

NATIONAL INSTITUTE FOR FUSION SCIENCE

Collection of Contributions from NIFS  
to 20th IAEA Fusion Energy Conference  
(Vilamoura, Portugal, 1-6 Nov. 2004)

NIFS-808

Jan. 2005

RESEARCH REPORT  
NIFS Series

Inquiries about copyright should be addressed to the Research Information Center,  
National Institute for Fusion Science, Oroshi-cho, Toki-shi, Gifu-ken 509-5292 Japan.  
E-mail: [bunken@nifs.ac.jp](mailto:bunken@nifs.ac.jp)

**<Notice about photocopying>**

In order to photocopy any work from this publication, you or your organization must obtain permission from the following organization which has been delegated for copyright clearance by the copyright owner of this publication.

Except in the USA

Japan Academic Association for Copyright Clearance (JAACC)  
6-41 Akasaka 9-chome, Minato-ku, Tokyo 107-0052 Japan  
Phone: 81-3-3475-5618 FAX: 81-3-3475-5619 E-mail: [jaacc@mtd.biglobe.ne.jp](mailto:jaacc@mtd.biglobe.ne.jp)

In the USA

Copyright Clearance Center, Inc.  
222 Rosewood Drive, Danvers, MA 01923 USA  
Phone: 1-978-750-8400 FAX: 1-978-646-8600

## Confinement and MHD stability in the Large Helical Device

O.Motojima 1), K.Ida 1), K.Y.Watanabe 1), Y.Nagayama 1), A.Komori 1), T.Morisaki 1), B.J.Peterson 1), Y.Takeiri 1), K.Ohkubo 1), K.Tanaka 1), T.Shimozuma 1), S.Inagaki 1), T.Kobuchi 1), S.Sakakibara 1), J.Miyazawa 1), H.Yamada 1), N.Ohyabu 1), K.Narihara 1), K.Nishimura 1), M.Yoshinuma 1), S.Morita 1), T.Akiyama 1), N.Ashikawa 1), C.D.Beidler 2), M.Emoto 1), T.Fujita 3), T.Fukuda 4), H.Funaba 1), P.Goncharov 5), M.Goto 1), T.Ido 1), K.Ikeda 1), A.Isayama 3), M.Isobe 1), H.Igami 1), K.Ishii 6), K.Itoh 1), O.Kaneko 1), K.Kawahata 1), H.Kawazome 7), S.Kubo 1), R.Kumazawa 1), S.Masuzaki 1), K.Matsuoka 1), T.Minami 1), S.Murakami 8), S.Muto 1), T.Mutoh 1), Y.Nakamura 1), H.Nakanishi 1), Y.Narushima 1), M.Nishiura 1), A.Nishizawa 1), N.Noda 1), T.Notake 9), H.Nozato 4), S.Ohdachi 1), Y.Oka 1), S.Okajima 10), M.Osakabe 1), T.Ozaki 1), A.Sagara 1), T.Saida 11), K.Saito 1), M.Sakamoto 12), R.Sakamoto 1), Y.Sakamoto 3), M.Sasao 11), K.Sato 1), M.Sato 1), T.Seki 1), M.Shoji 1), S.Sudo 1), N.Takeuchi 9), H.Takenaga 3), N.Tamura 1), K.Toi 1), T.Tokuzawa 1), Y.Torii 13), K.Tsumori 1), T.Uda 1), A.Wakasa 14), T.Watari 1), I.Yamada 1), S.Yamamoto 13), K.Yamazaki 1), M.Yokoyama 1), Y.Yoshimura 1)

1) National Institute for Fusion Science, 322-6 Oroshi-cho, Toki-shi, 509-5292, Japan

2) Max-Planck Institut fuer Plasmaphysik, Greifswald D-17491, Germany

3) Japan Atomic Energy Research Institute, Naka, 311-0193, Japan

4) Graduate School of Engineering, Osaka University, Suita, Osaka 565-0871,

5) Department of Fusion Science, School of Mathematical and Physical Science, Graduate University for Advanced Studies, Hayama, 240-0193, Japan

6) Plasma Research Center, University of Tsukuba, Tsukuba, 305-8577, Japan

7) Graduate School of Energy Science, Kyoto University, Uji 611-0011, Japan

8) Department of Nuclear Engineering, Kyoto University, Kyoto 606-8501, Japan

9) Department of Energy Engineering and Science, Nagoya University, 464-8603, Japan

10) Chubu University, Kasugai, Aichi, 487-8501, Japan

11) Graduate School of Engineering, Tohoku University, Sendai, 980-8579, Japan

12) Research Institute for Applied Mechanics, Kyushu University, Kasuga, 816-8580, Japan

13) Institute of Advanced Energy, Kyoto University, Uji, 611-0011, Japan

14) Graduate School of Engineering, Hokkaido University, Sapporo 060-8628, Japan

e-mail contact of main author: [motojima@LHD.nifs.ac.jp](mailto:motojima@LHD.nifs.ac.jp)

## **Abstract.**

The Large Helical Device (LHD) is a heliotron device with  $l = 2$  and  $m = 10$  continuous helical coils with a major radius of 3.5 – 3.9 m, a minor radius of 0.6 m, and a toroidal field of 0.5 – 3 T, which is a candidate among toroidal magnetic confinement systems for a steady state thermonuclear fusion reactor. There has been significant progress in extending the plasma operational regime in various plasma parameters by neutral beam injection (NBI) with a power of 13MW and electron cyclotron heating (ECH) with a power of 2MW. The electron and ion temperature have reached up to 10 keV in the collisionless regime and the maximum electron density, the volume averaged beta value and stored energy are  $2.4 \times 10^{20} \text{ m}^{-3}$ , 4.1% and 1.3 MJ, respectively. In the last two years, intensive study of the MHD stability providing access to the high beta regime and of healing of the magnetic island in comparison with the neoclassical tearing mode in tokamaks has been conducted. Local Island Divertor (LID) experiments also have been done to control the edge plasma aimed at confinement improvement. As for transport study, the transient transport analysis was executed for the plasma with an internal transport barrier (ITB) and a magnetic island. The high ion temperature plasma was obtained by adding impurities to the plasma to keep the power deposition to the ions reasonably high even at very low density. By injecting 72kW of ECH power, the plasma was sustained for 756 second without serious problems of impurities or recycling.

## 1. Introduction

A heliotron type device is a probable candidate among toroidal magnetic confinement systems as a thermonuclear fusion reactor under steady-state operation because it can confine plasma with only external coils and utilizing a well-defined divertor configuration. Compatibility between magnetohydrodynamics (MHD) stability and good confinement is one of the crucial issue in the Heliotron device, because there exists a trade off between the magnetic well and small drift of helically trapped particles from the magnetic flux surface [1]. When the plasma is shifted outward, the high  $\beta$  plasma will not be achieved because of the reduced confinement and the limited heating power, not because of the MHD instability. Ideal MHD instabilities universally have the potential for strongly limiting the operational regime of the plasma parameters in high  $\beta$  regime. In tokamaks, it is well known that the operational  $\beta$  limits are quite consistent with the theoretical predictions of ideal linear MHD theory [2,3]. On the contrary, in helical plasmas, a limited number of experimental research into the effects of pressure driven ideal MHD instabilities on the operational beta range has been reported, for examples, on Heliotron DR [4], the compact helical system (CHS) [5] and the Large Helical Device[6].

Large Helical Device (LHD) is a superconducting heliotron device (poloidal period number  $L = 2$ , and toroidal period number  $M = 10$ ) with a major radius of  $R_{ax} = 3.5 - 4.1$  m, an average minor radius of 0.6 m, magnetic field up to 3T, and heating neutral beam with negative ions with a beam energy of 150 – 180 keV[7,8] with a radius of tangency,  $R_{T\_NBI}$  of 3.65m - 3.7m. The high  $\beta$  experiment is done in the inward shifted configuration, where the confinement is good (and the  $\beta$  limit is low) enough to study the  $\beta$  limit in a heliotron device. Because the plasma pressure is still marginal for the  $\beta$  limit even in the inward shifted configuration, the improvement of confinement is required. The extended operation regimes, the development of control techniques and understanding of transport, especially in the plasma with an internal transport barrier[9-12] are discussed in this paper.

## 2.MHD study

### 2.1. High beta experiment

The operational highest beta value has been expanded from 3.2% to 4% in the last two years by increasing the heating capability and exploring a new magnetic configuration with a higher aspect ratio by changing the pitch parameter of the helical coil,  $\gamma(=n/2 \cdot a/R)$ , from 1.254 to 1.22[13]. This new configuration with higher aspect ratio is characterized by a smaller volume and smaller Shafranov shift than the standard configuration as seen in Fig1. Although

the MHD stability properties are expected to be even worse according to ideal MHD theory in this configuration ( $\gamma = 1.22$ ) than in the so-called standard configuration ( $\gamma = 1.254$ ), the smaller shift is considered to contribute to the central deposition of the neutral beam and hence the reduction of the direct loss of the beam by keeping the magnetic axis close to the tangential radius of the neutral beam (indicated by the shaded region in Fig.1) at higher beta.

Figure 2(a) shows typical MHD activities in a typical high-beta discharge with a magnetic axis of 3.6 m and a magnetic field of 0.45 T, respectively. As the electron density is increased by the gas puff, the volume averaged  $\beta$  value estimated from the stored energy measured with a diamagnetic loop,  $\langle \mathbf{b}_{\text{dia}} \rangle$ , increases and reaches 4% at 1.12sec. Here the  $\langle \mathbf{b}_{\text{dia}} \rangle$  is the diamagnetic beta value defined as  $4\mu_0/3 \cdot W_{\text{dia}} / (B_{\text{av0}}^2 V_{\text{p0}})$ , where  $W_{\text{dia}}$  is the diamagnetic energy. The  $B_{\text{av0}}$  and  $V_{\text{p0}}$  are the averaged toroidal magnetic field inside the plasma boundary and plasma volume, respectively, and both of them are estimated under vacuum condition. The  $\beta$  value estimated from the kinetic stored energy based on the measured electron temperature and density profiles is 3.3% assuming  $Z_{\text{eff}} = 1$ , while the  $\beta$  value due to beam pressure evaluated with the FIT[14] code is 1.5%. Here, it should be noticed that the  $\beta$  values estimated with kinetic measurements and with beam pressure calculation have relatively large uncertainties due to the lack of precise measurements of ion density and temperature profiles and due to the difficulty in evaluating the accurate orbit loss of high energy ions in the low magnetic field of 0.45T. The  $m/n = 1/1$  and  $2/3$  modes of the magnetic fluctuations excited in the edge region are dominantly observed in this discharge. Here  $m$  and  $n$  are the poloidal and toroidal mode-numbers of the magnetic fluctuations, respectively. The  $m/n = 1/1$  and  $2/3$  modes grow from 0.5s and their amplitudes increase with  $\langle \beta_{\text{dia}} \rangle$ . However, when  $\langle \beta_{\text{dia}} \rangle$  exceeds a certain value at 1.14 s, the  $m/n = 1/1$  mode is frequently interrupted.

The equilibrium reconstruction and stability analysis are done for this discharge by the 3-D MHD equilibrium code VMEC[15]. Figure 2(b) shows the experimentally observed beta gradients at  $\rho = 0.9$  in the  $R_{\text{ax}} = 3.6\text{m}$  and  $\gamma = 1.22$  configuration, where the rotational transform is estimated to be unity, as a function of  $\langle \beta_{\text{dia}} \rangle$ . The data were obtained in 0.45T to 1.75T operation. Here the  $\beta$  gradients are evaluated with kinetic pressure measurements and volume averaged  $\beta$  is given by diamagnetic loop measurements. The solid line in Fig.2(b) denote a contour of the low- $n$  ( $m/n = 1/1$ ) ideal MHD modes (with global mode structure) with  $\gamma_{\text{low-n}}/\omega_A = 0.5 \times 10^{-2}$  and  $1.0 \times 10^{-2}$  for currentless equilibria. The growth rate is calculated by a MHD stability analysis code (TERPSICHORE [16]). Here  $\omega_A = v_{A0}/R_0$ ,  $v_{A0}$  and  $R_0$  are the Alfvén velocity and the major radius at the magnetic axis. The dotted line is the stability boundary of Mercier modes (with a highly localized mode structure / high- $m$  limit) [17]. The change of the gradients is observed around  $\langle \beta_{\text{dia}} \rangle = 1.5\%$ , which corresponds to Mercier unstable region. However, the observed beta gradients at  $\rho=0.9$  increase with increasing beta up to  $\langle \beta_{\text{dia}} \rangle = 4\%$ . Here, the electron temperature profiles measured with a multi-channel

YAG Thomson scattering often show a local flattening at the rational surface, which is not included in the analysis using VMEC discussed above[18].

An important subject of investigation is the effect of  $\beta$  on confinement. Figure 3 shows the improvement factor ( $H_{ISS}$ ) of the global energy confinement time evaluated with the diamagnetic flux measurements on the ISS95 (International Stellarator Scaling 1995) empirical scaling[19] as a function of  $\langle \beta_{dia} \rangle$ . A serious degradation of a global energy confinement time has not been observed up to  $\langle \beta_{dia} \rangle \sim 4\%$ , and the enhancement factor is gradually reduced in  $\langle \beta_{dia} \rangle > 2\%$ . This gradual decrease of the enhancement factor is thought mainly to be due to the increase of the electron density (and plasma collisionality) to achieve a high  $\beta$  plasma, not due to MHD stability, since the gradual decrease of the enhancement factor is also observed in the plasma with low  $\beta$  values less than 1.5%). This is due to the weaker density dependence of the energy confinement time (weaker temperature dependence on thermal diffusivity) at higher plasma collisionality[20], while the density dependence of the energy confinement time of  $n_e^{0.5}$  (Gyro-Bohm type scaling) is assumed to be unchanged over a wide range of the collisionality in the ISS95.

## 2.2. Healing of Magnetic island

The suppression of the growth of the magnetic island at a rational surface in the high  $\beta$  regime is the other important issue of MHD, which has been considered to be a serious problem in tokamak plasmas known as the neoclassical tearing mode. In LHD, where the magnetic shear is negative, the magnetic island is healed rather than growing in contrast to the neoclassical tearing mode. The experiment in the plasma with an  $n/m = 1/1$  perturbation field clearly shows that this healing effect becomes more effective as the conductivity or the beta is increased[21,22]. The bootstrap current and Pfirsch-Schluter current are considered as candidates to cause healing of the magnetic island[23], however, the magnitude of these currents in the plasma with a magnetic island is too small to be sufficient for healing the magnetic island. Therefore the characteristic of magnetic island healing is considered to be one of the advantages of a heliotron configuration, because it gives more tolerance for the error magnetic field, which is difficult to be eliminated completely.

Figure 4(a) shows time evolution of the  $T_e$  profile at  $\phi=136^\circ$  after the hydrogen pellet injection in the case of  $R_{ax}=3.6$  m. This is a typical evidence of ‘healing’ events. The island appears after the pellet injection, but the island width ( $w$ ) is reduced as the temperature increases. Finally, the  $T_e$  profile returns to that before the pellet injection, and the island disappears. The island width in the plasma depends on the plasma parameters. In this experiment, it is observed that the magnetic island width decreases as  $T_e$  or beta increases. Figure 4(b) shows that the island width in vacuum is increased as the  $n=1$  coil current ( $I_N$ )

increases, but the island in the plasma suddenly appears when it surpasses the threshold of the current[21,24]. This is another aspect of ‘healing’. Here, the coil current is normalized to  $B_{ax}$ . The threshold level ( $I_N^*$ ) is increased as the beta increases, as shown in Fig.4(c).

### 3. Extended operation regime in LHD

#### 3.1 Edge control by Local island divertor

A local island divertor (LID) has been installed in the LHD plasma to increase edge pressure gradients to achieve better energy confinement time. As discussed in 2.2, LHD plasma shows a weaker density dependence of the global energy confinement time than the ISS95 scaling at higher density. This saturation at the higher density should be due to the lower collisionality near the plasma edge, because a stronger gas puff applied to achieve the high density causes a flat density profile. Therefore it is considered to be important to reduce the edge density keeping the lower collisionality and improve energy transport at the edge to achieve a good energy confinement time. The LID is a kind of pumped limiter inserted inside the  $n/m=1/1$  magnetic island produced at the plasma edge. Since LID head is inserted to the middle of the O-point of the magnetic island, the core plasma does not touch the limiter and the outward heat and particle fluxes do not directly go to the front of the limiter but flows to the backside of the LID limiter along the field lines across the separatrix [25,26].

In the present experiment with LID as is mentioned above, a factor of  $\sim 1.2$  improvement of the energy confinement time has been observed over the ISS95 at higher electron density (larger energy confinement time) regime as seen in Fig5(a). This amount of reduced enhancement of energy confinement time is thought to be due to the increase of the edge temperature gradient as seen in Fig5(b). Although the minor radius of the plasma is reduced by inserting the LID head into the magnetic island produced by an  $n/m = 1/1$  external perturbation field, the core electron temperature does not drop because of the larger electron temperature. At the moment, the experiments are restricted to the relative low density (due to technical reason related to the plasma operation), where the absolute value of the energy confinement is low, because the pumping exceeds the capability of efficient central fuelling. In order to achieve the improvement at higher density, more efficient central particle fuelling such as due to beam fuelling or a pellet with a higher speed is required. Another characteristic of the plasma with LID configuration is low radiation level. A significant impurity shielding is observed in the plasma with the LID configuration in the Ne puff experiments. In this discharges, there is a large positive radial electric field observed at the X-point of the magnetic island in the LID configuration[Fig5(c)]. This positive radial electric field contributes to the exhaust of impurities and prevents the radiation collapse, while the negative electric field and its shear contribute to the improvement of heat transport.

### 3.2 Control of radial electric field by shift of magnetic axis

A change in the magnitude and radial profiles of the helical ripples will be the most straightforward tool to control the radial electric field. The reason is that the radial electric field in LHD is determined by the ambipolar condition of ion flux and electron flux that are trapped in helical ripples[27]. In LHD, the radial profiles of the helical ripples can be controlled by the shift of the magnetic axis from 3.9m to 3.5m.[28] . Figure 6 shows the radial profiles of the radial electric field for the ion root (large neoclassical flux with negative  $E_r$  in the high collisionality regime), electron root (small neoclassical flux with positive  $E_r$  in the low collisionality regime) and the transition regime (between ion root and electron root) for various configurations with different helical ripple profiles. When the helical ripple increases gradually towards the plasma edge ( $R_{ax}=3.9m$ ), the electron root region extends to half of the plasma minor radius and the radial electric field shear produced is relatively weak. However, when the helical ripple increases sharply at the plasma edge ( $R_{ax}=3.5m$ ), the electron root region is localized at the plasma edge and strong radial electric field shear is produced. These results show that a strong magnetic field shear can be obtained at the plasma edge by shifting the magnetic axis inward rather than shifting the magnetic axis outward, where the electron root condition becomes achievable even at higher collisionality.

The electron density at the transition from ion root to electron root is  $0.7 \times 10^{19} m^{-3}$  for the plasma with the magnetic axis of 3.5m, while it is  $1.3 \times 10^{19} m^{-3}$  for the plasma with the magnetic axis of 3.9m. The higher critical electron density for the plasma with magnetic axis of 3.9m can be explained by the larger magnitude of helical ripples and these characteristics are consistent with the prediction by neoclassical theory[29,30].

### 3.3 Density limit and radiation collapse

It is important to study the mechanism of radiation collapse to extend the density limit, since the plasma is terminated by the radiation collapse at the density limit. The radial electric field is expected to be negative in the high density limit. In the latest experimental campaign in LHD, line-averaged densities of up to  $1.6 \times 10^{20} m^{-3}$  have been sustained for more than 0.7 s by 11 MW neutral beam injection using gas puff fuelling. In addition, using multiple hydrogen pellet injection, the density has been increased to  $2.4 \times 10^{20} m^{-3}$  transiently. Data from the most recent campaign also shows a limit which exceeds the Sudo limit [31] by a factor of approximately 1.4 as is seen in Fig.7(a). At the radiation collapse the thermal instability occurs, where the total radiation sharply increases because of the increase of cooling rate of impurities associated with the low edge temperature below 0.15keV at  $r = 0.9$

regardless of the input power and plasma density[20].When the thermal instability starts, the total radiation power  $P_{\text{rad}}$  is proportional to  $\bar{n}_e^3$ , while it usually is proportional to  $\bar{n}_e$  as demonstrated in Fig.7(b). The spontaneous increase of density and radiation power (which is proportional to  $\bar{n}_e$ ) precedes the thermal instability, especially in the plasma with higher impurity concentration. In order to study this spontaneous density increase before the radiation collapse, a short Ne puff was applied to the early phase of the discharges[28]. When the short Ne puff is applied to the early phase of the discharge with the pulse width of  $t = 0.5 - 0.68\text{s}$ , there is no spontaneous density increase and no radiation collapse as seen in Fig.8. In contrast, by slightly increasing the pulse width of Ne puff ( $t=0.5-0.7\text{s}$ ), a clear spontaneous increase of radiation power and density is observed, although the Ne puff is already turned off.

The radial electric field at  $\rho = 0.9$  starts to be more negative 0.5 sec before the radiation collapse, where the radiation loss due to NeVI and NeVII is maximum. The radial electric field becomes more and more negative until the radiation collapse. The change of radial electric field to more negative is due to the increase of collisionality (increase of electron density and decrease of temperature). When the radial electric field becomes more negative, the negative radial electric field causes the increase of impurity influx, because the exhausting effect by positive radial electric field disappears. In the discharge without radiation collapse, the radial electric field remains positive with no increase of electron density and radiation power. The ion temperature shows a significant drop to 0.15 keV and the thermal instability causing the radiation collapse starts. The role of positive electric field in preventing the spontaneous increase of the electron density and impurity radiation demonstrated in this experiment is also important in the LID configuration, because strong positive radial electric field is produced at the plasma edge as described in 3.1.

### **3.4 Achievement of high ion temperature with NBI**

At present, LHD has three tangential neutral beams lines with negative-ion-sources, of which are designed to have a high energy of around 180keV. They are effective tools for the experiment, but primarily contribute to the electron heating rather than the ion heating. To increase the ion temperature up to 10keV and to investigate the property of high ion temperature plasma, the experiments using the high-Z plasmas have been done with Ar- and/or Ne-gas fuelling to increase beam absorption and energy deposition to ions in low-density plasmas. Intensive Ne- and/or Ar glow discharge cleaning was applied to reduce the wall-absorbed hydrogen and increase the concentration of Ne and/or Ar ions. As a result, the ion temperature increases with an increase in the ion heating power normalized by the ion density, and the highest ion temperature obtained in LHD has increased from 5 keV to 10 keV in the last two years[32,33]. However, plasma with large concentration of high-Z impurity is

not be relevant for the future research aimed at nuclear fusion because of the large dilution of the fuelling. Therefore this is intended as a preparatory experiment to study the property of high ion temperature plasma up to 10keV and to demonstrate the high capability of LHD as a magnetic confinement device, before the installation of a neutral beam with the energy of 40 keV for the purpose of ion heating, which is planned to be installed in LHD in the near future.

The ion temperature increases with increasing normalized ion heating power in the plasma with Ar- and Ne-puff as seen in Fig.9(a). No distinct saturation has been observed. Figure 9(b) shows the time evolutions of ion and electron temperatures in the plasma with Ar-puff at  $t=0.5$ s. After an increase in the electron density due to the Ar gas-puff, the central ion temperature, measured with the Doppler broadening of an X-ray line of ArXVII, rapidly increases as the density decreases with the addition of NBI power, and stays at high values. The ion temperature reaches 10 keV at around  $t=1.65$ s with an injection power of 12.2 MW, around 30 % of which is absorbed at an electron density of  $0.37 \times 10^{19} \text{m}^{-3}$ . The electron temperature is also increased up to 4.3 keV, and, however, is much lower than the ion temperature. The observed beam slowing-down time after the NBI-off is as long as 1.2 s probably due to both the low electron density and the high electron temperature, and the ion and electron temperatures show an extremely slow decay after the beam turn-off.

### **3.5 Long pulse operation with ECH**

In the LHD, steady-state plasma heating by electron cyclotron (EC) wave with 72kW and ICRF with 500kW was achieved during 756 and 150 sec, respectively. A EC heated plasma with time-averaged radiation temperature of 240eV and density of less than  $1 \times 10^{18} \text{m}^{-3}$  was obtained. As for an ICRF heated plasma, plasma with electron and ion temperature of 2 keV and density of  $6 \times 10^{18} \text{m}^{-3}$  were sustained until the discharge was terminated by increase in radiation loss.

## **4 Transport study**

### **4.1 Property of particle transport**

Hollow density profiles are often observed in LHD, which is in contrast to the peaked density profiles observed in tokamak plasmas. A hollow profile even in the steady state suggests the existence of outward convective velocity in the core region, because the density profiles should be flat in the steady state in the plasma, where most of the particle source is localized at the plasma edge. In order to study the parameter dependence of diffusion and convective velocity in the plasma, a modulated gas puff is applied to the plasma [34].

The diffusion coefficient increases as the temperature is increased as seen in Fig10(a). The temperature dependence of the diffusion coefficient is  $T_e^{1.7+0.9}$  and  $T_e^{1.1+0.14}$  in the core ( $\rho < 0.7$ ) and the edge ( $\rho > 0.7$ ), respectively, both values are close to that expected by gyro-Bohm scaling of  $T_e^{1.5}$ . The dependence of edge diffusion on magnetic field is measured to be  $B^{-2}$ , which is also consistent with the prediction of gyro-Bohm scaling. These characteristics are supported by the fluctuation measurements using CO<sub>2</sub> laser scattering. Figure 10(b) shows that the convective velocity in the core becomes more positive, while the convective velocity in the edge becomes more negative as the temperature gradient is increased, which results in the density profile becoming more hollow associated with the increase of the temperature gradients at higher heating power.

## 4.2 Electron transport

An electron internal transport barrier (ITB) is characterized with the peaked electron temperature profile associated with the transition from ion root to electron root observed in the NBI sustained plasmas with centrally focused ECH [9-12]. The characteristics of the formation of the ITB depend on the direction of the neutral beam[35]. Figure 11(a) shows the increment of the electron temperature,  $\Delta T_e$ , at the plasma center by ECH power as a function of ECH power normalized by the electron density. The threshold power for the transition to the ITB plasma is clearly observed in the plasma with counter(CNTR) NBI in the direction that the beam driven current increases the rotational transform in the plasma. This is in contrast to that the central  $T_e$  increases almost linearly with the ECH power and no clear threshold power for the transition to ITB plasma is observed in the plasma with co(CO) NBI in the direction of decreasing rotational transform by beam driven current. The differences in the characteristics are due to the differences in rotational transform  $i$  and not due to the differences in the deposition profile. In the plasma with CNTR NBI, the rational surface of  $i/2\pi=1/2$  is located at half of the plasma minor radius, while the plasma with CO NBI has no  $i/2\pi=1/2$  rational surface because of the increase of central rotational transform above 0.5. As the magnetic axis shifts outward, the rational surface of  $i/2\pi=1/2$  moves toward the plasma edge and always exists in the plasma, regardless of the direction of the NBI, the difference in characteristics of the ITB between CO NBI and CNTR NBI becomes small.

The time lag that gives the maximum correlation at each position is plotted in Fig. 11(b)(c), together with power deposition profile of the modulated electron cyclotron heating (MECH) calculated by a ray tracing code. The incremental electron heat diffusivity,  $c_e$ , is evaluated from the slope of the time lag. The heat diffusivity normalized by the gyro-Bohm scaling  $T_e^{3/2} / B^2$  reduced from 8.0 to 3.8  $m^2 \cdot s^{-1} \cdot keV^{3/2} \cdot T^2$  with the increase of ECH power, which indicates an improvement of confinement. The flattening of the time lag observed at

$r = 0.4 - 0.55$  in Fig. 11 (c) is due to the appearance of a magnetic island at the rational surface of  $i/2\pi=1/2$ .

Another approach to estimate the incremental electron thermal diffusivity is cold pulse propagation induced by a tracer encapsulated solid pellet (TESPEL) [36] ablated near the plasma edge. The thermal diffusivity can be derived with transient transport analysis using the perturbed heat transport equation[37,38]. Figure 12(a) shows the radial profiles of thermal diffusivity evaluated using cold pulse propagation,  $\chi_{cp}$  and thermal diffusivity evaluated with power balance,  $\chi_{pb}$ . The significant reduction of the electron thermal diffusivity inside the ITB ( $2 \text{ m}^2/\text{s}$  inside and  $10 \text{ m}^2/\text{s}$  outside ITB) is observed both in the  $\chi_{cp}$  and  $\chi_{pb}$ . The temperature dependence of the thermal diffusivity,  $\alpha$ , where the electron thermal diffusivity is proportional to the temperature to the power of  $T_e$  as  $T_e^\alpha$  is an important parameter in the study of the plasma with an ITB. In L-mode, the parameter  $\alpha$  is positive and typically it is 1.5, which is predicted from the gyro-reduced Bohm scaling and is also consistent with the scaling of energy confinement in LHD. If the parameter  $\alpha$  stays positive, the formation of an ITB would never occur, because spontaneous increase of electron temperature during the formation of an ITB requires a negative  $\alpha$ . The transient transport analysis with a cold pulse indicates the existence of  $d\chi_e/dT_e$  and  $\alpha$  can be derived from  $d\chi_e/dT_e$  as  $\alpha = (T_e/\chi_e)(d\chi_e/dT_e)$ . As shown in Fig.12(b), the temperature dependence parameter,  $\alpha$ , derived from the cold pulse propagation with transient transport analysis also shows the same trend. The temperature dependence is positive ( $\alpha = 0.5 - 1.0$ ) outside the ITB, while it becomes negative inside the ITB and decreases down to -3 towards the magnetic axis. The observation of negative  $\alpha$  is considered to be the most significant evidence of an electron ITB in the plasma. In LHD the thermal diffusivity  $\chi_e$  depends on temperature,  $T_e$ , rather than the temperature gradient,  $\nabla T_e$ , ( $|\alpha| > |\beta|$ ), which is in contrast to the fact that the  $\chi_e$  depends on  $\nabla T_e$  rather than  $T_e$  ( $|\alpha| < |\beta|$ ) in tokamaks.

## 5 Summary

In the inner shifted configuration where the  $\beta$  limit is expected to be low (1.5% in the Mercier limit), high beta plasma with  $\langle \beta_{dia} \rangle = 4\%$  is obtained in the high aspect ratio configuration where the pitch parameter of helical coil,  $\gamma$ , is 1.22. The  $\beta$  values achieved significantly exceeds the linear MHD stability criteria, the Mercier limit and reaches to the region where the low-n ( $m/n = 1/1$ ) ideal MHD modes are predicted to be unstable. The difference in magnetic field configuration between a heliotron plasma and a tokamak plasma is positive shear and magnetic well in a tokamak and negative shear and magnetic hill in a heliotron plasma. The characteristic of magnetic island healing, which is considered to be advantageous for a reactor, is due to the negative magnetic shear which is common in a heliotron configuration. This is in contrast to the tendency of magnetic islands to grow in

tokamaks, where the magnetic field shear is typically positive. The negative magnetic shear is considered to contribute to the formation of an electron internal transport barrier[39,40]. The electron internal transport barrier is observed in a tokamak, when the magnetic shear changes its sign from positive to negative. In a heliotron plasma, where the magnetic field shear is negative, the electron internal transport barrier is usually observed with ECH heating in the electron root.

LID is now showing high capability as a powerful tool for edge control to achieve an improved confinement regime. It is an important role of the LHD project as a three dimensional currentless steady state magnetic confinement device to supply a high quality database for the plasma physics and sciences necessary to realize controlled nuclear fusion, which should be focused on 1) steady state physic, 2) high  $\beta$  physic, and 3) confinement improvement and edge control[39].

### **Acknowledgements**

The comparison experiments investigating the mechanism of confinement improvement especially in the electron internal transport barrier has been performed under the collaboration between JT60U and LHD group. The author would like to thank the technical staff for their support of the LHD experiments.

### **References**

- [1] O.Kaneko et al., Phys. Plasma 9 (2002) 2020.
- [2] M. Wakatani, Y. Nakamura and K.Ichiguchi, Fusion Eng. Design 15 (1992) 395.
- [3] ITER Physics Basis, Nuclear Fusion 39 (1999) 2137.
- [4] N. Yanagi et al, Nucl. Fusion 32 (1989) 1264.
- [5] S. Okamura et al, Nucl. Fusion 30 (1999) 1337.
- [6] K.Y. Watanabe et al, Fusion Sci. Tech. 46 (2004) 24.
- [7] O.Motojima, et al., Nucl. Fusion 43 (2003) 1674.
- [8] O.Motojima et. al., Fusion Science and Technology Vol 46 (2004) 1
- [9] T.Shimozuma et al., Plasma Phys Control Fusion 45 (2003) 1183.
- [10] K.Ida, et. al., Phys Rev Lett 91 (2003) 085003.
- [11] Y.Takeiri et al., Phys. Plasma 10 (2003) 1788
- [12] K.Ida, et. al., Phys plasmas 11 (2004) 2551
- [13] K.Y. Watanabe et al, this conference.
- [14] S. Murakami, Nuclear Fusion 36 (1996) 359.
- [15] S.P.Hirshman, Phys. Fluids 26 (1983) 3553.
- [16] W. A. Cooper, Plasma Phys. Control. Fusion 34 (1992) 1011.
- [17] A. H. Grasser, J. M. Green and J. L. Johnson, Phys. Fluids 18 (1975) 143.

- [18] S.Sakakibara et.al, proc. 31st EPS Conference on Plasma Phys. London, 28 June - 2 July 2004  
ECA Vol.28B, O-4.01 (2004).
- [19] U. Stroth et al, Nuclear Fusion 36 (1996) 1063.
- [20] B.Peterson, et al., this conference
- [21] Y.Nagayama, et a., this conference.
- [22] N. Ohyabu, et al., *Phys. Rev. Lett.* 88, (2002) 55005.
- [23] K. Narihara, et al., *Phys. Rev. Lett.* 87, (2001) 135002.
- [24] K.Ida et al., *Phys. Rev. Lett.* 88, (2002) 015002.
- [25] A.Komori, T.Morisaki, et al., this conference.
- [26] T.Morisaki, et al., Fusion Eng. Design 65 (2003) 475.
- [27] K.Ida, et. al., Phys Rev Lett 86 (2001) 5297.
- [28] K.Ida, et. al., this conference
- [29] L.M.Kovrizhnykh L.M. Nucl. Fusion 24 (1984) 435
- [30] M.Yokoyama, et al., Nucl. Fusion 42 (2002) 143.
- [31] S.Sudo et al, Nucl. Fusion 30 (1990) 11.
- [32] Y.Takeiri, et al., this conference
- [33] S.Morita, et al., Nucl. Fusion 43 (2003) 899.
- [34] K.Tanaka, et al., this conference
- [35] T.Shimozuma et al., this conference
- [36] S.Sudo, N.Tamura, K.Khlopenkov,et al., Plasma Phys. Control. Fusion 44 (2002) 129.
- [37] S. Inagaki, et al., *Phys. Rev. Lett.* 92 (2004) 55002.
- [38] S. Inagaki, et al., Plasma Phys Control Fusion
- [39] K.Ida et al., Plasma Phys Control Fusion 46 (2004) A45
- [40] S. Inagaki, et al., this conference

## Figure captions

Fig.1 Shafranov shift as a function of beta value for the configurations of  $R_{ax}=3.6$  and  $\gamma=1.254$  and  $\gamma=1.22$ .

Fig.2 (a) Time evolution of averaged electron density and averaged  $\beta$  value and magnetic fluctuation of m/n mode and (b) kinetic beta gradients at  $\rho=0.9$  ( $t/2\pi = 1$ ) in  $\langle\beta\rangle$ - $d\beta/d\rho$  diagram.

Fig.3 The improvement factor of effective energy confinement as a function of (a) beta value for the plasma with  $R_{ax}=3.6m$ ,  $B=0.45-1.75T$  and  $\gamma = 1.22$ .

Fig.4 Time evolution of the  $T_e$  profile with the  $n=1$  external field. The hydrogen pellet is injected at  $t = 1.0sec$ . (b) Normalized coil current vs. island width ( $w$ ) in vacuum (open circles) and in plasma (closed circles). (c) beta vs. threshold of the normalize coil current.

Fig.5 (a) comparison of energy confinement time observed to the that predicted by the ISS95 scaling and (b) radial profiles of electron temperature for the plasma with helical divertor configuration (open circles) and LID configuration (closed circles) in LHD and (c) radial profiles of radial electric field with magnetic island (LID configuration) and without magnetic island (limiter configuration).

Fig.6 (a) Radial profiles of radial electric field for the plasma with a magnetic axis of (a) 3.5m (inward shift configuration) and (b) 3.9m (outward shift configuration) with  $\gamma = 1.254$ .

Fig.7. Comparison of achieved electron density to Sudo scaling and (b) total radiation power as a function of electron density.

Fig.8 Time evolution of (a) normalized total radiation power, (b) radial electric field, (c) ion temperature at  $\rho = 0.9$  for the discharges with and without radiation collapse for the plasma with magnetic axis of 3.6m.

Fig. 9 (a) Ion temperature as a function of the direct ion heating power normalized by the ion density in the plasma with Ar- and Ne-puff and (b) time evolution of electron and ion temperature in a low-density high-Z plasma.

Fig.10 (a) Electron temperature dependence of diffusion coefficient and (b) convective velocity as a function of the temperature gradient.

Fig.11 (a) Electron temperature increases at the center and peripheral are plotted as a function of density-normalized ECH power and time lag of ECE signals from MECH is plotted versus normalized minor radius for (b) CNTR NBI heated plasma and (c) Co NBI heated plasma. Electron heat diffusivities estimated from heat pulse propagation velocity are also indicated in the figures.

Fig.12 The radial profiles of the electron heat diffusivity where  $\beta = (\nabla T_e / \chi_e)(d\chi_e / d\nabla T_e)$ . and (b) the  $T_e$  dependence factor of  $\chi_e$ ,  $\alpha$ , estimated by cold pulse propagation. The heat diffusivity estimated by power balance is also plotted.

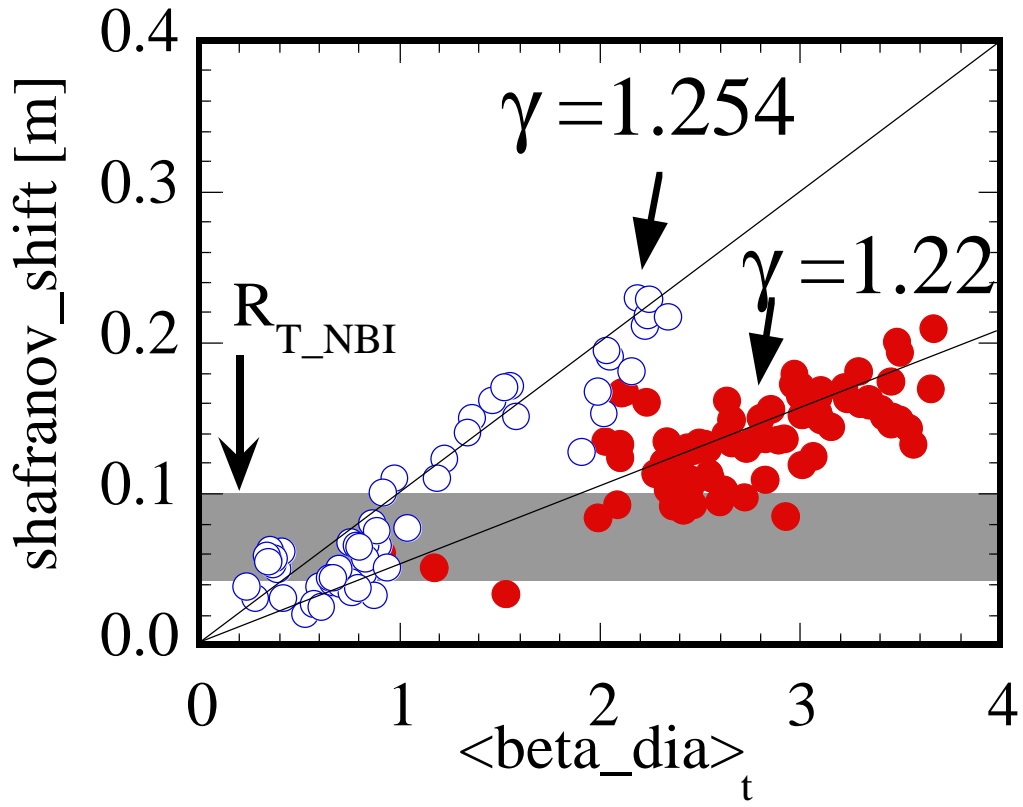


Fig.1.

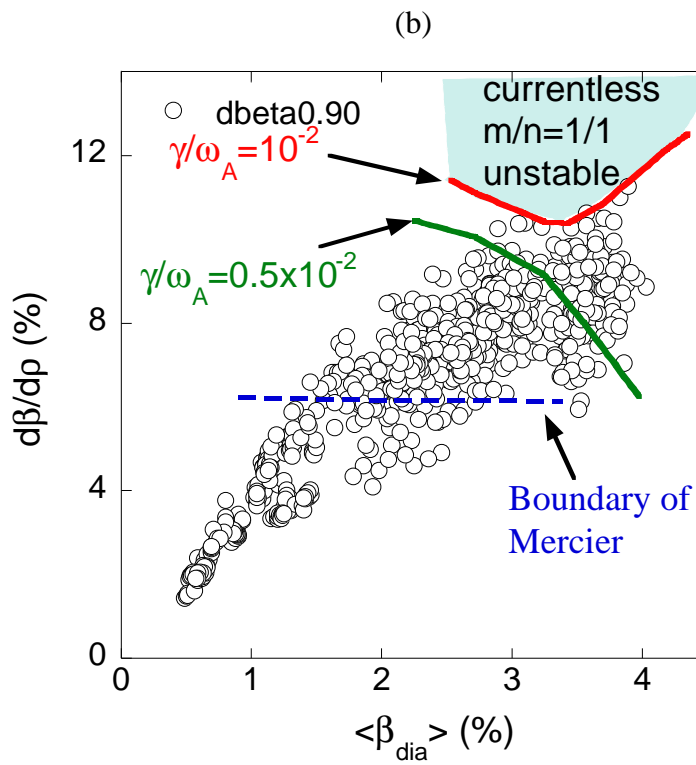
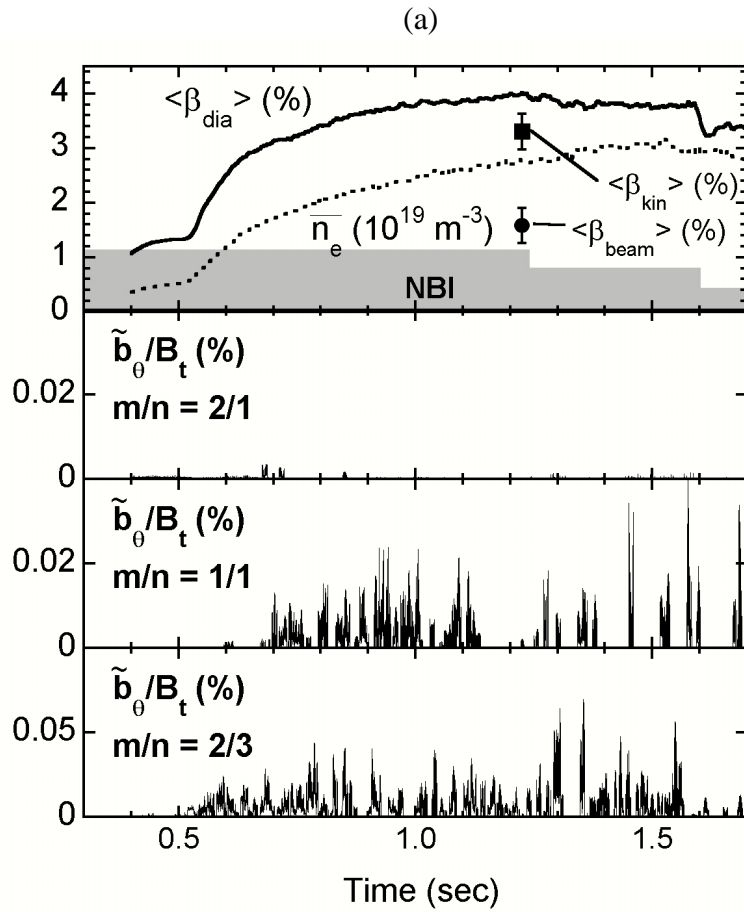


Fig.2 (a)

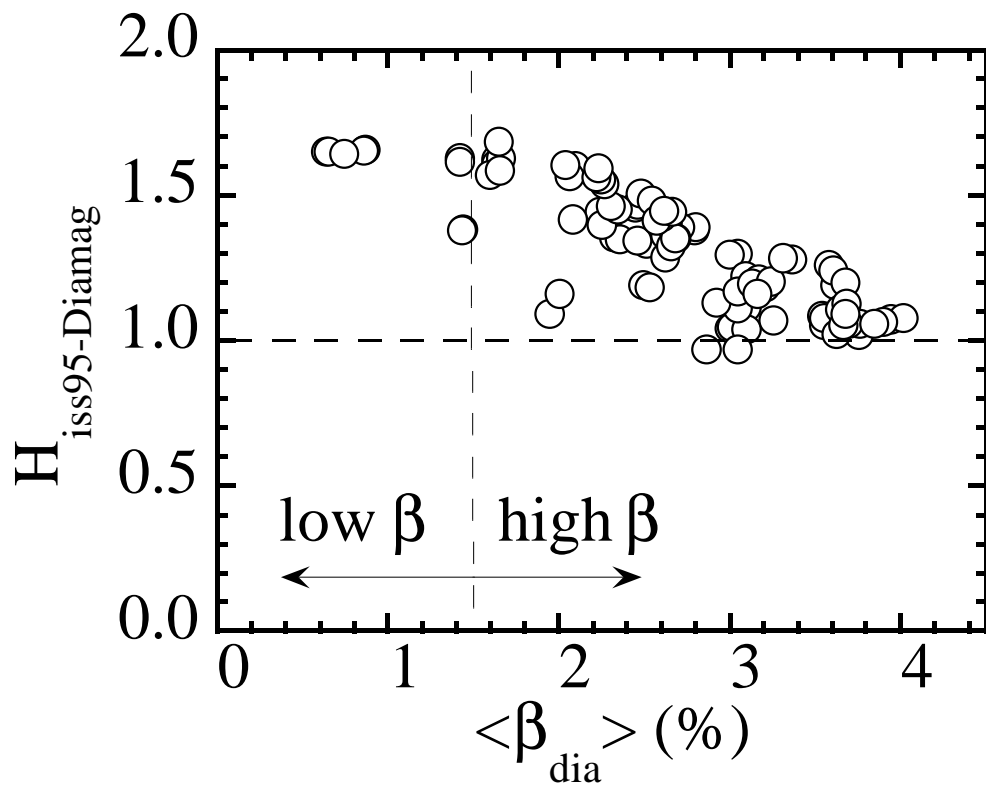


Fig.3

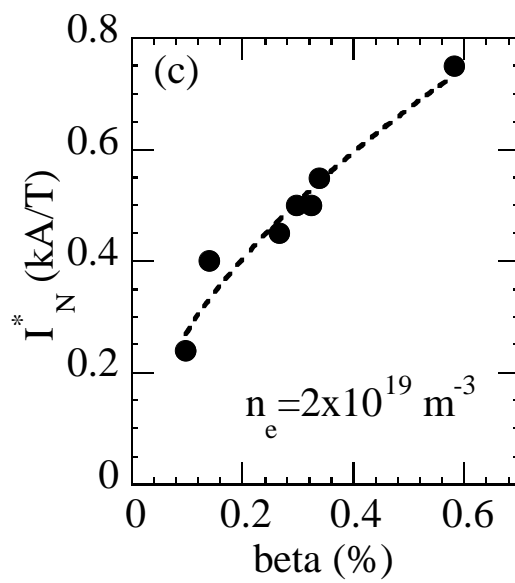
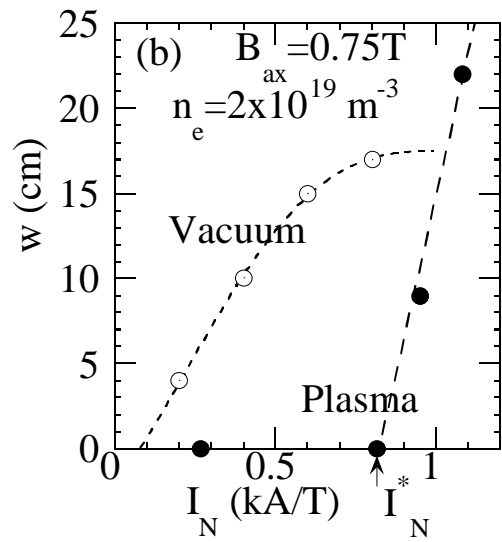
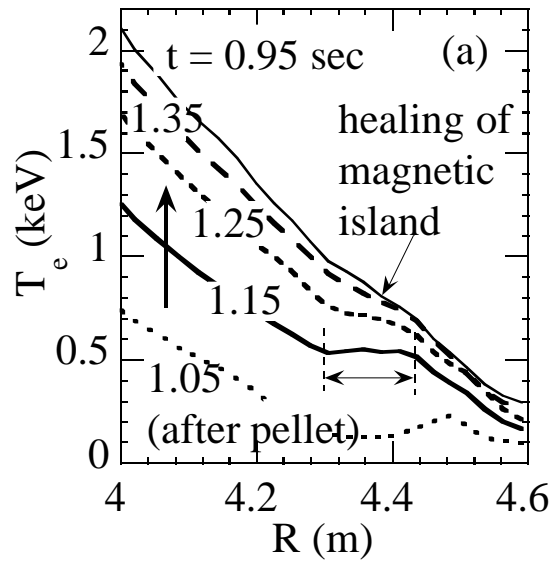


Fig.4

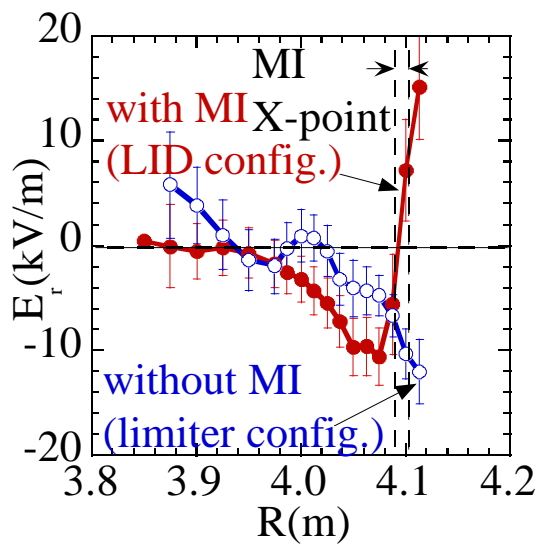
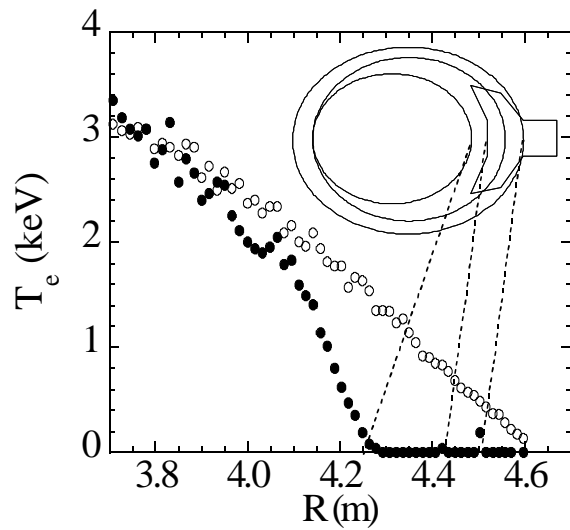
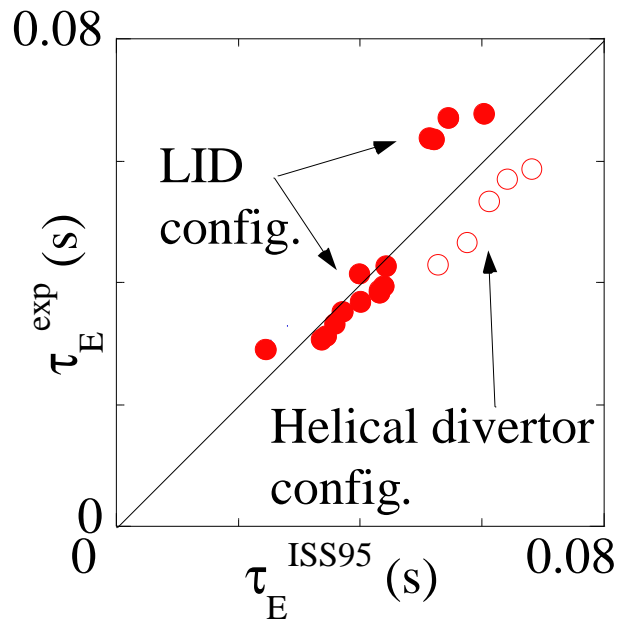


Fig.5

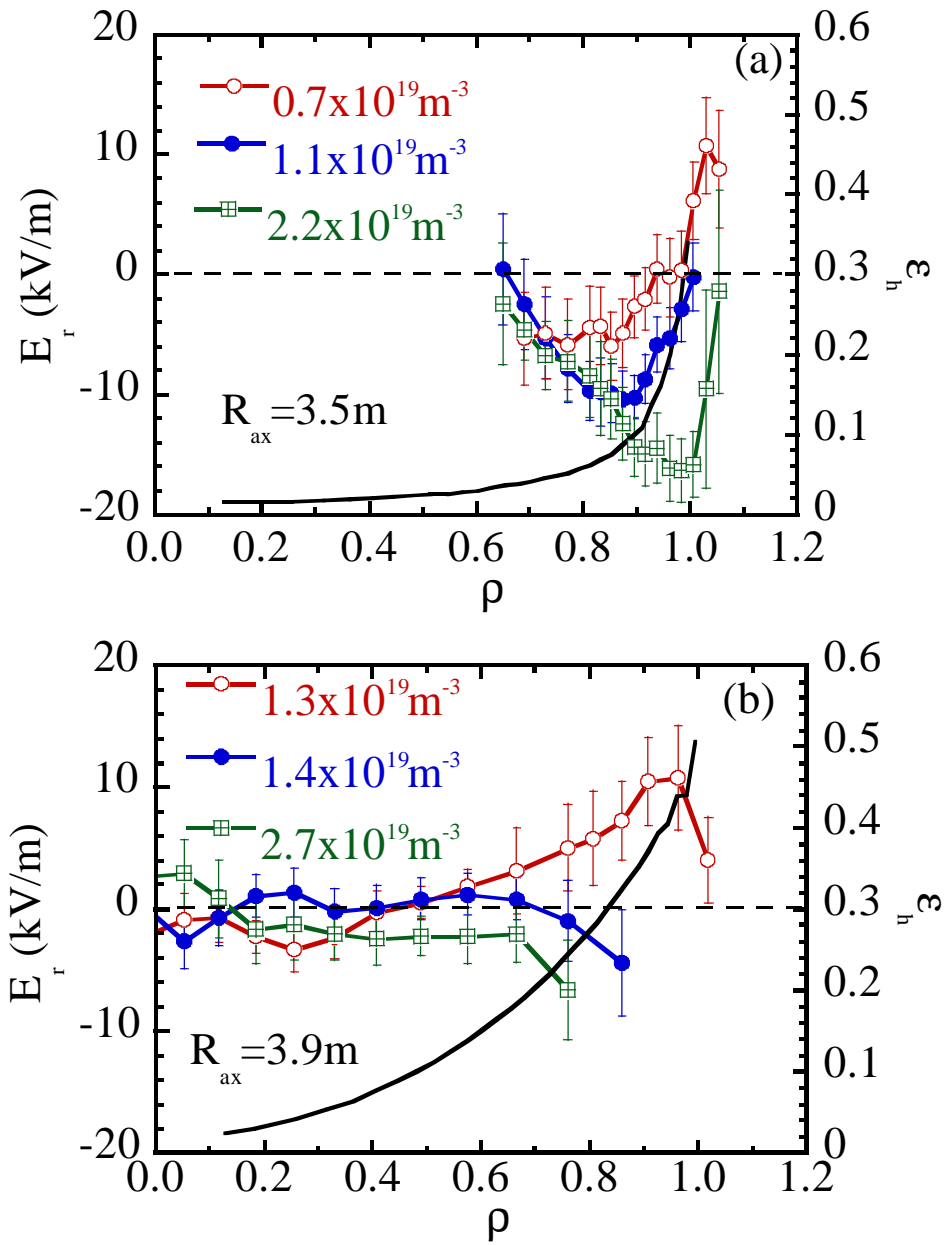


Fig.6

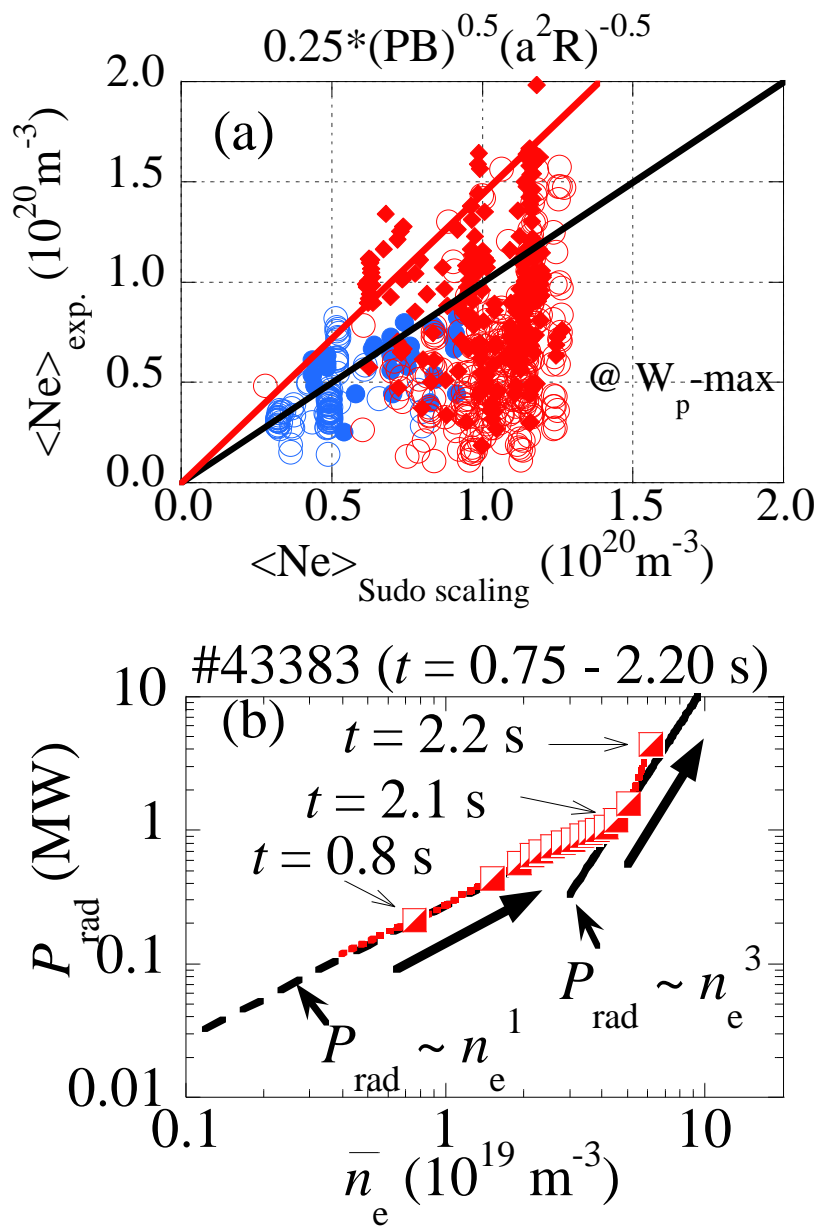


Fig.7.

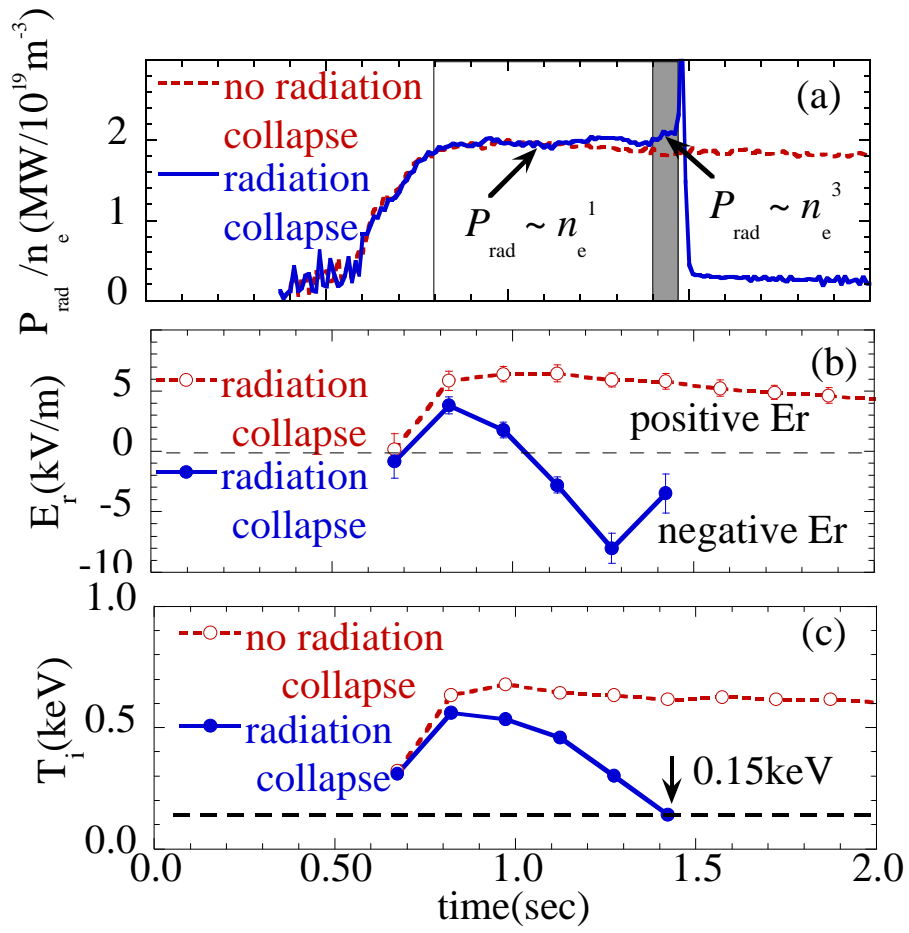


Fig.8

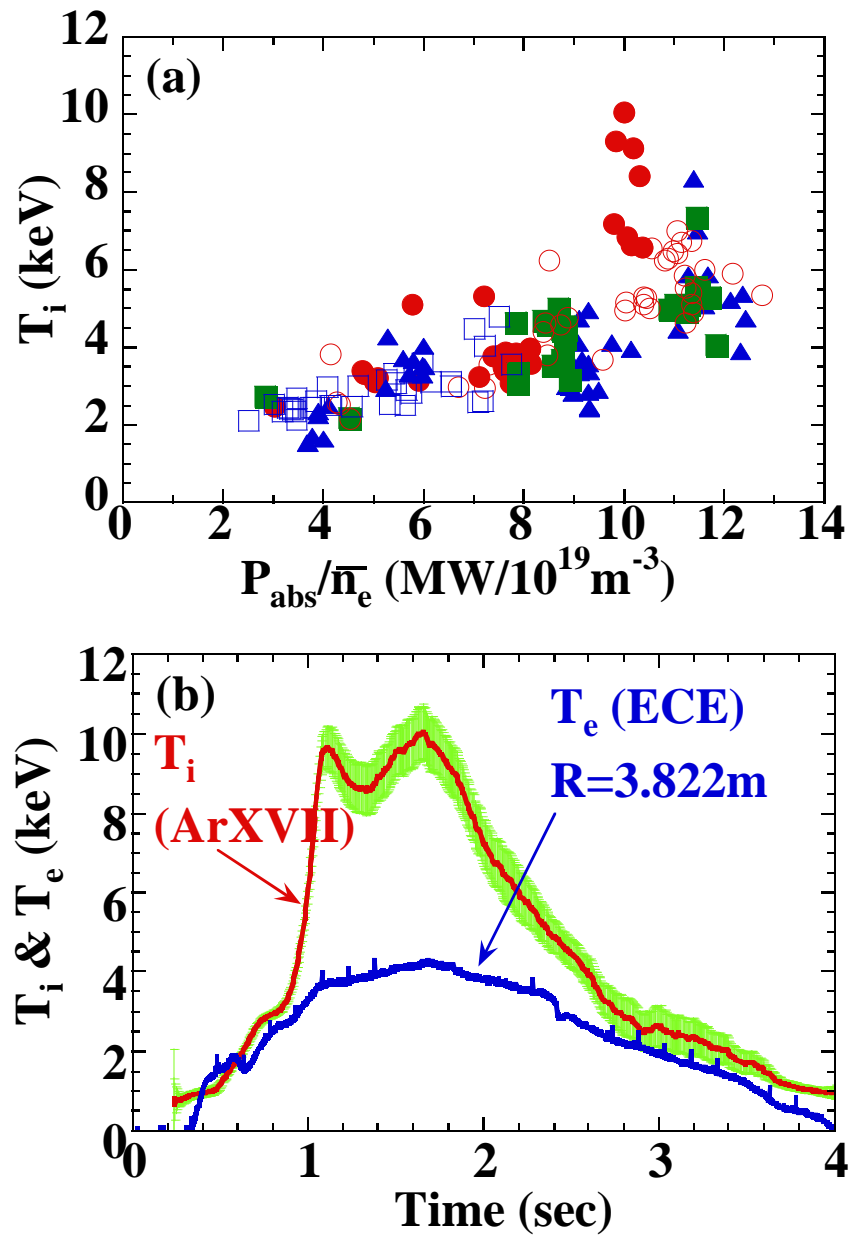


Fig. 9

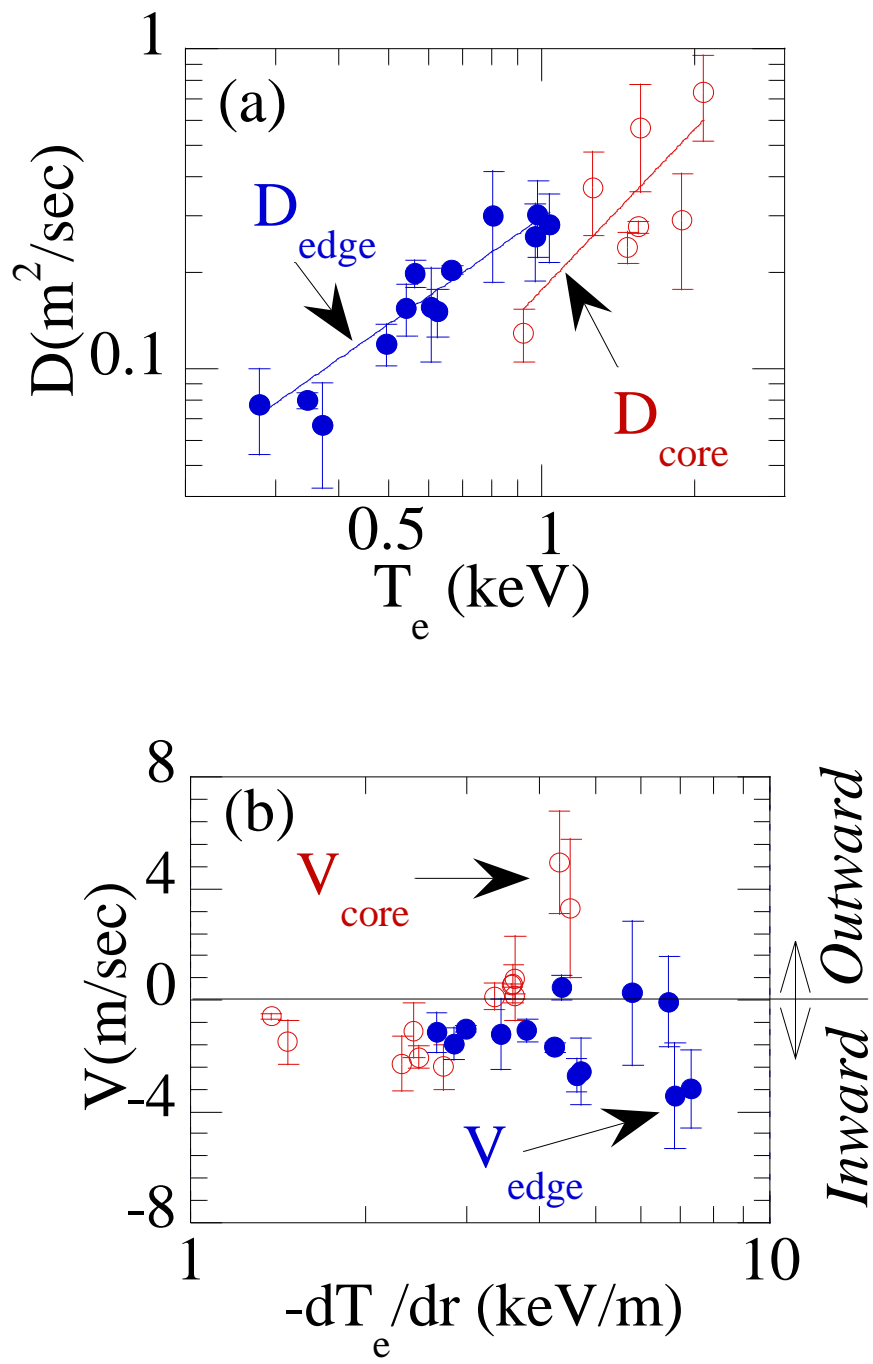


Fig.10

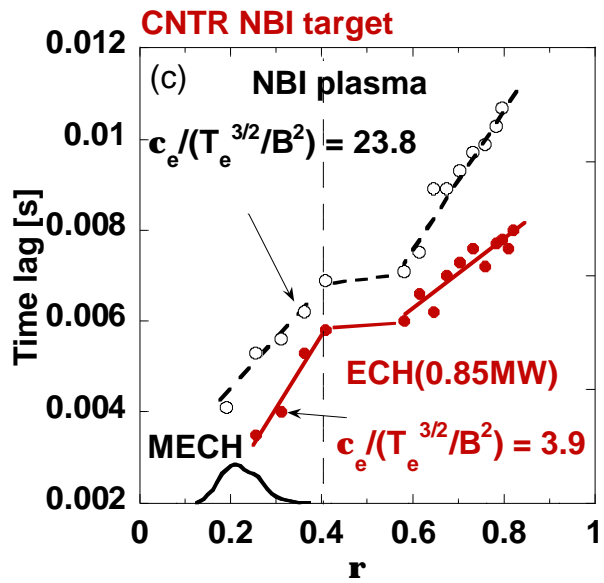
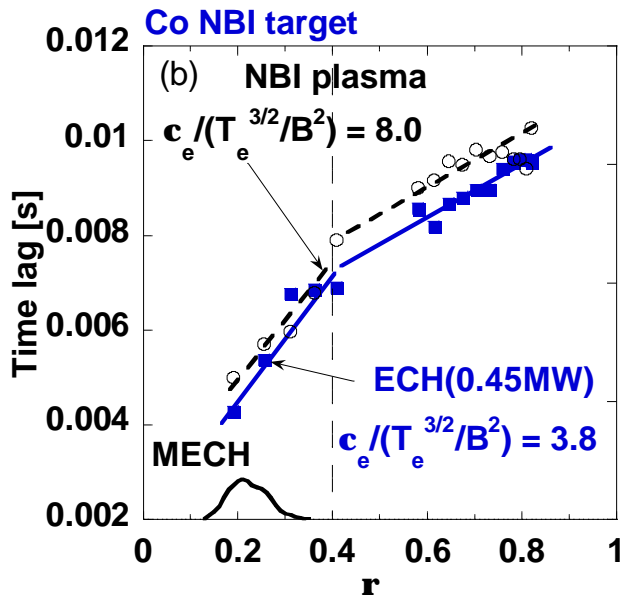
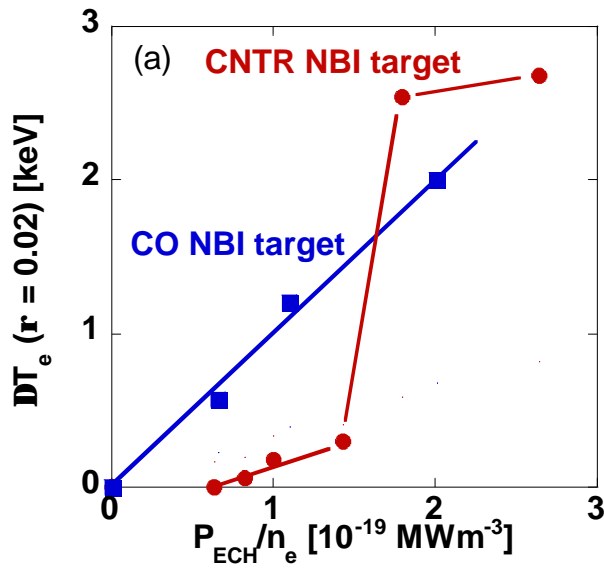


Fig.11

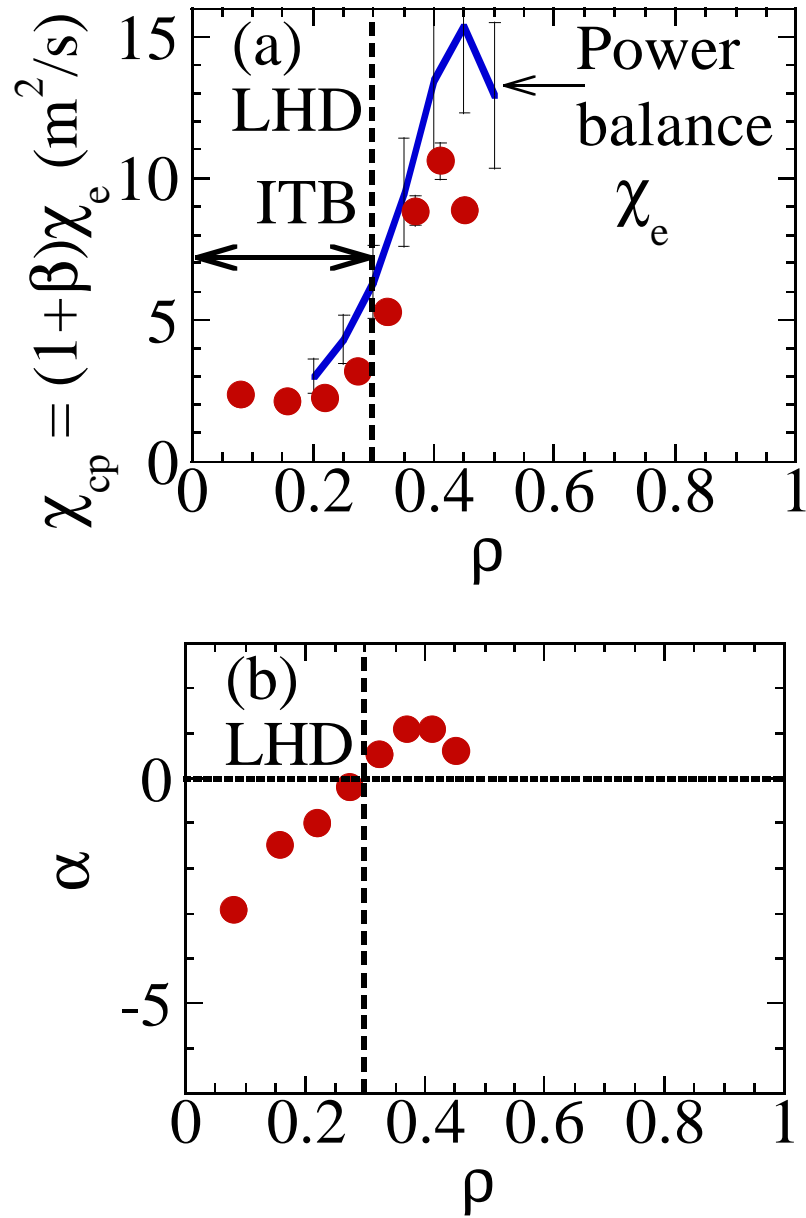


Fig.12

## Confinement Study of Net-Current Free Toroidal Plasmas Based on Extended International Stellarator Database

H.Yamada 1), J.H.Harris 2), A.Dinklage 3), E.Ascasibar 4), F.Sano 5), S.Okamura 1),  
J.Talmadge 6), U.Stroth 7), A.Kus 3), S.Murakami 8), M.Yokoyama 1), C.D.Beidler 3),  
V.Tribaldos 4), K.Y.Watanabe 1)

- 1) National Institute for Fusion Science, Toki, Gifu 509-5292, Japan
- 2) Australian National University, Canberra, Australia
- 3) Max-Planck-Institut für Plasmaphysik, EURATOM Association, Greifswald, Germany
- 4) CIEMAT, Madrid, Spain
- 5) Institute of Advanced Energy, Kyoto University, Uji, Kyoto, Japan
- 6) University of Wisconsin, Madison, USA
- 7) University of Kiel, Kiel, Germany
- 8) Department of Nuclear Engineering, Kyoto University, Kyoto, Japan

e-mail contact of main author: hyamada@lhd.nifs.ac.jp

**Abstract.** International collaboration of a stellarator confinement database has been progressing. About 2500 data points from major 9 stellarator experiments have been compiled. Robust dependence of the energy confinement time on the density and the heating power has been confirmed. Dependences on other operational parameters, i.e., the major and minor radii, magnetic field and the rotational transform  $\iota$ , have been evaluated using inter-machine analyses. In order to express the energy confinement in a unified scaling law, systematic differences in each subgroup should be quantified. An *a posteriori* approach using the confinement enhancement factor on ISS95 yields a new scaling expression ISS04v03;  $\tau_E^{ISS04v3} = 0.148 a^{2.33} R^{0.64} P^{-0.61-0.55} \bar{n}_e^{0.85} B^{0.41} \iota_{2/3}$ . Simultaneously, the configuration dependent parameters are quantified for each configuration. The effective helical ripple shows correlation with these configuration dependent parameters.

### 1. Introduction

Stellarators are widely recognized as the main alternative to the tokamak as a toroidal fusion reactor. A large experiment has extended parameters, and theoretical and design studies have developed advanced configurations for the next generation of experiments. The configuration space of possible stellarator designs is so large that comparative studies of experimental behavior are important to making choices that lead to an attractive reactor. Both experimental and theoretical confinement studies have been intensively conducted in a variety of concepts for a long time.

In 1995, a collaborative international study used available data from medium-sized stellarator experiments, i.e. W7-AS, ATF, CHS, and Heliotron-E to derive the ISS95 scaling relation for the energy confinement time [1]

$$\tau_E^{ISS95} = 0.079 a^{2.21} R^{0.65} P^{-0.59} \bar{n}_e^{0.51} B^{0.53} \iota_{2/3}^{0.4} \quad (1)$$

with the root mean square error (RMSE) in the logarithmic expression of 0.091. Here the units of  $\tau_E$ ,  $P$  and  $\bar{n}_e$  are s, MW and  $10^{19} \text{m}^{-3}$ , respectively, and  $\iota_{2/3}$  is the rotational

transform at  $r/a = 2/3$ . This expression is dimensionally correct and can be rephrased into an expression by important non-dimensional parameters,

$$\tau_E^{ISS95} \propto \tau_{Bohm} \rho^{*-0.71} \beta^{-0.16} \nu_b^{*-0.04},$$

where  $\rho^*$  and  $\nu_b^*$  are defined by the ion gyro radius normalized by the plasma minor radius and the collision frequency between electrons and ions normalized by the bounce frequency of particles in the toroidal ripple, respectively.  $\beta$  is the ratio of the plasma kinetic pressure to the magnetic field pressure. ISS95 is characterized by a weak gyro-Bohm nature and no definitive dependence on  $\beta$  and collisionality. Since ISS95, new experiments, i.e., LHD [2], TJ-II [3], Heliotron J [4], and HSX [5], most with different magnetic configurations, have started. In LHD, parameter dependences similar to ISS95 have been found but there exists a systematic improvement on it [6]. Also, collisionality independence like that in ISS95 has been confirmed in the deep collisionless regimes ( $\nu_b^* \approx 0.05$ ) when geometrical optimization of neoclassical transport is applied [7]. Confinement improvement with divertor operation also has been taken into account for W7-AS [8,9]. Extension of the confinement database aims at confirmation of our previous understanding of ISS95 and examination of possible new trends in confinement performance of stellarators. We have started to revise the international stellarator database, incorporating these new data, so as to deepen understanding of the underlying physics of confinement and its relationship to magnetic configuration details and improve the assessment of stellarator reactors.

## 2. Extension of International Stellarator Confinement Database

About 2500 data points have been compiled in the database to date from nine stellarators, i.e., ATF, CHS, Heliotron E, Heliotron J, HSX, LHD, TJ-II, W7-A and W7-AS. 1747 data representing typical discharges have been used for this study. The largest device, LHD ( $R/a = 3.9 \text{ m} / 0.6 \text{ m}$ ) has extended the parameter regime to substantially lower  $\rho^*$  and  $\nu_b^*$  regimes which are 3-10 $\times$  closer to the reactor regimes than those of the mid-size devices [10] (Fig. 1). Heliotron lines (Heliotron E, ATF, CHS and LHD) have colinearity between the aspect ratio and the rotational transform  $\iota$ . This obtains because the transform scales as the number of toroidal field periods  $M$ , which scales as  $R/a$ . Therefore,

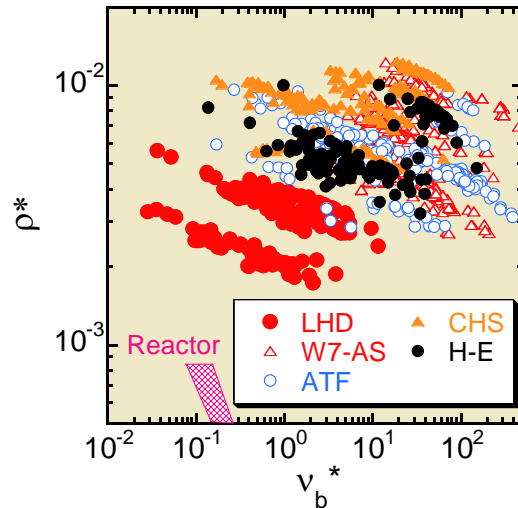


FIG.1. Parameter regime of data in the international stellarator database on the space of normalized gyro radii  $\rho^*$  and collisionality  $\nu_b^*$ .

Therefore,

the  $\kappa$  dependence tends to be statistically unstable for the data from heliotrons. W7-AS alone, which has contrasting  $\kappa$  profile to heliotrons, can not provide the size and  $\kappa$  dependences simultaneously. In the extended database, however, data from the flexible heliac TJ-II allows us to investigate the  $\kappa$  dependence over a much larger variation ( $1.3 < \kappa < 2.2$ ) than is available in the other experiments. Data from HSX has not been employed yet in the present combined analysis since non-thermal electrons characterize plasma confinement there.

The present database contains scalar data of parameters described in ref.[1], the format of which is similar to the ITER H-mode database [11]. The web page of the international stellarator confinement database is jointly hosted by National Institute for Fusion Science and Max-Planck-Institut für Plasmaphysik, EURATOM Association, and available at <http://iscdb.nifs.ac.jp/> and <http://www.ipp.mpg.de/ISS>.

### 3. Towards a Unified Scaling

A simple regression analysis of the entire data set (except for HSX) using the same parameters as in ISS95 yields

$$\tau_E^{REG} = 0.30 a^{2.07} R^{1.02} P^{-0.60} \bar{n}_e^{-0.58} B^{1.08} \tau_{2/3}^{-0.16} \propto \tau_{Bohm} \rho^*^{-1.95} \beta^{0.14} v_b^*^{-0.18} \quad (2)$$

with RMSE = 0.101. This expression is characterized by very strong gyro-Bohm as a similar analysis of heliotron lines has suggested [12], and a weak negative dependence on the rotational transform. The former trend is attributed to the fact that the energy confinement time in LHD with smaller  $\rho^*$  (in other words, larger dimension) is better than the gyro-Bohm prediction in comparison with other heliotrons. However, application of expression Eq.2 to data from a single device leads to contradictory results. For example, comparison of dimensionally-similar discharges in LHD indicates that the transport lies between Bohm and gyro-Bohm scalings [6]. Rotational transform scans in TJ-II also show that  $\tau_E$  is proportional to the power of 0.35-0.6 [13], which contradicts the weak  $\kappa$  dependence of Eq.2. It is also pointed out that Eq.2 is not dimensionally correct.

We conclude that while Eq.2 is useful for unified data description as a reference, its application is limited to the available data set alone and is not valid

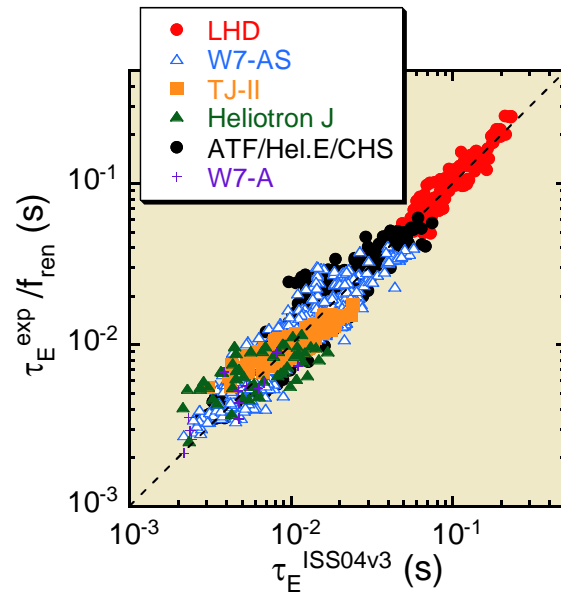


FIG.2. Comparison of energy confinement in experiments and predicted by ISS04v3. Experimental data is corrected by a renormalization factor  $f_{ren}$ .

for extrapolation. Data inspection and experience from inter-machine studies suggest necessity to introduce a magnetic configuration dependent parameter in order to supplement the set of regression parameters and resolve this seemingly contradictory result. A systematic gap between W7-AS and heliotron/torsatrons was noted during the earlier studies on the ISS95 scaling. A recent example showing the pronounced effect of magnetic configuration variation even in a single device has come from comparison of the performance of configurations with shifted magnetic axes in LHD. A discharge with an inward shift of the magnetic axis from  $R_{ax}=3.9$  m to  $R_{ax}=3.6$  m, results in a doubling of  $\tau_E$  for similar operational parameters  $a$ ,  $P$ ,  $\bar{n}_e$ ,  $B$  and  $\iota$  [6]. Therefore, acceptance of a systematic difference in different magnetic configurations is a prerequisite for derivation of a useful unified scaling law. A deterministic parameter characterizing the magnetic configuration has not been identified yet, but certainly involves the details of the helically corrugated magnetic fields. Since the configuration dependent parameter is not available now, an enhancement factor on ISS95 is first used expediently for renormalization to describe the magnetic configuration effect. This process is based on the conjecture that parametric dependence expressed by ISS95 is robust for stellarators and the enhancement factor on ISS95 reflects some configuration effects. One renormalization factor is defined by the averaged value of experimental enhancement factors for each configuration (subset). Iteration of a regression analysis of data normalized by this factor specific to configurations tends to converge into the following expression :

$$\tau_E^{ISS04\nu^3} = 0.148 a^{2.33} R^{0.64} P^{-0.61} \bar{n}_e^{-0.55} B^{0.85} \iota_{2/3}^{0.41} \propto \tau_{Bohm} \rho^{*-0.90} \beta^{-0.14} v_b^{*-0.01} \quad (3)$$

with RMSE =0.026 (see Fig.2). In this process, weighting of the square root of the number of each subset is applied. This expression appears more comprehensive than Eq.2. The leading coefficient is determined so as to give an renormalization factor of 1 for the case with  $\iota < 0.48$  in W7-AS, and Fig. 3 shows the resultant renormalization factor for subsets  $f_{ren}$  with different configuration. The confinement improvement by a factor of 2 when the magnetic axis is shifted from  $R_{ax}=3.9$  m to  $R_{ax}=3.6$  m in LHD can be seen clearly. The systematic difference for the cases with high rotational transform ( $\iota > 0.48$ ) and low one ( $\iota < 0.48$ ) in W7-AS has been also found in this analysis.

The robustness of the unified expression can be checked by examining its dependence on individual parameters. Figure 4 (a) and (b) show the exponent of density and heating

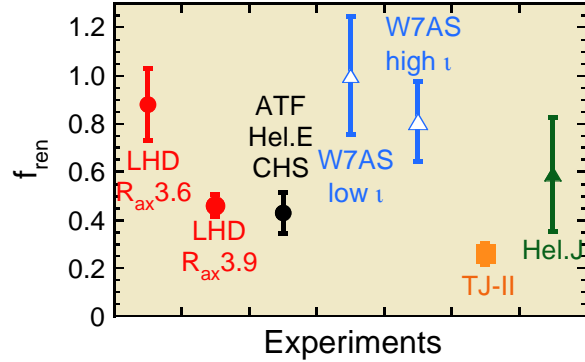


FIG.3. Renormalization factors for devices considered. Data of W7-AS are divided into two groups with low  $\iota$  ( $< 0.48$ ) and high  $\iota$  ( $\geq 0.48$ ).

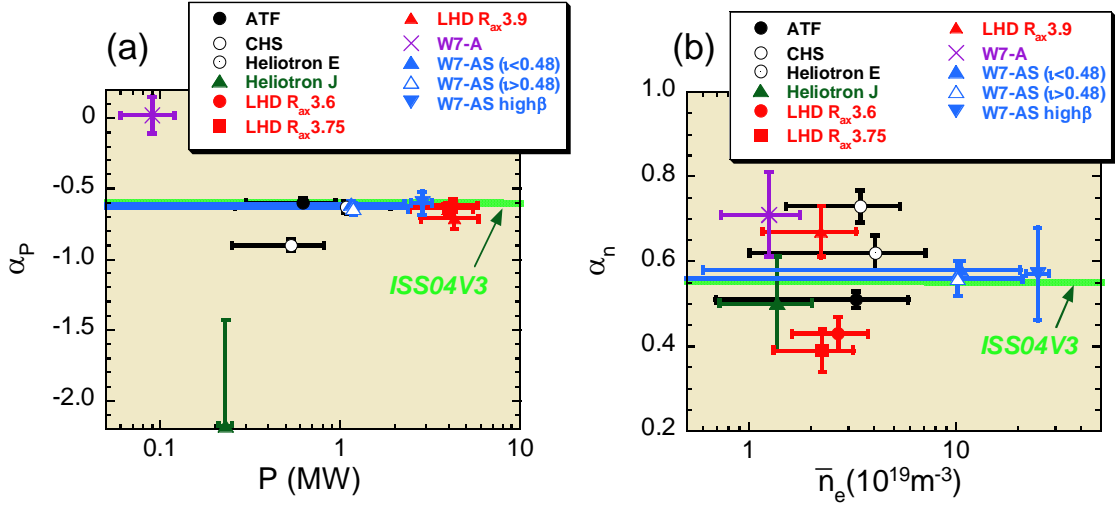


FIG.4. Exponents of (a) heating power and (b) density dependences in each subgroup with their parameter ranges.

power dependences, i.e.,  $\tau_E \propto P^{\alpha_P} \bar{n}_e^{\alpha_n}$  in a single experiment (configuration) with their parameter ranges, respectively. In these analyses, parameter dependences other than the density and the heating power are fixed as described by ISS04v03. Although some subgroups show significant deviation from the scaling, this discrepancy occurs mainly at low parameter values. Therefore, density and power dependences like  $\tau_E \propto P^{-0.61} \bar{n}_e^{0.55}$  can be found as general trends in subgroups. On the contrary, the magnetic field dependence in subgroups appears not to be consistent with ISS04v03. Therefore the magnetic field scaling is a result of inter machine regressions, which means that its statistical nature is different from variable quantities like power and density.

#### 4. Discussion

These results motivate future directions for stellarator confinement studies. The first step is clarification of the hidden physical parameters to interpret the renormalization factor shown in Fig.3. It is reasonable to suppose that this renormalization factor is related to specific properties of the helical field structure of the devices. A leading candidate is the effective helical ripple,  $\varepsilon_{\text{eff}}$  [14], which is defined from the neoclassical flux in the  $1/\nu$  regime,

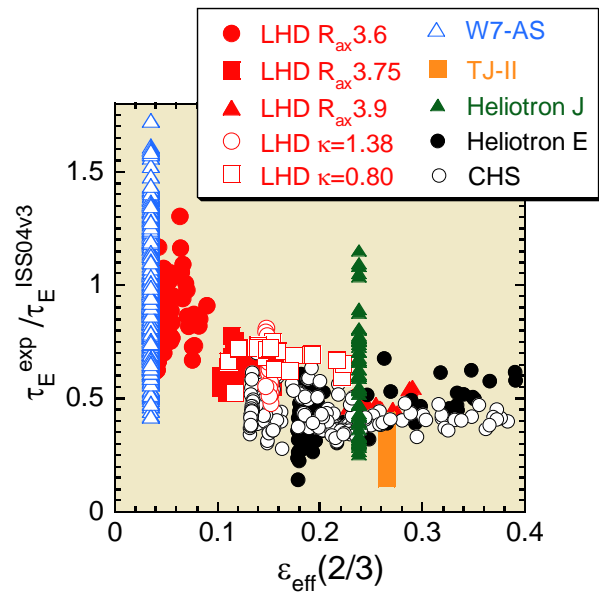


FIG.5. Confinement enhancement factor as a function of  $\varepsilon_{\text{eff}}$  at  $r/a=2/3$ .

which is proportional to  $\varepsilon_{\text{eff}}^{3/2}$ . The values of  $\varepsilon_{\text{eff}}$  have been calculated rigorously by the numerical codes, DCOM [15], DKES[16] and MOCA[17]. These codes have been successfully benchmarked for several configurations [18]. Figure 5 shows the correlation of  $\varepsilon_{\text{eff}}$  with the enhancement of confinement times with respect to the unified scaling law ISS04v3. The upper envelope resembles an  $\varepsilon_{\text{eff}}^{-0.4}$  dependence, however, detailed studies on  $\varepsilon_{\text{eff}}$  behaviour are required as the data indicate, e.g. large scattering of W7-AS and Heliotron J data. Also the expression of a power law of  $\varepsilon_{\text{eff}}$  diverges to infinity when it approaches zero (ideal tokamak case). Hence, a simple power law is expected to fail. Although all data in the database are not located in the collisionless regime where the neoclassical transport is enhanced,  $\varepsilon_{\text{eff}}$  can be related to effective heating efficiency through the neoclassical-like losses of high energetic particles and anomalous transport through flow damping due to neoclassical viscosity. Also neoclassical conduction loss of ions should be carefully looked into although the anomalous transport is generally predominant in electron heat transport. Due to the aforementioned reasons, an incorporation of that factor to a unified scaling is premature at present.

The second potential geometrical parameter is that given for the neoclassical flux in the plateau regime. This factor corresponds to the effect of elongation in tokamaks. The formulation is available in ref.[19] and here the geometrical factor that is the ratio of dimensionless fluxes in the cases of stellarator with many harmonics and tokamaks with only toroidal ripple, i.e.,  $\Gamma_{\text{stell}}/\Gamma_{\text{tok}}$  is considered. Figure 6 shows the correlation of this plateau factor  $\Gamma_{\text{stell}}/\Gamma_{\text{tok}}$  with the enhancement of confinement times with respect to the unified scaling law ISS04v3. The envelope of the data shows the trend that a smaller factor of  $\Gamma_{\text{stell}}/\Gamma_{\text{tok}}$  leads to good confinement although the scattering of data is larger than in the case of  $\varepsilon_{\text{eff}}$ . It should be noted that there is colinearity between  $\varepsilon_{\text{eff}}$  and  $\Gamma_{\text{stell}}/\Gamma_{\text{tok}}$  generally. However, an elongation scan in LHD ( $\kappa=0.8-1.38$ ) has excluded this colinearity, which has not indicated significance of  $\Gamma_{\text{stell}}/\Gamma_{\text{tok}}$  dependence (compare open squares and open circles in Fig.6). Therefore,  $\varepsilon_{\text{eff}}$  is more likely to be the essential configuration factor than is the plateau factor  $\Gamma_{\text{stell}}/\Gamma_{\text{tok}}$ .

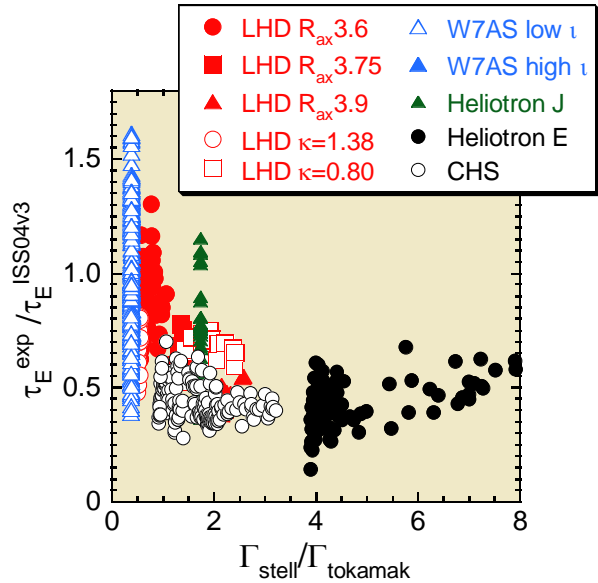


FIG.6. Confinement enhancement factor as a function of the plateau factor at  $r/a=2/3$ .

## 5. Conclusions

International collaboration on the stellarator confinement database has progressed significantly. About 2500 data points from 9 major stellarator experiments have been compiled. Robust dependence of the energy confinement time on the density and the heating power have been confirmed, and dependences on other operational parameters, i.e., the major and minor radii, magnetic field and the rotational transform  $\iota$ , have been evaluated using inter-machine analyses. In order to express the energy confinement in a unified scaling law, a systematic offset between each configuration data subgroup must be admitted. This factor is correlated with the magnetic geometry. A confinement enhancement factor on ISS95 is used for a posteriori approach. This procedure converges into the ISS04v03 expression;

$$\tau_E^{ISS04v3} = 0.148 a^{2.33} R^{0.64} P^{-0.61} \bar{n}_e^{0.55} B^{0.85} \iota_{2/3}^{0.41}.$$

The configuration dependence of confinement can usefully be expressed as a renormalization factor for ISS04v03. There are many potential candidates for this configuration factor: the effective helical ripple, the neoclassical flux in the plateau regime, fractions of direct-loss orbits and trapped particles, etc. In studies to date, the effective helical ripple shows correlation with the confinement enhancement factor.

While the explicit incorporation of this factor in a unified scaling is still premature, the correlation encourages a systematic comparative study of other potential configuration-dependent effects on stellarator confinement. The results of such studies will provide important guidance for the optimization of stellarator configurations and operational techniques.

## Acknowledgements

We are grateful to the LHD, W7-AS, TJ-II, Heliotron-J and HSX experimental groups for their contribution to the updated international stellarator database. In particular, discussions and communications with Drs. R.Brakel, V.Dose, K.Ida, Y.Igithkhanov, H.Maassberg, D.Mikkelsen, Y.Nakamura, R.Preuss, F.Wagner, A.Weller and K.Yamazaki are appreciated. The international stellarator database activity is organized under the auspices of IEA Implementing Agreement for Cooperation in Development of the Stellarator Concept.

## References

- [1] STROTH, U., et al, Nucl. Fusion **36** (1996) 1063.
- [2] IYOSHI, A., et al., Nucl. Fusion **39** (1999) 1245.
- [3] ALEJALDRE, C., et al., Plasma Phys. Control. Fusion **41** (1999) A539.
- [4] OBIKI, T., et al., Nucl. Fusion **41** (2001) 833.

- [5] ANDERSON, F.S.B., et al., Fusion Technol. **27** (1995) 273.
- [6] YAMADA, H., et al., Nucl. Fusion **41** (2001) 901.
- [7] YAMADA, H., et al., Plasma Phys. Control. Fusion **43** (2001) A55.
- [8] MCCORMICK, K., et al., Phys. Rev. Lett. **89** (2002) 015001.
- [9] WELLER, A., et al., Plasma Phys. Control. Fusion **45** (2003) A285.
- [10] MOTOJIMA, O., et al., Nucl. Fusion **43** (2003) 1674.
- [11] ITER PHYSICS BASIS, Nucl. Fusion **39** (1999) 2175.
- [12] YAMAZAKI, K., et al., in proc. 30th EPS Conf. on Contor. Fusion and Plasma Phys. (St.Petersburg, 7-11 July 2003) ECA Vol.27A, P-3.16.
- [13] ASCASIBAR, E., et al., to appear in Nucl. Fusion.
- [14] BEIDLER, C.D. and HITCHON, W.N.G., Plasma Phys. Control. Fusion **36** (1994) 317.
- [15] MURAKAMI, S., et al., Nucl. Fusion **42** (2002) L19.
- [16] VAN RIJ, W.I., HIRSHMAN, S.P., Phys. Fluids B **1** (1989) 563.
- [17] TRIBALDOS, V., Phys. Plasmas **8** (2001) 1229.
- [18] BEIDLER, C.D., et al., in proc. 30th EPS Conf. on Contor. Fusion and Plasma Phys. (St.Petersburg, 7-11 July 2003) ECA Vol.27A, P-3.2.
- [19] RODRIGUEZ-SOLANO RIBEIRO, SHAING, K.C., Phys. Fluids **30** (1987) 462.

## Effects of global MHD instability on operational high beta-regime in LHD

K.Y.Watanabe 1), S.Sakakibara 1), Y.Narushima 1), H.Funaba 1), K.Narihara 1), K.Tanaka 1), T.Yamaguchi 2), K.Toi 1), S.Ohdachi 1), O.Kaneko 1), H.Yamada 1), Y.Suzuki 3), W.A.Cooper 4), S.Murakami 5), N.Nakajima 1), I. Yamada 1), K.Kawahata 1), T.Tokuzawa 1), A.Komori 1) and LHD experimental group

- 1) National Institute for Fusion Science, 322-6 Oroshi, Toki, 509-5292, Japan
- 2) The Graduate University for Advanced Studies, Toki 509-5292, Japan
- 3) Graduate School of Energy Science, Kyoto Univ., Kyoto, 606-8224, Japan
- 4) Centre de Recherches en Physique des Plasmas, Association Euratom / Confederation Suisse, EPFL, 1015 Lausanne, Switzerland
- 5) Department of Nuclear Engineering, Kyoto Univ., Kyoto 606-8501, Japan

e-mail contact of main author: kiyowata@LHD.nifs.ac.jp

**Abstract.** In the Large Helical device (LHD), the operational highest averaged beta value has been expanded from 3.2% to 4% in last two years by increasing the heating capability and exploring a new magnetic configuration with a high aspect ratio. Although the MHD stability properties are considered to be unfavourable in the new high aspect configuration, the heating efficiency due to neutral beams and the transport properties are expected to be favourable in a high beta range. In order to make clear the effect of the global ideal MHD unstable mode on the operational regimes in helical systems, specially the beta gradients in the peripheral region and the beta value, the MHD analysis and the transport analysis are done in a high beta range up to 4% in LHD. In a high beta range of more than 3%, the maxima of the observed thermal pressure gradients in the peripheral region are marginally stable to a global ideal MHD instability. Though a gradual degradation of the local transport in the region has been observed as beta increases, a disruptive degradation of the local transport does not appear in the beta range up to 4%.

### 1. Introduction

A Heliotron device is a probable candidate of toroidal magnetic confinement systems as thermonuclear fusion reactor under steady-state operation because it can confine plasma with only external coils and install a well-defined divertor configuration. However, it is theoretically predicted that it has a disadvantage with respect to pressure driven magneto-hydrodynamics (MHD) instabilities [1]. Ideal MHD instabilities have a possibility to strongly limit the operational regime of the plasma parameters such as beta, pressure gradient and/or so on. In tokamaks, it is well known that the operational beta limits are quite consistent with theoretical predictions of ideal linear MHD theory [2]. On the contrary, in helical plasmas, a limited number of systematic studies about the effect of pressure driven ideal MHD instabilities on the operational beta range in experiments have been reported, for examples, on Heliotron DR [3], the compact helical system (CHS) [4] and the Large Helical Device (LHD) [5,6]. In the recent papers on LHD [5,6], the relationships between the unstable condition of the pressure driven MHD modes and the experimentally observed pressure gradients at some resonant rational surfaces based on the consistent MHD equilibrium with the measured plasma parameters data like the plasma stored energy, toroidal current, electron density and temperature profiles, which are enabled by powerful profile measurement systems, have been reported. According to them, the pressure gradients in the core region (a normalized minor radius,  $\rho \sim 0.5$ ) are governed by the ideal global MHD instability driven by pressure gradients. When a growth rate of the low-n ideal MHD unstable mode is applied as an index of the criteria, the pressure gradients do not exceed it. However, we have not obtained any conclusive results on the effects of the ideal global MHD instability in the peripheral region

( $\rho \sim 0.9$ ) on the operational regimes because the achieved beta values have not been high enough to reach a clear conclusion about this. Generally speaking, in heliotron devices, the global MHD mode in the core region is unstable in the intermediate beta range and it is stable in the high beta range. On the other hand, because the instability in the peripheral region is more unstable as the beta becomes higher, it is considered that the behaviour of the instability in the peripheral region limits the operational beta range, and it should be studied systematically.

MHD studies from the other aspects of the above have been done in previous LHD experiments as the followings. With regard to the MHD fluctuations with the resonance in the core region, stabilization due to spontaneous generation of magnetic well has been verified in the experiment [7]. MHD modes excited in the edge region have been observed even in the low- $\beta$  regime, and amplitudes of edge resonant modes such as  $m/n=2/3$  mode are considerably enhanced in the H-mode plasma with steep edge pressure gradient [8]. A disruptive degradation of an improvement factor of the global energy confinement time had not been observed up to  $\langle \beta_{\text{dia}} \rangle \sim 3\%$  [5,9].

Recently the increase of heating capability and a new magnetic configuration with a high aspect ratio by changing the pitch parameter of helical coil,  $\gamma$ , enables exploration of the operational beta range up to 4% in LHD. LHD is a Heliotron device (poloidal period number  $L=2$ , and toroidal period number  $M=10$ ) with a major radius of  $R_{\text{ax}}=3.5\text{-}4.1$  m, an averaged minor radius of 0.6 m, magnetic field,  $B_t$ , up to 3T, and heating neutral beam with negative ion with beam energy of 150-180keV. The new configuration with higher aspect ratio ( $\gamma=1.22$ ) is characterized by a smaller volume and smaller Shafranov shift than the so-called standard configuration ( $\gamma=1.254$ ). Although the MHD stability properties are expected even worse theoretically in this configuration ( $\gamma=1.22$ ) than the standard configuration because the magnetic well formation due to small Shafranov shift in a high beta range is reduced, the small shift is considered to contribute to the central deposition of neutral beam and hence the reduction of the direct loss of the beam by keeping the magnetic axis close to the tangential radius of the neutral beam in a high beta range. Moreover, the small volume is favourable for the extension of the operational density range according to a density limit empirical scaling, and the MHD equilibrium properties are favourable because of the small shift. Figure 1 shows the improvement factor ( $H_{\text{ISS}}$ ) of the global energy confinement time on the ISS95 (International Stellarator Scaling 1995) empirical scaling [10] in the new high aspect configuration as a function of  $\langle \beta_{\text{dia}} \rangle$ . Here  $H_{\text{ISS-diamag}}$  and  $H_{\text{ISS-kin}}$  are based on the diamagnetic flux measurement and the electron temperature and density profile measurements under the assumption of  $Z_{\text{eff}}=1$  and  $T_i=T_e$ , respectively. The  $\langle \beta_{\text{dia}} \rangle$  is the diamagnetic beta value defined as  $(2W_{\text{dia}}/3V_{\text{p0}})/(B_{\text{av0}}^2/2\mu_0)$ , where  $W_{\text{dia}}$  is the diamagnetic energy. The  $B_{\text{av0}}$  and  $V_{\text{p0}}$  are averaged toroidal magnetic field inside the plasma boundary and plasma volume, respectively, and both of them are estimated under vacuum conditions. A disruptive degradation of both global energy confinement times based on the diamagnetic flux measurement and the profile measurements have not been observed up to  $\langle \beta_{\text{dia}} \rangle \sim 4\%$ . However, the enhancement factors are gradually reduced as beta increases.

In this paper, in order to study the role of ideal pressure driven MHD modes on the operational regime in

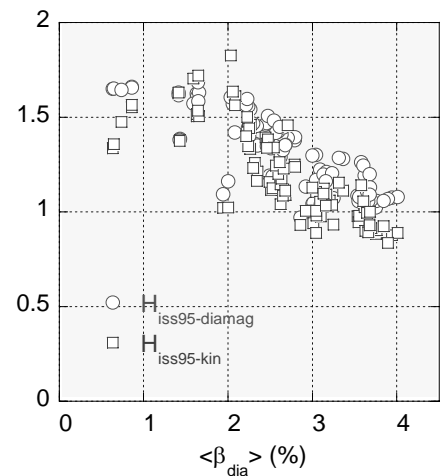


FIG.1 The improvement factor of effective energy confinement as a function of beta value.

LHD, especially in the peripheral region, we compare between the experimentally observed pressure gradients at peripherally located resonant rational surfaces and the theoretically predicted unstable region for ideal pressure driven MHD instabilities in the new high aspect configuration with  $R_{ax}=3.6m/\gamma=1.22$ , where the achieved beta value has been extended to 4%. And we study the relationships between the local transport property and the ideal MHD analysis results up to  $\langle\beta_{dia}\rangle\sim 4\%$ . We also show the typical behaviour of the MHD property in the high aspect configuration.

## 2. Typical high-beta discharge and MHD analysis

Figure 2 shows typical MHD activities in high-beta discharge in the high aspect configuration with  $R_{ax}=3.6m/\gamma=1.22$ . The  $B_t$  is set at 0.5 T. The  $\langle\beta_{dia}\rangle$  increases as the electron density increases. Three neutral beams are injected to this plasma and the deposition power is about 6.9 MW at 1.725s. At 1.74s the  $\langle\beta_{dia}\rangle$  reaches the maximum,  $\langle\beta_{dia}\rangle\sim 3.8\%$ . At the time,  $\langle\beta_{kin}\rangle$  and  $\langle\beta_{beam}\rangle$  reach  $\sim 3.2\%$  and  $\sim 1.0\%$ , respectively. Here  $\langle\beta_{kin}\rangle$  and  $\langle\beta_{beam}\rangle$  are the thermal component and the beam component of the beta value, respectively.  $\langle\beta_{kin}\rangle$  is estimated twice as the electron beta gradients with an assumption of  $Z_{eff}=1$  and  $T_i=T_e$ , where the electron temperature and density profiles are measured by Thomson scattering and FIR measurements, respectively. The beam pressure is estimated based on the Monte Carlo technique and the steady state Fokker-Plank solution [11]. It should be noted that the beam pressure is expected to be  $\sim 30\%$  of the thermal pressure in LHD typical high beta discharges because the operational density range is relatively low ( $n_e < 3\times 10^{19}m^{-3}$ ) due to a low density limit, the electron temperature is relatively high as shown in Fig.3 and NB injected power is large. A drop of the  $\langle\beta_{dia}\rangle$  after 1.85s is due to the termination of a beam injector.

The  $m/n=1/1, 2/3$  and  $2/5$  modes excited in the edge region are dominantly observed in this discharge. Here  $m$  and  $n$  are the poloidal and toroidal mode-numbers of the magnetic fluctuation, respectively. The  $m/n=1/1$  and  $2/3$  modes grow from 0.7s and their amplitudes increase with  $\langle\beta_{dia}\rangle$ . However, when  $\langle\beta_{dia}\rangle$  exceeds a certain value at 1 s, the  $m/n=1/1$  mode is frequently

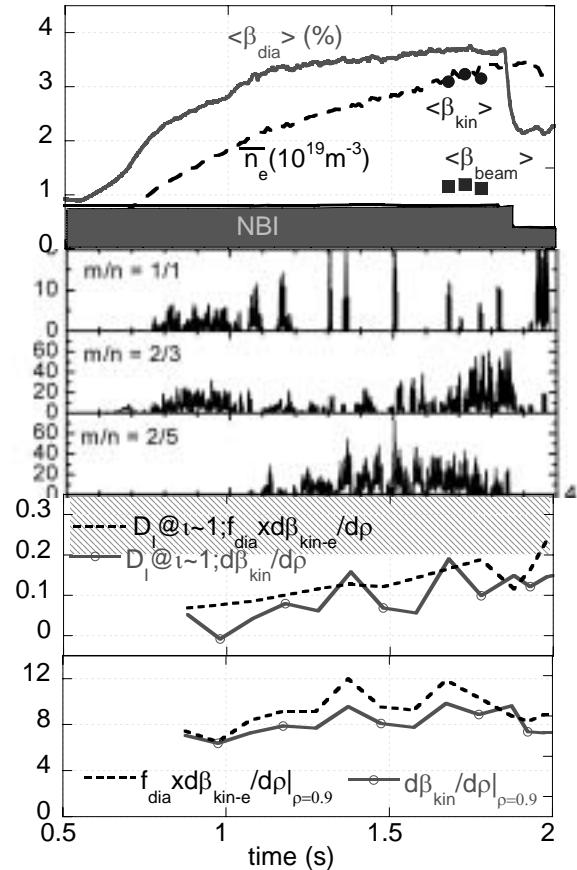


FIG.2 Temporal changes of plasma parameters in high-beta discharge.

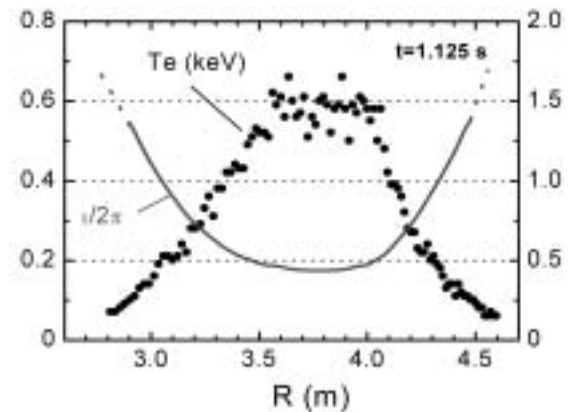


FIG.3  $T_e$  and iota profiles at 1.125 s in Fig.2 discharge.

interrupted and the amplitude of  $m/n=2/3$  mode starts to decrease. Then  $\langle \beta_{\text{dia}} \rangle$  starts to increase suddenly, and the amplitude of the  $m/n=2/5$  mode increases after that. At 1.75s, the degradation of  $\langle \beta_{\text{dia}} \rangle$  occurs with the growth of the  $m/n=2/3$  mode and the reduction of the  $m/n=2/5$  amplitude, although the heating and the supply of  $\text{H}_2$  gas are still maintained. The bottom figure of Fig.2 shows the temporal changes of the thermal pressure gradient,  $d\beta_{\text{kin}}/d\rho$  and the pressure gradient including the beam effect,  $f_{\text{dia}} \times d\beta_{\text{kin-e}}/d\rho$  around the  $m/n=1/1$  resonant surface. Here we assume beam pressure gradients are proportional to the electron beta gradients,  $d\beta_{\text{kin-e}}/d\rho$ , and the sum of the thermal pressure and the beam pressure coincides with the stored plasma energy measured by the diamagnetic flux loop ( $f_{\text{dia}}$  is set to let  $f_{\text{dia}} \times \langle \beta_{\text{kin-e}} \rangle$  is equal to  $\langle \beta_{\text{dia}} \rangle$ ). Both pressure gradients increase with  $\langle \beta_{\text{dia}} \rangle$ . The  $d\beta_{\text{kin}}/d\rho$  saturates at 1.1 s. After the  $m/n=1$  mode is suppressed at 1.2s, the gradient increases again. The Mercier parameter  $D_1$ , which is well used as the index of high- $n$  ideal stability, indicates the MHD mode is unstable because of the reduction of magnetic shear due to finite-beta effect. In this discharge, the low- $n$  ideal mode is expected to be stable because the  $D_1$  is less than 0.2. Then, the observed  $m/n=1/1$  mode is considered to be a resistive mode.

The equilibrium reconstruction is done for this discharge by the 3-D MHD equilibrium code VMEC [12], and  $T_e$  and rotational transform profiles are shown in Fig.3 as an example. The flattening structures of  $T_e$  profiles are found, for example, near the  $m/n=1/1$  resonant surface. These asymmetrical structures are often observed in high-beta discharges, and however, it is difficult to apply such profiles to the present equilibrium reconstruction. This flattening may contribute to the stabilization of the ideal and resistive modes. One of possibilities for the formation of the asymmetrical profile in periphery is due to variation of magnetic surfaces such as the growth of the intrinsic magnetic island due to an error field in finite beta plasmas [13].

Figure 4 shows changes of the amplitudes of observed MHD modes as a function of  $\langle \beta_{\text{dia}} \rangle$  in the  $\gamma = 1.22$  configuration. Although the  $m/n=2/1$  mode excited in core region has been observed in the  $\langle \beta_{\text{dia}} \rangle$  range of less than 2.5% in previous experiments, this mode disappears in the high-beta regime. The resonant surfaces with  $\iota=1$  are located at  $\rho \sim 0.9$  and their resonant modes are dominantly observed in the  $\langle \beta_{\text{dia}} \rangle$  range with more than 2.5%. While the amplitude of the  $m/n=1/1$  mode increases with  $\langle \beta_{\text{dia}} \rangle$ , it disappears or is intermittently observed when  $\langle \beta_{\text{dia}} \rangle$  exceeds 2.8%. Although the changes of the amplitudes of  $m/n=2/3$  and  $1/2$  modes are similar to the case of the  $m/n=1/1$  mode, the threshold  $\langle \beta_{\text{dia}} \rangle$  where the mode disappears is higher. The  $m/n=2/5$  mode appears when  $\langle \beta_{\text{dia}} \rangle$  exceeds

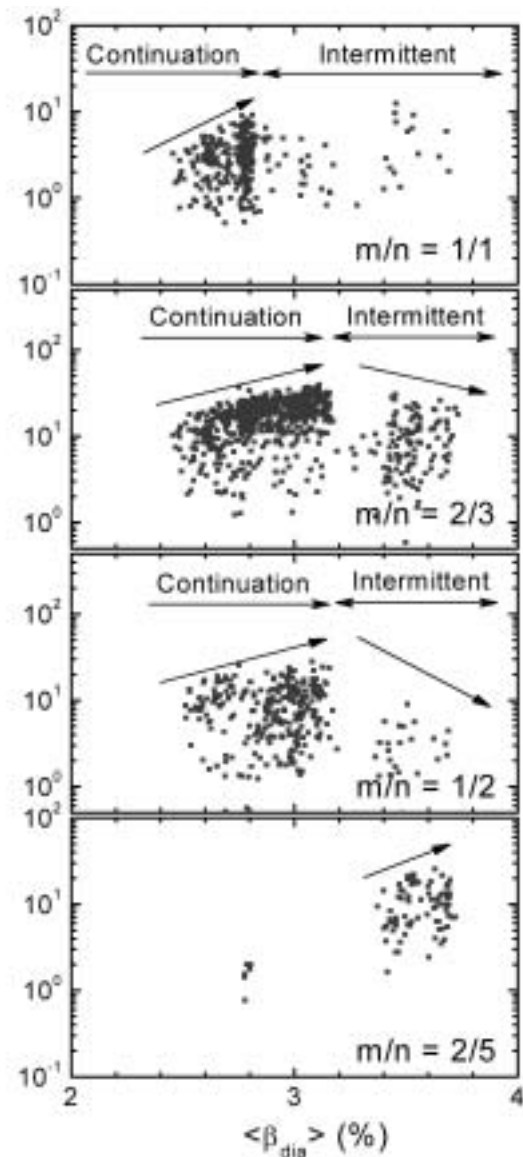


FIG.4 Beta dependence of MHD modes

3.4%, the amplitudes still increase with  $\langle \beta_{\text{dia}} \rangle$  in the present  $\langle \beta_{\text{dia}} \rangle$  range. These phenomena suggest that the stable region is expanded from the inner region to the outer one. The destabilization of the MHD mode just outside the "stable" region may be caused by the steep pressure gradient outside the profile flattening as shown in Fig.3.

### 3. Relationships between the prediction of linear MHD stability and the experiments

Here, we consider the effect of the global ideal MHD mode in the peripheral region on operational regimes. Figure 5 shows the experimentally observed beta gradients in the peripheral region ( $\rho=0.9$ ,  $\iota \sim 1$ ) in the high aspect configuration with  $R_{\text{ax}}=3.6\text{m}/\gamma=1.22$  as a function of  $\langle \beta_{\text{dia}} \rangle$ . The data were obtained in 0.45T to 1.75T operation. Symbols in Fig.5 correspond to the observed thermal beta gradients. Solid and dashed lines denote contours of the low-n ( $m/n=1/1$ ) ideal MHD modes (with global mode structure) with  $\gamma_{\text{low-n}}/\omega_A=10^{-2}$  and  $5 \times 10^{-3}$  for currentless equilibria. The growth rate is calculated with a MHD stability analysing code (TERPSICHORE [14]). Here  $\omega_A=v_{A0}/R_0$ ,  $v_{A0}$  and  $R_0$  are the Alfvén velocity and the major radius at the magnetic axis. The dotted lines are the stability boundary of Mercier modes (with a highly localized mode structure / high-m limit) [15]. The observed beta gradients at  $\rho=0.9$  increases with the beta up to  $\langle \beta_{\text{dia}} \rangle=4\%$ . The change of the gradients are observed around  $\langle \beta_{\text{dia}} \rangle=1.5\%$ , which corresponds to the Mercier unstable region. The envelope of the observed thermal pressure gradients in the beta range of  $\langle \beta_{\text{dia}} \rangle=3-4\%$  looks to coincide with a contour of the growth rate of the  $m/n=1/1$  ideal MHD mode,  $\gamma_{\text{low-n}}/\omega_A=10^{-2}$ .

Now we consider the beam pressure effect on the global ideal MHD instability. According to a global ideal MHD stability analysis, the achieved thermal beta gradients are in a marginal stable region of the global MHD instability even around  $\langle \beta_{\text{dia}} \rangle \sim 4\%$ . As shown in section 2, typical LHD high beta operations are done in low magnetic field and with high NBI power, where the beam pressure is fairly large. Figure 6 shows beta gradients including the beam component as a function of  $\langle \beta_{\text{dia}} \rangle$ . Here we assume the beam pressure gradients are proportional to the electron beta gradients, and the sum of the thermal pressure and the beam pressure is the diamagnetic plasma energy as shown section 2. The other situations are the same as in Fig.5. The change of the beta gradients around  $\langle \beta_{\text{dia}} \rangle=1.5\%$  observed in Fig.5 almost disappears in Fig.6. The beta gradients including beam effects are in the unstable region of the low-n ideal MHD instability. Even where the global ideal MHD mode is expected to be unstable, the beta gradients increase as the beta increases. These results suggest that either the beam pressure

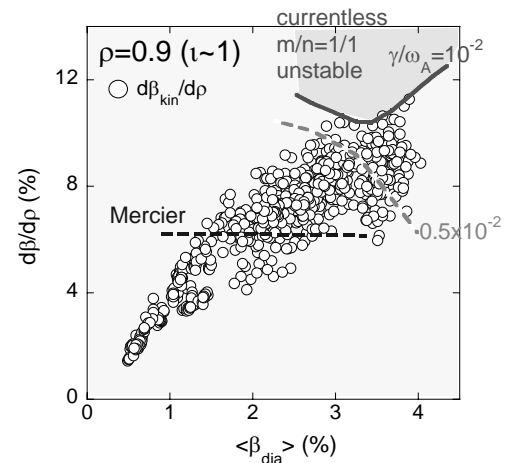


FIG.5 The observed thermal beta gradients at  $\rho=0.9$  in  $\langle \beta \rangle$ - $d\beta/d\rho$  diagram.

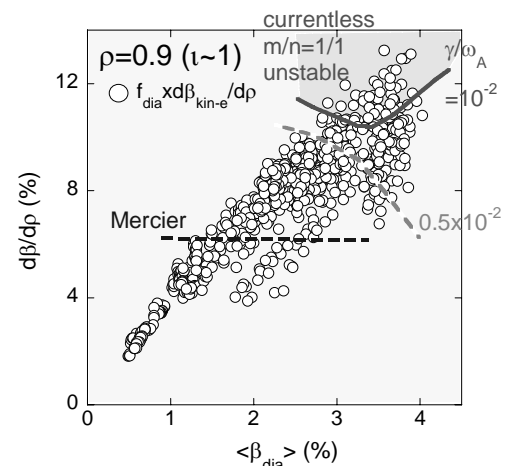


FIG.6 A beta gradient including a beam component at  $\rho=0.9$  in  $\langle \beta \rangle$ - $d\beta/d\rho$  diagram.

does not contribute the global ideal MHD instabilities or/and the beam pressure profiles may be broader than what is assumed here.

In order to know the effects of the beam component of the pressure on the ideal MHD mode, we need more detail information of the beam pressure. Moreover, we need larger heating power and/or the same kind of experimental study in a configuration with a higher aspect ratio. High heating power leads to high-density operation according to a density limit empirical scaling and/or the high magnetic field operation keeping the achieved beta value, where the contributions of the beam component on the total beta value are expected to be reduced. A configuration with a high aspect ratio is favourable from a viewpoint of the suppression of the loss of the NBI heating power in the high beta range, and its small volume leads to the extension of the operational density range. They also lead to the reduction of the contribution of the beam component.

#### 4 Transport properties in high beta ranges

In order to analyse a local transport property in the peripheral region from a viewpoint of pressure gradients, we introduce a parameter,  $X$ , proportional to the heating power and inversely proportional to the beta gradient as follows,

$$X = Q_{\rho=0.9} / \left( - \frac{\partial \beta_{kin}}{\partial r} \Big|_{\rho=0.9} S_{\rho=0.9} \frac{B^2}{2\mu_0} \right), \quad (1)$$

where  $r$  is a minor radius, and  $Q_{\rho=0.9}$  and  $S_{\rho=0.9}$  are the heat flux due to input power at  $\rho=0.9$  and an area of the  $\rho=0.9$  magnetic surface, respectively. When a density is constant, the parameter coincides with the effective heat conductivity. Squares in Fig.7 show  $X$  normalized by a heat conductivity based on the so-called gyro-reduced Bohm model at  $\rho=0.9$ , as a function of  $\langle \beta_{dia} \rangle$ . Circles show the beta gradients at  $\rho=0.9$ , which extracted from the data shown in Fig.5. The normalized  $X$  gradually increases with  $\langle \beta_{dia} \rangle$ . The disruptive degradation of  $X$  is not observed around  $\langle \beta_{dia} \rangle = 3-4\%$ , where the global ideal MHD modes is predicted to be marginally stable. However, the maxima of the normalized  $X$  suddenly increase when the beta gradients are in the Mercier unstable region, where resistive MHD modes are unstable and there is a possibility that the high- $n$  ballooning mode is unstable. The effect of the resistive modes and the high- $n$  ballooning modes on the transport properties is a future subject.

According to a local transport analysis, the local transport in the peripheral region is not seriously affected by the global ideal MHD modes around  $\langle \beta_{dia} \rangle = 3-4\%$ . However, as shown in Fig.1, a gradual degradation of a global energy confinement on beta value is observed based on the ISS95 transport model. Figure 8 shows the electron density normalized by density limit proposed by Sudo et al. [16],  $H_{Sudo}$ , as a function of beta value. High beta discharges are done in a high collisionality range close to the density limit,  $H_{Sudo} > 0.5$  in  $\langle \beta_{dia} \rangle > 2\%$  and  $H_{Sudo} \sim 1$  in  $\langle \beta_{dia} \rangle \sim 4\%$ . According to a recent LHD transport scaling analysis in the high collisionality [17], the dependence of the global energy confinement time on the electron density changes from the ISS95 scaling,  $\tau_E \sim n_e^{0.51}$  in the low collisionality range to  $\tau_E \sim n_e^{0.28}$  in the high

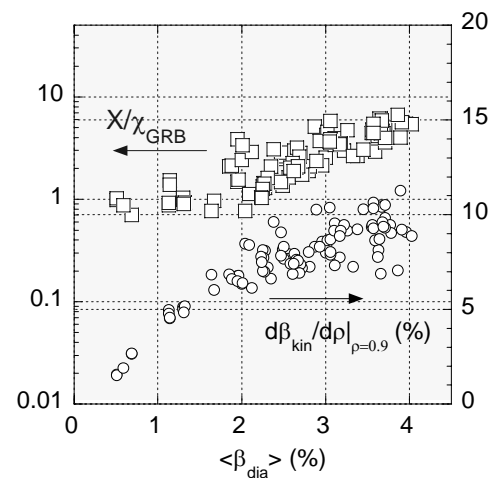


FIG.7 A normalized parameter,  $X$  at  $\rho=0.9$  as a function of the beta value.

collisionality range. When we apply the new scaling law, a degradation of global energy confinement time is still observed. According to another scaling model, it is pointed out that the global confinement time scales according to the effective helical ripple of the magnetic field,  $\varepsilon_{h\text{-eff}}$  [18]. In a high beta range,  $\varepsilon_{h\text{-eff}}$  becomes larger than that in vacuum because of a Shafranov shift. The gradual degradation of global confinement time may follow this model. Moreover, it is reported that the broad heat deposition profile leads to the degradation of confinement time in LHD [19]. In low field operations, the heat deposition due to NBI is expected to be broad. This is another candidate of the explanation for the degradation of global energy confinement time.

## 5 Summary and discussion

In the Large Helical device (LHD), the operational highest averaged beta value has been expanded from 3.2% to 4% in last two years by increasing the heating capability and exploring a new magnetic configuration with a higher aspect ratio. Although the MHD stability properties are considered to be unfavourable in the new high aspect configuration, the heating efficiency due to neutral beam and the transport properties are expected to be favourable in the high beta range. In helical systems, in order to make clear the effect of the global ideal MHD unstable mode on the operational regimes, specially the beta gradients in the peripheral region and the total beta value, the MHD analysis and the transport analysis are done for the high beta operation up to  $\langle \beta_{\text{dia}} \rangle \sim 4\%$  in LHD. In a beta range of  $\langle \beta_{\text{dia}} \rangle = 3 \sim 4\%$ , the global ideal MHD mode resonant with the peripheral rational surface,  $\iota = 1$ , is marginal stable for the observed thermal component of beta gradients, that is, growth rates of a global ideal MHD mode are always below a value,  $\gamma_{\text{low-n}}/\omega_A = 10^{-2}$ . However, the beta gradients including a beam component do not appear to be sensitive to the growth rates of a global ideal MHD mode. The beam pressure effect on the global ideal MHD instability is still unclear.

The local transport in the peripheral region and the global energy confinement are not seriously affected by the global ideal MHD instability around  $\langle \beta_{\text{dia}} \rangle = 3 \sim 4\%$ , where the global ideal MHD modes is expected unstable. The reason may be that the global ideal MHD instability around  $\langle \beta_{\text{dia}} \rangle = 3 \sim 4\%$  is marginally stable. In order to make sure the effect of the global ideal MHD instability in the peripheral region on a local transport and a global energy confinement, we need larger heating power and/or the same kind of experimental study in a configuration with a higher aspect ratio.

Here we analyse the operational regimes based on a linear MHD theory. We know that the achieved pressure gradients are in the non-linear saturation phase. However, since it has not been clear how the pressure driven MHD instability affect the experimental operation regimes of the helical

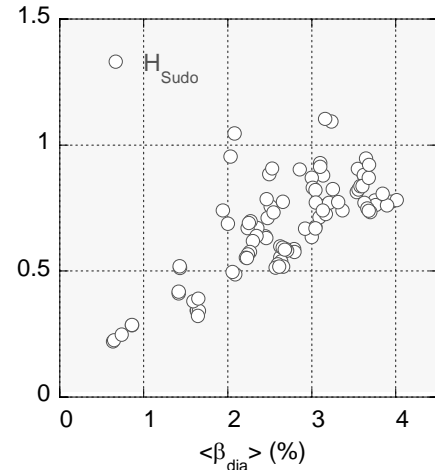


Fig.8 Electron density normalized by density limit proposed by Sudo et al.

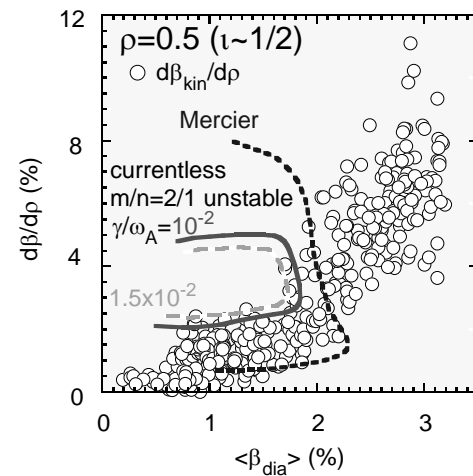


FIG.9 The observed thermal beta gradients at  $\rho = 0.9$  in  $\langle \beta \rangle - d\beta/d\rho$  diagram.

systems, our approach (evaluating the experimentally achievable pressure gradients by the linear growth rate and/or Mercier parameter) would be useful, because it could be a reference for more complicated non-linear analyses, and a criterion for a reactor design. Figure 9 shows the relationship between the experimentally observed thermal beta gradients in the core region ( $\rho=0.5$ ,  $\iota\sim 1/2$ ) and the theoretically predicted unstable region for ideal pressure driven MHD instabilities in the standard configuration with  $R_{ax}=3.6m/\gamma = 1.254$  [5,6]. Symbols correspond to the observed thermal beta gradients. Solid and dashed lines denote contours of the low-n ( $m/n=2/1$ ) ideal MHD modes with  $\gamma_{low-n}/\omega_A=10^{-2}$  and  $1.5\times 10^{-2}$  for currentless equilibria. In the core region, the maxima of the achieved pressure gradients seem to saturate against the contour of  $\gamma_{low-n}/\omega_A= 1.5\times 10^{-2}$  in the range of  $\langle\beta_{dia}\rangle = 1\sim 1.8\%$ . When  $\langle\beta_{dia}\rangle$  exceeds  $\sim 1.8\%$ , the maximum achieved pressure gradient more than doubles. Roughly speaking,  $\gamma_{low-n}/\omega_A= 1\sim 1.5\times 10^{-2}$  from the results of Figs.5 and 9 is considered a good index to determine the condition that the global ideal MHD instability limits the operational regime. For further verification, we need to extend the above comparative analyses between the experimental results and the theoretical prediction based on a linear theory to many magnetic configurations in LHD.

The authors deeply acknowledge the LHD experiment group for their great effort of LHD operation and maintenance.

## References

- [1] WAKATANI, M., NAKAMURA, Y., and ICHIGUCHI, K., Fusion Eng. Design 15 (1992) 395.
- [2] ITER Physics Basis, Nuclear Fusion 39 (1999) 2137.
- [3] YANAGI, N., et al., Nucl. Fusion 32 (1989) 1264.
- [4] OKAMURA, S., et al, Nucl. Fusion 30 (1999) 1337.
- [5] WATANABE, K.Y., et al, Fusion Sci. Tech. 46 (2004) 24.
- [6] WATANABE, K.Y., et al, J. Plasma and Fusion Res. Ser, 6, (to be published).
- [7] SAKAKIBARA, S., Nucl. Fusion 41 (2001) 1177.
- [8] TOI, K., et al., Nucl. Fusion 44 (2003) 217.
- [9] YAMADA, H., et al., Plasma Phys. Control. Fusion 43 (2001) A55.
- [10] STROTH, U., et al, Nuclear Fusion 36 (1996) 1063.
- [11] HIRSHMAN, S.P., Phys. Fluids 26 (1983) 3553.
- [12] NAGAYAMA, Y., et al., this conference.
- [13] MURAKAMI, S., Nuclear Fusion 36 (1996) 359.
- [14] COOPER, W. A., Plasma Phys. Control. Fusion 34 (1992) 1011.
- [15] GRASSER, A.H., GREEN, J.M., and JOHNSON, J.L., Phys. Fluids 18 (1975) 143.
- [16] SUDO, S., et al, Nucl. Fusion 30 (1990) 11.
- [17] MIYAZAWA, J., et al, J. Plasma and Fusion Res. (to be submitted).
- [18] YAMADA, H., et al., this conference.
- [19] YAMADA, H., et al., Nucl. Fusion 43 (2003) 749.

## Electrostatic fluctuation and fluctuation-induced particle flux during formation of the edge transport barrier in the JFT-2M tokamak

T. Ido 1), Y. Miura 2), K. Hoshino 2), Y. Hamada 1), Y. Nagashima 1), H. Ogawa 2), K. Shinohara 2), K. Kamiya 2), A. Nishizawa 1), Y. Kawasumi 1), Y. Kusama 2), JFT-2M group 2)

1) National Institute for Fusion Science, Oroshi-cho, Toki-shi, Gifu, 509-5292, Japan

2) Naka Fusion Research Establishment, Japan Atomic Energy Research Institute, Naka-machi, Naka-gun, Ibaraki 311-0193, Japan

e-mail contact of main author : ido@LHD.nifs.ac.jp

**Abstract.** The electrostatic fluctuation with Geodesic-Acoustic-Mode (GAM) frequency is observed in L-mode plasmas. The fluctuation has the poloidal wave number ( $k_\theta$ ) of  $(-2 \pm 24) \times 10^{-3} \text{ (cm}^{-1}\text{)}$ , that corresponds to the poloidal mode number of 1.5 or less, and the radial wave number ( $k_r$ ) of  $0.94 \pm 0.05 \text{ (cm}^{-1}\text{)}$ , that is corresponds to  $k_r \rho_i = 0.26 < 1$ . The amplitude of the fluctuation changes in the radial direction; it is small near the separatrix and it has maximum at 3 cm inside the separatrix. The relation between the amplitude of potential fluctuation and that of density fluctuation is the same as that of the predicted GAM. The fluctuation is probably GAM.

The envelope of ambient density fluctuation and the potential fluctuation have a significant coherence at the GAM frequency. Thus, it is clearly verified that the fluctuation with the GAM frequency correlates with the ambient density fluctuation. The fluctuation with the GAM frequency affects the particle transport through the modulation of the ambient fluctuation. But the effect is not large, and it is not a sufficient condition to form the edge transport barrier and to drive the intermittent particle flux.

### 1 Introduction

It is thought that the transport of magnetically confined plasmas is mainly caused by plasma turbulence. The clarification of the feature of the turbulence is an important issue to predict the transport of plasma and to estimate the performance of future machines such as International Thermonuclear Experimental Reactor (ITER).

Recently, zonal flow [1] is getting a lot of attention as a cause of the saturation of the turbulence through the energy transfer due to the nonlinear coupling of the turbulence and through the suppression of turbulence due to the shear of zonal flow [2, 3]. Some experimental results indicate the existence of zonal flow [4, 5, 6, 7, 8].

In this study, the potential and density fluctuations are measured directly and simultaneously with a heavy ion beam probe (HIBP), and the existence of Geodesic-Acoustic-Mode (GAM) [9, 10] which is a branch of zonal flow is investigated. Moreover, the correlation between GAM and ambient fluctuation is examined directly, and the influence on the particle flux is studied.

### 2 Experimental Setup

The HIBP can measure a local electrostatic potential ( $\phi$ ) directly even in high temperature plasmas with a high temporal and spatial resolution. Singly charged heavy ion beam, called the primary beam, is injected into the magnetically confined plasma. A part of the primary beam is charged doubly through the electron impact ionization and it is called the secondary beam. Since the charge number increases by one, the total energy of the ion changes by the potential energy at the ionization point. Therefore,  $\phi$  at the ionization point can be obtained through the measurement of the difference in the kinetic energies between the primary and the secondary beam ion. Moreover, the secondary beam current ( $I_{HIBP}$ ) reflects the electron density

and temperature. In this experiment, the contribution of the temperature is smaller than that of the density [11]. Thus, the density fluctuation  $\tilde{n}_e$  can be inferred through the fluctuation of the secondary beam current ( $\tilde{I}_{HIBP}$ ). When the path integral effect is negligible, the normalized  $\tilde{I}_{HIBP}$  is equivalent to the normalized  $\tilde{n}_e$ ;  $\tilde{n}_e/n_{e,0} \sim \tilde{I}_{HIBP}/I_{HIBP,0}$ .

In this study, the characteristics of the electrostatic fluctuation, especially focusing the fluctuation with the GAM frequency, are studied with the HIBP [12] in the JFT-2M tokamak.

The JFT-2M tokamak is a medium-sized tokamak with a major radius (R) of 1.3 m and an averaged minor radius (a) of 0.3 m. The experiments are performed with an upper single null divertor configuration and  $\nabla B$  drift of ion is toward X-point. The fueling gas species is deuterium.

The HIBP on JFT-2M can measure 7 sample volumes simultaneously: the density fluctuation can be measured in all the 7 sample volumes and the potential can be measured in 4 or 5 sample volumes of them, which depends on the injection condition. The radial width of each sample volume is about 6 mm according to a beam trajectory calculation [13]. The arrangement of sample volumes is determined through the Larmor radius of the beam, that is the combination of the magnetic field strength ( $B_t$ ) and the beam energy ( $W_0$ ). When  $W_0 = 350$  keV, the sample volumes are aligned in nearly minor-radius-direction in  $B_t$  of 1.17 T and in the poloidal direction in  $B_t$  of 1.28 T. In addition to that, the sample volumes can be moved in the radial direction with the electrostatic sweeper. Thus, the radial profile in wide range are measured through changing the sweep voltage.

### 3 Temporal behavior and frequency spectra of the electrostatic fluctuation

First, the temporal behavior of the electrostatic fluctuation is shown. Figure 1 shows the temporal behavior of a typical discharge. In this shot,  $B_t = 1.17$  T, the plasma current is 190 kA and the  $q_{95}$ , which is the safety factor at the flux surface that encloses 95 % of the total poloidal flux, is 2.9. The neutral beam (NB) is injected in the co-direction from 700 ms to 800 ms and its power is 700 kW.

After the sawtooth crash at 725 ms, large spikes start to appear in  $D_\alpha$  intensity and negative spikes are shown in  $I_{HIBP}$ . It indicates that the formation of the transport barrier starts intermittently but it is not sustained. The SX intensity from the scrape off layer (SOL) and  $D_\alpha$  intensity drop clearly after a sawtooth crash at 735.5 ms. They indicate the transition to the ELM-free H-mode. The fluctuation in the intensity of the secondary beam, which reflects density fluctuation ( $\tilde{n}_e$ ), exists with the broad frequency spectrum in L-mode, and it is suppressed at the L-H transition (Fig.1(d)). The potential fluctuation( $\tilde{\phi}$ ) shows the similar behavior except that a significant fluctuation with the frequency of about 15 kHz is observed during L-mode (702 - 725 ms) (Fig.1(f)). The potential fluctuation with the frequency of 15 kHz exists in L-mode (and Ohmic phase in other discharge) and disappear at about 725 ms, when the intermittent formation of the transport barrier starts.

## 4 Characteristics of electrostatic fluctuation with the GAM frequency

### 4.1 Frequency spectra

The power spectra of the potential ( $\tilde{\phi}$ ) and normalized density fluctuations ( $\tilde{n}_e/n_{e0}$ ) are shown in Fig.1(g) and (h). A significant peak with the frequency of about 15 kHz appears. The predicted GAM frequency ( $\sqrt{(T_i + T_e)}/M_i/2\pi R$ ) [10] is 19 kHz, where  $M_i$  is the mass of the ion, R is 1.54 m, the ion temperature ( $T_i$ ) is  $340 \pm 40$  eV measured with charge exchange

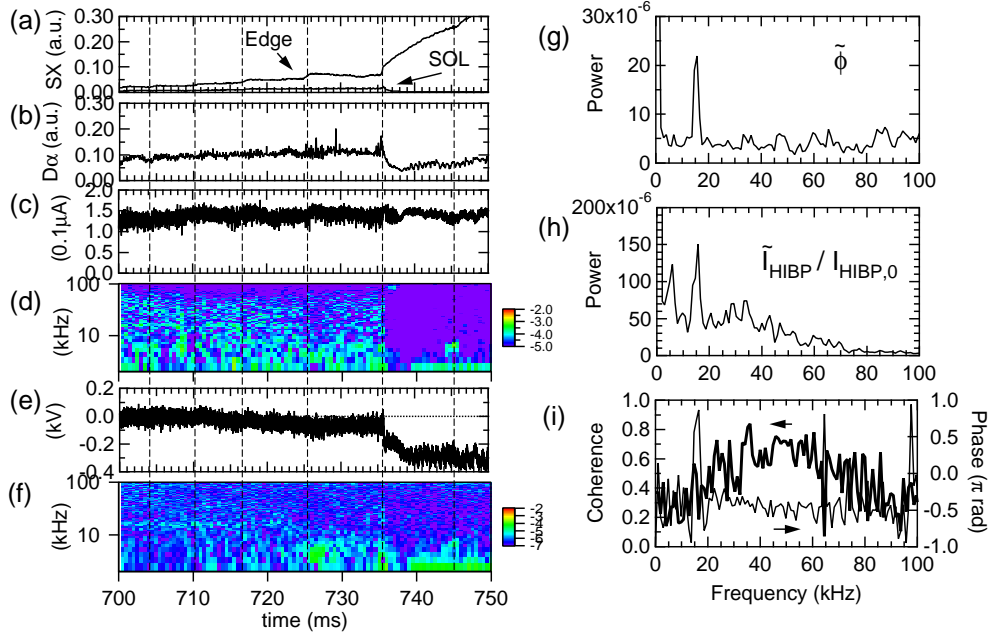


Fig. 1: (a) Chord integrated soft x-ray(SX) intensities from the edge ( $\rho \sim 0.85$ ) and SOL ( $\rho \sim 1.1$ ), where  $\rho$  is the distance of the chord from the plasma center normalized by the minor radius. (b)  $D_\alpha$  intensity in the divertor. The vertical dashed lines indicate the timing of the sawteeth crash. (c)(d) the secondary beam intensity ( $I_{HIBP}$ ) and its spectrum at 1.4 cm inside the separatrix and its spectrum, (e)(f) electrostatic potential ( $\phi$ ). (g)(h) power spectra of the electrostatic potential fluctuation ( $\tilde{\phi}$ ) and fluctuation of normalized  $I_{HIBP}$ , which is normalized density fluctuation ( $\tilde{n}_e/n_{e,0}$ ), during L-mode, (i) coherence between  $\tilde{\phi}$  and normalized  $\tilde{I}_{HIBP}$

spectroscopy (CXS), and the electron temperature ( $T_e$ ) is assumed to be the same as  $T_i$ . The frequency of the peak in the power spectra is similar to the predicted GAM frequency. The word ‘‘GAM frequency’’ and  $f_{GAM}$  are used as the frequency of the peak near the predicted GAM frequency in this paper, and the physical value (A) with the GAM frequency is expressed as  $A(f_{GAM})$ .

The coherence and phase difference between  $\tilde{\phi}$  and  $\tilde{n}_e/n_{e,0}$  is shown in Fig.1(c). The fluctuations with the broad frequency spectrum indicate high coherence, and the phase difference is near  $\pi/2$ . On the other hand, the fluctuations with  $f_{GAM}$  indicate lower coherence than the above fluctuation, but the coherence is higher than that of the ambient fluctuation around  $f_{GAM}$ . The phase difference is  $\pi$ , and it is quite different from the phase difference of the fluctuations with the broad frequency. The results mean the fluctuations consist of 2 different components at least; one is the fluctuation with the GAM frequency and the other is the ambient fluctuation with the broad frequency spectrum.

## 4.2 Radial profile of the amplitude

The radial profile of the amplitude of the potential fluctuation with the GAM frequency ( $\tilde{\phi}(f_{GAM})$ ) is measured. The HIBP can measure the potential at 4 sample volumes simultaneously. The sample volumes range over about 1 cm in the radial direction, when they are aligned in nearly radial direction. In order to measure the radial profile of the amplitude of  $\tilde{\phi}(f_{GAM})$ , the positions of the sample volumes are changed every shot. The profile is shown in Fig.2(b), where each shot is identified with different marks. The amplitude is almost the same in same position

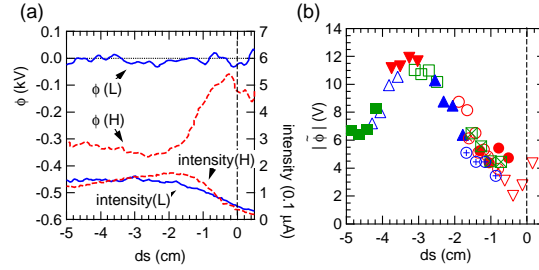


Fig. 2: (a) The radial profiles of  $\phi$  and  $I_{HIBP}$  in L- and H-mode. (b) The radial profiles of the amplitude of  $\tilde{\phi}(f_{GAM})$  in L-mode. The horizontal axis is the distance from the separatrix and the negative sign means the inside of the separatrix.

even in the different shot, thus the shots are reproducible. The the amplitude of  $\tilde{\phi}(f_{GAM})$  is small near the separatrix, it reaches to the maximum value at about 3 cm inside the separatrix.

The maximum of the  $\tilde{\phi}(f_{GAM})$  is about 4 % of the stationary potential in H-mode plasma [14, 16], and the peak of the profile is inside the position where the steady  $E \times B$  flow shear is maximum in H-mode. It indicates  $\tilde{\phi}(f_{GAM})$  may not be very important for L-H transition.

### 4.3 Coherence in the poloidal direction

In order to measure the coherence in the poloidal direction, the sample volumes are ordered in the poloidal direction on almost the same magnetic surface. For the purpose, the magnetic field is 1.28 T, and the other parameters are fixed and  $q_{95} = 3.2$ . The position of the sample volumes are at 1 cm inside the separatrix. The density fluctuation (7 sample volumes), potential and potential fluctuation (4 sample volumes) are measured simultaneously under this condition. The sample volumes are at intervals of 7 mm in the poloidal direction.

The frequency spectra of  $\tilde{\phi}$  and normalized  $\tilde{n}_e$  are shown in Fig.3(a). Although a peak exists around  $f_{GAM}$  in the spectrum of  $\tilde{\phi}$ , there is no significant peak in the spectrum of normalized  $\tilde{n}_e$ . The reason is that the fluctuation with  $f_{GAM}$  is weak and the ambient density fluctuation is strong near the separatrix.

The coherence between the fluctuations is shown in Fig.3(b) and (c). The distance between the sample volumes is 7 mm and 21 mm, respectively. As the distance between the sample

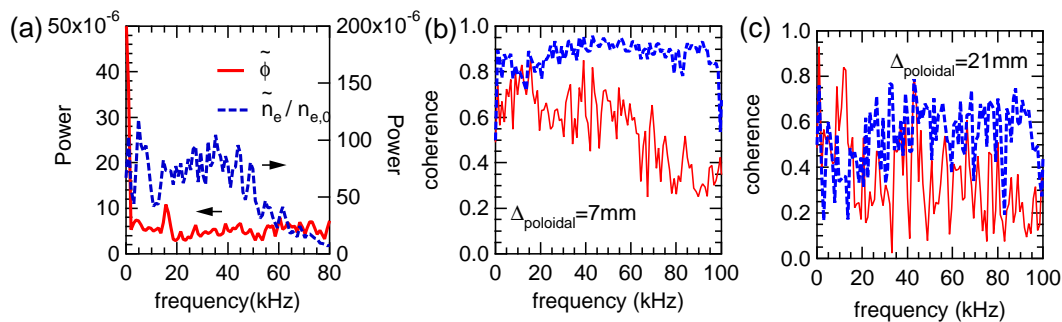


Fig. 3: (a) power spectra of  $\tilde{\phi}$  and normalized  $\tilde{n}_e$ . (b) Coherence. The sample volumes are at 7 mm apart. (c) Coherence. The sample volumes are at 21 mm apart. The solid line is of  $\tilde{\phi}$  and the dashed line is of  $\tilde{n}_e$ .

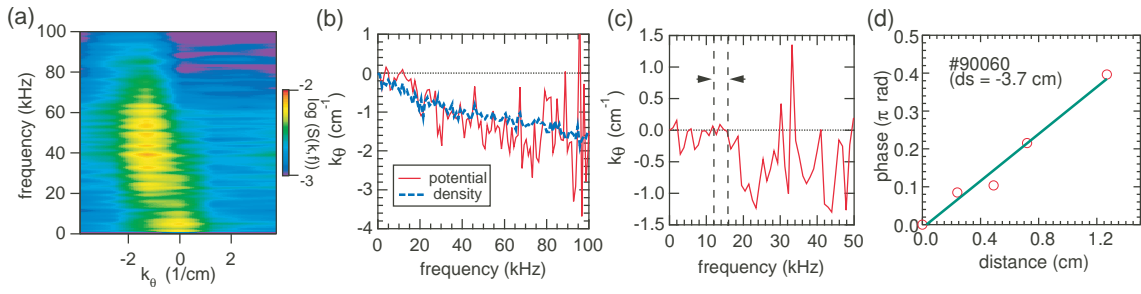


Fig. 4: (a) Dispersion relation of the normalized  $\tilde{n}_e$ . (b) Dispersion relation evaluated with phase difference. The sample volumes are at 7 mm apart. (c) Dispersion relation evaluated with phase difference. The sample volumes are at 21 mm apart. The solid line is of  $\tilde{\phi}$  and the dashed line is of  $\tilde{n}_e$ . (d) phase delay of  $\tilde{\phi}(f_{GAM})$  in the radial direction. The horizontal axis is the distance between sample volumes.

volumes is larger, the coherence between  $\tilde{n}_e$  signals is smaller in all frequency range. The coherence between  $\tilde{\phi}$  signals shows the similar tendency except that  $\tilde{\phi}$  near the GAM frequency keeps high coherence. That means the correlation length of  $\tilde{\phi}(f_{GAM})$  is longer than that of the ambient fluctuation in the poloidal direction.

#### 4.4 Wave number

First, the poloidal wave number ( $k_\theta$ ) is estimated. The sample volumes can be aligned on almost the same magnetic surface with intervals of 7 mm in the poloidal direction as mentioned above, so we can measure  $k_\theta$  of 4.5 (cm<sup>-1</sup>) or less. The dispersion relation of the density fluctuation is estimated with Fast Fourier Transform (FFT) (Fig. 4(a)). The dominant components exist in the frequency range of 40 - 60 kHz and  $k_\theta$  of 1 - 2 (cm<sup>-1</sup>). Its poloidal mode number is about 60 - 120.

Because the potential fluctuation is measured only in 4 sample volumes, it is difficult to estimate the dispersion relation with FFT. Thus, the dispersion relation is estimated through the phase difference ( $\Delta\phi$ ) between the signals from different sample volumes:  $k_\theta = \Delta\phi/\Delta l_p$ , where  $\Delta l_p$  is the distance between the sample volumes. The estimated dispersion relation of  $\tilde{\phi}$  is shown in Fig. 4(b). The distance of the sample volumes is 7 mm. It is similar to that of  $\tilde{n}_e$ . However,  $k_\theta$  around the GAM frequency is almost zero unlike that of  $\tilde{n}_e$ . That is due to  $\tilde{\phi}(f_{GAM})$  which has long correlation length in the poloidal direction, so  $k_\theta$  of  $\tilde{\phi}(f_{GAM})$  is estimated using the signals from the sample volumes located at 21 mm apart (Fig.4(c)). The phase difference around the GAM frequency is small, and the  $k_\theta$  is estimated as  $k_\theta = (-2 \pm 24) \times 10^{-3}$  (cm<sup>-1</sup>). The poloidal mode number is 1.5 or less. It does not contradict the predicted structure of GAM ( $m=0$ ).

Next, in order to estimate the radial wave number ( $k_r$ ), the sample volumes are set in the radial direction by means of optimization of the magnetic field strength and the energy of the injected heavy ion beam:  $B_t = 1.17$  T and  $W_0 = 350$  keV. The interval of the sample volumes is about 2.5 mm in the radial direction. The phase difference of  $\tilde{\phi}(f_{GAM})$  measured near 3.7 cm inside the separatrix is shown in Fig.4(d)). The  $k_r$  is estimated as  $k_r = \Delta\phi_r/\Delta ds$ , where  $\Delta\phi_r$  is the phase difference and  $\Delta ds$  is the distance between the sample volumes, and  $k_r = 0.94 \pm 0.05$  (cm<sup>-1</sup>). Evaluating  $k_r$  through  $|E_r| = |-\partial\phi/\partial r| = |k_r\phi|$  in Fig.2, it is consistent with the above  $k_r$ . The Larmor radius of the deuteron ( $\rho_i$ ) is 0.28 cm, where the ion temperature is 380 eV and the magnetic field strength is about 1 T, so  $k_r\rho_i = 0.26 < 1$ .

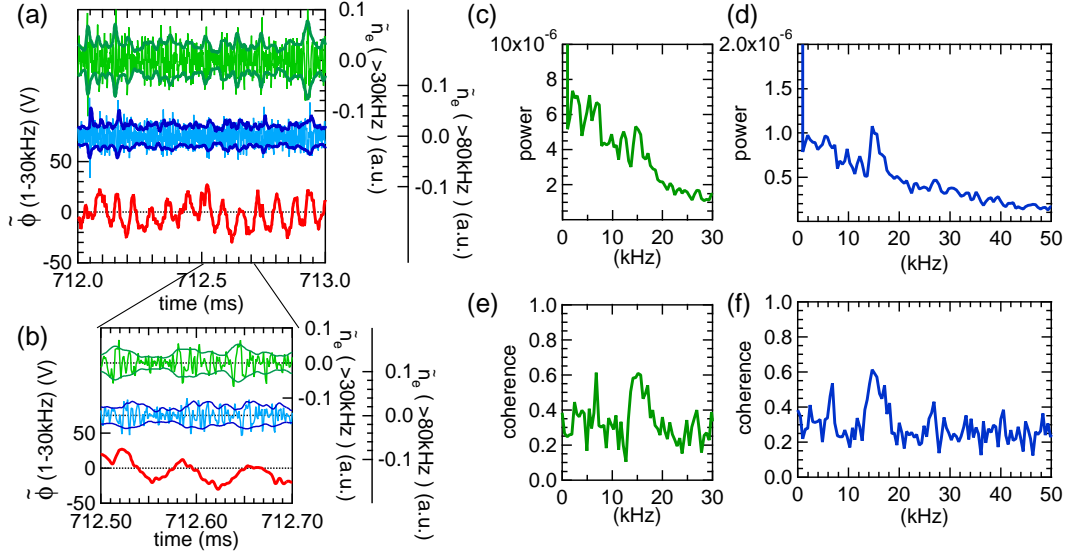


Fig. 5: Relation between  $\tilde{n}_e$  and  $\tilde{\phi}$ . (a):  $\tilde{n}_e$  with a frequency of 30 kHz and higher,  $\tilde{n}_e$  with a frequency of 80 kHz and higher, and  $\tilde{\phi}$  with a frequency from 1 to 30 kHz. The envelope of  $\tilde{n}_e$  is also shown. (b): Expanded view of (a). (c) and (d): power spectra of the envelope of  $\tilde{n}_e$  in (a). (e) and (f): coherence between  $\tilde{\phi}$  and the envelope of  $\tilde{n}_e$ .

#### 4.5 The amplitude of $\tilde{\phi}$ and normalized density fluctuation

The relation between the amplitude of  $\tilde{\phi}$  and normalized  $\tilde{n}_e$  of GAM is predicted as following equation [1]:  $|\tilde{n}_e(f_{GAM})/n_{e,0}| = \sqrt{2}k_r\rho_i |e\tilde{\phi}(f_{GAM})/T_e|$ . In the experiment, the right hand side of the equation is  $11 \times 10^{-3}$  at -3.7 cm inside the separatrix, where  $k_r\rho_i = 0.26$  estimated in the previous section,  $|\tilde{\phi}(f_{GAM})|$  is about 11 V (Fig.2(b)), and  $T_e = 380$  eV assuming  $T_e = T_i$  measured with CXS. The measured  $\tilde{n}_e(f_{GAM})/n_{e,0}$  is about  $9 \times 10^{-3}$ , thus the observed fluctuation with  $f_{GAM}$  has the same character as that of the predicted GAM.

### 5 Relation between the fluctuation with the GAM frequency and ambient fluctuation

The fluctuation with  $f_{GAM}$  probably produces the shear flow as inferred from Fig.2, so it possibly suppresses the ambient fluctuation. Originally, GAM is produced through nonlinear coupling of the turbulence. Therefore, it can regulate the power of the ambient fluctuation.

In order to see the temporal behavior of the amplitude of the ambient fluctuation, the envelope of  $\tilde{n}_e$  is evaluated (Fig.5(a) and (b)). The envelope is evaluated with Hilbert transform and a low pass filter whose cut-off frequency is 30 kHz. The envelope oscillates and it indicates the amplitude of  $\tilde{n}_e$  is modulated.

The frequency spectra of the envelopes of  $\tilde{n}_e$  with a frequency of 30 kHz or higher ( $\tilde{n}_e(f > 30 \text{ kHz})$ ) and 80 kHz or higher ( $\tilde{n}_e(f > 80 \text{ kHz})$ ) are shown in Fig.5 (c) and (d), respectively. A significant peak appears around the GAM frequency in each spectrum. It indicates  $\tilde{n}_e$  is modulated with the GAM frequency.

The coherence between the envelope of  $\tilde{n}_e$  and  $\tilde{\phi}(f_{GAM})$  is shown in Fig.5(e) and (f). There is a peak around the GAM frequency in each figure. Therefore, the modulation of  $\tilde{n}_e$  is closely related with the  $\tilde{\phi}(GAM)$ . It possibly shows the self-regulated mechanism of plasma turbulence with zonal flow (GAM).

Compared with the modulation of  $\tilde{n}_e(f > 80 \text{ kHz})$  with  $f_{GAM}$ , that of  $\tilde{n}_e(f > 30 \text{ kHz})$  is weaker

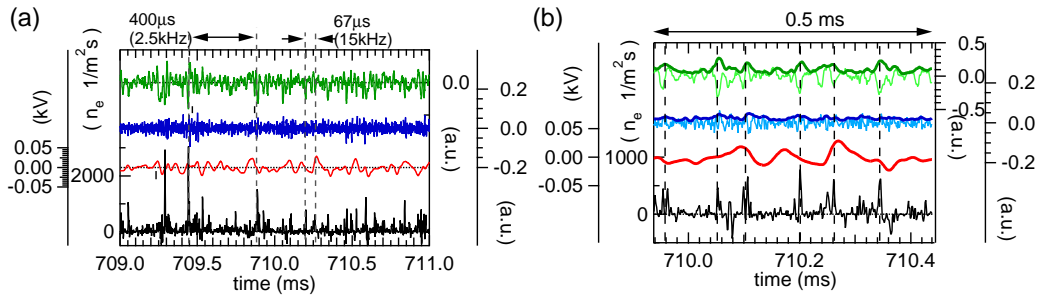


Fig. 6: (a)  $\tilde{n}_e$  with a frequency of 30 kHz and higher,  $\tilde{n}_e$  with a frequency of 80 kHz and higher,  $\tilde{\phi}$  with a frequency from 1 to 30 kHz, and  $\Gamma_f$  in L-mode. (b) the expanded view of (a). The envelope of  $\tilde{n}_e$  is also shown.

than the modulation with the lower frequency ( $<10\text{kHz}$ ). It may indicate that the turbulence with higher frequency is suppressed more efficiently by the oscillating shear flow of GAM [15].

## 6 Influence on the particle transport

The particle flux induced by the electrostatic fluctuation ( $\Gamma_f$ ) can be estimated with  $\tilde{E}_\theta$  and  $\tilde{n}_e$  measured with the HIBP;  $\Gamma_f = \tilde{n}_e \tilde{E}_\theta / B_t$ . The  $\tilde{E}_\theta$  is measured by the HIBP through alignment of the sample volumes on the same magnetic surface as described in section 4.3.

In L-mode, the average particle flux  $\langle \Gamma_f \rangle$  is about  $(80 \pm 40) \times n_e(r_{sv})$  ( $1/\text{m}^2 \text{ s}$ ), where  $n_e(r_{sv})$  is the local electron density in the sample volume. Assuming that the particle confinement time is 50 ms which is 5 times the energy confinement time, the particle flux ( $\Gamma$ ) is roughly estimated at about  $20 \times 10^{19}$  ( $1/\text{m}^2 \text{ s}$ ). The experimental result is  $\langle \Gamma_f \rangle \sim (80 \pm 40) \times 10^{19}$  ( $1/\text{m}^2 \text{ s}$ ), where  $n_e(r_{sv}) = 1 \times 10^{19}$  is assumed.  $\Gamma_f$  is the same as  $\Gamma$  in the order, so the measured  $\Gamma_f$  is possibly a major component of the total particle flux.

The measured  $\Gamma_f$  during L-mode is shown in Fig.6. It indicates intermittent behavior. Some spikes appear at intervals of about  $67 \mu\text{s}$ , which corresponds to  $f_{GAM}$ . They coincide with the increase in the amplitude of  $\tilde{n}_e$  as shown in Fig.6(b), thus the fluctuation with  $f_{GAM}$  affects the particle transport through the modulation of the ambient fluctuation. Larger spikes with longer period (several hundreds  $\mu\text{s}$ ) also appear in Fig.6(a), and it probably shows the existence of some other mechanism of the intermittent transport.

In this shot, bursting fluctuation appears with the repetition frequency of about 4 kHz just after the start of the formation of the edge transport barrier. After the burst continues for about 9 ms, and  $\tilde{E}_\theta$  and  $\tilde{n}_e$  are suppressed and the transition to the ELM-free H-mode occurs. The burst means the formation and disappearance of a weak transport barrier repeat at intervals of about 4 kHz [16].  $\tilde{\phi}(f_{GAM})$  and any spike with a time interval of GAM period does not appear in the burst phase. Therefore, other mechanism play the important role for the formation of the transport barrier.

## 7 summary

The characteristic electrostatic potential fluctuation measured by the HIBP is found to have the theoretically predicted characters of GAM: the frequency, the structure in the poloidal direction, wave numbers in radial and poloidal direction, and the relation between amplitude of  $\tilde{\phi}(f_{GAM})$  and that of  $\tilde{n}_e(f_{GAM})$ . Therefore, the fluctuation considered to be GAM.

The high coherence between the envelope of ambient fluctuation and the fluctuation with  $f_{GAM}$  clearly indicates that the modulation of the ambient fluctuation and the fluctuation with  $f_{GAM}$  is closely related.

The measured particle flux indicates the intermittent behavior. The fluctuation with  $f_{GAM}$  affects the particle transport through the modulation of the ambient fluctuation, however, it seems that the intermittent flux can not be explained only with the effect of GAM. And, it does not appear in H-mode and bursting phase but in L-mode and Ohmic phase. Therefore, other mechanism play the important role for the formation of the transport barrier.

### **Acknowledgement**

We are grateful to Professor K. Itoh, Professor K. Toi, Dr. A. Fujisawa, Dr. Y. Kishimoto, Dr. T. Matsumoto, and Dr. N. Miyato for fruitful discussions, and Dr. H. Ninomiya, Dr. M. Kikuchi, Dr. H. Kimura, Dr. M. Azumi, Dr. H. Kishimoto, Professor M. Fujiwara, and Professor O. Motojima for the continuous encouragement. We would like to thank Dr. Y. Uesugi for valuable suggestions. This work was carried out as a joint work under the Facility Utilization Program of JAERI.

### **References**

- [1] For review, see P. H. Diamond, S.-I. Itoh, K. Itoh, and T.S. Hahm, Plasma Phys. Control. Fusion in press
- [2] Z. Lin, T. S. Hahm, W. W. Lee, W. M. Tang, and R. B. White, Science **281** (1998) 1835
- [3] P. H. Diamond and et al., in Proceedings of the 17th IAEA fusion energy conference, Yokohama, 1998 **4** 1421. (International Atomic Energy Agency, Vienna, Austria, 1999)
- [4] M. G. Shats and W. M. Solomon, Phys. Rev. Lett. **88** (2002) 045001
- [5] G.R. McKee, and et al., Phys. Plasma, **10** (2003) 1712
- [6] G.S. Xu, B.N. Wan, and J. Song, M. Li, Phys. Rev. Lett. **91** (2003) 125001
- [7] A. Fujisawa and et al., Phys. Rev. Lett. in press
- [8] Y. Hamada and et al., submitted to Nucl. Fusion
- [9] N. Winsor, J. L. Johnson, and J. M. Dawson, Phys. Fluids **11** (1968) 2448
- [10] K. Hallatschek and D. Biskamp, Phys. Rev. Lett. **86** (2001) 1223
- [11] A. Fujisawa, H Iguchi, S. Lee, and Y. Hamada, Rev. Sci. Instrum. **68** (1997) 3393
- [12] T. Ido, and et al., Rev. Sci. Instrum. **70 partII** (1999) 955
- [13] T. Ido, and et al., Plasma Phys. Control. Fusion **41** (1999) 1013
- [14] T. Ido, and et al., Phys. Rev. Lett., **88** (2002) 055006
- [15] T.S. Hahm, and et al., Phys. Plasma, **6** (1999) 922
- [16] Y. Miura, and et al., Nucl. Fusion, **41** (2001) 973

## Configuration Dependence of Energetic Ion Driven Alfvén Eigenmodes in the Large Helical Device

S. Yamamoto 1), K. Toi 2), N. Nakajima 2), S. Ohdachi 2), S. Sakakibara 2),  
C. Nührenberg 3), K.Y. Watanabe 2), S. Murakami 4), M. Osakabe 2), N. Ohyabu 2),  
K. Kawahata 2), M. Goto 2), Y. Takeiri 2), K. Tanaka 2), T. Tokuzawa 2), K. Narihara 2),  
Y. Narushima 2), S. Masuzaki 2), S. Morita 2), I. Yamada 2), H. Yamada 2),  
LHD experimental group

1) Institute of Advanced Energy, Kyoto University, Uji, Japan

2) National Institute for Fusion Science, Toki, Japan

3) Max-Planck-Institute für Plasmaphysik, IPP-Euratom Association, Greifswald, Germany

4) Graduate School of Engineering, Kyoto University, Kyoto, Japan

e-mail contact of main author: syama@iae.kyoto-u.ac.jp

**Abstract.** Energetic ion driven Alfvén eigenmodes (AEs) such as toroidicity-induced AEs (TAEs) and helicity-induced AEs (HAEs) have been observed in neutral beam injection (NBI) heated plasmas of the Large Helical Device (LHD). It is important to clarify the configuration dependence of AEs because the existence and stability of them sensitively depend on the magnetic axis position and plasma beta. These parameters are scanned for the study of the configuration dependence of AEs in LHD. We have studied the energetic ion driven AE in plasmas obtained in three types of magnetic configuration. In order to identify the observed AEs, we have compared between the experimental data and the global mode analysis using CAS3D3. In the configuration with high magnetic shear, two TAEs with  $m\sim 2/n=1$  ( $m, n$ : poloidal and toroidal mode number) and  $m\sim 3/n=2$  are typically observed. In the configuration with medium magnetic shear, a number of TAE with  $n=2\sim 5$  are simultaneously observed. In the configuration with low magnetic shear, a number of bursting TAE are observed. We have studied the observed region of AEs in parameter space composed of the resonance and the stability conditions. From these studies of AE using global mode analysis in three-dimensional magnetic configurations, continuum damping of which damping rate depends on the magnetic shear is thought to be an important role in stabilizing AEs in LHD.

### 1. Introduction

Alfvén eigenmodes (AEs) destabilized by the energetic alpha particles are paid much attention in the physics design of a Deuterium-Tritium (D-T) reactor including the International Thermonuclear Experimental Reactor (ITER) [1]. Energetic alpha particles in a fusion reactor would resonate with MHD modes in course of the slowing down process and destabilize these MHD modes. In turn, the MHD modes would enhance radial transport of alpha particles before thermalization. This would quench fusion burn. Moreover, thus ejected energetic alpha particles might lead to significant damage of the first wall of a fusion reactor. For these reasons, energetic ion driven MHD instabilities such as toroidicity-induced Alfvén eigenmode (TAE) are being extensively studied in many major tokamaks [2] and helical systems [3-5] using energetic ions generated by the neutral beam injection (NBI) and/or ion cyclotron range of frequency heating (ICRH) as well as DT fusion reactions.

Alfvén eigenmodes such as TAEs and helicity-induced AEs (HAEs) [6,7] are observed in NBI heated plasma of the Large Helical Device (LHD) [8-10]. It is important to clarify the configuration dependence of AEs because the existence and stability of them sensitively depend on the radial profiles of the rotational transform  $\iota/2\pi$  ( $=1/q, q$ : safety factor) and the magnetic shear  $s$  ( $=\rho dq/[d\rho/q]$ ). These quantities in low  $\beta$  plasmas of LHD are basically determined by the magnetic axis position of the vacuum field ( $R_{ax}$ ). The finite plasma  $\beta$  effect and net plasma current  $I_p$  can considerably modify these quantities  $\iota/2\pi$  and  $s$ . In the plasma

of  $R_{ax}=3.6$  m, the magnetic shear tends to decrease with the increase in plasma  $\beta$  and finally changes the sign in the central region when averaged  $\beta$  approaches to  $\beta \sim 3\%$ . We have scanned the parameters  $R_{ax}$ ,  $\beta$  and  $I_p$  for the study of the configuration dependence of energetic ion driven AEs in LHD. We present experimental results of AEs observed in LHD and clarify the mode structures through comparison to numerical results by global mode analysis code for three-dimensional (3D) plasmas, CAS3D3 [11].

## 2. Observation of Alfvén Eigenmodes

We have studied the energetic ion driven AEs in NBI-heated plasma obtained in the following three types of magnetic configuration: (i) low  $\beta$  ( $<1\%$ ),  $R_{ax}=3.6$  m plasma with high magnetic shear, (ii) low  $\beta$  ( $<1\%$ ),  $R_{ax}=3.5$  m plasma with medium magnetic shear, and (iii) high  $\beta$  ( $>2\%$ ),  $R_{ax}=3.6$  m plasma with weak magnetic shear. The radial profiles of  $\iota/2\pi$  and  $s$  are shown in Fig. 1.

### 2.1. Configuration (i): High Magnetic Shear ( $R_{ax}=3.6$ m, low $\beta$ )

In the configuration (i), two TAEs with  $m \sim 2/n=1$  ( $m, n$ : poloidal and toroidal mode number) and  $m \sim 3/n=2$  are typically observed. A typical discharge in which the TAEs are observed is shown in Fig. 2, where hydrogen beams with the energy of  $E_{NBI}=150$  keV and the power of  $P_{NBI} \sim 4$  MW are tangentially co- and counter-injected into a helium plasma at  $R_{ax}=3.6$  m and magnetic field strength  $B_t=1.3$  T. After  $t \sim 0.65$  s, coherent magnetic fluctuations of which frequencies are scaled with the dependence of  $1/(n_e)^{1/2}$  are detected. In this phase, the parallel beam velocity  $v_{b\parallel}$  exceeds  $v_A/3$  ( $v_A$ : Alfvén velocity). A hydrogen ice pellet is injected into the LHD plasma at  $t \sim 0.8$  s, then electron density suddenly increases and coherent magnetic fluctuations are suppressed. The  $m \sim 2/n=1$  mode with the frequency  $f_{exp}=40 \sim 52$  kHz (at  $t=1.6$  s) and  $m \sim 3/n=2$  mode with  $f_{exp}=55 \sim 68$  kHz (at  $t=1.6$  s) are excited after  $t \sim 1.1$  s. As seen from the calculated TAE gap frequencies ( $f_{TAE}=v_A/4\pi R_{ax}$ : dotted and broken curves) shown in Fig. 2(a), the observed frequencies of the former mode and the latter mode respectively lie in the  $n=1$  TAE gap formed by  $m=2$  and 3, and  $n=2$  TAE gap formed by  $m=3$  and 4 poloidal mode coupling.

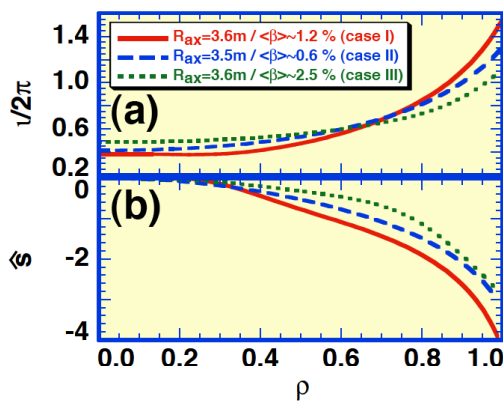


FIG. 1. Radial profiles of (a) rotational transform and (b) magnetic shear for the configuration (i), (ii) and (iii).

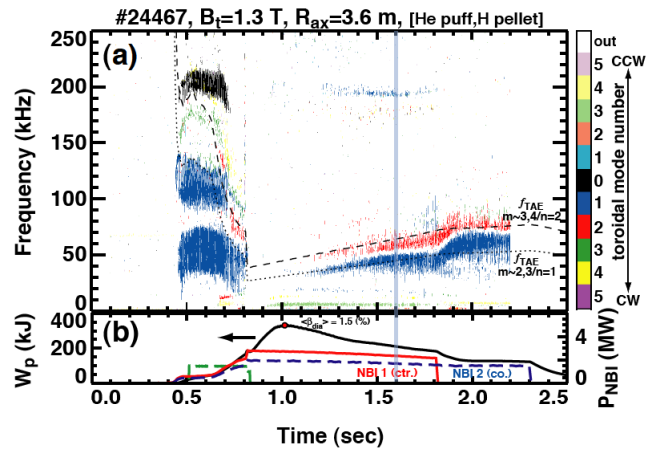


FIG. 2. Typical discharge where TAEs with  $m \sim 2/n=1$  and  $m \sim 3/n=2$  are observed in the plasma of  $R_{ax}=3.6$  m with high magnetic shear (configuration (i)).

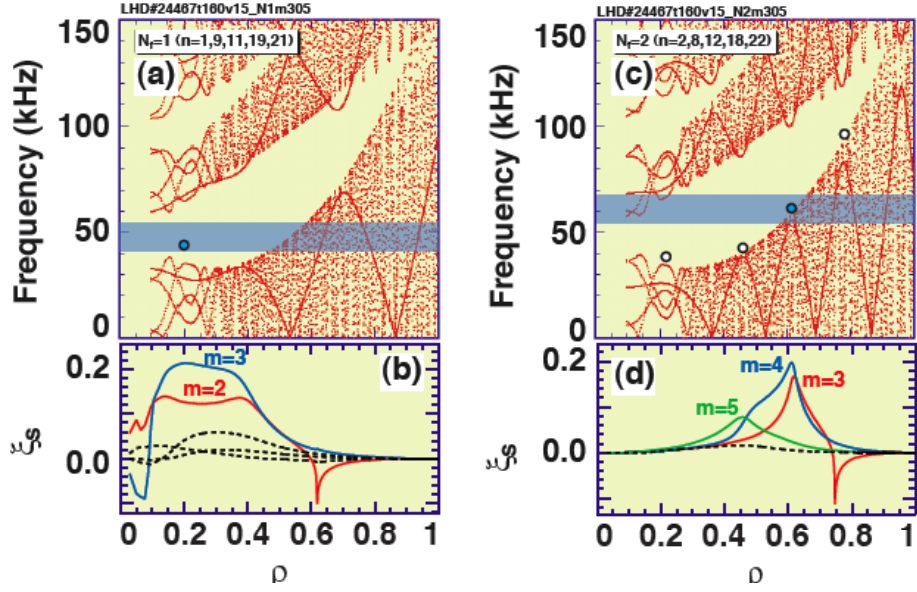


FIG. 3. Shear Alfvén spectra for (a)  $N_f=1$  and (d)  $N_f=2$ , and radial profile of discrete mode for (b)  $n=1$  and (d)  $n=2$ , of which frequency agree well with that of observed mode.

We compare these observed frequencies at  $t=1.6$  s in the plasma shown in Fig. 2 with the global mode analyses by CAS3D3 that are calculated for 3D magnetic configurations, where toroidal mode coupling is taken into account. The plasma compressibility is ignored (adiabatic index:  $\gamma \sim 0$ ) because the plasma  $\beta$  is not so high and shear Alfvén wave does not couple with sound wave. Shear Alfvén continua in the 3D case are also shown in Fig. 3(a) for  $N_f=1$  and in Fig. 3(c) for  $N_f=2$  ( $N_f$ : the number of toroidal mode family), where the toroidal mode coupling among  $n=\pm 1, \pm 9, \pm 11, \pm 19$  and  $\pm 21$  Fourier modes is taken into account for  $N_f=1$  and  $n=\pm 2, \pm 8, \pm 12, \pm 18$  and  $\pm 22$  modes for  $N_f=2$ . The shaded zone in Figs. 3(a) and (c) indicates the frequency of the observed mode. As seen from Fig. 3(a), the observed mode frequency lies in the innermost  $n=1$  TAE gap, which is formed by  $m=2$  and 3 poloidal mode coupling. The observed frequency intersects with the Alfvén continua with  $n=1$  at the edge of  $\rho \sim 0.65$ . The discrete mode of which eigenfunction has a peak at  $\rho \sim 0.18$  is marked by the open circle in Fig. 3(a) and its frequency agrees well with the observed mode frequency. The eigenfunction shown in Fig. 3(b) is basically composed by dominant two poloidal harmonics  $m=2$  and 3, and localized in the plasma core where magnetic shear is quite weak. The  $m \sim 2/n=1$  observed mode indicates a character of a core-localized type TAE (C-TAE) with even parity. The  $n=1$  C-TAE would not suffer from strong continuum damping near the plasma core with very low magnetic shear. The observed frequency of  $n=1$  C-TAE intersects with a lot of Alfvén continua for high- $n$  modes in the outer plasma region ( $0.45 < \rho < 0.65$ ). However, the  $n=1$  C-TAE would not suffer from continuum damping due to the high- $n$  modes belonging to  $N_f=1$  mode family. Therefore, the continuum damping due to the high- $n$  modes introduced by the toroidal mode coupling is quite weak in LHD as same as CHS [5]. The higher frequency mode ( $f_{\text{exp}}=55 \sim 68$  kHz) of  $m \sim 3/n=2$  is also analyzed by CAS3D3 code, as shown in Fig. 3(c). The calculated eigenfunction is shown in Fig. 3(d). As seen from these figures, the discrete mode mainly consists of three Fourier components with  $m=3, 4$  and 5, and intersect with the  $n=2$  shear Alfvén continuum at the  $\rho \sim 0.75$ . The eigenfunction of the observed  $m \sim 3/n=2$  mode extends radially from the gap toward central region with low magnetic shear. This mode exhibits a feature of global type TAE (G-TAE) and is different from the character of the observed  $n=1$  C-TAE.

## 2.2. Configuration (ii): Medium Magnetic Shear ( $R_{ax}=3.5$ , low $\beta$ )

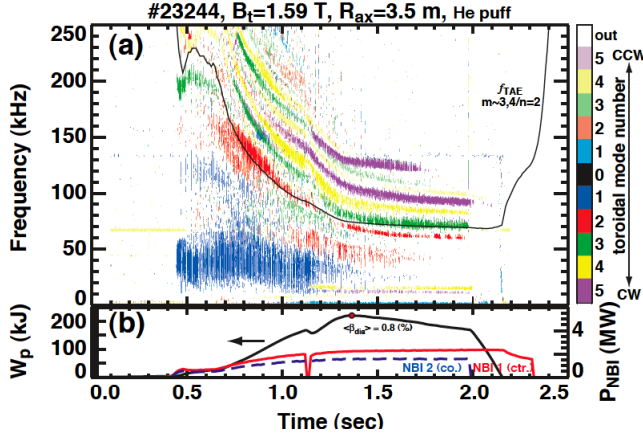


FIG. 4. Typical discharge where a number of TAEs are simultaneously observed in the plasma of  $R_{ax}=3.5$  m with medium magnetic shear (case (ii)).

In the configuration (ii), of which magnetic shear is smaller than that of  $R_{ax}=3.6$  m (configuration (i)), a number of TAE with  $n=2\sim 5$  are simultaneously observed, as shown in Fig. 4. These modes in the frequency range of 50 kHz to 250 kHz are excited in the time window of  $v_b/\nu_A > 1/3$ , having the mode numbers of  $m\sim 3/n=2, \sim 4/3, \sim 5/4$  and  $\sim 6/5$ . The frequency separation between neighboring modes is explained not by the effect of Doppler shift due to the toroidal plasma rotation, but by the TAE gap location of each modes. The calculated shear Alfvén continua with  $N_f=2$  and 5 at  $t=1.5$  s are shown in Figs.

5(a) and (c). The shaded zones in Fig. 5 indicate the observed frequencies of the mode  $f_{exp}=64\sim 67$  with  $m\sim 3/n=2$ , and  $98\sim 102$  kHz with  $m\sim 6/n=5$ , respectively. A lot of discrete modes are found in respective TAE gaps and the peak of each eigenfunction is represented by the solid circle in the Figs. 5(a) and (c). The calculated eigenfunctions for observed mode with  $n=2$  and 5 are shown in the Figs. 5(b) and (d). In contrast with the  $m\sim 3/n=2$  TAE observed in the configuration (i) (Figs. 3(d)), the TAE with  $n=2$  shown in Fig. 5(b) consists of two dominant Fourier components  $m=3$  and 4. This has a feature of “gap localized TAE” [10]. The TAEs with  $n=5$  shown in Fig. 5(d) consist of some poloidal components and localize around the TAE gap in the plasma outer region ( $\rho > 0.6$ ). The observed mode of  $f_{exp}=98\sim 102$  kHz with  $n=5$  would be EAEs existing in the

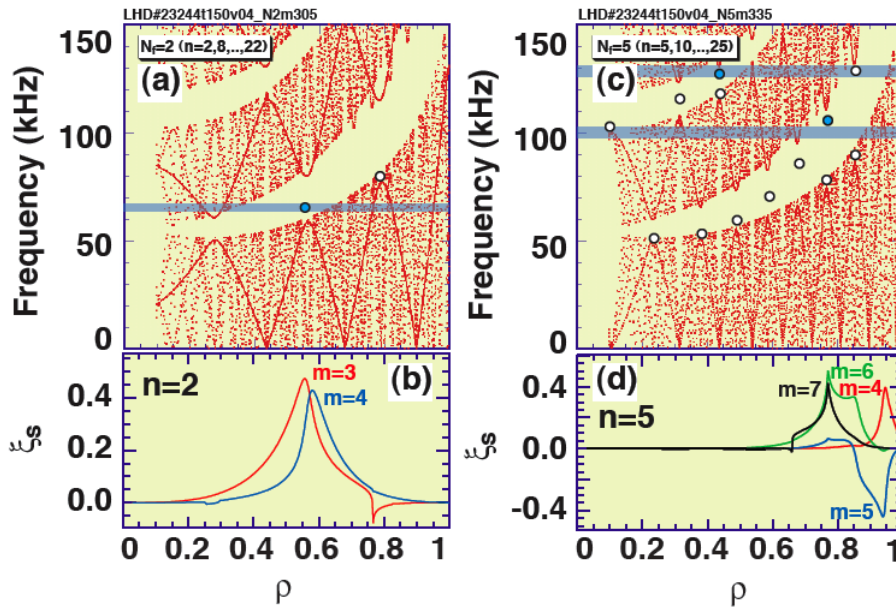


FIG. 5. Shear Alfvén spectra for (a)  $N_f=2$  and (d)  $N_f=5$ , and radial profile of discrete mode for (b)  $n=2$  and (d)  $n=5$ , of which frequency agree well with that of observed mode.

plasma core region ( $\rho \sim 0.1$ ). However, the dominant  $m$  number of observed modes ( $m \sim 6/n=5$ ) does not agree with that of EAE. In conclusion, the observed modes with  $n=5$  are thought to be TAEs existing in the outer region of  $\rho > 0.6$ . On the other hand, the observed highest frequency mode of  $f_{\text{exp}} \sim 129$  kHz is thought to be  $n=5$  EAE of which gap locates at  $\rho \sim 0.4$ .

### 2.3. Configuration (iii): Low Magnetic Shear ( $R_{\text{ax}}=3.6$ m, high $\beta$ )

In the configuration (iii), of which magnetic shear is further reduced from the core to the plasma peripheral region due to increased  $\beta$  even in the configuration of  $R_{\text{ax}}=3.6$  m, a number of bursting TAE are observed, as shown in Fig. 6. It is noted that bursting TAE appreciably affect the energetic ion transport and/or bulk plasma confinement because some plasma parameters, such as plasma stored energy  $W_p$  and  $H_{\omega}$ , are simultaneously modulated with bursting TAEs. The calculated shear Alfvén continuum with  $N_f=2$  at  $t=1.4$  s and the eigenfunction of the discrete mode are shown in Figs. 7(a) and (b), respectively. The TAE gaps are well aligned from the plasma core to the edge with fairly large gap width because of low magnetic shear and large Shafranov shift due to the finite  $\beta$  effect. The CAS3D3 analysis has demonstrated that the eigenfunction of TAE is widely extended from the core to the edge, clearly exhibiting G-TAE character (Fig. 7(b)). Accordingly, the G-TAE having bursting characteristics is strongly excited because of high pressure gradient region of energetic ions moves toward the edge and the growth rate of the mode will overcome continuum damping.

Beside the observation of TAEs, high frequency mode with  $n=2$ , of which frequency is about eight times higher than that of TAE gap, are newly observed in the plasma shown in Fig. 6. The coherent modes in the range of  $180 < f_{\text{exp}} < 220$  kHz are observed after  $t=1$  s. The observed modes are identified to be  $n=2$  and propagate in the diamagnetic drift direction of energetic ions. These modes are thought to be Alfvén eigenmodes, because the frequencies of these

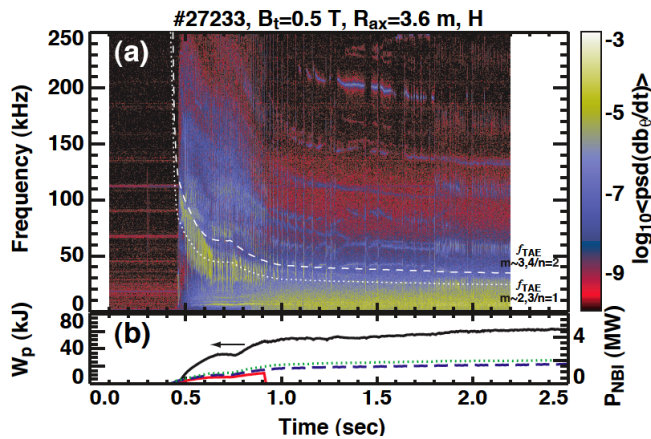


FIG. 6. Typical discharge where a number of bursting TAEs and a HAE are simultaneously observed in the high  $\beta$  plasma of  $R_{\text{ax}}=3.6$  m with low magnetic shear (case (iii)).

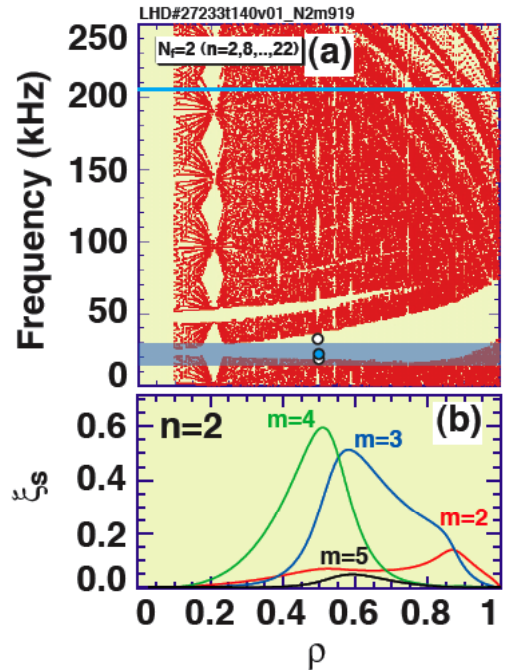


FIG. 7. Shear Alfvén spectra for (a)  $N_f=2$  and radial profile of discrete mode for  $n=2$  of which frequency agree well with that of observed mode. The observed frequency of HAE is also shown by blue solid line.

modes are proportional to the Alfvén velocity  $v_A$ . The toroidal mode coupling related to 3D magnetic configuration leads to a generation of new spectral gap, which is related to the helical fields components. In this new gap, the HAEs can be excited by the energetic ions. We compare these observed frequencies at  $t=1.4$  s of the plasma shown in Fig. 6 with the shear Alfvén spectrum for  $N_f=2$  as shown in Fig. 7. The HAE gap has a good alignment from the plasma core toward the edge. The continua with high- $n$  mode exist in HAE gap and the new continua inside HAE gap might be produced by the absence of helical symmetry of helical field components. The former continua may not affect the low- $n$  modes because the toroidal mode coupling is weak and the latter continua may affect the low- $n$  modes. The solid line in Fig. 7 indicates the measured frequency of magnetic fluctuation. The frequency lies in the HAE gap at the plasma edge ( $\rho \sim 0.8$ ) and intersects newly generated continua inside the HAE gap location. We predict that the modes would be excited in despite of the suffering of continua damping. The pressure profile of energetic ions is predicted to be flat because the Larmor radius of passing energetic ion reaches up to 10 % of plasma radius. Therefore, the pressure gradient of energetic ion has a peak near the plasma edge and the growth rate of the mode may be significantly large enough to overcome the damping. It is concluded from these analyses that the observed high frequency modes are thought to be HAEs.

### 3. Parametric Study for AEs

MHD instabilities will be destabilized by the energetic ions when a certain threshold conditions are satisfied. As regard to the AEs, the linear growth rate being proportional to the pressure gradient of energetic ions must be large enough to overcome the damping rate of the waves. This condition may be translated to the condition for the averaged beam beta  $\langle \beta_{b//} \rangle$ . Moreover, the velocity of energetic ions  $v_{b//}$  is required to satisfy the resonance condition with the Alfvén wave. The TAE resonance condition for the fundamental excitation is  $v_{b//}/v_A > 1$  and sideband excitation via the drift modulation of energetic ion orbit is  $v_{b//}/v_A > 1/3$ . We have investigated the excitation conditions of TAE and HAE in the parameter space of  $\langle \beta_{b//} \rangle$  and  $v_{b//}/v_A$  in the configurations of  $R_{ax}=3.6$  m and 3.5 m, changing various plasma parameters  $\langle n_e \rangle$ ,  $B_t$ ,  $P_{NBI}$ , and ion species (H/He). As shown in Fig. 8 for TAEs and Fig. 9 for HAEs, the parameters are scanned over wider range of  $\langle \beta_{b//} \rangle \leq 10$  % and  $v_{b//}/v_A \leq 4$ , compared with that in major tokamaks, W7-AS and CHS. It is clearly seen from Fig. 8 that the TAEs with  $m \sim 3/n=2$

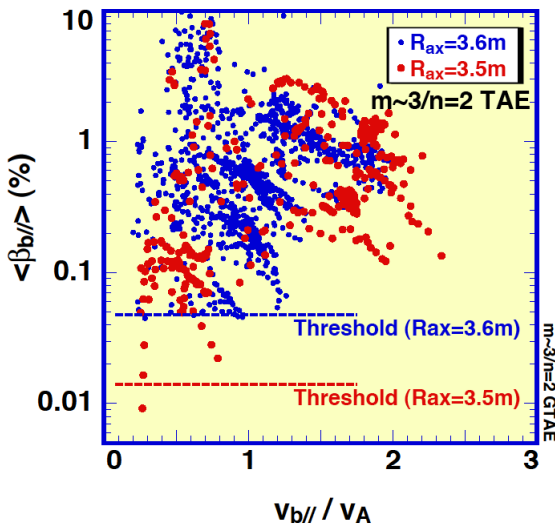


FIG. 8. Excitation region for  $m \sim 3/n=2$  G-TAEs in configuration of the  $R_{ax}=3.6$  m (blue circle) and 3.5 m (red circle).

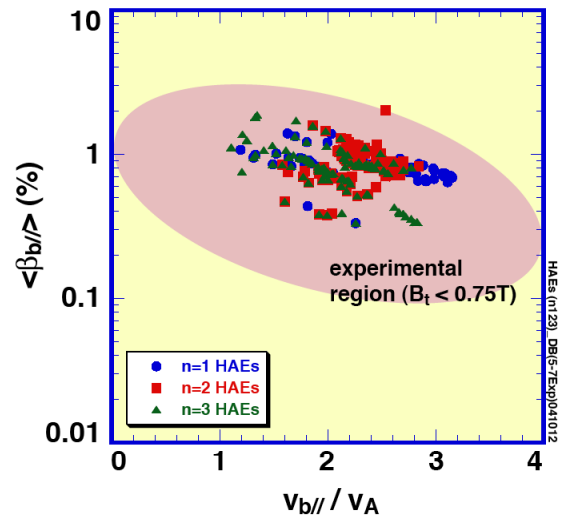


FIG. 9. Excitation region for HAEs with  $n=1,2,3$  in configuration of the  $R_{ax}=3.6$  m and  $B_t > 0.75$  T.

are destabilized in the condition of  $0.3 < v_{b//}/v_A < 2.0$  and  $\langle \beta_{b//} \rangle > 0.05$  % for  $R_{ax}=3.6$  m plasma (configuration (i) and (iii)), and  $0.3 < v_{b//}/v_A < 2.3$  and  $\langle \beta_{b//} \rangle > 0.01$  % for  $R_{ax}=3.5$  m plasma (configuration (ii)), respectively. This indicates that the TAEs are excited via sideband excitation ( $v_{b//}/v_A > 1/3$ ) as well as fundamental excitation ( $v_{b//}/v_A > 1$ ). TAEs are not observed in the region of  $v_{b//}/v_A > 2.3$  that corresponds to higher electron density. This result may be explained by fewer amounts of resonant energetic ions to destabilize TAEs against various damping mechanisms. The difference in the excitation threshold of  $m \sim 3/n=2$  G-TAEs in the  $R_{ax}=3.5$  m and  $R_{ax}=3.6$  m plasmas seems to be related to the difference of the damping rate. The  $m \sim 3/n=2$  G-TAEs would suffer from continuum damping, of which damping rate depends on the magnetic shear near the plasma edge. It is speculated that the damping rate of continuum damping of  $m \sim 3/n=2$  G-TAEs in the  $R_{ax}=3.6$  m plasmas are higher than that in the  $R_{ax}=3.5$  m plasmas, because the magnetic shear at edge of  $R_{ax}=3.6$  m plasma is larger than that in  $R_{ax}=3.5$  m plasma. The HAEs are only observed in the configuration of  $R_{ax}=3.6$  m and  $\beta \geq 2$  %. The HAEs with  $n=1 \sim 3$  are destabilized in the range of  $\langle \beta_{b//} \rangle \geq 0.4$  % and  $1 \leq v_{b//}/v_A \leq 3.2$ . This range of  $v_{b//}/v_A$  is consistent with the fundamental excitation of HAE with  $n=1 \sim 3$ .

#### 4. Summary

In NBI-heated LHD plasmas, various Alfvén eigenmodes destabilized by the energetic ions have been observed. The configuration dependence of AEs has been investigated for typical three configurations with high, medium and low magnetic shear. The frequencies of observed AEs agree well with the results from global mode analysis code CAS3D3 for three-dimensional plasmas. For the observed AEs, the eigenfunctions are also calculated by the code. The characteristic feature of these observed TAEs are identified, that is, core localized TAE (C-TAE), global TAE (G-TAE) and gap-localized TAE. Moreover, a new AE, that is, HAE has been observed for the first time in a certain condition. We have studied the excitation condition of G-TAEs in the configuration of  $R_{ax}=3.5$  m and  $R_{ax}=3.6$  m. These studies of AEs excitation in three magnetic configurations of LHD suggest that continuum damping plays an important role in stabilizing AEs.

#### Acknowledgements

The authors thank Professor O. Motojima (Director General of NIFS) and Professor M. Fujiwara (former Director General of NIFS) for their continuous encouragements. The authors also appreciate LHD technical group for their excellent operation of LHD. In particular, one of the authors (S.Y.) acknowledges the support by a 21st century program of "Establishment of COE on Sustainable Energy System" from JSPS, and is grateful to the Heliotron J staff of Kyoto University for stimulating discussions and continuous encouragements. This research is supported in the part by Grant-in-Aid for Scientific Research from JSPS, No.12480127 and from MEXT, No.16082209.

#### References

- [1] ITER Physics Expert Group on Energetic Particles, Heating and Current Drive Expert Group, ITER Physics Basic Editors, Nucl. Fusion **36** (1999) 2471.
- [2] WONG, K.L., Plasma Phys. Control. Fusion **41** (1999) R1.
- [3] WELLER, A., et al., Phys. Plasmas **8** (2001) 931.
- [4] TAKECHI, M., et al., Phys. Rev. Lett. **83** (1999) 312.
- [5] TOI, K., et al., Nucl. Fusion **40** (2000) 1349.

- [6] NAKAJIMA, N., CHENG, C.Z. and OKAMOTO, M., Phys. Fluids B **4** (1992) 1115.
- [7] KOLESNICHENKO, Ya.I., et al., Phys. Plasmas **8** (2001) 491.
- [8] TOI, K., et al., Plasma Phys. Control. Fusion **46** (2004) S1.
- [9] YAMAMOTO, S., et al., Phys. Rev. Lett. **91** (2003) 245001.
- [10] YAMAMOTO, S., et al., submitted to Nucl. Fusion.
- [11] NUEHRENBERG, C., Phys. Plasmas **6** (1999) 137.

## Density Limit Studies in the Large Helical Device

B. J. Peterson, J. Miyazawa, K. Nishimura, S. Masuzaki, Y. Nagayama, N. Ohyaabu, H. Yamada, K. Yamazaki, T. Kato, N. Ashikawa, Yuhong Xu<sup>1</sup>, A. Yu. Kostrioukov<sup>2</sup>, Yi Liu<sup>3</sup>, R. Sakamoto, M. Goto, K. Narihara, M. Osakabe, K. Tanaka, T. Tokuzawa, M. Shoji, H. Funaba, S. Morita, T. Morisaki, O. Kaneko, K. Kawahata, A. Komori, S. Sudo, O. Motojima and the LHD Experiment Group

National Institute for Fusion Science, Toki-shi, Gifu-ken 509-5292 JAPAN

<sup>1</sup>Forschungszentrum Juelich, Juelich, Germany

<sup>2</sup>St. Petersburg Technical University, St. Petersburg, Russia

<sup>3</sup>Southwest Institute of Physics, Chengdu, China

e-mail contact of main author: [peterson@LHD.nifs.ac.jp](mailto:peterson@LHD.nifs.ac.jp)

PACS 52.55.Hc, 52.25.Vy, 52.25.Fi

**Abstract.** Steady state densities of up to  $1.6 \times 10^{20} \text{m}^{-3}$  have been sustained using gas puff fuelling and NBI heating up to 11 MW in the Large Helical Device (LHD). The density limit in LHD is observed to be  $\sim 1.6$  times the Sudo limit. The density is ultimately limited by radiative collapse which is attributed to the onset of a radiative thermal instability of the light impurities in the edge region of the plasma based on several observations. First of all the onset of the radiative thermal instability is tied to a certain edge temperature threshold. Secondly, the onset of thermal instability occurs first in oxygen and then carbon as expected from their cooling rate temperature dependencies. Finally, radiation profiles show that as the temperature drops and the plasma collapses the radiating zone broadens and moves inward. In addition, comparison with the total radiated power behaviour indicates that Carbon is the dominant radiator. Two dimensional tomographic inversions of AXUVD array data and comparison of modelling with images of radiation brightness from imaging bolometers and indicate that the poloidal asymmetry which accompanies the radiative collapse is toroidally symmetric. In addition to the operational density limit where the discharge is terminated by radiative collapse, a confinement limit has been recognized in LHD. This confinement limit appears at lower density than the operational density limit, similar to the saturated ohmic confinement observed in tokamaks. To investigate the physics behind this degradation, the parameter dependence of the thermal diffusivity,  $\mathbf{c}$ , has been investigated. While the temperature dependence in ISS95 is as strong as the gyro-Bohm model of  $\mathbf{c} \propto T_e^{1.5}$ , weaker  $T_e$  dependence of  $\mathbf{c}$

$\propto T_e^{0.5}$  appears in the high-density regime. Such weak  $T_e$  dependence results in the weak density dependence of the global energy confinement as  $\tau_E \propto \bar{n}_e^{-1/3}$ .

## 1. Introduction

Density limit is an important issue for future fusion reactors since the fusion reaction rate is a function of the density squared. In tokamaks an empirical density limit (Greenwald limit) has been observed which scales with the plasma current density. Densities above the Greenwald limit have been achieved primarily in tokamaks using pellet injection to achieve peaked density profiles, indicating that the density limiting process is related to the physics of the edge plasmas. As the density limit in a tokamak is approached, the MARFE phenomenon is commonly observed and the discharge is ultimately terminated by a current disruption which can cause considerable damage to the device from induced currents and runaway electrons [1].

On the other hand, the operational density in stellarators is not limited by current disruption as in tokamaks, nor is the Greenwald limit directly applicable to net-current free plasmas. Studies on Heliotron-E resulted in an empirical density limit scaling law (Sudo limit) which is proportional to the square root of the product of the input power density and the magnetic field [2]. In the W7-AS stellarator, using a graphite limiter configuration, the density limit was attributed to power imbalance due to strong radiation from heavy impurities from the core of the plasma. This study also revealed a density limit scaling law very similar to the Sudo limit [3]. With the addition of a graphite island divertor in W7-AS, at high densities the radiation profile became hollow with the pumping out of impurities from the core and much higher steady state densities of up to  $3.5 \times 10^{20} \text{ m}^{-3}$  could be achieved. However, when the higher deposited power was considered the previously derived scaling law was still obeyed [4].

Initial investigations into the density limit on the Large Helical Device (LHD) [5] have indicated that the density in LHD is limited by a radiative thermal instability which results in the collapse of the plasma at a limit which is 1.4 times the Sudo limit. This collapse is characterized by a poloidal asymmetry in the radiation and density with the high density and high radiation region on the inboard side. Further investigation of this phenomenon showed that the poloidal asymmetry also appears in the electron temperature profiles (lower temperature on the inboard side) as the plasma column contracts [6]. Measurements with imaging bolometers indicated that the radiation asymmetry was located on the inboard side slightly below the midplane [7]. Also, after boronization of the vacuum

vessel wall, indeed, the radiation loss,  $P_{\text{rad}}$ , decreases about 20 ~ 50 %, compared at similar density and input power,  $P_{\text{abs}}$ , and the density limit increases 20 ~ 50 % [8]. These results indicate the importance of  $P_{\text{rad}}$  on density limit studies. However, the thermal instability is typically triggered even when  $P_{\text{rad}}$  is less than a half of  $P_{\text{abs}}$ . These observations call for an investigation of the role of  $P_{\text{rad}}$  and the exploration of the mechanism which triggers or enhances the thermal instability.

Confinement properties in the high-density region are also important as degradation of confinement in the edge region may be related to the onset of the thermal instability. Other than the operational density limit where the discharge is terminated by radiative collapse, a confinement limit has been recognized in LHD. The energy confinement times,  $t_E$ , of the moderate density LHD plasmas are well reproduced by the international stellarator scaling 95 (ISS95), which has strong positive density dependence as  $t_E \propto \bar{n}_e^{0.51}$ . In the high-density regime, however, the energy confinement is lower than the prediction of ISS95 [9]. This confinement limit appears at lower density than the operational density limit, similar to the saturated ohmic confinement observed in tokamaks. To investigate the physics behind this degradation, the parameter dependence of the thermal diffusivity,  $\kappa$ , is investigated.

In this paper we expand on this research, reporting the most recent results of efforts to increase the density in LHD and investigating the density limit from various perspectives including the plasma behaviour in the divertor region, confinement degradation at high density, etc.

## 2. Peak density parameters and scaling in LHD

LHD is the largest superconducting heliotron-type fusion device with an averaged minor radius of  $a = 0.65$  m and a major radius of the plasma axis of 3.6 m [10]. In the latest experimental campaign in the Large Helical Device (LHD), line-averaged densities of up to  $1.6 \times 10^{20} \text{m}^{-3}$  have been sustained for more than 0.7 s by 11 MW neutral beam injection using gas puff fuelling. An example of one of these high density discharges is shown in Figure 1. This value of density corresponds to 1.36 times Sudo scaling, which is close to what was observed previously. In addition, using multiple hydrogen pellets, the density has been increased to over  $2 \times 10^{20} \text{m}^{-3}$  transiently as shown in Figure 2.

Data from the most recent campaign also shows a limit which exceeds the Sudo limit by a factor of approximately 1.6 (see Figure 3) as was seen in previous studies [5,6].

### 3. Evolution of parameters leading to radiative collapse at the density limit

#### 3.1 Evolution of bulk parameters

The terminal phase of a typical discharge with radiative collapse is shown in Fig. 4. During the steady state portion of the discharge prior to 2 s, the radiation is proportional to the line-averaged density,  $\bar{n}_e$ . This phase ends when the radiative thermal instability is triggered as indicated by the sharp increases in  $P_{\text{rad}}$  and the light impurities emission. After this point the radiation increases rapidly and its dependence on the density becomes stronger than linear (as seen in Figure 5) as the plasma column starts to contract. The critical time ( $t_c = 2.1$  s in Fig. 4 and Fig. 5) of the onset of the thermal instability is defined as when  $P_{\text{rad}}$  is proportional to  $\bar{n}_e^3$  (see Fig. 4(e) and Fig. 5, where  $x = (dP_{\text{rad}}/dt/P_{\text{rad}}) / (d\bar{n}_e/dt/\bar{n}_e)$ , which we call the density exponent given by  $P_{\text{rad}} = \bar{n}_e^x$ ). The density exponent of 3 is somewhat arbitrarily chosen as being well above one. This gives us a convenient means to quantify the onset of the thermal instability for comparing various discharges. Fig. 6 shows the evolution of the electron temperature at  $r = 0.9$  versus the line-averaged density. The temperature increases as the plasma is heated and the stored energy increases, then peaks as the stored energy saturates. In an attempt to maintain constant pressure and stored energy the temperature then decreases as the density continues to increase with gas puffing. The white circles indicate the points in time,  $t_c$ , where  $x = 3$ , which we defined as the onset of the thermal instability. These points occur invariably at a temperature at  $r = 0.9$  of 150 eV. At this time, when the thermal instability is initiated, the edge (at  $r = r/a = 0.9$ ) temperature is consistently observed to decrease to about 150 eV regardless of the input power and plasma density as is seen in Fig. 6 and regardless of the magnetic axis position, the puffed gas or the density as seen in Fig. 7. This characteristic edge temperature is insensitive to  $P_{\text{abs}}$  and  $\bar{n}_e$  as long as the wall condition is maintained, confirming that the onset of the thermal instability is closely tied to the edge plasma temperature. While we believe the thermal instability is triggered further out in minor radius at a lower electron temperature, we do not have good measurements in that range of electron temperature

(below 50 eV), therefore we have chosen  $r = 0.9$  for our analysis point. After  $t_c$  the temperature at  $r = 1$  has dropped below the measurable limit of 50 eV, which is the temperature below which the oxygen radiation grows, rapidly leading to the onset of the radiative thermal instability as seen in Fig. 4(c). This is followed  $\sim 50$  ms later by  $C_{III}$  which becomes unstable at a lower electron temperature. The radiation is also enhanced after  $t_c$  as the hot plasma column shrinks leaving an increasingly larger volume of low temperature plasma in which the light impurities radiate strongly. After  $t_c$  the edge temperature decreases faster than that at the core (Fig. 4(d)), presumably due to radiative cooling in the edge by light impurities. Comparison of the growth rate of the  $O_V$  radiation in Fig. 4(c) with the decay rate of the stored energy in Fig. 4(a) also indicates that the edge radiative losses are responsible for the confinement degradation.

### 3.2 Radiated power fraction

Comparison of the input power of the NBI and the radiated power from the bolometer in Fig. 4(b) indicates that the total radiated power fraction is around 40% at the onset of the thermal instability at  $t_c$  and then increases rapidly to transiently exceed the input power at the collapse. This level of radiated power fraction is commonly observed at the onset of the thermal instability leading to radiative collapse as is seen in Fig. 8 in data from the third and fourth campaigns of LHD. These are for discharges with hollow radiation profiles or low levels of metallic impurities from the stainless steel walls during discharges using the graphite helical divertor. However, much higher radiated power fractions of up to 100% were observed without collapse in discharges using a stainless steel divertor [11] or a stainless steel limiter [12] with significant levels of radiation from the core resulting from metallic impurities. This indicates that the edge radiation from lighter impurities is playing the primary role in determining the onset of the thermal instability and the collapse of the plasma at the density limit. It should be noted that this estimate of the total radiated power is not based on power balance, but on the volume integration of the radiation profiles for the region inside the last closed flux surface and the ergodic edge region obtained by tomographic inversion of bolometer array signals [13]. Thus, it does not include the divertor leg region whose radiation is difficult to estimate due to the limited number of detectors, uncertainty regarding the size of the radiating volume

and the toroidal and poloidal asymmetries in this region. Therefore the neglect of this region may result in an underestimation of the total radiated power.

### **3.3 Edge parameters and role of light impurities**

Since the dominant intrinsic light impurities are oxygen and carbon they should be responsible for the strong increase in the radiation from the edge. First we consider the radiation brightness from the divertor, core and edge plasmas in Fig. 9 as the discharge shown in Fig. 4 collapses. One notes that the onset of the thermal instability, as defined by the red dashed line when  $x = 3$  for the total radiation, is followed by the development of the previously observed asymmetry in the radiation as the radiation from the inboard channel starts to diverge from the channel located near the outboard edge of the plasma. At the same time the radiation from the divertor leg region is increasing, but not as dramatically as the radiation from the inboard side. The ion-saturation current from the divertor probe begins to drop with the onset of the thermal instability and the radiation asymmetry as it approaches a detached state. Finally, considering the density exponents of the light impurities signals, CIII and OV, and the radiated power, one notes that the thermal instability begins in the OV, but that the CIII signal most closely matches the total radiated power indicating that the carbon is the dominant impurity. This temporal progression makes sense in that the oxygen should radiate at a higher temperature, and therefore the thermal instability should begin earlier in the oxygen as the edge temperature drops. Also, the above suggestion, that carbon is the dominant impurity, is consistent with observations before and after boronization, that while the reduction of OV radiation is stronger than that seen in the reduction of CIII, the reduction in CIII more closely matches the reduction in the total radiated power [8].

### **3.4 Evolution of radiation profiles during collapse**

In Fig. 10 the evolution of the radiated power density profile from the bolometer array at the horizontally elongated cross-section [13] is shown. In the steady state portion of the discharge the profile is hollow. After the onset of the thermal instability the strongly radiating zone broadens and moves inward minor radially. Also one notes some indication of growth in the core radiation. At the edge of the plasma one notes the radiation reaches a maximum then decreases, then increases again.

This is also seen in the inboard channel of the bolometer in Fig. 8 and may be related to the two peaks observed in the cooling rate of the impurities as a function of electron temperature. One should take care in the quantitative evaluation of the radiation profile during the collapsing phase as the asymmetry in the radiation signal may lead to errors in the tomographic inversion. These errors should be mitigated in this case by the orientation of the array which fans out vertically while the asymmetry has an inboard-outboard nature.

### 3.5 Radiation asymmetry at collapse

As was seen in Fig. 9 and as was reported previously [5,6,7] a MARFE-like asymmetry is observed during the radiative collapse in various diagnostics including two resistive bolometer arrays, Thomson scattering and the FIR interferometer, each located at a different toroidal angle spread through one half of the torus. All of these diagnostics indicate that the low temperature, high density, high radiation region is located on the inboard side, suggesting that this poloidally asymmetric feature is toroidally symmetric. In Fig. 11 we show the results of two imaging bolometers [13] at two different times, compared with images calculated from models of the radiation. The left hand set of images come from the steady state period of the discharge which has a poloidally and toroidally symmetric hollow profile which is confirmed by the images calculated from a toroidally and poloidally symmetric hollow radiation profile. In the left hand set of images, the data from the imaging bolometers taken from later in the same discharge during the radiative collapse are compared with images calculated from the same hollow profile multiplied by a poloidally asymmetric (yet toroidally symmetric) term given as

$$S(\mathbf{r}, \mathbf{q}) = S(\mathbf{r}) \cdot [1 + F(\mathbf{q})] \quad \text{and} \quad F(\mathbf{q}) = \left( (1 + \cos(\mathbf{q} + 150)) / 2 \right)^{50}.$$

This data shows the high radiation region moving to the inboard side slightly below the midplane as reported earlier [7].

In Fig. 12 the tomographic reconstructions for the same shot and time slices as in Fig. 11 are shown from two arrays of AXUV diodes which are mounted in a semi-tangential cross-section on LHD [13]. This is at a toroidal location which is one third of the way around the machine from the

imaging bolometers described earlier. The data shown is from the same discharge and time slices shown in Fig. 11. At the toroidal location of these arrays a gas puff valve is located directly beneath the arrays. The strong signal at the bottom of figure 12(a) comes from the puffed in gas. Besides this feature the radiation is rather symmetric. In Fig. 12(b) the high radiation zone has moved to the inboard side, but at a poloidal angle which is closer to the horizontal midplane than that seen in Fig. 11. The comparison in Fig. 11 of the model with the data taken together with the results from the diodes in Fig. 12 and other diagnostics mentioned above indicates that this phenomenon is toroidally symmetric, which is another aspect which it has in common with a MARFE.

#### 4. Confinement in the high-density regime

Energy confinement time compared with ISS95 scaling declines in high-density and high-collisionality regime as shown in Fig. 13. This degradation mainly results from the loss of a strong, positive density dependence as in ISS95. Although the shallow penetration of the heating beams in the high-density regime is also a possible cause, it is not sufficient to explain the degradation from ISS95.

In the gyro-Bohm model, the thermal diffusivity is predicted to increase with  $T_e^{1.5}$ . The dimensionless form of ISS95 has a gyro-Bohm like parameter dependence and this is reflected in the strong positive density dependence. The electron temperature dependence of the effective thermal diffusivity,  $\mathbf{c}_e^{\text{eff}}$ , is shown in Fig. 14. In the high-collisionality (low-temperature) regime, a weak temperature dependence of  $\mathbf{c}_e^{\text{eff}} \propto T_e^{0.5}$  appears. As the temperature increases, a stronger temperature dependence as predicted by the gyro-Bohm model ( $\mathbf{c}_e^{\text{eff}} \propto T_e^{1.5}$ ) and/or neo-classical theory ( $\mathbf{c}_e^{\text{eff}} \propto T_e^{4.5}$ ) appears. These temperature dependences are observed independent of  $\mathbf{r}$ . The weak temperature dependence of  $\mathbf{c}_e^{\text{eff}} \propto T_e^{0.5}$  leads to the weak density dependence of the energy confinement time of  $t_E \propto \bar{n}_e^{-1/3}$ . Therefore, the degradation from ISS95 in the high-density regime can be attributed to the change in the temperature dependence of the thermal diffusivity.

#### 5. Discussion

That LHD plasmas can achieve high density steady state discharges at levels which are 1.6 times the Sudo limit has been confirmed with the most recent data taken at NBI powers of up to 11 MW. The assumption that the collapse of the plasma at the density limit is caused by a radiative thermal instability is supported by several observations. (1) There is a threshold edge temperature below which the radiative thermal instability is initiated, leading to the collapse. (2) As the plasma collapses, radiation from oxygen increases first (since it radiates at a higher temperature) followed by carbon (radiating at a lower temperature) which is the dominantly radiating intrinsic impurity. (3) Radiation profiles show that as the temperature drops and the plasma collapses, the radiating zone broadens and moves inward. Additional evidence that the poloidally asymmetric feature observed during the collapse is toroidally symmetric indicates that this phenomenon is a toroidal effect, as in a tokamak MARFE, and is not related to the geometry of the magnetic field nor of the vacuum vessel, both of which are highly three-dimensional in LHD. Finally, studies show that confinement in the high density regime is degraded compared to ISS95 scaling due to a weakening temperature dependence of the thermal diffusivity. This degradation of confinement as density increases leads to an even more rapid drop in the temperature thereby more rapidly reaching the edge threshold temperature where the onset of the radiative thermal instability is triggered.

It is interesting that while LHD does not have any considerable plasma current which can disrupt and terminate the discharge at high density as in a tokamak, there are several common features of the density limiting phenomena in both types of devices. One is a role played by the edge plasma and the other is the MARFE-like asymmetries observed. Several questions remain unanswered regarding the collapse of the plasma in LHD. While we have evidence that the radiation from carbon is playing a key role in the radiative collapse, it is not clear if the rapid increase in radiation can be solely attributed to the dropping edge temperature leading to an increase in the cooling rate, or if the impurity density might be increasing due to some enhanced transport or recycling. Recent measurements of radial electric field during the collapse indicate that transition of the edge electric field from positive to negative due to an increase of the density may be contributing to the inward flux of impurities [14]. Further clarification of these issues will require detailed transport modeling of spectroscopic data from during the plasma collapse.

While the density limit in LHD appears to be well above the scalings seen for other helical devices, this study does not provide a new scaling for LHD. One difficulty in deriving such a scaling is in determining the criteria for the selection of the density to be used in the scaling study. In previous studies the value of the density used was that taken when the stored energy reached a maximum in time. However this does not necessarily represent the maximum attainable density. We would suggest that a future scaling study for LHD use, as a criteria for the selection of the density, the onset of the thermal instability as defined in this paper as the point when the radiation increases as the third power of the density. Experiments on LHD (not reported in this paper) using cessation of gas puffing or addition of NBI power to recover from the collapse after the onset of the thermal instability indicate that the level of density achieved at the onset of the thermal instability may be sustainable using the appropriate feedback mechanism (for instance the inboard/outboard asymmetry observed in the bolometer array brightness signals) to avoid the collapse.

- [1] GREENWALD, M., Plasma Phys. Control. Fusion **44** (2002) R27.
- [2] SUDO, S., et al., Nucl. Fusion **9** (1990) 11.
- [3] GIANNONE, L., et al., Plasma Phys. Control. Fusion **42** (2000) 603.
- [4] GIANNONE, L., et al., Plasma Phys. Control. Fusion **44** (2002) 2149.
- [5] PETERSON, B.J., et al., Phys. Plasmas **8** (2001) 3861.
- [6] XU, YUHONG, et al., Nucl. Fusion **42** (2002) 601.
- [7] ASHIKAWA, N., et al., J. Nucl. Mater. **313-316** (2003) 1103.
- [8] NISHIMURA, K., et al., J. Plasma Fusion Res. **79** (2003) 1216.
- [9] YAMADA, H., et al., Nucl. Fusion **43** (2003) 749.
- [10] MOTOJIMA, O., et al., this conference, submitted to Nuclear Fusion
- [11] PETERSON, B.J., et al., Nucl. Fusion **41** (2001) 519.
- [12] PETERSON, B.J., et al., J. Nucl. Mater. **313-316** (2003) 1178.
- [13] PETERSON, B.J., et al., Plasma Phys. Control. Fusion **45** (2003) 1167.
- [14] IDA, K., et al., this conference, submitted to Nuclear Fusion

## Figure Captions

Fig. 1. Typical waveforms of a high density discharge using gas puff fuelling (shot #46289) (a) line-averaged density and gas-puff timing, (b) deposited NBI power, (c) spectroscopy signals from OV and CIII, and (d) total plasma stored energy and total radiated power.

Fig. 2. Typical waveforms of a high density discharge using gas puff and hydrogen pellet fuelling (shot #47492) (a) line-averaged density and gas-puff timing, (b) deposited NBI power, (c) spectroscopy signals from OV and CIII, and (d) total plasma stored energy and total radiated power.

Fig. 3. Density limit scaling for LHD data taken at the timing of maximum stored energy plotted versus the Sudo limit. Green line indicates a factor of 1.6.

Fig. 4 Typical waveforms of a discharge terminated by radiative collapse in LHD for shot 43383.

Fig. 5 Radiated power dependence on density for LHD shot 43383.

Fig. 6 Evolution of edge electron temperature at  $r = 0.9$  as a function of line-averaged density for varying input powers.

Fig. 7 Edge ( $r = 0.9$ , open symbol) and core ( $r = 0.1$ , solid symbol) electron temperature dependence on line-averaged density for Hydrogen (red) and Helium (blue) puffing and axis positions at the onset of the thermal instability, when  $x = 3$ .

Fig. 8 Radiated power fraction versus density at the onset of the thermal instability for collapsing shots (triangles) and at the peak density for non collapsing shots (circles) from the third and fourth campaigns in LHD.

Fig. 9 Time evolution of bolometer brightness, divertor ion saturation current, and the density exponent for the total radiated power, CIII and OV data shown in Fig. 4.

Fig. 10 Evolution of radiated power density profile during radiative collapse of shot 43383. Red dashed line indicates the onset of the radiative instability ( $x = 3$ ).

Fig. 11 IRVB radiation brightness image (d) data from (u) upper and (t) tangential ports during the (s) steady state and (a) asymmetric phases of the discharge compared with reconstructions from (m) model profiles.

Fig. 12 Two dimensional tomographic images of radiation intensity measured with AXUVD arrays in LHD for the same shot and time slices shown in Fig. 11.

Fig. 13 Degradation from ISS95 in the high-collisionality regime.

Fig. 14 Electron temperature dependence of the effective thermal diffusivity.

## Figures

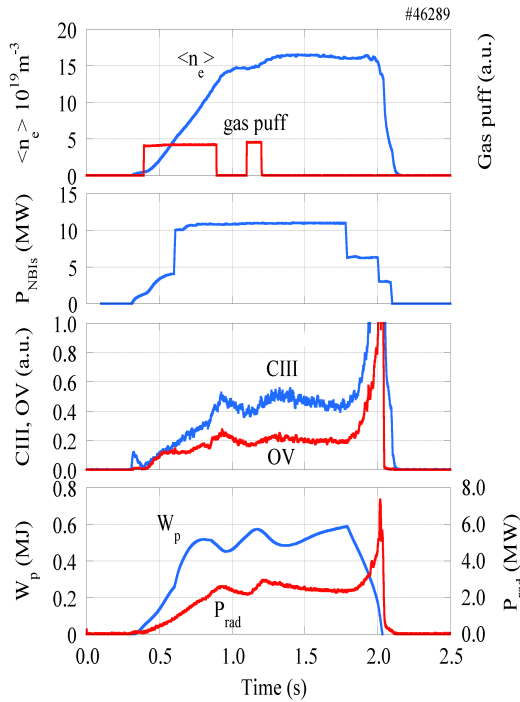


Fig. 1. Typical waveforms of a high density discharge using gas puff fuelling (shot #46289) (a) line-averaged density and gas-puff timing, (b) deposited NBI power, (c) spectroscopy signals from OV and CIII, and (d) total plasma stored energy and total radiated power.

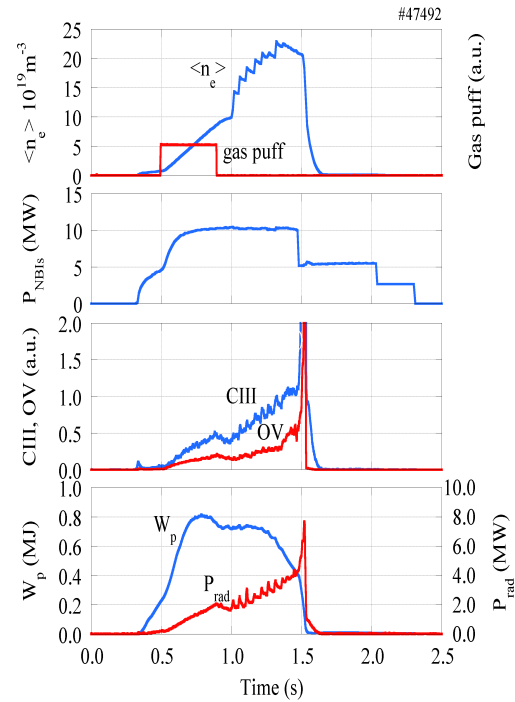


Fig. 2. Typical waveforms of a high density discharge using gas puff and hydrogen pellet fuelling (shot #47492) (a) line-averaged density and gas-puff timing, (b) deposited NBI power, (c) spectroscopy signals from OV and CIII, and (d) total plasma stored energy and total radiated power.

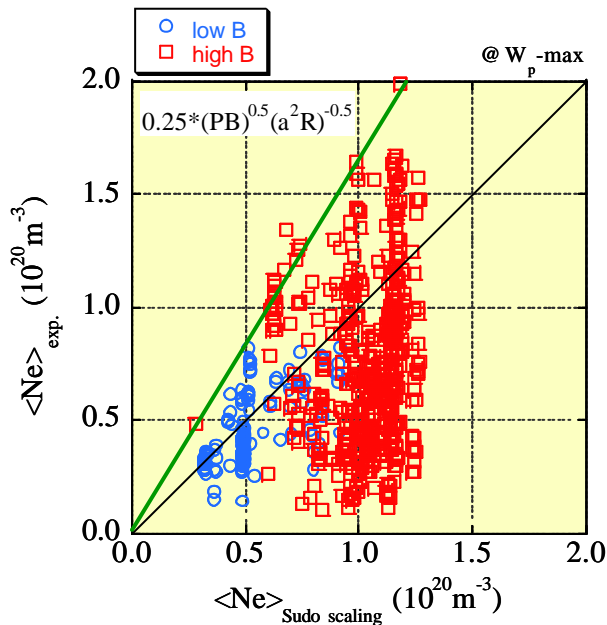


Fig. 3. Density limit scaling for LHD data taken at the timing of maximum stored energy plotted versus the Sudo limit. Green line indicates a factor of 1.6.



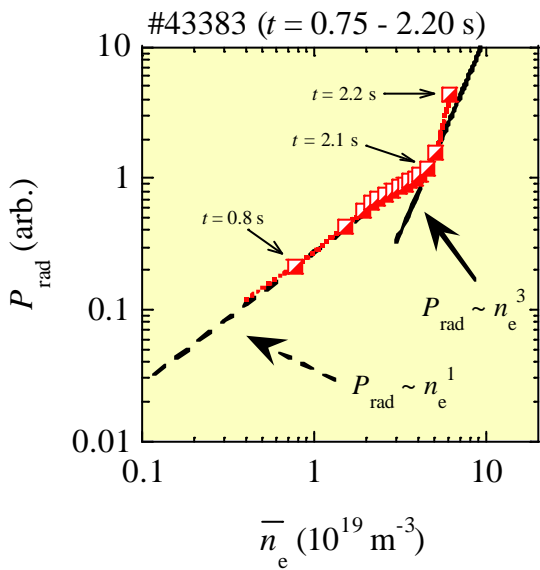


Fig. 5 Radiated power dependence on density

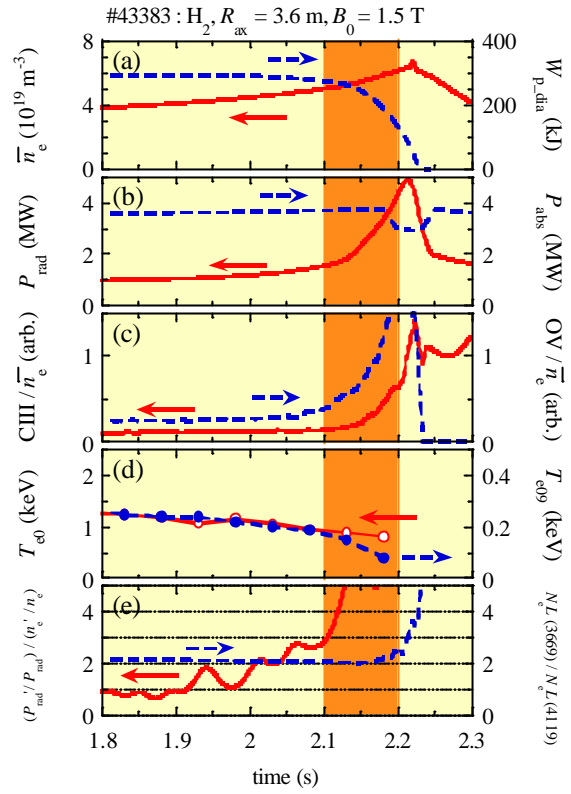


Fig. 4 Typical waveforms of a discharge terminated by radiative collapse in LHD.

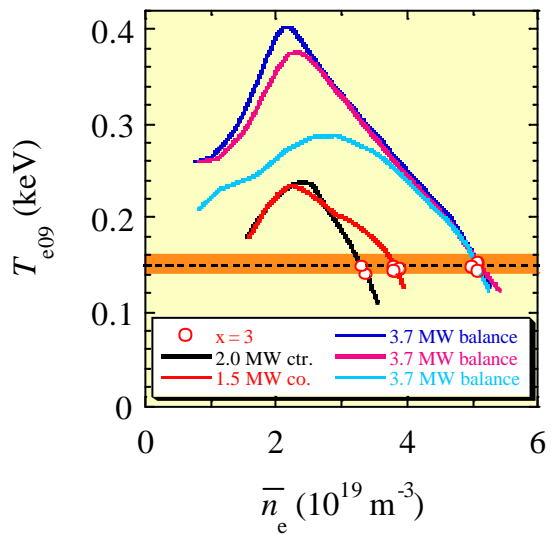


Fig. 6 Evolution of edge electron temperature at  $r = 0.9$  as a function of line-averaged density for varying input powers.

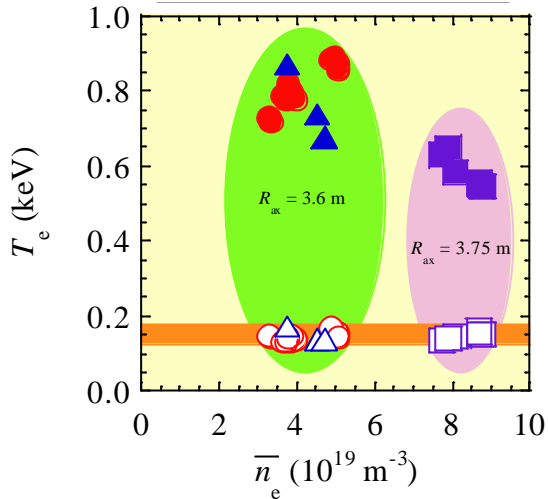


Fig. 7 Edge ( $r = 0.9$ , open symbol) and core ( $r = 0.1$ , solid symbol) electron temperature dependence on line-averaged density for Hydrogen (red) and Helium (blue) puffing and axis positions at the onset of the thermal instability, when  $x = 3$ .

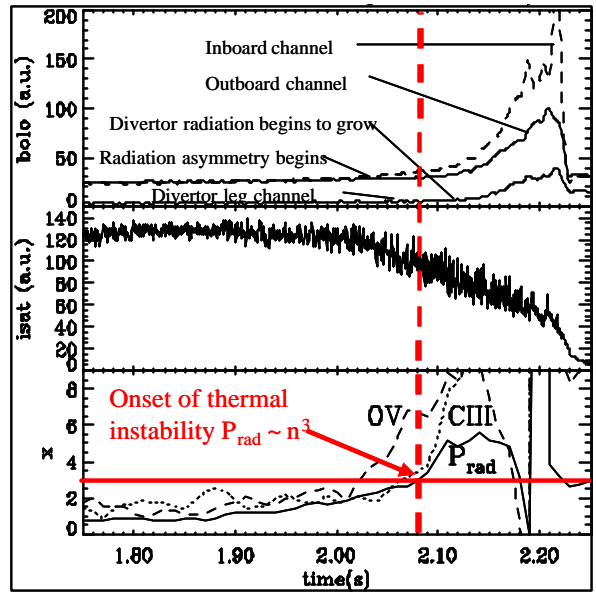


Fig. 9 Time evolution of bolometer brightness, divertor ion saturation current, and the density exponent for the total radiated power, CIII and OV data shown in Fig. 4.

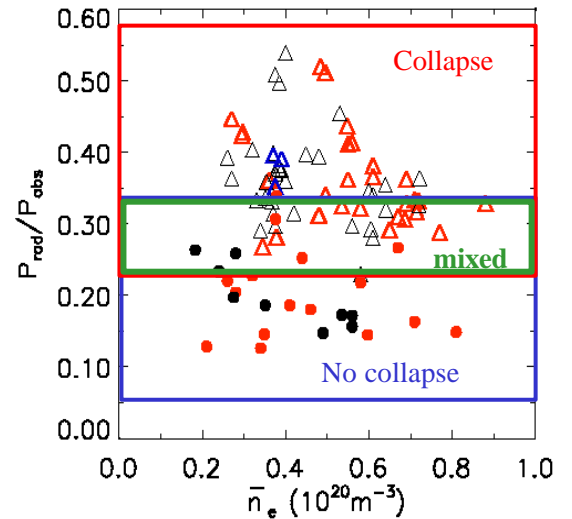


Fig. 8 Radiated power fraction versus density at the onset of the thermal instability for collapsing shots (triangles) and at the peak density for non collapsing shots (circles) from the third and fourth campaigns

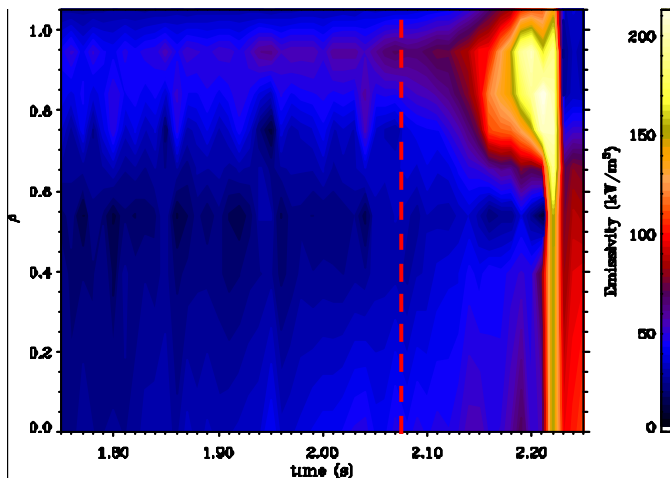


Fig. 10 Evolution of radiated power density profile during radiative collapse of shot 43383. Red dashed line indicates the onset of the radiative instability ( $x = 3$ ).

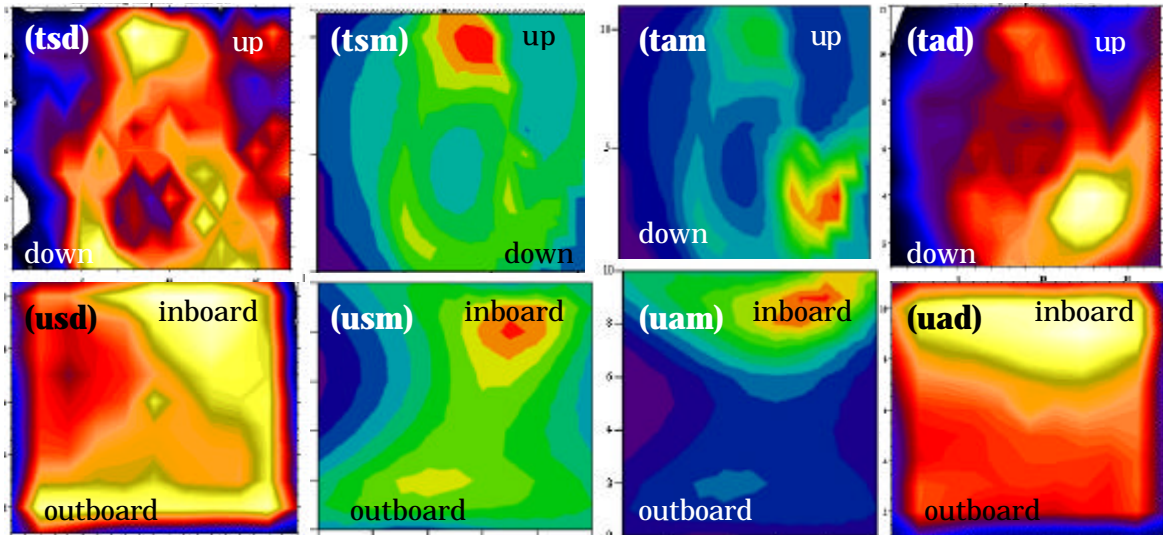


Fig. 11 IRVB radiation brightness image (d) data from (u) upper and (t) tangential ports during the (s) steady state and (a) asymmetric phases of the discharge compared with reconstructions from (m) model profiles.

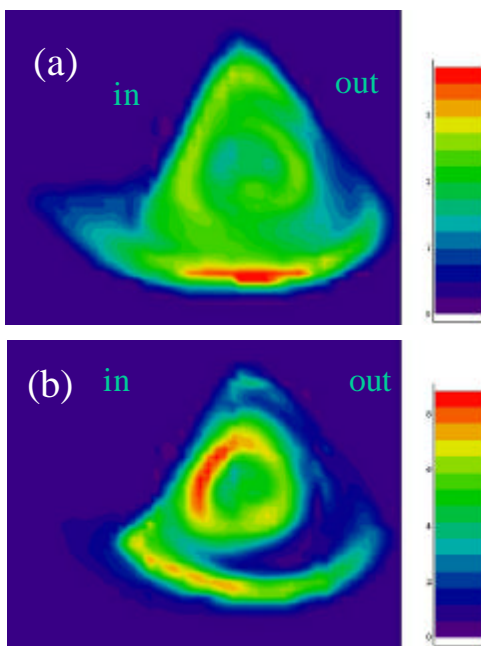


Fig. 12 Two dimensional tomographic images of radiation intensity measured with AXUVD arrays in LHD for the same shot and time slices shown in Fig. 11.

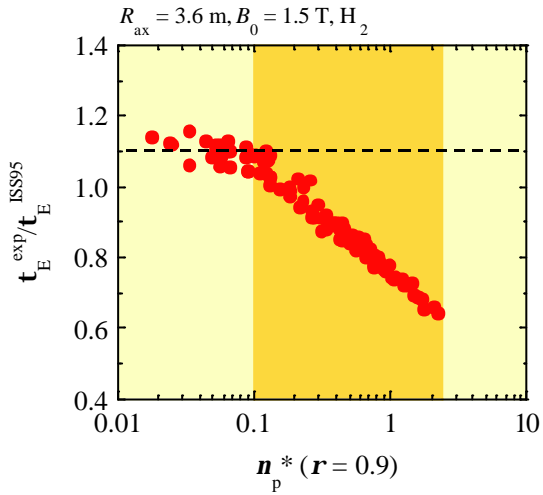


Fig. 13 Degradation from ISS95 in the high-collisionality regime.

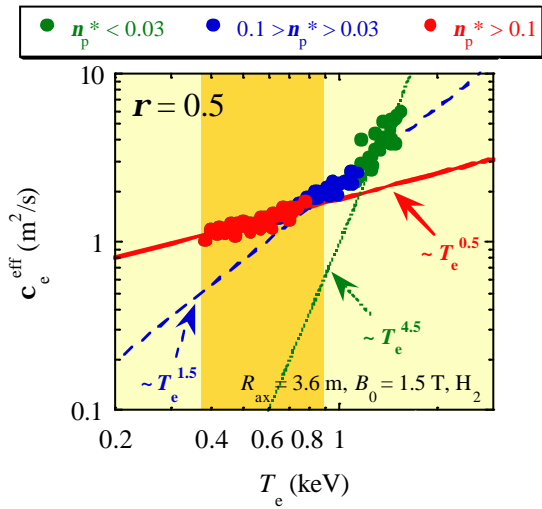


Fig. 14 Electron temperature dependence of the effective thermal diffusivity.

## Edge and Internal Transport Barrier Formations in CHS

S. Okamura 1), T. Minami 1), T. Akiyama 1), T. Oishi 2), A. Fujisawa 1), K. Ida 1), H. Iguchi 1), M. Isobe 1), S. Kado 3), K. Nagaoka 1), K. Nakamura 1), S. Nishimura 1), K. Matsuoka 1), H. Matsushita 1), H. Nakano 1), M. Nishiura 1), S. Ohshima 1), A. Shimizu 1), C. Suzuki 1), C. Takahashi 1), K. Toi 1), Y. Yoshimura 1), M. Yoshinuma 1), CHS group

1) National Institute for Fusion Science, Oroshi 322-6, Toki 509-5292, Japan

2) Graduate School of Engineering, The University of Tokyo, Tokyo 113-8656, Japan

3) High Temperature Plasma Center, The University of Tokyo, Tokyo 113-8656, Japan

e-mail contact of main author: okamura@nifs.ac.jp

**Abstract.** Edge transport barrier (ETB) formation was observed in CHS. Sharp decrease of  $H\alpha$  emission indicates the quick transition of edge particle transport. Increase of the density gradient at the edge was measured by various profile diagnostics and the improvement of the global energy confinement was confirmed based on the stellarator confinement scaling. The heating power threshold exists. The transition and back transition is controlled by the heating power. The local density measurement by the beam emission spectroscopy shows intermittent burst of the low frequency fluctuations during the ETB formation phase. The ETB formation together with the electron temperature increase (electron ITB) in the core region were observed for the NBI discharges without ECH.

### 1. Introduction

The formation of transport barriers is an important research topic in the plasma confinement study for fusion research. Various types of transport barriers have been found in tokamaks and stellarators and physical mechanism of their formation has been studied intensively. In the Compact Helical System (CHS), which is a low-aspect-ratio middle size stellarator ( $R=1$  m,  $a=0.2$  m, toroidal period number  $N=8$ ), the H-mode discharge had been found in 1993 [1] which was the first finding in stellarators, simultaneously with the Wendelstein 7AS experiment [2]. This operation needed the control of the rotational transform at the plasma edge using an ohmic current created by the special operation of the poloidal coil current ramping. As well as the edge transport barrier (ETB) formation in the H-mode, the internal transport barrier (ITB) was found in CHS [3], also for the first time in the stellarator research. In the research of ITB, clear increase of the electron temperature and the potential at the central region of the plasma were measured for ECH plasmas. Now the ITB formation in stellarator has become popular for various devices. In addition to the electron ITB, new type of ITB was reported in the last FEC meeting [4] where the transport barriers were formed for both electrons and ions in the plasma with ECH and NBI heating. This type of ITB is unique for CHS experiment, which has not been observed in other stellarators yet.

In this conference, we report a new type of ETB formation (H-mode) in CHS experiment [5, 6]. This type of ETB discharges does not need ohmic current control. Sufficient level of NBI heating power is necessary for the transition which was not available in the previous H-mode study (threshold power for the transition clearly exists). With a large drop of the  $H\alpha$  emission, the edge density starts to increase due to the formation of the transport barrier for the particle flow. Since these ETB transition appears during the NBI phase without ECH, the electron

temperature profile does not change much for most cases. However special discharges were found where the electron temperature increases together with density. The best case gives two times increase of electron temperature with the profile indicating the formation of the electron ITB without ECH. In this paper, characteristics of a new type of ETB will be described from various points of view and electron profile measurements for the combined ETB and ITB formation will be given.

## 2. Global Parameter Changes with ETB Formation

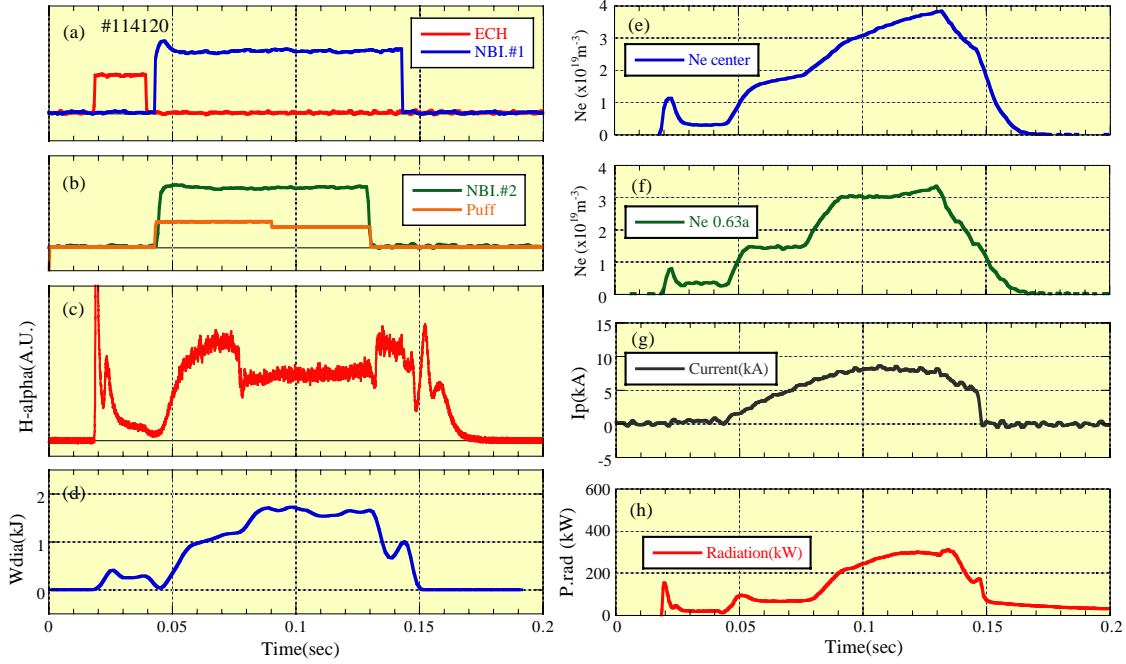


FIG. 1 Time traces of basic plasma parameters for NBI discharges with ETB formation. (a) and (b): ECH, NBI and gas puffing, (c)  $H\alpha$  emission, (d) diamagnetic energy, (e) line averaged electron density for central chord, (f) the same for edge chord, (g) plasma current and (h) total radiation power.

Figure 1 shows time traces of plasma global parameters showing the transition to the ETB formation and the back transition. The experimental condition of those discharges is as follows. The plasma volume is about  $0.7 \text{ m}^3$  and its surface area is about  $7.5 \text{ m}^2$ . The magnetic field strength is  $0.95 \text{ T}$  at the magnetic axis. The profile of the rotational transform has a strong stellarator type shear at the plasma edge. It is  $0.3 (=1/q)$  at the magnetic axis and slightly higher than 1 at the edge. The characteristics of magnetic surface parameters (rotational transform and magnetic well) is sensitive to the major position of the plasma and its (toroidally averaged) ellipticity. The cross section of CHS plasma is an ellipse (ellipticity is about 2) which rotates along the torus. The ellipticity we control by the axisymmetric poloidal field is the toroidally averaged one. The configuration shown in Fig. 1 has the magnetic axis position  $R_{ax} = 92.1 \text{ cm}$  and the ellipticity  $\kappa = 1.22$ .

Two neutral beams are injected into the low density hydrogen plasma created by the ECH heating (53 GHz, 200 kW). Both beams are installed tangentially to the torus making co-injection. Beam energy for two NBIs are 40 and 30 keV, respectively, and the maximum port-

through injection power is about 800 kW for each. Such an arrangement is essential for supplying sufficient heating power for the ETB transition because the counter-injection gives large direct loss of beam ions. As shown in Fig.1, the plasma is sustained by NBI and density increases with gas puffing. After 35 msec from the starting of NBI, a spontaneous transition appears in the plasma edge region which is clearly shown by the sharp drop of H $\alpha$  emission signal. The estimated NBI deposition power is about 0.6 MW before the transition. The delay time between the start of NBI heating and the transition largely depends on the magnetic configuration and the heating power. Figure 1 shows two chord signals of HCN interferometer at the center (e) and the normalized minor radius of 0.63 (f). These data show that the density profile becomes slightly peaked during the NBI heating phase with the edge density staying almost constant. After the transition at 78 msec, the edge density starts to increase making a flatter profile and the diamagnetic plasma energy increases as well (volume averaged beta is 0.6 % after the transition). The total radiation loss from the plasma also starts to increase. When the NBI.#2 is turned off and the heating power is decreased, the back transition appears. The plasma current is a combination of the bootstrap current and the beam driven current. The current level of 8 kA in this shot gives the increase of the edge rotational transform of 0.035 which is not larger than the ambiguity of the edge value given from the equilibrium calculation.

### 3. Local Profile Measurements

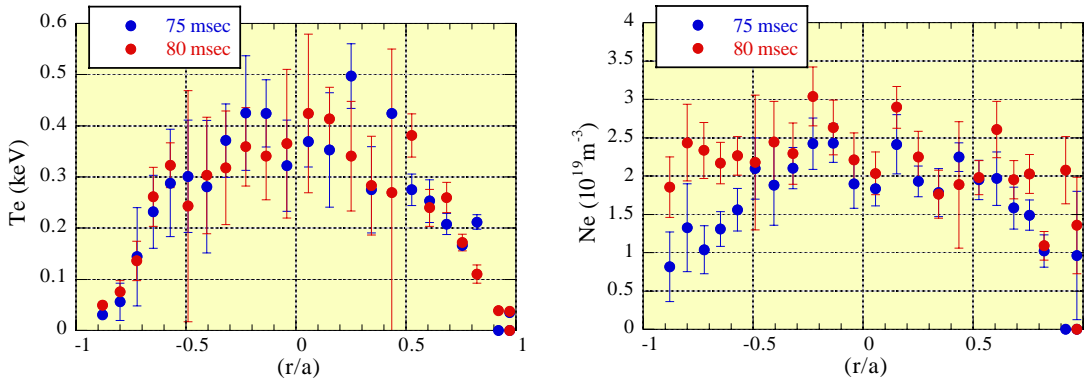


FIG. 2 YAG Thomson scattering measurements for electron temperature (left) and density (right). Blue point profile is before the transition and red one is after the transition.

The change of density profile at the transition was clearly measured by the YAG Thomson scattering system in CHS which gives full profiles of electron temperature and density every 5 msec. Figure 2 shows measured profiles of the same discharge shown in Fig.1 at 75 msec (just before the transition) and 80 msec (after the transition). The edge density increases after the transition making the large density gradient at the plasma boundary. However the temperature profiles does not change much for this discharge.

Edge density profile measurement was made also by the lithium beam probe system [7]. Accelerated neutral lithium beam (15 keV) was injected into the plasma edge region and the Li I resonance line emission excited by the electrons was measured along the beam. This diagnostic gives the electron density profiles for larger area at the boundary where the electron temperature is not high enough for the standard Thomson scattering system which is designed for taking plasma core temperature profile. Figure 3 shows the variation of the edge density

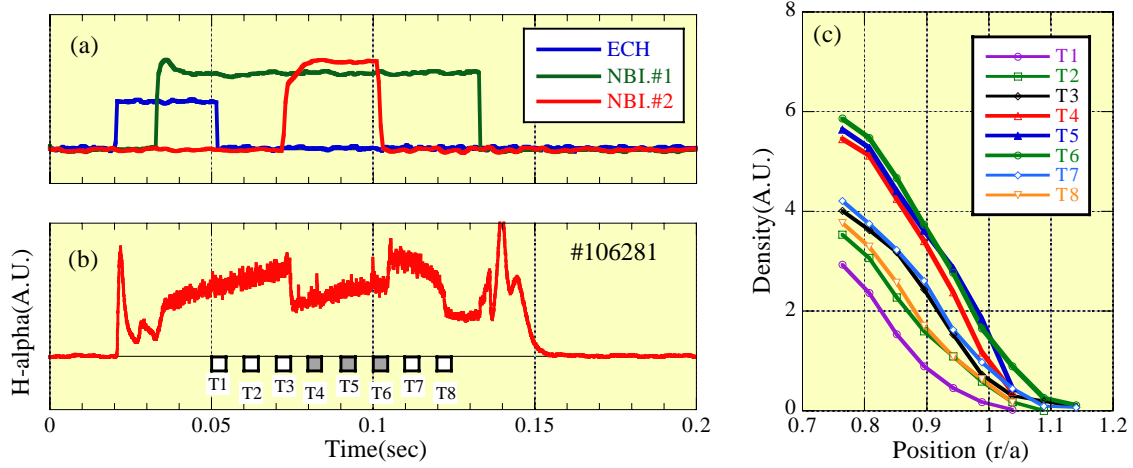


FIG. 3 Density profiles measured by lithium beam probe. Data averaging periods are shown in (b). Position in (c) is plotted as a function of averaged minor radius.

profiles for whole period of the discharge. In this discharge, the second beam NBI.#2 is injected for shorter period (from 72 msec to 102 msec) than NBI.#1 in order to confirm the transition to ETB and the back transition controlled by the heating power. The increase of the edge density is observed for time periods from T4 to T6 where the ETB is formed.

Another local density measurement in CHS is the beam emission spectroscopy (BES) which measures  $H\alpha$  emission of high energy hydrogen beam excited by electrons [8]. NBI.#2 is used for the beam source for BES measurement. An eight channel array of visible detectors is installed for getting the spatial density profile near plasma edge region. Since this system has the high frequency response ( $< 100$  kHz), local fluctuation measurement is also made which is discussed later. Figure 4 shows the time variation of three BES channels for the discharge with ETB formation. When the ETB is formed at 70 msec, BES signals looking at inside of the last closed magnetic surface (LCMS) rapidly increase and the BES signal for the outside of LCMS drops indicating the suppression of the outward particle flow by the transport barrier. After forming the large density gradient, the edge density increases and finally stays constant. In the  $H\alpha$  emission signal, a pre-phase of the drop is recognized where the BES signal inside the plasma starts to increase (Fig.

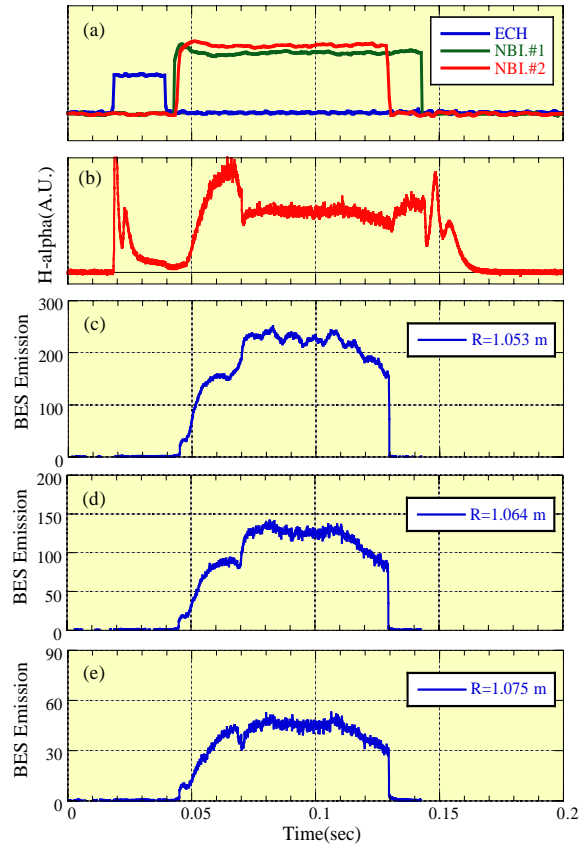


FIG. 4 BES measurements of local electron density. Calculated LCMS is between measurement position of (d) and (e)

4(c)) while others do not change at all.

#### 4. Dependence of ETB Formation on Heating Power

Heating power threshold is clear for the ETB formation in CHS. When the heating power is decreased, the time delay between the starting of NBI heating and the spontaneous transition becomes larger. If the heating power is close to the power threshold, sequence of short spikes of  $H\alpha$  emission signal appears indicating the dithering between the H and L state [5]. When the heating power is decreased further, the spontaneous switching between two states appears and finally no transition occurs for the heating power below the threshold.

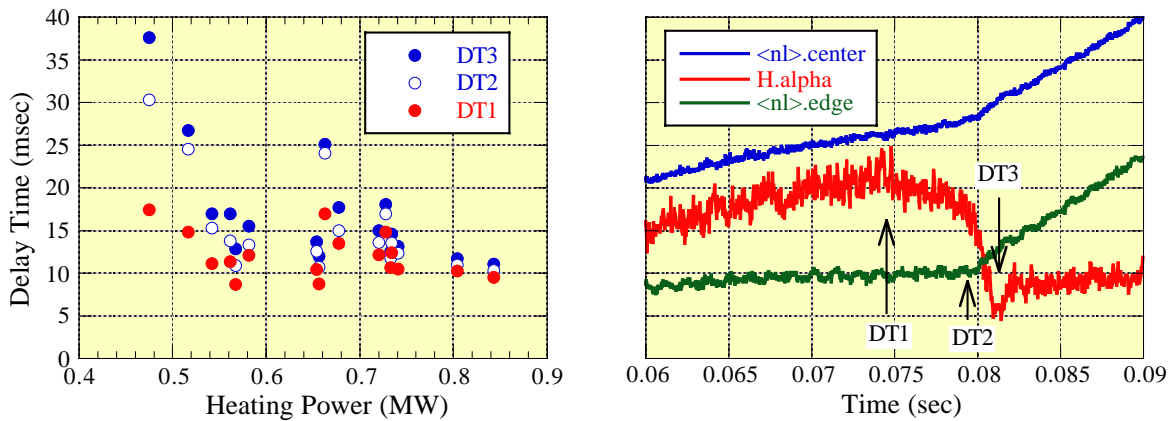


FIG. 5 Time delay of  $H\alpha$  signal drop after NBI start as a function of heating power. Three characteristic instants are shown in right figure.

Figure 5 shows the dependence of time delay of the transition from the starting of NBI as a function of deposition power. The magnetic configuration with  $R_{ax} = 92.1$  cm and  $\kappa = 1.11$  was used. In this configuration, the delay time of the transition from the start of NBI heating is generally much shorter than the case in Fig. 1. Three timings are taken corresponding to the various phase of  $H\alpha$  emission change shown in the right figure. DT1 is the beginning of whole transition phenomena.  $H\alpha$  signal starts to decrease slowly in the pre-phase between DT1 and DT2. The quick decrease of the signal appears between DT2 and DT3. Although we do not have complete understanding of these phases, local particle dynamics might be related to these phases of  $H\alpha$  signal (e.g., BES signal in Fig. 4(c) shows slow increase in the pre-phase). When the heating power is decreased down to the power threshold, the delay of the quick drop phase is increased while the starting of the pre-phase does not change so much. Even though the timing of the quick drop is delayed, the speed of signal drop does not change much. But finally main drop of the signal becomes slow at the power threshold.

The heating power threshold is about 0.5 MW for the density of  $2 \times 10^{19} \text{ m}^{-3}$ . For the lower density plasma ( $1.5 \times 10^{19} \text{ m}^{-3}$ ), the power threshold is decreased roughly proportionally. On the other hand, the gas puffing is necessary condition for making the ETB formation. ETB does not appear for very low density plasmas without gas puffing. The power threshold obtained in the CHS experiment can be compared with the tokamak H-mode threshold scaling because it consists only of the density, magnetic field and device size parameters [9]. CHS power threshold is roughly two times larger.

## 5. Confinement Improvement

Due to the formation of ETB, the plasma energy increases by about 40% as is shown in Fig. 1. The analysis of discharges with and without ETB based on the global energy confinement scaling is shown in Fig. 6. Data are taken from the density scanning experiment (with gas puffing control) where the NBI port through power was kept almost constant (1.3 to 1.4 MW). In this experiment, the magnetic configuration with  $R_{ax} = 92.1$  cm and  $\kappa = 1.11$  was used. Data for 'Good ETB' were obtained with the wall conditioning of strong titanium gettering. Maximum diamagnetic energy during the discharge is taken for  $W_p$ . If the plasma density does not reach the threshold level during the initial phase of discharge, ETB is not formed even though the density in the later phase rises up. The diamagnetic energy divided by the scaling factor for the NBI deposition power is plotted as a function of the averaged density. Confinement scaling from the new international cooperation for stellarators is used [10]. The black dotted line is from this scaling for the middle size heliotron type devices with CHS parameters. Three fitting curves are added according to the density scaling law with different coefficients. The formation of ETB makes confinement improvement above the scaling law. The intense wall conditioning improves additionally the confinement.

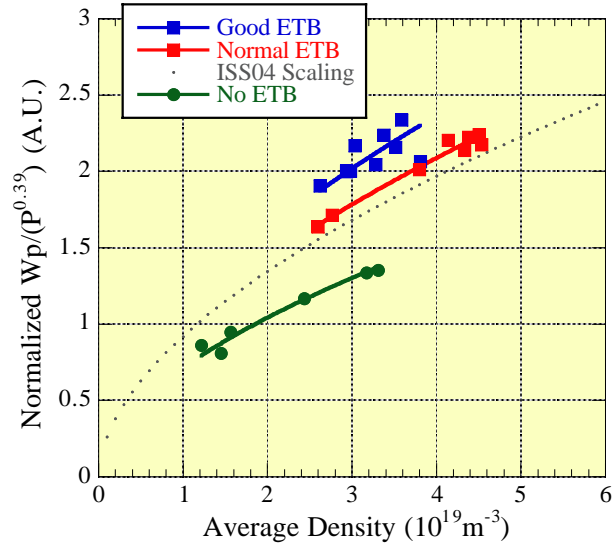


FIG. 6 Plasma energy normalized by the scaling factor for  $P$  as a function of averaged density.

## 6. Fluctuation Measurement by BES

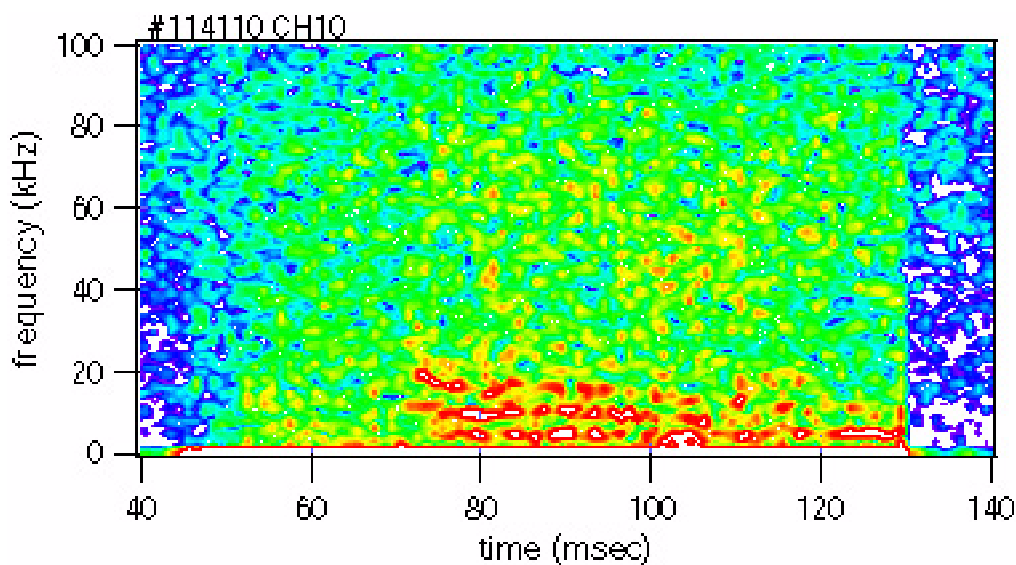


FIG. 7 Time variation of power spectrum in BES signal just inside LCMS. Red color corresponds to largest power. ETB is formed at about 70 msec.

High frequency components in the BES signal were analyzed in order to compare the fluctuation level in the L and H phase. During the H phase with ETB formation, low frequency fluctuations appear near the plasma boundary. Figure 7 shows the time variation of the spectrum profile of BES signal looking at just inside LCMS for the same discharge shown in Fig. 4. The fluctuation level is largest for this channel among all 8 channels observing across LCMS. Logarithmic value of power spectrum is shown by colors (red is highest). After the ETB formation at 70 msec, fluctuation level rises with the frequency of about 5 kHz and its harmonics. They appear intermittently with the period of a couple of msec. From the detailed analysis of initial time variation of those fluctuations and the density profile, it is confirmed that those fluctuation starts after the formation of a steep density gradient at the plasma edge. The physical mechanism of those fluctuations and its effect on the transport has not been understood. From BES edge density fluctuation measurements so far, we have not observed any evidence of the suppression of fluctuation level during ETB phase.

### 7. ETB with Temperature Increase in the Core Region

As was mentioned in section 3, for most discharges the electron temperature profile does not change much with the ETB formation. However we observe occasionally the increase of the electron temperature in the core region just after the ETB formation. This increase of the temperature cannot be understood by the increase of the heat deposition with the increased density because the increase of heating power is only proportional to the density at maximum. There must be the transport improvement or the transport barrier. Such an increase of the electron temperature appears only in a short time (10 to 20 msec) because of the rapid density increase with the ETB formation. Systematic study for the operational condition of those mode and the method of making the phenomena steady are necessary.

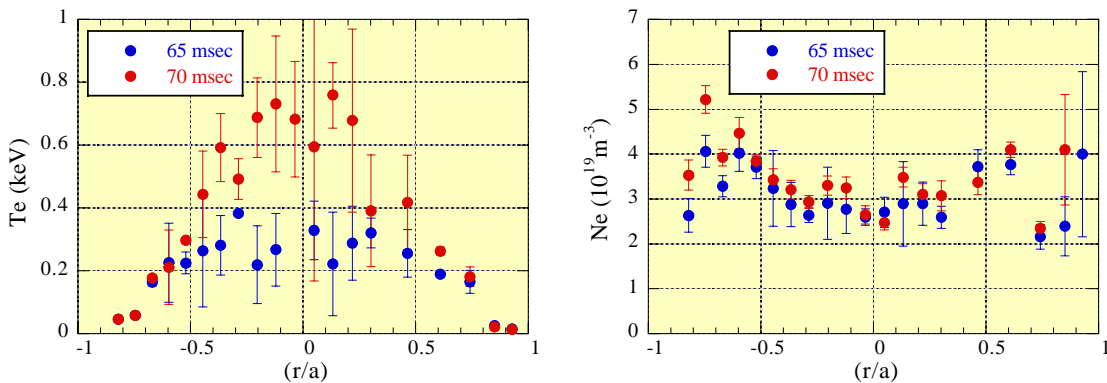


FIG. 8 Electron temperature and density profiles for ETB discharge with simultaneous ITB.

Figure 8 shows one example of electron density and temperature profiles of an ETB discharge with the raised electron temperature in the core. The profile shape of the electron temperature is very similar to the ITB discharge in CHS [4]. However in the previous ITB experiment, the electron temperature increase and the steep temperature gradient are made after the application of ECH. In this ETB discharge, the ECH for the target plasma production is turned off before the transition. More important difference is the plasma density. In the previous ITB experiment, there was a clear density threshold for the ITB formation at  $0.4 \times 10^{19} \text{ m}^{-3}$  (lower density operation is necessary). The mechanism for the creation of the electric field shear is considered to be given by the intersection of the positive and negative electric field region

(electron root and ion root) created by the neoclassical non-ambipolar diffusion process in stellarators. With this reason, we called this type of ITB as neoclassical ITB (N-ITB). The ITB formation in the present experiments should have a different physical mechanism because the neoclassical electron root cannot be created for such a density and temperature region.

## 8. Discussion and Summary

Following to the series of ITB physics studies in stellarator initiated by CHS experiment in 1999, the NBI discharges with ETB formation (H-mode) has been extensively studied. Those experiments became possible because of the improved heating efficiency of two NBIs by arranging them in co-injection together instead of balanced injection. Clear drop of  $H\alpha$  emission signal was observed and the quick increase of the edge density was measured by YAG Thomson and BES. The experiments confirming the existence of heating power threshold clearly showed that the transition is controlled by the amount of heat flow through the plasma boundary. The time delay of the transition from the start of NBI depends on the heating power. It also depends very sensitively to the magnetic configuration (more important is the edge rotational transport value). The physical mechanism to determine the instant of transition is an important topic for the future study. The electron temperature does not increase much for most discharges. However large increase of the electron temperature was observed for the limited number of discharges where the temperature gradient appeared for the density of  $2 \times 10^{19} \text{ m}^{-3}$  which is well above the density threshold for the previous ITB experiments in CHS. Further study of this type of confinement improvement is essential for fusion research for stellarators.

## REFERENCES

- [1] TOI, K., et al., Plasma Physics and Controlled Nuclear Fusion Research (Proc. Conf. Wurzburg, 1992), IAEA, Vienna (1993) vol. 2, 461.
- [2] ERCKMANN, V. et al., Phys. Rev. Lett. **89** (1993) 2086.
- [3] FUJISAWA, A., et al., Phys. Rev. Lett. **82** (1999) 2669.
- [4] MINAMI, T., et al., Fusion Energy 2002 (Proc. 19th Int. Conf., Lyon, 2002), CD-ROM file EX/C4-3.
- [5] OKAMURA, S., et al., J. Plasma Fusion Res. **79** (2003) 977.
- [6] OKAMURA, S., et al., Plasma Phys. Control. Fusion **46** (2004) A113.
- [7] NAKAMURA, K., et al., Rev. Sci. Instrum. (2004) in printing.
- [8] OISHI, T., et al., Rev. Sci. Instrum. **75** (2004) 4118.
- [9] SNIPES, J.A., et al., Fusion Energy 2002 (Proc. 19th Int. Conf. Lyon, 2002), CD-ROM file CT/P-04.
- [10] YAMADA, H., et al., 31th EPS Conf. on Contror. Fusion and Plasma Phys. ECA Vol. 28G, P-5.099 (2004)

## Experimental Studies of Zonal Flows in CHS and JIPPT-IIU

A. Fujisawa, K. Itoh, H. Iguchi, K. Matsuoka, S. Okamura, A. Shimizu, T. Minami, Y. Yoshimura, K. Nagaoka, C. Takahashi, M. Kojima, H. Nakano, S. Ohshima, S. Nishimura, M. Isobe, C. Suzuki, T. Akiyama, K. Ida, K. Toi, S.-I. Itoh<sup>1</sup> and P. H. Diamond<sup>2</sup>, CHS group.

Y. Hamada, A. Nishizawa, T. Ido, T. Watari, Y. Kawasumi and JIPPT-IIU group.

*National Institute for Fusion Science, Oroshi-cho, Toki, Japan 509-5292*

<sup>1</sup>*RIAM, Kyushu Univ., Kasuga, Japan 816-8580*

<sup>2</sup>*University of California, San Diego, La Jolla, California, U. S. A., 92093-0319*

e-mail: fujisawa@nifs.ac.jp

**Abstract.** Zonal flow is now one of central topics for transport study in toroidal plasmas, and its detection is a challenging experimental subject. This paper introduces trials to identify zonal flows in toroidal plasmas, i.e., CHS and JIPPT-IIU, with HIBPs. The main results are the first confirmation of the existence of residual zonal flows, and findings of coherent oscillations that can be the Geodesic Acoustic Modes in CHS and JIPPT-IIU.

### 1. Introduction

Plasma turbulence has been studied for over a half century as a mechanism to govern the transport in toroidal plasmas. One of the successful achievements in this field is that the shear of mean radial electric field (or perpendicular flow) can suppress turbulence and transport to result in improved confinement modes [1-4]. Recently, the other players in regulating plasma transport, *zonal flows* [5,6], have come into the transport study in toroidal plasmas. The importance of zonal flow study becomes crucial to give a precise prediction of the plasma transport, in particular, the performance of International Thermonuclear Experimental Reactor (ITER) [7-9].

The zonal flows can be driven exclusively by nonlinear interactions with turbulence, on the other hand, the meso-scopic structure of zonal flows has an effect on plasma turbulence through time-varying ExB shearing. Direct nonlinear simulations have, in fact, confirmed the mutual interaction between zonal flows and turbulence, and their essential role in turbulence and transport [10-15]. However, only a few experimental trials have been performed to identify zonal flows and their effects on confinement [16-23].

In toroidal plasmas, two major branches of zonal flows are expected, i.e., a residual flow of nearly zero frequency, and an oscillatory flow termed Geodesic Acoustic Modes (GAMs) [24,25]. These zonal flows appear in electric field fluctuation symmetric ( $m=n=0$ ) on magnetic flux surface with finite radial wave numbers. Hence, direct measurement of electric field is essential to identify the zonal flows. Advantageously, heavy ion beam probes (HIBP) are able to measure electric field of the plasma interior. This paper presents the first experimental detection, using the HIBPs, of the residual zonal flows in CHS [26], together with findings of coherent oscillation presumed as GAMs in CHS [26] and JIPPT-IIU [27].

### 2. Heavy Ion Beam Probe

In the diagnostics, the energy difference between injected and detected beams corresponds to the plasma potential at the ionization point. Hence, the fluctuation of the

beam energy represents to the potential fluctuation. Besides, the fluctuation of detected beam intensity gives information of density fluctuation, as

$$\tilde{I}_{\text{det}}/I_0 = \tilde{n}_e/n_e - \int \tilde{n}_e S_1 dl_1 - \int \tilde{n}_e S_2 dl_2, \quad (1)$$

where  $I_0$ ,  $S_1$ , and  $S_2$  mean the initial beam intensity, electron impact ionization cross-section from singly ionized state to the others, and the one from doubly charged state to the others, respectively. The local density fluctuation can be estimated from that of the detected current fluctuation (i.e.,  $\tilde{I}/I_{\text{det}} \approx \tilde{n}_e/n_e$ ), if the plasma density is sufficiently low to neglect the integral terms.

Heavy ion beam probes are often capable to simultaneously measure several adjacent points of plasma along the beam orbit. Difference between potentials at two channels gives a measure of electric field, i.e.,  $E\delta r = -(\phi(\rho_2) - \phi(\rho_1))$ . The potential fluctuation at a point  $\rho_2$  can be written by electric field fluctuation and potential fluctuation at an adjacent position  $\rho_1$  along the orbit in a symbolic manner,

$$\tilde{\phi}(\rho_2) = -\tilde{E}\delta r + \tilde{\phi}(\rho_1) \approx -\tilde{E}\delta r + \int_a^{\rho_1} \tilde{E} dl, \quad (2)$$

Consequently, potential fluctuation should contain the integrated fluctuation of electric field along the beam orbit, similarly to the path integral effects of density fluctuation. Therefore, the local electric field measurement is superior in the detection of the zonal flows, although the measurements need higher signal-to-noise ratio than that of potential fluctuation.

### 3. Experimental Results of CHS

#### 3-1. Experimental Conditions

The Compact Helical System (CHS) is a helical device with the major and minor radii being  $R=1.0\text{m}$ ,  $a=0.20\text{m}$ , respectively. The magnetic field strength of CHS is up to 2T. The CHS is equipped with two HIBP systems. As is shown in Fig. 1(a), the locations of two HIBPs are apart approximately by 90 degree in the toroidal direction. Both HIBPs have almost the same geometrical characteristics with their maximum energy of 200keV. Each of them is capable to measure three adjacent positions in the plasma. The necessary beam energy is  $\sim 70$  keV, using cesium, for this magnetic field strength of 0.88T in order to see the plasma center.

The experiments were performed in plasmas produced with electron cyclotron resonance heating of  $\sim 200$  kW. The plasma parameters are, magnetic field strength  $B=0.88$  T, density  $n_e \sim 5 \times 10^{12} \text{cm}^{-3}$ , electron temperature  $T_e \sim 1\text{keV}$ , ion temperature  $T_i \sim 0.1$  keV, ion Larmor radius  $\rho_i \sim 0.1\text{cm}$ , time scale of micro-instabilities  $\Omega^* \sim 50\text{kHz}$  with  $k_{\text{perp}}\rho_i \sim 0.3$  and energy confinement time  $\tau_E \sim 2.5\text{ms}$  (or the characteristic frequency  $\tau_E^{-1}/2\pi \sim 0.1\text{kHz}$ ).

#### 3-2. Spectra of potential and electric field fluctuations

Electric field fluctuation has been measured with dual HIBPs. Figure 1(b) shows a spectrum of the electric field fluctuation, and its coherence between two toroidal locations; here potential difference,  $E\delta r = -(\phi(\rho_2) - \phi(\rho_1))$ , is just termed ‘*electric field*’ for simplicity. The observed radial location is  $r_{\text{obs}} = 12 \pm 0.5$  cm, or two thirds of plasma minor radius. Here, the Fast Fourier Transform (FFT) technique is applied for sequential windows taken from the stationary period of  $\sim 80$  ms. Spectrum in Fig. 1(b) is a shot-average of the ensembles. The signal-to-noise ratio for the measurement is the maximum since detected beam current is largest around the observation point. The fluctuation in the low frequency range ( $< \sim 1\text{kHz}$ ) shows a high coherence ( $\sim 0.6$ ) between two toroidal locations. The coherence can become

closer to one in an appropriate period of a single shot. The fluctuation with the long-range correlation in this frequency regime should represent the residual zonal flow.

For comparison, Fig. 1(c) shows the corresponding spectrum of potential fluctuation, and coherence between potentials. Their characteristics are obviously different in power and coherence. Particularly, in the frequency range from 1 kHz to 10 kHz, the potential fluctuation power is much larger than that of the electric field as the frequency is lower. The potential power decreases as  $P \sim f^{-1.9}$ , while the power of electric field as  $P \sim f^{-0.6}$  in the range from  $\sim 1$  kHz to  $\sim 10$  kHz. On the other hand, the coherence of power is quite high around  $\sim 2$  kHz ( $\sim 0.9$  at the maximum). The difference in power and coherence suggests presence of significant coherent fluctuations with this low frequency range in outer region of the observation radius.

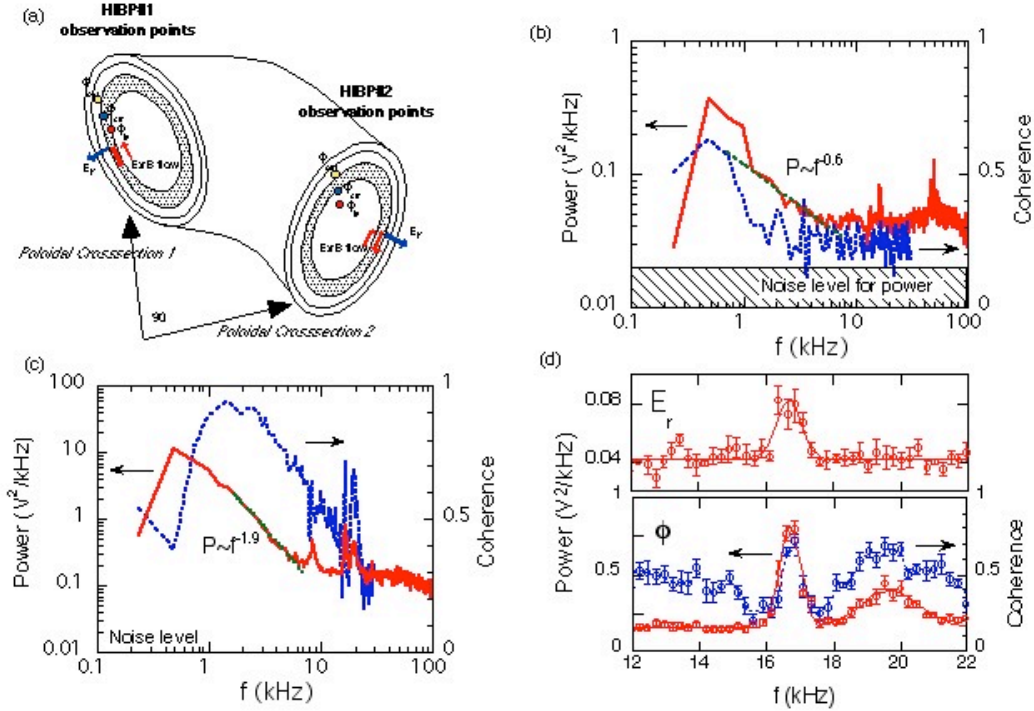


Figure 1. (a) Geometry of dual heavy ion beam probes on CHS, (b) Fluctuation spectrum of electric field and coherence between two toroidal locations. The hatched region represents noise level of measurements of electric field fluctuation power. (c) Power and coherence in potential fluctuation. (d) Expanded views of power spectrum of electric field fluctuation (upper), and power spectrum of potential and coherence between potentials (lower).

Figure 1(d) shows expanded views around the peak for power spectra of potential and electric field, and coherence in potential between two toroidal locations. In the power spectrum of electric field shows a sharp peak at  $f \sim 16.5$  kHz with a width of  $\sim 1$  kHz. On the other hand, the power spectrum of potential fluctuation, two peaks at  $f \sim 16.5$  and  $f \sim 20.0$  kHz can be found. These peaks show quite high coherence up to  $\sim 0.8$ , although a significant coherence cannot be evaluated owing to the poorer signal-to-noise ratio for electric field fluctuation. In this experimental condition, the theoretically expected GAM frequency is  $c_s/2\pi R \sim 17$  kHz, with  $c_s$  being the ion sound velocity. Consequently, the prediction of frequency and long-range correlation suggests that the electric field fluctuation of  $f \sim 16.5$  kHz should represent a GAM.

The other peak at  $f \sim 20$  kHz could be also a GAM, which is interfused into potential fluctuation due to the effect of electric field integral (in Eq. (2)). This mode should be located

on an outer region of the observation point ( $r_{\text{obs}} \sim 12$  cm), owing to its absence in spectrum of electric field fluctuation. The sharpness of both peaks in potential suggests that ‘GAM’ may have eigenmode-like characteristics in localization and frequency. Otherwise, the ‘GAM’ should appear as broader band structure in potential spectrum owing to its dependence on temperature varying with radius.

### 3-2. Spatio-temporal Structure of Residual Zonal Flow

The electric field fluctuation of  $f < \sim 1$  kHz shows a long-range correlation. The fluctuation, the residual zonal flows, can be extracted by using a numerical filter. The numerical filter is defined as  $\phi_f(t) = \int_{t-\infty}^{t+\infty} f(t-t')\phi(t')dt'$  with  $f(t-t') = \left(1/\sqrt{2\pi\tau_f^2}\right)\exp[-(t-t')^2/2\tau_f^2]$ . The time constants for high and low frequency cut-off are selected here as  $\tau_f = 0.3$  ms and  $\tau_f = 1.0$  ms, respectively. The extremely low frequency is removed to avoid the effects of plasma movement or changes in plasma. The filter property has a peak around 0.5 kHz with the width of  $\sim 1$  kHz in frequency domain. This property corresponds to the coherence curve indicated in Fig. 1(b).

Figures 2(a) and (b) shows examples of the processed electric field. In the case of Fig. 2(a), the observation points of dual HIBPs are located on the same magnetic flux surface, while the observation points in Fig. 2(b) are located in slightly different magnetic flux surfaces. The waveforms of both cases alter temporally in a synchronized way. Obviously, the former and the latter cases show phase difference of  $\sim 0$  and  $\sim \pi/2$ , respectively. No phase-shift of this fluctuation on a magnetic flux surface demonstrates the toroidal symmetry ( $n=0$ ) of electric field fluctuation. The fact also supports the poloidal symmetry ( $m=0$ ), with an assumption that the electric field is constant on a magnetic field line (see ref. [26] in detail). On the other hand, a finite phase shift in Fig. 2(b) indicates that the coherent fluctuation should have a radial structure.

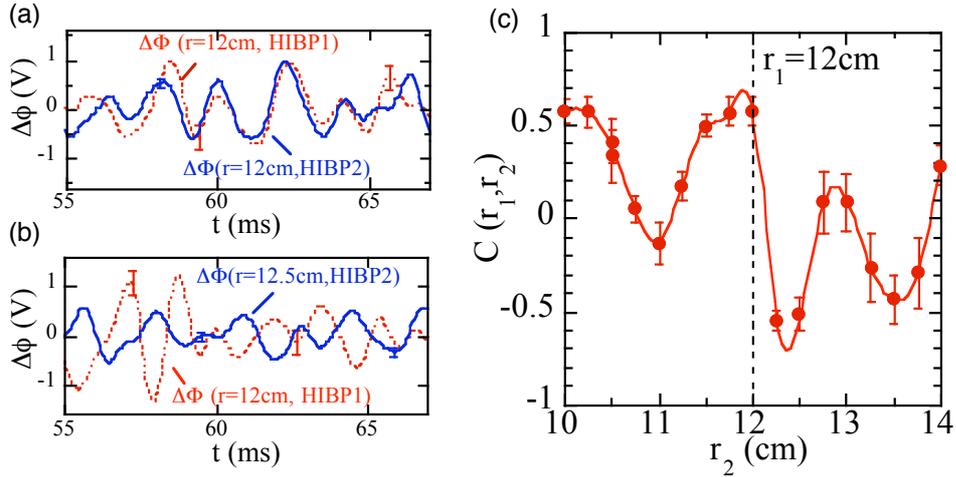


Figure 2. Spatio-temporal structure of residual zonal flows in CHS. (a) Waveforms of electric fields at two toroidal locations,  $\Delta\phi$ , on the same flux magnetic surface. (b) Those on slightly different magnetic flux surfaces. (c) Radial structure of zonal flows represented in cross-correlation coefficients.

The radial structure can be inferred as follows. The electric field fluctuation could be expressed as  $E(r) = -\tilde{E}_z(r) - \tilde{E}_r(r)$ , where the  $E_z$  and  $E_r$  represent the residual zonal flow

and the others, respectively. An analysis using cross-correlation technique can give a rough radial structure of the zonal flow;  $C(r_1, r_2) = \langle E(r_1) \cdot E(r_2) \rangle / \sqrt{\langle E^2(r_1) \rangle \langle E^2(r_2) \rangle}$ , where  $\langle \rangle$  means the time-average. Supposed that  $\tilde{E}_z(r) = E_z \cos(k_r r - \omega t)$  and  $E_T/E_z$  is sufficiently small, the correlation function is reduced to  $C(r_1, r_2) \cong (1 - E_T^2/E_z^2) \cos k_r(r_1 - r_2)$ . Dual HIBP systems allow us to perform this manner of analysis. The result, shown in Fig. 2(c), demonstrates that the electric field fluctuation (or residual zonal flow) should have a radial structure with the dominant wavelength of  $\sim 1$ cm. These results provide clear evidence to show existence of electric field fluctuation symmetric on a magnetic flux surface, with finite radial wavelength, that is, zonal flow.

## 4. Experimental Results of JIPPT-IIU

### 4-1. Experimental Conditions

JIPPT-IIU is a tokamak with the major and minor radii being 0.93m and 0.23m, respectively. The maximum field strength is 3T. The JIPPT-IIU is equipped with a single HIBP. The maximum energy of this HIBP is 500 keV. An excellent feature with this HIBP is that the system has multiple channels available (6 at maximum) to observe adjacent positions in the poloidal cross-section of the plasma. Figure 3a illustrates sets of observation points for three different values of beam energy; 450 keV, 300keV and 250 keV. Neighboring five or six marks represent a set of observation points that can be observed simultaneously.

The experiments are performed in ohmically heated plasmas with toroidal current of 200kA. The safety factor is about 4.3 at the edge, and the plasma density  $1 \times 10^{13} \text{ cm}^{-3}$  and the central electron temperature about 1keV.

### 4-2. Fluctuation Spectra and Correlation Analysis

The potential fluctuation measurements revealed the existence of coherent activity of potential in the core region of the plasma. Figure 3(b) is an example of potential fluctuation spectra. The spectrum shows the existence of a peak around  $\sim 45$  kHz with the width of  $\sim 5$  kHz. The observation points are indicated by an arrow in Fig. 3(a); the normalized minor radius of the observed location is  $\rho \sim 0.2$ , and an expanded view of the observed points is shown as the inset.

In this case, the coherent activity is found in every five observation points; those are located within  $\pm 1$ cm around the central magnetic flux surface. The cross-correlation functions of these points are shown in Fig. 3(c). Every function shows quite similar characteristics. These curves are well fitted with the function of  $C(\tau) = C(0) \exp(-\tau/\tau_{\text{Decay}}) \cos(2\pi f\tau)$  with almost the same parameters;  $C(0) \sim 0.8$ ,  $\tau_{\text{Decay}} \sim 55 \mu\text{s}$ , and  $f \sim 46 \text{ kHz}$ . The feature suggests the poloidal (or  $m=0$ ) symmetry of the modes, if the integral effects are neglected (see Eq. (2)). In the measurements on other sets of multiple observation points, a tendency is found that the correlation could decrease as the observation points become aligned in radial direction. This tendency suggests that the high correlation may not be simply ascribed to the integral effects of electric field fluctuation.

The measurements of the coherent activities in potential were performed for other sets of observation points. The survey allows us to investigate the radial dependence of the amplitude and the frequency of the oscillatory mode. The dependences are shown in Fig. 3(d). It is easily found that both amplitude and frequency increases toward the core. This tendency is quantitatively consistent with the theoretical expectation of GAM frequency,  $f \sim c_s/R$ . The

increase of the amplitude could be related to the decrease of flow damping rate (i.e., ion-ion collisionarity) toward the core. These facts qualitatively support that the oscillation could be GAM.

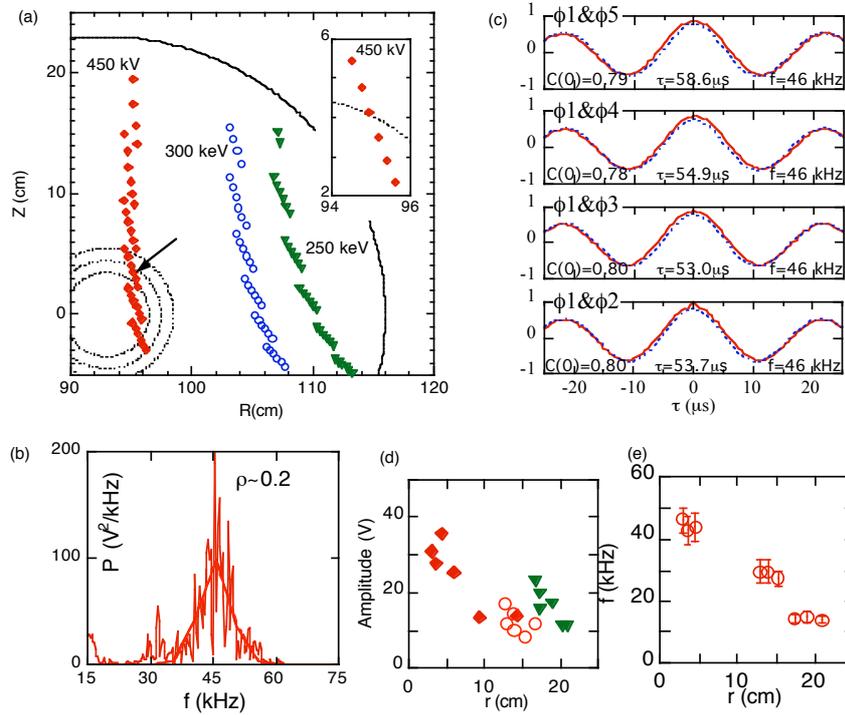


Figure 3. (a) Sets of observation points of HIBP on JIPPT-IIU for three different beam energies (450 keV, 300 keV, 250 keV). The inset shows an expanded view of the set of observation points indicated by the arrow. (b) Potential fluctuation spectrum at the observation point indicated by the arrow in Fig. 3(a). (c) Cross-correlations (red lines) between channels. The dashed blue lines represent the fitting curves. The numbers ( $C(0)$ ,  $\tau_{\text{Decay}}$ ,  $f$ ) are the fitting parameters used for the curve. (d) The radial dependence of the amplitude of coherent oscillation, and (e) The radial dependence of frequency.

## 5. Discussion and Summary

### 5-1. Zonal Flows and Confinement

Zonal flow and turbulence can be regarded as a system that exchanges energy between them. Then, energy distribution between zonal flow and turbulence can be an important factor to determine plasma confinement since the symmetrical characteristics of zonal flow cannot contribute to any radial transport. Therefore, an increase in zonal flow energy should result in better improvement. In CHS, a result is available to show a relation between zonal flow, turbulence and confinement. In other words, a clear difference is found between the amplitude of the zonal flow among cases with and without a transport barrier [28].

Figure 4 shows an example of a change in zonal flow amplitude before and after a back-transition. In Fig. 4(a), two waveforms of potential are shown; one indicates clear transition feature at  $t \sim 70$  ms, while the other shows no change at that time. This means that the former HIBP observes a point inside the barrier. Besides, the detected beam intensities of the latter HIBP around the central channel show opposite characteristics; the inside signal rises but the outside decreases at the transition time. The fact strongly suggests that the central channel of the latter HIBP should be exactly located on the barrier foot-point.

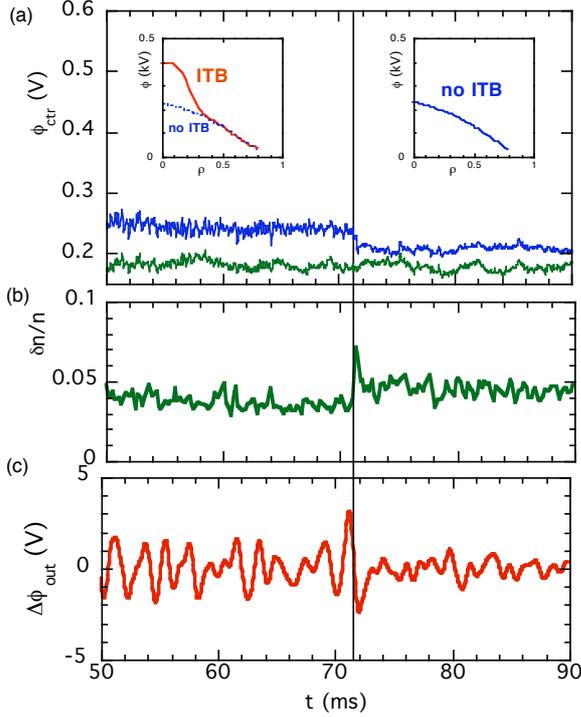


Figure 4. Change in zonal flows and fluctuation with and without transport barrier. (a) Waveforms of potentials at the barrier foot point and barrier inside. The insets show potential profiles before and after the transition. (b) Waveforms of density fluctuation, and (c) waveforms of amplitude of zonal flow at the barrier.

0.05~0.1 kV/m, with an assumption of volume distance being  $\Delta r_{\text{eff}} \sim 1.5$  cm. The amplitude of zonal flow seems rather small, although the absolute value can become a factor larger by taking into account the beam focusing property and a finite size of sample volumes. On the other hand, the huge amplitude of ‘GAM’ in JIPPT-IIU can give a much larger zonal electric field.

The smaller value of the residual zonal flow in CHS, could be ascribed to the flow damping mechanism due to the inhomogeneity of magnetic field (or large parallel viscosity). Actually, the charge exchange recombination spectroscopic measurements confirmed that the toroidal flows driven by parallel-injected neutral beam are quite small compared to those of tokamaks [29]. This feature, large damping rate of zonal flow, can explain the different characteristics in transport between tokamaks and the helical device. In this sense, the symmetry of magnetic configuration can be a key factor to design plasma confinement devices with high confinement performance.

### 5-3. Summary

In summary, we have introduced the HIBP measurements in NIFS. One of the major achievements in the measurements is to show the presence of the residual zonal flows and their fundamental characteristics in CHS. This is the first identification of the residual zonal flow in a toroidal plasma. Besides, the other branch of zonal flow, GAM, is suggested to exist in CHS and JIPPT-IIU. The experimental confirmation of existence of zonal flows should

Figures 4b and Fig. 4c show the density fluctuation (in the frequency range of more than  $f \sim 2$  kHz) and zonal flow amplitudes in the HIBP at the barrier foot point, respectively. After the back-transition, the zonal flow amplitude decreases with a simultaneous increase in the density fluctuation amplitude. Note that the relative increase in the local density fluctuation after the back-transition can be actually larger if the path integral effect is taken into account. As a result, this observation indicates that large energy distribution to zonal flow could be a cause of confinement improvement in the barrier region. Also this result may - the ITB characterized by stronger zonal flow - suggest an important role of an interplay between zonal flow and turbulence fluctuation in transport.

### 5-2. Viscosity and zonal flows

According to the waveforms in Figs. 2(a) and (b), the observed amplitude of the residual zonal flow is  $\sim 1$  V. The absolute value of zonal electric field is

enhance the prospect of plasma burning in the ITER. The presented works, trial for the identification of zonal flows, are the prologue to start a new age of plasma turbulence research.

### Acknowledgements

This work is partially supported by the Grant-in-Aids for Scientific Research (No. 15360497) and Specially-Promoted Research (No. 16002005). The authors also express a great appreciation to Director General O. Motojima and Prof. Emeritus M. Fujiwara for their continuous encouragements and supports.

### References

- 1) Yoshizawa, A. , Itoh, S. -I., Itoh, K., ‘Plasma and Fluid Turbulence’ (Institute of Phys. Pub., Bristol and Philadelphia, 2003).
- 2) Biglari, H., Diamond, P. H., Terry, P. W., Phys. Fluids B **2** 1 (1990);
- 3) Itoh, S.-I., and Itoh K., J. Phys. Soc. Jpn. **59**, 3815 (1990).
- 4) Hasegawa A., Maclennan, C. G., and Kodama, Y., Phys. Fluids **22**, 2122 (1979)
- 5) Diamond, P. H. *et al*, in Proceedings of the 17th IAEA fusion energy conference, Yokohama, 1998 **vol. 4** 1421-1428.(International Atomic Energy Agency, Vienna, Austria, 1999).
- 6) Diamond, P. H., Itoh, K., Itoh, S.-I., Hahm, T. S., Plasma Phys. Control. Fusion in press.
- 7) Glanz, J., Science **274**, 1600 (1996).
- 8) Lin, Z., Hahm, T. S., Lee, W. W., Tang, W. M., White, R. B., Science **281**, 1835 (1998).
- 9) Rosenbluth, M. N., Hinton, F. L., Phys. Rev. Lett. **80**, 724 (1998).
- 10) Hasegawa, A., Wakatani, M., Phys. Rev. Lett. **59**, 1581 (1987).
- 11) Hammet, G., et al., Plasma Phys. Control. Fusion **35**, 973 (1993).
- 12) Waltz, R. E., Kerbel, G. D., Milovich, J., Phys. Plasmas **1**, 2229 (1994)
- 13) Dimits, A. M., et al., Phys. Plasmas **7**, 969 (2000).
- 14) Hallatshek, K., Phys. Rev. Lett. **84**, 5145 (2000).
- 15) Scott, B. D., Phys. Plasmas **7**, 1845 (2000).
- 16) Watanabe, T. -H., Sugama, H., Phys. Plasmas **9**, 3659 (2002).
- 17) Hamada, H., et al., Fusion Eng. Design **34-35**, 663 (1997).
- 18) Schoch, P. M., Connor, K. A., Demers, D. R., Zhang, X., Rev. Sci. Instrum. **74** 1846 (2003).
- 19) Shats, M. G., Solomon, W. M., Phys. Rev. Lett. **88**, 045001 (2002).
- 20) Xu, G.S. et al., Phys. Rev. Lett. **91**, 125001 (2003)
- 21) McKee, G. R. *et al.*, Plasma Phys. Control. Fusion **45**, A477 (2003).
- 22) Moyer, R. A., Tynan, G. R., Holland, C., Burin, M. J., Phys. Rev. Lett. **87**, 135001 (2001).
- 23) Diamond, P. H., *et al.* Phys. Rev. Lett. **84**, 4842 (2000).
- 24) Winsor, N., Johnson, J. L., and Dawson, J. M., Phys. Fluids **11**, 2448 (1968).
- 25) Hallatshek, K., Biskamp, D., Phys. Rev. Lett. **86** 1223 (2001).
- 26) Fujisawa, A., et al., Phys. Rev. Lett. in press.
- 27) Hamada, Y., submitted to Nucl. Fusion.
- 28) Fujisawa, A., *et al.* Phys. Rev. Lett. **82**, 2669(1999).
- 29) Ida, K., Yamada, H., Iguchi H., et al., Phys. Rev. Lett. **67** 58(1991).

# Edge Plasma Control by Local Island Divertor in LHD

A. Komori<sup>1</sup>, T. Morisaki<sup>1</sup>, S. Masuzaki<sup>1</sup>, M. Kobayashi<sup>1</sup>, Y. Feng<sup>2</sup>, M. Shoji<sup>1</sup>, N. Ohyabu<sup>1</sup>, K. Ida<sup>1</sup>, K. Tanaka<sup>1</sup>, K. Kawahata<sup>1</sup>, K. Narihara<sup>1</sup>, S. Morita<sup>1</sup>, B. J. Peterson<sup>1</sup>, R. Sakamoto<sup>1</sup>, S. Sakakibara<sup>1</sup>, H. Yamada<sup>1</sup>, K. Ikeda<sup>1</sup>, O. Kaneko<sup>1</sup>, S. Kubo<sup>1</sup>, J. Miyazawa<sup>1</sup>, K. Nagaoka<sup>1</sup>, H. Nakanishi<sup>1</sup>, K. Ohkubo<sup>1</sup>, Y. Oka<sup>1</sup>, M. Osakabe<sup>1</sup>, D. Reiter<sup>3</sup>, F. Sardei<sup>2</sup>, T. Shimozuma<sup>1</sup>, Y. Takeiri<sup>1</sup>, K. Tsumori<sup>1</sup>, K. Y. Watababe<sup>1</sup>, I. Yamada<sup>1</sup>, Y. Yoshimura<sup>1</sup>, M. Yoshinuma<sup>1</sup>, O. Motojima<sup>1</sup> and LHD Experimental Group<sup>1</sup>

<sup>1</sup>National Institute for Fusion Science, Toki, Gifu 509-5292, Japan

<sup>2</sup>Max-Planck-Institute fuer Plasmaphysik, Euratom Association, D-17493 Greifswald, Germany

<sup>3</sup>Institute fuer Plasmaphysik, Forschungszentrum Juelich GmbH, Euratom Association, Trilateral Euregio Cluster, 52425 Juelich, Germany

## Abstract.

In the Large Helical Device (LHD) program, one of the key research issues is to enhance helical plasma performance through the edge plasma control. For the first time in the LHD program, the edge plasma control was performed with a local island divertor (LID) that is a closed divertor, utilizing an  $m/n = 1/1$  island generated externally by 20 small perturbation coils, and fundamental LID functions were demonstrated experimentally. It was found that the outward heat and particle fluxes crossing the island separatrix flow along the field lines to the backside of the divertor head, where carbon plates are placed to receive the heat and particle loads. Accordingly high efficient pumping was demonstrated, which is considered to be the key in realizing high temperature divertor operation, resulting in an improvement of energy confinement. In the present experiment, relatively good energy confinement is achieved in the high density regime at a magnetic axis position,  $R_{ax}$ , of 3.75 m. Results of edge modelling are also presented by using the EMC3-EIRENE code.

**PACS numbers:** 52.55Hc

## 1. Introduction

The Large Helical Device (LHD) is a superconducting heliotron-type device at the National Institute for Fusion Science at Toki, Japan [1]. One of the key research issues in the LHD program is to control heat and particle fluxes to the wall and to enhance core plasma confinement. This control of the LHD edge plasma will primarily be done with a closed full helical divertor, which utilizes a natural separatrix in the edge region [1], as shown in Fig. 1(a). However, the closed full helical divertor is planned in the late stage of the LHD program. Instead we intended to use a local island divertor (LID) for the LHD edge plasma control [2]. The LID is a closed divertor that uses an  $m/n = 1/1$  island, as shown in Fig. 1(b). The technical ease of hydrogen pumping is the advantage of the LID over the closed full helical divertor because the hydrogen recycling is toroidally localized.

The core region in the LID configuration is surrounded by the separatrix of the island, so that the outward heat and particle fluxes cross the island separatrix, and flow along the field lines to the backside of the island [2]. The particles recycled there are pumped out by a

pumping system, designed to be a closed divertor system with overall pumping efficiency of larger than 30%. Unlike the conventional pump limiters, blades of the divertor head are located inside the island, thereby being protected from the high outward heat flux from the core. Thus there is no leading-edge problem.

High efficient pumping is the key in realizing high temperature divertor operation, where the divertor plasma with a temperature of a few keV is produced, resulting in a significant improvement of energy confinement [3]. A closed divertor also provides high plasma plugging efficiency required for the high recycling operation, where a low temperature and high density divertor plasma is produced for radiative cooling. These two operational modes can be realized in the LID [2]. These divertor functions allow the LID to pump out ionized impurities that are difficult to be pumped out in the presence of the magnetic field.

Recent results of the LID are described in this paper. The LID experiment has provided us critical information on the edge plasma behavior in the heliotron-type device, and helped us to optimize the design of the closed full helical divertor on LHD. It has also influenced the divertor design of W7-X [4], and helped us to explore advanced divertor concepts.

## 2. Experimental apparatus

The LID system consists of a divertor head, its driving system, a pumping duct, and an LID chamber and so on, in addition to 20 perturbation coils locating above and below the torus for controlling the islands [5]. The length of the LID head system is so long that the driving system requires the long LID chamber to take out the divertor head from the LHD vacuum vessel and to seal it up with a gate valve whose inner diameter is 1.4 m. These driving system and gate valve are necessary for maintaining the LID head system and performing experiments without the LID.

The size of the divertor head is  $0.99 \times 0.664$  m in the front view, and the area of the divertor head, which receives the particle flux, is  $\sim 0.3$  m<sup>2</sup>. The divertor head is divided into 8 elements, which consist of small planar carbon plates joined mechanically to a stainless-steel heat sink with a cooling tube, on the side that the particle flux strikes. The average heat flux onto the carbon plates was designed  $\sim 5$  MW/m<sup>2</sup> for 3 sec. Another side of the divertor head, facing the core plasma, is covered mainly with the molybdenum plates by mechanical joint to protect the heat sink from high-energy neutral particles produced by charge exchange.

The particles recycled on the carbon plates are pumped out by the pumping system, which has 8 cryogenic pumps with a hydrogen pumping speed of 42,000 l/sec. The effective pumping speed is  $1.3 \times 10^5$  l/sec at the gate valve located between the LID chamber and LHD vacuum vessel, and large enough to realize a molecular flow. The pumping capacity and maximum pumping flux are  $3 \times 10^5$  torr-l and 75 torr-l/sec, respectively. These satisfy the values required for the LID pumping system to control the LHD edge plasma. The gap between the divertor head and pumping duct was usually fixed at 0.1 m in our experiment in order to form a closed divertor configuration with high pumping efficiency.

## 3. Experimental results and discussion

Before the start of the LID experiment, the magnetic flux surface measurement was performed to assure the formation of the  $m/n = 1/1$  island. It was carried out using the diode technique, which utilizes an electron gun and a probe array. The experimental observations

agreed well with the numerical result, and hence, a clear generation of the  $m/n = 1/1$  island was demonstrated.

### 3.1. LID functions

The effect of the LID on plasma performance was studied mainly using hydrogen puffing NBI discharges at magnetic axis positions,  $R_{ax}$ 's, of 3.6 and 3.75 m with the toroidal magnetic field of  $\sim 2.75$  T. The NBI power,  $P_{NB}$ , was 4 - 10 MW. The plasma parameters change significantly with the LID. For example, the line-averaged electron density,  $\bar{n}_e$ , is reduced typically by a factor of  $\sim 2$  at the same gas puff rate, compared with discharges without the LID.

The ion saturation currents,  $I_{is}$ , were measured with the Langmuir probes located on the carbon plates of the helical divertor and the divertor head of the LID, respectively. The latter carbon plates are, of course, located on the backside of the divertor head, to which the heat and particle fluxes flow along the field lines of the  $m/n = 1/1$  island separatrix. It was clearly shown that the particle flux flowed to the helical divertor and struck upon its carbon plates, when the LID was turned off. No  $I_{is}$  signal was, of course, observed on the divertor head of the LID. On the contrary,  $I_{is}$  on the divertor head of the LID became large with the LID, while  $I_{is}$  on the carbon plate of the helical divertor was reduced to almost zero. This indicates that the LID carries out one of its functions, that is, collects almost all particle flux towards the helical divertor [5, 6]. To estimate the number of particles that strike upon the divertor head, we calculated the percentage  $P$  of the magnetic field lines that strike upon the divertor head, among a total of 240 field lines, which circulates around the torus 15 times [2]. The field lines started from the poloidally equally spaced points at distances of 0.04, 0.08 and 0.12 m from the last closed flux surface (LCFS) and toroidally at the same angle as the center of the divertor head. The perpendicular spreading of the starting points took into account the perpendicular diffusion of the particle flux to some extent. This calculation suggested that  $P$  reaches 90% when the size of the divertor head is larger than  $\sim 0.6$  m [2], and this was demonstrated experimentally.

Figure 2 shows the radial profiles of electron temperature,  $T_e$ , and  $I_{TS}$ , which is a measure of electron density,  $n_e$ , and measured with the Thomson scattering system. The magnetic axis position,  $R_{ax}$ , was 3.6 m. A comparison between two discharges with and without the LID was performed under the condition with almost the same  $\bar{n}_e$  of  $\sim 1.9 \times 10^{19} \text{ m}^{-3}$ . It was clearly demonstrated with the LID that the  $T_e$  profile is bounded by the inner separatrix of the island, while the low- $T_e$  plasma flows along the outer separatrix of the island. Since the toroidal position of the Thomson scattering system is 72 degrees apart from that of the LID head, the island separatrix can be seen to guide indeed particle fluxes to the LID head. The  $T_e$  profile with the LID rises steeply from the inner separatrix of the island, and the central  $T_e$  is as high as that without the LID. In the region outside the outer separatrix of the island, the low-temperature and low-density plasma is scraped off, which exists outside the LCFS without the LID, as shown in Fig. 2. Since almost no plasma exists between the outer separatrix of the island and the vacuum vessel, the recycling of particles is localized only near the LID head, located inside the pumping duct. This was confirmed by the  $H_\alpha$  emission measurement at the plasma periphery. The neutral particle pressure,  $p_{vv}$ , between the plasma and wall was also measured with a fast-ion gauge located on the vacuum vessel. When the LID was turned off,  $p_{vv}$  increased monotonically with  $\bar{n}_e$ . This is because strong gas puffing is necessary for the

production of the higher  $\bar{n}_e$  under the condition that the heating power is kept constant. Accordingly,  $p_{vv}$  increases with  $\bar{n}_e$ . When the LID was turned on, stronger gas puffing was necessary than that without the LID in order to realize the same  $\bar{n}_e$  as without the LID, because the pumping ability of particles is much higher than that without the LID. However, it was clearly shown that  $p_{vv}$  was almost constant and kept low, independently of  $\bar{n}_e$ , being different from the observations without the LID. This indicates that the number of recycled particles is small, and is reasonable because almost all the divertor plasma strikes upon the divertor head, and there is almost no particle flux to the wall and helical divertor, as mentioned before. The connection length of the magnetic field around the island, that is, from near the inner separatrix of the island on the equatorial plane to the divertor head is  $\sim 120$  m in this case, and will be shortened by increasing the perturbation coil currents further. Thus, the density along the outer separatrix of the island, as shown in Fig.2, will decrease significantly, and hence, the  $I_{TS}$  profile will agree with the  $T_e$  profile, which exists only inside the inner separatrix of the island.

The too effective pumping of ionized particles by the LID causes not only the low-density plasmas, but also a favourable aspect of preventing impurities from penetrating into the plasma, and this is an important function of the LID. Figure 3 shows radial profiles of radiation,  $P_{rad}$ , measured with the bolometer array, and depicted using the normalized radius,  $\rho$ , without the LID. Open and closed symbols represent the radiation profiles without and with the LID, respectively. A distinct difference between these two kinds of profiles is the radiation power itself, that is, the radiation power with the LID is about 50% lower than that without the LID over the entire plasma except for the plasma center in the relatively high-density operation. The highly radiated region is different in these two kinds of profiles. The radiation power is high in the region of  $\rho > 0.65$  without the LID, while it is localized in the island region outside the LCFS, as shown in Fig. 3. In the latter case, the cold plasma located in the island region, as shown in Fig. 2, may play an important role in the radiation process. The radiation power from the central region with the LID increases with  $\bar{n}_e$ , and exceeds that without LID at  $\bar{n}_e$  of  $\sim 2 \times 10^{19} \text{ m}^{-3}$ . The main sources of radiation are metallic impurities, which may be released from the LID head facing the plasma. There is a possibility that this central radiation may degrade the core plasma performance if the impurities accumulate further. In the neon (Ne) gas injection experiment to the hydrogen plasma, it was found that the Ne density with the LID is lower than that without the LID [6]. Accordingly the LID was demonstrated to be very effective for impurity screening. Another supporting evidence of impurity screening is tolerance to the radiation collapse with the LID. Figure 4 shows the time evolution of the total radiation power from the plasma, during the Ne injection, in the limiter (dashed line) and the LID (solid line) configurations. In the limiter configuration, the perturbation coils for generating the  $m/n=1/1$  island were switched off but the LID head was inserted as a limiter. It is found that the total radiation power was kept low in the LID configuration during the discharge, while it increased abruptly, leading to the radiation collapse in the limiter configuration.

### 3.3. Effect of LID on global confinement

As mentioned in section 3.1, it was found that the LID can affect the edge plasma through the effective particle control. The  $T_e$  and  $n_e$  profiles at the plasma periphery were realized with the LID, which are very similar to expected ideal ones.

In order to investigate the LID effect on the global confinement, the experiments were performed in the two magnetic configurations, that is, at  $R_{ax} = 3.60$  and  $3.75$  m, with various  $\bar{n}_e$ 's in the LID configuration. Figure 5 (a) shows the plasma stored energy,  $W_p$ , measured with diamagnetic loops, as a function of  $\bar{n}_e$ . The high density discharges in each configuration were achieved by hydrogen pellet injection. It can obviously be seen that the density range is limited less than  $\sim 7 \times 10^{19} \text{ m}^{-3}$  at  $R_{ax} = 3.60$  m, while it is extremely extended up to  $\sim 1.3 \times 10^{20} \text{ m}^{-3}$  at  $R_{ax} = 3.75$  m. Furthermore  $W_p$  tends to saturate in the high density regime at  $R_{ax} = 3.60$  m. On the other hand,  $W_p$  is not saturated against  $\bar{n}_e$  at  $R_{ax} = 3.75$  m. The improvement factor of the energy confinement time,  $\tau_E$ , over the ISS95 scaling law [7] was calculated for the  $R_{ax} = 3.60$  and  $R_{ax} = 3.75$  m configurations as a function of  $\bar{n}_e$ , as shown in Figs. 5 (b) and (c). The energy confinement time,  $\tau_E$ , with the LID was found to follow the ISS95 scaling law at  $R_{ax} = 3.60$  m in the low density regime, however it is worse in the high density regime than that without the LID, that is, with the standard LHD magnetic configuration. The energy confinement without the LID is usually about 1.5 times better than that of the ISS95 scaling law, when  $R_{ax}$  is at 3.60 m [8]. It is shown that the improvement factor decreases with  $\bar{n}_e$ . On the other hand, the improvement factor at  $R_{ax} = 3.75$  m with the LID is almost unity without degradation in the density range up to  $\sim 1.3 \times 10^{20} \text{ m}^{-3}$ . Much better confinement is achieved in the high density regime, compared with that without the LID, that is, the standard LHD magnetic configuration, as shown in Fig. 5 (c). Thus, it can be said that the confinement performance is actually improved by the LID at  $R_{ax} = 3.75$  m.

Although the reason is not clear for the different characteristics of confinement between the two configurations, that is, the  $R_{ax} = 3.60$  and  $3.75$  m configurations, some explanations can be considered from the present experimental results. First of all, the magnetic configuration itself is thought to affect the confinement. The separatrix of the island is located inside the region of the closed nested magnetic surfaces at  $R_{ax} = 3.6$  m, and hence, is isolated from an ergodic layer of the helical natural separatrix, while it touches the ergodic layer of the helical natural separatrix, and is ergodized a little at  $R_{ax} = 3.75$  m. In other words, the island at  $R_{ax} = 3.75$  m is located in the ergodic layer, that is, floating in the "ergodic sea". Thus, some field lines reach the target plates of the natural open helical divertor, instead of striking the LID head, because of their radial excursions due to the ergodic effect. Then, some amount of particle recycling occurs consequently on the target plates of the natural open helical divertor. In fact, a longer density decay time,  $\tau_p^*$ , suggesting higher particle recycling, was observed at  $R_{ax} = 3.75$  m, as shown in Fig. 6. Little difference between the two fuelling methods, that is, pellet injection and gas puff, can be seen, suggesting that the fuelling method has nothing to do with the recycling process. From the  $H_\alpha$  light emission from the plasma periphery, it can be also confirmed that the edge recycling at  $R_{ax} = 3.75$  m is larger than that at  $R_{ax} = 3.60$  m. Generally speaking, the number of recycling particle and its energy is larger than that of gas puffing. Therefore these recycled particles may contribute to an increase in  $\bar{n}_e$ .

Furthermore, there is another possibility that the particle recycling at the LID head is also high at  $R_{ax} = 3.75$  m, since the outer island separatrix may hit the leading edge of the LID head a little. This problem came from the design concept of the LID head. It was originally designed to fit the magnetic configuration at  $R_{ax} = 3.60$  m, since it showed the best performance of the confinement [8]. In order to estimate the particle recycling at the LID head precisely, the edge transport physics has been analyzed using the 3D fluid edge-transport code, EMC3 [9], coupled with the kinetic neutral transport code, EIRENE [10]. This EMC3-EIRENE code treats almost any three-dimensional geometries of plasma, magnetic field and

plasma facing components, and provides 3D profiles of plasma parameters, that is,  $n_e$ ,  $T_e$ , neutrals, and so on. Here, the EMC3-EIRENE code simulated a discharge with relatively low heating power, that is, with  $P_{NB}$  of  $\sim 1.4$  MW. The electron density,  $n_e$ , at the inner island separatrix was chosen to be  $\sim 1.2 \times 10^{19} \text{ m}^{-3}$ , taking into account the experimental observations. Figure 7 shows the 2D-ionization source profile on the poloidal cross section at the toroidal position of the LID head center. The cross section of the LID head is outlined against the coloured contour map. From these figures, one can easily identify the position, where the particle recycling is highest and the ionization occurs very frequently. It is found that the ionization source is concentrated at the backside of the LID head at  $R_{ax} = 3.60$  m, that is, the particle recycling is taken place inside the pumping duct. On the other hand, it can be seen at  $R_{ax} = 3.75$  m that the peak of the ionization locates at the edge of the LID head, that is, the outer island separatrix hits the leading edge of the LID head. In this situation the particle recycling occurs inside the island. Therefore recycling particles can contribute to an increase in  $\bar{n}_e$ . A pumping efficiency,  $\varepsilon$ , was also obtained at  $R_{ax} = 3.60$  m with the EMC3-EIRENE code to be 50 – 60 % under the definition of  $\varepsilon = \Gamma_{pump} / \Gamma_{head}$ , where  $\Gamma_{pump}$  and  $\Gamma_{head}$  are the particle flux pumped out by the LID and the particle flux guided to the LID head, respectively.

#### 4. Summary

The fundamental functions of the LID were clearly demonstrated. The particle flow is indeed guided to the divertor head along the island separatrix, and a high pumping efficiency is realized. The electron density,  $n_e$ , is bounded on the island separatrix as well as the electron temperature,  $T_e$ . Accordingly, almost no plasma exists between the outer island separatrix and the wall, and hence, a recycling rate of particles becomes low. This leads to a steep  $T_e$  gradient in the periphery, similar to that expected with the LID. Relatively good energy confinement is achieved in the high density regime at  $R_{ax} = 3.75$  m, which is improved much better than that at  $R_{ax} = 3.6$  m. The simulation using the EMC3-EIRENE code provides the reasonable results, explaining the experimental observations.

The first step was taken towards the enhancement of helical plasma performance with the LID. For remarkable improvement of plasma confinement, the plasma density should be controlled by central fuelling or by changing recycling rate. By checking the results obtained by the simulation using the EMC3-EIRENE code, further experimental verification is also necessarily expected.

#### References

- [1] IYOSHI, A., et al., “Design study for the Large Helical Device”, Fusion Technol. **17** (1990) 169
- [2] KOMORI, A., et al., “Local island divertor concept for LHD”, Plasma Physics and Controlled Nuclear Fusion Research 1994 (Proc. 15th Int. Conf. Seville, 1994), Vol. 2, IAEA, Vienna (1995) 773.
- [3] OHYABU, N., et al., “The large helical device (LHD) helical divertor”, Nucl. Fusion **34** (1994) 387.
- [4] GRIEGER, G., et al., “Physics and engineering studies for Wendelstein 7-X”, Plasma Physics and Controlled Nuclear Fusion Research 1990 (Proc. 13th Int. Conf. Washington, D. C., 1990), Vol. 3, IAEA, Vienna (1991) 525.

- [5] KOMORI, A., et al., “Initial results of local island divertor experiments in Large Helical Device”, *Fusion Sci. and Technol.* **46** (2004) 167.
- [6] MORISAKI, T., to be published in *Nucl. Mater.* (2005).
- [7] STROTH, U., et al., “Energy confinement scaling from the international stellarator database”, *Nucl. Fusion* **36** (1996) 1063.
- [8] YAMADA, H., et al., “Configuration flexibility and extended regimes in Large Helical Device”, *Plasma Phys. Control. Fusion* **43** (2001) A55.
- [9] FENG, Y., et al., “Transport in island divertors: physics, 3D modelling and comparison to first experiments on W7-AS”, *Plasma Phys. Control. Fusion* **44** (2002) 611.
- [10] REITER, D., Juelich Report (1984) 1947.

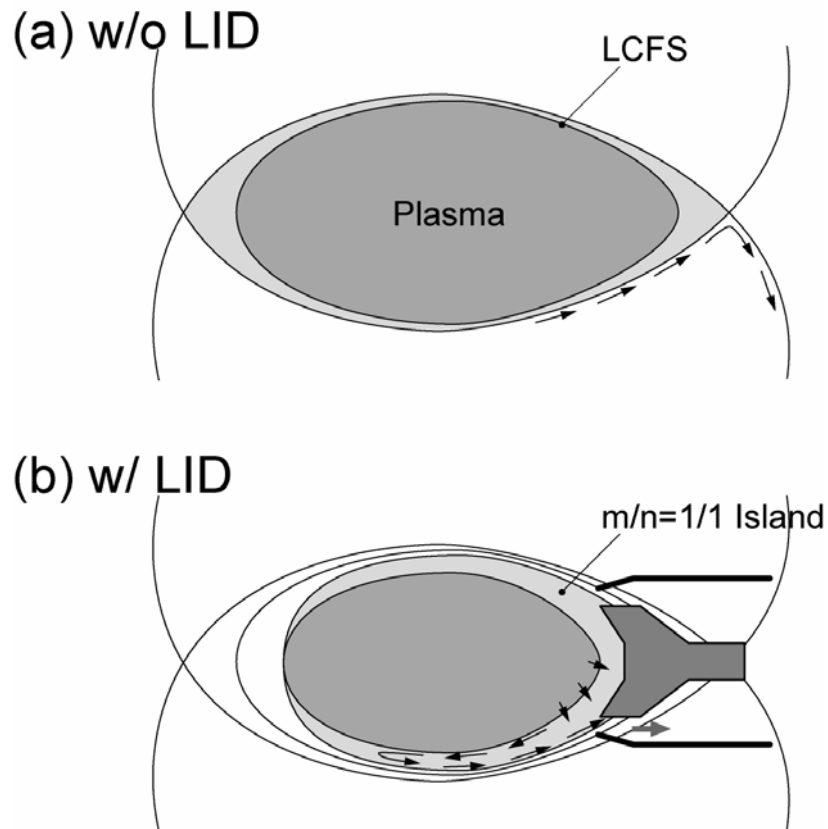


Fig. 1. Plasma cross sections (a) without and (b) with the LID. The intrinsic 1/1 island, due to error field, is eliminated with perturbation coils in (a), where LCFS represents the last closed flux surface. The experiment with the LID is the one, performed when the 1/1 island is formed and the divertor head is inserted, as shown in (b).

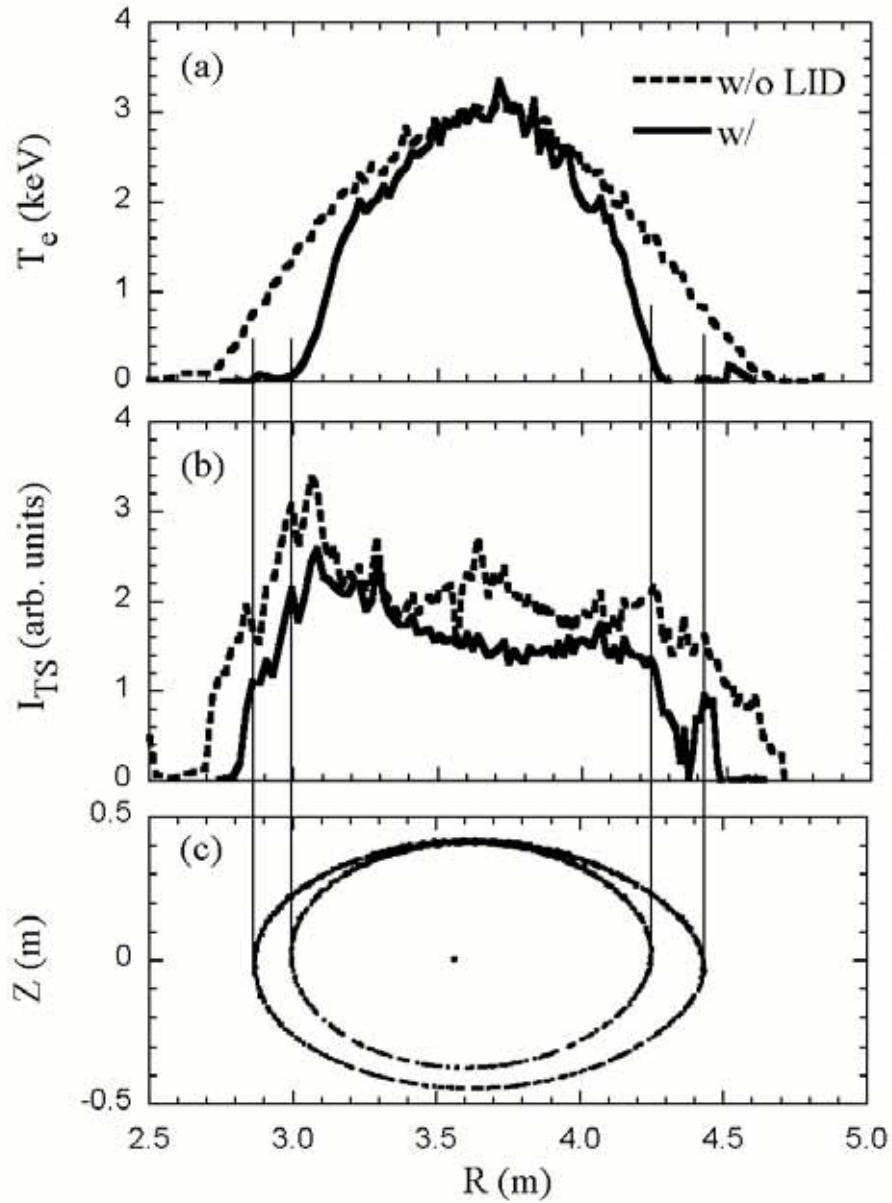


Fig. 2. Radial profiles of (a)  $T_e$  and (b)  $I_{TS}$  which is a measure of  $n_e$  measured with the Thomson scattering, with (solid line) and without (dashed line) the LID at  $R_{ax} = 3.6$  m. A Poincaré plot of the island separatrix at the toroidal position of the Thomson scattering system is also depicted in (c).

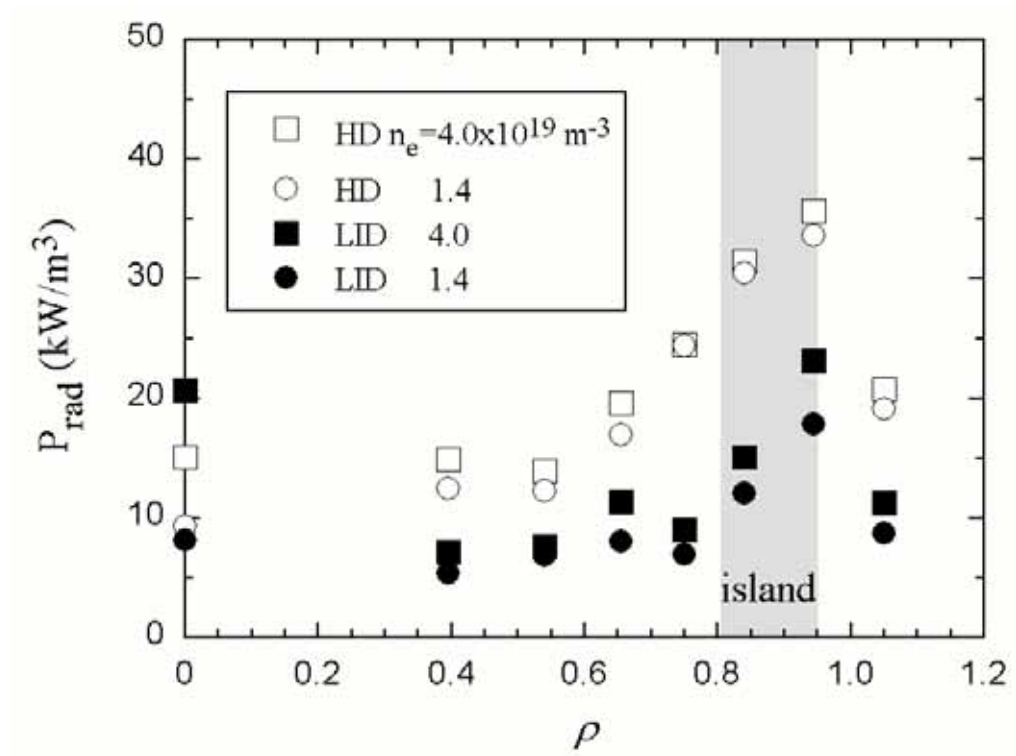


Fig. 3. Radiation profiles with (closed symbols) and without (open symbols) the LID, as a function of normalized radius  $\rho$  at  $R_{ax} = 3.6$  m. With the LID, the island is in the region of  $0.80 < \rho < 1.95$ .

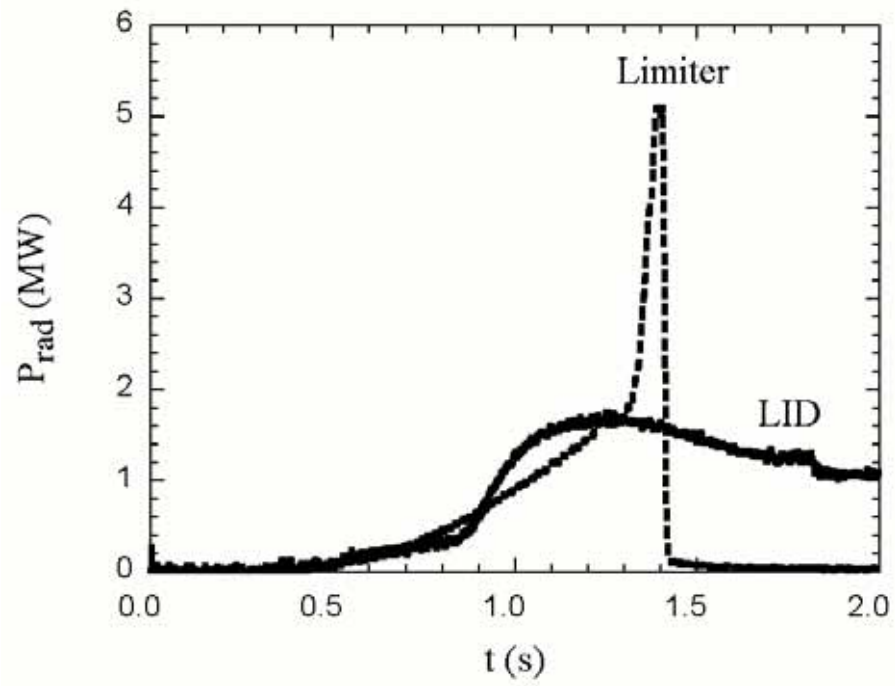


Fig. 4. Time behaviour of total radiation power,  $P_{rad}$ , from the plasma during Ne injection in the limiter (dashed line) and the LID (solid line) configurations.

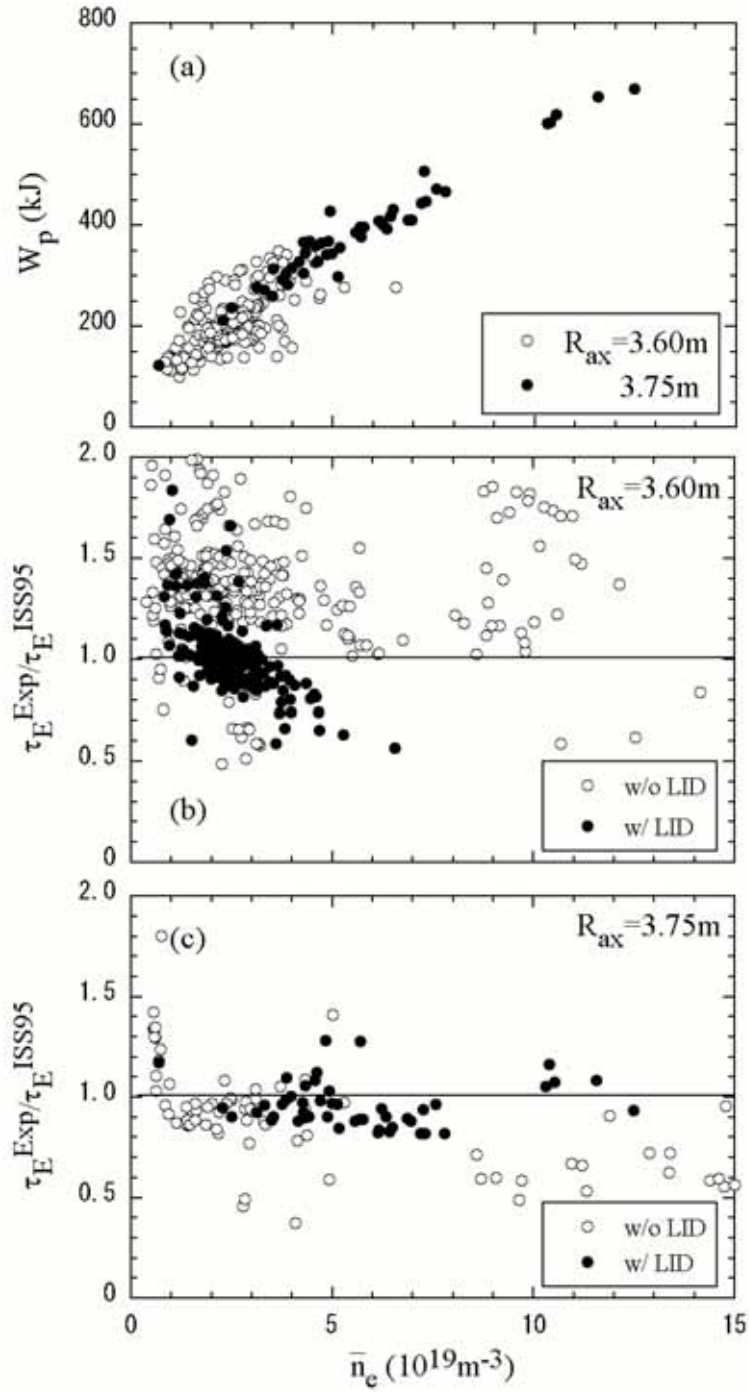


Fig. 5. (a) Achieved plasma stored energy  $W_p$  in the LID configuration. Improvement factor of the energy confinement time  $\tau_E$  from the ISS95 scaling law at (b)  $R_{ax}= 3.60$  m and (c)  $R_{ax}= 3.75$  m as a function of the line averaged density.

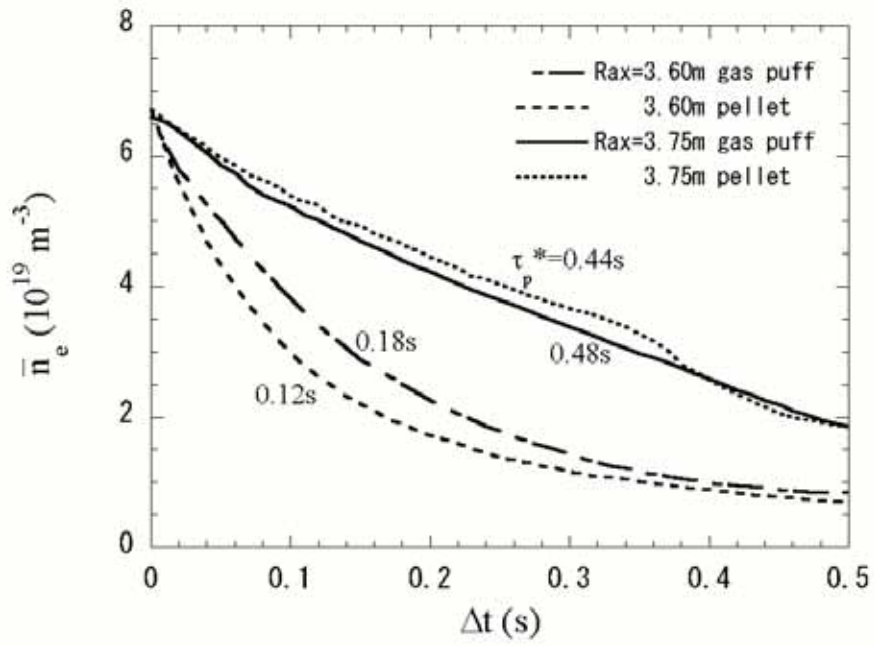


Fig. 6. Temporal evolution of  $\bar{n}_e$  after turning off the gas puffing, whose characteristic time provides the effective particle confinement time,  $\tau_p^*$ .

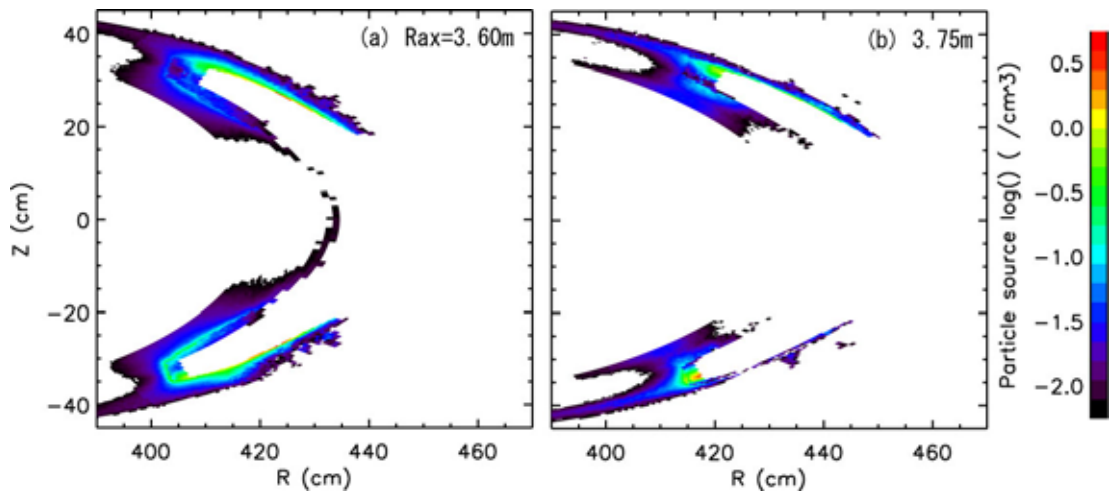


Fig. 7. 2D ionization source profile on the poloidal cross section at the LID head center. The cross section of the LID head is outlined against the colored contour map.

# Comparison of Transient Electron Heat Transport in LHD Helical and JT-60U Tokamak Plasmas

**S. Inagaki**<sup>†</sup> **H. Takenaga**<sup>‡</sup> **K. Ida**<sup>†</sup> **A. Isayama**<sup>‡</sup>  
**N. Tamura**<sup>†</sup> **T. Takizuka**<sup>‡</sup> **T. Shimozuma**<sup>†</sup> **Y. Kamada**<sup>‡</sup> **S. Kubo**<sup>†</sup>  
**Y. Miura**<sup>‡</sup> **Y. Nagayama**<sup>†</sup> **K. Kawahata**<sup>†</sup> **S. Sudo**<sup>†</sup> **K. Ohkubo**<sup>†</sup>  
**LHD Experimental Group and the JT-60U Team** §

<sup>†</sup> National Institute for Fusion Science, Oroshi-cho, Toki-shi, Gifu, 509-5292, Japan

<sup>‡</sup> Naka Fusion Research Establishment, Japan Atomic Energy Research Institute, Naka-machi, Naka-gun, Ibaraki 311-0193, Japan

**Abstract.** Transient transport experiments are performed in plasmas with and without Internal Transport Barrier (ITB) on LHD and JT-60U. The dependence of  $\chi_e$  on electron temperature,  $T_e$ , and electron temperature gradient,  $\nabla T_e$ , is analyzed by an empirical non-linear heat transport model. In plasmas without ITB, two different types of non-linearity of the electron heat transport are observed from cold/heat pulse propagation. The  $\chi_e$  depends on  $T_e$  and  $\nabla T_e$  in JT-60U, while the  $\nabla T_e$  dependence is weak in LHD. Inside the ITB region, there is no or weak  $\nabla T_e$  dependence both in LHD and JT-60U. A cold pulse growing driven by the negative  $T_e$  dependence of  $\chi_e$  is observed inside the ITB region (LHD) and near the boundary of the ITB region (JT-60U).

§ To whom correspondence should be addressed (inagaki@LHD.nifs.ac.jp)

## 1. Introduction

Helical systems and tokamaks are the most realistic concepts for magnetic confinement of thermonuclear plasmas. There are some similarities and differences in heat transport between helical systems and tokamaks. Similarities in transport are as following: (i) the radial heat transport is anomalously higher than neoclassical theory, (ii) the global energy confinement time shows similar parametric dependence and the power degradation of confinement is observed in both devices. Heat (and particle) transport in both devices are also considered to be driven by turbulent processes. On the other hand, one of the differences in heat transport is as following: the electron temperature,  $T_e$ , profile reacts weakly to changes of the heating deposition profile in tokamaks, however, this transport phenomenon, known as “profile stiffness” [1, 2], is weak or absent in helical systems. In fact, although the global confinement scaling is similar to ELMy H-mode scaling [3], no evidence for the tokamak-like stiffness is observed in the Large Helical Device (LHD). The physical models that can explain stiffness can be divided into two categories: local and non-local. Some local transport models based on temperature-gradient-driven turbulence indicate that the heat transport is non-linear and thus the electron heat diffusivity,  $\chi_e$ , has a dependence on  $T_e$  and/or  $\nabla T_e$  [4, 5]. Especially, the non-linear models based on the “critical gradient scale length” can explain some of tokamak-type stiffness [6]. Therefore, the validity of non-linear transport models based on turbulence should be clarified in helical systems. To study the non-linearity of heat transport, transient transport analysis is recognized as a very powerful tool because it can yield  $\partial q_e / \partial \nabla T_e$  and  $\partial q_e / \partial T_e$ , here  $q_e$  is the electron heat flux [7]. Thus the transient response should be explained by the first-principle transport models as well as the steady state profiles. In addition, the transient analysis is the only technique which can obtain information to answer the interesting question of whether transport in magnetically confined plasmas is determined by local plasma parameters or not.

Theoretically, the magnetic configuration influences turbulence in many aspects. Hence, comparison of heat transport features between tokamak and helical systems would reveal the importance of the magnetic configuration for transport and be very useful to gain a comprehensive understanding of the turbulent transport in toroidal devices because their magnetic configurations are quite different (e.g. aspect ratio and safety factor,  $q$ , profile). In spite of its importance for the transient analysis, there was a few comparisons of the transient experiments between helical and tokamak plasmas because of a few experiments of transient transport in helical plasmas. Particularly, there is no comparison of transient transport experiments in plasma with Internal Transport Barriers (ITBs) between helicals and tokamaks. Recent experimental progress on LHD and JT-60U enables us to make more an extensive comparison of the transient response in plasmas not only without ITB but also with ITB. In this paper, the newly obtained results of transient transport experiments are reported and the characteristics of electron heat transport obtained from transient analysis are compared between LHD and JT-60U plasmas.

To perturb the core region of LHD and JT-60U plasmas, heat and cold pulse propagation techniques are used. Multi-channel heterodyne radiometers and a multi-channel grating

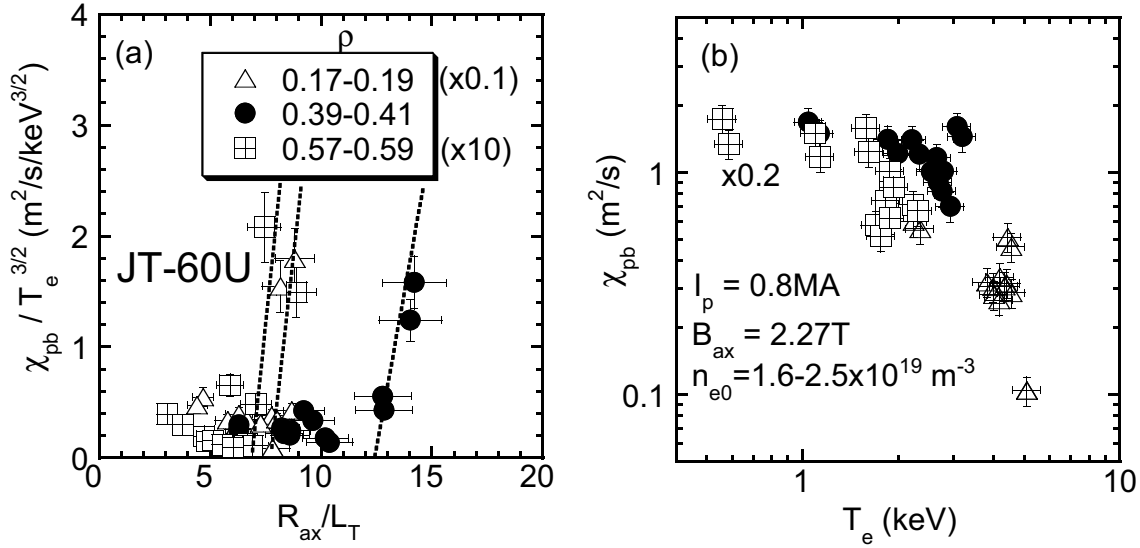


FIG. 1. (a)  $L_T$  and (b)  $T_e$  dependence of  $\chi_e$  at different radii in the JT-60U NBI plasmas. The  $\chi_e$  is normalized by the gyro-Bohm  $T_e$  dependence in (a).

polychromator are used to track the small  $T_e$  perturbations at different radii in both devices [8, 9]. The second harmonics of the X-mode is optically thick in typical LHD and JT-60U plasmas and the  $T_e$  measured by electron cyclotron emission agrees well with that by Thomson scattering in this experiments.

## 2. Static heat transport features

To clarify the non-linearity of heat transport, the transient response should be compared with the steady state transport features, thus the static transport analysis is still important. Figure 1(a) shows the temperature gradient scale length,  $L_T^{-1} = -\nabla T_e / T_e$ , dependence of  $\chi_e$  (obtained from the static analysis i.e. the power balance analysis) in the JT-60U positive shear plasmas (the magnetic field at axis,  $B_{ax} = 2.27\text{T}$ , the plasma current,  $I_p = 0.8\text{MA}$ , the collisionality,  $\nu_* = 0.01 - 0.1$ , the normalized gyro-radius,  $\rho_* = 4 - 10 \times 10^{-3}$ ). The critical gradient scale length is suggested in JT-60U. No sharp dependence of  $\chi_e$  on  $T_e$ , however, is observed in the power balance analysis (see Fig. 1(b)). On the other hand, the "critical gradient scale length" is unclear in the LHD inward shifted configuration (major radius at the magnetic axis,  $R_{ax} = 3.5\text{m}$ , an averaged plasma radius,  $a_p = 0.58\text{m}$ ). Figure 2(a) shows the  $T_e$  and temperature scale length,  $L_T^{-1} = -\nabla T_e / T_e$ , dependence of  $\chi_e$  in the LHD NBI plasmas ( $\nu_* = 0.1 - 0.3$ ,  $\rho_* = 3 - 4 \times 10^{-3}$ ). However, there is clear  $T_e$  dependence of  $\chi_e$  in the power balance analysis of LHD plasmas (Fig. 2(b)).

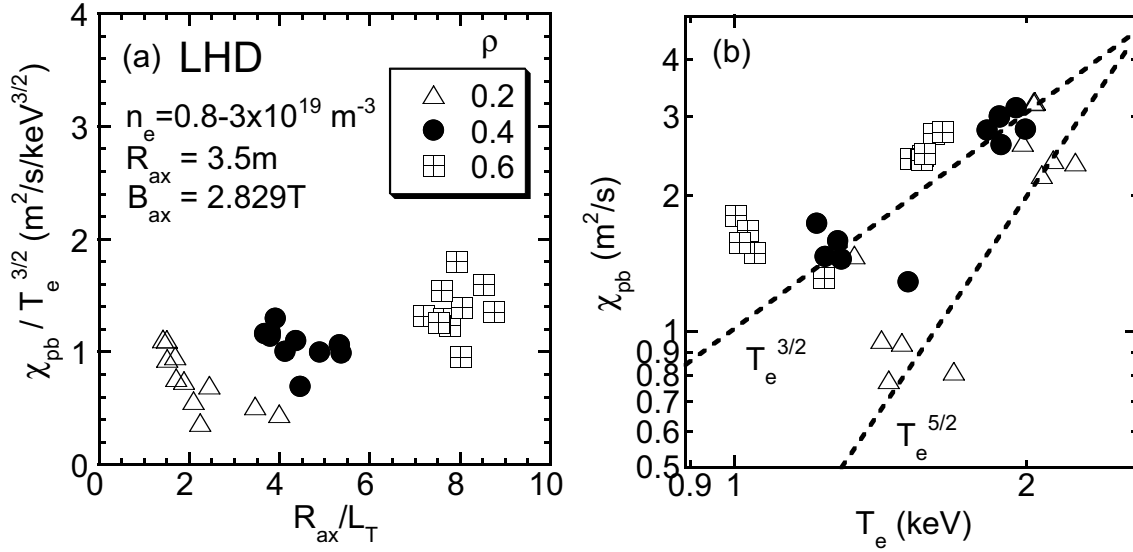


FIG. 2. (a)  $L_T$  and (b)  $T_e$  dependence of  $\chi_e$  at different radii in the LHD NBI plasmas. The  $\chi_e$  is normalized by the gyro-Bohm  $T_e$  dependence in (a).

### 3. Transient transport analysis

In order to induce a cold pulse, a tracer encapsulated solid pellet (TESPEL [10]) is injected into the LHD edge. Figure 3 shows the typical time evolution of cold pulse induced by TESPEL injection in the low power NBI plasma on LHD. The TESPEL ablates within 1ms and induces a local  $T_e$  decrease in the edge region through the ionization. The  $T_e$  perturbation propagates toward the core region (cold pulse propagation). Increases in the line average density,  $\bar{n}_e$ , and the total stored energy,  $W_p$ , are due to the increase in the edge density ( $\rho > 0.6$ ) because of the particle source from TESPEL.

To study the non-linearity between heat flux and temperature gradient in toroidal plasma, the transient transport analysis is carried out with a simple non-linear model for  $\chi_e$  written as  $\chi_e \propto T_e^\alpha |\nabla T_e|^\beta$ . By using this model, the perturbed electron heat transport equation can be written as,

$$\frac{3}{2} n_e \frac{\partial \delta T_e}{\partial t} = \nabla \cdot \left( n_e (1 + \beta) \chi_e \nabla \delta T_e - n_e \alpha \chi_e \frac{\delta T_e}{L_T} \right). \quad (1)$$

Here  $n_e$ ,  $\nabla T_e$ ,  $T_e$  and  $\chi_e$  are static values obtained just before TESPEL injection,  $\delta T_e = T_e(r, 0) - T_e(r, t)$  and  $\chi_e$  can be estimated by the power balance analysis. The  $n_e$  increases in the ablation region ( $\rho > 0.6$ ) while it doesn't change in core region within the accuracy of the Abel inversion. The particle diffusivity, which is estimated by gas-puff modulation experiments [11], is much smaller than  $\chi_e$  and thus the particle transport effects on the cold pulse propagation are neglected in LHD. When the heat flux perturbation,  $\delta q_e(r, t)$ , and the perturbation scale length,  $L_{\delta T_e}$ , are defined as

$$\delta q_e(r, t) = \frac{1}{r} \int_0^r \frac{3}{2} n_e \frac{\partial \delta T_e}{\partial t} \rho d\rho, \quad L_{\delta T_e}(r, t) = (\nabla \delta T_e / \delta T_e)^{-1},$$

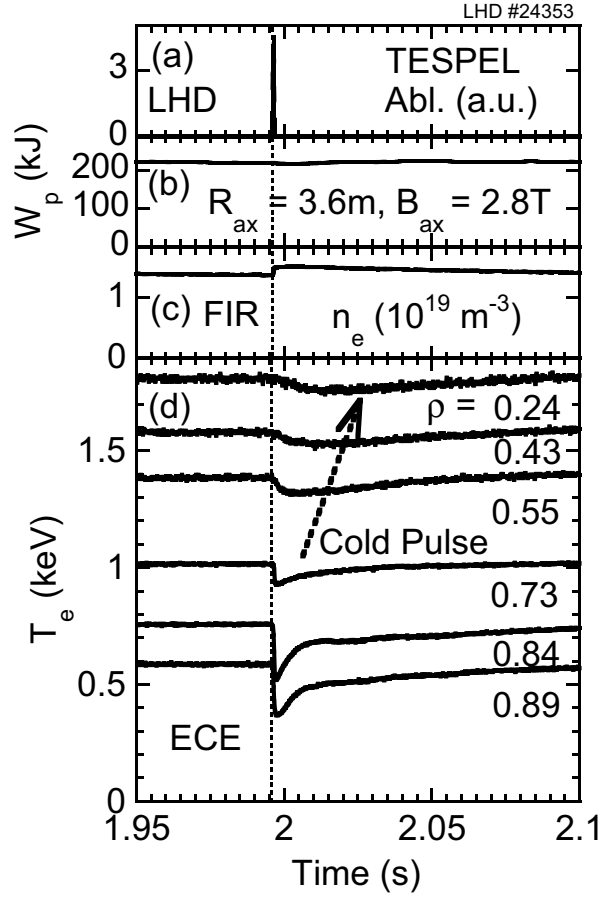


FIG. 3. Typical time evolutions (a) TESPEL ablation light, (b)  $W_p$ , (c)  $\bar{n}_e$  and (d)  $T_e$  at different radii in the cold pulse experiment.

Eq. 1 can be written as

$$\frac{\delta q_e}{n_e \delta T_e} = \frac{\chi_{tr}}{L_{\delta T_e}} - V_{tr}, \quad (2)$$

here  $\chi_{tr} = (1 + \beta)\chi_e$ ,  $V_{tr} = \alpha\chi_e L_T^{-1}$  and  $r$  is the averaged minor radius. Figure 4 shows the typical time trace of plasma in the gradient - flux space for a cold pulse propagation. The fact that data points indeed lay on a straight line allows us to determine  $\beta$  and  $\alpha$  from the slope and intercept of a line.

#### 4. Transient transport experiments without internal transport barrier

The cold pulse experiments are performed mainly in low power NBI plasmas ( $P_{NB} < 3\text{MW}$ ) on LHD inward shifted configuration (same as that shown in Fig. 2). The typical  $\chi_{tr}$  obtained from the transient analysis based on the empirical non-linear transport model is shown in Fig. 5. The heat diffusivity estimated by power balance analysis,  $\chi_{pb}$ , is also shown in Fig. 5(b). The small difference between  $\chi_{pb}$  and  $\chi_{tr}$  indicates a weak  $\nabla T_e$  dependence of  $\chi_e$  ( $\beta \ll 1$ ) in LHD. A weak  $\nabla T_e$  dependence of  $\chi_e$  is also shown in W7-AS [12]. On the contrary, the  $T_e$

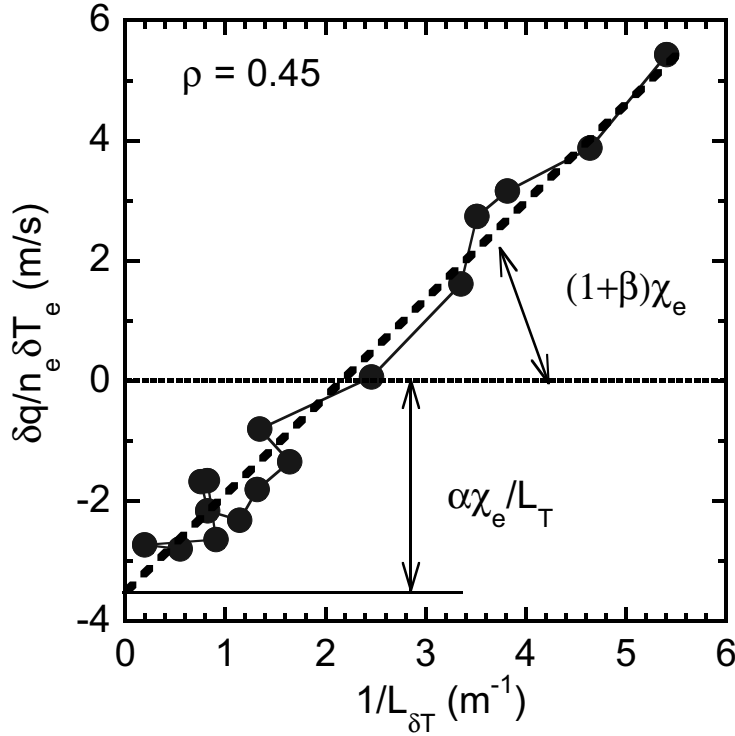


FIG. 4. Typical behavior of plasma in the perturbed gradient vs the perturbed heat flux space.

dependence of  $\chi_e$  is indicated in Fig. 5(c). A gyro-Bohm like  $T_e$  dependence ( $\alpha = 3/2 - 5/2$ ) can explain the obtained  $\alpha$ .

The cold pulse experiments are performed in the different magnetic configuration on LHD ( $R_{ax} = 3.6\text{m}$ ) as shown in Fig. 6. Although the beam deposition profile and the  $\chi_e$  profile are different in the  $R_{ax} = 3.6\text{m}$  configuration from the  $R_{ax} = 3.5\text{m}$  configuration, the weak  $\nabla T_e$  and the gyro-Bohm like  $T_e$  dependences ( $\beta \sim 0$  and  $\alpha = 3/2 - 5/2$ ) are also observed. Both configurations have the negative magnetic shear and the magnetic hill. The cold pulse experiments in much more magnetic configurations in LHD should be carried out to discuss the magnetic configuration effects on the non-linearity of heat transport more quantitatively.

Although the  $\alpha$  in the edge region is more important to compare the  $T_e$  dependence of  $\chi_e$  with the global energy confinement and it has not obtained by transient analysis,  $T_e$  dependence of  $\chi_e$  can be considered as one of the candidates to explain the power degradation of the global confinement in LHD [3]. In high NB power cases, however, the non-local  $T_e$  rise, which is discussed later, appears and it makes hard to decouple the non-linearity of  $\chi_e$  from observations. The non-locality is also suggested in the W7-AS experiments [12].

To perturb the core region of JT-60U plasma, the short pulse (100ms) ECH injection is carried out. Figure 7(a) shows the typical response of  $T_e$  to a step of the injected ECH power ( $P_{EC} \sim 1\text{MW}$ ) in the core region. Here, the peak of ECH power deposition is located at  $\rho \sim 0.6$ , and there is no ECH power source in the region of  $\rho < 0.3$ . The heat pulse propagates from edge to core similarly to the cold pulse and thus the transient analysis with

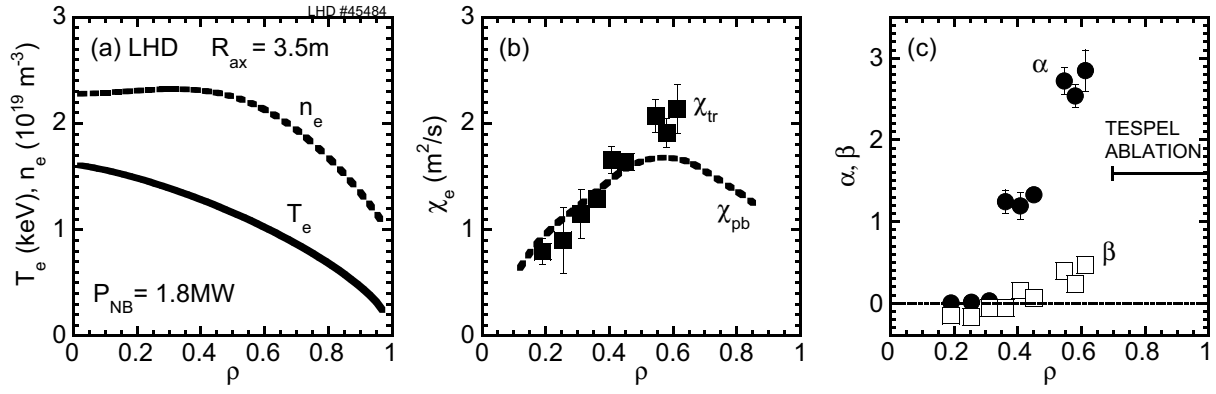


FIG. 5. Radial profiles of (a)  $T_e$  and  $n_e$  just before the TESPEL injection, (b)  $\chi_{tr}$  and  $\chi_{pb}$ , (c)  $\beta$  (the index of  $\nabla T_e$  dependence of  $\chi_e$ ) and  $\alpha$  (the index of  $T_e$  dependence of  $\chi_e$ ) in the  $R_{ax} = 3.5m$  configuration.

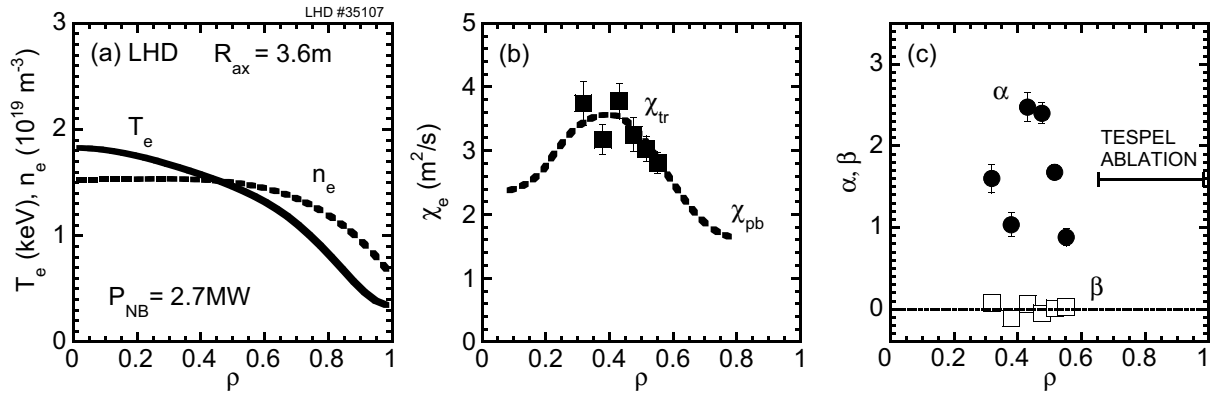


FIG. 6. Radial profiles of (a)  $T_e$  and  $n_e$  just before the TESPEL injection, (b)  $\chi_{tr}$  and  $\chi_{pb}$ , (c)  $\beta$  (the index of  $\nabla T_e$  dependence of  $\chi_e$ ) and  $\alpha$  (the index of  $T_e$  dependence of  $\chi_e$ ) in the  $R_{ax} = 3.6m$  configuration.

an empirical non-linear  $\chi_e$  model, which is discussed above, can be applied (see Fig. 7(b)). The  $\chi_{tr} = 0.16m^2/s$  is obtained in an ohmic plasma while the  $\chi_{tr}$  increases in the NBI plasma ( $0.24m^2/s$ ) due to the increase in  $T_e$  or  $\nabla T_e$ . To compare the  $\nabla T_e$  dependence of  $\chi_e$  with the critical gradient length model, both  $\chi_{tr}$  and  $\chi_{pb}$  are plotted as a function of  $R_{ax}/L_T$  (see Fig. 7(c)). The  $\chi_{pb}$  and the  $\chi_{tr}$  are normalized by  $T_e^{3/2}$  to decoupled the gyro-Bohm  $T_e$  dependence. The dependence of  $\chi_{pb}$  on  $R_{ax}/L_T$  may be changed at  $R_{ax}/L_T = 6 - 8$  i.e. the temperature-gradient-driven mode may be switched on above  $R_{ax}/L_T = 6-8$  and  $\chi_e$  has  $\nabla T_e$  dependence, and thus the enhancement of  $\chi_{tr}$  ( $\chi_{tr} > \chi_{pb}$ ) may be observed at  $R_{ax}/L_T = 6-8$ . The transient (and also the static) experiments in plasmas with much lower and much higher  $R_{ax}/L_T$  are required to clarify the critical value more precisely. The  $\nabla T_e$  dependence factor  $\beta$  decreases from 3 to 1.6 with the increase in  $R_{ax}/L_T$ , while the  $T_e$  dependence factor  $\alpha = 0.5 - 2$  is not different from that obtained in the LHD plasma.

There are differences in non-linearity of  $\chi_e$  between LHD and JT-60U plasmas without

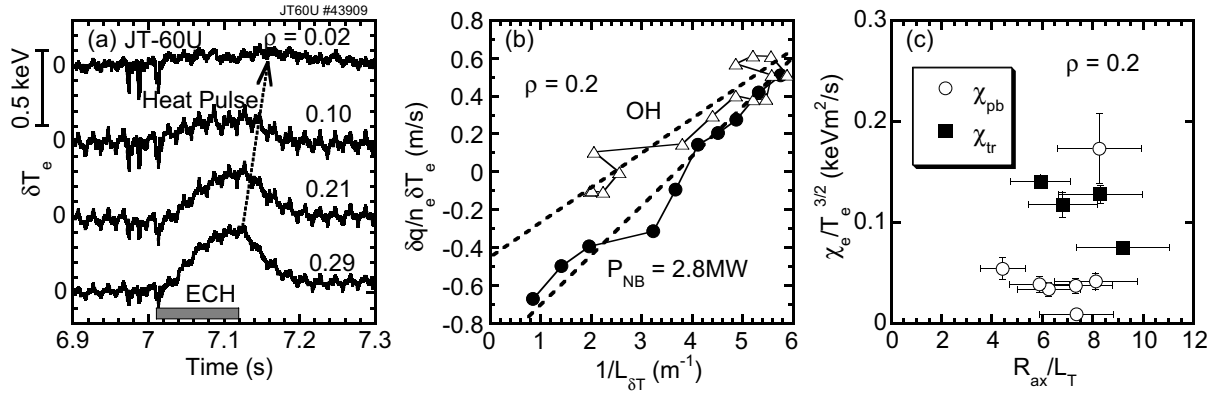


FIG. 7. (a) Time evolution of  $T_e$  perturbations induced by a step of the ECH in JT-60U ( $\rho < 0.3$ ), (b) typical behavior of ohmic and NBI plasmas in the perturbed gradient and the perturbed heat flux space ( $I_p = 0.8$  MA), (c)  $R_{ax}/L_T$  dependence of  $\chi_{pb}$  and  $\chi_{tr}$ , here the  $\chi_{pb}$  and the  $\chi_{tr}$  are obtained in the density region of  $n_{e0} = 1.6 - 2.5 \times 10^{19} \text{ m}^{-3}$ .

ITBs. The  $T_e$  dependence of  $\chi_e$  is larger than  $\nabla T_e$  dependence in LHD plasma. On the other hand, a  $\nabla T_e$  dependence of  $\chi_e$  is observed in JT-60U plasma. For the stabilization of micro-turbulence, the local shear is a critical parameter [13]. The influence of local and global shear on turbulence may be one of the candidates to explain the difference in the non-linearity between LHD and JT-60U plasmas.

## 5. Cold pulse propagations in plasmas with electron internal transport barrier

The transport barriers are considered to be formed by the suppression of turbulence-induced transport both in helical systems and tokamaks. The transition of radial electric field triggers the formation of the electron ITB (e-ITB) in the LHD [14], while a negative magnetic shear is more important parameter in the formation of e-ITB in JT-60U [15]. In addition, the temperature scale length dependence on the heating power are different between the LHD and the JT-60U plasmas [15]. The difference in the power dependence indicates the difference in the dependence of  $\chi_e$  on  $T_e$  and/or  $\nabla T_e$  between the LHD and the JT-60U plasmas. Transient experiments are relevant for these issues to be clarified.

The e-ITB is formed when the ECH is focused on the magnetic axis in LHD ( $P_{EC} \sim 0.8$  MW,  $P_{NB} \sim 2$  MW,  $R_{ax} = 3.5$  m,  $a_p = 0.58$  m,  $\bar{n}_e = 0.7 \times 10^{19} \text{ m}^{-3}$ ), and it is formed in the reversed shear plasma [16] on JT-60U ( $P_{NB} = 7.6$  MW,  $R_{ax} = 3.4$  m,  $a_p = 0.94$  m,  $\bar{n}_e = 1.5 \times 10^{19} \text{ m}^{-3}$ ,  $I_p = 1$  MA). Typical time evolutions of cold pulse propagation and radial profiles of target plasmas are shown in Fig. 8. There is also an ion barrier ( $T_{i0} = 7$  keV) in the JT-60U plasma, while neither ion nor  $n_e$  ITBs are present in LHD ( $T_{i0} = 1.8$  keV). The cold pulse propagation technique is also used to perturb the ITB plasmas. The TESPEL (in LHD) and the pellet (in JT-60U) are injected to the edge of e-ITB plasmas. A unique feature of cold pulse propagation is observed. When the cold pulse approaches the ITB foot, the negative peak of the cold pulse is enhanced both in JT-60U and LHD as shown in Fig. 9.

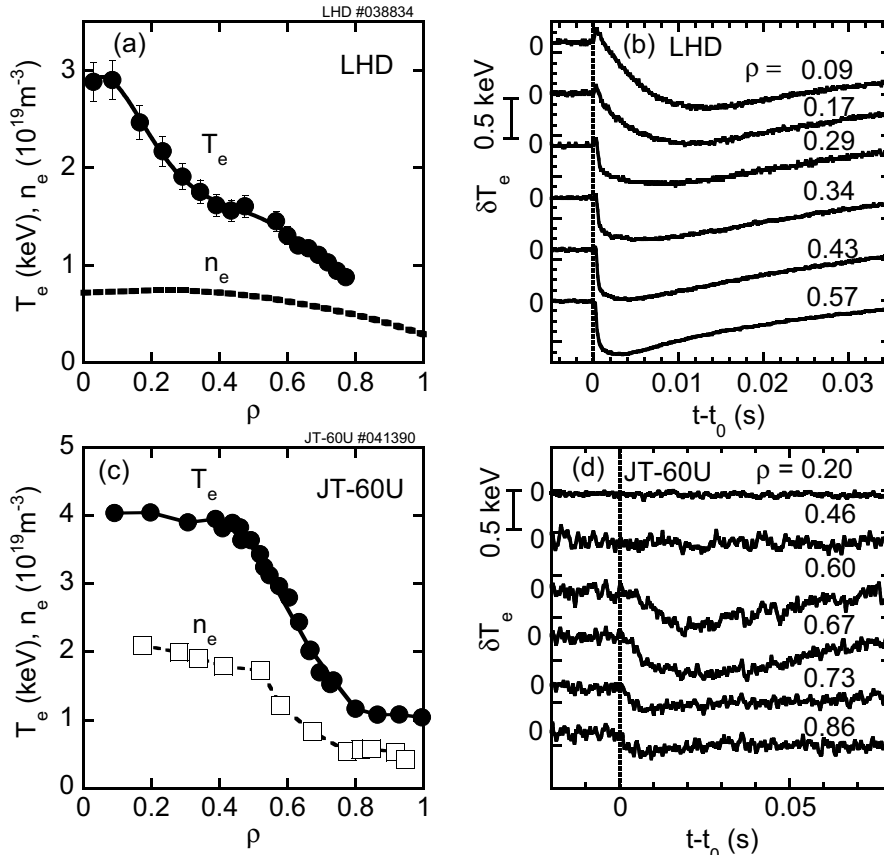


FIG. 8. Radial profiles of e-ITB plasmas just before TESPEL/Pellet injection and time response of  $T_e$  to edge cooling in LHD ((a) and (b)) and JT-60U ((c) and (d)). The TESPEL/Pellet is injected at  $t = t_0$ .

Here, no evidence of a significant plasma shift induced by the TESPEL/PELLET injection is observed. In the JT-60U plasma, the peak of the cold pulse can not enter the ITB region, thus the enhancement of the cold pulse is localized near the ITB boundary region. The cold pulse is damped strongly to zero further inside the ITB region, and thus there is no perturbation in the core. A similar phenomena is observed in the strong ITB plasma sustained by a high level of heating power in JET [17]. On the other hand, the enhancement of the cold pulse is observed inside the ITB region in LHD. However, the cold pulse propagation is slowing down inside the ITB. The simple diffusive nature (heat flux is proportional to temperature gradient) cannot explain this enhancement of the cold pulse. The non-linear dependence of  $\chi_e$  on  $T_e$  and/or  $\nabla T_e$  is required. Figure 10 shows the strong reduction of  $\chi_{tr} = (1 + \beta)\chi_e$  inside the ITB region (see (a) and (c)) in both devices. The small difference between  $\chi_{tr}$  and  $\chi_{pb}$  indicates  $\beta = 0$  (i.e. the ITB is in a “weak or not stiff” region). The vanishing of  $\nabla T_e$  dependence of  $\chi_e$  in JT-60U may be due to the strong reduction of the turbulence-driven-transport inside the ITB. The growth of the cold pulse peak can be explained by the convective-like term driven by the  $T_e$  dependence of  $\chi_e$  (see Eq. 1) because the transient transport analysis indicates the strong negative  $T_e$  dependence of  $\chi_e$  ( $\chi_e$  decreases with an increase in  $T_e$ ). Figure 10 (b) and

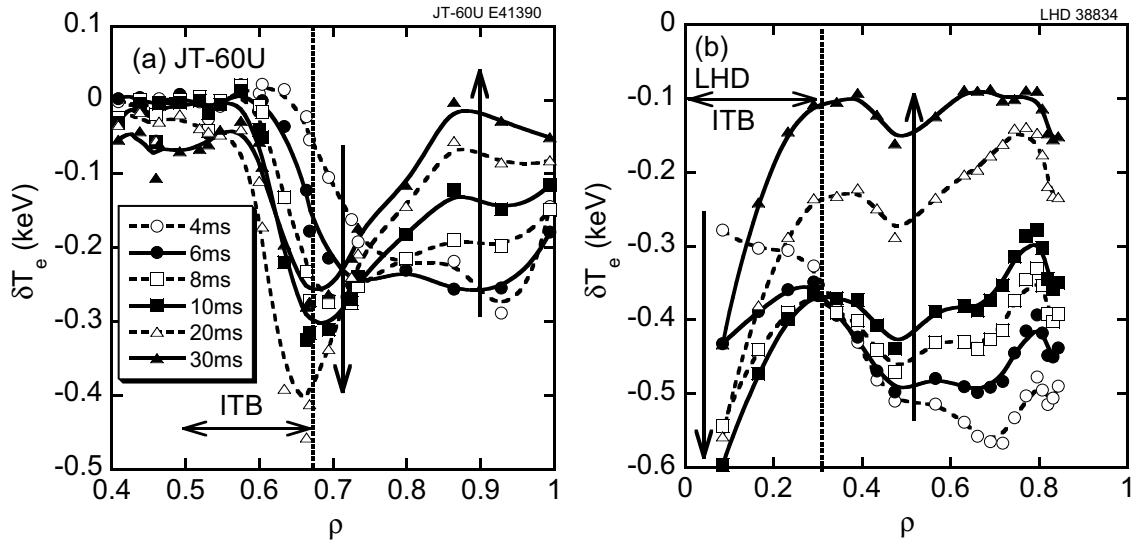


FIG. 9. Time evolution of radial profile of  $T_e$  perturbation in (a) JT-60U and (b) LHD. The TESPEL/Pellet is injected at  $t = 0$ s.

(d) show the  $T_e$  dependence factor  $\alpha$  of  $\chi_e$ . The negative  $T_e$  dependence ( $\alpha < 0$ ) is observed inside the ITB in LHD, while it is observed not only inside the ITB but also outside the ITB in JT-60U. The transport just outside the ITB region in JT-60U, where the flat  $T_e$  and  $q$  profiles are observed, may be different qualitatively from the transport shown in Fig. 7. Although the physical mechanisms that could be responsible for this negative  $T_e$  dependence of  $\chi_e$  are unclear yet (any gyro-Bohm models can not provide  $\alpha < 0$ ), the negative  $T_e$  dependence indicates the qualitative change in turbulence effects on transport. The  $q$  profile effect may be a key issue that should be clarified because both plasmas in Fig. 10 have the negative magnetic shear configuration.

## 6. Non-local effects in transport

Several recent experiments in LHD and JT-60U, however, point to the importance of non-local effects in the turbulent-induced transport [18]. Rapid cold pulse propagations are observed both in LHD and JT-60U. The typical time evolution of core temperature response to the edge cooling in JT-60U high- $\beta_p$  ELMy H-mode plasma ( $P_{NB} = 18\text{MW}$ ,  $R_{ax} = 3.3\text{m}$ ,  $a_p = 0.93\text{m}$ ,  $\bar{n}_e = 3 \times 10^{19}\text{m}^{-3}$ ,  $I_p = 1.8\text{MA}$ ) is shown in Fig. 11(a). The core  $T_e$  begin to decrease before diffusive transport effect (calculated by  $\chi_{pb}$ ) reaches this region, and the magnitude of cold pulse is larger than that predicted by diffusion. To explain this prompt response of core  $T_e$  by the non-linearity of  $\chi_e$ , the strong  $\nabla T_e$  dependence of  $\chi_e$  is required (see simulation result in Fig. 6(a)). This strong  $\nabla T_e$  dependence is not consistent with the power degradation observed in JT-60U. One of the non-linear but local models (e.g. ITG-based models [19]) can explain such a strong  $\nabla T_e$  dependence, however, there is no evidence of rapid changes in the fluctuations or  $T_i$  profile. It has been observed that the non-local response to edge cold pulses often have reversed polarity, with the core  $T_e$  increasing in response to edge cooling

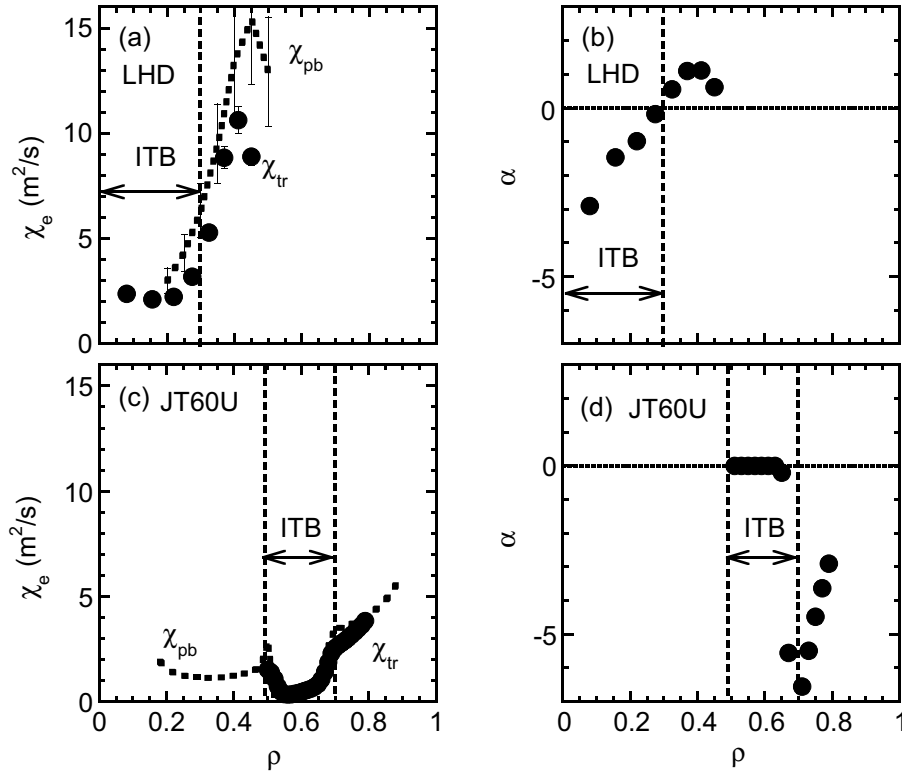


FIG. 10. Radial profiles of the the transient and power balance heat diffusivity in (a) LHD and (c) JT-60U and the  $T_e$  dependence factor of  $\chi_e$  in (b) LHD and (d) JT-60U.

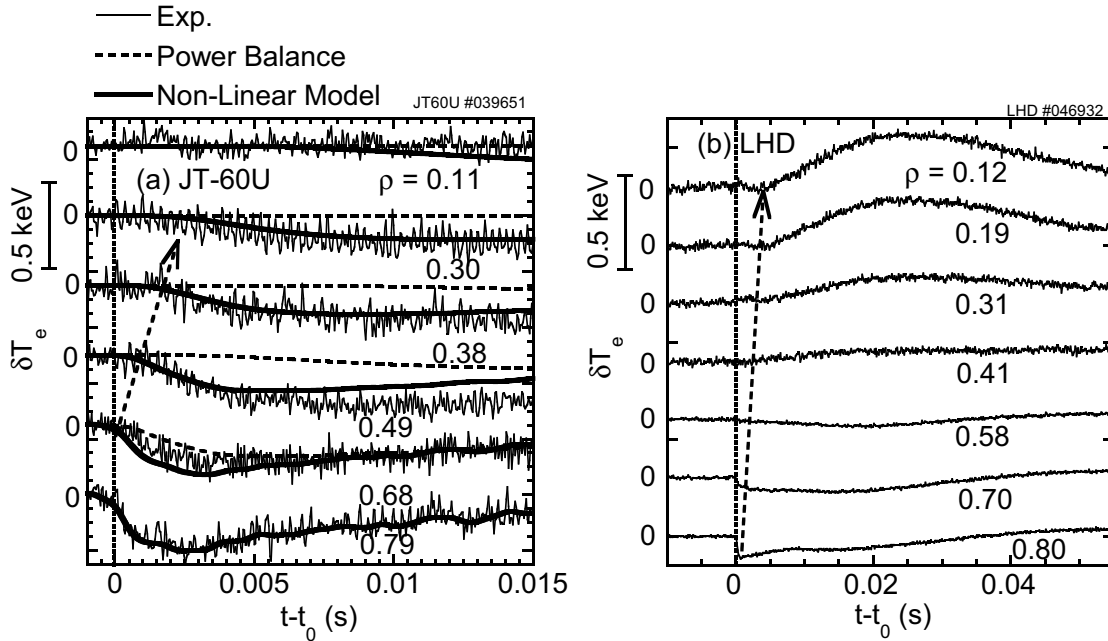


FIG. 11. Time evolution of  $T_e$  perturbations at different radii in (a) JT-60U high- $\beta_p$  ELMy H-mode plasma and (b) LHD ECH + NBI plasma. The simulation results with the linear  $\chi_e$  model ( $\chi_e = \chi_e$  i.e.  $\alpha = 0, \beta = 0$  in the non-linear model) and the non-linear  $\chi_e$  model ( $\alpha = 0, \beta = 9$ ) are also shown in (a). The TESPEL is injected at  $t = t_0$ .

in many tokamaks [20, 21]. While such a phenomenon, which can not be explained by the local diffusive model even if the heat flux is a non-linear function of  $\nabla T_e$  and  $T_e$ , has not been reported so far in helical systems. However, a first observation of the reverse of  $\delta T_e$  polarity in helical systems is done in LHD, and thus the strong non-local effects in helical systems is evident as well as in tokamaks. The typical  $T_e$  response to the edge cooling in LHD is shown in Fig. 11(b). The TESPEL is injected to the edge of plasma ( $P_{EC} \sim 0.8\text{MW}$ ,  $P_{NB} \sim 2\text{MW}$ ,  $T_{e0} = 3\text{keV}$ ,  $\bar{n}_e = 1 \times 10^{19}\text{m}^{-3}$ , same magnetic configuration as Fig. 2). The cold pulse produced in the edge region ( $\rho > 0.8$ ) is strongly reduced in the region of  $0.4 < \rho < 0.6$ , and thus neither  $T_e$  nor  $\nabla T_e$  are changed significantly by the cold pulse propagation. In spite of no change in temperature and its gradient, a sudden rise of  $T_e$  is observed in the central region ( $\rho < 0.4$ ). This indicates an abrupt reduction of  $\chi_e$  unrelated to  $\nabla T_e$  and/or  $T_e$ . Unfortunately, plasma goes back to normal condition after 20ms from TESPEL injection as well as in tokamaks. There are some discoveries in the characteristics of the non-local  $T_e$  rise observed in LHD, (1) The non-local  $T_e$  rise is also observed in plasmas sustained by pure ECH, (2) The formation of e-ITB is triggered by a non-local  $T_e$  rise in LHD when the plasma is heated by just below the critical power, (3) The non-local  $T_e$  rise is also observed in the e-ITB plasma. These new observations will help to make a physical picture of the turbulence, which can explain both non-linearity and non-locality in transport. Especially, observation (1) indicates the plasma current itself is irrelevant to the non-local transport mechanism. Moreover, the similarities of the non-local  $T_e$  rise between tokamaks and LHD allow us to conclude that the magnetic shear is not important in the non-local transport. The non-local  $T_e$  rise in LHD is unclear in the high- $n_e$  and low- $T_e$  region ( $n_e > 1.5 \times 10^{19}\text{m}^{-3}$ ,  $T_e < 2.0\text{keV}$ ) just as TFTR scaling predicts [21]. The non-local  $T_e$  rise, however, has not been observed in JT-60U even if  $n_e$  and  $T_e$  are in condition, which is predicted by TFTR scaling.

## 7. Summary

Cold/Heat pulse propagation experiments in LHD and JT-60U show the following electron heat transport features. (i) Cold pulses in no-ITB plasma in LHD ( $v_* = 0.1 - 0.3$ ,  $\rho_* = 3 - 4 \times 10^{-3}$ ) show a gyro-Bohm like  $T_e$  dependence of  $\chi_e$ . On the other hand, heat pulse propagations show not only the gyro-Bohm like  $T_e$  dependence of  $\chi_e$  but also the  $\nabla T_e$  dependence of  $\chi_e$  in the core region ( $\rho < 0.3$ ) of JT-60U plasma ( $v_* = 0.01 - 0.1$ ,  $\rho_* = 4 - 10 \times 10^{-3}$ ). (ii) No or weak  $\nabla T_e$  dependence inside the ITB is found both in LHD and JT-60U reverse shear plasmas. The negative  $T_e$  dependence of  $\chi_e$  is found inside the ITB in LHD and inside and outside the ITB in JT-60U. (iii) The prompt cold pulse propagation in a high- $\beta_p$  ELMy H-mode plasma in JT-60U and the reverse of cold pulse polarity in low density plasmas ( $n_e < 1 - 1.5 \times 10^{19}\text{m}^{-3}$ ) are evidence for non-local heat transport.

## Acknowledgments

We are grateful to the technical groups for their excellent support. The part of this work was carried out as a joint work under the Facility Utilization Program of JAERI.

## References

- [1] F. Wagner *et al* , Phys. Rev. Lett. **56** (1986) 2187
- [2] J. D. Callen *et al* , Phys. Fluids B **4** (1992) 2142
- [3] H. Yamada *et al* , Nucl. Fusion **43** (2003) 749
- [4] W. Horton *et al* , Phys. Fluids **31** (1988) 2971
- [5] F. Romanelli and S. Briguglio, Phys. Fluids **B 2** (1990) 754
- [6] F. Ryter *et al* , Phys. Rev. Lett. **86** (2001) 5498
- [7] N. J. Lopes Cardozo, Plasma Phys. Control. Fusion **37** (1995) 799
- [8] Y. Nagayama *et al* , Rev. Sci. Instrum. **70** (1999) 1021
- [9] A. Isayama *et al* , Rev. Sci. Instrum. **73** (2002) 1165
- [10] S. Sudo *et al* , Plasma Phys. Control. Fusion **44** (2002) 129
- [11] K. Tanaka *et al* , submitted to Nucl. Fusion
- [12] L. Gianone *et al* , Nucl. Fusion **32** (1992) 1985
- [13] R. Waltz and A. Boozer, Phys. Fluids B **5** (1993) 2201
- [14] T. Shimozuma *et al* , Plasma Phys. Control. Fusion **45** (2003) 1183
- [15] K. Ida *et al* , Plasma Phys. Control. Fusion **46** (2004) A45
- [16] T. Fujita *et al* , Phys. Rev. Lett. **78** (1997) 2377
- [17] P. Mantica *et al* , Plasma Phys. Control. Fusion **44** (2002) 2185
- [18] S. V. Neudatchin *et al* , Plasma Phys. Control. Fusion **44** (2002) A383
- [19] M. Kotschenreuther *et al* , Phys. Plasmas **2** (1995) 2381
- [20] K. W. Gentle *et al* , Phys. Rev. Lett. **74** (1995) 3620
- [21] M. W. Kissick *et al* , Nucl. Fusion **38** (1998) 821

## Transition Phenomena and Thermal Transport Property in LHD Plasmas with an Electron Internal Transport Barrier

T. Shimozuma<sup>1</sup>), S. Kubo<sup>1</sup>), H. Idei<sup>2</sup>), S. Inagaki<sup>1</sup>), N. Tamura<sup>1</sup>), K. Ida<sup>1</sup>), I. Yamada<sup>1</sup>),  
K. Narihara<sup>1</sup>), S. Muto<sup>1</sup>), M. Yokoyama<sup>1</sup>), Y. Yoshimura<sup>1</sup>), T. Notake<sup>3</sup>), K. Ohkubo<sup>1</sup>),  
T. Seki<sup>1</sup>), K. Saito<sup>1</sup>), R. Kumazawa<sup>1</sup>), T. Mutoh<sup>1</sup>), T. Watari<sup>1</sup>)  
and LHD Experimental Group

1) National Institute for Fusion Science, 322-6 Oroshi-cho, Toki-city, Gifu 509-5292, Japan

2) Kyushu University, Kasuga, Fukuoka 816-8580, Japan

3) Dept. of Energy Eng. and Sci., Nagoya University, Nagoya 464-8603, Japan

e-mail contact of main author: shimozuma.takashi@LHD.nifs.ac.jp

**Abstract.** Two kinds of improved core confinement were observed during centrally focused Electron Cyclotron Heating (ECH) into plasmas sustained by Counter (CNTR) and Co Neutral Beam Injections (NBI) in the Large Helical Device (LHD). One shows transition phenomena to the high-electron-temperature state and has a clear electron Internal Transport Barrier (eITB) in CNTR NBI plasma. Another has no clear transition and no ECH power threshold, but shows a broad high temperature profiles with moderate temperature gradient, which indicates the improved core confinement with additional ECH in Co NBI plasma. The electron heat transport characteristics of these plasmas were directly investigated by using the heat pulse propagation excited by Modulated ECH (MECH). The difference of the features could be caused by the existence of the  $m/n=2/1$  rational surface or island determined by the direction of NBI beam-driven current.

### 1. Introduction

In recent years, many efforts to elucidate the mechanism of improved confinement with internal transport barriers have been extensively made. There are comprehensive review articles for both tokamak [1] and stellarator devices [2]. For stellarator machines, in special, many interesting phenomena have been observed related with intense local heating by electron cyclotron heating (ECH), such as formation of ITBs [3-6], achievement of the electron root [7], the bifurcation phenomena of radial electric field [8] and transient behavior like pulsation [9]. These phenomena are interpreted to be induced by creation of ambipolar radial electric field due to unbalance of electron and ion losses, decrease of electron heat diffusivity under the existence of such electric field and suppression of turbulence by the shear of radial electric field [2].

In the Large Helical Device (LHD), high electron temperature over 10keV and transition behavior to such state with the formation of ITB have been achieved by means of high power ECH over 2MW and using strongly focused mirror antennas. In experiments, neutral-beam-driven currents modify the profiles of rotational transform  $\iota/2\pi$ , and two different kinds of improved confinement were observed. In this paper, using the techniques of heat pulse propagation generated by modulated ECH (MECH), we tried to elucidate the mechanisms of realization of these discharges.

This paper is organized as follows. At first the experimental apparatus and configuration are explained in Sec. 2. In Section 3, the feature of ITB plasmas in LHD and the transition phenomena to the high-central- $T_e$  state induced by external perturbations are given. The method and analyzed results of MECH technique for various target plasmas are described in Sec. 4. Finally discussions and summary will be given in Sec. 5

## 2. Experimental Configuration

LHD is the largest heliotron-type device ( $l=2$ ,  $m=10$ ) with superconducting helical coils and poloidal coils. The major and the averaged minor radii of the produced plasmas are typically 3.5m and 0.6m, respectively. The ECH system consists of two 82.7GHz and two 84GHz gyrotrons for fundamental resonance heating, and four 168GHz gyrotrons for second harmonic heating at 3T [10]. In the present experiments 82.7GHz power was injected from the antenna installed in the upper port (upper antenna), 84GHz power was launched from the antenna in the lower port (lower antenna) as shown in Fig.1 (a). The upper and lower antennas are installed in the toroidal section with the vertically elongated cross section. The beam waist radii at the focal point are 15mm in the radial direction for the upper antenna, and 30mm for the lower antenna. The MECH power of 168GHz was injected from upper antenna.

The electron temperature profiles are measured by a Thomson scattering system at about 110 positions in the equatorial plane of the horizontally elongated toroidal section, with a spatial resolution of 20 - 35mm [11]. For  $T_e$  measurements with higher time resolution, a multi-channel radiometer system was installed to detect electron cyclotron emission (ECE) at the low magnetic field side (32 channels, spatial resolution: 10 - 70mm) [12].

A schematic of the time sequence in NBI, ECH and pellet injection is illustrated in Fig. 1 (b). The target plasmas were produced by NBI and additional ECH was turned on at the flat top of the discharge in Fig. 1 (b). The typical line-averaged electron density was  $0.5 - 0.7 \times 10^{19} \text{ m}^{-3}$ . The MECH pulse (50% duty, modulation frequency was 35Hz) was superposed during the ECH pulse. The direction of beam-driven currents was changed by switching the injection direction of NBI.

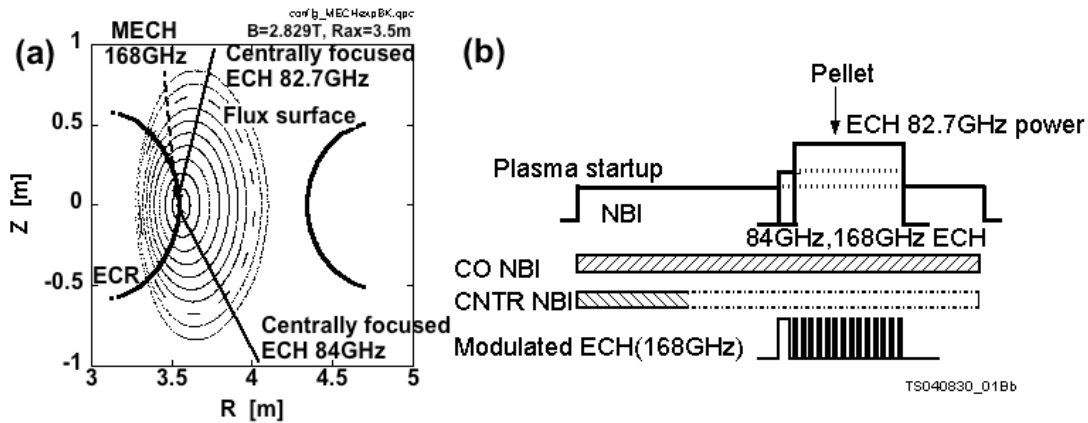


FIG. 1. Experimental configuration is shown in (a) with ECH injection direction. (b) Typical time sequence in NBI, ECH and pellet injection.

## 3. Feature of Electron ITB and Transition Phenomena Triggered by External Perturbations

Clear formation of an eITB was observed in CNTR NBI sustained plasmas with centrally focused ECH [3]. The electron temperature profile of the plasma shows a clear foot position and a steep gradient around normalized minor radius  $\rho=0.3$ . On the formation of the ITB, some transition phenomena to the high-electron-temperature state were observed, which could

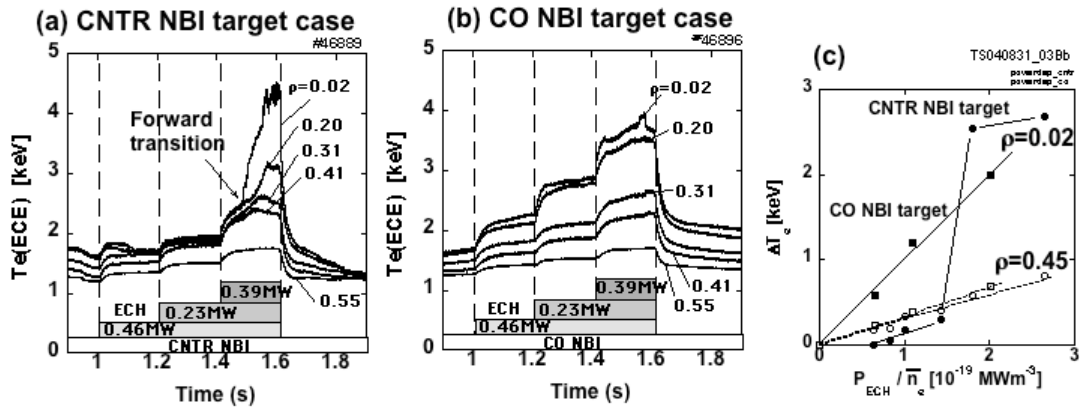


FIG. 2. Electron temperature evolutions for stair-like ECH power injection into (a) CNTR and (b) Co NBI sustained plasmas. Electron temperature increases at the center and periphery are plotted as a function of density-normalized ECH power in (c).

be triggered by the external perturbations, such as additional ECH power, slight density decrease, small pellet injection and so on. To clarify the transition phenomena by additional ECH, injection power was increased in a staircase pattern. Figure 2 (a) and (b) show the time evolution of the electron temperature measured by ECE at several normalized radii,  $\rho$ , for the CNTR and Co NBI target plasmas, respectively. There was a clear forward transition to the high-central- $T_e$  state in the only CNTR NBI plasma as shown in Fig. 2 (a). A decay time of the central  $T_e$  is longer than one at the periphery and of Co NBI case. The increment of the electron temperature,  $\Delta T_e$ , at the plasma center by ECH power is plotted in (c) as a function of ECH power normalized by the electron density. Obvious ECH power threshold can be noticed for the case of the CNTR NBI plasma. On the other hand, there is no threshold power in the Co NBI case, and the central  $T_e$  increases almost linearly with ECH power and moves to the high- $T_e$  state.

A transition to the high- $T_e$  state could be also induced by slight density decrease. During additional ECH injected into a CNTR NBI sustained plasma, central electron temperature spontaneously built up at latter half of the ECH pulse shown in Fig. 3 (a). The line-averaged

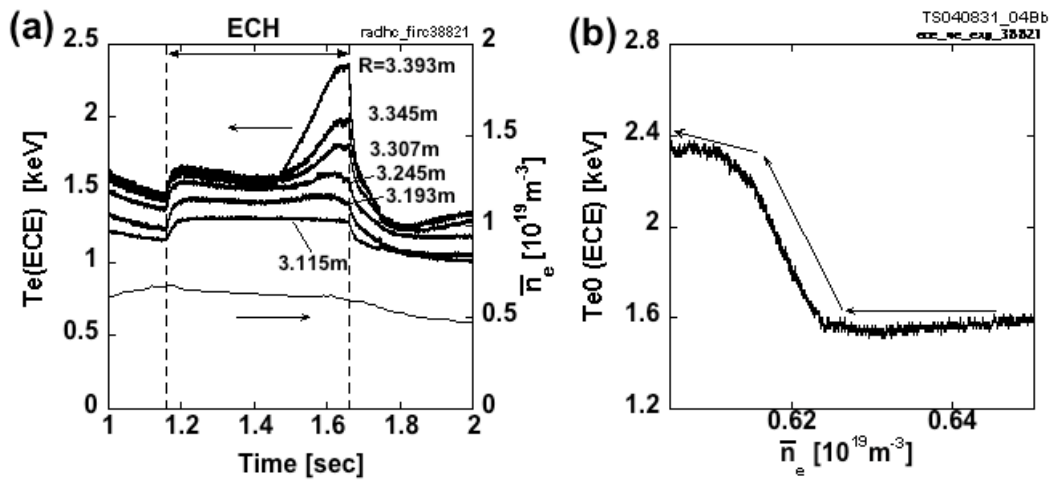


FIG. 3. High- $T_e$  transition induced by a little density decrease. Time evolution of electron temperature measured by ECE is plotted in (a). The central electron temperature is plotted as a function of line-averaged electron density in (b).

electron density gradually decreased during ECH pulse, then the transition happened. In Fig. 3 (b) the central electron temperature  $T_{e0}$  is plotted as a function of line-averaged electron density. A little density decrease of  $10^{17} \text{ m}^{-3}$  led to about 1keV temperature rise. Another high- $T_e$  transition was triggered by small pellet (TESPEL) injection due to edge-plasma cooling as shown in Fig. 4. The CNTR NBI sustained plasma was heated additionally by ECH, though the ECH power level was below the threshold value for transition. After TESPEL injection at 1.645s, central electron temperature up to  $\rho=0.3$  increased after cooling of edge plasma within 3ms. The increase of the line-averaged density was below  $1 \times 10^{18} \text{ m}^{-3}$  by the pellet injection for this case.

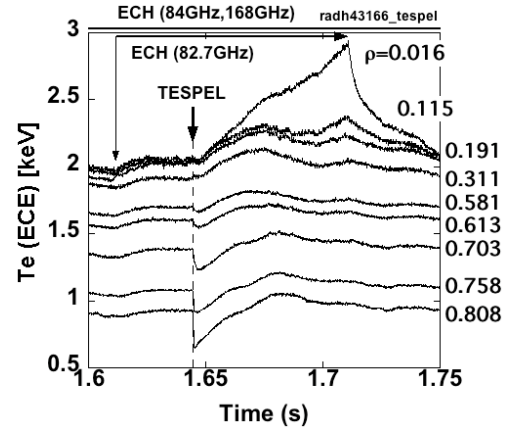


FIG. 4. Transition was triggered by small pellet injection even though ECH power level was below the threshold value for transition.

#### 4. Heat Transport Analysis by Modulated ECH in High $T_e$ Plasmas

Direct observation of the existence of the transport barrier was tried by means of heat pulse propagation excited additional modulated ECH power (168GHz, 0.2MW, 35Hz, and duty 50%). Target plasmas for investigation are NBI reference and NBI plus ECH plasmas. The modulation frequency was precedently optimized for heat pulse propagation in view of the sampling time of ECE and MECH pulse width. Figure 5 (a) shows temperature oscillation measured by ECE at each radial position for a typical CNTR NBI sustained plasma. The scale of the vertical axis is the same for all frames. The maximum amplitude of  $\Delta T_e$  is about 50eV at  $\rho=0.02$ . The Fourier spectrum of the ECE signal at  $\rho=0.02$  is shown in Fig. 5 (b). The peaks

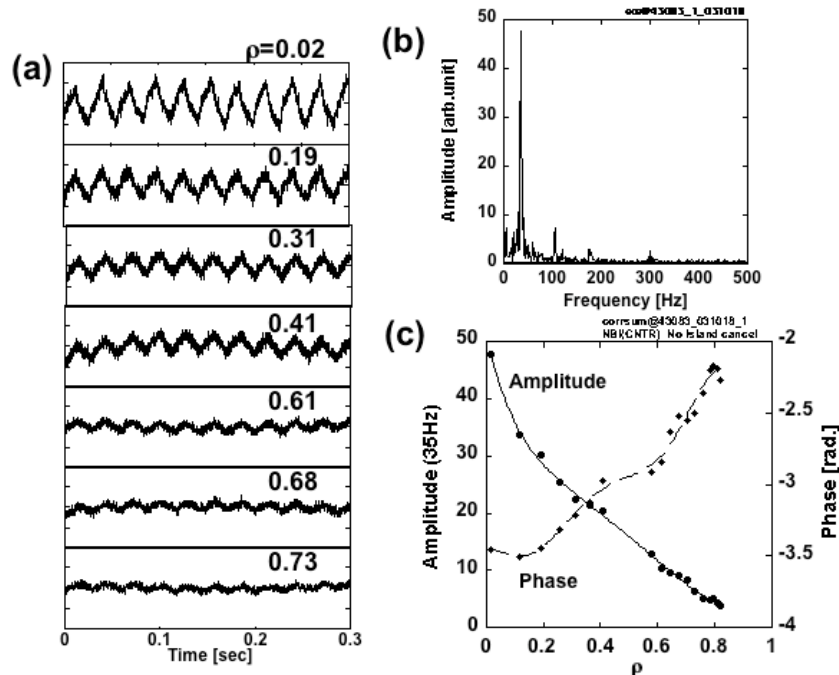


FIG. 5. ECE signal processing excited by MECH. (a) Time evolution of ECE signal at each radial position plotted in the same vertical scale. (b) Fourier spectrum of ECE signal at  $\rho=0.02$ . (c) Radial profile of 35Hz component of the frequency spectrum, both amplitude and phase profiles.

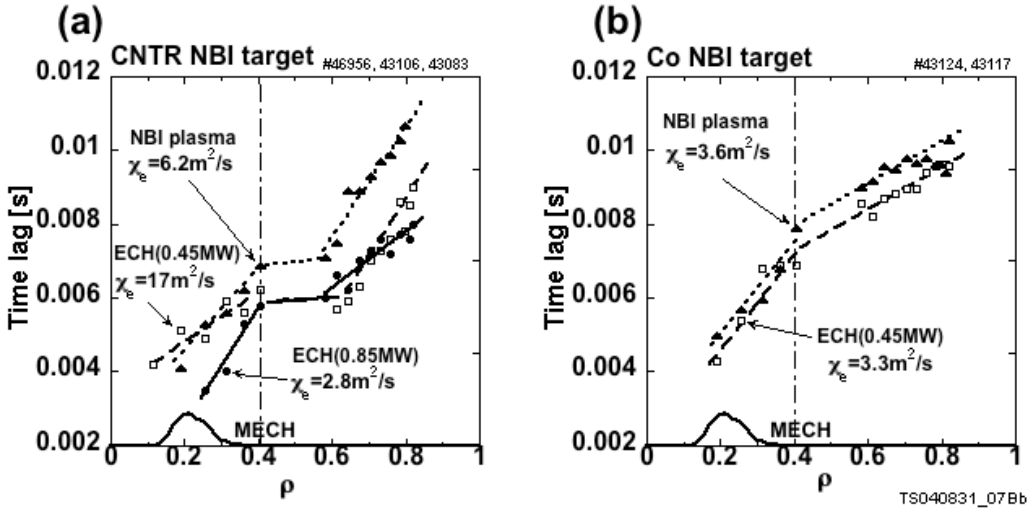


FIG. 6. Time lag of ECE signals from MECH is plotted for normalized minor radius. (a) CNTR NBI sustained plasma, (b) Co NBI case. The closed triangles, open squares and closed circles correspond to the data of NBI reference plasma, NBI plasma with 0.45MW ECH power and NBI plasma with 0.85MW ECH power, respectively. Electron heat diffusivities estimated from heat pulse propagation velocity are also indicated in the figures.

of the fundamental (35Hz), third (105Hz) and fifth harmonics (175Hz) can be identified. The Fourier amplitude and phase of the modulation frequency (35Hz) are plotted in Fig. 5 (c). A time lag of ECE signal rise at each radial position from MECH ON timing is determined by the correlation calculation between each ECE signal and MECH signal, which is defined as follows.

$$\text{Corr}(S_{MECH}, S_{ECE})(\rho, t) = \int_{-\infty}^{\infty} S_{MECH}(\tau + t) S_{ECE}(\rho, \tau) d\tau, \quad (1)$$

where  $S_{MECH}(t)$  is an MECH signal and  $S_{ECE}(\rho, t)$  is a calibrated ECE signal at  $\rho$  position.

The time lag that gives the maximum correlation at each position is plotted in Fig. 6, together with power deposition profile of the MECH calculated by a ray tracing code. The incremental electron heat diffusivity,  $\chi_e$ , is evaluated from the relation,  $\chi_e = V^2 / (4\pi f_{mod})$ , assuming a constant value of  $\chi_e$  and slab model within  $\rho = 0.4$ , where  $V$  is a propagation velocity of the heat pulse that is calculated from the ratio of the propagation distance and the time lag. The modulation frequency of MECH is denoted by  $f_{mod}$ . The evaluated  $\chi_e$  values are also described in the figure. Remarkable difference of propagation behavior can be noticed between CNTR and Co cases. As shown in Fig. 6 (a), the heat diffusivity in the core region ( $\rho < 0.4$ ) once increased with ECH power injection (0.45MW), and then drastically decreased by injection of more ECH power above the threshold value. This behavior and spatial change of  $\chi_e$  within  $\rho = 0.4$  by the ECH power increase (0.45 to 0.85MW) imply an improved confinement and a barrier structure within  $\rho = 0.4$ . On the other hand, the heat diffusivity in the Co NBI sustained plasma was not changed so much by superposition of ECH power. Considering additional ECH power, the confinement is not degraded even with ECH power injection. The heat diffusivity normalized by the gyro-Bohm scaling  $T_e^{3/2} / B^2$  reduced from 8.0 to 3.8  $\text{m}^2 \cdot \text{s}^{-1} \cdot \text{keV}^{-3/2} \cdot \text{T}^2$  with the power increase by ECH, which means a kind of improved confinement except an anomalous transport part.

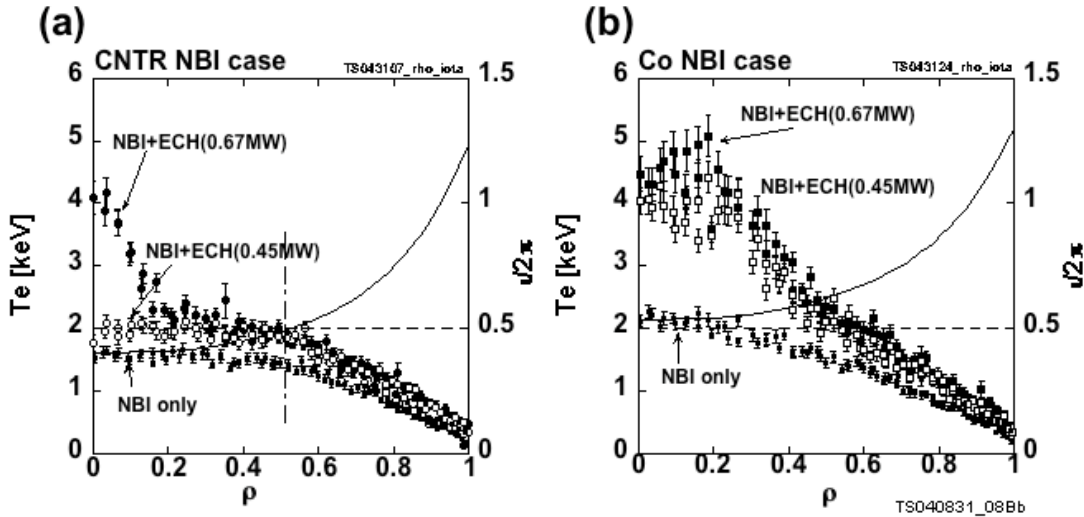


FIG. 7. Electron temperature profiles for NBI, NBI+ECH(0.45MW), NBI+ECH(0.67MW) plasmas. Target plasmas are sustained by (a) CNTR injected and (b) Co injected NBI.

There is a difference in the direction of NBI-driven currents between CNTR and Co injections, i.e., a profile difference of the rotational transform,  $u/2\pi$ . An equilibrium calculation including the beam-driven current shows that a rational surface of  $u/2\pi=1/2$  exists around the position  $\rho=0.5$  for the CNTR case, while no such surface exists in the Co NBI plasma. Figure 7 (a) and (b) shows typical electron temperature profiles for CNTR and Co NBI sustained plasmas with calculated rotational transform profiles. The CNTR NBI-driven current reduces the rotational transform in the core region from the value for the vacuum magnetic field, and  $u/2\pi=1/2$  appears in the plasma. The flattening of a time lag from  $\rho=0.4$  to 0.55 in Fig. 6 (a) suggests the existence of the  $m/n = 2/1$  island where the quick radial propagation can be driven by the fast parallel heat transport on the separatrix of the island.

## 5. Discussions and Summary

The determining factor of the ITB foot position is one of key factors to elucidate a complex

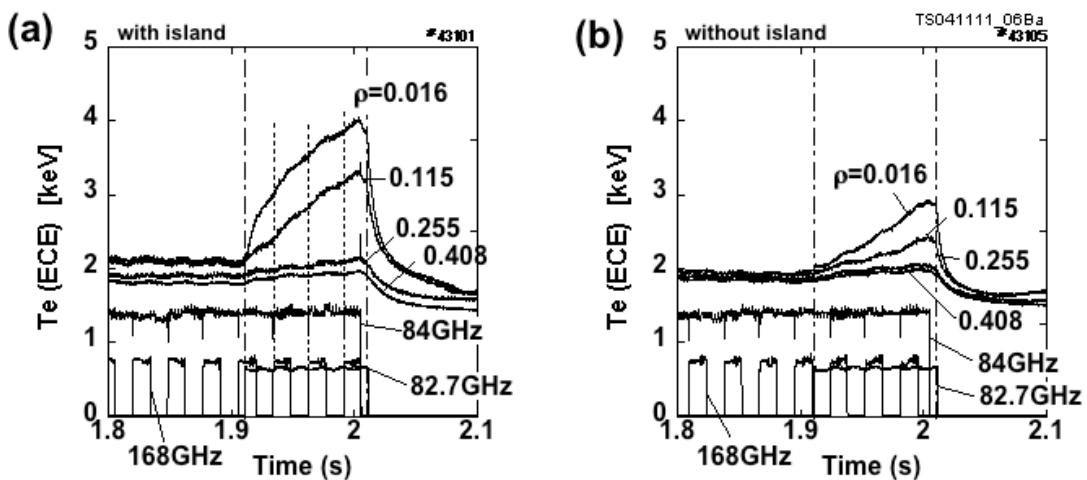


FIG. 8. Effect of the island-cancellation magnetic field on the transition to the high- $T_e$  during additional ECH (82.7GHz) (a) with the island (b) without the island.

dynamics of barrier formation mechanism. To clarify the effect of existence of 2/1 natural island on the high- $T_e$  transition, cancellation magnetic field was superposed by means of external perturbation coils. Figure 8 shows the effect of the island-cancellation field on the CNTR NBI target plasma during additional ECH injection (a) with the natural island and (b) without the island. Increase of the central electron temperature is large and smooth for the plasma with the island. This experimental evidence assures that the existence of the 2/1 island is a candidate of the triggering mechanism of radial electric field bifurcation [13], and the electric field domain interface could suppress the anomalous transport, resulting in the formation of an ITB [14,15].

On the other hand, in the Co NBI case, the electron heat transport in the core region was not changed, although ECH power was injected into the core region ( $\rho < 0.2$ ). The ambipolarity condition of electron and ion fluxes predicts the existence of positive radial electric field over wide range. The generated radial electric field could improve the core confinement neoclassically except a part of anomalous transport. The neoclassical electron-root plasma seems to be realized in the core region.

In summary, two types of improved core confinement were realized by centrally focused ECH in the NBI-sustained LHD plasmas. These plasmas could be controlled by the direction of NBI-driven current. In the CNTR injection case, the temperature profile in the core had a narrow profile and steep temperature gradient, and an electron ITB was established in the core region. Transition behavior to the high- $T_e$  state was sometimes observed, which was triggered by some external perturbations, such as additional ECH power, a little decrease of density, small pellet injection and so on. In the Co NBI case, plasma that had a broad high- $T_e$  profile and moderate temperature gradient was realized. This plasma had no threshold ECH power for transition to high- $T_e$  state. Characteristics of the heat transport in these plasmas were directly measured by heat pulse propagation generated by additional modulated ECH. In special, the formation process of the ITB was investigated. The existence of 2/1 island or low order rational surface may facilitates the transition to high- $T_e$  state and the formation of an ITB with a steep temperature gradient in the CNTR NBI plasmas. On the other hand, in the Co NBI injection plasma, which has a broad high- $T_e$  profile and no clear ECH power threshold, the positive radial electric field (electron-root) could improve core confinement in the neoclassical means, though a part of anomalous heat transport still exists.

## References

- [1] WOLF, R.C., "Internal transport barriers in tokamak plasmas", *Plasma Phys. Control. Fusion* **45** (2003) R1.
- [2] FUJISAWA, A., "Experimental studies of structural bifurcation in stellarator plasmas", *Fusion* **45** (2003) R1.
- [3] SHIMOZUMA, T., et al., "Formation of electron internal transport barrier by highly localized electron-cyclotron-resonance heating in the large helical device", *Plasma Phys. Control. Fusion* **45** (2003) 1183.
- [4] TAKEIRI, Y., et al., "Formation of electron internal transport barrier and achievement of high ion temperature in large helical device", *Phys. Plasmas* **10** (2003) 1788.
- [5] IDA, K., et al., "Characteristics of electron heat transport of plasma with an electron internal-transport barrier in the large helical device", *Phys. Rev. Lett.* **91** (2003) 085003.
- [6] ESTRADA, T., et al., "Electron internal transport barrier formation and dynamics in the plasma core of the TJ-II stellarator", *Plasma Phys. Control. Fusion* **46** (2004) 277,

- [7] MAASSBERG, H., et al., "The neoclassical electron root feature in the Wendelstein-7-AS stellarator", *Phys. Plasmas* **7** (2000) 295.
- [8] FUJISAWA, A., et al., "Dynamic behavior of potential in the plasma core of the CHS heliotron / torsatron", *Phys. Rev. Lett.* **79** (1997) 1054.
- [9] FUJISAWA, A., et al., "Discovery of electric pulsation in a toroidal helical plasma", *Phys. Rev. Lett.* **81** (1998) 2256.
- [10] SHIMOZUMA, T., et al., "ECH system and its application to long pulse discharge in large helical device", *Fusion Eng. Design* **53** (2001) 525.
- [11] NARIHARA, K., et al., "Design and performance of the Thomson scattering diagnostic on LHD ", *Rev. Sci. Instr.* **72** (2001) 1122.
- [12] NAGAYAMA, Y., et al., "Electron cyclotron emission diagnostics on the large helical device", *Rev. Sci. Instr.* **70** (1999) 1021.
- [13] SHAING, K.C., et al., "Plasma and momentum transport processes in the vicinity of a magnetic island in a tokamak", *Nucl. Fusion* **43** (2003) 258.
- [14] TODA, S., et al., "Theoretical study of the hysteresis characteristic of electric fields in helical plasmas", *Plasma Phys. Control. Fusion* **43** (2001) 629.
- [15] ESTRADA, T., et al., "Transient behaviour in the plasma core of TJ-II stellarator and its relation with rational surfaces", *Plasma Phys. Control. Fusion* **44** (2002) 1615.

# Control of the radial electric field shear by modification of the magnetic field configuration in LHD

K.Ida† M.Yoshinuma† M.Yokoyama† S.Inagaki† N.Tamura†  
B.J.Peterson† T.Morisaki† S.Masuzaki† A.Komori†  
Y.Nagayama† K.Tanaka† K.Narihara† K.Y.Watanabe†  
C.D.Beidler‡ LHD experimental group

† National Institute for Fusion Sciences, Toki, Gifu 509-5292, Japan

‡ Max-Planck Institut fuer Plasmaphysik, Greifswald D-17491, Germany

**Abstract.** Control of the radial electric field,  $E_r$ , is considered to be important in helical plasmas, because the radial electric field and its shear are expected to reduce neoclassical and anomalous transport, respectively. In general, the radial electric field can be controlled by changing the collisionality, and positive or negative electric field have been obtained by decreasing or increasing the electron density, respectively. Although the sign of the radial electric field can be controlled by changing the collisionality, modification of the magnetic field is required to achieve further control of the radial electric field, especially producing a strong radial electric field shear. In the Large Helical Device (LHD) the radial electric field profiles are shown to be controlled by the modification of the magnetic field by 1) changing the radial profile of the helical ripples,  $\varepsilon_h$ , 2) creating a magnetic island with an external perturbation field coil and 3) changing the local island divertor coil current.

PACS numbers: 52.55.Hc, 52.50.Sw, 52.50.Gj

## 1. Introduction

Since the radial electric field and its shear was recognized to play an important role on the improvement of transport, the control of the radial profile of the radial electric field is one of the important tools to improve confinement in toroidal plasmas. In tokamak plasmas, the transition of the radial electric field is observed to be associated with the transition from L-mode to H-mode plasma[1, 2]. In stellarator and Heliotron plasmas, the transition of the radial electric field is triggered by the neo-classical non-ambipolar ion and electron flux, and the radial electric field becomes positive (in the electron root) when the plasma collisionality is low enough, while it is negative (in the ion root) at higher collisionality. Associated with transition of radial electric field from negative (ion root) to large positive (electron root), the reduction of electron thermal diffusivity is observed in CHS, Wendelstein-7AS and LHD plasmas[3, 4, 5, 6, 7] Therefore

it is important to investigate the technique to control radial electric field profiles and understand the physics behind them. In this paper, the control of the radial electric field profiles and the effect of radial electric field on transport especially particle/impurity transport are described.

## **2. Control of Radial electric field**

The Large Helical Device (LHD) is a Heliotron device (poloidal period number  $L = 2$ , and toroidal period number  $M = 10$ ) with a major radius of  $R_{ax} = 3.5 - 4.1$  m, an average minor radius of 0.6 m, magnetic field up to 3T, and heating neutral beam with negative ions with a beam energy of 150 - 180 keV. Typically two-thirds of the total beam energy is deposited to the electrons, because of this high beam energy. The radial electric field ( $E_r$ ) is derived from the poloidal and toroidal rotation velocity and pressure gradient of Neon impurity measured with charge exchange spectroscopy[8] at the mid plane in LHD (vertically elongated cross section) using radial force balance. The radial force balance equation can be expressed as  $E_r = (en_I Z_I) - 1(dp_I/dr) - (v_\theta B_\phi - v_\phi B_\theta)$ , where  $B_\phi$  and  $B_\theta$  are the toroidal and poloidal magnetic field and  $Z_I$ ,  $n_I$ ,  $p_I$  are the ion charge, density and pressure of the measured impurity, respectively. The Large Helical Device (LHD) has  $n/m=1/1$  external perturbation coils. The size of the magnetic island can be controlled up to 10cm by changing the current of the perturbation coils. The spatial resolution of the measurements of the radial electric field using the charge exchange spectroscopy is determined by the length of integration of the signal along the line of sight within the beam width of the neutral beam. The spatial resolution becomes poor near the plasma center and relatively good near the plasma edge and it is +/- 1.5cm at the  $R=4.05$ m. In this experiment, radial profiles of electron density are measured with FIR and CO2 laser interferometers, while the electron temperature profiles are measured with a YAG Thomson scattering system and ion temperature profiles are measured with charge exchange spectroscopy. The total radiation power is measured with a bolometer.

### *2.1. Helical ripple strength*

Since the radial electric field in LHD is determined by the ambipolar condition of ion flux and electron flux that are trapped in the helical ripples, a change in the magnitude and radial profiles of helical ripples will be the most straightforward tool to control the radial electric field[9]. In LHD, the radial profiles of helical ripples can be modified by a shift of the magnetic axis from 3.5m to 3.9m as seen in Fig.1.

Figure 2 shows the radial profiles of the radial electric field for the ion root (large neoclassical flux with negative  $E_r$  in the high collisionality regime), electron root (small neoclassical flux with positive  $E_r$  in the low collisionality regime) and the transition regime (between ion root and electron root) for various configurations with different helical ripple profiles. When the helical ripple increases gradually towards the plasma edge ( $R_{ax}=3.75$ m, 3.9m), the electron root region extends to half of the plasma minor

radius and the radial electric field shear produced is relatively weak. However, when the helical ripple increases sharply at the plasma edge ( $R_{ax}=3.5\text{m}$ ), the electron root region is localized at the plasma edge and strong radial electric field shear is produced. When the magnitude of the helical ripple is suppressed to a low level ( $R_{ax}=3.6\text{m}$ ), the transition region of the radial electric field is located at  $\rho = 0.9$ , not at the plasma edge, because there is no increase in the helical ripple at the plasma edge in this configuration. These results show that a strong magnetic field shear can be obtained at the plasma edge by shifting the magnetic axis inward rather than shifting the magnetic axis outward, where the achievement of electron root itself is relatively easy (even with higher collisionality).

The measured radial profile of the radial electric field is consistent with that estimated from neoclassical calculation. Figure 3 shows the radial profiles of electric field estimated with the neoclassical calculation using the model profile of temperature and density. Two examples of radial electric field are presented, one is a radial electric field profile in the electron root plasma with low density and the other is a radial electric field profile in the ion root plasma with high density. The transition between electron root and ion root is localized near the plasma edge ( $\rho > 0.8$ ) for the plasma with magnetic axis of 3.5m, while it is located in the plasma core ( $\rho < 0.8$ ) for the plasmas with magnetic axes of 3.6, 3.75 and 3.9m. The difference in the radial profile of the radial electric field is due to the difference in the radial profile of the helical ripple.

The electron density at the transition from ion root to electron root is  $0.7 \times 10^{19}\text{m}^{-3}$  for the plasma with the magnetic axis of 3.5m, while it is  $1.3 \times 10^{19}\text{m}^{-3}$  for the plasma with the magnetic axis of 3.9m. The difference in critical electron density can be explained by the differences in the magnitudes of the helical ripples. As seen in Fig.4, the transition from ion root to electron root occurs when the collisionality normalized by the bounce frequency of helically trapped particles decreases below 0.1, which is consistent with the prediction by neoclassical theory[10, 11]. In the plasmas with large helical ripples ( $R_{ax}=3.75\text{m}$ ,  $3.9\text{m}$ ), a reduction of the thermal diffusivity is observed associated with the transition from the ion root to the electron root. However, there is no reduction of the thermal diffusivity observed associated with the transition in the plasma with small ripples ( $R_{ax}=3.5\text{m}$ ,  $3.6\text{m}$ ), because neoclassical transport is always smaller than anomalous transport.

## *2.2. Magnetic island*

Formation of the magnetic island is considered to be a useful tool to produce strong radial electric field shear at the boundary of the magnetic island, since the plasma flow is expected to be damped inside the magnetic island. The size of the magnetic island in the plasma is normally smaller than that expected by the vacuum magnetic field because the healing effect[12]. This healing effect becomes larger in the plasma with lower collisionality[13, 14]. The island structure of the radial electric field was investigated for the medium density plasma in the ion root and radial electric field shear is observed at the boundary of the magnetic island[15]. This raised the question as to whether radial

electric field shear can be produced in the electron root plasma, where the collisionality might be too low to produce a magnetic island. Figure 5(a) show the radial electric field profiles for various currents of the  $n/m=1/1$  external coils for the electron root. When the  $n/m=1/1$  perturbation field due to LID current is small enough there is no magnetic island structure observed. As the perturbation field is increased, a clear magnetic island structure appears in the radial profiles of the radial electric field. The radial electric field becomes zero at the magnetic island ( $R= 4.00\text{m} - 4.08\text{m}$ ). Relatively large radial electric field shear is produced at both boundaries of the magnetic island. As shown in Fig.5(b), there is no magnetic island observed at normalized LID currents less than  $250\text{A/T}$ , because of the healing of the magnetic island. However, when the normalized LID current exceeds  $300\text{A/T}$ , the magnetic island suddenly appears and the size of the magnetic island jumps to close to that expected from the calculated vacuum magnetic flux surface. The location of the magnetic island (center of magnetic island at the mid-plane) moves inside when the  $n/m=1/1$  perturbation field becomes strong as shown in Fig5(c). When the size of the magnetic island is large, the location of the center of the magnetic island is consistent with that expected from vacuum magnetic flux surfaces. However, the location of the magnetic island moves to the inner side as the LID current is increased, although the LID current does not affect the location of the magnetic island in vacuum as seen in Fig.5(b) The shift of location of the magnetic island is observed in the electron root plasma but not in the ion root plasma[15].

Because the radial electric field shear may exist at the boundary of the magnetic island, the transport barrier may start near the boundary of magnetic island. In fact the magnetic island contributes to the formation of an electron internal transport barrier (ITB) near the threshold power of ECH for the transition to ITB in LHD[16]. Therefore it is considered that the magnetic island may contribute to the formation of the ion internal transport barrier, which has not been observed in LHD yet. The radial electric field itself is expected to affect the particle transport especially impurity transport[17, 18, 19], which is in contrast to the radial electric field shear effect on the energy transport. In the CHS experiment, the impurities tend to accumulate at the plasma axis and the impurity and electron density profiles tend to peaked in plasmas with negative electric field, while the impurity is exhausted and impurity and density profiles are hollow in plasmas with positive electric field[20]. Therefore it is expected that the positive electric field should contribute to suppress the influx of impurities and prevent the radiation collapse.

Figure 6 shows the radial profile of the radial electric field for the plasma in the electron root with a helical divertor (standard configuration) and ion root with a limiter configuration and a Local Island Divertor (LID)[21] configuration, where a part of the magnetic island is connected to the local island divertor head. The measured radial profiles of the radial electric field are consistent with those estimated by neoclassical calculation for the electron root plasma with the helical divertor and ion root plasma with a limiter configuration. In the divertor (LID) configuration, a large positive electric field with a sharp radial electric field shear is observed, while the radial electric field

is negative for the plasma with a limiter configuration. The sign of the radial electric field changes from negative to positive by crossing the X-point of the magnetic island. This positive electric field is considered to be produced by the electron loss along the magnetic field line toward the LID limiter head. The radial electric field estimated from neoclassical theory becomes more negative towards the plasma edge, while the radial electric field measured becomes positive towards the plasma edge. There is a large discrepancy in radial electric field between the measurements and neoclassical prediction near the X-point, because the electron loss along the magnetic field line is not included in the neoclassical calculation. Since this positive electric field is located in the region of the direct electron loss, the radial electric field shear in this region could not contribute to the improvement of the electron transport. However, the radial electric field at the edge plays a role in preventing the influx of impurities into the plasma with an LID configuration.

### **3. Role of Radial electric field on impurity transport**

The role of positive radial electric field in preventing the impurity influx is observed in experiments in the plasma with radiation collapse. When the short Ne puff is applied to the plasma in the early phase of the discharge, there are two type of discharges; one is a steady state discharge without radiative collapse, the other is a transient discharge resulting in radiative collapse even when the Ne puff is already turned off [Fig7(a)]. The 10 % increase of Ne puff (from 180ms pulse width to 200ms pulse width) early in the discharge causes this difference. Therefore there should be a feedback mechanism in the radiation collapse related to the increase of the electron density. The temperature dependence of the cooling coefficient results in the sharp increase of radiation power proportional to  $n_e^3$ [22]. However the spontaneous gradual increase of radiation power proportional to  $n_e^1$  well before the radiation collapse ( $t = 0.8 - 1.4$ sec). can not be explained by increase of cooling rate. There should be a feedback mechanism relating particle and/or impurity transport and radial electric field. As seen in Fig.7, the radial electric field starts to be more negative 0.5 sec before the radiative collapse. The radial electric field becomes more and more negative until the radiative collapse. The change of radial electric field to more negative is due to the increase of the collisionality (increase of electron density and decrease of temperature). When the radial electric field becomes more negative, the negative radial electric field causes an increase of the impurity influx, because the exhausting effect by positive radial electric field disappears. In the discharge without radiation collapse, the radial electric field remains positive with no increase of the electron density and radiation power. The ion temperature shows a significant drop down to 150eV just before the radiation collapse. Associated with decreasing temperature, the NeX intensity also drops because the fully ionized neon decreases by the recombination process. These drops are not observed in the discharge without radiation collapse. These data shows there are two steps in the discharge towards the radiative collapse. Until just before the radiative collapse ( $t < 1.27$  sec), there is no

significant drop of temperature. Negative electric field causes the increase of density and the radial electric field becomes more negative due to the increase of collisionality. This feedback process between the negative radial electric field and the increasing electron density should be the most important process. Just before the radiation collapse ( $t > 1.27$  sec), the feedback process between the decreasing temperature and increasing cooling rate also is considered to be important.

Figure 8(a)(b) show the time slice of the radial electric field and the ion temperature in the discharge, which is terminated by radiative collapse. The negative electric field is localized near the plasma edge at  $r = 0.8 - 0.9$ . Just before the radiative collapse ( $t = 1.43$  sec), the negative radial electric field region extends to more inside of the plasma ( $\rho < 0.7 - 0.8$ ) and the edge radial electric field becomes less negative at  $t = 1.42$ s. Although the negative electric field is localized in the narrow region ( $\delta\rho = 0.1$ ), the drop of ion temperature is observed in the wide region. The decrease of intensity of the charge exchange line of NeX just before the radiation collapse is due to the recombination of fully ionized Neon associated with the drop of the electron temperature. These observations show that the positive electric field is quite important to avoid the radiation collapse and are consistent with the experimental results in the LID configuration, where the impurity influx is shielded by the strong positive electric field near the X point of the magnetic island[23].

#### **4. Discussions**

The strong shear of the radial electric field is demonstrated to be produced inside the plasma by controlling the helical ripple and the magnetic topology (magnetic island and LID configuration) to trigger an internal transport barrier and reduce impurity influx. The radial electric field shear is demonstrated to be controlled by the modification of the helical ripple associated with the shift of the magnetic axis, while the sign of the radial electric field is controlled by the collisionality. The magnetic configuration with a sharp gradient in the helical ripple is considered to be more appropriate for creating the strong radial electric field shear. The magnetic island produces the radial electric field shear at the boundaries of the magnetic island and hence contributes to trigger the formation of an internal transport barrier in the electron root plasma. The transient improvement of the ion transport in the ion root is also observed after the pellet injection with the assistance of  $n/m=1/1$  island. This is due to the fact that the increase of the electron density gradient by pellet injection is transient and there is not enough particle source to sustain the density gradient. This improvement is expected to be sustained in the steady state by increasing ion heating power and beam fueling using a low energy beam of 40 keV, which is planned to be installed in LHD in the near future to increase the heating power to ions. In addition to the temperature dependence of the cooling rate, the feedback mechanism in which negative electric field causes an increase of the density, which results in a more negative electric field, is crucial to the process of radiative collapse. The role of radial electric field is found to be quite important to prevent the

influx of impurities and avoid the radiative collapse. The positive electric field observed in the LID configuration is considered to play an important role for impurity shielding. Therefore the improvement of thermal transport and impurity exhaust are achieved by the control of radial electric field profiles in LHD.

The authors would like to thank the LHD technical staff for their effort to support the experiments in LHD. This work is partly supported by a grant-in-aid for scientific research of MEXT Japan.

## References

- [1] R.J.Groebner, K.H.Burrell, and R.P.Seraydarian, Phys. Rev. Lett. 64, (1990) 3015
- [2] K.Ida, et. al., Phys Rev Lett 65 (1990) 1364.
- [3] A.Fujisawa, et. al., Phys Rev Lett 82 (1999) 2669.
- [4] U.Stroth, et. al., Phys Rev Lett 86 (2001) 5910.
- [5] T.Shimozuma et al., Plasma Phys Control Fusion 45 (2003) 1183.
- [6] K.Ida, et. al., Phys Rev Lett 91 (2003) 085003.
- [7] Y.Takeiri et al., Phys. Plasma 10 (2003) 1788
- [8] K.Ida, S. Kado, Y. Liang, Rev. Sci. Instrum. 71 (2000) 2360.
- [9] K.Ida, et. al., Phys Rev Lett 86 (2001) 5297.
- [10] C.D.Beidler et al., Plasma Physc. Controll. Fusion 36 (1994)317
- [11] M.Yokoyama, et al., Nucl. Fusion 42 (2002) 143.
- [12] K.Narihara, et al., Phys Rev Lett 87 (2001) 35002
- [13] N.Ohyabu et al., Phys Rev Lett 88 (2002) 55005
- [14] Y.Nagayama et al., submitted to Nucl. Fuion.
- [15] K.Ida, et al., Phys Rev Lett 88 (2002) 015002.
- [16] K.Ida, et. al., Phys plasmas 11 (2004) 2551.
- [17] K.Ida, et. al., Phys Rev Lett 68 (1992) 182.
- [18] Y.Nakamura, et. al., Nucl Fusion 43 (2003) 219.
- [19] K.Ida, et. al., Plasma Phys Control Fusion 45 (2003) 1931.
- [20] K.Ida et. al., Phys Plasmas 08 (2001) 1.
- [21] A.Komori et al., submitted to Nucl. Fuion.
- [22] B.J.Peterson et al., submitted to Nucl. Fuion.
- [23] T.Morisaki et al., J. Nucl. Mater to be published

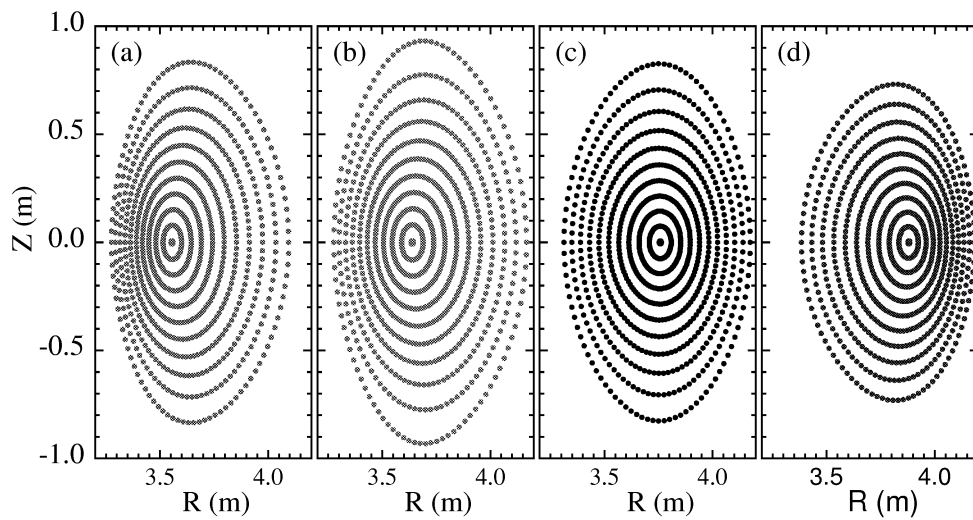


**Figure 1.** (a) Poloidal cross section of the magnetic flux surface for plasmas with various magnetic axis,  $R_{ax}$  of (a) 3.5m, (b) 3.6m, (c) 3.75m, and (d) 3.9m.

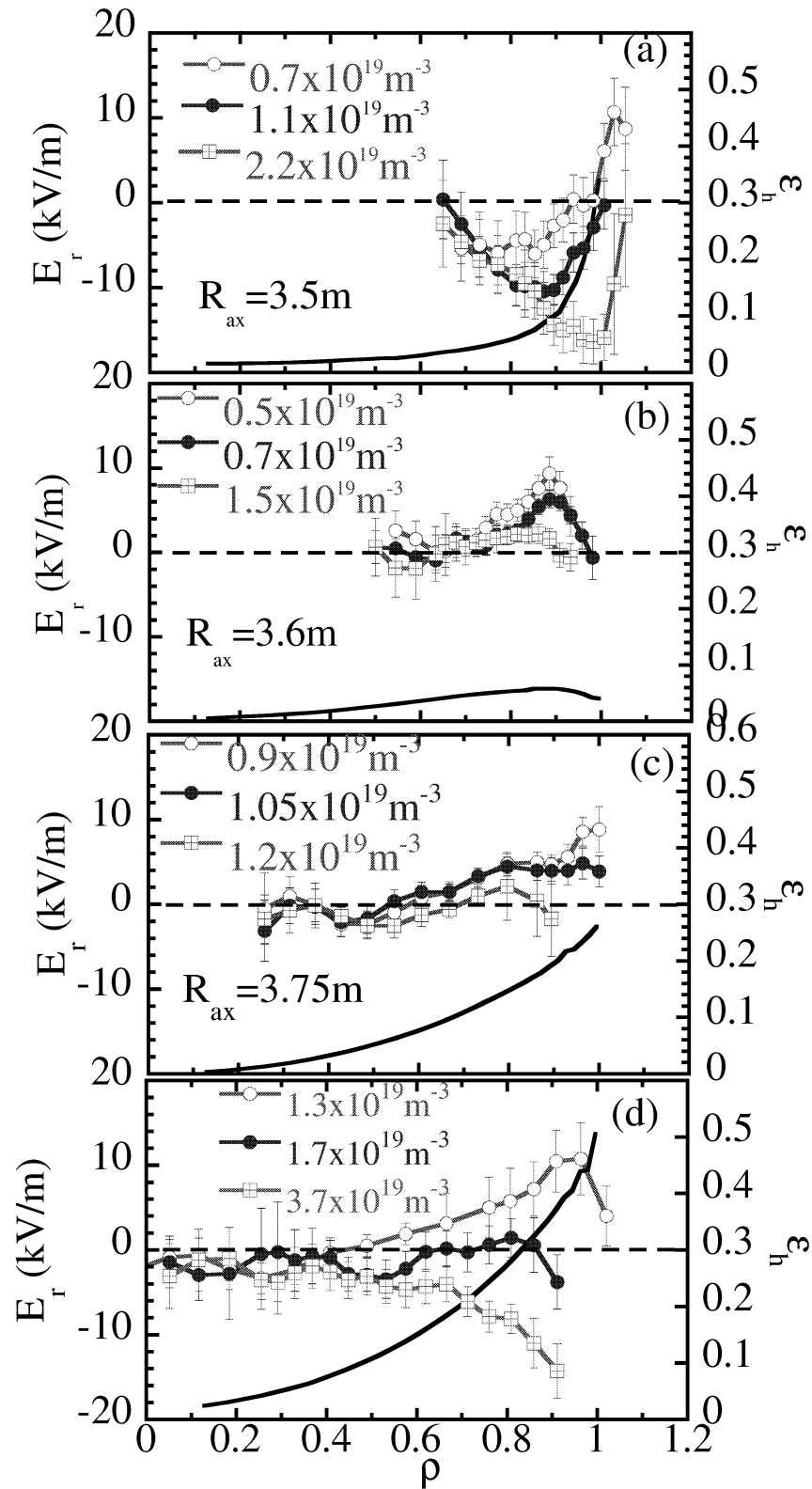


**Figure 2.** Radial profiles of radial electric field,  $E_r$  and helical ripple  $\epsilon_h$  for plasmas with various magnetic axis,  $R_{ax}$  of (a) 3.5m, (b) 3.6m, (c) 3.75m, and (d) 3.9m.

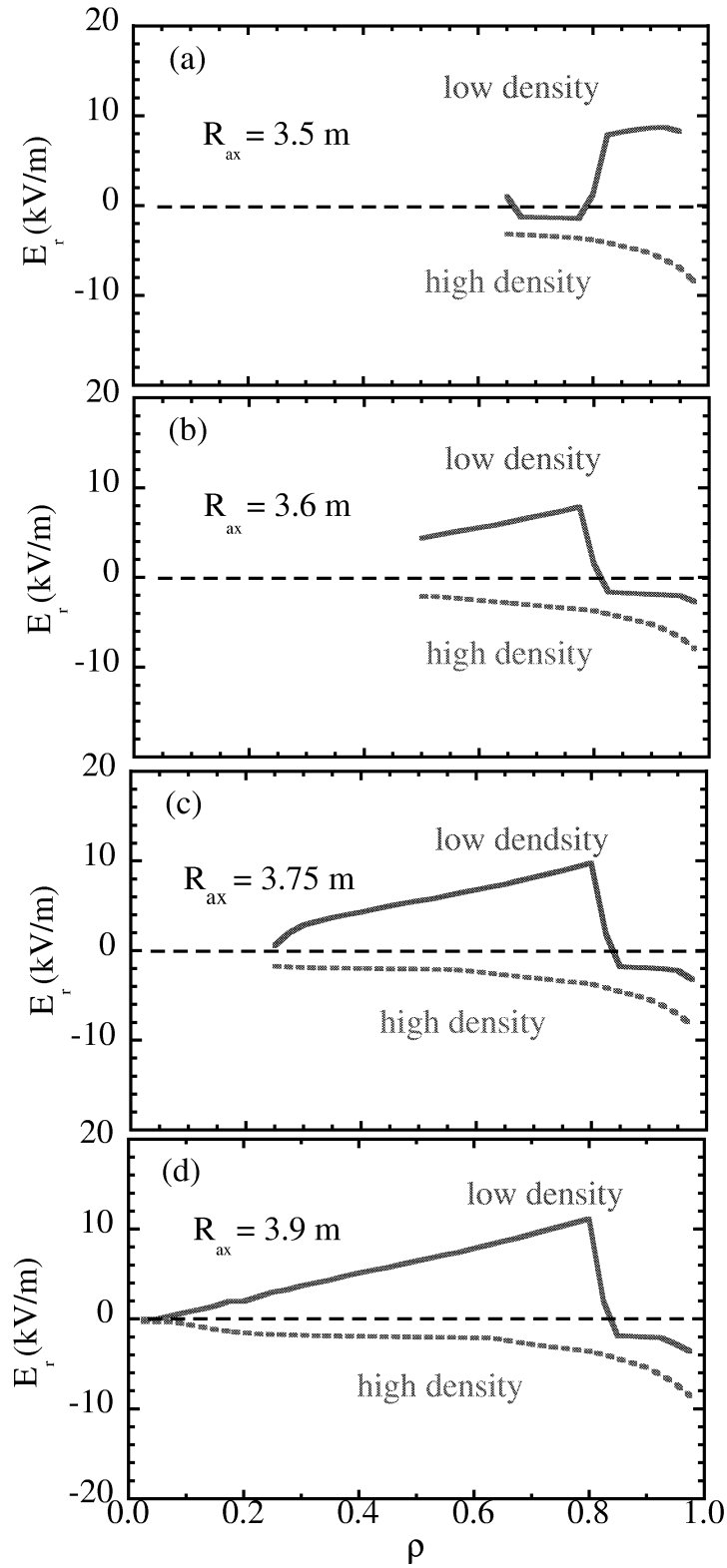


**Figure 3.** Radial profiles of radial electric field,  $E_r$  calculated with NC theory for plasmas with various magnetic axis,  $R_{ax}$  of (a)3.5m, (b)3.6m, (c)3.75m, and (d)3.9m.

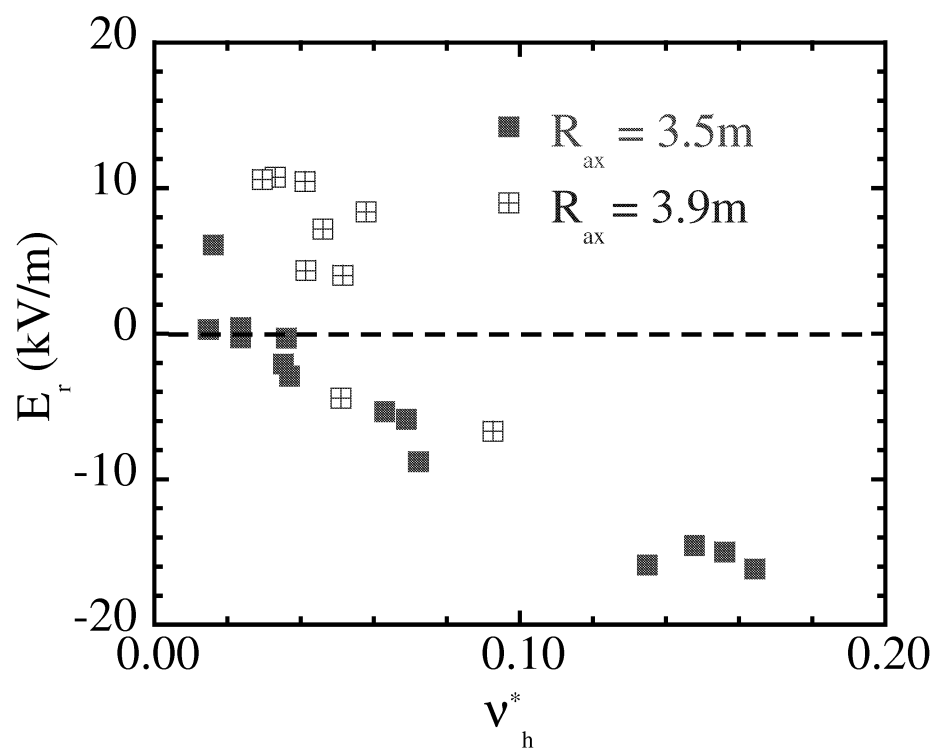


**Figure 4.** Radial electric field as a function of collisionality normalized by the bounce frequency of helically trapped particles.

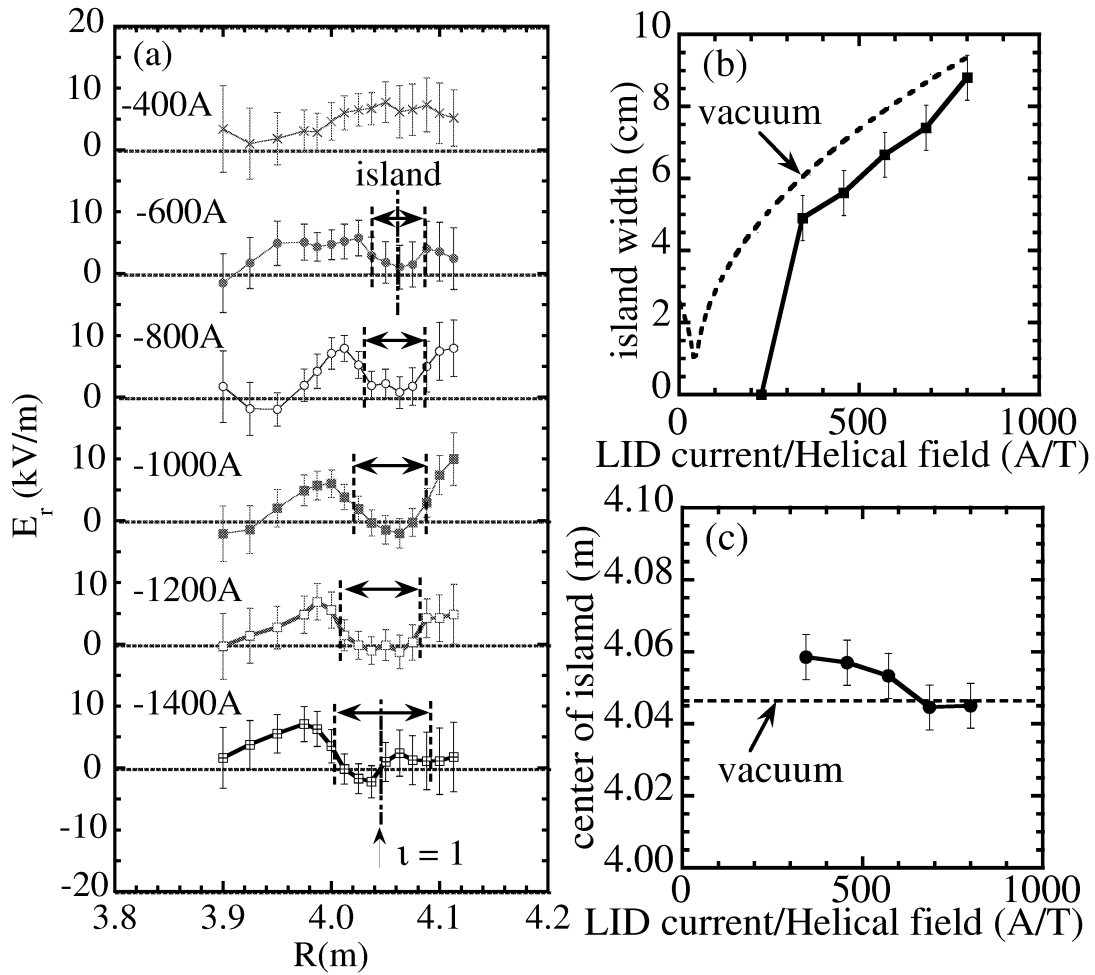


**Figure 5.** (a) Radial profiles of radial electric field with magnetic island for the plasma in the electron root (b) width of magnetic island at the mid-plane and (c) position of center of magnetic island as a function of LID perturbation field normalized by helical magnetic field.

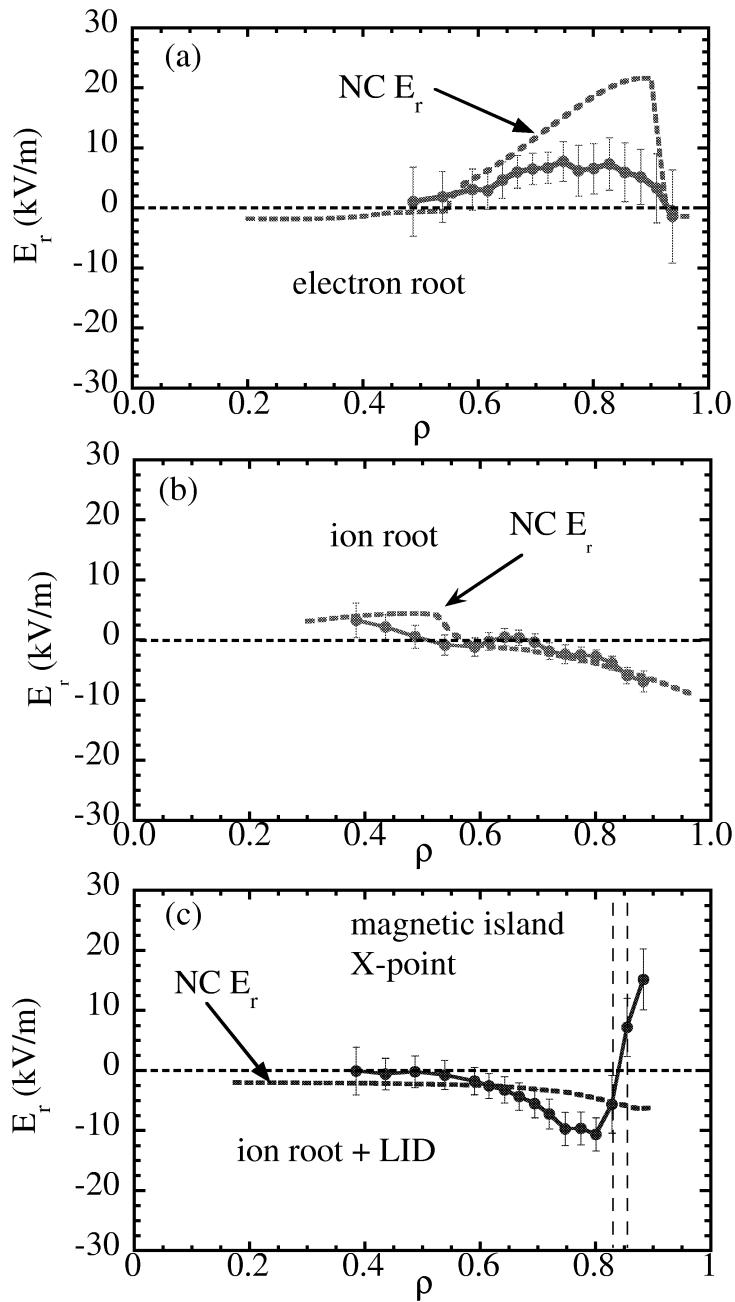


**Figure 6.** Radial profiles of radial electric field measured and neoclassical prediction (dotted lines) for the plasmas (a) in the electron root (b) ion root in limiter configuration and (c) ion root with a local island divertor configuration.

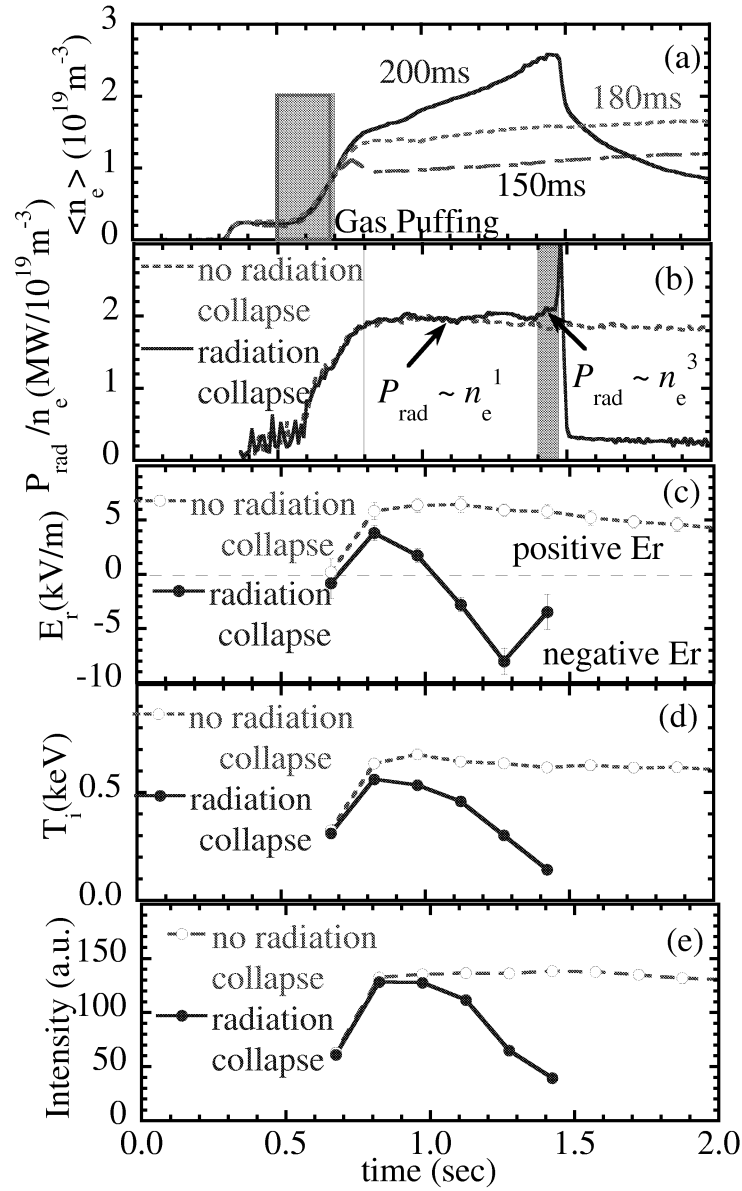


**Figure 7.** Time evolution of (a) line averaged electron density (b) normalized total radiation power (c) radial electric field (d) ion temperature and (e) NeX intensity at  $\rho = 0.89$  for the discharges with and without radiation collapse.

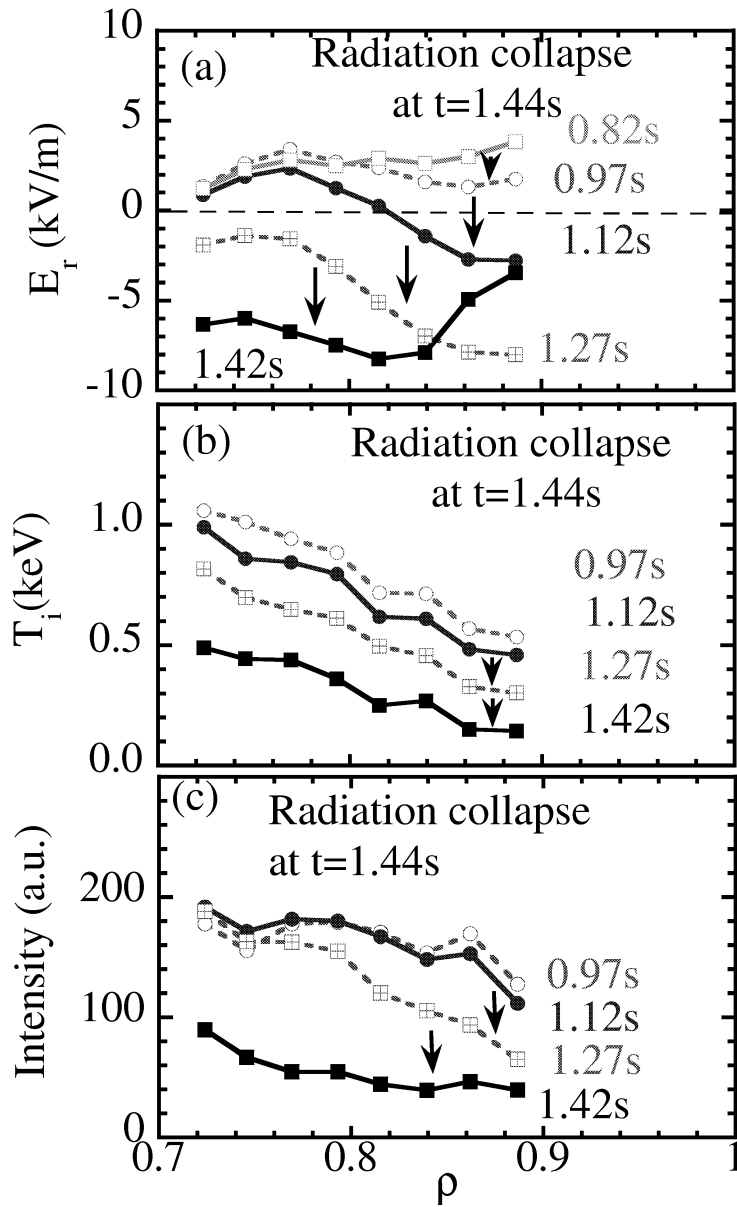


**Figure 8.** Radial profiles of (a) radial electric field, (b) ion temperature and (c) intensity of charge exchange line NeX in the discharges with radiation collapse.

## High-Ion Temperature Experiments with Negative-Ion-Based NBI in LHD

Y. Takeiri 1), S. Morita 1), K. Tsumori 1), K. Ikeda 1), Y. Oka 1), M. Osakabe 1), K. Nagaoka 1), M. Goto 1), J. Miyazawa 1), S. Masuzaki 1), N. Ashikawa 1), M. Yokoyama 1), S. Murakami 2), K. Narihara 1), I. Yamada 1), S. Kubo 1), T. Shimozuma 1), S. Inagaki 1), K. Tanaka 1), B.J. Peterson 1), K. Ida 1), O. Kaneko 1), A. Komori 1), and LHD Experimental Group 1)

1) National Institute for Fusion Science, Toki 509-5292, Japan

2) Department of Nuclear Engineering, Kyoto University, Kyoto 606-8501, Japan

e-mail contact of main author: takeiri@nifs.ac.jp

**Abstract.** High-Z plasmas have been produced with Ar- and/or Ne-gas fuelling to increase the ion temperature in the LHD plasmas heated with the high-energy negative-ion-based NBI. Although the electron heating is dominant in the high-energy NBI heating, the direct ion heating power is much enhanced effectively in low-density plasmas due to both an increase in the beam absorption (ionisation) power and a reduction of the ion density in the high-Z plasmas. Intensive Ne- and/or Ar-glow discharge cleaning works well to suppress dilution of the high-Z plasmas with the wall-absorbed hydrogen. As a result, the ion temperature increases with an increase in the ion heating power normalized by the ion density, and reaches 10 keV. An increase in the ion temperature is also observed with an addition of the centrally focused ECRH to the low-density and high-Z NBI plasma, suggesting improvement of the ion transport. The results obtained in the high-Z plasma experiments with the high-energy NBI heating indicate that an increase in the direct ion heating power and improvement of the ion transport are essential to the ion temperature rise, and that a high-ion temperature would be obtained as well in hydrogen plasmas with low-energy positive-NBI heating which is planned in near future in LHD.

### 1. Introduction

In the Large Helical Device (LHD), which is the world-largest superconducting helical device [1], it is quite important to investigate the confinement properties of high-ion temperature plasmas. Achievement of high temperature plasmas should also indicate the confinement ability of the high-energy ions. The high-electron temperature plasmas have been already achieved with centrally focused ECRH [2], and the improvement of electron confinement was observed due to suppression of the anomalous transport in the electron-ITB plasmas [3,4]. The LHD is equipped with three tangential negative-NB injectors in which the nominal injection energy of hydrogen beam is as high as 180 keV [5]. The LHD-NBI system was designed for achievement of high- $n_T$  plasmas and the injection energy was determined for the target density of  $(3 - 5) \times 10^{19} \text{ m}^{-3}$ . Against low-density hydrogen plasmas, then, most of the beam power goes to electrons due to the high injection energy and a large fraction of the injected neutral beam passes through the plasma without ionisation. As a result, the achieved ion temperature has been below 2 – 3 keV in hydrogen discharges using the negative-NBI [6]. There are two scenarios to raise the ion temperature in the LHD. One is to increase the direct ion heating power, and the other is to improve the ion transport. While plasma heating with low-energy positive-NBI systems would be effective to increase the ion-heating fraction so as in the present large tokamaks, we realized the enhancement of the ion heating power effectively by producing high-Z plasmas at low density [3,6,7]. The ion temperature was increased to 5 keV by Ne-gas puffing with an increase in the direct ion heating power [3,6]. However, dilution of the high-Z plasmas with hydrogen from the wall prevented the further increase in the ion temperature. We have performed the Ne- and/or Ar-glow discharge cleaning for reduction of the wall-absorbed hydrogen, and achieved the further increase in the ion temperature up to 10 keV with Ar-gas puffing. On the other hand, the transport

improvement is expected in the neoclassical electron root plasmas with positive radial-electric field [8], which was confirmed for electrons in the electron-ITB plasmas in the LHD with the centrally focused ECRH [3,4,9]. We have superposed the centrally focused ECRH to the high-Z NBI plasma as one approach to improve the ion transport, and observed an increase in the ion temperature. In the followings, we present the high-ion temperature experiments with the high-Z plasmas heated by the high-energy negative-NBI system in the LHD, with views of effectiveness of the high-Z glow discharge cleaning, plasma properties including high-energy ion behaviour in the high-Z discharges, and effect of the superposition of the ECRH to the high-Z NBI plasmas.

## 2. Negative-Ion-Based NBI system and ECRH system

The neutral beam injection (NBI) system in the LHD, which is characterized by high-energy NB injection produced through negative ions, consists of three tangential injectors, each of which has two large negative-ion sources [5,10]. One injector has the opposite injection direction to the other two injectors. The nominal injection energy is 180 keV and the beam species is hydrogen. The injection power has gradually increased year by year since the NBI system was operational in 1998, and reached 13 MW in the previous campaign. The achieved injection energy and power with one injector are 186 keV and 5.7 MW, respectively [11]. High-power neutral beams are injected usually for 2 sec with high reliability, and the injection duration can be extended over 100 sec with reduced power [12]. The shine-through beam, passing through the plasma without ionisation, is incident on the beam-facing armour tiles installed inside the LHD vacuum vessel. The shine-through power is estimated with a calorimeter array on the armour tiles, and the port-through injection power is determined with the shine-through power measurement [13].

The electron cyclotron resonance heating (ECRH) system employs 168GHz, 84GHz, and 82.7GHz gyrotrons, and each microwave is injected on the equatorial plane as a strongly focused Gaussian beam using vertical and horizontal antenna systems with quasi-optical mirrors [14]. In the experiments, the second-harmonic heating with two 82.7 GHz gyrotrons is utilized. The power deposition profile is estimated with ray tracing including a weakly relativistic effect.

## 3. Glow Discharge Cleaning with High-Z Gas

Since the ionisation cross-section for the injected beam is larger in the higher-Z plasmas, the beam absorption (ionisation) rate is increased especially for low-electron density plasmas in the high-Z discharges. Considering a reduced number of ions in the high-Z plasmas, the direct ion heating power is much enhanced even with the high-energy NBI heating. To realize such high-Z plasmas at low density the wall conditioning is important, because the high-Z plasmas should be diluted with the residual hydrogen during the discharge and a degree of the dilution be large in the low-density plasmas. For reduction of the wall-absorbed hydrogen intensive Ne- and/or Ar-glow discharge cleaning was performed. Figure 1(a) shows the ratio of the H<sub>2</sub> partial pressure to the total pressure before the start of the main discharges (after the glow discharge cleaning). In this case the high-Z experiments were made for three successive days (Jan. 13–15, 2004) and the Ne-glow discharge cleaning was performed for 64 hours prior to a series of the high-Z experiments. As shown in Fig. 1(a), the H<sub>2</sub> partial pressure after the high-Z glow discharge cleaning was much reduced compared with that after the H<sub>2</sub>-glow discharge

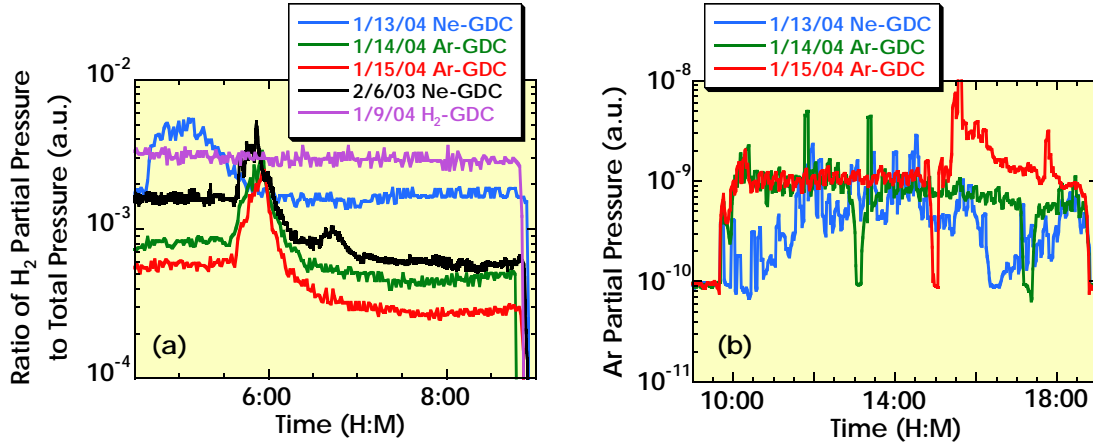


FIG. 1. (a) Ratio of the H<sub>2</sub> partial pressure to the total pressure after the glow discharge cleaning (before the start of the main discharges). Ti-gettering was applied after the Ne- or Ar-glow discharge cleaning and was not done after the H<sub>2</sub>-one. (b) Ar partial pressure during the main discharges. The Ar gas was mainly puffed for the discharges. At around 15:00 on 1/15/04 the experiments were moved to high-density hydrogen discharges.

cleaning on the other day (Jan. 9, 2004). After the first-day experiment the Ar-glow discharge cleaning was applied during the successive two nights (Jan. 14 and 15, 2004). It is found that the H<sub>2</sub> partial pressure was reduced day by day, indicating reduction of the wall-absorbed hydrogen. It seems that the Ar-glow discharge cleaning is more effective for reduction of the H<sub>2</sub> partial pressure compared with the Ne-one (Feb. 6, 2003 is the successive third day of the Ne-glow discharge cleaning). The Ar partial pressure during the high-Z main discharges is shown in Fig. 1(b) for the three successive high-Z experiments (Jan. 13–15, 2004) in which the plasma was produced mainly with Ar gas-puffing. In the first day (Jan. 13) when the Ne-glow discharge cleaning was applied before the main discharges, the Ar partial pressure was gradually increased due to Ar gas-puffing in the main discharges, and it was decreased while the main discharge was suspended. In the second day (Jan. 14) when the Ar-glow discharge cleaning was applied, the Ar partial pressure showed a higher value than that in the first day, and it was slowly decreased as the main discharge progressed. The Ar partial pressure was maintained at a high value without a decrease in the third day (Jan. 15) when the second Ar-glow discharge cleaning was applied. After the high-Z experiments (around 15:00 on Jan. 15), the Ar partial pressure increased due to the following high-density H<sub>2</sub> discharge experiments. The successive two-nights of Ar-glow discharge cleaning should replace the wall-absorbed hydrogen with argon and be effective for the reduction of the residual hydrogen.

## 4. High-Ion Temperature in High-Z Discharges

### 4.1. Enhancement of Beam-Absorption Power

The ionisation (absorption) rate of the injected neutral beam is estimated with measurement of the shine-through power [13]. Figure 2 shows the ratio of the plasma absorption power to the port-through power of the injected neutral beams as a function of the line-averaged electron density. The beam absorption rate is fitted to  $1 - \exp(-\sigma_{\text{eff}} n_e \ell)$  using the line-density  $n_e \ell$ , and, then,  $\sigma_{\text{eff}}$  represents the effective cross-section for the ionisation of neutral beam. In the figure, the absorption rates are plotted for two cases, the conventional hydrogen discharges and the Ne- or Ar-seeded discharges after the Ne-glow discharge cleaning. The plasma

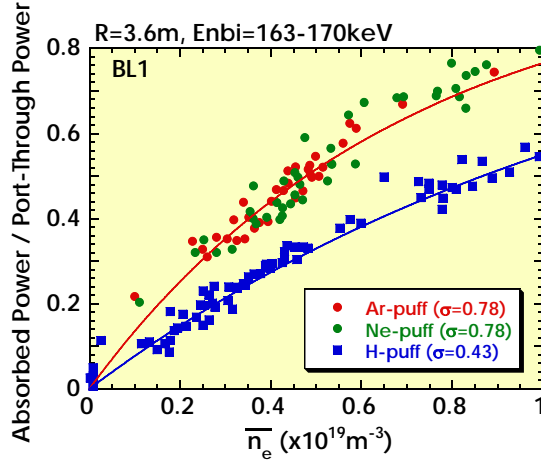


FIG. 2. Ratio of the plasma absorbed power to the port-through power of the injected neutral beams as a function of the line-averaged electron density for the Ar-, Ne-, and H<sub>2</sub>-puffed plasmas. The injected beam energy ranges 163 – 170 keV. The data are fitted to  $1 - \exp(-\sigma n_e l)$  using the line-density  $n_e l$ .

absorption power is enhanced in the Ne- or Ar-seeded plasmas compared with the H<sub>2</sub>-puffed ones, and the effective cross-section for the beam ionisation is about 1.8 times larger. In low-electron density plasmas below  $0.5 \times 10^{19} \text{m}^{-3}$ , the plasma absorption power is increased 1.6 times in the Ne- or Ar-seeded plasmas. Since the ion density is reduced compared with the electron density in the high-Z plasmas, the direct ion heating power is much enhanced. Consequently, with the high-Z discharges, the ion heating power by the high-energy NBI can be increased even in the low-density plasmas. In other words, with a view of the ion heating, the high-energy NBI heating in the high-Z plasmas is equivalent to the low-energy NBI heating in hydrogen discharges where the ion heating is dominant, although the plasma characteristics such as the collisionality are not the same. As shown in Fig. 2, the  $\sigma_{\text{eff}}$  is not so different between the Ne- and the Ar-seeded plasma. The  $\sigma_{\text{eff}}$  for the Ar-seeded plasma after the Ar-glow discharge cleaning also indicates nearly the same value as the Ne- or Ar-seeded plasma after the Ne-glow discharge cleaning.

#### 4.2. Achievement of 10-keV Ion Temperature

Figure 3(a) shows the time evolutions of various plasma parameters in an Ar-puffed plasma after the Ar-glow discharge cleaning. After an increase in the electron density due to the Ar gas-puffing, the central ion temperature, measured with the Doppler broadening of an X-ray line of ArXVII, rapidly increases as the density decreases with an addition of another NBI power, and stays at high values. The ion temperature reaches 10 keV at around  $t=1.65\text{s}$  with an injection power of 12.2 MW, around 30 % of which is absorbed at an electron density of  $0.37 \times 10^{19} \text{m}^{-3}$ . The electron temperature is also increased up to 4.6 keV, and, however, is much lower than the ion temperature. The observed beam slowing-down time after the NBI-off is as long as 1.2 sec probably due to both the low electron density and the high electron temperature, and the ion and electron temperatures show an extremely slow decay after the beam turn-off. The parallel beam-pressure should be large. The high-energy ion spectra measured with a Si-FNA detecting perpendicularly are shown in Fig. 3(b). At  $t=0.8-1.0\text{s}$  before the ion temperature rise, the high-energy ion spectrum is depressed less than 30 keV. On the other hand, no depression is observed on the spectrum at  $t=1.6-1.8\text{s}$  and the high-energy ion flux is increased when the ion temperature rises to 10 keV, indicating that the injected high-energy particles are slowing-down to the thermal energy without large loss. As shown in Fig. 3(c), the density profile becomes peaked ( $t=1.64\text{s}$ ) with a reduction of the density in outer plasma region at around  $\rho=0.8$  as the ion temperature increases, compared with that before the temperature increase ( $t=0.88\text{s}$ ) showing hollow or flat profiles.

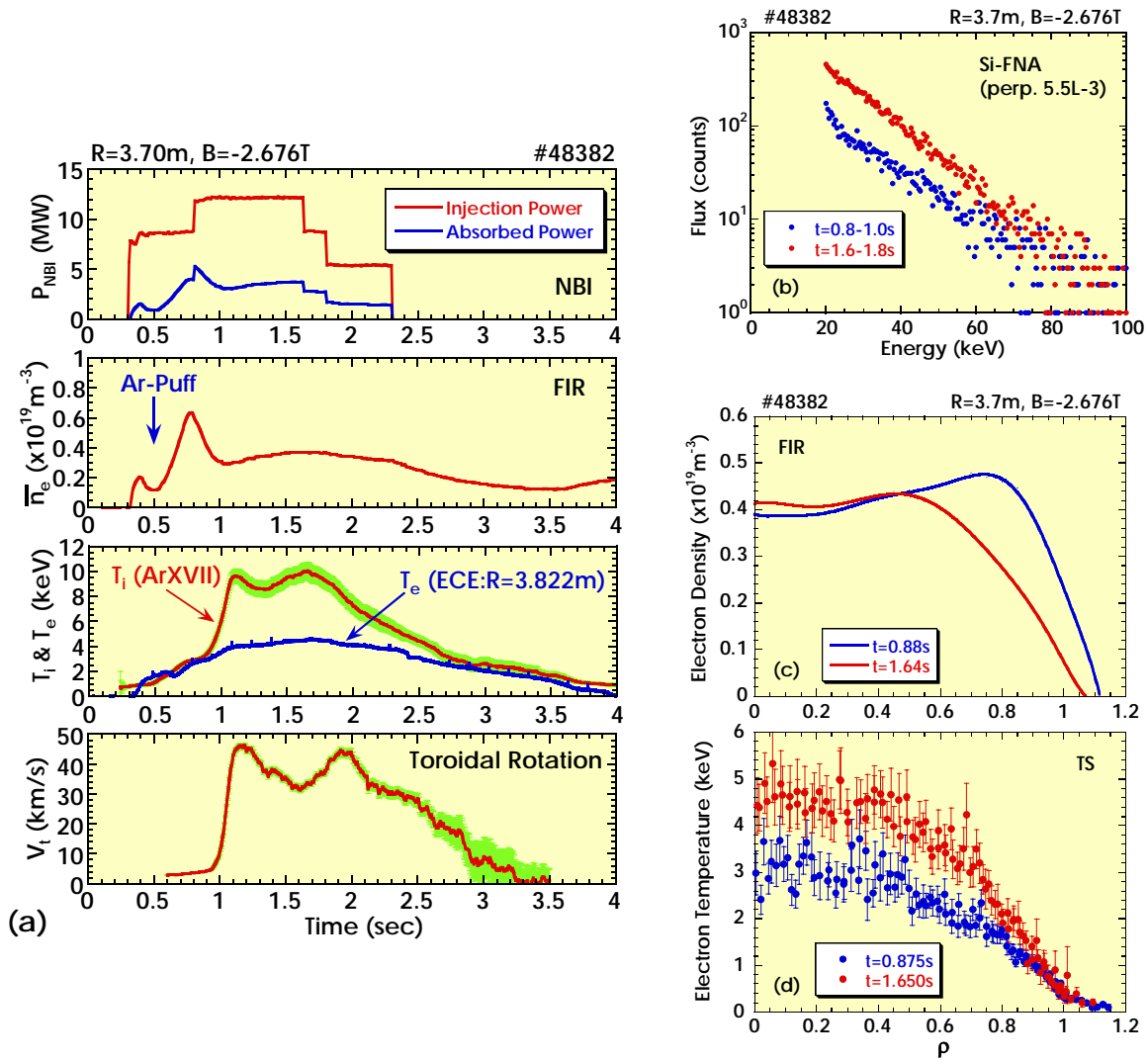


FIG. 3. (a) Time evolutions of the injection and absorption powers, the line-averaged electron density, the ion and electron temperatures, and the toroidal rotation velocity (from the top). (b) High-energy ion spectra measured with a perpendicularly detected Si-FNA. The fluxes are plotted as integrated counts for  $t=0.8-1.0$ s and  $t=1.6-1.8$ s. (c) Electron density and (d) electron temperature profiles at  $t=0.88$ s and  $t=1.65$ s.

Corresponding to the density peaking, the electron temperature profile shows a steep gradient at around  $\rho=0.8$ , as shown in Fig. 3(d). Theoretical calculation of neoclassical ambipolar flux considering multi-ion species indicates generation of a strong positive radial-electric field at around  $\rho=0.8$ , suggesting a confinement improvement there. A large toroidal rotation is observed corresponding to an increase in the ion temperature as shown in Fig. 1(a), and the toroidal rotation velocity reaches 46 km/s, which is about 30 % of the Ar-thermal velocity, suggesting also a confinement improvement in the high-ion temperature plasmas with the high-Z discharge.

### 4.3. Properties of High-Z and High-Ion Temperature Plasmas

It is important to clarify the properties of high-Z and high-ion temperature plasmas. From a measurement of the recombination  $H\alpha$  intensity at the plasma termination, the H ion density is roughly estimated to be 25 – 40 % of the electron density, and this ratio is not so changed

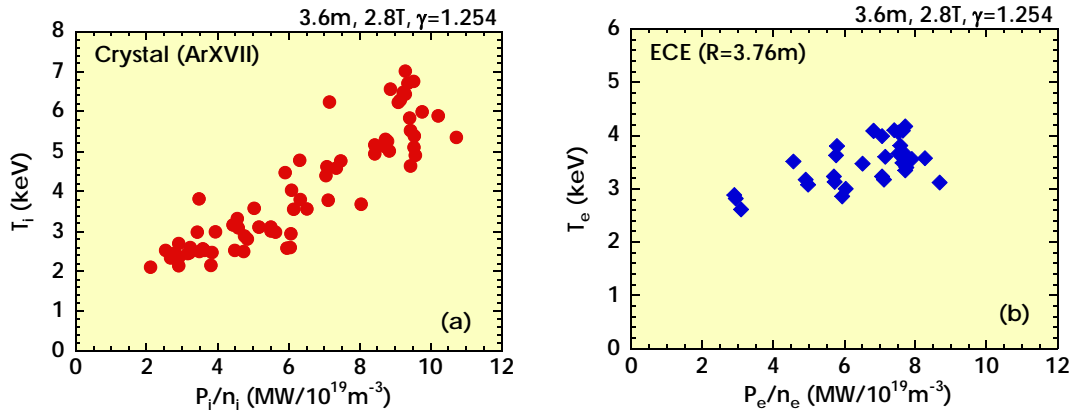


FIG. 4. (a) Ion temperature as a function of the ion heating power normalized by the ion density. (b) Electron temperature as a function of the electron heating power normalized by the electron density. The Ne or Ar gas is puffed and intensive Ne-glow discharge cleaning was applied for a series of high-Z experiments. The magnetic axis position is 3.6m.

in a series of low-density and high-Z discharges. Thus, the H ions seem to dominate the species number ratio even in the high-Z plasmas. The  $Z_{\text{eff}}$  is around 7 and around 12 if the other ion species is Ne alone and Ar alone, respectively. Although the other possible impurity is C in the LHD with carbon divertors, the  $Z_{\text{eff}}$  is thought to range 7 – 12 in the Ne and Ar discharges, and the total ion density should be 30 – 46 % of the electron density. Then, the ion heating power is around a third of the NBI-absorption power. Here, we can estimate the ion heating power normalized by the ion density. Compared with the hydrogen discharges, the normalized ion heating power is much enhanced by a factor of 4 - 5 in the high-Z and low-density plasmas by both an increase in the beam absorption power and a reduction of the ion density. Figure 4(a) shows the ion temperature as a function of the normalized ion heating power for the Ar- and Ne-puffed plasmas after the Ne-glow discharge cleaning. It is found that the ion temperature is increased with an increase in the normalized ion heating power in the Ar- and Ne-puffed plasmas and that no distinct saturation of the increase in the ion temperature has been observed. The electron temperature as a function of the electron heating power normalized by the electron density is also shown in Fig. 4(b). The electron temperatures for the normalized heating power show similar values to the ion temperatures although the dependency is not so clear due to a narrower power range. It seems that the ion and electron temperatures are increased with increases in the direct ion and electron heating powers, respectively. Since the collisionalities of high-Z and H ions are considered to be in plateau regime, the dependence of the ion temperature is not directly applied to the hydrogen discharges in collisionless regime. However, the experimental results obtained in the high-Z discharges indicate that there is a possibility to achieve a high-ion temperature as well in hydrogen discharges if the direct ion heating power is increased to the same power density as that in the high-Z discharges.

Assuming that the ionised hydrogen particles of 180keV – 3MW are confined for 1 sec, corresponding to the beam slowing-down time, the hydrogen ion density deriving from the injected beam is  $0.35 \times 10^{19} \text{ m}^{-3}$ . Therefore, it is considered that the hydrogen ions in the high-Z discharges are mainly supplied from the injected beam. In other words, it would be difficult to realize the further high-Z discharges with the NBI heating.

#### 4.4. Ion Temperature Rise with Superposition of ECRH

When centrally focused ECRH is superposed on the NBI plasmas, improvement of the electron transport was observed in LHD. This improvement is correlated with realization of the electron root where the positive radial-electric field is generated due to neoclassical ambipolar flux [3,4,8,9]. However, no definite increase in the ion temperature has been observed, probably because the ion heating power is too small in low-density hydrogen plasmas due to the high injection energy. Figure 5(a) shows the comparison between the NBI-only plasma and the NBI+ECRH plasma in low-density and Ne-puffed discharges after the Ar-glow discharge cleaning. By the superposition of the ECRH of 470 kW the electron temperature is much increased to 3 keV from 2 keV, and accordingly the ion temperature is also increased by a factor of 1.5. Note that the integration time of the  $T_i$  measurement is 150 – 300 ms. Since the electron-ion heat exchange time is as long as a few seconds for Ne, Ar, or H ions and an increase in the ion heating ratio by the electron temperature rise is as small as about 10 %, it is suggested that the ion temperature increase is due to an improvement of the ion transport. Comparison of the electron density and temperature profiles between the NBI-only plasma and the NBI+ECRH plasma is shown in Figs. 5(b) and (c), respectively. As shown in Fig. 5(c), with the superposition of the ECRH the electron temperature profile forms a steep gradient at  $\rho=0.4-0.6$ , just outside of the injection region of the focused ECRH at around  $\rho=0.3$ . As the neoclassical calculation of the ambipolar flux considering multi-ion species shows generation of a positive radial-electric field in a region outside around  $\rho=0.4$  with the superposition of the ECRH, there is a possibility of improvement of the ion transport in the electron root. Although the density profile usually becomes hollow with applying the ECRH, it becomes peaked with a reduction of outer region density in the NBI+ECRH plasma

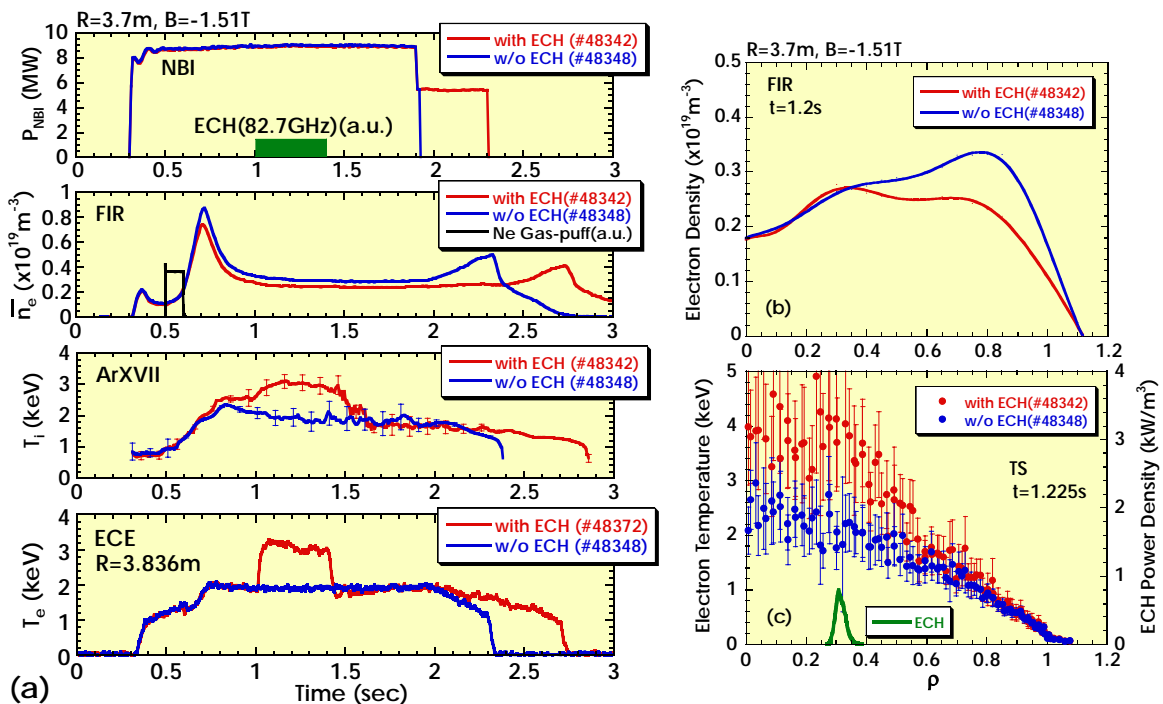


FIG. 5. (a) Time evolutions of the NB injection powers and the ECRH timings, the line-averaged electron densities, the ion temperatures, and the electron temperatures (from the top), for the NBI-only plasma and the NBI+ECRH plasma of the Ne-puffed discharges. (b) Electron density and (c) electron temperature profiles at  $t=1.2\text{s}$  for the NBI-only and the NBI+ECRH plasmas. The ECRH power deposition profile is also indicated in (c). The magnetic axis position is 3.7m.

with a rise in the ion temperature, as shown in Fig. 5(b). The correlation of the increase in the ion temperature and the density peaking is recognized in the high-Z plasmas including the impurity pellet injection, and the particle transport would be changed in the high-Z plasmas with high-ion temperature.

## 5. Concluding Remarks

The high-Z discharges are utilized for high-ion temperature experiments with high-energy negative-ion-based NBI heating, in which the electron heating is dominant usually in hydrogen discharges. In the high-Z plasmas the beam absorption (ionisation) rate is increased and the plasma ion density is reduced, resulting in much enhancement of the effective ion heating power by a factor of 4 – 5. The ion temperature is increased with an increase in the ion heating power normalized by the ion density, and reaches 10 keV in an Ar-seeded discharge. In the high-ion temperature plasmas realized in the high-Z discharges, there are observations suggesting transport improvement. The toroidal rotation velocity is increased corresponding to the increase in the ion temperature, and the density profile becomes peaked with a reduction of outer density at around  $\rho=0.8$ , where the electron temperature gradient becomes steep with a theoretical calculation result of generation of a strong positive radial-electric field. Intensive Ar- and/or Ne-glow discharge cleaning is effective to reduction of the wall-absorbed hydrogen with which the high-Z plasmas are diluted. With superposition of the centrally focused ECRH on the NBI-heated high-Z plasma, an increase in the ion temperature is observed, suggesting improvement of the ion transport in the neoclassical electron root.

Two scenarios for increasing the ion temperature, i.e., to increase in the direct ion heating power and to improve the ion transport, are experimentally demonstrated with high-Z plasmas in LHD. The high-Z plasmas heated by high-energy negative-NBI is equivalent to the hydrogen plasmas heated by low-energy positive-NBI in that the effective ion heating power is large, although the plasma parameters such as collisionality are not necessarily the same. The positive-NBI heating, which is planned in near future in LHD, could demonstrate to increase the ion temperature in hydrogen discharges.

## References

- [1] O. Motojima, *et al.*, Phys. Plasmas **6** (1999) 1843.
- [2] S. Kubo, *et al.*, Proc. 19th IAEA Fusion Energy Conf., Lyon, 2002, EX/C4-5Rb.
- [3] Y. Takeiri, *et al.*, Phys. Plasmas **10** (2003) 1788.
- [4] T. Shimosuma, *et al.*, Plasma Phys. Control. Fusion **45** (2003) 1183.
- [5] O. Kaneko, *et al.*, Nucl. Fusion **43** (2003) 692.
- [6] S. Morita, *et al.*, Nucl. Fusion **43** (2003) 899.
- [7] Y. Takeiri, *et al.*, Proc. 30th EPS Conf., St. Petersburg, 2003, P-2.171.
- [8] M. Yokoyama, *et al.*, Nucl. Fusion **42** (2002) 143.
- [9] K. Ida, *et al.*, Phys. Rev. Lett. **91** (2003) 085003.
- [10] Y. Takeiri, *et al.*, Rev. Sci. Instrum. **71** (2000) 1225.
- [11] K. Tsumori, *et al.*, this Conference, FT/1-2Rb.
- [12] Y. Takeiri, *et al.*, Plasma Phys. Control. Fusion **42** (2000) 147.
- [13] M. Osakabe, *et al.*, Rev. Sci. Instrum. **72** (2001) 586.
- [14] T. Shimosuma, *et al.*, Fusion Eng. Design **53** (2001) 525.

# Classical and non-classical confinement properties of energetic ions on LHD

M.Osakabe, S.Murakami\*<sup>1</sup>, T. Seki, S.Yamamoto\*<sup>2</sup>, K.Toi, S.Sakakibara, O.Kaneko, K.Saito, Y.Takeiri, M.Isobe, T.Saida\*<sup>3</sup>, T.Ozaki, M.Sasao\*<sup>3</sup>, K.Tanaka, K.Narihara, and LHD-experimental Group

*National Institute for Fusion Science, Toki 509-5292, Japan*

*\*1Department of Nuclear Engineering, Kyoto University, Kyoto, Japan*

*\*2Institute of Advanced Energy, Kyoto University, Gokasho, Uji, 611-0011, Japan*

*\*3Dept. of Quantum Science and Energy Engineering, Tohoku University, Sendai, Japan*

Corresponding author's email address: osa@nifs.ac.jp

## Abstract

The confinement properties of tangentially injected energetic particles are experimentally investigated on the Large Helical Device(LHD). The local confinement times of energetic particles are evaluated by experiments and have good correlation with pitch-angle scattering times in the core region and with charge exchange loss times in the edge regions. Thus, the classical process is considered to be the dominant process of the energetic particle confinement on LHD. In addition to these classical effects, the enhanced energetic particle transports induced by MHD-instabilities are observed on LHD. These effects become significant at low magnetic field( $B_t \sim 0.75$ ) configurations.

## I. Introduction

Confinement of energetic particles is one of the most important issues in helical devices since a large helical ripple has a significant influence on the topology of energetic particle orbits. Following three topics are considered to be important in the energetic particle confinement studies in helical devices: (1) The confinement property of energetic particle during its slowing-down process, (2) the wave-particle interactions between energetic particles and waves, e.g., ICRF-wave or MHD-instabilities, and (3) the effect of radial electric field on the confinement property of energetic particles. In realizing a helical fusion reactor, we need to investigate these influences on  $\alpha$ -heating. In this paper, we will focus on the first and the second topics of the energetic particles on LHD.

On LHD, a series of experiments with a short pulse(blip) of tangential neutral beam(NB) injection was performed to investigate the confinement property of tangentially injected energetic particles. The NB-blip method is a well-known experimental technique in investigating the confinement property of energetic particles for neutron diagnostics and charge-exchange(CX) neutral diagnostics, and are widely applied to many devices[1-9]. We have developed new experimental method based on Maximum Entropy and Maximum Likelihood Method(MEMLM) to analyze the CX neutral diagnostics during NB-blip

experiments. The method was applied to LHD to evaluate the confinement time of passing particles on its birth orbits.

During the high-beta experiments of LHD, fast changes of energetic neutral particle fluxes were observed with the MHD bursts on the signals of a tangential CX neutral diagnostic. The signals of neutral particles at high energy (typically  $\sim 130$ -keV) were simultaneously increased with the MHD-bursts. The signal increase of lower energy particles occurred with a certain delay time for the increase of the high energy particles. It seems that the increased neutral flux has a characteristic time of energy decay. This phenomenon was typically observed when the magnetic field strength is lower than 0.75[T].

In this paper, we will describe and discuss the classical and non-classical aspects of energetic particle confinements on LHD. In Sec. 2, we will show the experimental apparatus. The confinement property of the energetic particles being evaluated by the NB-blip experiments are described in Sec. 3. The interaction of MHD-instabilities with energetic particles are shown and discussed in Sec.4. Sec.5 is a summary.

## 2. Experimental Set-up

On LHD, NBs are tangentially injected by using three beam-lines (one for co.-NB and two for counter-NB) which are based on the negative-ion sources[10]. Each beam line has two ion sources and the tangency radii of these ion-sources are 3.63[m] and 3.77[m], respectively. To investigate the confinement property of passing energetic particles, the E//B-type CX neutral particle analyzer(NPA)[11] is installed on the tangential port, which is located at 10 cm below the mid-plane. The NPA is placed to measure the counter-NB particles for the LHD standard magnetic field direction. The NPA is horizontally movable and its scanning angle is from 0-deg. to 9-deg., where these angles are defined by the angle between the normal of the port and the NPA line of sight. The NPA has 39 energy-channels and 3 mass-column (117channels in total). The measurable energy range of the NPA is  $0.5 \leq E/A \leq 200$  [keV amu], where E and A denote the energy and the mass number of the measured particle, respectively. The electron density and temperature distributions are obtained by the FIR interferometer and YAG Thomson scattering measurement, respectively. Figure 1 shows a plot of the pitch-angles to the normalized minor radii ( $\rho = r/a$ ) along the center lines of ion sources of a counter-NB and the

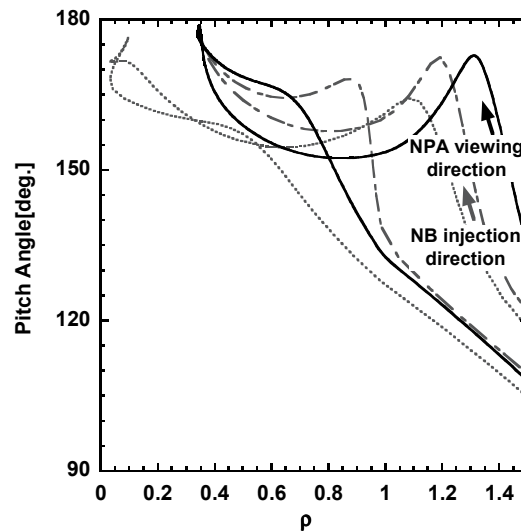


FIG.1. Pitch-angles and normalized minor-radii distributions along the center line of the outer ion-source of a counter-NB. (gray center-dashed curve) and of the inner ion-source (gray dashed curve). Those along the E//B-NPA line of sight are shown by a black solid-curve for the scanning angle of 0-deg.

E//B-NPA sight line at 0-deg.position. Considering the width of the beam, this graph shows that the E//B-NPA observes the injected energetic particles directly.

### 3. Evaluation of energetic particle confinement by NB-blip experiments

Figure 2 shows typical waveforms of NB-blip experiments. The blipped particles were injected at 150keV with 20ms pulse duration and 250ms cycle. As shown in this figure, the influence of the NB-blip injection on the plasma parameters are negligible. The flux decay of blipped particles during their slowing-down process from 150keV down to 55keV was evaluated by using a tangential Charge eXchange Neutral Particle Analyzer (CXNPA). Analysis is done using the data in the period between  $t=1.0$  and  $2.3s$ , as indicated by the gray area in Fig.2. The NPA data are accumulated according to the blip-cycle to obtain the better statistics.

Using the waveforms of the NPA for blipped-particles at the injection energy( $\psi_0(t)$ ) as a response function ( $R_\theta(t) \equiv \psi_0(t)/\alpha$ ), the contribution of energetic particles on the location of  $\rho$  to the waveform of the NPA for blipped particles at the energy ( $E_i$ ) can be expressed by  $w_i(\rho)R_\theta(t-\tau_i)$  if we neglect the effect of energy diffusion in the slowing-down process. Here, the  $\alpha$  is the normalized parameter so that it makes the integration of  $R_\theta(t)$  over time unity and the  $\tau_i$  is the slowing-down time from the injection energy to the energy of  $E_i$ . Therefore, the waveform of the NPA at  $E_i$  for the blipped particles can be written as;

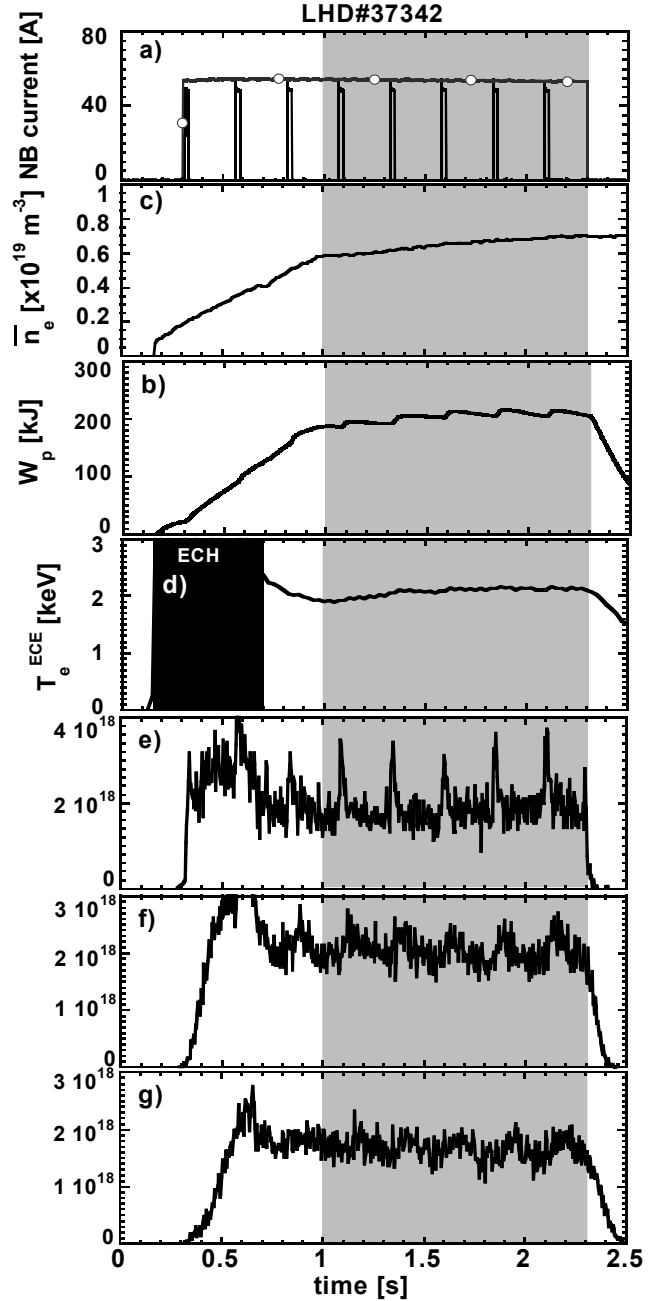


FIG. 2. Typical waveforms at an NB-blip experiment. (a) Beam current of counter-NB for plasma sustention (solid-lines) and for blip injections (solid-lines with open circles), (b) plasma stored energy, (c) line averaged electron density, (d) central electron temperature are shown. The neutral flux of (e) 148keV, (f) 110keV, and (g) 83keV, which are measured by E//B-NPA are also shown.

$$\begin{aligned}
\psi_i(t) &= \int_{l_{close}}^{l_{distant}} w_i(\rho(l)) R_0(t - \tau_i(\rho(l))) dl \\
&= \int_{\tau_{min}}^{\tau_{max}} (w_i^1(\tau_i)(dl_1/d\rho) - w_i^2(\tau_i)(dl_2/d\rho))(d\rho/d\tau_i) R_0(t - \tau_i) d\tau \\
&= \int_{\tau_{min}}^{\tau_{max}} w_i'(\tau_i) R_0(t - \tau_i) d\tau_i
\end{aligned} \tag{1}$$

where  $l$  is a path length along the NPA sight line. The  $l_{close}$  and  $l_{distant}$  correspond to the lengths of the close plasma edge to the NPA-port and of the distant edge, respectively. The  $\tau_{min}$  is the minimum of  $\tau_i$  on the path and is usually the value of  $\tau_i$  at the edges, while the  $\tau_{max}$  is the maximum and is usually the value at the closest point to the plasma center on the path. The subscript of  $l$  and superscript of  $w$  denote the region of the path. The  $l_1$  and  $w^1$  are for the region within the point of  $\tau_i = \tau_{max}$ , while the  $l_2$  and  $w^2$  are for the region beyond the point.

We have to note all of the information, such as the density profile of the bulk neutrals( $n_0(\rho)$ ), the density profile of the energetic particles( $n_{bi}(\rho)$ ) at  $E_i$ , the charge exchange reaction rate( $\sigma_{cx}v$ ), and reionization loss effect of escaping neutrals( $\exp(-(\sigma_{cx} + \sigma_{ion}) \int_{l_{close}}^l n_i dl')$ ) contribute to  $w_i'(\rho)$ . In those quantities, only the density of energetic particles( $n_{bi}(\rho)$ ) is unknown variables when the bulk plasma is in quasi-steady state condition. The rest are constant in time or can be evaluated. Therefore, the confinement ratio of energetic particles ( $n_{bi}(\rho)/n_{b0}(\rho)$ ) can be obtained from the ratio  $w_i'(\rho)/w_o'(\rho)$  with the correction of CX-reaction rate and reionization loss of escaping neutrals. We do not need to know the bulk neutral density and the birth energetic ion density profiles since they appear both in the denominator and in the numerator of the ratio and are canceled out. Only assumptions we have made are that the energy loss of the particle is given by the classical deceleration rate and that the particles are staying on the same orbit

To evaluate the  $w_i'(\rho)$ , we need to deconvolute the integral of Eq(1). For the deconvolution, we had developed an technique based on the Maximum Entropy and Maximum Likelihood Method (MEMLM) [12]. Confinement times of energetic particles were evaluated from the decay time of  $w_i'(\rho)$ . In Fig.3, the confinement times of energetic particles( $\tau_{exp.}$ ), which were evaluated from NB-blip experiments, are compared to the pitch-angle scattering time( $\tau_{90-deg.}$ ) and charge exchange loss time( $\tau_{cx.}$ ) for LHD-plasmas of  $Rax=3.6[m]$  and  $Bt=2.5[T]$ . These times are calculated from plasma parameters of the discharges and are averaged along the orbit of the measured energetic particles. In Fig.3, the confinement times of energetic particles have good correlation with the pitch-angle scattering times at the core region, i.e.  $r/a \leq 0.83$ , and with the charge exchange loss time at the edge ( $r/a=0.95$ ). This result indicates the confinement times of tangential energetic particles are explained by the classical theory with orbit effect at high magnetic field configurations.

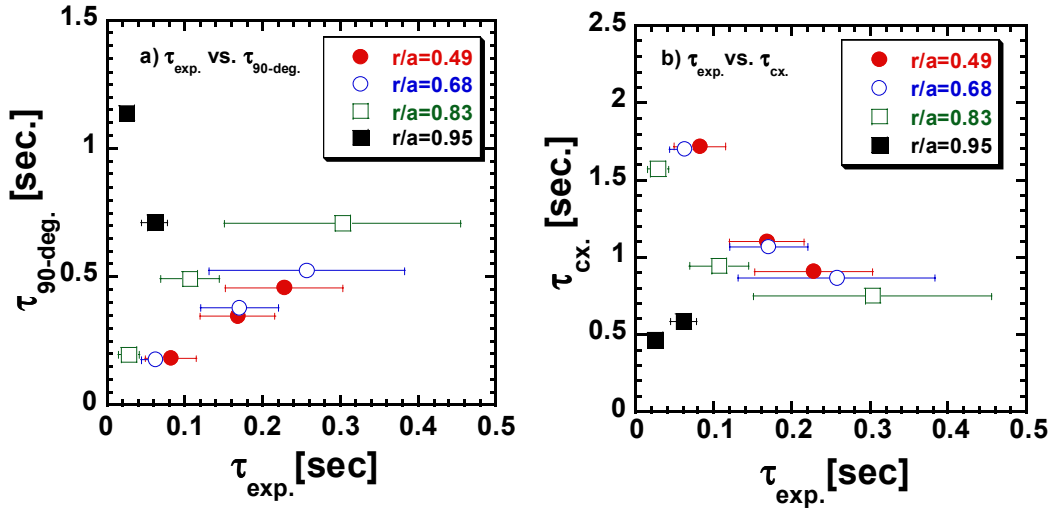


FIG. 3. Correlations of particle confinement time ( $\tau_{\text{exp}}$ ) to (a) the 90-degree pitch-angle scattering time ( $\tau_{90\text{-deg.}}$ ) and to (b) the charge exchange loss time ( $\tau_{\text{cx}}$ ) for LHD plasmas of  $R_{\text{ax}}=3.6[\text{m}]$  and  $B_t=2.5[\text{T}]$  configuration. In evaluating the pitch angle scattering time and charge exchange loss time, the particle energy of 100keV is assumed. The neutral density profile is obtained from AURORA code.

#### 4. Interaction of MHD-instabilities on energetic particle confinement

In addition to these classical effects on the energetic particle transport, we have observed the other effect when the magnetic field strength is low ( $B_t \sim 0.75$ ). With this magnetic field strength, the tangential NPA signals are often modulated by MHD-bursts, while the NB is continuously injected [13]. Figure 4 shows the typical waveforms of a Mirnov-coil signal and NPA signals. As shown in this figure, the high energy components ( $>113\text{keV}$ ) of NPA signals were increased during MHD-bursts. The flux increase at lower energy component had some time delay and this delay became larger as the energy became lower. The mode analysis of the MHD-burst at  $t=0.943\text{s}$  indicates that the burst was TAE of  $n=2$  [14].

In Fig.4(d), the peak position of signal increase at each NPA energy channel is shown. The decay time of the flux peak was obtained by exponential fitting of the peak positions and was about 4.3ms. In

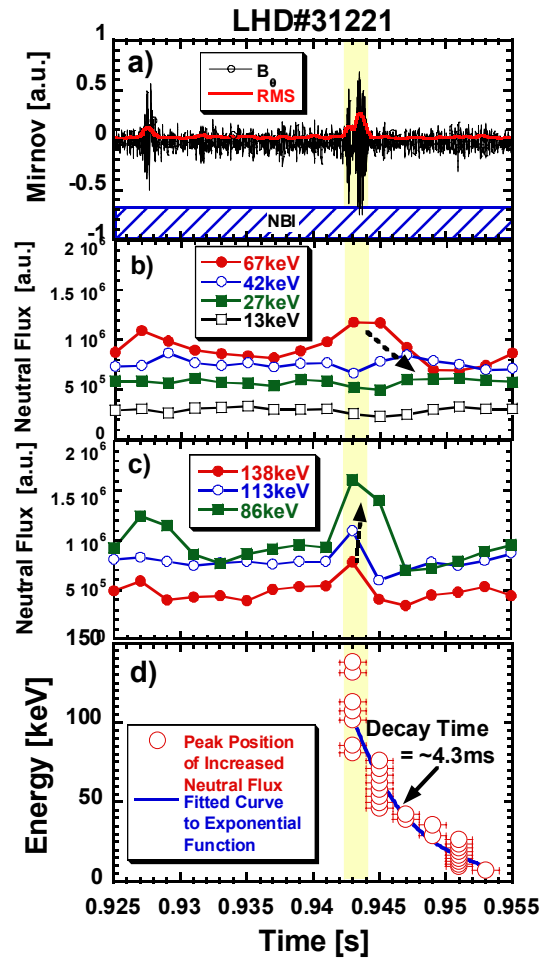


FIG. 4. Typical waveforms of (a) mirnov-coil and (b, c) NPA signals when the NPA signals fluctuate with a MHD-burst. (d) The peak position of NPA signals are shown with circles.

Fig.5, the energy decay times of the NPA flux peak associated with the MHD-bursts are compared to the inverse of the line averaged electron densities. This figure indicates that the delayed signal increase in the lower energy region can be explained by the result of energy slowing-down of the increased particles at the high energy region with the MHD-burst. But, the signal increase in the high energy region cannot be explained by the classical process.

Comparing the decay time in Fig.4(d) to the slowing-down times of particles which were circulating on the NPA sight line, it turned out that the increased particles were on the orbit which is circulating around  $r/a=0.57$ (Fig.6(a)). This orbit had a maximum probability to stay at  $r/a\sim 0.75$ , where the TAE gap of  $n$ (toroidal mode number)=2 and  $m$ (poloidal mode number)=3~4 locates (Fig.6(b) and (c))[15]. This suggests that the signal increase with the MHD burst at the high energy region is due to the result of enhanced transport of energetic particles by the TAE-mode.

## 5. Summary

Confinement properties of passing energetic particles are investigated on LHD using NB-blip method. The confinement time of the particle on the passing orbit is consistent with classical theory when the magnetic field strength is high. The energetic particle confinement was influenced by the TAE-mode. The influenced particle has a maximum probability on the gap of the mode.

## References

- [1] R.J.Goldston, et al.,Nucl.Fusion **15**(1975)651
- [2] W.W.Heidbrink, et al.,Nucl.Fusion **28**(1988)1897
- [3] W.W.Heidbrink, et al., Phys. Fluids **B2**(1990)4
- [4] W.W.Heidbrink, et al., Phys. Fluids **B3**(1991)3167
- [5] K.Tobita, et al.,Nucl.Fusion **34**(1994)1097
- [6] E.Ruskov, et al.,Nucl.Fusion **35**(1995)1099

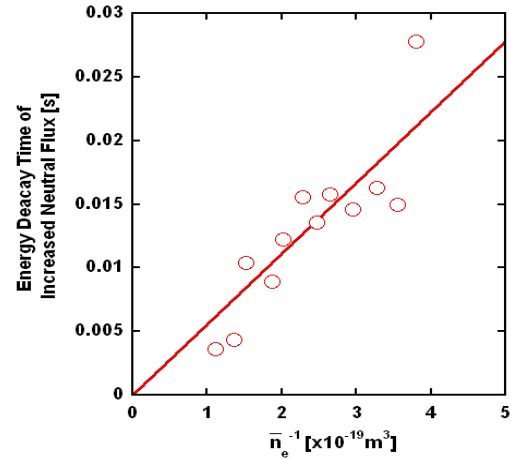


FIG. 5. inverse line averaged electron densities versus measured energy decay time of flux peak associated with MHD-bursts.

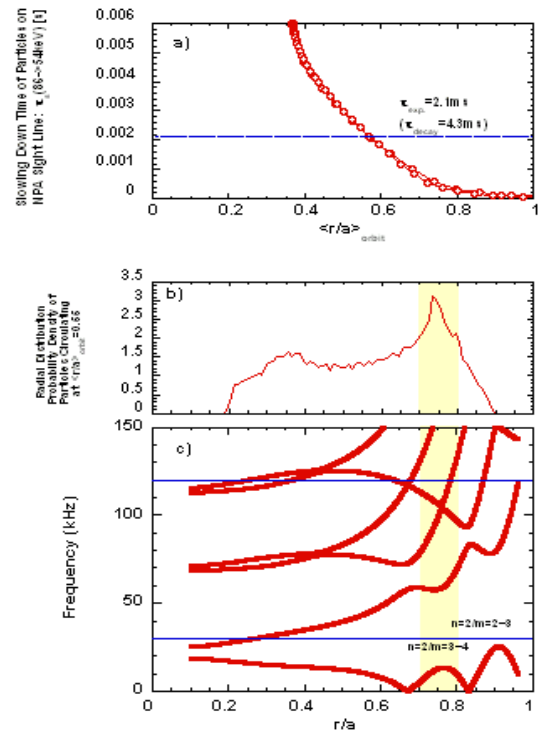


FIG. 6. (a) Orbit averaged energy slowing-down time of a particle circulating on the NPA sight line (red-lines with open circles). The energy deceleration time from 86keV to 54keV is used as an energy slowing-down time. The blue line indicates the corresponding deceleration time to the energy decay time of 4.3ms. (b) the probability of a particle staying at a certain minor radius for the orbit of  $\langle r/a \rangle_{\text{orbit}} = 0.57$ . (c) The shear-Alfvén spectrum for the toroidal mode number  $n=2$ . The blue line indicates the frequency range of the MHD burst shown in Fig.4(a).

- [7] M.Isobe, et al.,Nucl.Fusion **37**(1997)437
- [8] M.Isobe, et al.,Nucl.Fusion **41**(2001)127
- [9]W.W.Heidbrink, et al.,Plasma Phys. **9**(2002)28
- [10] O.Kaneko, et al., Nucl.Fusion **43** (2003) 692.
- [11] S.S.Medley, et al., Rev. Sci. Instrum.**69** (1998) 2651
- [12] M.Osakabe, et al., to be published in RSI.
- [13] M.Osakabe, et al., Proc. 30th EPS Conf. (2002) P1-083
- [14] K.Toi, et al., PPCF **46**, S1(2004)
- [15] S.Yamamoto, et al., this conference paper EX/5-4Rb

## Magnetic Field Structure and Confinement of Energetic Particles in the LHD

T. Watanabe 1), Y. Matsumoto 2), M. Hishiki 2), S. Oikawa 2), H. Hojo 3), M. Shoji 1), S. Masuzaki 1), R. Kumazawa 1), K. Saito 1), T. Seki 1), T. Mutoh 1), A. Komori 1) and LHD Experimental Group 1)

1) National Institute for Fusion Science, Oroshi, Toki, Gifu 509-5292, Japan

2) Graduate School of Engineering, Hokkaido University, Sapporo 060-8628, Japan

3) Plasma Research Center, University of Tsukuba, Tsukuba 305-8577, Japan

e-mail contact of main author: watanabe.tsuguhiro@toki-fs.jp

**Abstract.** The LHD achieves high-performance plasma confinement by the coordination of magnetic surface region and chaotic field line layer. It is theoretically and experimentally shown that drift surfaces exist for highly energetic particles being extended over the last closed flux surface (LCFS) in the LHD. Those particles are considered as lost particles due to the loss-cone in the previous theories, where the analyses are limited inside the LCFS. The present theory predicts that the LHD has no loss-cone and that highly energetic particles confined over the LCFS exist. These are consistent with the LHD experimental results in both the ion cyclotron range of frequency (ICRF) heating experiments and the low magnetic field neutral beam injection (NBI) heating experiments. From particle orbit analyses and studies on the connection length of diverter field lines, it is also shown that plasma can exist in the chaotic field line layer located outside the LCFS in the LHD. The plasma in the chaotic field line layer is clearly detected by CCD-cameras in the LHD experiment. This ambient plasma might be expected to have the role of a kind of an impregnable barrier for the core plasma, which suppresses both the MHD instabilities and the cooling of the core plasma due to charge exchange processes. The line-tying effects of diverter field lines that are slipped out from the chaotic field line layer can also stabilize the ballooning mode and the vertical displacement events of plasma column.

### 1. Introduction

Helical system is a fully 3-D system. The freedom of fully 3-D system not only realize disruption-free plasma confinement system but also bring various optimization scheme for plasma confinement. Main issues for optimization are MHD stable high-beta equilibrium and good particle confinement characteristics [1, 2]. The current research of optimization of helical system postulate that high temperature plasma is confined only in the magnetic surface region. On the other hand, the present paper claim that the LHD (the Large Helical Device) achieves high-performance plasma confinement by the coordination of magnetic surface region and chaotic field line layer.

The LHD uses superconducting magnets with  $\ell/m = 2/10$  and  $R_0/a \simeq 3.9\text{ m}/0.6\text{ m}$  heliotron-type magnetic field configuration with continuous winding helical coils and without the toroidal coil, where  $\ell$  and  $m$  are the poloidal and toroidal mode numbers of helical coils respectively.  $R_0$  and  $a$  are the major radius of the device and the average minor radius of plasma, respectively. The characteristics of the LHD magnetic field are the high magnetic shear configuration in the peripheral region and the existence of the chaotic field line layer which surrounds the LCFS. Lines of force outside the LCFS show a fractal structure and create a chaotic field line layer[3].

The drastically improved plasma has been obtained through the LHD experiments started in 1998. In the recent experiments, the maximum averaged beta value  $\langle \beta_{dia} \rangle$  of 4% was obtained [4] by high power NBI heating up to 12MW in the configuration with  $R_{ax} = 3.6\text{ m}$  and  $B_{ax} = 0.45\text{ T}$ , where  $R_{ax}$  and  $B_{ax}$  are magnetic axis position and toroidal magnetic field at  $R_{ax}$  respectively. Up to now, the beta collapse phenomenon has not been reported in the LHD experiment.

In the past, many ICRF experiments suffered from a rise in impurities. Furthermore, the ICRF heating in helical systems has been considered to be questionable because of the poor confinement property of the perpendicularly accelerated high-energy particles. The helically trapped particles have large orbit size in the radial direction. Then, it was thought that the helically trapped particles tend to diffuse and would escape out by orbit loss. However, high performance for the plasma heating in the ICRF experiments of the LHD has been shown as follows [5, 6, 7]: 1) High heating efficiency is found, which increases with the increase of the plasma temperature. 2) High-energy particles with energies up to 500 keV are produced by ICRF heating. [7]. 3) Plasma with a high stored energy can be sustained for more than 12 minutes by ICRF heating only[8]. In the 8th campaign of LHD experiment (2004,

Nov.), the LHD sustained plasma (average density  $\simeq 0.7 \times 10^{19} \text{ m}^{-3}$ , central ion temperature  $\simeq 2 \text{ keV}$ ) for more than 12 minutes with ICRF of  $P_{ICRF} \simeq 0.6 \text{ MW}$ . The total injection power to plasma is almost 430 MJ, in this discharge. Energy spectrum of protons reaches to 600 keV.

It will be difficult to explain these experimental results comprehensively by plasma confinement only in magnetic surface region.

The large pressure gradient can be formed beyond the stability criterion for the Mercier mode [9]. The maximum value of volume average plasma beta of the LHD increases favorably year by year [10]. Theoretically, it is shown that the LHD has potentiality of high beta plasma confinement and the chaotic field line layer play a key role for this efficient plasma confinement in the LHD [11].

It was shown LHD type magnetic configuration has large particle-orbit loss region [12]. The boundary of loss region was determined by the condition that helically trapped particle orbits intersect the LCFS, because analysis was restricted inside of the LCFS.

If a large loss-cone exists in the LHD, high performance plasma production and its sustainment by ICRF would be impossible in the LHD. Because, ICRF heating in the LHD produce helically trapped particles, mainly. The present paper, however, claim that the LHD has no loss-cone owing to the coordination of magnetic surface region and chaotic field line layer. An example of a 'loss-cone particle' in the previous theories is shown in FIG.1. Magnetic field configuration is 'standard' one ( $R_{ax} = 3.75 \text{ m}$ ). Poincaré plots of a 150 keV proton are shown by magenta color dots. Initial pitch angle (angle between velocity and magnetic field) is chosen as  $\chi_0 = 3\pi/8$ . This figure shows that the particle orbit is constrained by three constants of motion (Energy  $E$ , magnetic moment  $\mu$  and longitudinal invariant  $J_{\parallel}$ ) and the Poincaré plots form clear banana shapes. Then this particle is a completely confined particle in collision-less case. On the other hand, if we restrict analyses only inside the LCFS, this particle become a loss-cone particle because the banana shape Poincaré plots intersect the LCFS as shown in this figure (cyan color plots show the Poincaré plot of lines of force).

Furthermore, FIG.1 shows that particle motion of a helically trapped particle is almost independent of magnetic surface. This nature does not change even in the 'inward shifted' magnetic axis case ( $R_{ax} = 3.6 \text{ m}$ ) as shown in Fig.2. Highly energetic particles orbit cannot be changed though a little change of vertical magnetic field can change the magnetic surface.

Another important issue of the helical system is a particle confinement of the transition orbit. If the initial pitch angle,  $\chi_0$ , is located between the one for the passing particle and the one for the reflecting particle, particle iterates the passing particle motion and reflecting particle motion. In this case, the longitudinal invariance breaks ( $J_{\parallel} \neq \text{const.}$ ) and life time of transition particle become finite. The life time of transition particle is partially controllable by magnetic field intensity, particle energy and machine size. In the usual operating range of the LHD ( $B_{ax} \simeq 2.75 \text{ T}$ ,  $E \lesssim 180 \text{ keV}$ ), the life-time of transitional particle is sufficiently long compared to the transit time ( $= a/\sqrt{E/M}$ ,  $M$ : mass of charge). Then the LHD has no loss-cone. Transition particle crisscross in a magnetic surface region. Numerical example of a particle motion of the transition orbit is shown in FIG.3.

After the 3rd campaign of LHD experiment (2000, Mar), melt-down of leading edge of stainless tube for the

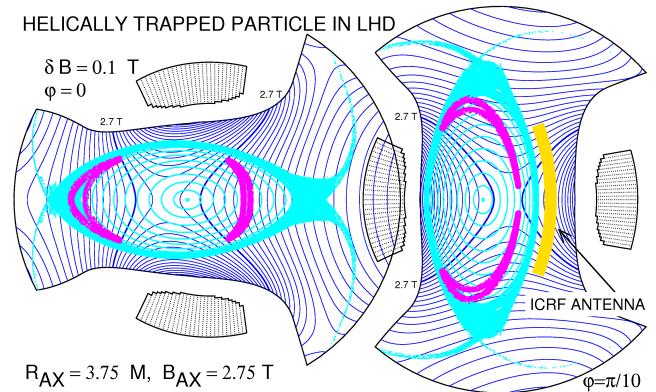


FIG.1. An Example of a 'loss-cone' particle in the previous theories, where the analyses are limited inside the LCFS. Magnetic field is the 'standard' configuration ( $R_{ax} = 3.75 \text{ m}$ ). Initial conditions of particle motion is given by  $R_0 = 4.2 \text{ m}$ ,  $z_0 = 0$ ,  $\varphi_0 = 0$ ,  $E = 150 \text{ keV}$ ,  $\chi_0 = 3\pi/8$ . Magenta (cyan) color dots show the Poincaré plots of a proton orbit (lines of force). Cross sections of vacuum vessel, helical coils and ICRF antenna are also shown. Contour plot of the magnetic field strength  $B$  is also shown by blue lines (increment of the contour  $\delta B = 0.1 \text{ T}$ ).  $\varphi$  represents the toroidal angle of the cross section.

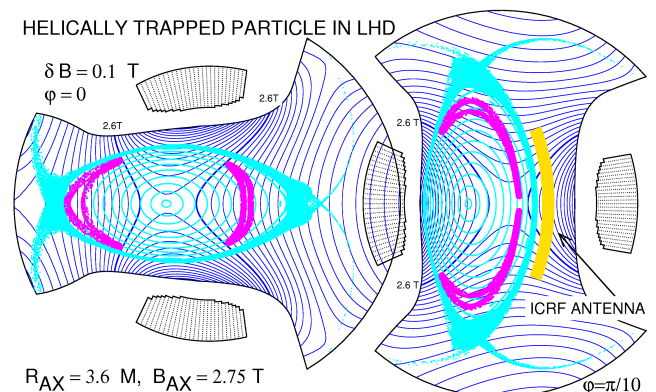


FIG.2. Effect of 'inward shift' of magnetic axis in the LHD. Magnetic axis is shifted inside ( $R_{ax} = 3.6 \text{ m}$ ) and other parameters are same to the case of FIG.1.

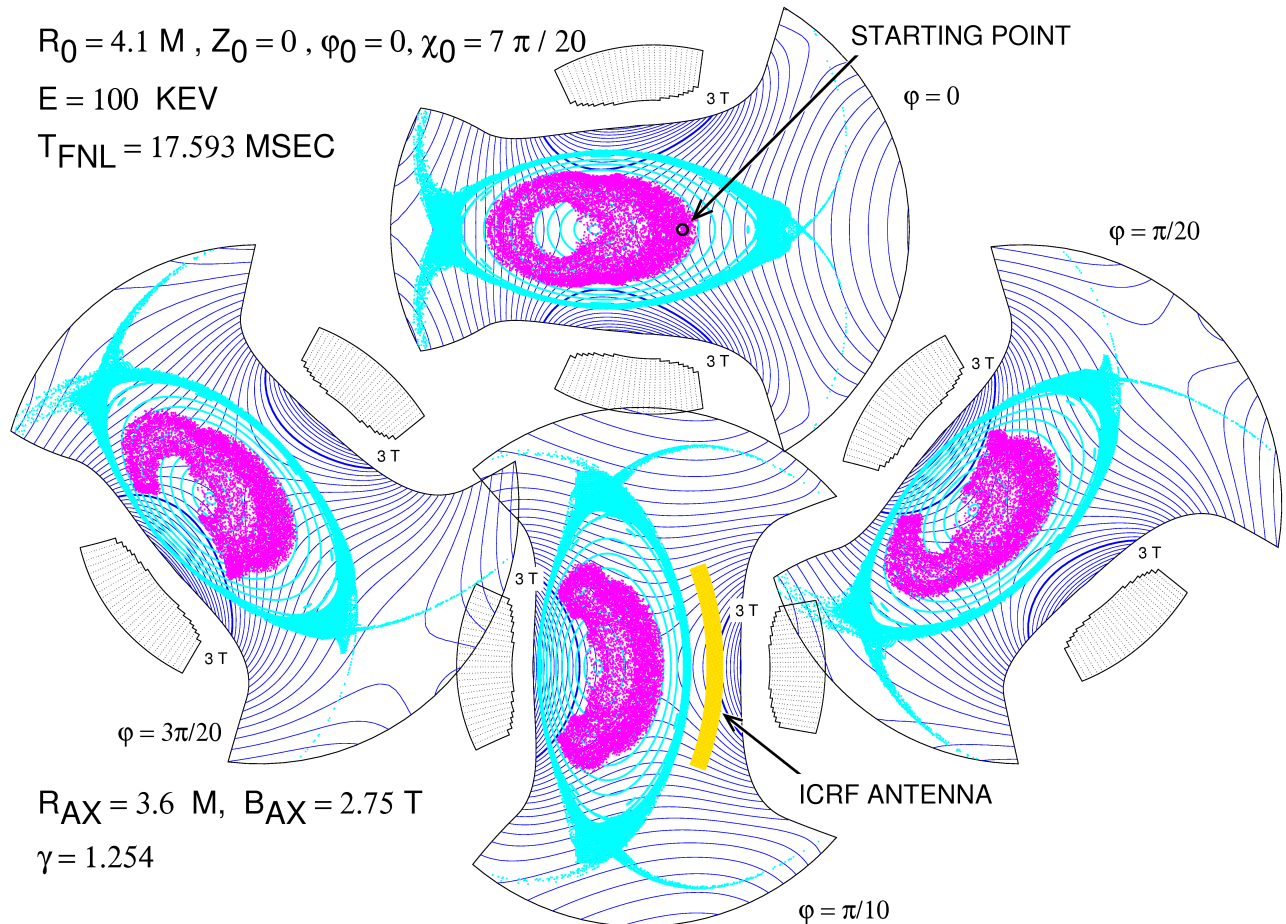


FIG.3. Poincaré plots of a transition orbit particle. Parameters of magnetic field configuration and initial conditions of particle motion are shown in the figure. The particle orbits is still stays inside of magnetic surface (computation is terminated at  $t = 2222 \times 2\pi R_0 / \sqrt{E/M} \simeq 17.593 \text{ msec}$ ).

pellet injection was found. After the 5th campaign of LHD experiment (2002, Mar), the erosion of the edge of the NBI armor tile was found. Those equipments were installed enough outside the LCFS. These phenomena suggest the existence of the high-energy particle drift surface extending outside the LCFS in low  $B_{ax}$  case.

The magnetic field structure and the particle orbit must be elucidated to obtain higher performance of the plasma confinement and to evade troubles with high-energy NBI particles in low  $B_{ax}$  case. We have developed highly accurate magnetic field computation codes [13, 14] and the multi-dimensional highly accurate spline interpolation scheme [15]. In addition, we have developed an original rotating helical coordinate system, where the metric tensor is not used, in conformity to the shape of LHD plasma[16]. The 3D-grid structure can be arranged in the vacuum vessel with relatively small main memory of computer. We have derived the equation of lines of force and the equation of particle motion in the rotating helical coordinate system[16]. These computing tools were integrated into a computer code, LHDMSVIEW, in which a higher order (8-stage, 6-order) Runge-Kutta scheme [17] is adopted as the integrator of differential equations. In the present study, we investigate the magnetic field structure and the particle orbits using the LHDMSVIEW.

In Sec.2 the detail of magnetic field configuration including the chaotic field line layer is reviewed and detail of particle orbit nature is summarized in Sec.3. Sec.4 is devoted to a summary and discussions.

## 2. Magnetic field configuration of the LHD

Here, we examine the details of magnetic structure which sustain the LHD plasma in high performance. Helical system has no a priori integral invariant of lines of force. The equation of lines of force is a nearly integrable Hamiltonian system. The magnetic surface of helical system coexists always with magnetic islands and chaotic field line layer. We define the chaotic field line layer as the region where the outside of the LCFS and the connection length (length of lines of force until reaching vacuum vessel wall)  $l_c$  exceed the two helical pitch ( $l_c \geq 2 \times 2\pi R_0/m$ ). Then the lines of force in the chaotic field line layer always connect from wall to wall of vacuum vessel except the magnetic islands region imbedded in the chaotic field layer. The diverter field lines are defined as the lines of force connecting to the vacuum vessel wall, in the chaotic field line layer.

$$R_{AX} = 3.6 \text{ M}, B_{AX} = 2.75 \text{ T}, \gamma = 1.254$$

CONNECTION LENGTH  $L_C$   
(TOROIDAL TURNS)

RED :  $1 < L_C \leq 2$

YELLOW:  $2 < L_C \leq 10$

GREEN:  $10 < L_C \leq 20$

CYAN :  $20 < L_C \leq 30$

BLUE :  $30 < L_C$

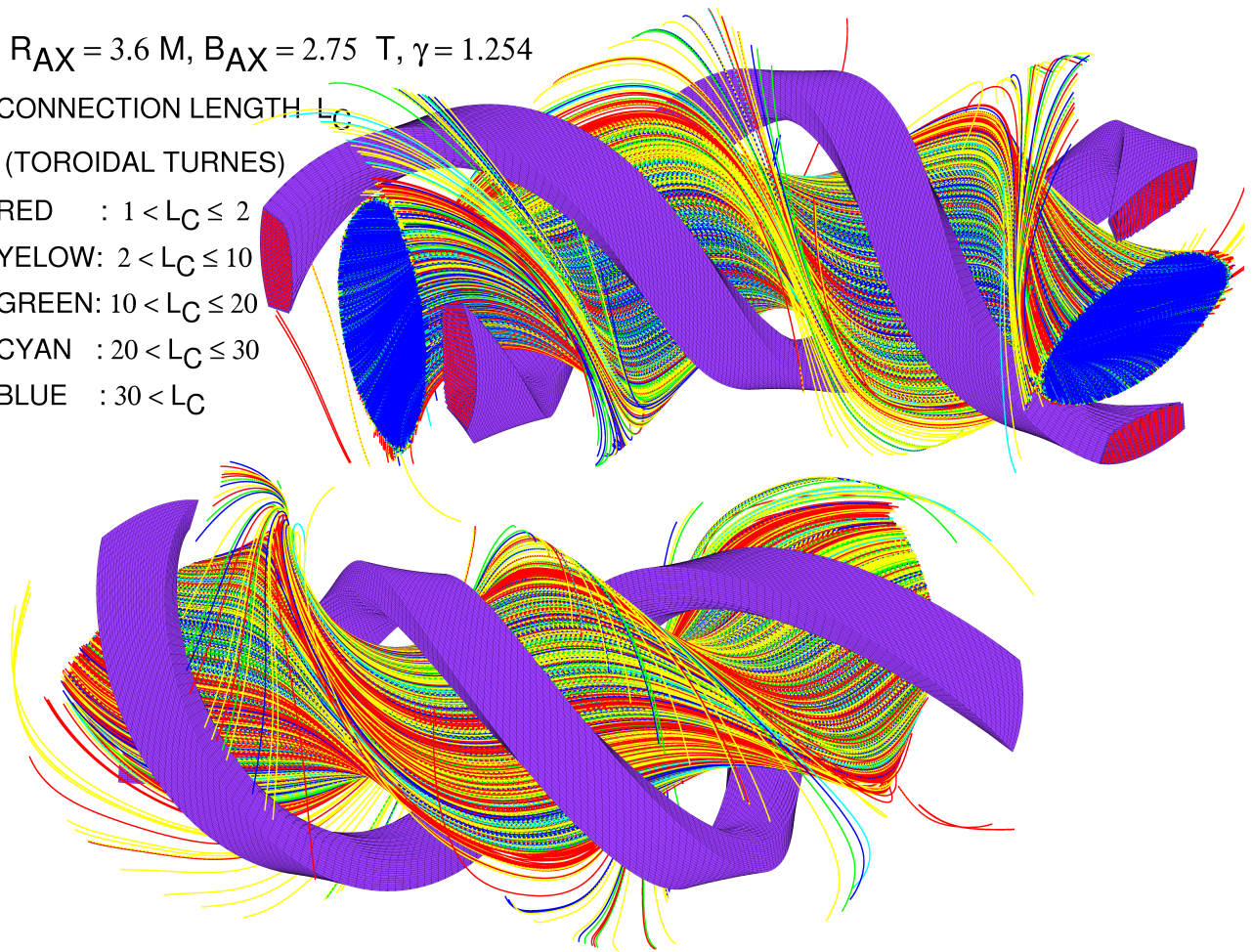


FIG.4. Lines of force in chaotic field line layer surrounding the outside of the LCFS. Helical coils are also plotted. All field lines terminate at footprints in the diverter plates (the diverter plates are not drawn). The lines of force are classified depending on the connection length with different color. It is shown that the connection length of lines of force closely surrounding the LCFS exceed 30 toroidal turns ( $\simeq 800\text{m}$  : shown by the blue lines). The lines of force that are slipped out from the chaotic field line layer reach the diverter plates soon.

The LHD magnetic field is produced with the continuous winding helical coils and without the toroidal coil. Both ends of elliptic magnetic surface is located approximately on a radius of the helical gyration of the helical coils and the toroidal magnetic field decreases very much at the ends of magnetic surface as shown in FIG.3. Then, a characteristic of the LHD magnetic field is the high magnetic shear configuration in the peripheral region of plasma column and create many small islands in the chaotic field line layer. So, lines of force outside the LCFS show a fractal structure [3] and connection length of diverter field lines pass through the neighborhood of LCFS becomes very long (in the order of 10 km) [18]. In contrast, lines of force that are slipped out from the chaotic field line layer reach the vacuum vessel wall soon in the order of 1.5 ~ 2.0 m because of no toroidal coil. The 3D view of diverter field lines are shown in FIG.4. Fractal structure of connection lengths of diverter field lines is shown in FIG.5.

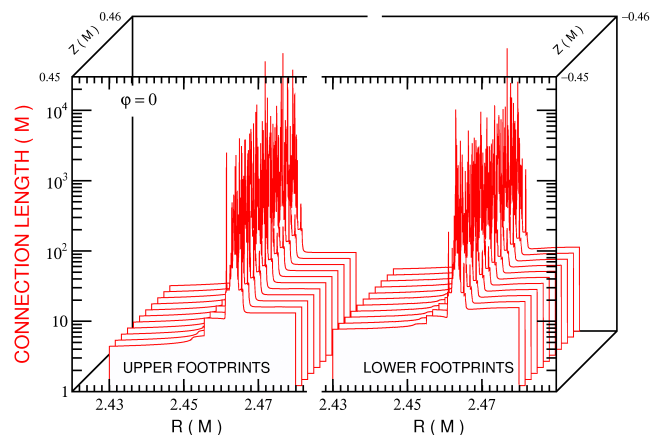


FIG.5. Distribution of connection length of diverter field lines. Starting point of computations are placed in square boxes of a poloidal section ( $\varphi = 0$ ) near footprints. Magnetic field configuration is the 'standard' one ( $R_{ax} = 3.75 \text{ m}$ ).

The chaotic field line layer can sustain low temperature ambient plasma due to the long connection length of

lines of force and mirror confinement effect of helical ripple nature of magnetic field [18]. This low temperature ambient plasma is clearly observed always by the CCD camera in the LHD experiment. The CCD camera view of the LHD plasma and the structure of chaotic field lines are compared in detail. The CCD image and the numerical 3D view of chaotic field lines are completely corresponding each other as shown in FIG.6.

The characteristics of lines of force outside the LCFS and the plasma contained in the chaotic field line layer have been bringing the following advantage for the high performance of plasma confinement in the LHD. (1) The very long connection length of the diverter field line can reduce the heat load to the diverter plate without losing high-performance of core plasma confinement. (2) The chaotic-field-line-layer plasma can protect the core plasma from the cooling down effect by neutrals outside the plasma (role of the plasma blanket). The penetration of neutral atoms to the core plasma are prevented by the chaotic-field-line-layer plasma [19]. (3) The chaotic-field-line-layer plasma stabilizes the interchange mode due to the neutralization of the charge separation that causes the instability. (4) The lines of force that are slipped out from the chaotic field line layer reach the vacuum vessel wall soon. Then, it is expected in chaotic field line layer that the plasma pressure can be sustained stably by the line-tying effect of the field lines [20].

### 3. Energetic particle orbit in the LHD

Particle confinement and formation of magnetic surface in a non-axisymmetric system is based on the adiabaticity of the longitudinal invariant  $J_{\parallel}$ . Adiabatic invariants can be obtained by averaging over the rapid oscillation of action variables in a Hamiltonian system. In a helical system, the slow variation for  $J_{\parallel}$  is caused by the rotational transform of lines of force, and the rapid oscillation is caused by passing of one helical period (for passing particles and for lines of force) or by helical trapped bounce motion (for trapped particles). If the adiabaticity of the particle motion is weaker (stronger) than the adiabaticity of the line of force, the particle confinement region becomes smaller (larger) than a magnetic surface region.

For passing particles, the  $\mathbf{B} \times \nabla B$  drift motion decides the strength of the adiabaticity. The drift motion in the region placed between helical coils (weak  $|\mathbf{B}|$  region), negate partially the slow variation of  $\mathbf{B}$  caused by the rotational transform of lines of force, if velocity component along the magnetic field  $\mathbf{B}$  is positive as shown in FIG.7. Then, passing particles with  $v_{\parallel} > 0$  have stronger adiabaticity than adiabaticity of magnetic surface and can be confined over the LCFS. Furthermore, this drift motion pushes the particle orbit to the inside region of starting magnetic surface. Then, in general, high-energy passing particles inside of the LCFS with  $v_{\parallel} > 0$  does not reach to the diverter plate,

On the contrary, the  $\mathbf{B} \times \nabla B$  drift motion of passing particle with  $v_{\parallel} < 0$  reinforce the slow variation of  $\mathbf{B}$  caused by the rotational transform of lines of force, as shown in FIG.7. Then, passing particles with  $v_{\parallel} < 0$  have weaker adiabaticity than adiabaticity of magnetic surface and loss region present in the magnetic surface region. Furthermore, this drift motion pushes the particle orbit to the outside region of starting magnetic surface. Then, in general, high-energy particle (positive ion) loss from the magnetic surface region is limited with  $v_{\parallel} < 0$  particles.

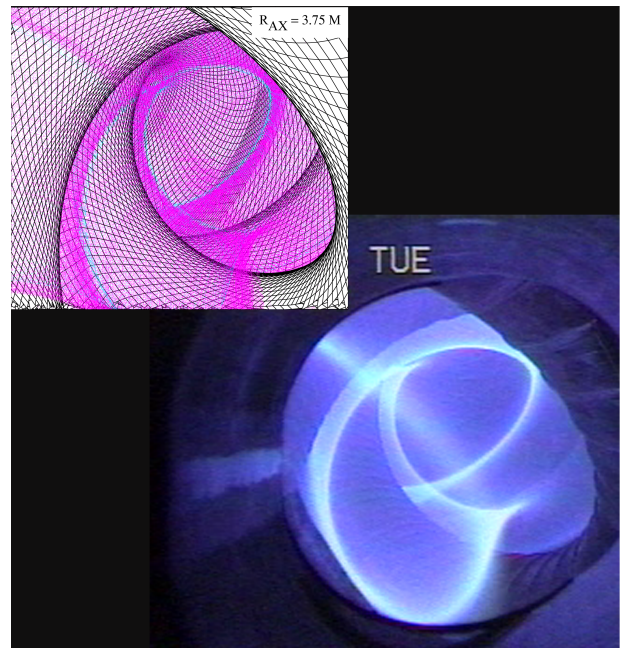


FIG.6. Numerical 3D view of chaotic field lines(left upper) and the CCD camera view of the LHD plasma(right lower).

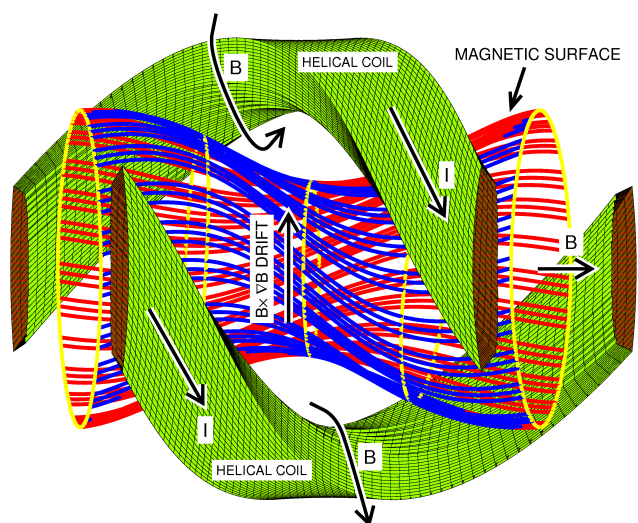


FIG.7. Lines of force (shown by blue and red lines) and the direction of  $\mathbf{B} \times \nabla B$  drift motion for a positive ion. The cross sections of the magnetic surface are also shown by yellow lines.

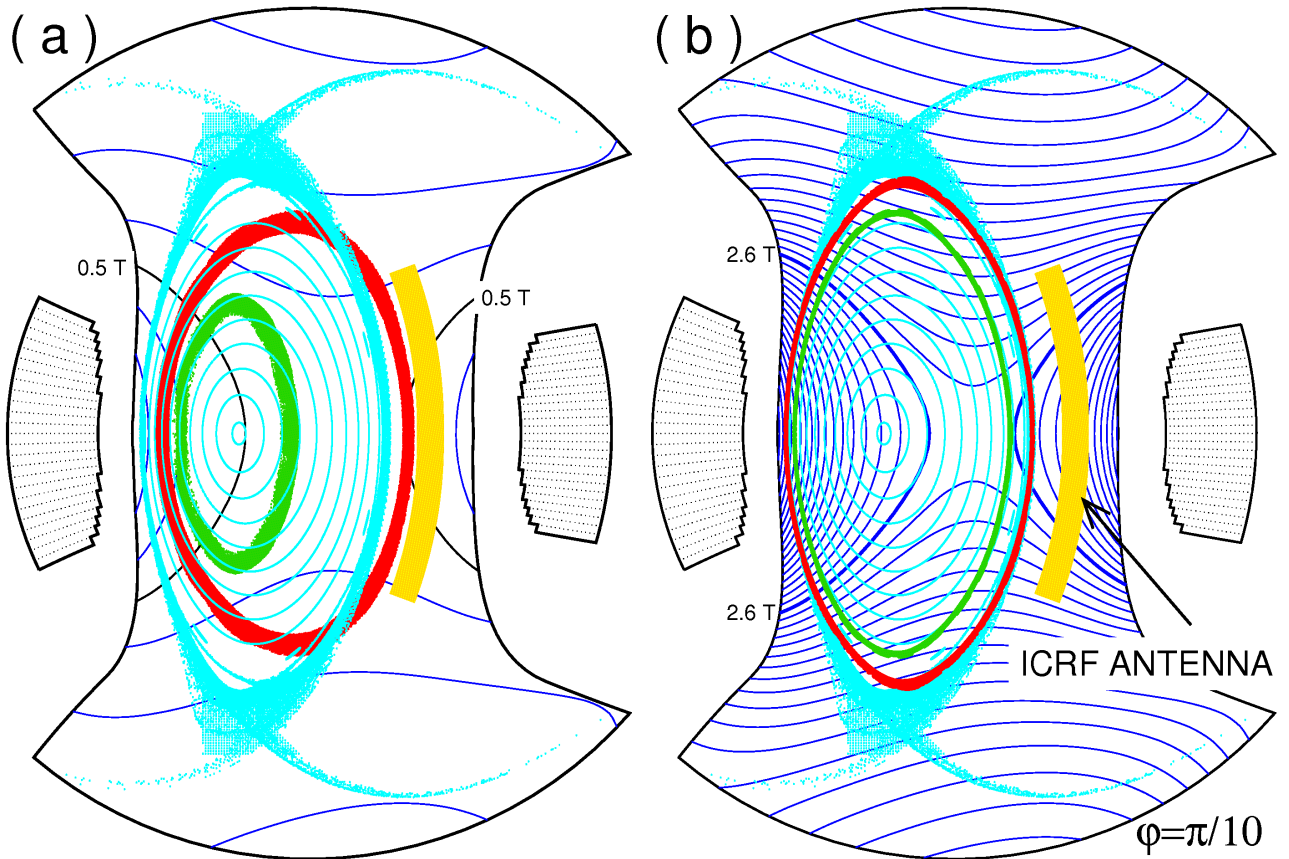


FIG.8. Relations between the magnetic surface, the outermost drift surfaces and magnetic field intensity are shown by the Poincaré plots at the poloidal cross section of  $\varphi = \pi/10$ . Red (green) color dots show the almost outermost drift surface of co-NBI (counter-NBI) particle with  $E = 180$  keV. Cyan color dots show the structure of lines of force. Position of magnetic axis is 'inward shifted' one ( $R_{ax} = 3.6$  m). (a) Low magnetic field case ( $B_{ax} = 0.5$  T). (b) Standard magnetic field case ( $B_{ax} = 2.75$  T).

In the LHD magnetic configuration, then, it is easy to confine the  $v_{\parallel} > 0$  passing particle than the  $v_{\parallel} < 0$  passing particle. Co-NBI is more effective than counter-NBI for the LHD plasma heating. In a usual LHD operating range ( $B_{ax} \simeq 2.75$  T,  $E \lesssim 180$  keV), this difference is small as shown in FIG.8(b). Confinement region of counter-NBI particles are slightly smaller than the LCFS and confinement region of co-NBI particles reach even the boundary of chaotic field line layer exceeding the LCFS. However, in low magnetic field operation case, the effect of the  $\mathbf{B} \times \nabla B$  drift motion increase. The drift surface of co-NBI can extend fairly outside the LCFS and the drift surface of counter-NBI is reduced fairly compared with the LCFS as shown in FIG.8(a).

The existence of drift surface extending outside the magnetic surface was verified by several experimental results in the LHD. After the 3rd campaign of LHD experiment (2000, Mar), melt-down of leading edge of stainless tube for the pellet injection was found. After the 5th campaign of LHD experiment (2002, Mar), the erosion of the edge of the NBI armor tile was found. The drift surface of co-NBI in low magnetic field case had intersected with these equipments as shown in FIG.9.

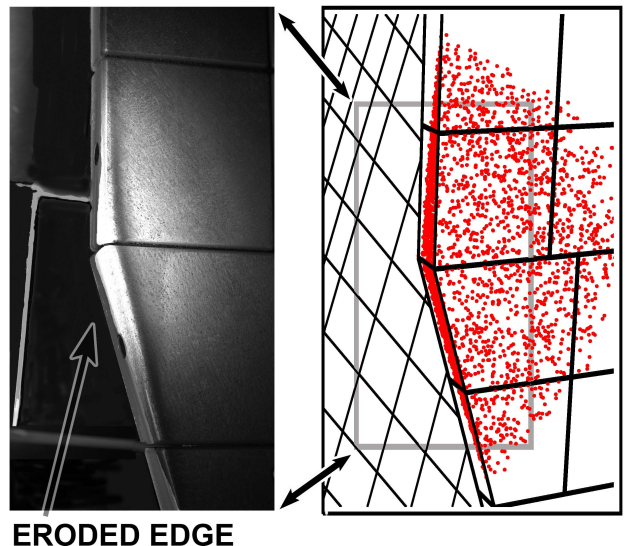


FIG.9. A close-up photograph of the eroded edge of NBI armor tile (the left hand side). The right hand side shows the interference of the corresponding armor tiles and the almost outermost drift surface of 180keV co-NBI particles in the case of  $B_{ax} = 0.5$  T (shown by red puncture plots on the armor tiles). The vacuum vessel wall of the LHD is also drawn.

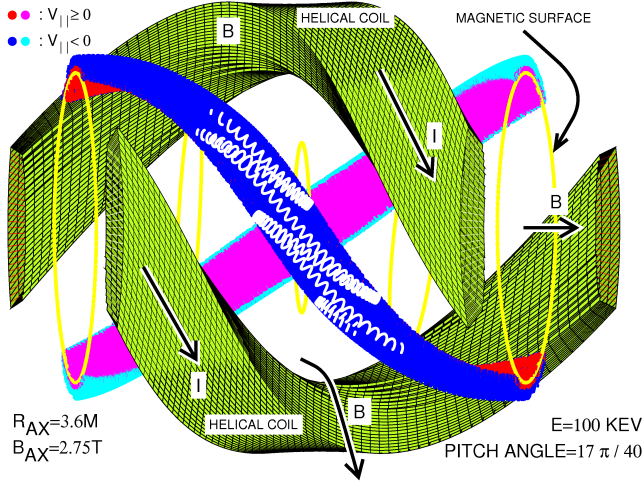


FIG.10. Stereoview of a trapped particle (proton) orbit. Magnetic field configuration is the 'inward shifted' configuration ( $R_{ax} = 3.6$  m,  $B_{ax} = 2.75$  T). Initial condition of particle orbit is given by  $R_0 = 4.5$  m (5 cm inside from the LCFS),  $z_0 = 0$ ,  $\varphi_0 = 0$ ,  $\chi_0 = 17\pi/40$ ,  $E = 100$  keV. When  $v_{\parallel} \geq 0$  ( $v_{\parallel} < 0$ ), particle positions are plotted by red (blue) dots. Particle orbits are traced until 17.593 msec ( $= 2222 \times 2\pi R_0 / \sqrt{E/M}$ ). A part of orbit is plotted by white dots. The cross sections of magnetic surface of the starting position are plotted by yellow dots. Helical coils of one helical pitch are also shown. This figure shows clearly that  $v_{\parallel} \leq 0$  particles are located always the outside of  $v_{\parallel} \geq 0$  particles.

The periodic length is another important key factor to decide the strength of the adiabaticity of particle motion. Short period is favorable for the particle confinement. Since the LHD generates the plasma confinement magnetic field with the continuous winding helical coils, helical mirror trapped particles can circulate around the magnetic axis as shown in FIG.10. The helically trapped particles are trapped in weak  $|B|$  region placed between helical coils along field lines. The basic periodic length of particle motion becomes the bounce period, which is smaller than the helical period. Then the helical trapped particles can manifest stronger adiabaticity and can be confined more effectively compared with the passing particles and the magnetic surface. This is very convenient for high performance of ICRF heating [21]. The mirror confined plasma becomes possible even in the chaotic field line layer [18].

We have confirmed numerically the high performance of ICRF heating process in the LHD. At the beginning, we have executed the numerical computations of collision-less proton orbit starting from the core plasma region to clarify the ICRF heating process in the LHD. RF field is assumed to be

$$\mathbf{E}(r, \varphi, z) = (0, 0, E_0 \sin \omega t), E_0 = 20 \text{ kV/m}, \quad (1)$$

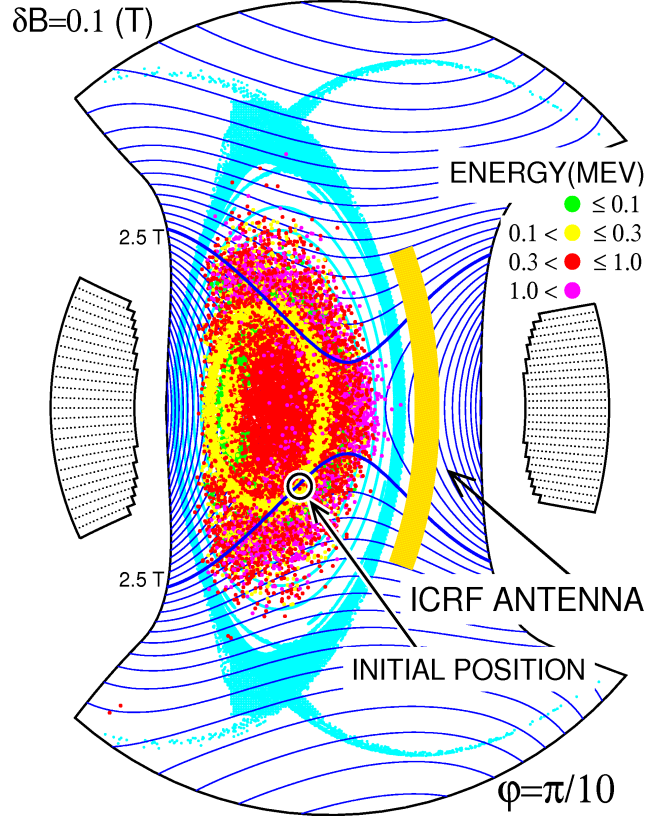


FIG.11. Poincaré plot of ICRF heated 11 protons started with energy  $E = 100$  kV. Starting position of all protons are same as shown in the figure. Initial pitch angles of 11 protons are distributed as  $\chi_0 = n\pi/10$ , ( $n = 0, \dots, 10$ ). The colors of puncture dots are classified by the energy of the protons.

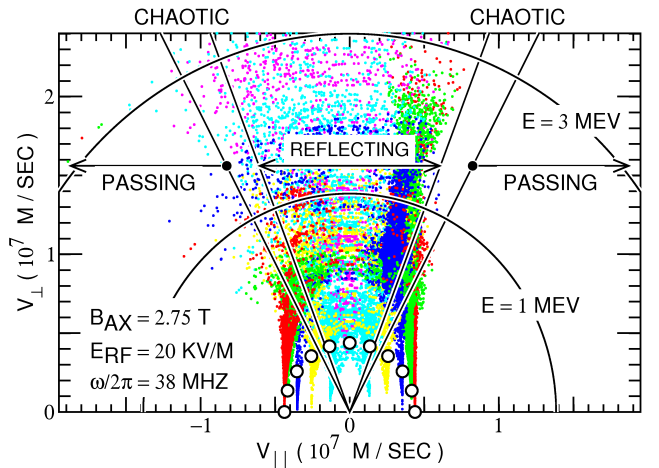


FIG.12. Poincaré plots of ICRF heated protons in  $(v_{\parallel}, v_{\perp})$  plane at  $\varphi = \pi/10$  poloidal cross section. Parameters are the same as those of FIG.11. Colors of dots are classified according to the initial pitch angles. The chaotic orbit regions have no degradation effect for heating process. Particles are lost to the vacuum vessel wall along the diverter field lines with  $v_{\parallel} < 0$  when  $E \gtrsim 1$  MeV. The phase space is classified to passing, chaotic and reflecting region from the field intensity distribution along the line of force.

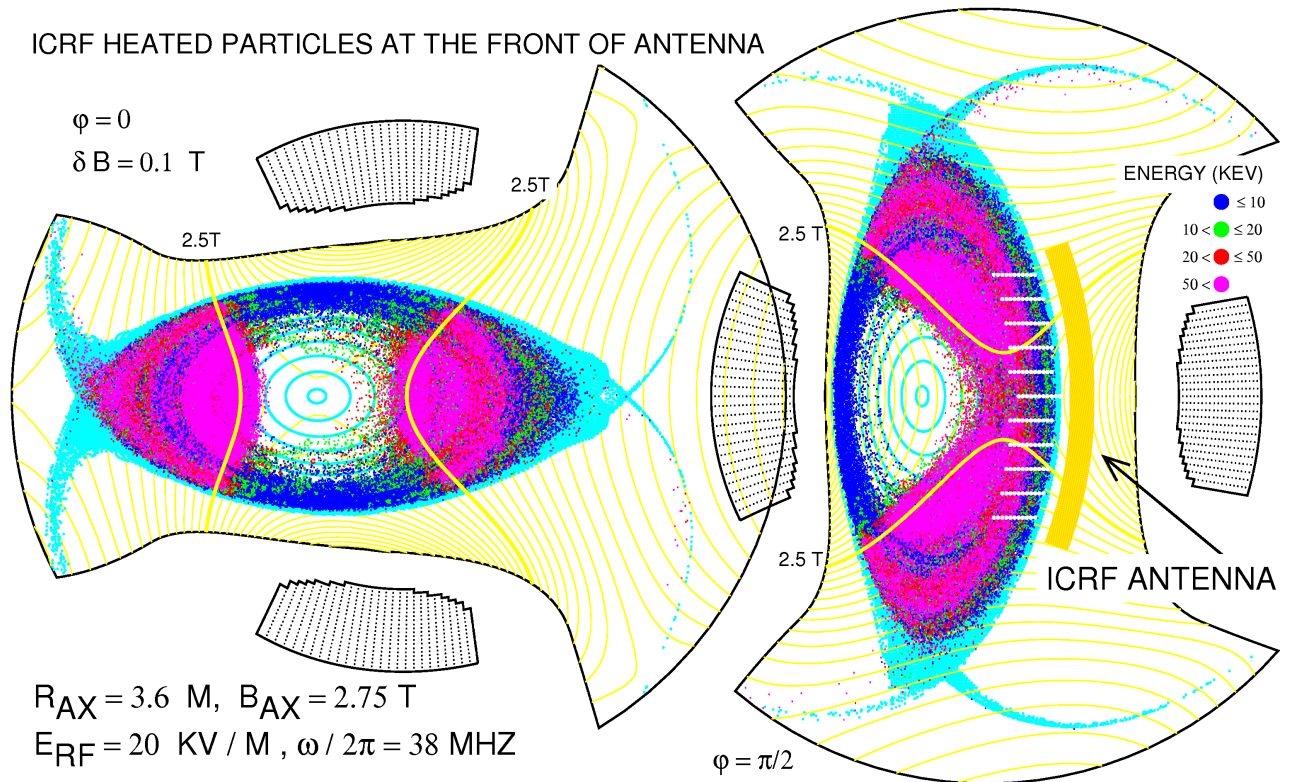


FIG.13. ICRF heating process due to the near field of ICRF antenna.  $B_{ax} = 2.75$  T,  $R_{ax} = 3.6$  m are assumed. Colors of puncture plots represent the energies of protons ( $E \leq 10$  keV : blue,  $10 < E \leq 20$  keV : green,  $20 < E \leq 50$  keV : red,  $50 < E$  : magenta), whose initial energy are assumed to be  $E_0 = 2$  keV. Initial position of protons are shown by white dots plotted in front of the antenna. Initial pitch angle are distributed as  $\chi_0 = n\pi/5$ , ( $n = 0, 1, \dots, 5$ ). ICRF resonance layer is shown by the bold yellow lines ( $B = 2.5$  T line). Lines of force are shown by small cyan color dots.

where frequency  $\omega/2\pi = 38$  MHz, the resonance magnetic field intensity is 2.5 T. The magnetic axis has no ICRF resonance field intensity as shown in FIG.11 ('saddle type' configuration,  $B_{ax} = 2.75$  T). Initial energy of protons is set equal to 100 keV. The starting point of all particles (total 11 protons) is chosen on the ICRF resonance layer in core plasma region ( $r = 3.78$  m,  $z = -0.31$  m,  $\varphi = \pi/10$ ) and initial pitch angles are distributed as  $\chi_0 = n\pi/10$ , ( $n = 0, 1, \dots, 10$ ) as shown by open circles in FIG.12. Poincaré plots of ICRF heated particles are shown in FIG.11. The perpendicularly accelerated high-energy particles pass through the chaotic orbits region. Due to the chaotic orbits nature (see FIG.3), ICRF heated particles with very high energy ( $E \gtrsim 0.5$  MeV: shown by red and magenta dots in FIG.11) distribute almost all core plasma regions.

An illustrative result is shown in FIG.12, which shows the Poincaré plots in  $(v_{\parallel}, v_{\perp})$  at  $\varphi = \pi/10$  poloidal cross section (the starting poloidal section of particles). ICRF resonance heating accelerate particles in  $v_{\perp}$  direction mainly, in the initial stage. An accelerated particle crosses the chaotic orbit regions without any degradation effect, and changes to a reflecting particle. Energy increment of reflecting particle becomes large (density of dots become sparse). Particles are lost to the vacuum vessel wall along the diverter field lines with  $v_{\parallel} < 0$  when  $E \gtrsim 1$  MeV.

Vacuum wavelength of ICRF field ( $\omega/2\pi = 38$  MHz) is very long. But the strap of the LHD's ICRF antenna has relatively wide (width  $\simeq 0.3$  m, height  $\simeq 1.2$  m) [22]. Then the near field of ICRF antenna can reach up to the depth of about 0.3 m in front of the antenna without severe damping. Then, we have studied the ICRF heating process of peripheral plasma that

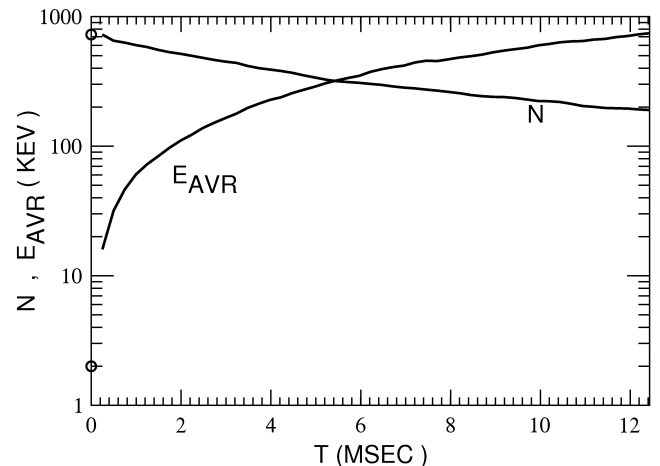


FIG.14. The time trace of average energy  $E_{avr}$  and total number  $N$  of protons corresponding to the Poincaré plot shown by FIG.13. Initial energy and total number are shown by open circles.

uses the near rf electric field in front of the ICRF antenna. The rf field is assumed to be

$$\mathbf{E}(r, \varphi, z) = (0, 0, E_0 \exp \left\{ - \left( \frac{\varphi - \pi/2}{d} \right)^4 \right\} \sin \omega t), \quad (2)$$

where  $E_0 = 20 \text{ kV/m}$ ,  $\omega/2\pi = 38 \text{ MHz}$  and  $d (= 1/4)$  is an index that shows the broadening of ICRF field to the toroidal direction. Initial position of protons are distributed up to the depth of 10 cm from the LCFS to the core plasma region in front of the ICRF antenna as shown in FIG.13. Initial Energy  $E_0$  of protons are 2 keV and initial pitch angle is distributed uniformly from 0 to  $\pi$  ( $\chi_0 = n\pi/5$ ,  $n = 0, 1, \dots, 5$ ). The total particle number is  $6 \times 11 \times 11 = 726$ . The maximum tracking time is 12.4 msec ( $= 222 \times 2\pi R_0 / \sqrt{E_0/M}$ ). Poincaré plot of ICRF heated protons, FIG.13, shows that relatively deep core region is possible to be heated by ICRF near-field. Energy of many chaotic orbits particle exceeds 50 keV even in relatively short time ( $\simeq 12.4 \text{ msec}$ ). Furthermore, we can confirm that the all lost particles flow out along diverter field lines with  $v_{\parallel} < 0$ .

The time trace of average energy and total number of protons are shown in FIG.14. This result shows that ICRF heating process in the LHD magnetic configuration is very much promising. Production of MeV range protons will be possible by the LHD.

The LHD has succeeded in sustaining the plasma (average density  $\simeq 0.5 \times 10^{19} \text{ m}^{-3}$ , central temperature  $\simeq 2 \text{ keV}$ ) during the 150 sec by ICRF ( $P_{ICRF} \simeq 0.5 \text{ MW}$ ) alone in 6th campaign experiment (2003). The plasma was terminated by uncontrollable plasma density rise. At that time, the CCD camera observed red-hot striation on the vertically installed diverter plate (standing diverter plate) as shown in FIG.15. These phenomena have suggested the production of energetic protons in front of the ICRF antenna.

To clarify these experimental results, we have studied numerically the ICRF heating of the plasma outside of LCFS. The ICRF near-field accelerate low energy ( $= 10 \text{ eV}$ ) protons starting from the ICRF resonance layer as shown in FIG.16. Average values of the maximum energy ( $E$ ) and the life-time ( $\tau$ ) of each particles show clear jumps near the border of chaotic field line layer (BCFL). The FIG.16 shows that ions, whose starting points are located inside the BCFL, begin to be confined and begin to be accelerated repeatedly. The position of the LCFS is not significant for the ICRF heated ions. This is consistent with the theoretical prediction for helically trapped particle motion in the LHD. ICRF near-field can start up efficiently the LHD plasma. Ions, whose starting points are located outside the BCFL, increase energy (up to almost 7 keV) by one-path ICRF resonance heating and flow out immediately. These outflow ions made a clear diverter trace on the standing diverter plate. The CCD image of the red-hot striation observed in ICRF heating in the 6th campaign of LHD experiment was completely reproduced by this diverter trace as shown in FIG.15.

#### 4. Summary and discussions

Magnetic field structure in the peripheral region of the LHD has studied numerically with high accuracy. We

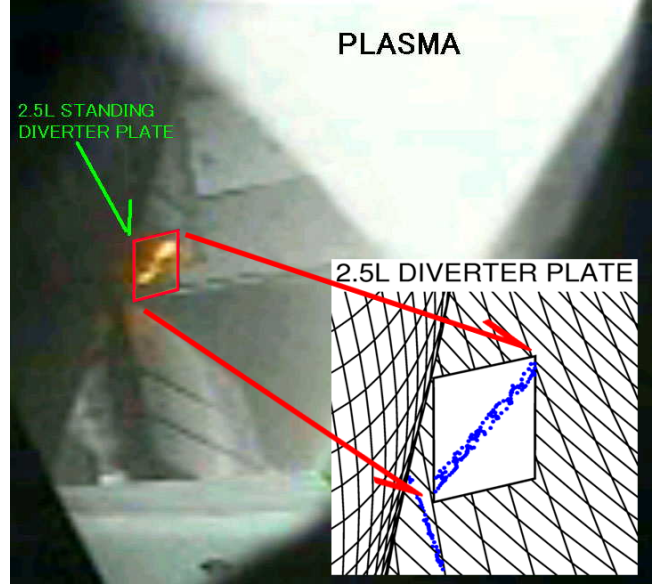


FIG.15. Red-hot striation observed in ICRF heating in the 6th campaign of LHD experiment and a numerical result (the lower right corner).

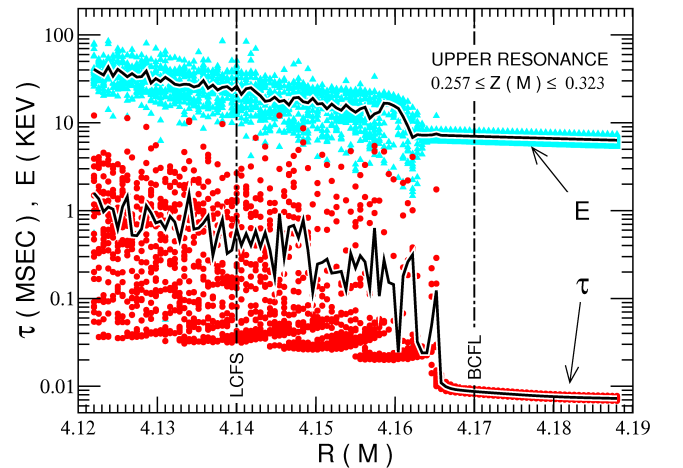


FIG.16. ICRF resonance heating in front of the antenna in the case of  $B_{ax} = 2.75 \text{ T}$ ,  $R_{ax} = 3.6 \text{ m}$ ,  $E_{rf} = 20 \text{ kV/m}$ ,  $\omega/2\pi = 38 \text{ MHz}$ . The ordinate represents the energy (shown by cyan dots) and the life-time (shown by red dots) of ions. Initial position of ions is located on the upper ICRF resonance layer ( $\varphi = \pi/2$ ,  $0.257 \leq z(\text{m}) \leq 0.323$ ,  $r$ : abscissa). Mean values of energy and the life-time are shown by bold line. The position of the LCFS and the borders of chaotic field line layer (BCFL) are also shown by thin chained line.

have confirmed that low temperature ambient plasma is always present in the LHD chaotic field line layer outside of the LCFS because of the very long connection length of chaotic-field-line and the mirror confinement effect of helical ripple nature of the LHD magnetic field. This is proved by the detailed comparison of the CCD camera view of the LHD plasma and the numerically obtained 3D view of chaotic field lines. Both images are corresponding each other completely. The ambient plasma in the chaotic field line layer brings the following advantage for the high performance of plasma confinement in the LHD. (1) Reduction of heat load to the diverter plate without losing high-performance of core plasma confinement because of very long connection length of lines of force. (2) The role of the plasma blanket effect. (3) Stabilization effect against MHD instabilities.

The particle orbits were traced numerically both in the presence and in the absence of ICRF field by directly solving the equation of motion in LHD magnetic field configuration. The particle loss boundary was set at the vacuum vessel wall, ICRF antennas and NBI armor tiles.

In the LHD configuration, the  $\mathbf{B} \times \nabla B$  drift motion decreases the rotational transform of particle (positive ion) motion when  $v_{\parallel} > 0$ . Then, it is easy to confine the  $v_{\parallel} > 0$  passing particle than the magnetic surface. The outermost drift surface of passing particles of  $v_{\parallel} > 0$  can extend over the LCFS. In a usual LHD operating range ( $B_{ax} \simeq 2.75$  T,  $E \lesssim 180$  keV), this difference is small, however, in low magnetic field operation case, the drift surface of co-NBI can extend fairly outside the LCFS. The numerical prediction of the drift surface being extended over the LCFS is verified by the LHD experiments.

The LHD generates the plasma confinement magnetic field with the continuous winding helical coils. Then helical mirror trapped particle can circulate around the magnetic axis, and can manifest stronger adiabaticity and can be confined more effectively compared with the passing particles. This property is verified numerically and is very convenient for ICRF heating of the LHD plasma.

The confinement of LHD plasma is improved by the 'inward shift' of magnetic axis [9]. However, the orbit of the highly energetic ion hardly changes according to this 'inward shift' of magnetic axis as shown in FIG.1-3. Here, we examine the change in the magnetic surface structure brought by the 'inward shift' of magnetic axis. The FIG.17 shows the rotational transform  $\iota/2\pi$  and the specific volume  $U$  of the magnetic surface in the case of the 'standard' ( $R_{ax} = 3.75$  m) and the 'inward shifted' ( $R_{ax} = 3.6$  m) configurations. This figure shows that the rotational transform at the LCFS  $\iota_{LCFS}/2\pi$  is different in the case of the 'standard' configuration and in the case of the 'inward shifted' configuration. Because the LCFS should not be destroyed by resonant perturbations, the rotational transform at the LCFS should be an irrational number that is 'far' from rational numbers. The FIG.18 shows the 'numbers' of neighboring rational number. The fact that should do special mention, is that the numerically obtained rotational transform in the case of  $R_{ax} = 3.6$  m is almost equal to the golden mean ( $= (1 + \sqrt{5})/2$ ). This means that the LCFS of 'inward shifted' case is robust against perturbations, because the golden mean is the irrational number least easily approximated by

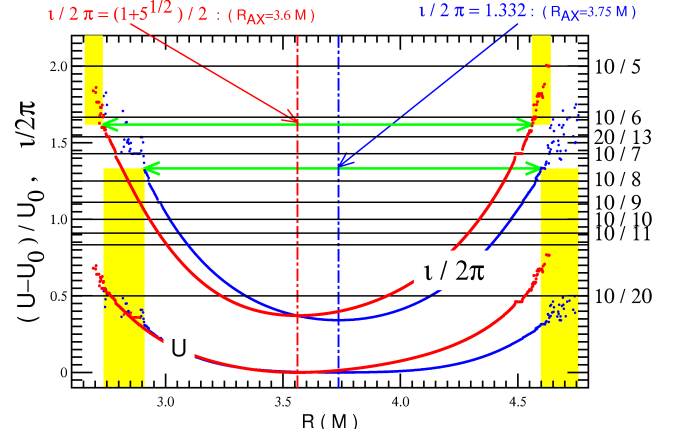


FIG.17. Magnetic structure of the LHD in the case of the 'standard' ( $R_{ax} = 3.75$  m : shown by blue lines) and the 'inward shifted' ( $R_{ax} = 3.6$  m : shown by red lines) configurations. Distributions of the rotational transform,  $\iota/2\pi$ , and the specific volume,  $U$ , are shown. The abscissa is the radial position  $r$  at  $\varphi = 0$  poloidal section ( $z = 0$ ).  $U_0$  is the specific volume at the magnetic axis. The position of the magnetic axis is shown by chained lines. The range of magnetic surface and the value of  $\iota_{LCFS}/2\pi$  are shown by green lines. Chaotic field line layers are indicated by yellow-daubed range.

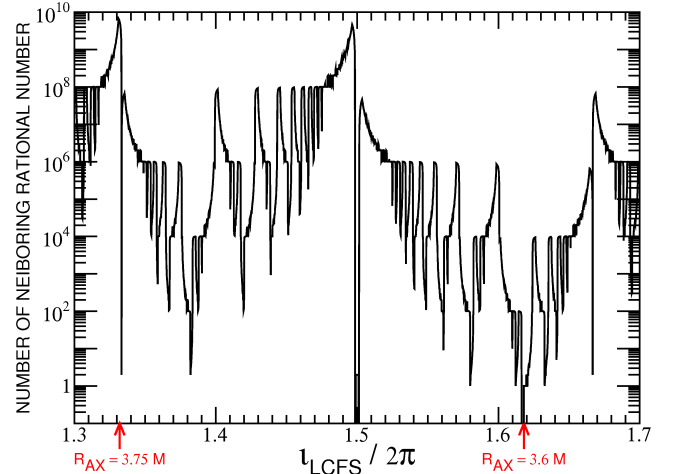


FIG.18. Numbers of neighboring rational number which satisfy the relation  $|b - a| \leq 10^{-3}$ . The rational number  $a$  and  $b$  are expressed by the continued fractions

$$a, b = 1 + \frac{1}{n_1 + \frac{1}{n_2 + \cdots + \frac{1}{n_i}}}, \quad (1 \leq n_i \leq 100, 1 \leq i \leq 6)$$

The values of the rotational transform at the LCFS of the LHD are also indicated by the red arrows.

rationals [23]. In the 'standard' case ( $R_{ax} = 3.75$  m), on the other hand, the  $\iota_{LCFS}/2\pi$  is very close to the low order rational number ( $= 4/3$ ) and the number of neighboring rational is very many, and the thickness of the chaotic field line layer is relatively thick (see FIG.17). Volume of magnetic surface ( $= V_{LCFS}$ ) and the volume of chaotic field line layer ( $= V_{chaos}$ ) are as follows.

$$\begin{aligned} V_{LCFS} &\simeq 27.0 \text{ m}^3, V_{chaos} \simeq 5.0 \text{ m}^3 & \text{for } R_{ax} = 3.75 \text{ m} \\ V_{LCFS} &\simeq 30.0 \text{ m}^3, V_{chaos} \simeq 2.1 \text{ m}^3 & \text{for } R_{ax} = 3.60 \text{ m} \end{aligned}$$

Therefore, it will be difficult to explain all the improvements of plasma confinement by the small difference ( $\simeq 10\%$ ) of the  $V_{LCFS}$ , only. The volume of the chaotic field line layer,  $V_{chaos}$ , has twice or more differences in 'standard' configuration and 'inward shifted' configuration. The difference of this volume ( $= V_{chaos}$ ) might be related to the difference of the plasma confinement performance. The relation between the confinement performance and the value of  $\iota_{LCFS}/2\pi$  is an interesting issue in the future.

In the 6th campaign LHD experiment, ICRF long pulse discharge terminate less than 3 minutes due to uncontrollable density increase. Red hot striation of the standing diverter plate was observed as mentioned in Sec.3. The standing diverter plate was replaced to new type diverter plate after the 6th campaign. The coolability for the new plate is reinforced about 3 times or more compared with the old plate. The present paper predict that low energy protons just after ionization near ICRF antenna are dangerous for the local heat load to diverter plates. In the 8th campaign, the position of the gas puffing is kept away from the ICRF antenna and a red hot striation of a standing diverter plate has not yet been observed including the long pulse discharge more than 12 minutes. So, the prediction of the present paper is consistent with present experiments.

Stabilization effect of the chaotic-field-line-layer plasma against MHD instabilities are an interesting item in the future experiment of the LHD.

## References

- [1] NÜHRENBERG, J., LOTZ, W., MERKEL, P., NÜHRENBERG, C., SCHWENN, U., STRUMBERGER, E., *Transactions of Fusion Technology*, **27** (1995) 71.
- [2] SPONG, D.A., HIRSHMAN, S.P., LYON, J.F., BERRY, L.A., STRICKLER, D.J., WARE, A.S., *IAEA-CN-116/IC/P6-51*, (2004).
- [3] AKAO, H., *J. Phys. Soc. Jpn.*, **59** (1990) 1633.
- [4] SAKAKIBARA, S., et al., *Proc. 31st EPS Conference on Plasma Phys. London, ECA*, **28B**, O-4.01 (2004)
- [5] SAITO, K., KUMAZAWA, R., MUTOH, T., SEKI, T., WATARI, T., TORII, Y., et al., *Nuclear Fusion*, **41** (2001) 1021.
- [6] TORII, Y., WATARI, T., KUMAZAWA, R., SAITO, K., MUTOH, T., SEKI, T., SHIMPO, F., NOMURA, G., WATANABE, T., TAKEUCHI, N., et al., *Plasma Phys. Control. Fusion*, **43** (2001) 1191.
- [7] MUTOH, T., KUMAZAWA, R., SEKI, T., SAITO, K., WATARI, T., TORII, Y., et al., *Nuclear Fusion* **43** (2003) 738.
- [8] MUTOH, T., et al., *private communications*, (2004).
- [9] YAMADA, H., KOMORI, A., et al, *Plasma Phys. Control. Fusion*, **43** (2001) A55.
- [10] MOTOJIMA, O., IDA, K., WATANABE, K.Y., NAGAYAMA, Y., KOMORI, A., MORISAKI, T., et al, *IAEA-CN-116/OV/1-4*, (2004).
- [11] WATANABE, T., HOJO, H., *J. Plasma Fusion Res. SERIES*, **5** (2002) 487.
- [12] SANUKI, H., TODOROKI, J., KAMIMURA, T., *Phys. Fluids B*, **2** (1990) 55.
- [13] WATANABE, T., *Kakuyugo Kenkyu*, **63** (1990) 482[in Japanese].
- [14] WATANABE, T., OUCHI, A., *Kakuyugo Kenkyu*, **64** (1990) 397[in Japanese].
- [15] WATANABE, T., *Trans. JSIAM*, **1** (1991) 101[in Japanese].
- [16] WATANABE, T., AKAO, H., *J. Plasma Fusion Res.*, **73** (1997) 186[in Japanese].
- [17] SARAFYAN, D., *J. Math. Anal. & Appl.*, **40** (1972) 436.
- [18] MATSUMOTO, Y., OIKAWA, S., WATANABE, T., *J. Phys. Soc. Jpn.*, **71** (2002) 1684.
- [19] GOTO, M., MORITA, S., *Phys. Rev.*, **E 65** (2002) 26401.
- [20] KADOMTSEV, B.B., "Reviews of Plasma Physics, 2", (ed. by M.A. Leontovich) Consultant Bureau, New York, (1966) 174.
- [21] MATSUMOTO, Y., NAGAURA, T., OIKAWA, S., WATANABE, T., *Jpn. J. Appl. Phys.*, **43** (2004) 332.
- [22] WATARI, T., MUTOH, T., KUMAZAWA, R., SEKI, T., SAITO, K., TORII, Y., et al., *Nuclear Fusion*, **41** (2001) 325.
- [23] JACKSON, E.A., "Perspectives of nonlinear dynamics, volume 2" (Cambridge University Press, New York) (1994) 63.

# Experiment of Magnetic Island Formation in Large Helical Device

Y. Nagayama, K. Narihara, Y. Narushima, N. Ohyabu, T. Hayashi, K. Ida, S. Inagaki, D. Kalinina<sup>1</sup>, R. Kanno, A. Komori, T. Morisaki, R. Sakamoto, S. Sudo, N. Tamura, T. Tokuzawa, H. Yamada, M. Yoshinuma, and LHD experimental group

National Institute for Fusion Science, Toki 509-5292, Japan and

<sup>1</sup>The Graduate University for Advanced Studies, Hayama 240-0193, Japan

(Dated: December 10, 2004)

Magnetic island formation is experimentally investigated in the Large Helical Device (LHD). The  $(m, n) = (1, 1)$  vacuum magnetic island is generated by using the local island diverter (LID) field, where  $m$  and  $n$  are the poloidal and toroidal mode numbers, respectively. The island width depends on plasma parameters (the electron temperature and the  $\beta$ ) and the magnetic axis position. In the case of  $R_{ax} = 3.53$  m, the magnetic island in the plasma is larger than that in the vacuum field. Here,  $R_{ax}$  is the major radius of the magnetic axis. In the case of  $R_{ax} = 3.6$  m, the magnetic island is not generated when the error field is less than the threshold, which is increased as the  $\beta$  is increased. Evidence of island current is obtained when the magnetic island is formed due to a small error field. However, the mechanism that generates the island is not known yet.

PACS numbers:

## I. INTRODUCTION

Magnetic islands play important roles in fusion and space plasmas. MHD instabilities create magnetic islands by magnetic reconnection, and cause sawtooth oscillations in tokamaks[1] and in helical systems[2]. In tokamaks, a seed island is enlarged due to the neoclassical effect, which is called Neoclassical Tearing Mode (NTM), and it degrades the plasma performance[3]. Actually, large magnetic islands due to NTM have been observed in the case of the beta degradation in TFTR[4].

In helical systems, it has been considered that the magnetic island structure, which is formed by an error field, could grow and degrade the plasma confinement seriously. Figure 1 shows a typical example of the confinement degradation due to spontaneous magnetic island formation in the Large Helical Device (LHD), which is the largest superconducting heliotron-type fusion device with an averaged minor radius of  $a = 0.65$  m and a major radius of the plasma axis ( $R_{ax}$ ) of 3.6 m[5]. Usually, in the case of smaller  $R_{ax}$ , a magnetic island can be generated easily. Fig. 1 shows time evolution of NBI power (arbitrary unit),  $\beta$ , averaged electron density, temperature at  $R = 4.2$  m of plasmas with island (solid line: Shot 39559) and without island (broken line: Shot 39558),  $T_e$  profiles with (closed circles) and without (open circles) island. Confinement degradation is caused 0.3 seconds after small change of NBI. As shown in Fig. 1(e), a magnetic island is generated although the error field is minimized.

The  $(m, n) = (1, 1)$  error field can be controlled using the external field in LHD. Here,  $m$  and  $n$  are the poloidal and toroidal mode numbers, respectively. In LHD, it has been observed that the heat conduction in the magnetic island is extremely smaller than that in the main plasma[6]. This indicates that the island structure is isolated from the main plasma. Also, in LHD, it has been observed that the island size is sometimes significantly

reduced in the plasma [7, 8]. This is called ‘healing’ of the island. To control the island width is a key issue in the development of a helical fusion reactor.

This paper will present the magnetic island formation in LHD. Confinement of plasma in helical systems is based on the assumption that the flux surface in the plasma can be created by the external field. If so, the magnetic island that is made by an error field should stay in plasma. This paper will show that an island due to the error field sometimes enlarges in the plasma. Under different conditions, however, a large island as wide as 20 % of the minor radius in the vacuum magnetic surface disappears in the plasma due to ‘healing’.

## II. GENERATION OF MAGNETIC ISLAND

### A. LID Field

In LHD, 10 pairs of modular vertical field coils are installed top and bottom in order to produce a  $(1, 1)$  field. By adding the  $(1, 1)$  field, a static magnetic island can be formed around the  $\iota/2\pi = 1$  surface. Since these coils are installed to form an  $(1, 1)$  island for the local island diverter (LID) [9], these coils are sometimes called LID coils and the  $(1, 1)$  field made by the LID coil current ( $I_{LID}$ ) is sometimes called the LID field. Figures 2(a,b) show the calculated flux surface in the plasma cross-section at  $\phi = 342^\circ$  and  $\phi = 126^\circ$ , respectively. Here, the toroidal angle  $\phi$  is defined as the angle from the border between the port sections 3 and 4, and the positive sign is defined as the direction of counter-clockwise in the top view. The flux surface in the vacuum field is measured by a scanning multi-channel detector array that detects an electron beam, which is injected from the electron emission diode. The electron beam is also scanned. The calculated flux surfaces are consistent with those measured in the vacuum field.

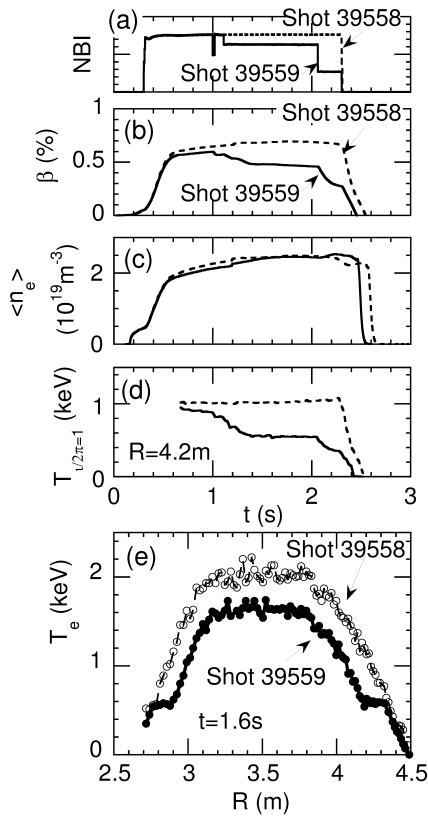


FIG. 1: Time evolution of (a) NBI power (arbitrary unit), (b)  $\beta$ , (c) averaged electron density, (d) temperature at  $R = 4.2$  m of plasmas with island (solid line: Shot 39559) and without island (broken line: Shot 39558). (e)  $T_e$  profiles with (closed circles) and without (open circles) island.

## B. Measurement of Magnetic Island

In this experiment, the width of the magnetic island in the plasma is estimated as a flat region in the electron temperature ( $T_e$ ) profile. The reason is as follows: the border of the island is a closed flux surface, which is nested by a field line. The electrons run along the field line with very high speed. So, the border of the island is isothermal. If the heat deposition inside the island is very high, the  $T_e$  at the O-point of the island can be higher than that on the border. However, since the island width is much narrower than the main plasma, the temperature difference between the O-point and the border is usually not big enough to be recognized. Therefore the  $T_e$  profile in the island region looks flat. In LHD, the  $T_e$  profile is measured using YAG laser Thomson scattering installed at  $\phi = 342^\circ$  and the ECE diagnostics at  $\phi = 126^\circ$ . Figure 2(c,d) show the  $T_e$  profiles measured by Thomson scattering at  $\phi = 342^\circ$  and at  $\phi = 126^\circ$  by ECE diagnostics (a scanning Michelson interferometer), respectively. Flat regions around  $R = 2.8$  m and  $R = 4.2$  m in the  $T_e$  profile (Figure 2(c,d)) correspond to the magnetic island in the vacuum flux surface Figure 2(a,b), respectively. There-

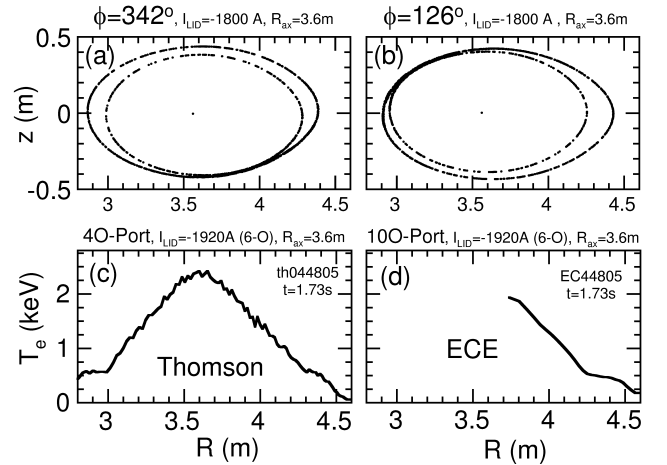


FIG. 2: (a) calculated flux surface at  $\phi = 342^\circ$ , (b) calculated flux surface at  $\phi = 126^\circ$ . (c)  $T_e$  profile measured by Thomson scattering at  $\phi = 342^\circ$ , (d)  $T_e$  profile measured by ECE diagnostics at  $\phi = 126^\circ$ .

fore, a flat region in the  $T_e$  profile is considered to be the magnetic island.

## C. Healing of Magnetic Island

A typical example of the ‘healing’ of a magnetic island is shown in Fig. 3. Parameters for the plasma configuration are as follows:  $R_{ax} = 3.6$  m,  $B_{ax} = 2.75$  T and  $I_{LID} = -1200$  A. Time evolutions of the  $\beta$ , the line averaged electron density and the  $T_e$  at  $R = 3.76$  m are shown in Fig. 3(a), (b), and (c), respectively. The plasma is heated by NBI with power of 9 MW. The hydrogen ( $H_2$ ) ice pellet is injected at  $t = 1$  s. After the ice pellet injection, the electron density and the  $\beta$  are quickly increased, as shown in Fig. 3(a-b). Figure 3(d) shows the time evolution of the  $T_e$  profile after the ice pellet injection. The  $T_e$  profile is measured by the ECE diagnostics at  $\phi = 126^\circ$ . The calculated island width ( $w$ ) in the vacuum is about 12 cm, but the island is not observed before the pellet injection ( $t = 0.95$  s), as shown in Fig. 3(d). This is the ‘healing’ of the magnetic island.

The electron temperature drops due to the ice pellet injection, and right after the ice pellet injection ( $t = 1.05$  s) the temperature profile near the island region is lower than the surrounded region. Soon, the temperature starts to recover, and the wide island appears at  $t = 1.15$  s. The width of the island is 12 cm, which is as large as the calculated width of the magnetic island in the vacuum field. As  $T_e$  increases, the island width decreases. Finally, the  $T_e$  profile returns to that before the pellet injection, and the island disappears. This experiment clearly shows that the island width in the plasma changes as  $T_e$  changes.

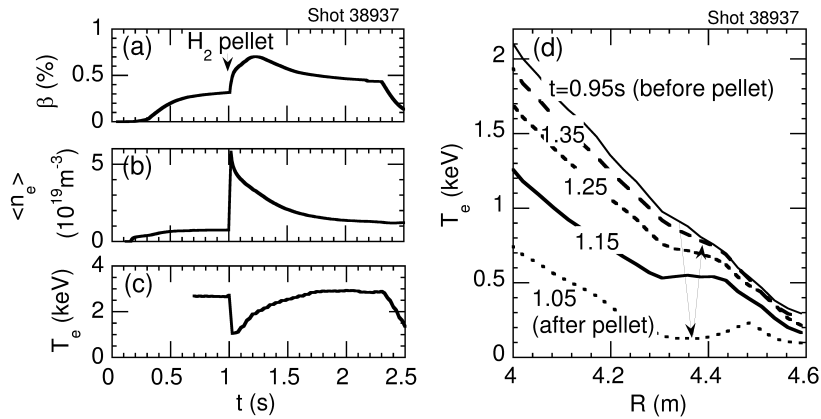


FIG. 3: Time evolution of (a)  $\beta$ , (b) line averaged electron density ( $\langle n_e \rangle$ ), (c) electron temperature at  $R = 3.76$  m, (d)  $T_e$  profile with the (1, 1) external field ( $I_{\text{LID}} = -1200$  A).

### III. ISLAND WIDTH

#### A. Parameter Dependence of the Island Width

The island width varies with the plasma parameters ( $T_e$  and  $\beta$ ). Figure 4(a) and (b) shows the island width ( $w$ ) versus  $T_e$  and  $\beta$  in the magnetic island, respectively. The major radius of the magnetic axis is 3.6 m. The experiment is done for various magnetic field, but the normalized LID coil current by  $B_{\text{ax}}$  ( $I_{\text{LID}}/B_{\text{ax}}$ ) is about 430 A/T. This LID field generates the magnetic island width of 12 cm in the vacuum field. There are two types of tendency indicated by a solid line (type A) and a broken line (type B). In the case of high field (open circles), the island width decreases as  $T_e$  increases (type A). In the case of low field (closed circles), the island width decreases as the  $\beta$  increases (type B).

It looks like the data belonging to type A (solid line) have the opposite tendency to those of type B (broken line). The reason may be as follows: The healing effect by  $T_e$  is weaker when  $T_e$  is lower than 0.6 keV. Higher  $\beta$  can be obtained at higher density and at lower field, where  $T_e$  is lower and the healing effect by  $T_e$  is weak. So, it looks like the data indicated by the closed circles have a tendency opposite to the type A (solid line) in Fig. 4(a). The high  $T_e$  plasma is obtained in the low density plasma with the high field, where the  $\beta$  is lower and the healing effect by the  $\beta$  is weak. Therefore, it appears that the data indicated by open circles have a tendency opposite to the type B (broken line) in Fig. 4(b).

#### B. Threshold of Island Formation

As shown in Fig. 4, the island width depends on the  $\beta$  when the vacuum magnetic island width is fixed. Figure 5(a) shows dependence of the island width ( $W$ ) on the vacuum magnetic island width ( $W_{\text{ex}}$ ) in the case of  $R_{\text{ax}} = 3.6$  m and  $B_{\text{ax}} = 0.75$  T. Here, the island width is

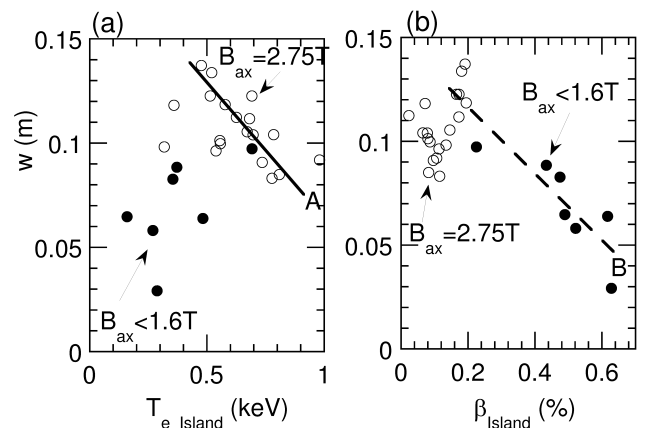


FIG. 4: (a) Island width vs. electron temperature in the island. (b) Island width vs.  $\beta$  in the island. The LID coil current is  $I_{\text{LID}}/B_{\text{ax}} = 400 \sim 460$  A/T. Open circles indicate the case of  $B_{\text{ax}} = 2.75$  T, and closed circles indicate the case of  $B_{\text{ax}} < 1.6$  T.

normalized by the plasma minor radius. In order to minimize the effect of  $T_e$ , the line averaged electron density ( $\langle n_e \rangle = 2 \times 10^{19} \text{ m}^{-3}$ ) is also fixed. As the vacuum magnetic island width is increased, the island width in vacuum is increased. In LHD plasmas, however, the island does not appear when the  $W_{\text{ex}}$  is less than a the critical vacuum magnetic island width ( $W_c$ ). The island in the plasma suddenly appears when it surpasses the threshold, where the island width in the vacuum is 17 % of the minor radius. This is another example of ‘healing’ of the island.

Figure 5(b) shows the relationship between the square of threshold ( $W_c$ ) and the  $\beta$  at the island. Here, the line averaged electron density ( $\langle n_e \rangle = 2 \times 10^{19} \text{ m}^{-3}$ ) is also fixed. The  $\beta$  is changed by changing the magnetic field and the heating power. As the  $\beta$  is increased, the critical vacuum magnetic island width is increased, as shown in Fig. 5(b).

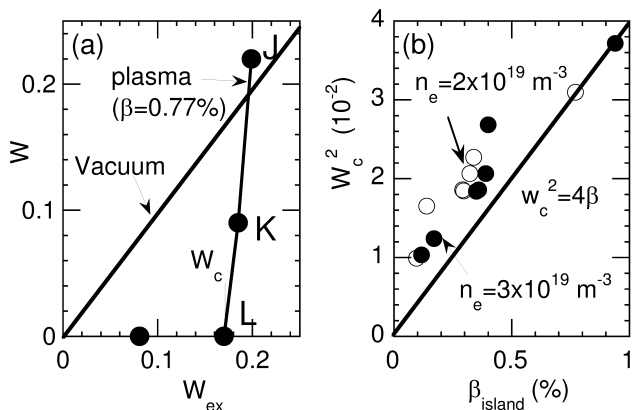


FIG. 5: (a) vacuum magnetic island width ( $W_{ex}$ ) vs. island width ( $W$ ) in plasma (closed circles). (b)  $\beta$  vs. square of the critical vacuum magnetic island width ( $W_c$ ).

## IV. ISLAND CURRENT

### A. Evidence of Island Current

In LHD, the radial magnetic field on the mid plane is measured by 10 large coils installed on the outboard side at every port. The toroidal angle of the coils are from  $\phi = 18^\circ$  to  $\phi = 342^\circ$ . Each coil has 10 turns and a cross-section of  $1 \text{ m}^2$ , so  $NS = 10 \text{ m}^2$ . Since the large coils are installed outside the vacuum vessel, the time response is not very good.

In the case of  $R_{ax} = 3.53 \text{ m}$  and  $B_{ax} = 2.8 \text{ T}$ , time evolutions of  $\beta$ , averaged electron density and  $T_e$  are shown in Fig. 6(a-c). The  $T_e$  profile is shown in Fig. 6(e). No LID field is applied. At  $t = 1.4 \text{ s}$ , hydrogen ice pellets are sequentially injected into the plasma. The density is increased and the temperature drops due to the pellet injection. The  $\beta$  is decreased after the pellet injection in this shot. In this shot, the magnetic island is formed after the  $\text{H}_2$  ice pellet injection due to the small residual error field, as shown in Fig. 6(e). This is the opposite phenomenon of ‘healing’. After the magnetic island is established,  $T_e$  drops significantly. This is a case when the magnetic island deteriorates the plasma confinement.

Since the island in the vacuum field is small, the horizontal magnetic field measured on the mid-plane should be generated by the island. Figure 6(d) shows time evolution of the radial magnetic field ( $B_r$ ), which is measured by large coils at  $\phi = 306^\circ$  and  $\phi = 162^\circ$ . Right after the pellet injection,  $B_r$  signals change the sign and start to increase. Figure 6(f) shows the polar plot of  $B_r$ . The open circle and broken line indicate the  $B_r$  in the case without island, and the closed square and solid line indicate the  $B_r$  in the case with island. These lines are the (1, 1) component, as  $B_r^{n=1} = b_{r1} \cos(\phi - \phi_0)$ , where parameters  $b_{r1}$  and  $\phi_0$  are obtained by the least square fitting to the experimental data that is marked by circles and squares. When the island is not observed ( $t = 1.4$

s), the  $B_r^{n=1}$  is small, as shown in Fig. 6(e). When the island is observed ( $t = 3.7 \text{ s}$ ), the  $B_r^{n=1}$  is large.

The amplitude of  $B_r^{n=1}$  is the highest at  $\phi \sim 155^\circ$  and  $\phi \sim 335^\circ$  and vanishes at  $\phi \sim 60^\circ$  and  $\phi \sim 240^\circ$ . Figure 7 shows the schematic view of the plasma cross-section, where the  $m = 1$  current flows and generates the radial field ( $B_r$ ). When the  $B_r$  is a maximum, the current should be in the top and the bottom. So, at  $\phi \sim 335^\circ$  the current that generates the  $B_r^{n=1}$  flows in the top and the bottom of the plasma cross section. As shown in Fig. 6(d), the  $m = 1$  island appears on both sides of the  $T_e$  profile at  $\phi = 342^\circ$ . So, the X-point and the O-point of the island are located in the top and the bottom in the plasma cross-section at  $\phi \sim 342^\circ$ . Therefore, the large negative  $B_r$  at  $\phi = 342^\circ$  is made by the  $m = 1$  current flowing at the O-point and/or the X-point of the island. Since the (1, 1) island is formed on the  $\iota/2\pi = 1$  flux surface, the  $m = 1$  current could be called the (1, 1) current. Therefore, the (1, 1) magnetic island is generated by the (1, 1) current on the  $\iota/2\pi = 1$  flux surface, when the error field is small in a helical system.

Assuming the plasma is cylindrical and the island width is thin, the width of the (1, 1) island can be estimated, as  $w^2 = 2\mu_0 I_s / r_s B_{ax}$ , and the magnetic field at the probe can be written as  $B_r = -(\mu_0 r_s I_s / 4R_{ax} r_p^2) \cos\theta$ , where  $I_s$  is the island current,  $r_s$  is the minor radius of the island, and  $r_p$  is the minor radius of the magnetic probe. Since the estimated magnetic field is 10 % less than the observed one and the observed phase is as is expected, it can be claimed that the amplitude and the phase of the magnetic field is consistent with the (1, 1) island current.

### B. Calculation of Pfirsch-Schluter Current

The Pfirsch-Schluter current is related to the  $\beta$  and it may have an  $m = 1$  component. It can be obtained by the equilibrium calculation. The ‘HINT’ code [10] is useful for calculating the 3-dimensional magneto-hydrodynamic (MHD) equilibrium of a high  $\beta$  plasma with a magnetic island structure. The result of a calculation using the ‘HINT’ code shows that the ‘healing’ of a high  $m$  island is obtained due to the Pfirsch-Schluter current. However, a clear ‘healing’ of a (1, 1) island has not been obtained. So the ‘healing’ cannot be explained by the Pfirsch-Schluter current only.

## V. DISCUSSION

There are threshold and bi-stable conditions for the generation of island. In the case of  $R_{ax} = 3.53 \text{ m}$ , the magnetic island is generated by external perturbations, such as the drop of NBI heating power and the injection of hydrogen ice pellets. Once the island is generated, the width is quickly increased. In the case of  $R_{ax} = 3.6 \text{ m}$ , the magnetic island is generated when the threshold

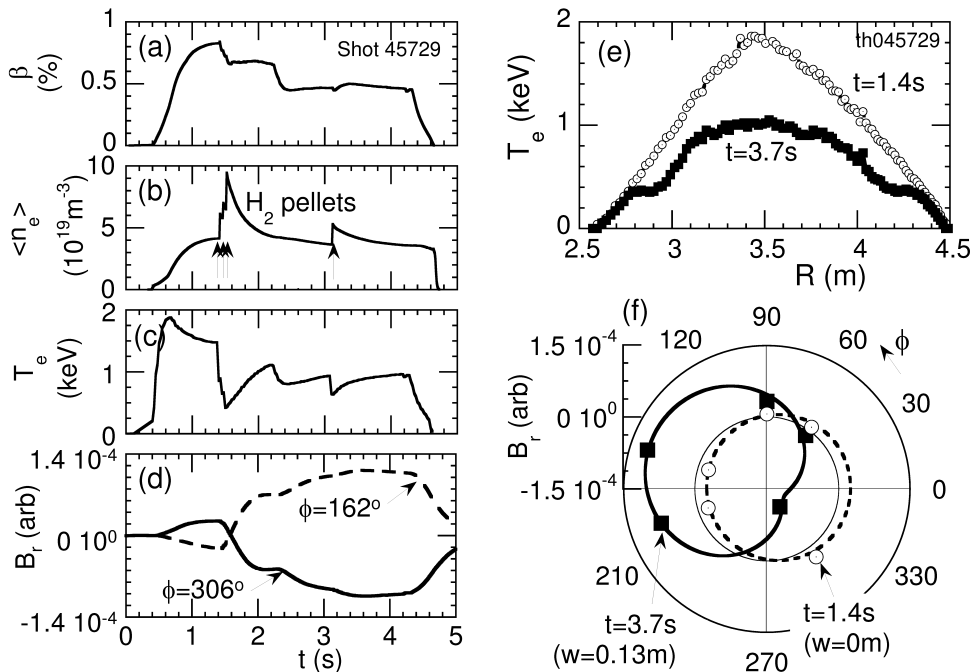


FIG. 6: Time evolution of (a)  $\beta$ , (b) averaged electron density, (c) temperature, (d) radial magnetic field at  $\phi = 306^\circ$  (solid line) and at  $\phi = 162^\circ$  (broken line), (e) electron temperature profile at  $\phi = 342^\circ$ , (f) the polar plot of  $B_r$  versus toroidal angle in case of  $R_{\text{ax}} = 3.53$  m without the LID field. Closed lines indicate the (1,1) component. Circular thin solid line indicates  $B_r = 0$ .

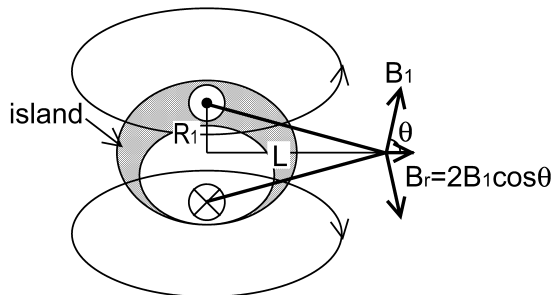


FIG. 7: Schematic view of the plasma cross-section, where the  $m = 1$  current flows and generates the horizontal field..

of the external error field surpasses the threshold. With a small excess of the threshold, the wide island is generated. However, the island that is formed by cooling plasma with ice pellet injection in the case of  $R_{\text{ax}} = 3.6$  m does not have a bi-stable feature.

In this experiment, we have observed that the island formation is related to the plasma parameters ( $T_e$  and the  $\beta$ ) and the magnetic axis position. In the case of  $R_{\text{ax}} = 3.6$  m, the island width is usually narrower than that in vacuum. In the case of low  $T_e$ , the island width is reduced as the  $\beta$  is increased. In the case of low  $\beta$ , the island width is reduced as the  $T_e$  is increased. Often, the island is not generated even if the island width in vacuum is as large as 17 % of the plasma minor radius.

In the case of  $R_{\text{ax}} = 3.53$  m, however, the island width is wider than that in the vacuum. The magnetic axis position is related to the stability. As the  $R_{\text{ax}}$  becomes larger, the interchange mode becomes less unstable. The island width is decreased as the  $\beta$  is increased. Since the interchange mode becomes less stable as the  $\beta$  becomes higher, the MHD instability may not be related to the island generation, directly.

In helical systems, the plasma current is not necessary to create the magnetic island, since it is formed in the vacuum field. A basic question is whether a current flows in the plasma when ‘healing’ the magnetic island. In this experiment, the horizontal field is detected on the mid-plane when the magnetic island is generated from the small residual error field. The amplitude and phase of the observed magnetic field is consistent with the assumption that the island is generated by the island current.

It is still unknown what mechanism generates the island current in the plasma with higher  $T_e$  and lower  $\beta$ . In the case of a higher  $\beta$  plasma, a possible mechanism is the Pfirsch-Schluter current, which is generated to maintain the equilibrium and is related to the  $\beta$ . Since the 3-dimensional equilibrium calculation using the ‘HINT’ code, which can treat the Pfirsch-Schluter current precisely, shows that the (1, 1) island width does not change due to the  $\beta$ , the reduction of island width may not be directly related to the Pfirsch-Schluter current. The bootstrap current is another possible mechanism that is related to the  $\beta$ . The bootstrap current density is higher

in the region where the pressure gradient is higher. The pressure gradient is very low inside the island and is high in the vicinity of the island. Therefore the bootstrap current density may have the (1, 1) structure. A difficulty of this argument is as follows: Once the island is shrunk, the (1, 1) mode of the bootstrap current density is disappeared. So, if the bootstrap current triggers the healing, it cannot maintain the healing. Bi-stable mechanism that maintain the 'healing' has been unknown, yet.

## VI. CONCLUSION

In conclusion, the generation and the 'healing' of the magnetic island are investigated using the LID field in

LHD. The generation of an island due a small error field is caused in the case of  $R_{ax} = 3.53$  m, and the 'healing' of the island is caused in the case of  $R_{ax} = 3.6$  m. The 'healing' effect is more enhanced as the  $\beta$  or the  $T_e$  increases. When the island is generated from the small residual error field, the (1, 1) horizontal magnetic field is observed. This is the first observation of the evidence of the island current in helical systems. Further theoretical research is required to understand the generation of the magnetic island in helical systems. The magnetic island formation has a bi-stable state sometimes. The magnetic island dynamics should be considered in designing a helical fusion reactor, because of very high values of  $\beta$  and  $T_e$ .

- 
- [1] Nagayama, Y., et al., 1996 *Phys.Plasmas* **3** 1647.
  - [2] Nagayama, Y., et al., 2003 *Phys.Rev.Lett.* **90** 205001.
  - [3] Chang, Z., et al., 1995 *Phys.Rev.Lett.* **74** 4663.
  - [4] Nagayama, Y., et al., 1996 *Phys.Plasmas* **3** 2631.
  - [5] Motojima, O., et al., "Confinement and MHD stability in the Large Helical Device", submitted to Nucl. Fusion.
  - [6] Inagaki, S., et al., 2004 *Phys.Rev.Lett.* **92** 55002.
  - [7] Narihara, K., et al., 2001 *Phys.Rev.Lett.* **87** 135002.
  - [8] Ohyabu, N., et al., 2002 *Phys.Rev.Lett.* **88** 55005.
  - [9] Komori, A., et al., "Edge Plasma Control by Local Island Divertor in LHD", submitted to Nucl. Fusion.
  - [10] Harafuji, K., Hayashi, T., Sato, K., 1989 *J.Comput.Phys.* **81** 169.

## Microscopic Modification of Wall Surface by Glow Discharge Cleaning and its Impact on Vacuum Properties of LHD

M. Tokitani 1), M. Miyamoto 2), K. Tokunaga 3), T. Fujiwara 3), N. Yoshida 3), A. Komori 4), S. Masuzaki 4), N. Ashikawa 4), S. Inagaki 4), T. Kobuchi 4), M. Goto 4), J. Miyazawa 4), K. Nishimura 4), N. Noda 4), B.J. Peterson 4), A. Sagara 4) and LHD experimental group 4)

1) Interdisciplinary Graduate School of Engineering Science, Kyushu University, Kasuga, Fukuoka 816-8580, Japan

2) Department of Material Science, Shimane University, Matsue, Shimane, 690-8504, Japan

3) Research Institute for Applied Mechanics, Kyushu University, Kasuga, Fukuoka 816-8580, Japan

4) National Institute for Fusion Science, Oroshi, Toki, Gifu 509-5292, Japan

e-mail contact of main author: tokitani@riam.kyushu-u.ac.jp

**Abstract.** Glow discharge cleaning (GDC) is a widely used technique for wall conditioning in fusion experimental devices. Though the cleaning effects of GDC are essentially related to the microscopic modification of the wall surface, there are few reports about it. In the present study, samples of wall materials were exposed to GDC plasma of hydrogen, helium and neon in the Large Helical Device (LHD) by using the retractable material probe transfer system and examined microscopic modification by transmission electron microscopy (TEM) to understand the underlying mechanism of GDC. Based on the results of the material probe experiments, GDC of LHD was successfully improved. Reduction of the impurities in the LHD vacuum vessel was drastically improved by using Ne-GDC. In the case of Ne-GDC, the specimen surface was covered with very thick re-deposited layer of Fe and Cr. Due to its high sputtering efficiency and very shallow penetration, it is likely that neon atoms effectively sputtered surface contamination without remaining serious damage and themselves in the sub-surface region. Retained Ne can be successfully removed by the following short H-GDC.

### 1. Introduction

LHD is the largest heliotron-type plasma confinement device, and is equipped with superconducting magnetic coils. The first wall panels and the divertor plates of LHD are made of stainless steel (SUS316L) and isotropic graphite, respectively. The former is the major material in LHD, and the graphite area is only about 5 % of the total plasma facing area. The vacuum vessel temperature is limited up to 95 °C due to the cryogenic capability for superconducting magnetic coils. Wall conditioning is conducted by mild temperature (95 °C) baking, GDC and titanium or boron coating. Working gases for GDC are hydrogen (H), helium (He) and neon (Ne). Until the experimental campaign in 2002, He-GDC was most frequently conducted.

In large-size plasma confinement devices like LHD, GDC is applied as a convenient wall conditioning method. Helium is used for working gas in some cases. In case of the all stainless steel wall machine TJ-II stellarator, control of plasma density at medium and high power injection became difficult, because the helium implanted in the wall by He-GDC desorbed during main plasma discharge [1]. In case of LHD, in spite of pumping for 7 hours after He-GDC ( for about 8 hours), the residual helium gas was still detected in the vacuum vessel [2]. Such prolonged desorption of helium gas made the ICRF heating condition unstable, and helium leak test difficult. It is well known that helium atoms implanted into metals are deeply trapped by lattice defects such as vacancies and bubbles formed by their own irradiation even if they do not have sufficient energy for knock-on damage [3].

In order to solve these problems, the behavior of implanted helium in metals (stainless steel) must be investigated from a viewpoint of material science. In the present work,

therefore, microscopic modification and retention properties in metals exposed to He-, H-, Ne-GDC in LHD were studied and its impact on vacuum properties of LHD is discussed by using several kinds of analytical techniques complementally. Based on the experimental results more efficient GDC method in LHD was proposed.

## 2. Experimental Procedures

To examine the surface modification and retention properties in metals due to the He-, H- and Ne-GDC, GDC exposure experiments carried out in the LHD. Pre-thinned vacuum annealed stainless steel (SUS316L) disks of 3mm in diameter and stainless steel (SUS316L) plates of 0.1 mm thick were used as specimens. All specimens were electrochemically polished. The specimens mounted on the retractable material probe system attached to the LHD, which is the same electric potential as the vacuum vessel, were placed on a position similar to the first wall surface through the 4.5 lower port (4.5L) as shown in Fig. 1. The GDC-plasma was sustained with two electrodes inserted into the vacuum vessel from the 4.5 upper port (4.5U) and the 10.5 upper port (10.5U). Discharge parameters of the GDCs were summarized in table 1. Total fluence was roughly estimated at  $3.7 \times 10^{22}$  He/m<sup>2</sup>,  $4.1 \times 10^{22}$  H/m<sup>2</sup> and  $3.2 \times 10^{22}$  Ne/m<sup>2</sup> respectively, based on the total plasma-facing area of 780 m<sup>2</sup>. The temperature of the probe head during the GDCs was measured by thermocouples at the positions just beneath the specimens. It stayed almost constant near room temperature.

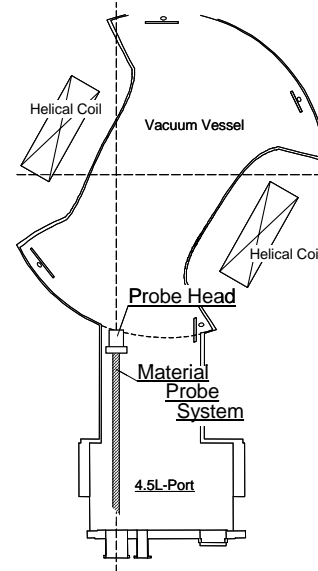


Fig. 1. Schematic view of the experimental position.

	Total discharge time	Voltage	Current
He-GDC	65h	200V	20A
H-GDC	71.5h	300V	20A
Ne-GDC	55h	200V	20A

Table 1. Discharge parameters of He, H and Ne-GDC.

After exposing to GDCs, microscopic damage, chemical composition and retention properties were examined by means of scanning electron microscopy (SEM), atomic force microscopy (AFM), transmission electron microscopy (TEM), energy dispersive spectroscopy (EDS) and thermal desorption spectroscopy (TDS). For cross-sectional observation of the damaged area, focus ion beam (FIB) technique was used to make a cross-sectional thin TEM sample [4].

Additional deuterium irradiation to the specimen pre-exposed to He-, H- and Ne-GDC was carried out in order to confirm the change of deuterium retention properties due to the GDCs. Samples of SUS316L ( $10 \times 10 \times 0.1$  mm<sup>3</sup>) exposed to GDCs were irradiated with 2 keV-D<sup>+</sup> at room temperature up to dose of  $1 \times 10^{22}$  D<sup>+</sup>/m<sup>2</sup>. And then the specimens were transferred into a TDS apparatus, where the thermally desorbed deuterium gas was measured with a high-resolution quadrupole mass spectrometer by heating up to 1400 K with a ramping rate of 1 K/s. This device makes it possible to distinguish the small difference in mass of helium (<sup>4</sup>He: m=4.0026 amu) and deuterium gas (D<sub>2</sub>: m=4.0282 amu) [5]. Desorption rate of deuterium was quantitatively calibrated by comparing with helium standard leak with specific

relative ionization efficiency.

### 3. Results and Discussion

#### 3.1. Microscopic modification and impurity depositions by GDCs

Fig. 2 shows TEM images of the pre-thinned SUS316L specimens exposed to He-, H- and Ne-GDC for 65h, 71.5h and 55h, respectively. The incident energy of these GDCs was at most about 200 eV, 300 eV and 200 eV, respectively. The temperature of the specimen holder during GDCs stayed almost constant near room temperature.

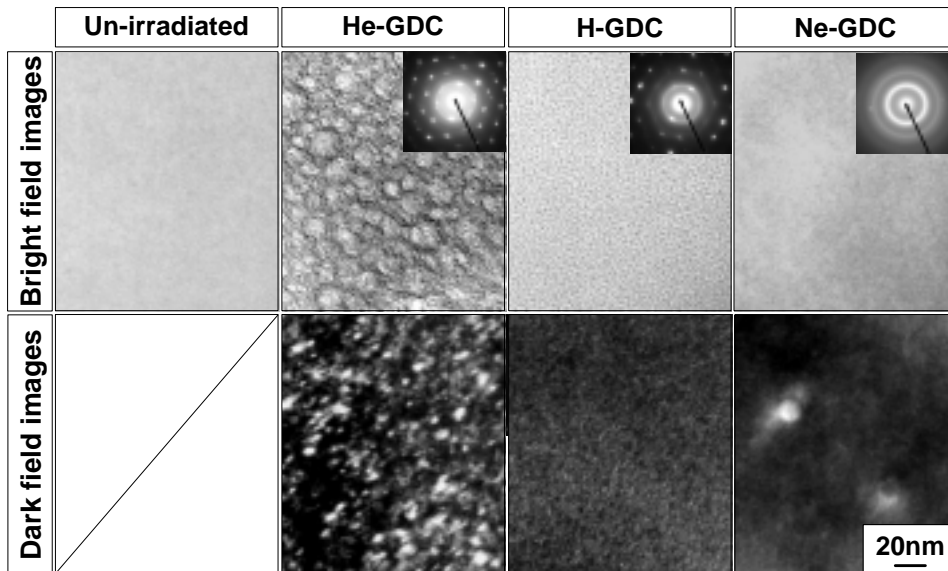


Fig. 2 TEM images after three GDCs, bright field images at large deviation parameter condition (upper series). White dot contrast in dark field images show dislocation loops (lower series).

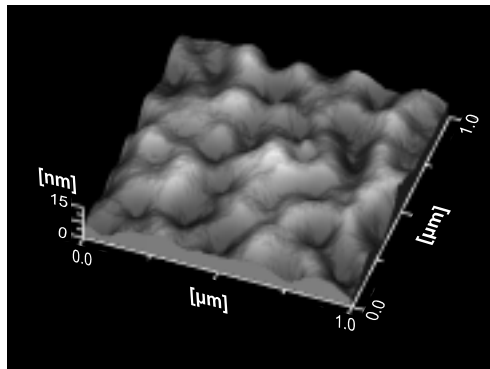


Fig. 3 Surface morphology of SUS316L after exposed to a He-GDC as observed by AFM.

Special features of He-GDC were rather strong sputtering erosion and heavy damage at the subsurface region; formation of dense bubbles with size of 2-20 nm, dislocation loops and cracks connecting the bubbles. Such a heavy damage structure was formed in spite of low incident energy. It is known that despite of insufficient irradiation energy

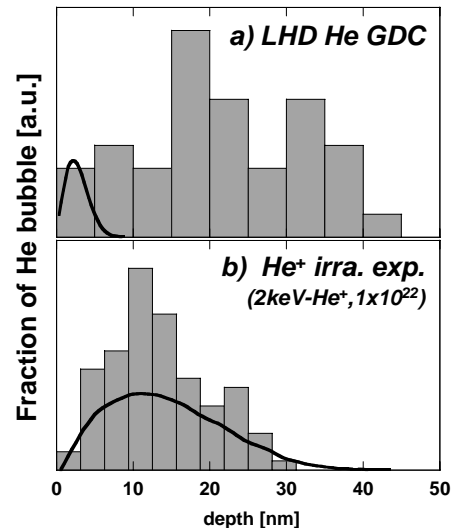


Fig. 4 (a) Depth distribution of helium bubbles in SUS316L exposed to He-GDC and (b) irradiated with 2keV-He<sup>+</sup> at room temperature to a fluence of  $1 \times 10^{22}$  He/m<sup>2</sup>. Depth distribution of the helium calculated by TRIM91-code was also plotted together.

for knock-on damage, injected helium atoms aggregate by themselves without any pre-existing vacancies and form dense helium bubbles [3]. Surface morphology obtained by a high resolution micrograph of AFM observation of the SUS316L specimen after the exposure is shown in Fig. 3. The surface is covered with dimples of about 200-400 nm in size. They are probably formed by exfoliation of blisters. Such large dimples and large bubbles have not been observed for a irradiation with 2 keV-He<sup>+</sup> at room temperature with comparable fluence [6]. In the case of helium ion irradiation experiment at room temperature, very dense helium bubbles of about 1-2 nm and dislocation loops were observed. Formation of dense helium bubbles, exfoliation of blisters and cracks lead to the increase of the effective surface area of the materials. It is expected that the increase in surface area causes adsorption of impurities gas existing in the vacuum vessel.

The depth distribution of helium bubbles formed in SUS316L exposed He-GDC is plotted in Fig. 4 together with the depth distribution of the helium calculated by TRIM91-code for 200 eV-He<sup>+</sup>. The data for irradiation experiment with 2keV-He<sup>+</sup> at room temperature is also plotted in the Fig. 4 for comparison. In case of He-GDC, the helium bubble was distributed deeper than the injected range. In contrast, in case of helium ion irradiation, distribution of a helium bubble agrees well with the injected range. This difference seems to be the result of the concentration of vacancies formed by knock-on process. In the case of 2 keV-He<sup>+</sup>, almost all the injected helium is trapped by the radiation induced vacancies which are formed in the helium injected range. In He-GDC case, since radiation induced vacancies are not formed, injected helium atoms can diffuse far deeper than the injected range, until it form their stable clusters. It is likely that some part of helium trapped in the heavily damaged region may release gradually through the nano-cracks connecting the bubbles and the surface. The prolonged helium release currently observed at LHD after He-GDC can be explained from this mechanism [2]. As shown in Fig. 5, desorption of helium is also affected by hydrogen discharge; in spite of no helium supply from outside, helium content in plasma increased during hydrogen discharges performed just after He-GDC. Fig. 6 shows the TDS spectrum of helium after He-GDC, with a ramping rate of 1 K/s. Retention of significant amount of helium was clear. Most of them desorbs at low temperatures between room temperature (300 K) and 750 K. This fact corresponds with the undesired desorption of helium observed in LHD during the discharges with hydrogen gas puffing.

On the other hand, accumulation of defects such as bubbles was not observed in the specimens exposed to H-GDC and Ne-GDC

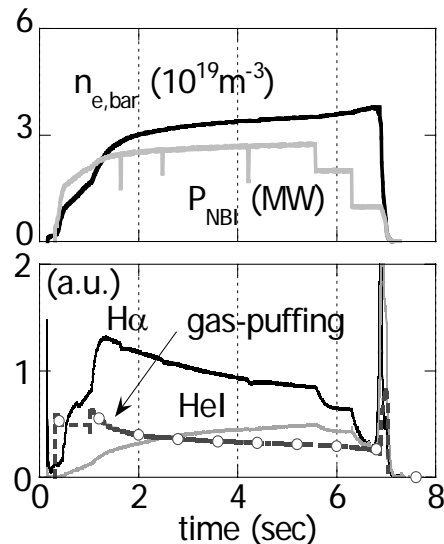


Fig 5. A typical discharge after He-GDC with hydrogen gas-puffing. (#26500)

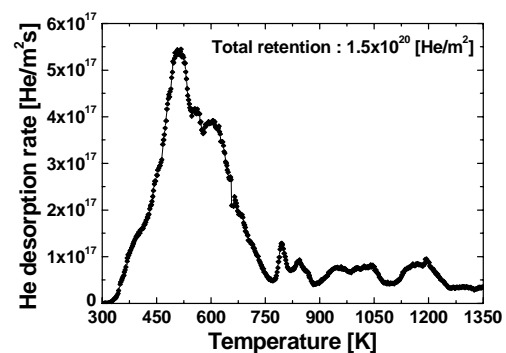


Fig 6. Thermal desorption spectrum of helium obtained from SUS316L after He-GDC.

(see Fig. 1). After exposure, impurity deposits were also identified on the specimens. Fig. 7 shows the electron diffraction pattern and the dark field image of deposition layer formed on SUS316L specimens exposed to GDCs. White contrasts show individual crystal grains of deposits. Especially, in case of Ne-GDC, the contrast of diffraction pattern is the clearest. This means that the specimen surface was covered with thick deposition layer. Due to its high sputtering efficiency, about ten times higher than that of helium, and very shallow penetration, it is likely that neon atoms effectively sputtered surface contamination without remaining serious damage and themselves in the sub-surface region. The element of deposition layers detected by EDS is mainly Fe and Cr, which were probably sputtered from the first wall of LHD (SUS316L). In the case of H-GDC, because the energy is insufficient for knock-on damage, the irradiation damage was not formed. Furthermore, due to its low sputtering efficiency, re-deposition of impurities is also very little (see Fig. 7).

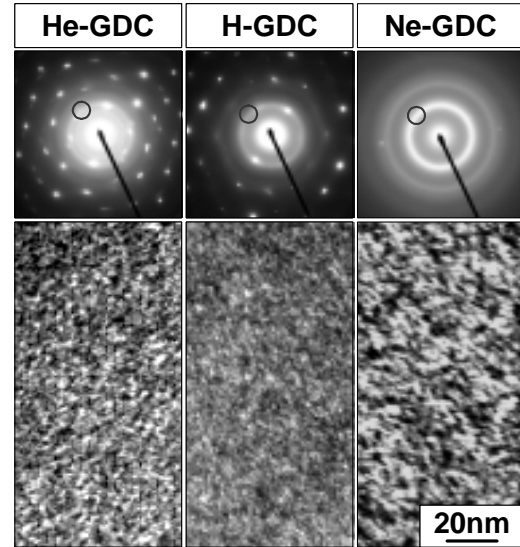


Fig. 7 Electron diffraction pattern and the dark field image of deposition layer formed on SUS316L exposed to GDCs. White dots show individual crystal grains of deposits.

### 3.2. Cross-sectional observation by FIB technique

In order to clearly understand of the depth distribution of internal damage, cross-sectional TEM observations were performed by using FIB technique. The results were shown in Fig. 8. Position of the top incident surface is noted by the arrows in each micrograph. In case of He-GDC (Fig. 8 (a)), very heavy damage such as large bubbles formation and surface roughening occurred in the top surface layer of about 10 nm thick (noted by (1) in the figure). It is considered that re-deposited materials such as Fe and Cr (see Fig. 7) also exist in this layer. In the second surface layer noted (2), about 30 nm thick, small helium bubbles (1-2 nm) were formed in the matrix. This result corresponds well with that of stereoscopic observation shown in Fig. 4. In contrast, for Ne-GDC (Fig. 8 (b)), re-deposited layer of 2-3 nm thick was clearly formed on the top surface (noted (3)) but no observable defects exist in both deposited layer and matrix. These results indicate that smooth surface without heavy damage can be obtained by Ne-GDC.

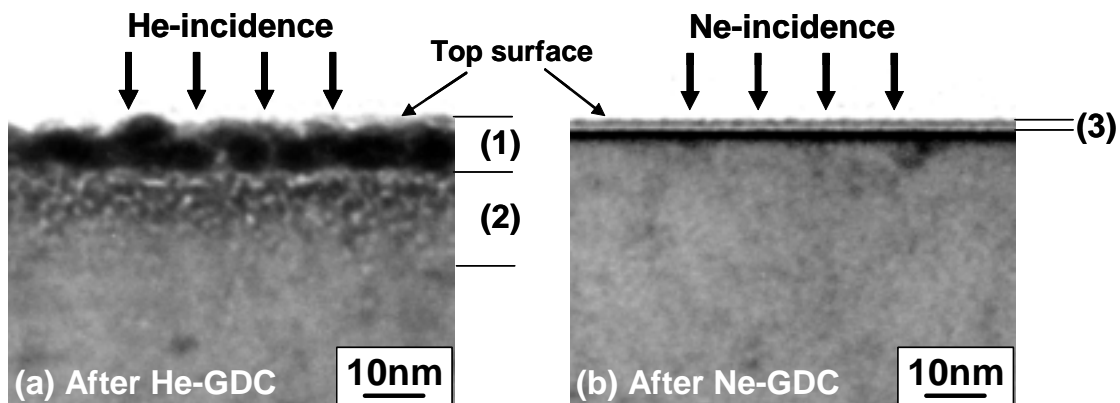


Fig. 8 Cross-sectional TEM observation on SUS316L by using a FIB technique. (a) After exposed to He-GDC, (b) after exposed to Ne-GDC.

### 3.3. Retention of deuterium after GDCs

Fig. 9 shows TDS of deuterium injected in the SUS316L specimens pre-exposed to He-(65h), H-(71.5h) and Ne-GDC(55h). Deuterium irradiation was performed subsequently at room temperature with 2 keV-D<sup>+</sup> up to dose of  $1 \times 10^{22}$  D<sup>+</sup>/m<sup>2</sup> is plotted in Fig. 9 (a), and without pre-exposes case (fresh specimen) was also shown in Fig. 9 (b). In case of the fresh one, thermal desorption spectra of deuterium is broad, and desorption is continued from 300 K to 500 K, but a sharp peak has appeared in the samples exposed to GDCs. The total retention is shown in Fig. 10. The fresh specimen has the highest deuterium retention. Namely, it was shown that the total retention of deuterium becomes lower by performing GDCs. Its mechanism is not understood well at the present, but it may have influenced that the oxide thin film of the surface was removed by performing GDCs. It was reported that an oxide film at the surface affects the retention and the diffusion of deuterium [7,8].

He-GDC showed highest deuterium retention and Ne-GDC showed lowest deuterium retention among the three GDCs. In the case of He-GDC, most of the injected deuterium ions (2 keV) are stopped in the heavily damaged layer of about 40 nm (see Fig. 4), because their projected range is about 20 nm. Therefore, it is considered that possible trapping sites for deuterium injected in the sample exposed to He-GDC is helium bubbles and strong stress field around them. It was reported that the stress fields around the highly pressurized helium bubbles in tungsten act the effective trapping sites of deuterium [9]. In contrast with He-GDC, Ne-GDC showed lowest retention of deuterium. Sufficient amount of trap sites for injected deuterium does not exist, because radiation induced defects are scarcely formed.

In case of H-GDC, desorption temperature shifts to lower side comparing with He-GDC, Ne-GDC and even the fresh specimen case. Most of the retained deuterium detraps up to 95 °C. We can say that this is one of a surface cleaning effect of H-GDC. This result indicates that it is possible in LHD to remove hydrogen effectively from the surface treated by H-GDC by the usual baking at 95 °C.

### 3.4. Improvement of GDC

Based on the results of the material probe experiments mentioned above, improved GDC technique was proposed; a two-step GDC method, combination of a Ne-GDC for efficient

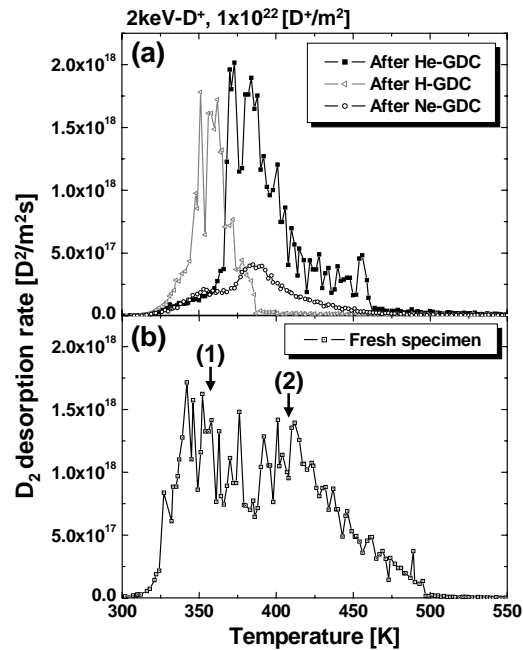


Fig. 9 Thermal desorption spectra of deuterium (a) with pre-exposes of GDCs and (b) without pre-exposes (Fresh specimen).

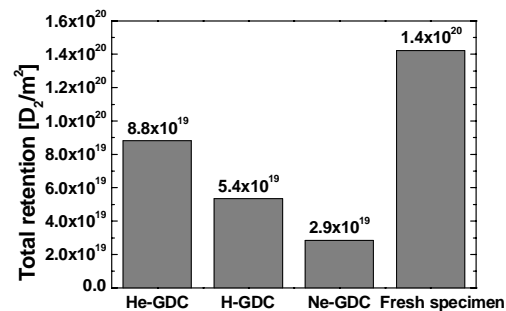


Fig. 10 Total desorption of deuterium in SUS316L, After GDCs and fresh specimen.

sputtering of surface contamination and a successive short H-GDC to desorb Ne retained during the first Ne-GDC. At the beginning of the experimental campaign in 2003, this two-step method was conducted to shorten the wall conditioning process and suppress the undesired desorption of the working gas of the GDC. Fig. 11 shows the reduction of partial pressure of  $M=28$  (CO) measured by quadrupole mass spectrometer during He-GDC and Ne-GDC. The decay time for Ne-GDC is much shorter and the achieved partial pressure was one order lower than those for He-GDC. These results are due to the high sputtering yield and very shallow penetration of Ne-GDC. After the Ne-GDC phase, H-GDC was conducted to remove implanted Ne in the first wall panels and the divertor plates. The partial pressure of Ne was reduced to the initial level after about 12 hours of H-GDC.

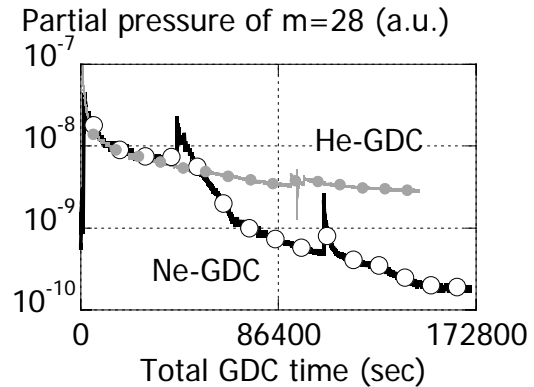


Fig. 11 Partial pressure of  $m=28$  versus total GDC time.

#### 4. Summary

The material probe experiments were carried out by exposing the SUS316L specimens to three different types of GDCs in LHD. Special features of He-GDC were rather strong sputtering erosion and heavy damage at the subsurface region; formation of dense bubbles with size of 2-20 nm, dislocation loops and cracks connecting the bubbles. The surface is covered with large dimples which seem to be formed by exfoliation of blisters. Such a heavily damaged structure leads to an increase of the effective surface area of a LHD vacuum vessel wall. It was suggested that He-GDC has a disadvantage as a wall conditioning. On the other hand, in cases of H-GDC and Ne-GDC, irradiation damages were not observed, though the surface was covered by re-deposited layer for Ne-GDC.

Depth distribution of damage and re-deposited layer was observed by cross sectional TEM technique using FIB. In case of Ne-GDC, smooth surface and no heavy damage was confirmed.

The influence of the GDCs on the deuterium retention was also examined. The sample exposed to He-GDC showed highest deuterium retention while Ne-GDC showed lowest. In case of H-GDC, most of deuterium desorbs up to 95°C.

It is considered that Ne-GDC and H-GDC is more suitable for GDC. At the beginning of the experimental campaign in 2003, Ne-GDC was conducted for efficient wall conditioning, due to its high sputtering efficiency and very shallow penetration. After the Ne-GDC phase, short H-GDC was conducted to remove implanted Ne.

It should be emphasized that understanding of characteristic feature of the microscopic processes of damage and surface modification for each GDC with different working gas was very effective for improvement of wall conditioning process of LHD.

**References**

- [1] D. Tafalla, F.L. Tabares, J. Nucl. Mater. 290-293 (2001) 1195-1198
- [2] H. Suzuki et al., J. Nucl. Mater. 313-316 (2003) 297-301
- [3] H. Iwakiri et al., J. Nucl. Mater. 283-287 (2000) 1134-113
- [4] S. Rubanov et al., Micron 35 (2004) 549-556
- [5] S. Hiroki et al., J. Nucl. Mater. 224 (1995) 293-298
- [6] M. Tokitani et al., J. Nucl. Mater. 329-333 (2004) 761-765
- [7] Y. Ishikawa et al., Vacuum, 47, 6-8, 701-704 (1996)
- [8] T. Hino et al., J. Nucl. Mater. 329-333 (2004) 673-677
- [9] H. Iwakiri et al., J. Nucl. Mater. 307-311 (2002) 135-138

## Experimental study of particle transport and density fluctuation in LHD

K.Tanaka<sup>1)</sup>, C. Michael<sup>1)</sup>, A. Sanin<sup>1)</sup>, L.N. Vyacheslavov<sup>1)</sup>, K.Kawahata<sup>1)</sup>, S. Murakami<sup>3)</sup>, A. Wakasa<sup>4)</sup>, H. Yamada<sup>1)</sup>, J. Miyazawa<sup>1)</sup>, S. Morita<sup>1)</sup>, T. Tokuzawa<sup>1)</sup>, T.Akiyama<sup>1)</sup>, M.Goto<sup>1)</sup>, K. Ida<sup>1)</sup>, M. Yoshinuma<sup>1)</sup>, I.Yamada<sup>1)</sup>, M. Yokoyama<sup>1)</sup>, S. Masuzaki<sup>1)</sup>, T. Morisaki<sup>1)</sup>, R.Sakamoto<sup>1)</sup>, H.Funaba<sup>1)</sup>, A.Komori<sup>1)</sup> and LHD experimental group

1)National Institute for Fusion Science, 322-6 Oroshi, Toki, 509-5292, Japan

2)Budker Institute of Nuclear Physics, 630090, Novosibirsk, Russia

3)Department of Nuclear Engineering, Kyoto University, Kyoto 606-8501, Japan

4)Graduate School of Engineering, Hokkaido University, Sapporo, 060-8628, Japan

e-mail contact of main author: ktanaka@LHD.nifs.ac.jp

**Abstract.** A variety of electron density ( $n_e$ ) profiles have been observed in Large Helical Device (LHD). The density profiles change dramatically with heating power and toroidal magnetic field ( $B_t$ ) under the same line averaged density. The particle transport coefficients, i.e., diffusion coefficient ( $D$ ) and convection velocity ( $V$ ) are experimentally obtained in the standard configuration from density modulation experiments. The values of  $D$  and  $V$  are estimated separately in the core and edge. The diffusion coefficients are found to be a strong function of electron temperature ( $T_e$ ) and are proportional to  $T_e^{1.7 \pm 0.9}$  in the core and  $T_e^{1.1 \pm 0.14}$  in the edge. Edge diffusion coefficients are proportional to  $B_t^{-2.08}$ . It is found that the scaling of  $D$  in the edge is close to gyro-Bohm-like in nature. Non-zero  $V$  is observed and it is found that the electron temperature gradient can drive particle convection, particularly in the core region. The convection velocity in the core reverses direction from inward to outward as the  $T_e$  gradient increases. In the edge, convection is inward directed in most cases of the present data set. It shows a modest tendency, being proportional to  $T_e$  gradient and remaining inward directed. However, the toroidal magnetic field also significantly affects the value and direction of  $V$ . The density fluctuation spectrum varies with heating power suggesting that it has an influence on particle transport. The value of  $k_{\perp} \rho_i$  is around 0.1, as expected for gyro-Bohm diffusion. Fluctuations are localized in both positive and negative density gradient regions of the hollow density profiles. The fluctuation power in each region is clearly distinguished having different phase velocity profiles.

### 1. Introduction

Particle transport of bulk ions and electrons is one of the most important issues of magnetically confined plasma research. However, compared with energy transport study, fewer works have been done. This is because of the difficulties of the experimental estimation of the particle source and the existence of the convection term in the particle balance equation. These make estimation of particle transport coefficients, i.e., diffusion coefficients ( $D$ ) and convection velocity ( $V$ ) impossible from simple particle balance analysis in the equilibrium state. Large Helical Device (LHD) is a large heliotron whose operational envelope extends towards the fusion relevant regime. Although thermal transport has been discussed in many reports, this is the first systematic study of the bulk ion and electron particle transport in LHD. The diffusion coefficients and convection velocities are separately estimated from the propagation of periodically modulated density by controlling the gas puff.

In most of the operational regimes of LHD, particle transport is dominated by anomalous transport. Therefore, experimental study of the turbulence is also important. In this paper, characteristics of electron density fluctuations, which can play a role on particle confinements, are also described.

### 2. Density profiles in LHD

The density profiles in LHD change with the magnetic configuration, magnetic field strength, and heating power. This is because the characteristics of particle transport are determined by these experimental conditions. Figure 1 show  $T_e$  and  $n_e$  profiles at different neutral beam injection (NBI) heating power. The magnetic configuration is the so-called standard configuration, whose magnetic axis position ( $R_{ax}$ ) is 3.6m. This configuration has the largest plasma volume and achieves the highest stored energy and best energy confinement improvement [4].

As shown in Fig.1 (a),  $T_e$  increases with increasing heating power. The shape of the  $T_e$  profiles remains parabolic and peaked at the center almost regardless of the heating power. On the other hand,  $n_e$  profiles change dramatically from peaked one to hollowed one with increase of the heating power. The value of  $n_e$  is non-zero at the last closed flux surface (LCFS), which is labeled as having a normalized radius  $\rho$  equal to 1, although  $T_e$  is almost zero at this position. This is due to the existence of an ergodic region, which has finite connection length and located outside of LCFS. The plasma can be confined in this ergodic region. It is known from measurements of the spatial profile of  $H_\alpha$  radiation that the peak of particle source is always located outside of LCFS surface when  $n_e$  at  $\rho = 1$  is higher than  $1 \times 10^{18} \text{m}^{-3}$ . In addition, particle fuelling from NBI is negligible in these cases. Therefore, the distinction between  $n_e$  profiles in Fig.1 (b) is not due to the difference of the particle source deposition but due to the dissimilarity in the transport. The density profiles also vary with magnetic configuration. At similar collision frequencies, the  $n_e$  profiles tend to become more hollow as  $R_{ax}$  increases [5]. In this paper, we concentrate only on the dependence of particle transport on heating power and  $B_t$  in standard configuration. The heating scheme used is NBI, whose power is scanned from 1MW to 8.5MW in this series of experiments. The line averaged density is almost kept constant to be free from the density dependence of the particle transport. Investigated plasmas lie in the plateau and so-called  $1/v$  region, where helical ripple transport is enhanced. The normalized collisionality ( $v_{*h} = v_{ei} q R / \epsilon_{h,eff}^{1.5} v_{th}$ ) is 0.26~2.6 at  $\rho=0.75$ . The gas species is hydrogen.

### 3. Density Modulation Experiments in LHD

The particle flux can be written as the sum of diffusion and convection terms as follows:

$$\Gamma = -D\nabla n_e + n_e V . \quad (1)$$

The particle balance equation is the following:

$$\frac{\partial n_e}{\partial t} = -\nabla \cdot \Gamma + S = -\frac{1}{r} \frac{\partial}{\partial r} r \Gamma + S . \quad (2)$$

Here,  $S$  is a particle source rate. If the particle source, which is located at the edge, is modulated, the density perturbation propagates from the edge to the core. The parameters  $D$  and  $V$  characterize this propagation. From the analysis of modulated components,  $D$  and  $V$  can be determined independently of the absolute value of the particle source [6], which is difficult to estimate experimentally. For this analysis, the source profiles (only relative shape) from 1-D calculations of the neutral penetration [7] are used.

Figures 2 (a) and (b) show the amplitude and phase profiles of line-integrated measurements for two discharges measured by the multi channel far infrared interferometer [2]. Modulation frequencies of 2, 5 and 10Hz are chosen to get several periods during the density flat top interval to ensure accurate measurements of phase and amplitude. A 5 Hz modulation was applied for the 5.2 MW heating case and 2 Hz modulation was applied for the 1 MW heating case. When core diffusion is lower, modulations cannot reach the core region

and results become insensitive to core transport. Modulations at lower frequency can penetrate deeper in the core. At lower heating power the diffusion is smaller as described in next section. So for the low diffusion case, a 2 Hz modulation was employed to estimate core diffusion coefficients. The modulation amplitude is kept less than 4 % of line averaged density in order to avoid modification of the underlying transport.

The modulated part of particle balance equation can be expressed in cylindrical geometry by the following equation:

$$\frac{\partial^2 \tilde{n}_e}{\partial r^2} + \left( \frac{1}{r} + \frac{1}{D} \frac{\partial D}{\partial r} - \frac{V}{D} \right) \frac{\partial \tilde{n}_e}{\partial r} - \left( \frac{V}{rD} + \frac{1}{D} \frac{\partial V}{\partial r} \right) \tilde{n}_e - i \frac{\omega}{D} \tilde{n}_e + \frac{\tilde{S}}{D} = 0. \quad (3)$$

Here, tilde symbols indicate modulated components;  $\omega$  indicates modulation frequency. The  $n_e$  tilde is complex function, which has both amplitude and phase information. The  $D$  and  $V$  are obtained from the fitting the solution of Eq. (3) to experimental data. Since the interferometer measures line integrated quantities, line-integrals of solutions to Eq. (3), parameterized by  $D$  and  $V$ , are fitted to the measured data.

Figure 2 shows examples of integrated modulation amplitude and phase at different heating power. A clear difference is observed between two cases. The amplitude and phase are calculated by the correlation analysis. The error bar is the uncertainty of the determination of phase and amplitude. The amplitude and phase profiles are calculated using model profiles of  $D$  and  $V$  as shown in Fig.3. Because the core and edge transport can be different, two fitting variables for both  $D$  and  $V$  are used. One is the core value ( $D_{\text{core}}$ ,  $V_{\text{core}}$ ) and the other is edge value ( $D_{\text{edge}}$ ,  $V_{\text{edge}}$ ). The profiles of  $D$  are assumed to be constant in the core and edge and change at  $\rho = 0.7$ . The value of  $V$  is zero at  $\rho = 0$  and  $V$  profiles are assumed to vary linearly with  $\rho$ , changing slope at  $\rho = 0.7$ . The values of  $V$  at  $\rho = 0.7$  and  $\rho = 1.0$  are taken to represent  $V_{\text{core}}$  and  $V_{\text{edge}}$  respectively. The transition points of  $D$  and  $V$  are fixed at  $\rho = 0.7$  in this series of analysis in order to make fitting more stable. As shown in Fig.2, measurements and calculation agree reasonably. The estimation errors of  $D$  and  $V$  in Fig.3 originate from estimation inaccuracy of modulation amplitude and phase.

## 4. Characteristics of transport coefficients

### 4.1 Particle Diffusion

As shown in Fig. 3 (a), the  $D$  is higher in the core than in the edge for both cases. Figure 4 shows the profile of electron thermal diffusion coefficients  $\chi_e$  obtained from power balance analysis by using PROCTR [7] code. Typically, the  $\chi_e$  profiles also show larger values in the core as well in LHD at standard configuration [5]. The predominance of core value of  $D$  and  $\chi_e$  was also observed in this series of modulation experiments. The lower values of  $D$  and  $\chi_e$  in the edge region are the reason for the steep edge gradients of  $n_e$  and  $T_e$ , which is observed in Fig.1 (a) and (b). The strong magnetic shear may play a role to stabilize microinstabilities and reduce diffusion in the edge region. The value of  $\chi_e$  is around one order magnitude larger than  $D$ . This is similar to the case of typical tokamak experiments.

A comparison of the experimentally determined  $D$  with a neoclassical estimate, calculated by the DCOM [9] code is presented in Fig. 5. In both cases, the experimental value is one order of magnitude larger than the neoclassical estimate. The diffusive particle flux is predominantly anomalous. This suggests that microturbulence plays an important role on diffusive flux.

The temperature dependence of  $D$  forms the basis for the investigation of the anomalous transport model. For Bohm-like diffusion, where particle transport is influenced by the long-wavelength fluctuations (up to plasma minor radius),  $D$  is proportional to  $T_e$ , while for gyro-Bohm-like diffusion, where short-wavelength fluctuations (around the ion gyro-radius) play a role,  $D$  is proportional to  $T_e^{1.5}$ . For this investigation, a systematic scan of NBI heating power ( $P = 1\sim 8.5\text{MW}$ ) keeping background density almost constant ( $n_{e\text{-bar}} = 1.2 \sim 1.5 \times 10^{19} \text{m}^{-3}$ ) is carried out at  $R_{\text{ax}} = 3.6\text{m}$ . The data set contains discharges at  $B_t = 2.8$  and  $2.75\text{T}$ . The small difference of  $B_t$  is not expected to affect the transport.

Figure 6 shows the  $T_e$  dependence of  $D_{\text{core}}$  and  $D_{\text{edge}}$ . The electron temperature in Fig.6 is the averaged value within  $\rho = 0.4 \sim 0.7$  for the core and  $\rho = 0.7 \sim 1.0$  for the edge. The data set include 2, 5, and 10Hz modulation frequencies. When core diffusion coefficients cannot be determined from fitting because of lower diffusion or higher modulation frequency, a spatially constant  $D$  was assumed. Then, the estimated  $D$  was taken as  $D_{\text{edge}}$ , because the analysis has sensitivity in the edge region in this case. The diffusion coefficient increases with  $T_e$  both in the core and edge regions. The fitted power-law scaling of the observed  $T_e$  dependences are  $D_{\text{core}} \propto T_e^{1.7 \pm 0.9}$  and  $D_{\text{edge}} \propto T_e^{1.1 \pm 0.14}$ . The difference of the  $T_e$  dependence in the core and edge suggests the existence of different types of turbulent transport in the core and edge. From the  $T_e$  dependence,  $D_{\text{core}}$  is gyro Bohm like rather than Bohm like. However, for the edge region the distinction between the two models is not as clear.

## 4. 2 Particle Convection

Hollow density profiles are observed in LHD in many discharges. This is a harsh contrast to tokamak plasmas, where most density profiles are peaked. As is shown in Fig.1, density profiles become hollow with an increase of  $T_e$ . The hollow density profiles clearly indicate the existence of the outward convection, because the particle source, which is localized out of LCFS, cannot maintain the hollow density profiles. In addition, density modulation experiments can estimate  $D$  and  $V$  separately, and results of many experimental discharges show an existence of the particle convection, which is the second term of Eq.(1). This fact suggests that off-diagonal terms of transport matrix contribute to the total particle flux. For example, to sustain the positive density gradient, which is observed at  $\rho = 0.6 \sim 0.9$  in 8.5MW heating case (see Fig.1(b)), in the equilibrium state, off-diagonal transport coefficients should determine the particle flux, since diffusion does not contribute to total particle flux in this region. The next question is which driving term or which gradient determines convective flux.

The change of the  $n_e$  profile in Fig.1 (b) suggests a correlation between  $V$  and  $T_e$  gradient. Figure 7 shows the  $T_e$  gradient dependence of  $V$ . The value of  $V$  at  $\rho = 0.7$  is considered to be  $V_{\text{core}}$ , and  $V_{\text{edge}}$  is considered to be the value at  $\rho = 1.0$ . The electron temperature gradient is the averaged over the region  $\rho = 0.4 \sim 0.7$  for core and  $\rho = 0.7 \sim 1.0$  for the edge. The edge convection is inward directed in the most cases. On the other hand,  $V_{\text{core}}$  changes direction from inward to outward with increasing of  $T_e$  gradient. The temperature gradient dependence of  $V_{\text{edge}}$  is not very clear although there is a modest tendency of decreasing  $V_{\text{edge}}$  with increasing  $T_e$  gradient. The dependence of  $V_{\text{core}}$  on  $T_e$  gradient is more pronounced. The core convection velocity shows a clear dependence on  $T_e$  gradient. Comparison with theoretical model of convection based on turbulence [10] is necessary for further understanding of the convection term.

## 4.3 The Effects of the Toroidal Magnetic Fields

The effect of  $B_t$  can give more clear remarks about whether diffusion is Bohm-like ( $D$  is proportional to  $B_t^{-1}$ ) or gyro-Bohm-like ( $D$  is proportional to  $B_t^{-2}$ ). The modulation experiments were done to study the effect of  $B_t$  on  $D$  and  $V$ . A comparison is made between two discharges at different  $B_t$  (1.49 and 2.75 T). In order to be free from the  $n_e$  and  $T_e$  dependence of  $D$  and  $V$ , the heating power and gas fuelling were adjusted to produce almost identical  $T_e$  profiles and similar line averaged density. The profiles of  $T_e$  and  $n_e$  are shown in Fig.8. The results for the estimated  $D$  and  $V$  are summarized in table.1. Since a relatively high modulation frequency of 10Hz was used to make the analysis possible during the short density flat top ( $\sim 1$ sec), a constant  $D$  profile, which mostly represents the edge value, is used for this analysis. The  $B_t$  dependence of  $D$ , which characterize the edge value is  $B_t^{-2.08}$ , which is very close to gyro-Bohm diffusion. Considering the  $T_e$  dependence ( $D_{\text{edge}} \propto T_e^{1.1 \pm 0.14}$ ), the edge diffusion is gyro-Bohm-like rather than Bohm-like. The gyro-Bohm nature is the same that of thermal diffusivity [4].

The effects of  $B_t$  is also seen in the character of the particle convection. At  $B_t = 1.49$ T, a strongly hollow profile was observed as shown in Fig.8 (b) and corresponding to this, the estimated  $V_{\text{core}}$  is outward directed. On the other hand, at  $B_t = 2.75$ T, flat density profiles are recorded as shown in Fig.8 (b) and the convection was observed to be inward directed in both the core and edge. As described in Section 4.2, the temperature gradient has clear correlation with  $V_{\text{core}}$ . However, the results in table 1 and Fig.8, indicate  $T_e$  gradient is not only parameter which drive core convection. For further investigation, the NBI power was scanned and modulation experiments were done at  $B_t = 1.5$ T.

Figure 9 shows comparison of  $T_e$  gradient dependence of  $V_{\text{core}}$  at low field ( $B_t = 1.5$ T) and high field ( $B_t = 2.75$  and 2.8T). The dataset at high field is the same data as one in Fig.7. The modulation frequency of the data set at low field was 2.5 and 5Hz. Because of the high recycling, averaged density could not be kept constant in this series of experiments. The density varies from 1.8 to  $5.0 \times 10^{19} \text{ m}^{-3}$  in the dataset at low field of Fig.9. As shown in Fig.9, at the same  $T_e$  gradient, the core convection tends to be higher and outward directed at lower field. Although the density dependence of  $V_{\text{core}}$  has to be kept in mind, the core convection reverses direction at higher  $T_e$  gradient at higher  $B_t$ .

## 5. Characteristics of Turbulence

As shown in Fig.5, diffusion is dominated by anomalous terms. To get a comprehensive picture of particle transport, it is necessary to measure microturbulence. The spectrum and spatial structure of fluctuations, dependence on the parameters of the discharge and correlation with transport characteristics can provide ideas to understand anomalous transport. In LHD, microturbulence was measured by using a  $\text{CO}_2$  laser Phase Contrast Imaging (PCI) Interferometer [11,12,13]. Since the length of scattering volume for the expected wavenumber region is larger than the plasma size for the  $10.6 \mu\text{m}$  infrared  $\text{CO}_2$  laser wavelength, no spatial resolution is expected along beam axis. However, by using strong magnetic shear of LHD, it is possible to get modest spatial resolution along the probe beam [14].

### 5.1 Spectrum Structure

The qualitative difference of the fluctuation spectra is observed at different NBI heating powers using PCI with 32-channel one-dimensional linear detector array. Figure 10 shows wavenumber ( $k$ ) and frequency ( $f$ ) spectra, which are measured by PCI at different heating power and similar line averaged densities. Spatial localization around the minor

radius was achieved by tilting the image of the detector array in plasma. The magnetic field shear is very strong in LHD. The field pitch angle reaches 40 degrees at the last closed flux surfaces compared with the zero angle in the plasma centre. The parallel wavenumber of fluctuations is much smaller than the perpendicular one. If the axis of one-dimensional detector array is set to be perpendicular to the particular magnetic field, only projections of fluctuations on the axis are recorded. The projected wavenumber at some other location becomes smaller as magnetic field direction is getting closer to the array axis, then contribution of signal decreases when projected wavenumber reaches the instrumental cut-off wavenumber. The axis of the linear detector image was set to be perpendicular to the magnetic field near upper last closed flux surfaces. Then signal is weighted here with a resolution around minor radius.

The measurements range of wavenumber and frequency ranges are  $k = 0.1 \sim 1.25\text{mm}^{-1}$  and  $f = 5 \sim 125\text{kHz}$  respectively. The measured wavenumber is comprised mostly of poloidal components. The peak wavenumber is  $0.2\text{ mm}^{-1}$  at 1MW heating and  $0.3\text{ mm}^{-1}$  at 6.5 MW heating. The value of  $k_{\perp}\rho_i$  is around 0.1, which is roughly equal to that expected for the gyro-Bohm diffusion model. In both case, fluctuation propagate in the electron diamagnetic direction in the laboratory frame.

As observed in Section 4.1, higher heating power causes larger diffusion. This observation can be compared with the properties of the fluctuations. As the diffusion coefficient is proportional to  $(\text{step size})^2/(\text{step time})$ , the anomalous component can be expressed as the  $(\text{eddy size})^2/(\text{eddy turnover time}) \sim (\text{frequency width})/(\text{wave number})^2$ . As shown in Fig.10, broad spectra in  $k$  are observed and the value of  $k$  at the peak of the wavenumber spectrum is reduced and the frequency spectrum is broadened at higher heating power. The change of the spectrum is qualitatively consistent with enhanced diffusion at higher heating power. The measured wavenumber is poloidal components, although radial components are more essential for transport. The shifting of peak wavenumber of radial components to lower values, when energy confinements degrade at lower  $B_t$ , is also observed in LHD [11]. Since the change in frequency spectrum width in Fig. 10 can be partly due to the increase of plasma rotation, simultaneous measurements of  $E_r$  or radial wavenumber-frequency spectrum, which is free from plasma rotation effects are necessary for more detailed discussion.

As shown in Fig.10, total fluctuation power is not very different or even slightly smaller at higher heating power, where diffusion is enhanced. This suggests that the fluctuation intensity is not the only parameter characterizing anomalous particle transport

## 5.2 Spatial Structure

Recently, a new technique was developed to measure spatial profile of fluctuations [12, 13]. By using a 48 (6 by 8) channel two-dimensional detector, it is possible to get fluctuation profile from single shot and single time by taking advantage of the strong magnetic shear. The one-dimensional PCI, which is described in the previous section, measures projected fluctuation picture to the axis of the array, which are integrated within measurements volume. The two dimensional PCI (2D PCI) records 2-D fluctuation picture integrated along injected beam direction as shown in Fig.11. This two-dimensional picture contains fluctuations propagating perpendicular to magnetic field lines, along the path of the probe beam. The propagation direction can be resolved by the spatial two-dimensional Fourier transform. The location of fluctuation can be determined from the position of the field, which is perpendicular to propagation direction.

The spatial profile of fluctuation power spectrum was measured by using 2D-PCI for  $k = 0.5 \sim 1.5\text{mm}^{-1}$  and  $f = 5 \sim 500\text{ kHz}$ . Figure 12 shows  $T_e$  and  $n_e$  profiles of target of the

measurements. The magnetic configuration is standard configurations ( $R_{ax}=3.6m$ ), which is the same as ones analyzed in section 2 ~ 4 and  $B_t$  is 2.75T. A peaked  $T_e$  and hollowed  $n_e$  profiles are observed as shown in Fig. 12. The density modulation was done for this discharge and shows outward convection in core, which is 0.24 m/sec at  $\rho = 0.8$  and inward convection at edge, which is -0.54 m/sec at  $\rho = 1.0$ . The diffusion coefficient was estimated to be  $0.05m^2/sec$  with spatially constant model.

Figure 13 shows contour plotting of the spectrum intensity in  $\rho$ -phase velocity space from laboratory frame. Maximum Likelihood Method (MLM) was applied to get fine spectrum resolution [15]. The maximum likelihood method has an advantage of fine spectrum resolution, but there are some uncertainties of the spectrum intensity. The several structures can be clearly seen in Fig.13, however, the intensity of each structure contains estimation error due to the nature of MLM.

Since fluctuations along beam axis in Fig.11 contribute to the signal, fluctuations from upper and lower of equatorial plane can be distinguished. The spectrum in positive and negative  $\rho$  region corresponds to top and bottom part of measured cross section in Fig.11. The poloidally rotating fluctuation as shown with blue arrow in Fig.11 have opposite direction in the top and bottom, therefore, poloidally rotating fluctuation components have a opposite sign in top and bottom region.

Asymmetries between top and bottom region is observed, however, the structures are similar in both regions. The spectrum consists of two parts. One is localized in positive gradient region, where  $|\rho| \leq 0.9$ , the other is localized in negative density gradient region, where  $|\rho| \geq 0.9$ . The phase velocity of the positive density gradient mode is close to  $E_r \times B_t$  poloidal rotation velocity with green lines in Fig.13. The radial electric field is calculated from ambipolar condition of neoclassical theory by GASRAKE code [16] with measured  $T_e$  and  $n_e$  profiles of Fig.12. The calculated  $E_r$  from neoclassical ambipolar condition reasonably agrees with measured  $E_r$  by charge exchange spectroscopy [17], which is not available in the discharge of Fig.12 and Fig.13.

On the other hand, spatial structure of the negative density gradient mode is complicated. Both electron and ion diamagnetic propagating components are observed. Presence of both electron and ion diamagnetic components, which is clearer in the bottom part, can be interpreted as an existence of strong velocity shear. The blue lines in Fig. 13 indicate velocity remainder after subtraction of drift velocity from  $E_r \times B_t$  poloidal rotation velocity. The drift velocity was calculated by the following equation with measured  $T_e$  and  $n_e$  profile in Fig.12.

$$V_{drift} = \frac{\nabla P}{en_e B_t} = \frac{k_B T_e}{e B_t} \left( \frac{1}{n_e} \frac{dn_e}{dr} + \frac{1}{T_e} \frac{dT_e}{dr} \right) \quad (4)$$

The blue lines pass the peak of the spectrum in edge region. This indicates negative density gradients mode propagates to ion diamagnetic direction with drift velocity in plasma frame. And the phase velocity changes rapidly in plasma edge making strong velocity shear. However, both calculated  $E_r \times B_t$  rotation and drift velocity is sensitive the profile of  $T_e$  and  $n_e$ . The measurements of  $E_r$  and more precise profile measurements of  $T_e$  and  $n_e$  profiles are necessary to confirm this.

The diffusion process is dominated by anomalous one as described in section 4.1. It is likely that convection is dominated by anomalous one as well, because total transport is anomalous one at standard configuration ( $R_{ax}=3.6m$ ). The fluctuations at positive density

gradient, where particle convection dominates particle transport, will contribute to particle convection and fluctuations in the negative density gradient region, where particle diffusion dominates particle transport, will contribute to particle diffusion. Observed difference of phase velocity indicates difference of underlying mechanisms of two modes.

## 6. Summary

Systematic studies using density modulation experiments were done to investigate particle transport characteristics at standard magnetic configuration in LHD. The density profiles vary with heating power and  $B_t$ . The edge diffusion coefficient is close to gyro-Bohm nature, where fluctuation wavelength around ion Larmor radius play an important role. The diffusion coefficient is larger in the core than at the edge. Particle convection is observed both in core and edge. The core convection velocity shows clear dependence on the  $T_e$  gradient. As the temperature gradient is increased,  $V_{\text{core}}$  changes direction from inward to outward. This is consistent with the fact that the density profile changes from peaked to hollow with an increase of heating power. However,  $B_t$  is also a key parameter to determine  $V_{\text{core}}$ . At higher  $B_t$ , the core convection reverse direction from inward to outward at larger  $T_e$  gradient. The edge convection velocity is inward directed in the most cases. A moderate tendency to decrease  $V_{\text{edge}}$  with increasing  $T_e$  gradient is also observed. The microturbulence measured by PCI shows qualitative correlation between measured spectrum and particle diffusion. Spatial profile of the turbulence measured by 2D PCI shows two different spatial structures. One localizes in positive density gradient region in core, the other localizes in negative density gradient region in edge. The former can contribute to particle convection, the latter can contribute to particle diffusion. More detailed systematic study of particle transport and characteristics of fluctuation about the density dependence and effect of magnetic configuration is underway and comparison with theoretical models of anomalous transport is planned.

## References

- [1] K. Narihara et al., Rev. Sci. Instrum., 72 (2001) 1122.
- [2] K. Kawahata et al., Rev. Sci. Instrum. **70**, (1999) 707.
- [3] K. Tanaka et al., Rev. Sci. Instrum. 75, (2004) 3429.
- [4] H. Yamada et al., in 18th Conference Proceedings of Fusion Energy 2000 (Sorrento, Italy 4-10 October 2000) IAEA (2001).
- [5] K. Tanaka et al., J. Plasma Fusion Res. Series, 4 (2001) 427.
- [6] K.W. Gentle et al., Plasma Phys. Contr. Fusion 29, (1987) 1077.
- [7] H.C. Howe, ORNL/TM-11521 (1990).
- [8] H. Yamada et al., Plasma Phys. Contrl. Fusion 44 (2002) A245.
- [9] S. Murakami et al., Nuclear Fusion 42 (2002) L19-L22.
- [10] X. Garbet et al., Phys. Rev. Lett. 91 (2003) 035001-1.
- [11] K. Tanaka et al., Rev. Sci. Instrum., Vol 74 (2003) 1633.
- [12] A. Sanin et al., Rev. Sci. Instrum. 75, (2004) 3439
- [13] L. N. Vyacheslavov et al., to be published 4<sup>th</sup> Triennial Special Issue of IEEE Transaction on Plasma Science.
- [14] S. Kado et al., Jpn. J. Appl. Phys., Part 1 34, (1995) 6492.
- [15] C. Michael et al., to be prepared for Rev. Sci. Instrum.
- [16] C.D. Beidler et al., Plasma Phys. Contr. Fusion 36, (1994) 317
- [17] K. Ida et al., Phys. Rev. Lett. 86 (2001) 5297.

TABLE I: *Effect of toroidal magnetic field  $B_t$  on particle diffusion and convection*  
*The positive and negative  $V$  indicate outward and inward convection respectively.*

Shot	Bt(T)	$D_{\text{edge}}(\text{m}^2/\text{sec})$	$V_{\text{core}}(\text{m}/\text{sec})$	$V_{\text{edge}}(\text{m}/\text{sec})$
48619	1.49	$0.43 \pm 0.13$	$5.43 \pm 2.89$	$-2.67 \pm 2.87$
48672	2.75	$0.12 \pm 0.004$	$-2.59 \pm 0.45$	$-3.32 \pm 0.28$

## Figure caption

*Fig.1 (a) Electron temperature and (b) density profiles under different NBI heating power. At  $R_{ax}=3.6m$ ,  $B_t=2.75T$  for 2.7 MW and 8.5MW heating,  $B_t=2.8T$  for 1MW heating. Temperature profiles are measured by Thomson scattering [1] and density profiles are measured by FIR [2] and  $CO_2$  [3] laser interferometers. Symbols in Fig.1 (a) indicate corresponding chord position of interferometers.*

*Fig.2 Comparison of modulation amplitude (a) and phase (b) profiles at different heating power. Circular and square symbols indicate measured value, lines indicate calculated values. A 5Hz modulation for 5.2MW and 2Hz modulation for 1MW injection were done.*

*Fig.3 (a) Estimated particle diffusion coefficients and (b) convection velocities. The dashed lines indicate upper and lower error. The positive and negative V indicate outward and inward convection respectively.*

*Fig.4 Profiles of electron thermal diffusion coefficients from power balance analysis.*

*Fig.5 Comparison between experimental values and neoclassical estimation of particle diffusion coefficients*

*Fig. 6 Electron temperature dependence of particle diffusion coefficients at  $R_{ax}=3.6m$ ,  $B_t=2.75, 2.8T$ .*

*Fig.7 The dependence of the convection velocity on electron temperature gradient*

*Fig. 8 Comparison of (a) electron temperature and (b) density profiles under different toroidal magnetic field.*

*Fig.9 The dependence of the core convection velocity on electron temperature gradient under different toroidal magnetic field*

*Fig.10 Comparison of (a) wavenumber and (b) frequency spectrum at different heating power*

*Fig.11 Measured cross section of phase contrast interferometer*

*Magnetic flux surfaces are shown every  $\rho = 0.1$  step from  $\rho = 0.1$  to 1.2. Magnetic configuration is standard configuration ( $R_{ax}=3.6m$ ). The red lines mark the path of  $CO_2$  laser beam.*

*Fig.12 (a) electron temperature and (b) density profiles during fluctuation measurements by two dimensional phase contrast imaging (2D PCI).  $R_{ax}=3.6m$ ,  $B_t=2.75T$ , NBI heating.*

*Fig.13 Contour plot of fluctuation power measured by 2D PCI. Dark color indicate stronger intensity. The dimension of the intensity is arbitrary unit. Positive and negative  $\rho$  indicate bottom and top part of measured position along beam axis in Fig.11 respectively. Positive velocity in top part and negative velocity in bottom part indicate electron diamagnetic direction. Negative velocity in top part and positive velocity in bottom part indicate ion diamagnetic direction. Green lines mark  $E_r \times B_t$  poloidal rotation velocity and Blue lines show remainder after subtraction ( $\nabla P \times B_t$ )-diamagnetic drift velocity from  $E_r \times B_t$  velocity.*

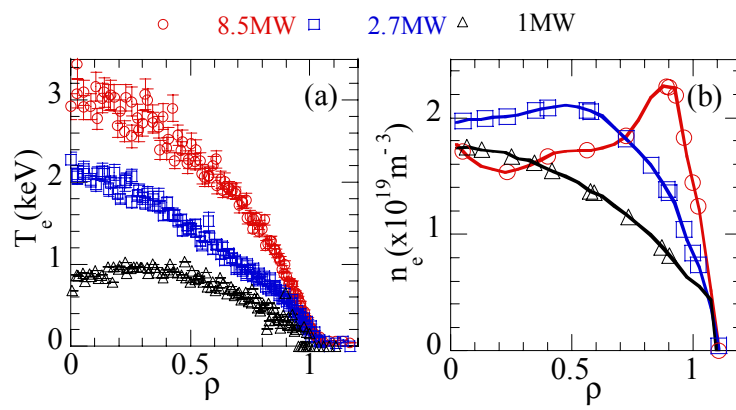


Fig.1

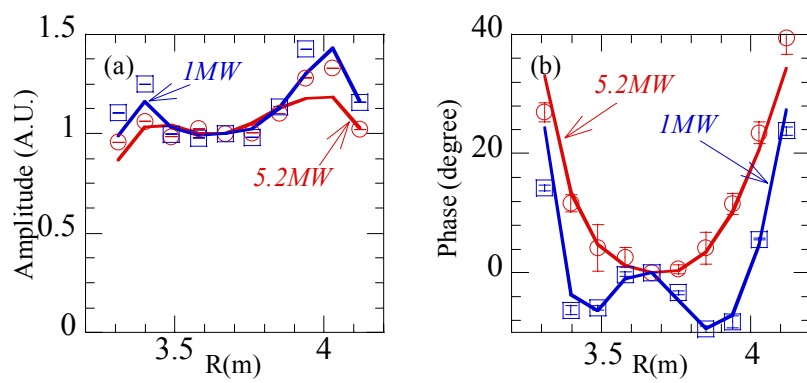


Fig.2

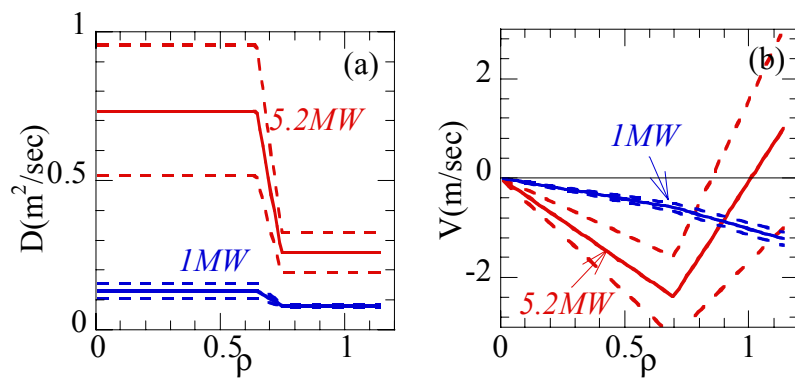


Fig.3

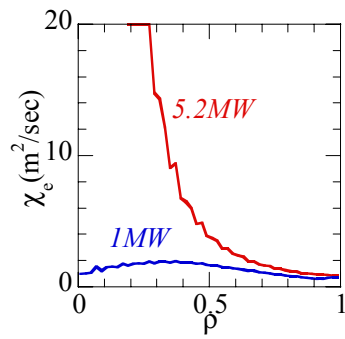


Fig.4

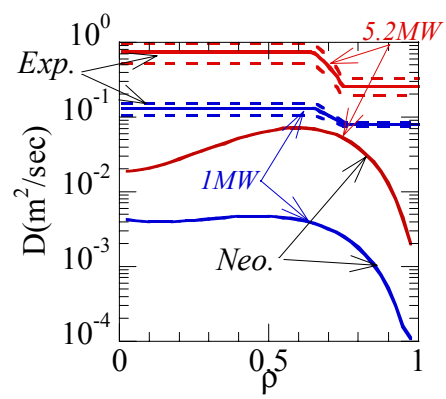


Fig.5

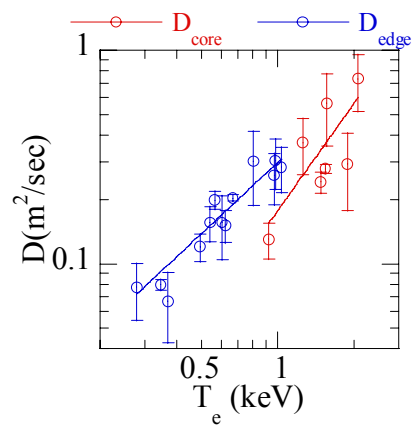


Fig.6

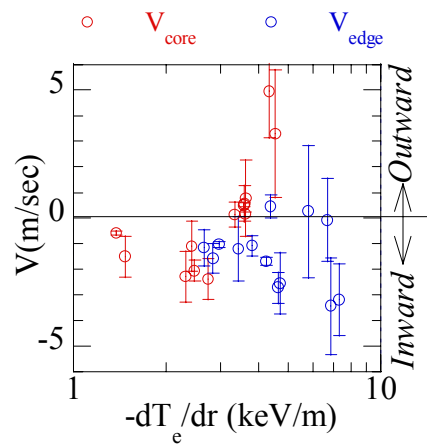


Fig.7

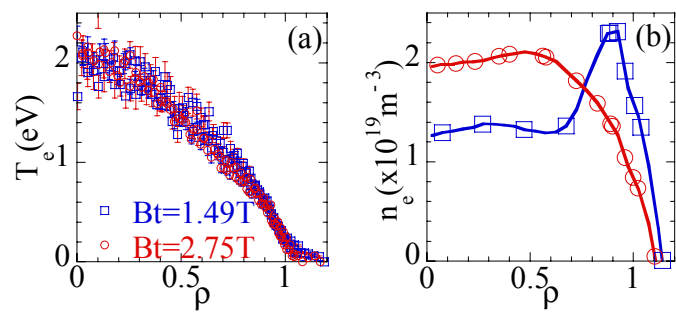


Fig.8

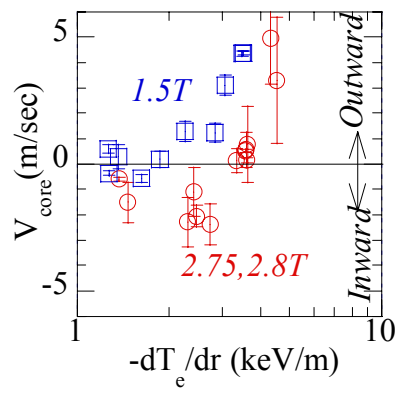


Fig.9

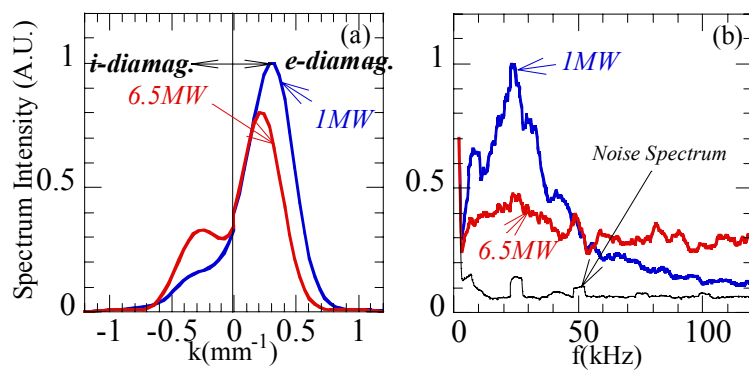


Fig.10

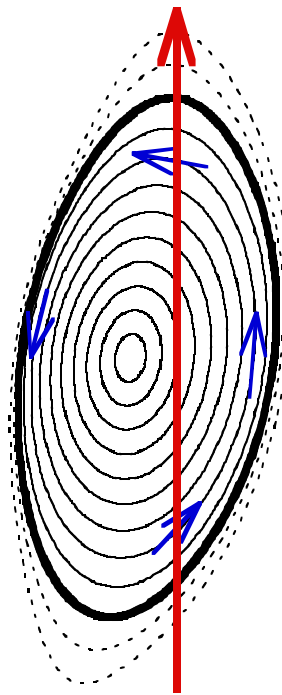


Fig.11

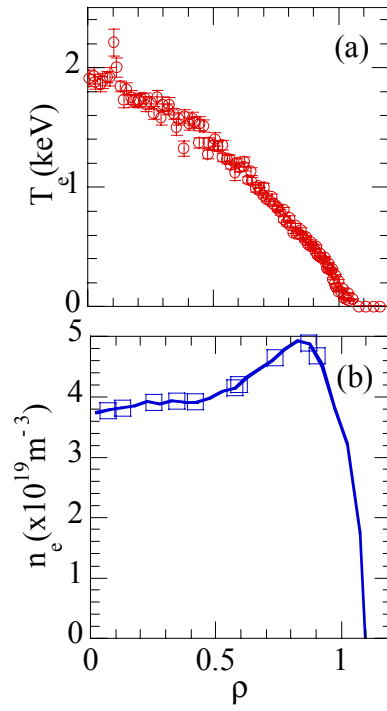


Fig.12

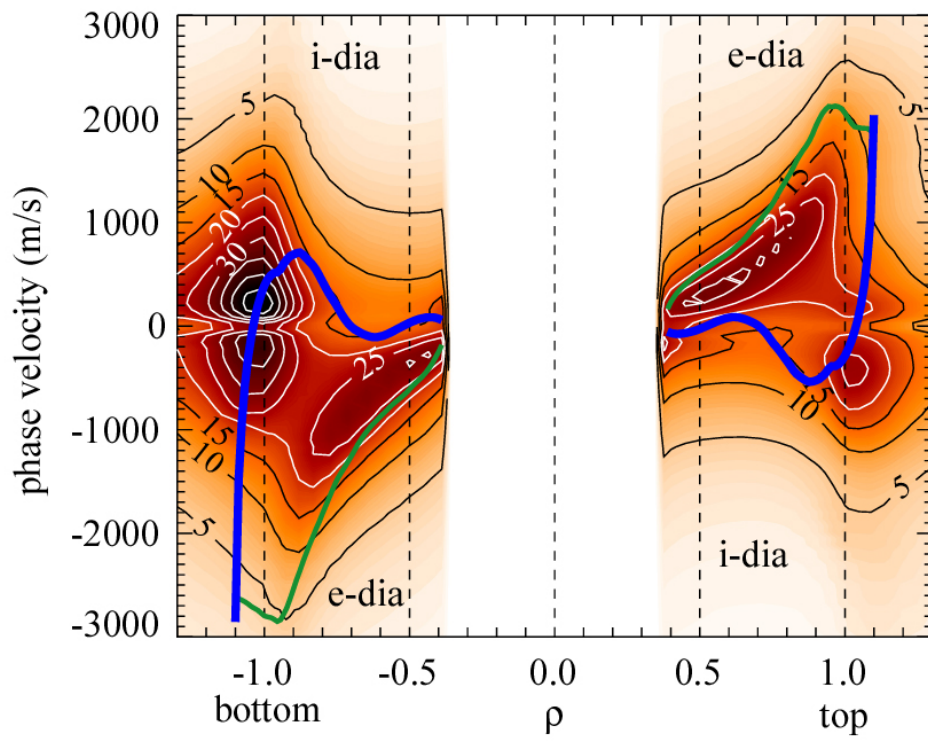


Fig.13

# Non-disruptive MHD Dynamics in Inward-shifted LHD Configurations

H. Miura<sup>1)</sup>, K. Ichiguchi<sup>1)</sup>, N. Nakajima<sup>1)</sup>, T. Hayashi<sup>1)</sup> and B.A. Carreras<sup>2)</sup>

1)National Institute for Fusion Science, 322-6 Oroshi, Toki, Gifu 509-5292, JAPAN

2)Oak Ridge National Laboratory, Oak Ridge, Tennessee 37831, USA

e-mail contact of main author:miura.hideaki@nifs.ac.jp

**Abstract.** Two kinds of nonlinear simulations are conducted to study behaviors of the pressure-driven modes in the Large Helical Device (LHD) plasma with the vacuum magnetic axis located at  $R_{ax} = 3.6\text{m}$  (so called inward-shifted configuration). One is the three-field reduced magnetohydrodynamic (RMHD) simulations. The other is the direct numerical simulations (DNS) of fully three-dimensional (3D) compressible MHD equations. The RMHD results suggest that the plasma behavior depends on the strength of the interaction between the unstable modes with different helicity. Similar plasma behaviors are also obtained in the DNS. In addition to some basic coincidence between RMHD and DNS, substantial toroidal flow generation is observed in the DNS. It is shown that toroidal flow can become stronger than the poloidal flow.

## 1 Introduction

The Large Helical Device (LHD) is a heliotron type device with a set of  $L=2/M=10$  helical coils with the major radius  $3.9\text{m}$  [1]. When the position of the vacuum magnetic axis  $R_{ax}$  is smaller than  $3.75\text{m}$ , the system is called “inward-shifted” configuration. Recent advances of the LHD experiments in inward-shifted configurations show that plasma is confined relatively well even though it passes through Mercier unstable region [2, 3]. It is reported in Refs.[2, 3] with  $R_{ax} = 3.6\text{m}$  vacuum magnetic axis, MHD instabilities with poloidal( $m$ ) and toroidal( $n$ ) Fourier modes  $(m, n) = (2, 1)$  appears in the course of the plasma pressure growth but disappears when the pressure (or the  $\beta$  value,  $\beta = 2p/|\mathbf{B}|^2$  where  $p$  is the pressure and  $\mathbf{B}$  represents the magnetic field vector) becomes sufficiently large. In stead of  $(2, 1)$ ,  $(1, 1)$  and  $(2, 3)$  modes whose resonant surfaces are in the neighbourhood of the outermost magnetic surfaces appear to dominate the fluctuations. Although these MHD instability are observed, the plasma confinement are maintained longer than we expect from its unstable properties of the configuration. It is now required to clarify the reason of the good confinement because it can bring about good confinement in further high- $\beta$  state.

An explanation for the good confinement in the linearly unstable region was proposed by Ichiguchi et al. based on the three-field RMHD simulations[4]. They found that strong overlap of the vortices with different helicity causes a disruptive phenomenon. They showed that such disruptive phenomenon can be suppressed by the self-organized deformation of the pressure profile which results from the nonlinear evolution of the interchange mode itself at lower  $\beta$  value. In the present study, this stabilization scenario is further confirmed for higher  $\beta$  value than those in the previous work.

Though the RMHD simulations have tractable natures to investigate the complex helical-toroidal system, the approximation used to derive the RMHD equations restrict their applicability. For example, the compressibility and poloidal motions are assumed to be negligible in the three-field RMHD equations. It is desirable to investigate effects of physical mechanism which are not incorporated in the RMHD system to study plasma dynamics more precisely and reach to a conclusive understanding. Here the direct numerical simulation (DNS) code of the 3D compressible and nonlinear MHD equations developed by Miura et al[5] are made use of for this purpose. The code

includes most of essences of MHD dynamics such as compressibility and toroidal flows. Hereafter we call these which are included in the DNS and not included in RMHD as “full MHD effects”. We examine how the full MHD effects appear in the plasma evolution in LHD from the view points of detailed MHD dynamics.

## 2 RMHD simulations

The RMHD simulations are conducted by the use of the NORM code. The toroidal geometry is incorporated by utilizing the toroidally averaged equilibrium quantities, which is obtained by using the 3D equilibrium calculated with the VMEC code[6]. Details of the code are given in Ref.[4]. In order to consider the stabilizing mechanism for the interchange mode in the LHD plasma, we have focused on the evolution of the pressure profile in the increase of the  $\beta$  value. In the present RMHD simulations, the magnetic Reynolds number is assumed to be  $S = 10^6$  and the fixed boundary condition is employed.

We start from the investigation of the interchange mode at  $\beta_0 = 0.5\%$ , where  $\beta_0$  denotes the  $\beta$  value at the magnetic axis. The initial equilibrium is calculated with the almost parabolic pressure profile of  $p_{eq} = p_0(1 - \rho^2)(1 - \rho^8)$  under the constraints of the no net current, where  $\rho$  is the square-root of the normalized toroidal flux. This pressure profile is consistent with the experimental data at low  $\beta$ . [7] This equilibrium is unstable against the linear ideal interchange mode. In the time evolution, the  $(m, n) = (5, 2)$ ,  $(7, 3)$  and  $(2, 1)$  modes are excited. However, all of them are saturated mildly without disruptive behavior. This is due to the fact that the vortices of the modes are localized around the corresponding rational surfaces, and therefore, they do not overlap each other. Such mild saturation results in the generation of the local flat regions in the average component of pressure profile  $\langle p \rangle$ , as shown by the blue line in FIG.1. Here  $\langle p \rangle$  is defined as  $\langle p \rangle = \oint \oint p d\theta d\zeta$ , where  $\theta$  and  $\zeta$  denote the poloidal and toroidal angles, respectively.

Next we consider the increase of the  $\beta$  value to  $\beta_0 = 1.0\%$ . In the nonlinear calculation with the initial pressure profile fixed to the parabolic one, a disruptive phenomenon is obtained[4]. In this case, the pressure in the central region is decreased in a short time. This phenomenon is caused by the significant overlap of the vortices due to the enhancement of the driving force. On the other hand, the actual pressure profile changes continuously in the increase of the  $\beta$  value. In order to simulate this situation, we employ the profile of the saturated pressure in the calculation at  $\beta_0 = 0.5\%$  as the initial pressure profile of the nonlinear calculation at  $\beta_0 = 1.0\%$ . In this case, the interaction of the vortices is weak and the unstable modes are mildly saturated as in the case of  $\beta_0 = 0.5\%$ . The disruptive phenomenon is suppressed because the locally flat structure in the initial pressure profile reduces the driving force at the resonant surfaces. The saturated average pressure profile is shown by the purple line in FIG.1.

In order to examine whether this mechanism explains the stable LHD plasma at higher  $\beta$  value, we investigate the nonlinear behavior at  $\beta_0 = 1.5\%$  by applying this scheme. The saturated pressure profile at  $\beta_0 = 1.0\%$  is employed as the initial profile. In the nonlinear evolution, the fluctuations are saturated mildly and the resultant pressure profile also shows the locally flat structure again. (See the red solid line in FIG.1.) Figure 2 shows the bird’s eye view of this pressure profile at  $\beta_0 = 1.5\%$ . The profile is not only locally flattened in the average component but also reorganized to have a precise structures corresponding to the poloidal mode number of the saturated mode at each resonant surface. This structure is formed by the local vortices of the interchange mode. This result shows that the disruptive phenomenon is suppressed by the local deformation of the pressure profile in the series of the  $\beta$  value. Thus, it still suggests that the self-organization of the pressure profile due to the interchange mode can be the main stabilizing mechanism in the LHD plasma.

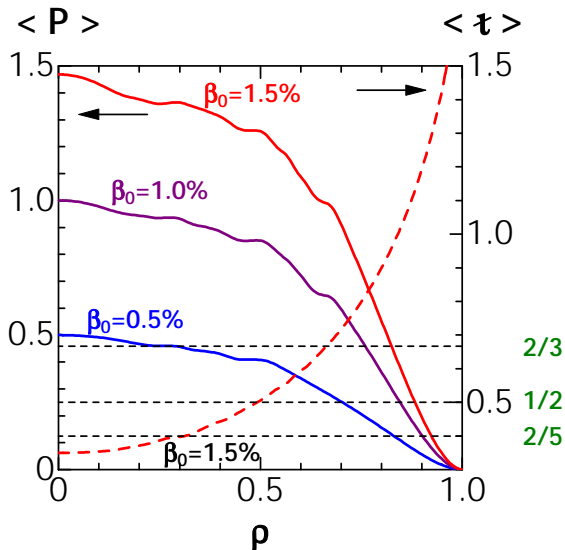


FIG. 1: Average pressure profile in the non-linear saturated stage in the series of the  $\beta$  value.

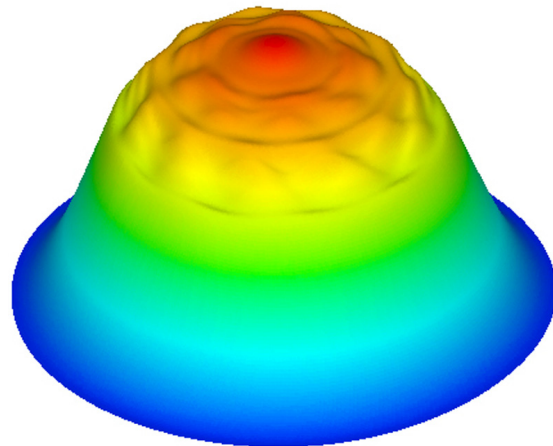


FIG. 2: Bird's-eye view of pressure profile at  $\beta_0 = 1.5\%$ .

### 3 DNS of full 3D compressible MHD

#### 3.1 Unstable Fourier mode growth

Here DNS of the 3D compressible and nonlinear MHD equations is conducted. We pay special attention to detailed MHD dynamics which are brought about by the full MHD effects. In the analysis we make use of the Boozer coordinate system *for the initial equilibrium*. The Boozer coordinates  $(\rho, \theta, \zeta)$  is obtained by the use of the HINT[8] and VMEC[6].

There are some numerical results which have been obtained earlier by the DNS code. The first work[5] is on simulations under the L=2/M=10 stellarator symmetry of the LHD, in which  $(m, n) \simeq (15, 10)$  and  $(20, 10)$  resistive ballooning modes are excited sequentially and saturated mildly. Next, full-torus DNS has been carried out[10, 11]. In the full-torus simulations, DNS under the stellarator symmetry are carried out prior to them so as to skip the long quasi-stationary period. (Hereafter we call the DNS under the stellarator symmetry prior to the full-torus simulation simply as the pre-calculation.) In FIG.3, the averaged pressure profile  $\langle p \rangle$  is shown as the function of  $\rho$ . The red solid line is the ideal MHD equilibrium with  $R_{ax} = 3.6m$  and  $\beta_0 = 4\%$  provided by the HINT code[8]. The green line represents  $\langle p \rangle$  of the initial condition for the full-torus simulation[10, 11] provided by the pre-calculation. It is seen in FIG.3 that the pressure gradient becomes less steep by the pre-calculation. In the full-torus simulation starting from the less-steep pressure gradient, the pressure-driven instability leads to formation of two pairs of mushroom-like structures of the pressure associated with the  $(m, n) = (2, 1)$  mode[10]. The structure formation is similar to those observed in RMHD simulations. Furthermore, we have found that toroidal flow grows as energetic as poloidal flows in the simulation[11]. In these earlier DNS, the pressure-driven modes are saturated mildly whether the system is under the stellarator symmetry or full-torus.

Since the plasma behaviors are sensitive to the initial pressure profile, the pre-calculations may have brought about qualitative changes to the plasma behaviors. It is worth carrying out the full-torus DNS starting from the HINT equilibrium, without the pre-calculation, and studying detailed physical process in it in order to find out what classifies the plasma behaviors disruptive or non-disruptive. For simplicity, we call the full-torus simulation starting from the pre-calculated initial

condition as “run 1” and the one starting from the HINT equilibrium as “run 2”. The magnetic Reynolds number is set  $S = 10^6$  in both runs. Figure 4 shows time evolutions of the kinetic energy  $K = \langle \rho_m \mathbf{v}^2 \rangle / 2$  and the poloidal contribution to it  $K_p = \langle \rho_m \mathbf{v}_p^2 \rangle / 2$  in runs 1 and 2, where  $\rho_m$ ,  $\mathbf{v}$  and  $\mathbf{v}_p$  are the mass density, the total velocity vector, poloidal part of the velocity, respectively. At early stages in the two runs, main parts of the kinetic energy  $K$  come from  $K_p$ . When  $K \simeq K_p$ , the fluid motions are nearly two-dimensional and the RMHD approximation is supported. The difference between  $K$  and  $K_p$  gradually becomes large gradually. The difference in run 1 is relatively large compared to that in run 2. We have to keep in mind the possibility that the pre-calculation in run 1 has worked to add 3D compressible perturbations[9] to the initial condition and led to early generation of toroidal flows. Though it is interesting to study whether the plasma obeys to 3D compressible perturbations or incompressible perturbations, it is a tough work and should be left for future work. After the linear growth, both runs 1 and 2 show two peaks of  $K$ . The saturation levels of run 2 are as large as twice of those in run 1, suggesting that the time evolution of the former is more violent than the latter. After the saturation of  $K$ ,  $K_p$  becomes much smaller than  $K$ . Namely, the toroidal flow dominates the fluid motions for  $t > 400\tau_A$ . Though FIG.4 shows only for  $t < 600\tau_A$ , we have carried out run 1 till  $t \simeq 1300\tau_A$  and verified that the kinetic energy decays monotonically after the saturation. Below, we concentrate on studying the dynamics in run 2 and try to find out qualitative views the full MHD effects.

Next we study the Fourier components of the pressure. Figure 5(a) is the time evolutions of the spatial power spectra of the pressure with low  $m$  and  $n$  wave numbers. We find that the  $(m, n) = (2, 1)$  mode grows exponentially first. The  $(1, 1)$  mode also grows exponentially and finally overcomes the  $(2, 1)$  modes. In the late stage of the evolutions  $t > 450\tau_A$ , the  $(1, 1)$  mode remains as the most dominant modes. In the points of views of the kinetic energy growth, the saturation time of the  $(2, 1)$  mode,  $t \simeq 400\tau_A$ , coincide with the first weak saturation of the kinetic energy  $K$  of run 2 in FIG.4, whereas the clearest saturation of  $K$  coincide with the saturation time of the  $(1, 1)$  mode. It implies that the kinetic energy saturates when the driving force, the pressure gradient, is lost.

Note that the  $(m, n) = (1, 1)$  mode has two stages of the exponential growth, before and after  $t \simeq 370\tau_A$  in FIG.5(a). The evolutions of the Fourier modes around the time are magnified in FIG.5(b). The growth of  $(1, 1)$  after the time is still exponential but slower than that before the time. Since the growth rate of this mode in the earlier stage is almost the same with that of the  $(2, 1)$  mode, the  $(1, 1)$  mode is considered being a side band of the  $(2, 1)$  mode. However, the  $(1, 1)$  mode becomes the dominant mode after the saturation of the  $(2, 1)$  mode and begin to grow with different growth rate. A crucial point is that the  $(3, 2)$  mode grows simultaneously and the distance between the three rational surfaces,  $\iota/2\pi = 1/2, 2/3$  and  $1/1$  are narrow. Furthermore, as is shown later, the  $(2, 1)$  and  $(3, 2)$  mode structures are overlapping to each other. Therefore, the situation is similar to the dangerous scenario suggested from the RMHD simulations.

In FIG.6(a) and (b), the Fourier modes resonant to  $\iota/2\pi = 1/2$  and  $2/3$  are shown respectively. These two rational surfaces are the most dangerous ones in the DNS under the stellarator symmetry, that is, for middle or high wave number Fourier modes. We find both in FIG.6(a) and (b) that the lowest modes grows first. The components of the lowest mode numbers have the largest growth rates at each rational surfaces because of the large viscosity and the higher modes grow later as the consequent of the nonlinear interactions.

In FIG.7, the mean profile of the pressure  $\langle p \rangle$  at some typical times are shown. At  $t = 450\tau_A$ , the mean profile of the pressure is quite different from the initial one. The pressure increase as the function of  $\rho$  at  $\rho < 0.3$ . The adverse pressure gradient is stable in the system, being consistent with the saturation of  $(2, 1)$  mode. At  $t = 600\tau_A$ , the pressure deformation proceeds. At this stage of the evolution, the magnetic surfaces are destroyed (figure is omitted) but there are remains of the magnetic surfaces, preventing the plasma from loosing the stored pressure instantaneously.

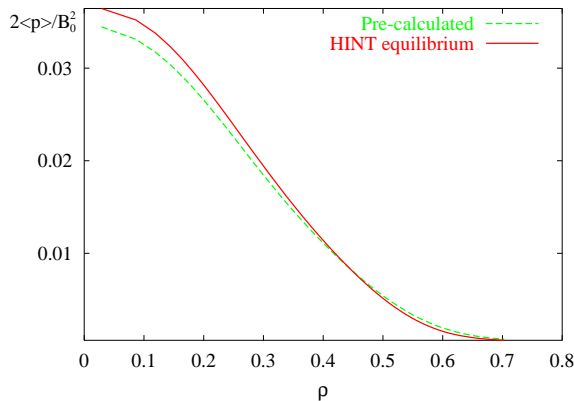


FIG. 3: Comparison of the initial pressure profile. The red line represents the ideal MHD equilibrium calculated by the HINT code. The green line represents the initial condition for run 1, provided by the pre-calculation under the stellarator symmetry. The vertical axis is normalized by  $|\mathbf{B}|^2/2$  of the HINT equilibrium.

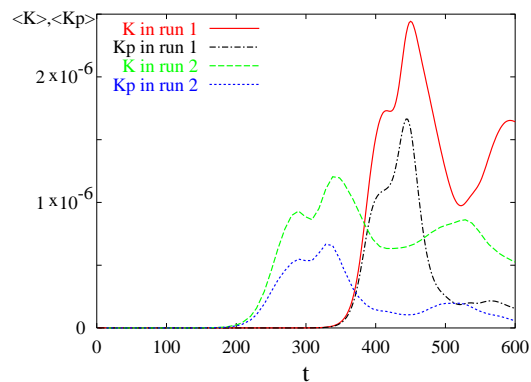


FIG. 4: Time evolution of the kinetic energy (green for run 1 and red for run 2) and poloidal contribution to it (blue and black for runs 1 and 2, respectively).

### 3.2 Flow generation and pressure deformation

The growth of unstable modes shown above are observed in a poloidal section. In FIG.8, the color contours of the pressure on a vertically-elongated poloidal section are shown for  $t = 350, 400$  and  $600\tau_A$ . The white lines represent streamlines drawn only by the poloidal velocity components. At  $t = 350\tau_A$ , the streamlines show formation of two anti-parallel vortex pairs associated with  $(2, 1)$  unstable modes. The two anti-parallel vortex pairs advect the pressure and mushroom-like pressure structures similar to those observed in run 1[10] are formed by the advection. At  $t = 400\tau_A$ , the streamlines show three vortex pairs. The emergence of the the third vortex pair is associated with excitations of  $(m, n) = (3, 2)$  modes seen in FIG.6(b). The third vortex pair is generated between the first two pairs, showing interactions of the  $(3, 2)$  and  $(2, 1)$  modes. At  $t = 600\tau_A$ , pressure deformation proceeds further. In these three figures, there are sinks or sources of the streamlines. They come from either the compressibility of fluid or from the toroidal contributions of the fluid motions. As far as we have verified by means of the visualization, generations of toroidal flows and occurrence of relatively large dilatation happens simultaneously at the same place.

In order to see the 3D properties of fluid motions, full-3D streamlines are drawn in FIG.9. Figures 9(a)-(c) are the 3D streamlines corresponds to FIG.8(a)-(c). In FIG.9(a)( $t = 350\tau_A$ ), contributions of the toroidal flows to the vortices are not very large and the fluid motions look like quasi-two-dimensional. However, some streamlines are convergent and advected toward the toroidal direction forming spirals of streamlines. It suggests that compressibility and toroidal flows play finite roles in the flow topology. In FIG.9(b)( $t = 400\tau_A$ ) it appears that the toroidal flow is as energetic as poloidal motions and in FIG.9(c) at  $t = 600\tau_A$  the toroidal flows overcome the poloidal motions. Recall here that the toroidal motions have longer length scale than the poloidal motions with the same wave number. Thus toroidal motions are less dissipated by the viscosity compared to the poloidal motions. It implies that the toroidal motions are slow to decay once they are excited and influence long time behaviors. We also note that the dominance of the toroidal over poloidal flows may be strengthened because of the disruptive nature of this run, because the generation of the poloidal motions are stopped in these cases. In fact, the toroidal flows are much more dominant in run 2 than in run 1, as has been seen in FIG.4.

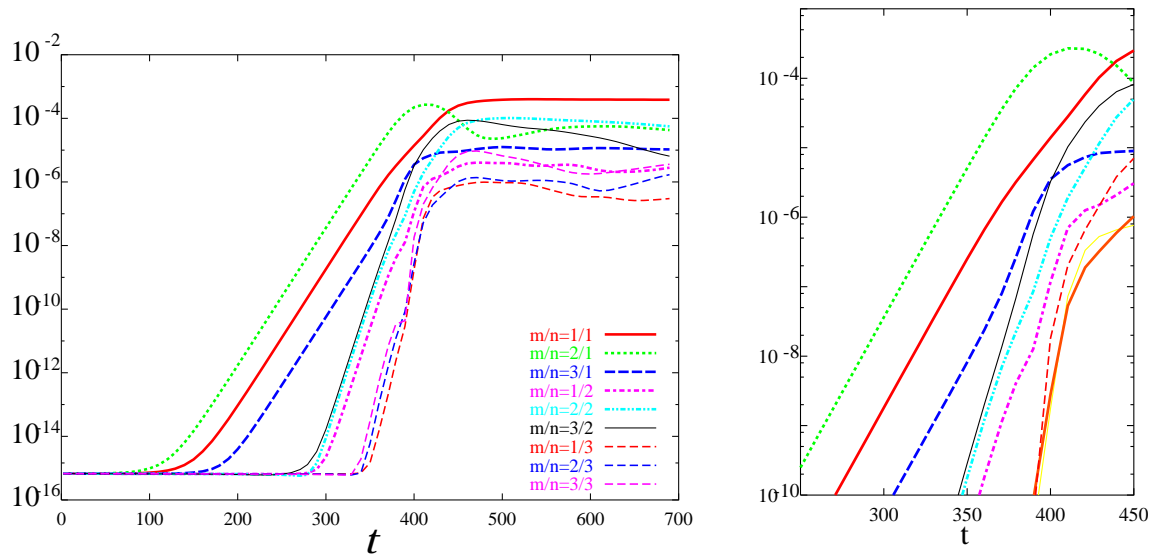


FIG. 5: Time evolutions of the Fourier power spectra of the pressure in Boozer coordinate.

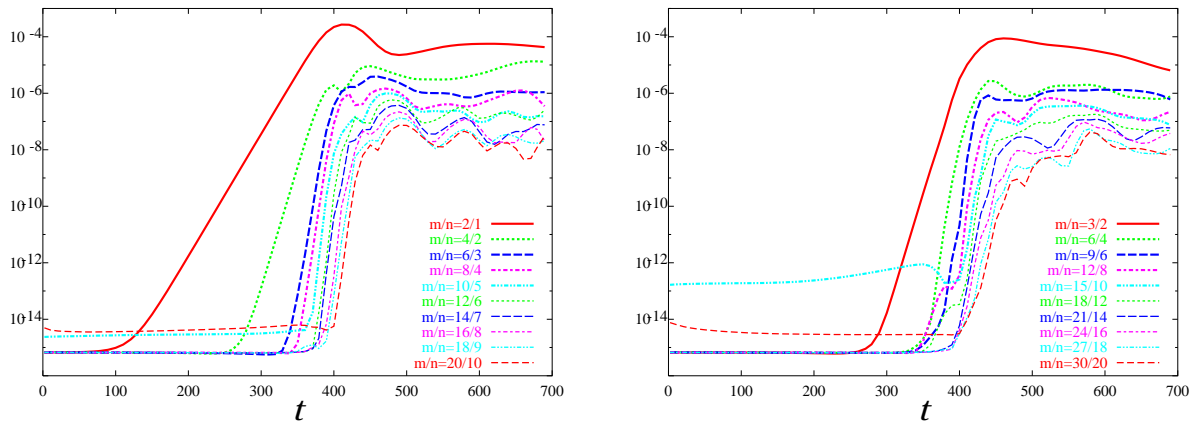


FIG. 6: Time evolutions of the spatial power spectra of the pressure associated with (a)  $\iota/2\pi = 1/2$  and (b)  $2/3$  rational surfaces. In (a), the lowest mode  $m/n = 2/1$  and its higher harmonics up to  $m/n = 20/10$  are shown. In (b), the lowest mode  $m/n = 3/2$  and its higher harmonics up to  $m/n = 30/20$  are shown.

## 4 Concluding Remarks

The dynamics of the pressure driven modes in LHD is investigated by means of the two kinds of simulations, RMHD and DNS. The RMHD simulations are carried out aiming to investigate plasma stabilization mechanism. The stabilizing scenario proposed in Ref.[4] is confirmed in the higher  $\beta$  value than the previous work. The basic dynamics suggested by the RMHD simulations is that the plasma can be non-disruptive when the interaction of the modes with different helicities is weak while it can be disruptive when the interaction is strong. The DNS results also look similar to the RMHD results especially in the pressure deformation. Either non-disruptive or disruptive results are observed depending on the initial pressure profile in the DNS.

One of the remarkable results of the DNS runs is the appearance of the substantial toroidal flow. The flow generation may be associated with the pressure deformation, because the fraction of the toroidal flow in the kinetic energy is larger in the disruptive run than that in the non-disruptive run. The 3D compressible perturbation may also be related with the generation. Further investiga-

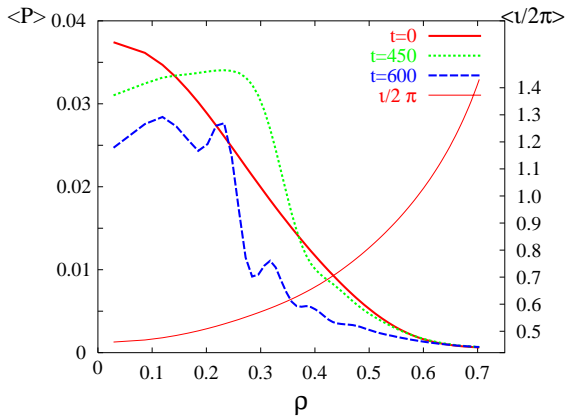


FIG. 7: The mean profile of the pressure at  $t = 0, 450$  and  $600\tau_A$ . The vertical axis is normalized by  $|\mathbf{B}|^2/2$  of the HINT equilibrium. The  $\iota$ -profile of the initial equilibrium is shown simultaneously and ticks of the  $\iota/2\pi$  is shown in the right-hand-side of the bounding box.

tion should be necessary to understand how the substantial toroidal flow generation influences the stabilization mechanism scenario based on the RMHD results.

In summary, some basic views for the stabilization mechanism suggested by the RMHD results seem to be supported by DNS. The influences of the toroidal flows and the other full MHD effects on the mechanism will be carefully studied.

## References

- [1] MOTOJIMA, O., et al., “Initial physics achievements of large helical device experiments”, *Phys. Plasmas* **6** (1999) 1843-1850.
- [2] YAMADA, H., et al., “Configuration flexibility and extended regimes in Large Helical Device”, *Plasma Phys. Control. Fusion* **43** (2001) A55-A71.
- [3] SAKAKIBARA, S., et al., “MHD characteristics in the high beta regime of the Large Helical Device”, *Nuclear Fusion* **41** (2001) 1177-1183.
- [4] ICHIGUCHI, K., et al., “Nonlinear MHD analysis for LHD plasmas”, *Nuclear Fusion* **43** (2003) 1101-1109.
- [5] MIURA, H., et al., “Nonlinear MHD Simulations in the Large Helical Device”, *Phys. Plasmas* **8** (2001) 4870.
- [6] HIRSHMAN, S.P., et al., “Three-dimensional free boundary calculations using a spectral Green’s function method”, *Comp. Phys. Comm.* **43** (1986) 143.
- [7] LIANG, Y., et al., “Measurement of Shafranov shift with soft x-ray CCD camera on large helical device”, *Plasma Phys. Control. Fusion* **44** (2002) 1383.
- [8] HARAFUJI, H., et al., “Computational Study of Three-Dimensional Magnetohydrodynamic Equilibria in Toroidal Helical Systems”, *J. Comp. Phys.*, **81** (1989) 169.
- [9] NAKAJIMA, N., et al., “Growth Rates and Structures of MHD Modes in Stellarator/Heliotron”, to appear in *J. Plasma Fusion and Res.* SER. **6**.
- [10] HAYASHI, T., et al., “Nonlinear MHD Simulations of Spherical Tokamak and Helical Plasmas”, 19th IAEA Fusion Energy Conference, Lyon, 2002, IAEA-CN-94/TH/6-3.
- [11] MIURA, H. and HAYASHI, T., “Low m/n modes behavior of MHD plasma in LHD”, to appear in *J. Plasma Fusion and Res.* SER. **6**.

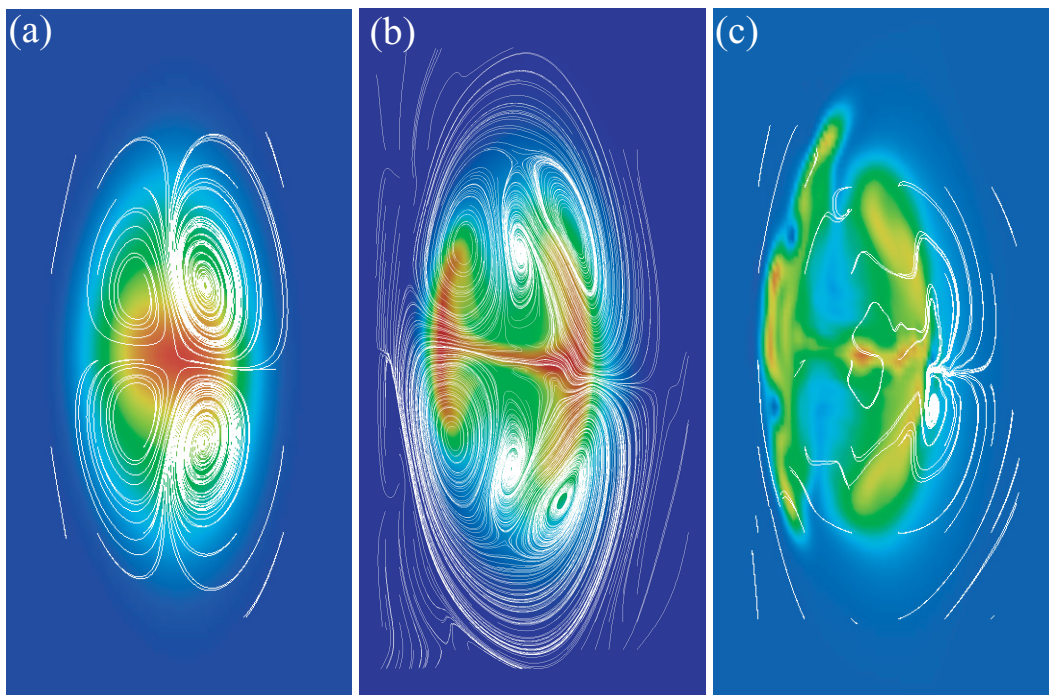


FIG. 8: Pressure contours and the two-dimensional streamlines on a vertically-elongated poloidal section at (a)  $t = 350$ , (b) 400 and (c)  $600\tau_A$ . Sink or sources of the streamlines are attributed to toroidal motions or compressibility of the fluids.

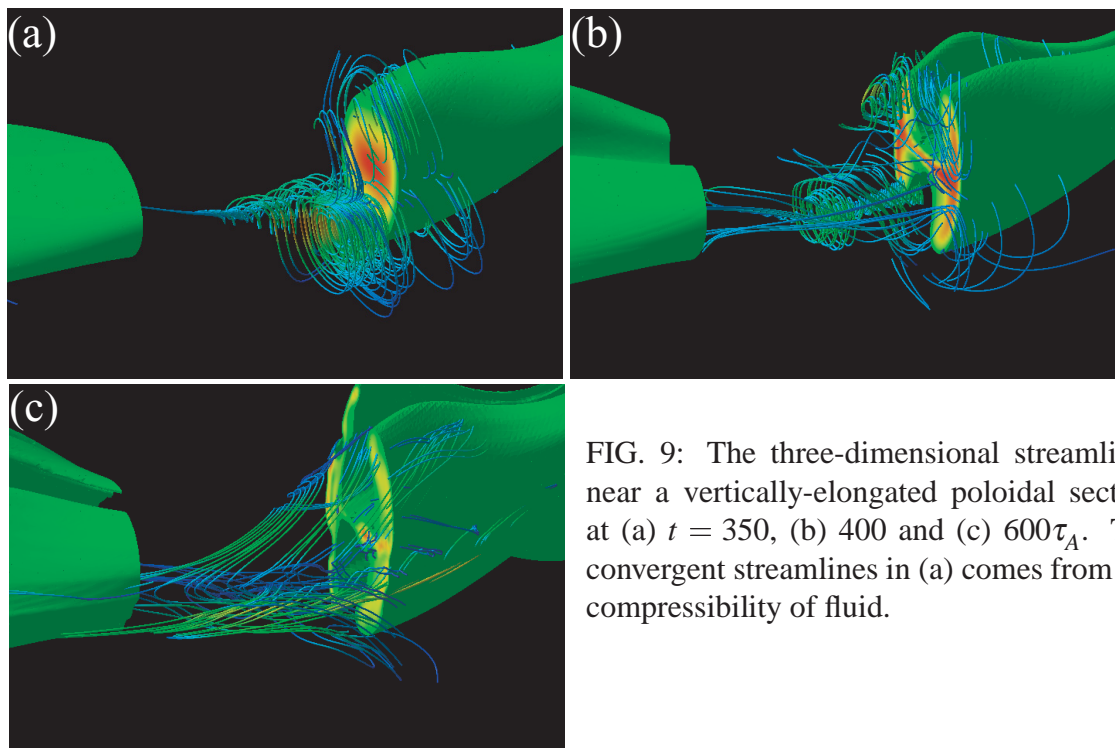


FIG. 9: The three-dimensional streamlines near a vertically-elongated poloidal section at (a)  $t = 350$ , (b) 400 and (c)  $600\tau_A$ . The convergent streamlines in (a) comes from the compressibility of fluid.

## Nonperturbative Effects of Energetic Ions on Alfvén Eigenmodes

Y. Todo 1), N. Nakajima 1), K. Shinohara 2), M. Takechi 2), M. Ishikawa 2), S. Yamamoto 3)

1) National Institute for Fusion Science, Toki, Japan

2) Naka Fusion Research Establishment, Japan Atomic Energy Research Institute, Naka, Japan

3) Institute of Advanced Energy, Kyoto University, Uji, Japan

e-mail contact of main author: todo@nifs.ac.jp

**Abstract.** Linear properties and nonlinear evolutions of an energetic-ion driven instability in a JT-60U plasma were investigated using a simulation code for magnetohydrodynamics and energetic particles. The spatial profile of the unstable mode peaks near the plasma center where the safety factor profile is flat. The unstable mode is not a toroidal Alfvén eigenmode (TAE) because the spatial profile deviates from the expected location of TAE and the spatial profile consists of a single primary harmonic  $m/n = 2/1$  where  $m, n$  are poloidal and toroidal mode numbers. The real frequency of the unstable mode is close to the experimental starting frequency of the fast frequency sweeping mode. The simulation results demonstrate that the energetic ion orbit width and the energetic ion pressure significantly broaden radial profile of the unstable mode. For the smallest value among the investigated energetic ion orbit width, the unstable mode is localized within 20% of the minor radius. This gives an upper limit of the spatial profile width of the unstable mode which the magnetohydrodynamic effects alone can induce. For the experimental condition of the JT-60U plasma, the energetic ions broaden the spatial profile of the unstable mode by a factor of 3 compared with the smallest orbit width case. The unstable mode is primarily induced by the energetic particles. It is demonstrated that the frequency shifts both upward and downward in the nonlinear evolution at the rate close to that of the fast frequency sweeping mode. In addition to the energetic particle mode in the JT-60U plasma, an investigation of TAE in an LHD-like plasma using the simulation code for the helical coordinate system is reported.

### 1. Introduction

Three types of frequency chirping instabilities, slow frequency sweeping (slow FS) mode, fast frequency sweeping (fast FS) mode, and abrupt large event (ALE) have been observed in the JT-60U plasmas heated with negative ion based neutral beam (NNB) injection [1, 2, 3, 4]. The frequencies of the three instabilities are in the range of shear Alfvén eigenmodes. The frequency sweeping of the slow FS mode has a good correlation with the equilibrium parameter evolution with a time scale  $\simeq 200$  ms. On the other hand, the time scales of the fast FS mode and the ALE are respectively 1-5 ms and 200-400  $\mu$ s, much shorter than the equilibrium time scale. The frequency of the fast FS mode shifts rapidly by 10-20 kHz in 1-5ms both upward and downward. The starting frequency of the fast FS mode changes in the time scale of the equilibrium parameter evolution and follows the toroidal Alfvén eigenmode (TAE) [5, 6] gap frequency.

We have investigated the fast FS mode in a JT-60U plasma using a simulation code for magnetohydrodynamics (MHD) and energetic particles, MEGA [7]. We reported that there is an unstable mode near the plasma center and a frequency sweeping close to that of the fast FS mode takes place [8]. The ratio of the linear damping rate ( $\gamma_d$ ) to the linear growth rate ( $\gamma_L$ ) in the simulation is consistent with the hole-clump pair creation which takes place when  $\gamma_d/\gamma_L$  is greater than 0.4 [9, 10].

In Ref. [8], we called the unstable mode “nonlocal energetic particle mode (EPM)” and argued that it is different from the resonant type EPM [11, 12] and similar to the EPM which is predicted for ICRF heated plasma with reversed magnetic shear [13, 14]. However, it was shown numerically that the reversed-shear-induced Alfvén eigenmode (RSAE), which has properties similar to the global Alfvén eigenmode (GAE) [15], can exist in reversed shear plasmas [16]. In

Ref. [17] it is theoretically clarified that both toroidal MHD effects of second order in inverse aspect ratio and adiabatic response of energetic particles can establish an eigenmode localized near the magnetic surface where the safety factor takes the minimum value in reversed shear plasmas. This gives us a new viewpoint to investigate linear properties of the nonlocal EPM which we reported in Ref. [8]. We have carried out simulations for various energetic ion orbit widths and energetic ion pressures using the MEGA code and found that they have significant effects on the spatial profile of the unstable mode in the JT-60U plasma [18]. In this paper, we report the linear properties and the frequency sweeping of the nonlocal EPM in sections 3 and 4, respectively. The simulation model is described in section 2. Section 5 is devoted to an investigation of TAE in an LHD-like plasma using the simulation code for the helical coordinate system.

## 2. Simulation Model

The hybrid simulation model for MHD and energetic particles [19, 20, 7] is employed in the MEGA code. The plasma is divided into the bulk plasma and the energetic ions. The bulk plasma is described by the nonlinear full MHD equations. The electromagnetic field is given by the MHD description. This approximation is reasonable under the condition that the energetic ion density is much less than the bulk plasma density. The MHD equations with energetic ion effects are,

$$\frac{\partial \rho}{\partial t} = -\nabla \cdot (\rho \mathbf{v}), \quad (1)$$

$$\rho \frac{\partial}{\partial t} \mathbf{v} = -\rho \boldsymbol{\omega} \times \mathbf{v} - \rho \nabla \left( \frac{v^2}{2} \right) - \nabla p + (\mathbf{j} - \mathbf{j}_h) \times \mathbf{B} - \nu \rho \nabla \times \boldsymbol{\omega} + \frac{4}{3} \nu \rho \nabla (\nabla \cdot \mathbf{v}), \quad (2)$$

$$\frac{\partial \mathbf{B}}{\partial t} = -\nabla \times \mathbf{E}, \quad (3)$$

$$\frac{\partial p}{\partial t} = -\nabla \cdot (p \mathbf{v}) - (\gamma - 1) p \nabla \cdot \mathbf{v} + (\gamma - 1) [\nu \rho \omega^2 + \frac{4}{3} \nu \rho (\nabla \cdot \mathbf{v})^2 + \eta j^2], \quad (4)$$

$$\mathbf{E} = -\mathbf{v} \times \mathbf{B} + \eta \mathbf{j}, \quad (5)$$

$$\boldsymbol{\omega} = \nabla \times \mathbf{v}, \quad (6)$$

$$\mathbf{j} = \frac{1}{\mu_0} \nabla \times \mathbf{B}, \quad (7)$$

where  $\mu_0$  is the vacuum magnetic permeability and  $\gamma$  is the adiabatic constant, and all the other quantities are conventional. Here,  $\mathbf{j}_h$  is the energetic ion current density without  $\mathbf{E} \times \mathbf{B}$  drift.

The effect of the energetic ions on the MHD fluid is taken into account in the MHD momentum equation [Eq. (2)] through the energetic ion current. The MHD equations are solved using a finite difference scheme of fourth order accuracy in space and time. The drift-kinetic description is employed for the energetic ions. The  $\delta f$  method [21, 22, 23] is used for the energetic ions. The marker particles are initially loaded uniformly in the phase space. With the uniform loading employed in this work, the number of energetic beam ions that each marker particle represents is in proportion to the initial distribution function, namely the particle density in the phase space. It is important to start the simulation from the MHD equilibrium consistent with the energetic ion distribution. We solve an extended Grad-Shafranov equation developed in Ref. [24] in the cylindrical coordinates  $(R, \varphi, z)$  where  $R$  is the major radius coordinate,  $\varphi$  is the toroidal angle coordinate, and  $z$  is the vertical coordinate. The MEGA code is benchmarked with respect to the alpha-particle-driven  $n = 4$  TAE in the TFTR D-T plasma shot #103101 [25]. The destabilized mode has a TAE spatial profile which consists of two major harmonics  $m/n = 6, 7/4$  and frequency 215kHz. These results are consistent with the calculation with the NOVA-K code [26]. The linear growth rate obtained from this simulation, is  $8.7 \times 10^{-3}$  of

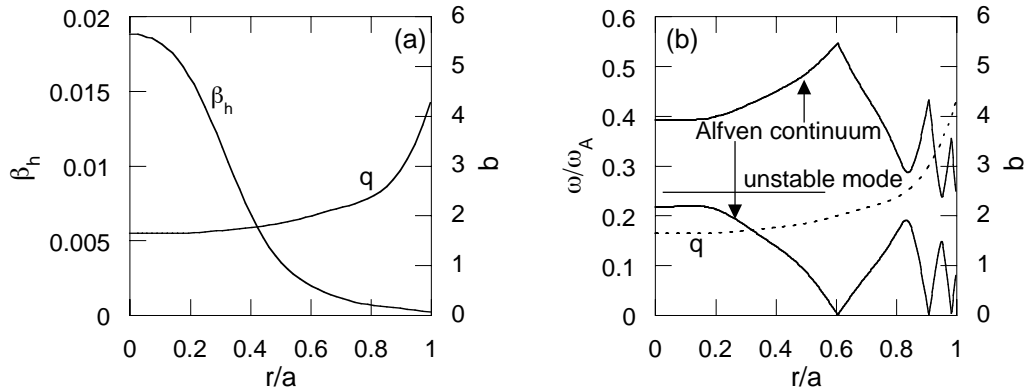


FIG. 1. Energetic ion beta ( $\beta_h$ ) profile and safety factor ( $q$ ) profile; (a). Frequency and location of the unstable mode with  $q$ -profile and the shear Alfvén continuous spectra with the toroidal mode number  $n = 1$ ; (b).

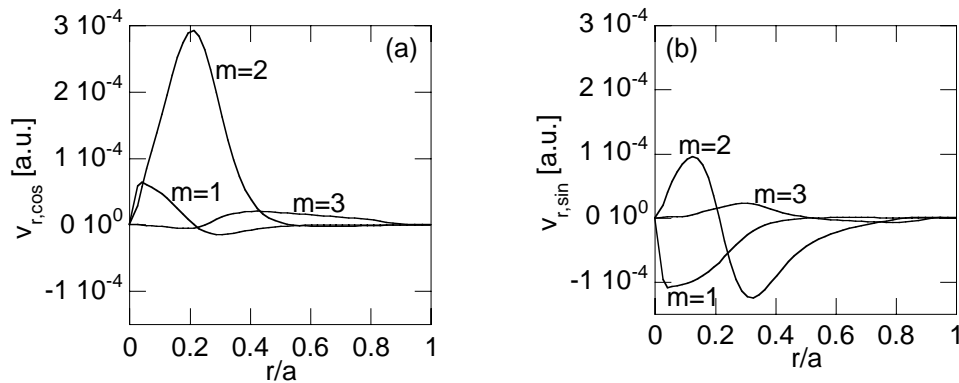


FIG. 2. Spatial profiles of (a) cosine part and (b) sine part of the unstable mode radial velocity  $\psi$  harmonics for  $\rho_{h\parallel}/a = 0.08$ . The toroidal mode number of all the harmonics is  $n = 1$ .

the mode frequency. This linear growth rate is close to what is observed in the previous particle simulation  $1.1 \times 10^{-2}$  [27] and calculated in the NOVA-K code  $8 \times 10^{-3}$  [26].

### 3. Nonlocal Energetic Particle Mode

#### 3.1. Instability in a JT-60U Plasma

The JT-60U discharge E36379 [3], where the fast FS mode was observed, was investigated using the MEGA code. The safety factor profile, bulk pressure profile, and density profile used in the simulation are based on the experimental data. The major and minor radii are  $R_0 = 3.4\text{m}$  and  $a=1.0\text{m}$ , respectively. The shape of the outermost magnetic surface in the simulation is circular while it was diverter-shaped in the experiment. The magnetic field at the magnetic axis is 1.2T. The bulk plasma and the beam ions are deuterium. The NNB injection energy is 346keV. The initial energetic ion distribution in the velocity space is assumed to be a slowing down distribution. The energetic ion velocity perpendicular to magnetic field is neglected because the NNB injection is tangential. The beam direction is parallel to the plasma current. The maximum velocity is assumed to be 80% of the injection velocity as the injection is not completely parallel to the magnetic field. This maximum velocity in the simulation corresponds roughly to the Alfvén velocity at the magnetic axis. The NNB injection and the collisions are neglected in the simulations in this paper. The number of marker particles used is  $5.2 \times 10^5$ . The numbers of

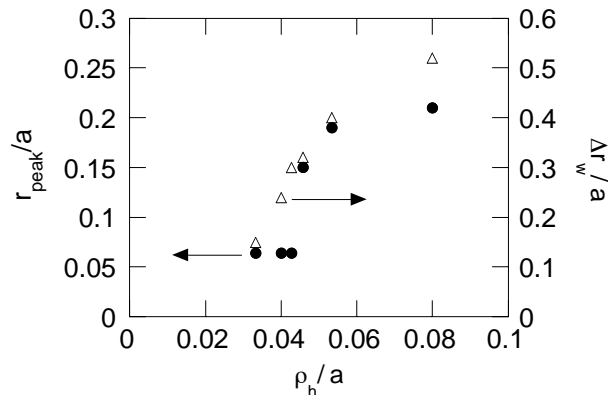


FIG. 3. Peak location ( $r_{peak}$ ) and radial width ( $\Delta r_w$ ) of the unstable mode spatial profile versus energetic ion parallel Larmor radius normalized by the minor radius.

grid points are (101, 16, 101) for the cylindrical coordinates ( $R, \varphi, z$ ).

A linearly unstable mode was investigated for energetic ion pressure profile based on a calculation using the OFMC code [28]. The OFMC code calculation gives classical distribution, which is established by the NNB injection and the particle collisions. Energetic ion redistributions and losses due to the ALE and the fast FS mode are not considered in the OFMC code calculation. The energetic ion pressure profile and  $q$ -profile used in the simulation are shown in Fig. 1(a). The central beta value is 1.9%. The ratio of energetic ion parallel Larmor radius, which is defined by the maximum parallel velocity and the Larmor frequency, to the minor radius  $\rho_{h\parallel}/a$  is 0.08. An unstable mode was found in the TAE range of frequency. Figure 1(b) shows the frequency and the location of the unstable mode. The location of the unstable mode is defined by the region where the total intensity of sine and cosine parts of the  $m/n = 2/1$  harmonic of radial velocity  $v_r$  is larger than 10% of the peak value. The frequency of the unstable mode is  $0.25\omega_A$  where  $\omega_A = v_A/R_0$  and  $v_A$  is the Alfvén velocity at the plasma center. The frequency corresponds to 52 kHz, which is close to the starting frequency of the fast FS mode. In Fig. 1(b) also shown are the  $n = 1$  shear Alfvén continuous spectra. The gap in the Alfvén continuous spectra at  $q = 2.5$  for  $m/n = 2, 3/1$  harmonics is located at  $r/a \sim 0.8$ . If the unstable mode is a TAE, it must be located at the gap ( $r/a \sim 0.8$ ) and must consist of two major harmonics. The unstable mode found in the simulation does not have the properties of TAE. Thus, we conclude it is not a TAE. The spatial profile of the radial velocity  $v_r$  of the unstable mode is shown in Fig. 2. The primary harmonic is  $m/n = 2/1$ , where  $m$  and  $n$  are the poloidal and toroidal mode numbers. Phases in all of the figures of radial velocity profile in this paper are chosen so as to maximize the cosine part of the intensity of the primary harmonic.

### 3.2 Effects of Energetic Ion Orbit Width

We have carried out simulations for various energetic ion orbit widths. Since the energetic ion orbit width is roughly given by  $q\rho_{h\parallel}$ , we solved the extended Grad-Shafranov equation for various  $\rho_{h\parallel}/a$  for the initial conditions of simulation. The Alfvén velocity, major and minor radii, energetic ion and bulk beta values, and energetic ion distribution in the velocity space are kept constant for all of the equilibria. For  $\rho_{h\parallel}/a = 0.02$ , no unstable mode was observed. The frequencies are roughly constant for all the cases. The peak locations and the radial widths of the unstable mode spatial profile are shown in Fig. 3. The radial width of the spatial profile is defined by the region where the total intensity of  $m/n = 2/1$  harmonic of radial velocity  $v_r$  is greater than 10% of the peak value. For the greater  $\rho_{h\parallel}/a$  values, the peak location moves radially outward and the radial width is broadened. The radial width of the mode spatial profile

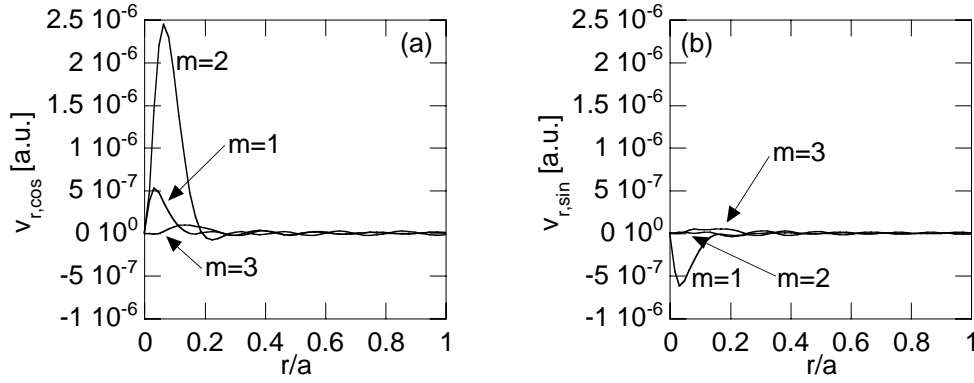


FIG. 4. Spatial profiles of (a) cosine part and (b) sine part of the unstable mode radial velocity  $v_r$  harmonics for  $\rho_{h\parallel}/a = 0.033$ . The toroidal mode number of all the harmonics is  $n = 1$ .

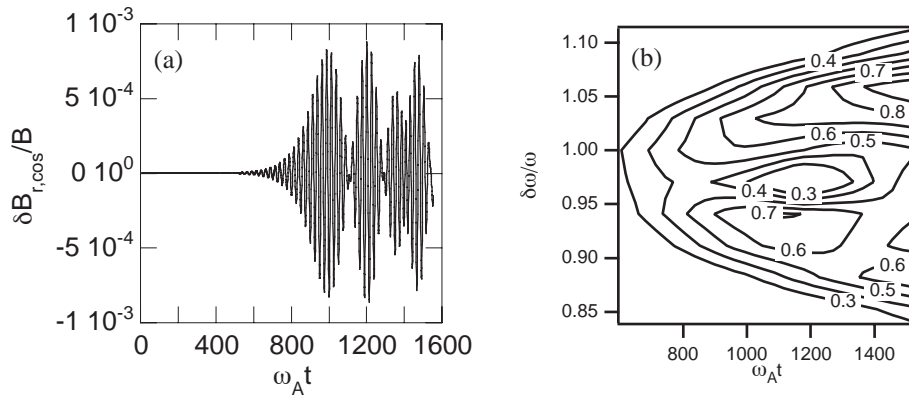


FIG. 5. Time evolution of (a) cosine part and (b) frequency spectrum of the radial magnetic field with the mode number  $m/n = 2/1$  for the reduced energetic ion distribution. A Gaussian time window  $\exp[-(t - t_0)^2 / (400\omega_A^{-1})^2]$  is used for the frequency spectrum analysis.

differs by a factor 3 between the smallest and largest orbit width. The energetic ion orbit width has significant effects on the mode spatial profile. The spatial profile of the unstable mode for the smallest orbit width with  $\rho_{h\parallel}/a = 0.033$  is shown in Fig. 4. The spatial profile is extremely localized near the plasma center. The sine component of  $m/n = 2/1$  harmonic of radial velocity  $v_r$  is negligibly small compared to the cosine part. The radial width of the unstable mode shown in Fig. 4 gives an upper limit of the radial width of a purely MHD eigenmode if it does exist. We have carried out simulations for various energetic ion pressures and found that the energetic ion pressure also has significant effects on the mode spatial profile.

The spatial width of the unstable mode with the smallest orbit width gives an upper limit of the spatial width which the MHD effects alone can induce. For the experimental condition of the JT-60U plasma, the energetic ions broaden the spatial profile of the unstable mode by a factor of 3 compared with the smallest orbit width case. The major part of the spatial profile of the unstable mode is induced by the energetic ions. It is concluded that the unstable mode is primarily induced by the energetic particles and the name “nonlocal EPM” [8] can be justified.

#### 4. Nonlinear Evolution of the Nonlocal EPM

In this section we report the results of the nonlinear simulation using the MEGA code. The viscosity and resistivity used in the simulation are  $2 \times 10^{-5} v_A R_0$  and  $2 \times 10^{-5} \mu_0 v_A R_0$ ,

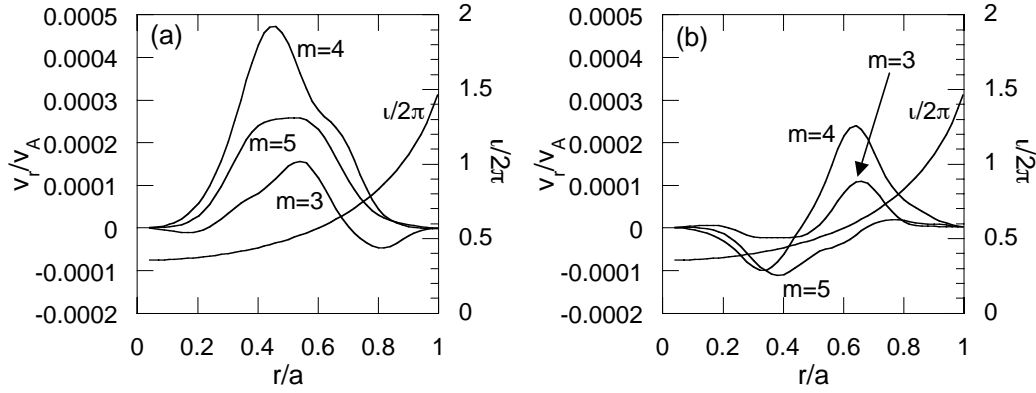


FIG. 6. Spatial profile of (a) cosine part and (b) sine part of radial velocity of the TAE in the LHD-like plasma with the toroidal mode number  $n = 2$  and the rotational transform profile.

respectively, where  $v_A$  is the Alfvén velocity at the magnetic axis and  $\mu_0$  the vacuum magnetic permeability. We consider a reduced energetic ion pressure profile because in the experiments redistributions and losses of energetic ions take place due to the fast FS mode and the ALE with time intervals much shorter than the slowing down time. The classical distribution gives an overestimate of the energetic ion pressure profile. Simulations which take into account the MHD activity, NNB injection, and collisions are needed to obtain self-consistent energetic ion distributions. It is, however, computationally too demanding and beyond the scope of this paper. We carried out a run where the energetic ion pressure is reduced to 2/5 while the spatial profile is the same as the classical distribution which is shown in Fig. 1(a). Figure 5(a) shows the time evolution of cosine part of  $m/n = 2/1$  harmonic of the radial magnetic field. An oscillation in amplitude takes place after saturation. The saturation level of the magnetic field fluctuation is  $\delta B/B \sim 8 \times 10^{-4}$ . It is found that the frequency shifts upward by 9% ( $\sim 5\text{kHz}$ ) and downwards by 9% ( $\sim 5\text{kHz}$ ) of the linear frequency in  $10^3$  Alfvén time ( $\sim 0.8\text{ms}$ ). This frequency shifts are close to those of the fast FS mode.

The frequency upshift and downshift due to the spontaneous hole-clump pair creation in a phase space was found by simulating a reduced kinetic equation when the linear damping rate ( $\gamma_d$ ) is greater than 0.4 of the linear growth rate without damping ( $\gamma_L$ ) [9, 10]. The theory predicts frequency shifts  $\delta\omega = 0.44\gamma_L(\gamma_d t)^{1/2}$ . This gives  $\delta\omega \sim 0.03\omega_A$  in  $10^3$  Alfvén time. This corresponds to 6 kHz. The rate of the frequency shifts in the simulation results is consistent with what the theory predicts.

## 5. Toroidicity-induced Alfvén Eigenmode in an LHD-like Plasma

The MEGA code has been successfully extended to simulate helical plasmas using the helical coordinate system which is employed in the MHD equilibrium code, HINT [29]. The relation between the helical coordinates ( $u^1, u^2, u^3$ ) and the cylindrical coordinates ( $R, \varphi, z$ ) is

$$R = R_0 + u^1 \cos(hMu^3) + u^2 \sin(hMu^3), \quad (8)$$

$$\varphi = -u^3, \quad (9)$$

$$z = -[u^1 \sin(hMu^3) - u^2 \cos(hMu^3)], \quad (10)$$

where we take for the LHD plasmas  $M = 10$  and  $h = -0.5$ . The physics model and the numerical algorithm are the same as described in section 2. The vector calculations must be done using the covariant and contravariant vectors, because the helical coordinates are not orthogonal. The code is benchmarked for the MHD force balance and a test particle orbit in an MHD equilibrium calculated using the HINT code. In the simulation run reported in this paper, the

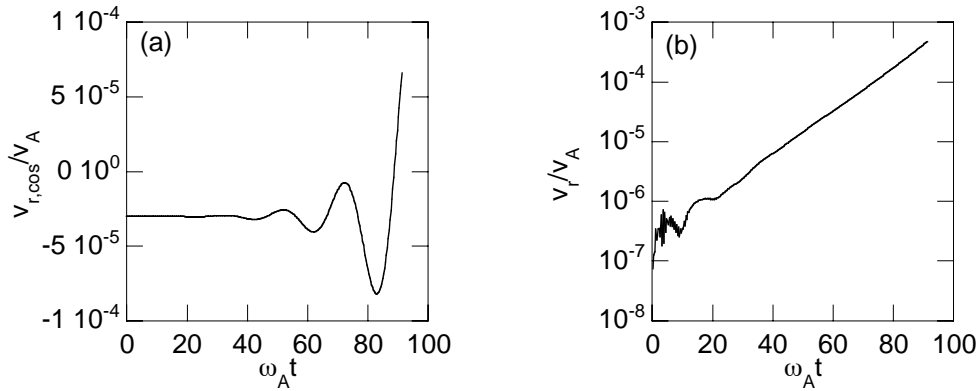


FIG.7 Time evolution of (a) cosine part and (b) amplitude of the radial velocity with the mode number  $m/n = 4/2$ .

numbers of grid points used are (91, 115, 1000) for  $(u^1, u^2, u^3)$  and the number of marker particles used is  $4 \times 10^6$ . A Boozer coordinate system was constructed to analyze the simulation data. The major and minor radii are  $R_0 = 3.73\text{m}$  and  $a = 0.89\text{m}$ , respectively. The magnetic field intensity at the magnetic axis is 0.5T and the Alfvén velocity divided by the hydrogen Larmor frequency is  $v_A/\Omega_i = 4.7 \times 10^{-2}$  m. The velocity distribution of energetic ions is a slowing-down distribution with the maximum velocity of  $1.2v_A$ . The perpendicular velocity of the energetic ions is neglected. The energetic ion beta value at the plasma center is 2%. A TAE with the toroidal mode number  $n = 2$  is destabilized. The spatial profile of the TAE is shown in Fig. 6. The dominant harmonics are  $m/n = 4, 5/2$ . The time evolutions of the cosine part and the absolute value of a radial velocity harmonic with the poloidal and toroidal mode numbers  $m/n = 4/2$  are shown in Fig. 7. It can be seen that the real frequency of the TAE is  $\omega/\omega_A \sim 0.29$  and the growth rate is  $\gamma/\omega_A \sim 0.081$ . The frequency and the location of the TAE are consistent with the theory [6].

### Acknowledgments

The authors would like to thank Drs. M. Okamoto, Y. Kusama, and T. Ozeki for valuable advice and continuous encouragement. The authors acknowledge helpful discussions with Dr. H. Miura on the Fourier analysis method in the Boozer coordinates for helical plasmas. Numerical computations were performed at the Man-Machine Interactive System for Simulation (MISSION) of National Institute for Fusion Science. This work was partially supported by Grants-in-Aid for Scientific Research of the Japan Society for the Promotion of Science (Nos. 14780396, 16560728).

### References

- [1] Y. Kusama, G. J. Kramer, H. Kimura *et al.*, Nucl. Fusion **39**, 1837 (1999).
- [2] G. J. Kramer, M. Iwase, Y. Kusama *et al.*, Nucl. Fusion **40**, 1383 (2000).
- [3] K. Shinohara, Y. Kusama, M. Takechi *et al.*, Nucl. Fusion **41**, 603 (2001).
- [4] K. Shinohara, M. Takechi, M. Ishikawa *et al.*, Nucl. Fusion **42**, 942 (2002).
- [5] C. Z. Cheng, L. Chen, and M. S. Chance, Ann. Phys. (N.Y.) **161**, 21 (1985).
- [6] C. Z. Cheng and M. S. Chance, Phys. Fluids **29**, 3659 (1986).

- [7] Y. Todo and T. Sato, *Phys. Plasmas* **5**, 1321 (1998).
- [8] Y. Todo, K. Shinohara, M. Takechi, and M. Ishikawa, *J. Plasma Fusion Res.* **79**, 1107 (2003), <http://jspf.nifs.ac.jp/Journal/2003.html>.
- [9] H. L. Berk, B. N. Breizman, and N. V. Petviashvili, *Phys. Lett. A* **234**, 213 (1997); **238**, 408(E) (1998).
- [10] H. L. Berk, B. N. Breizman, J. Candy, M. Pekker, and N. V. Petviashvili, *Phys. Plasmas* **6**, 3102 (1999).
- [11] L. Chen, *Phys. Plasmas* **1**, 1519 (1994).
- [12] C. Z. Cheng, N. N. Gorelenkov, and C. T. Hsu, *Nucl. Fusion* **35**, 1639 (1995).
- [13] H. L. Berk, D. N. Borba, B. N. Breizman, S. D. Pinches, and S. E. Sharapov, *Phys. Rev. Lett.* **87**, 185002 (2001).
- [14] F. Zonca, S. Briguglio, L. Chen, S. Dettrick, G. Fogaccia, D. Testa, and G. Vlad, *Phys. Plasmas* **9**, 4939 (2002).
- [15] K. Appert, R. Gruber, F. Troyon, and J. Vaclavik, *Plasma Physics* **24**, 1147 (1982).
- [16] A. Fukuyama and T. Akutsu, in proceedings of the 19th IAEA Fusion Energy Conference, 2002, Lyon (IAEA, 2003), TH/P3-14.
- [17] B. N. Breizman, H. L. Berk, M. S. Pekker, S. D. Pinches, and S. E. Sharapov, *Phys. Plasmas* **10**, 3649 (2003).
- [18] Y. Todo, K. Shinohara, M. Takechi, and M. Ishikawa, "Nonlocal energetic particle mode in a JT-60U plasma", to appear in *Phys. Plasmas*.
- [19] W. Park, S. Parker, H. Biglari, M. Chance, L. Chen, C. Z. Cheng, T. S. Hahm, W. W. Lee, R. Kulsrud, D. Monticello, L. Sugiyama, and R. White, *Phys. Fluids B* **4**, 2033 (1992).
- [20] Y. Todo, T. Sato, K. Watanabe, T. H. Watanabe, and R. Horiuchi, *Phys. Plasmas* **2**, 2711 (1995).
- [21] A. M. Dimits and W. W. Lee, *J. Comput. Phys.* **107**, 309 (1993).
- [22] S. E. Parker and W. W. Lee, *Phys. Fluids B* **5**, 77 (1993).
- [23] A. Aydemir, *Phys. Plasmas* **1**, 822 (1994).
- [24] E. V. Belova, N. N. Gorelenkov, and C. Z. Cheng, *Phys. Plasmas* **10**, 3240 (2003).
- [25] R. Nazikian, G. Y. Fu, S. H. Batha et al., *Phys. Rev. Lett.* **78**, 2976 (1997).
- [26] G. Y. Fu, R. Nazikian, R. Budny, and Z. Chang, *Phys. Plasmas* **5**, 4284 (1998).
- [27] Y. Chen, R. B. White, G. Y. Fu, and R. Nazikian, *Phys. Plasmas* **6**, 226 (1999).
- [28] K. Tani, M. Azumi, H. Kishimoto, and S. Tamura, *J. Phys. Soc. Jpn* **50**, 1726 (1981).
- [29] K. Harafuji, T. Hayashi, and T. Sato, *J. Comput. Phys.* **81**, 169 (1989).

## Boundary modulation effects on MHD instabilities in Heliotrons

N.Nakajima 1), S.R.Hudson 2), C.C.Hegna 3), and Y.Nakamura 4)

- 1) National Institute for Fusion Science, Oroshi-cho 322-6, Toki 509-5292, Japan
- 2) Princeton Plasma Physics Laboratory, P.O.Box 451, Princeton NJ 08543, USA.
- 3) Department of Engineering Physics, University of Wisconsin-Madison, WI 53706, USA.
- 4) Graduate School of Energy Science, Kyoto University, Uji, Kyoto 611-0011, Japan

e-mail contact of main author : nakajima@nifs.ac.jp

**Abstract** In three-dimensional configurations, the confinement region is surrounded by the stochastic magnetic field lines related to magnetic islands or separatrix, leading to the fact that the plasma-vacuum boundary is not so definite compared with tokamaks that the various modulations of the plasma-vacuum boundary will be induced around the stochastic region by a large Shafranov shift of the whole plasma, in especially high- $\beta$  operations. To examine such the modulation effects of the plasma boundary on MHD instabilities, high- $\beta$  plasmas allowing a large Shafranov shift are considered in the inward-shifted LHD configurations with the vacuum magnetic axis  $R_{ax}$  of 3.6m, for which previous theoretical analyses indicate that pressure-driven modes are significantly more unstable compared with experimental observations. It is shown that the boundary modulation due to a free motion of the equilibrium plasma has not only significant stabilizing effects on ideal MHD instabilities, but also characteristics consistent to experimental observations.

## 1 Introduction

Recently, high- $\beta$  plasmas with  $\langle\beta\rangle \sim 3\%$  have been established in the inward-shifted configurations with the vacuum magnetic axis  $R_{ax}$  of 3.6m [1], for which previous theoretical ideal MHD stability analyses show that pressure-driven modes are significantly more unstable compared with experimental observations [2]. There may be two types of thought to remove this discrepancy between theoretical and experimental results. One is to show the nonlinear saturation level of the linear modes may be too low to influence on the confinement performance and/or to show some two-fluid or kinetic effects added to MHD model may have strong stabilizing effects. The other is to reconsider the MHD equilibria themselves used in the linear and nonlinear stability analyses. It should be noted that, in the previous theoretical considerations, the MHD equilibria are mainly calculated under a fixed boundary corresponding to a *clear* Last Close Flux Surface (LCFS) of the vacuum magnetic field [2,3], and that, in the free boundary equilibrium calculations, an artificial material limiter is introduced to fix the plasma boundary, where the plasma pressure vanishes, on the clear LCFS of the vacuum magnetic field in the outboard of the horizontally elongated poloidal cross section [4]. Those methods to determine the MHD equilibria are based on the conjecture that the plasma do not expand beyond the clear LCFS of the vacuum field so much. In these analyses, the resultant MHD equilibria are strongly unstable against the pressure-driven ideal MHD modes in the inward-shifted LHD configurations. However, such a clear LCFS of the vacuum magnetic field is surrounded by unclear flux surfaces or stochastic magnetic field lines with a quite long connection length and a definite rotational transform, namely *averaged flux surfaces* with a quite long connection length and a definite rotational transform could exist in such a stochastic region. Thus, it is natural to consider that a movement of the equilibrium plasma into such a region is allowable and that a boundary modulation induced by the plasma free motion will lead to a state with lower free energy compared to that under the fixed boundary. Indeed, experimentally, it is fairly standard observation that the stochastic magnetic region surrounding nested flux surfaces holds confinement properties or pressure gradient due to long connection lengths of the magnetic field lines related to some magnetic structures [5].

In this work, analyses on MHD equilibria and stability are performed in order to show the significant stabilizing effects of the boundary modulation due to a free motion of equilibrium plasma with increasing  $\beta$  on the linearized ideal MHD stability, which may lead to removal of discrepancy between experimental and the previous theoretical results. For the MHD equilibrium calculations, vmec code [6] is used, where only currentless equilibria are considered for simplicity. For linearized ideal MHD stability analyses, cas3d3 code [7], based on the variational or energy principle, is used for low- $n$  compressible or incompressible perturbations ( $n$  is the toroidal mode number), under the constant mass density assumption.

## 2 Properties of the peripheral magnetic field

### 2.1 Vacuum magnetic field

The Poincare plots of the peripheral vacuum magnetic field in the horizontally elongated LHD poloidal cross section are shown in upper row of Fig. 1, for inward-shifted (left), standard (middle), and outward-shifted (right) configurations.

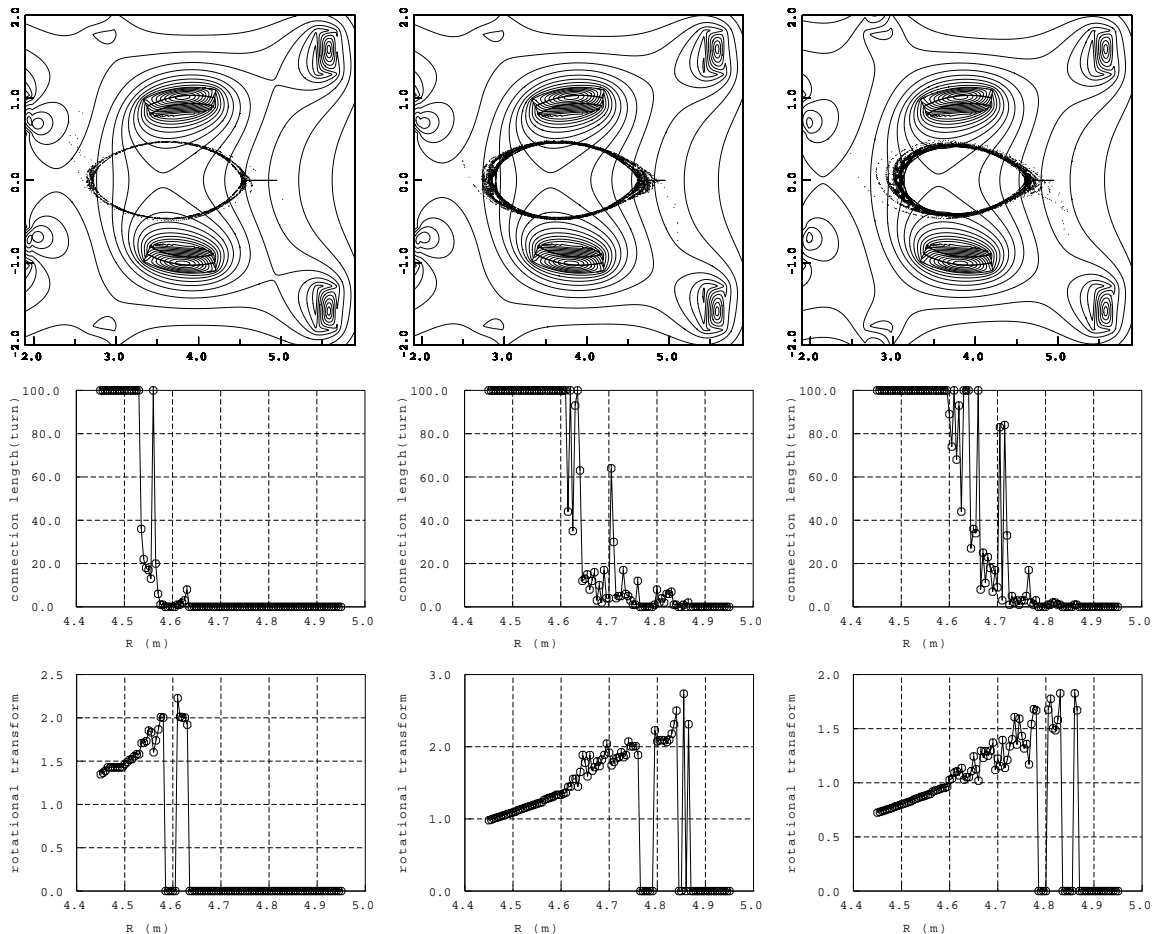


FIG. 1: Poincare plots (upper row), connection length or toroidal turns (middle row), and rotational transform  $\iota$  (lower row). Three columns correspond to inward-shifted (left), standard (middle), and outward-shifted (right) configurations. In the Poincare plots, the contours of magnetic field strength and the shape of helical coils are also shown by thin and thick solid lines, respectively.

From these figures, it is understood that the width of the peripheral region with stochastic magnetic field lines changes thick to thin according to the vacuum magnetic axis shift from outboard to inboard. The inward-shifted configurations are characterized as the configurations

with most thin width of the peripheral stochastic region. The middle row of Fig. 1 indicates the corresponding connection length (toroidal turn) of the magnetic field lines started from the equatorial plane ( $z = 0$ ) as a function of the major radius  $R$ . The corresponding rotational transform  $\iota$  is denoted in the lower row of Fig. 1, where  $\iota$  is set 0 when the connection length is shorter than one toroidal turn. From these two types of figures, it is understood that the region with a fairly long connection length (more than 100 toroidal turns  $\sim 2.2$  km) is limited by magnetic islands with  $\iota = 30/19 \sim 1.579$  (inward-shifted),  $\iota = 20/15 \sim 1.333$ , (standard) and  $\iota = 10/10 = 1$  (outward-shifted). In the inward-shifted configurations, a clear LCFS might be chosen around  $\iota = 1.48$  near the magnetic island with  $\iota = 30/20$ .

The region with a quite short connection length, for example, less than one toroidal turn, is considered to be direct loss region without plasma confinement. In contrast with it, the region with a long connection length and a definite rotational transform is considered to become a plasma confinement region with *averaged flux surfaces* depending on electron temperature and electron density there. Since the typical mean free path along a magnetic field line is around  $10 \sim 20$  m, the stochastic region consisting of field lines with a connection length of several 10 turns might be considered to be a confinement region with anomalous diffusion properties. Letting the magnetic field in this region be  $\vec{B} + \delta\vec{B}$  where  $\vec{B}$  and  $\delta\vec{B}$  are an averaged regular magnetic field and a fluctuating magnetic field, respectively, the electron thermal diffusion coefficient  $\chi_e$  might be estimated as

$$\chi_e = \frac{4v_{Te}\delta k_{\parallel}}{\pi^{3/2}\bar{k}_r^2} \begin{cases} \mathcal{R}^2 & \text{for } \mathcal{R} \leq 1 \\ \mathcal{R} & \text{for } \mathcal{R} \geq 1, \end{cases} \quad \mathcal{R} \equiv \left[ \frac{\pi L_{\parallel}\bar{k}_r^2}{8 \delta k_{\parallel}} \sum_m \left\langle \left( \frac{\delta B_{rmk_{\parallel}}}{B} \right)^2 \right\rangle_{k_{\parallel}} \right]^{1/2} \quad (1)$$

where  $L_{\parallel}$  and  $\delta k_{\parallel} \sim L_{\parallel}^{-1}$  is the parallel correlation length and the width of the parallel wave numbers contributing to the diffusion, respectively, and  $L_{\perp}$  and  $\bar{k}_r \gtrsim L_{\perp}^{-1}$  are the perpendicular (radial) correlation length and the typical radial wave number, respectively.  $\delta B_{rmk_{\parallel}}$  means the Fourier component of a radial fluctuating magnetic field with the poloidal mode number  $m$  and the parallel wave number  $k_{\parallel}$ , and  $v_{Te}$  is an electron thermal velocity. The formula given by Eq.(1) is derived from the Lagrange auto-correlation function by following the particle orbits without toroidal drift, where a renormalization effect is included and  $\mathcal{R} \ll 1$  corresponds to the quasi-linear limit. When the magnitude of the fluctuating magnetic field  $\delta\vec{B}$  is sufficiently small compared with the averaged regular field  $\vec{B}$ , the region with stochastic magnetic field lines might be treated as a confinement region with the electron thermal diffusion coefficient  $\chi_e$  given by Eq.(1). Based on this fact, the plasma-vacuum boundary could be chosen from averaged flux surfaces with a long connection length and a definite rotational transform in the stochastic region, and also a free equilibrium plasma motion could be allowed in such a stochastic region through the change of the vacuum magnetic field by the plasma current.

## 2.2 Finite- $\beta$ magnetic field

Properties of the peripheral magnetic field of finite- $\beta$  MHD equilibria are investigated by using HINT2 code (a new version of the original HINT code [8]). In HINT2 code, as well as HINT code, a relaxation method is used in order to obtain the MHD equilibrium without the assumption of the nested flux surfaces. Although the boundary of the calculation box is assumed to be a perfect conductor, the obtained MHD equilibrium is essentially free boundary equilibrium because no fixed boundary condition is introduced between plasma region and the vacuum region. The relaxation method is an iterative method consisting of 1) parallel relaxation of the pressure along fixed magnetic field lines and 2) perpendicular relaxation of the magnetic field for a fixed pressure profile. The parallel relaxation introduces an effective perpendicular transport of the pressure with respect to an averaged magnetic field  $\vec{B}$ , when

the magnetic field is decomposed into an averaged regular part  $\bar{\vec{B}}$  and a fluctuating part  $\delta\vec{B}$  (for clear nested flux surfaces,  $\delta\vec{B} = 0$ , so that there is no effective perpendicular transport). In such cases, the effective perpendicular transport coefficient  $\chi_{\perp}$  is proportional to  $\chi_e$  given by Eq.(1). Moreover, since the plasma pressure along the magnetic field lines with a short connection length is reset to 0, only the pressure along magnetic field lines with a long connection length is kept in the resultant MHD equilibrium.

Figure 2 shows the Poincare plots of the magnetic field lines of the finite- $\beta$  plasma for  $\langle\beta\rangle = 1.4\%$  (left column) and  $\langle\beta\rangle = 3.7\%$  (right column) in the inward-shifted configuration. As  $\beta$  increases, the width of the peripheral magnetic islands becomes wide, and stochastic magnetic field is created near the plasma periphery through islands-overlapping. Such a stochastic region penetrates from the plasma peripheral region to core region, as  $\beta$  increases. The pressure gradient still exists in the stochastic region with a long connection length and a definite rotational transform, and so, as well as the vacuum magnetic field, such a stochastic region should be treated as the plasma region with averaged flux surfaces.

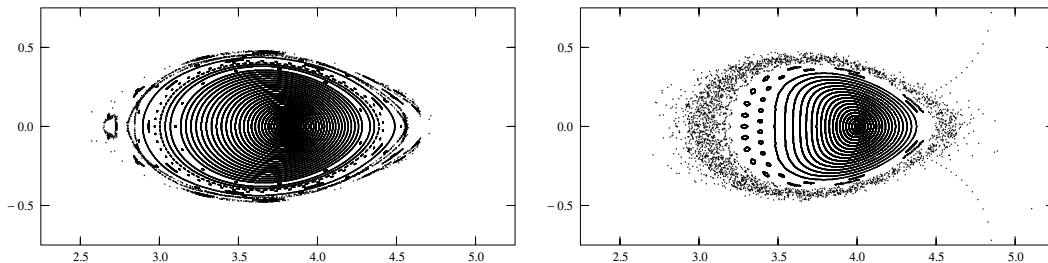


FIG. 2: Poincare plots of the magnetic field lines in the horizontally elongated LHD poloidal cross section for  $\langle\beta\rangle = 1.4\%$  (left column) and  $\langle\beta\rangle = 3.7\%$  (right column).

### 3 Properties of the ideal MHD stability

According to the consideration in the previous section, several MHD equilibria in the inward-shifted LHD configuration are chosen for linearized ideal MHD stability analyses. Essential point of the consideration is that an averaged flux surface could be chosen as a plasma-vacuum boundary from the region with stochastic magnetic field lines, when the connection length is long and the rotational transform is definite. However, there is still ambiguity which surface should be chosen. Moreover, it is not so easy to distinguish stabilizing or destabilizing effects due to the change of the local pressure gradient on the mode rational surface from those due to the geometrical change induced by the plasma free boundary motion. Thus, two types of approaches are chosen to specify the MHD equilibrium. One is to simulate the effects of the free boundary motion by introducing small boundary modulation to the boundary determined from the vacuum magnetic field. In this case, change of stabilizing or destabilizing effects due to the change of the local pressure gradient on the rational surfaces related to unstable modes is so weak that almost pure effects due to the boundary modulation on MHD stability might be observed. The other one is natural free boundary equilibrium calculations, where several averaged flux surfaces are chosen for comparison.

#### 3.1 In MHD equilibria with modulated fixed boundary

In the inward-shifted LHD configurations, the vacuum flux surfaces are so compressed into the helical coils inner side of torus that the bumpy deformation of the plasma boundary, expressed by the Fourier components with  $(m, n) = (0, \neq 0)$  ( $m$  and  $n$  are poloidal and toroidal mode numbers, respectively) is strongly enhanced. As  $\beta$  increases, the whole plasma moves from inner side of the torus to the outer side. Through this Shafranov shift, the enforced boundary shaping by external coils will be so reduced that the bumpy deformation of the plasma

boundary will diminish. In order to simulate the effects of the boundary modulation related to the bumpy components induced by the free boundary motion, four types of currentless MHD equilibria with different plasma boundary shapes, shown in Tab.1, are investigated under the fixed boundary condition for various  $\beta$ -values by using vmec code. The boundaries of Type  $S$  and  $L$  are determined from the vacuum nested flux surfaces without boundary modulations, where  $S$  and  $L$  indicate small and large plasma volume, respectively. The rotational transform at the plasma boundary is  $\iota = 1.36$  for Type  $S$  and  $\iota = 1.48$  for Type  $L$ , respectively. On the other hand, the boundaries of Type  $S$ -mod and  $L$ -mod are created from those of Type  $S$  and  $L$  by eliminating only the bumpy Fourier components from the plasma boundary spectrum. Broad pressure profiles, which is considered to be similar to experimentally obtained one,  $P(s) = P_0(1 - s)(1 - s^9)$  is used, where  $s$  is the normalized toroidal flux. The ideal MHD stability analyses for compressible perturbations are performed by using the cas3d3 code.

Type	$S$	$L$	$S$ -mod	$L$ -mod
boundary	vacuum	vacuum	modified $S$	modified $L$

TAB. 1 Boundary type of considered MHD equilibria

Figure 3 shows the contours of the flux surfaces and level surfaces of the vmec poloidal angles in the vertically elongated poloidal cross section of vacuum (left column) and finite- $\beta$  with  $\langle\beta\rangle = 3.0\%$  (right column) configurations with original  $L$  (upper row) and modulated  $L$ -mod (lower row) plasma boundary. It is understood from these figures that although the change of the plasma boundary shape by eliminating the bumpy components from the plasma boundary spectrum is quite small, considerable outward magnetic axis shift is induced.

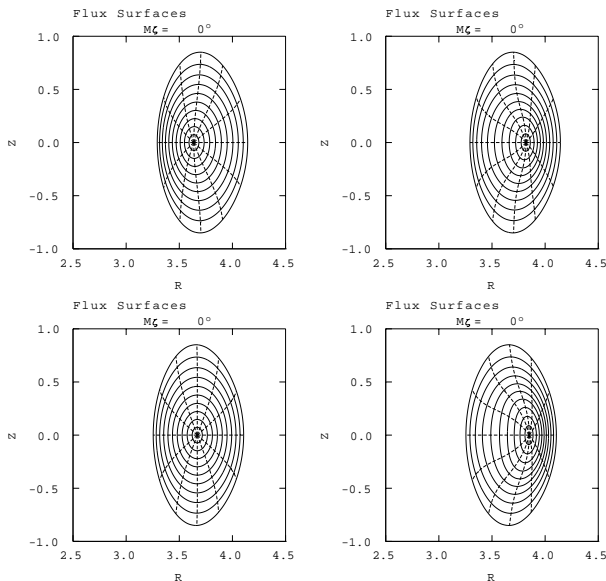


FIG. 3: Contours of the flux surfaces and level surfaces of the vmec poloidal angles in the vertically elongated poloidal cross section for vacuum (left column) and finite- $\beta$  with  $\langle\beta\rangle = 3.0\%$  (right column) configurations with original  $L$  (upper row) and modulated  $L$ -mod (lower row) plasma boundary.

This geometrical change of the flux surfaces leads to the significant change of the Mercier criterion as is shown in Fig. 4. Since the pressure gradient on each flux surface is fixed and  $\iota$  does not change so much, the change of the Mercier criterion  $D_I$  is considered to mainly come from the geometrical effects induced by the boundary modulation.

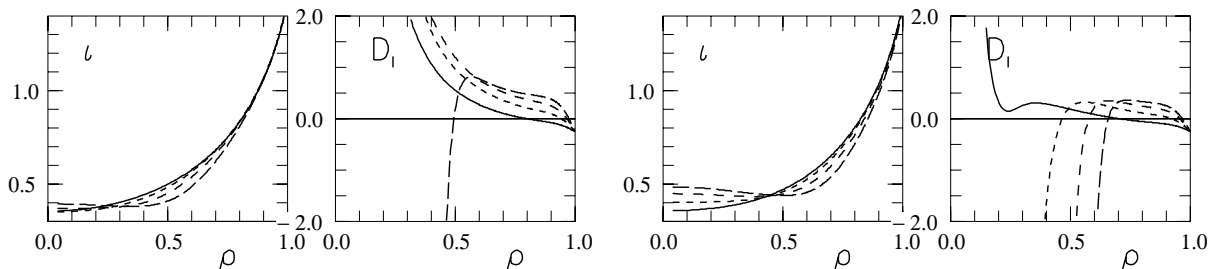


FIG. 4: Change of the rotational transform  $\iota$  and the Mercier criterion  $D_I$  with respect to  $\langle\beta\rangle$  for original  $L$  (left two columns) and modulated  $L$ -mod (right two columns) configurations, where  $\rho = \sqrt{s}$ . Solid lines correspond to the vacuum. Dashed lines correspond to  $\langle\beta\rangle = 1\%$ ,  $\langle\beta\rangle = 2\%$ , and  $\langle\beta\rangle = 3\%$  from short to long ones.

Figure 5 shows the growth rates normalized by the Alfvén transit time on the magnetic axis  $\gamma\tau_{A0}$  vs the toroidal mode number  $n$  for equilibria with original vacuum boundary (Type  $S$  and  $L$ ), where  $\gamma\tau_{A0} = 0.1$  corresponds to around  $40\mu\text{sec}$  for typical high- $\beta$  LHD operation parameters. Every magnetic field line at a Mercier unstable rational surface has unfavorable magnetic curvature in average, and so the toroidal mode coupling of perturbations inherent to helical systems becomes so weak there [9,10] that the toroidal mode number  $n$  can be used as a good quantum number. As  $\beta$  increases, unstable modes change from localized interchange modes with only single dominant Fourier mode, to localized interchange modes consisting of multiple Fourier components, and finally to ballooning modes, except for considerably low- $n$  modes, say,  $(m, n) = (2, 1)$ . As is understood from the comparison of stability analyses between fixed boundary (left column in Fig. 5) and free boundary (right column in Fig. 5), the perturbations become significantly more unstable and more global, when free radial motions of the perturbations are allowed on the plasma boundary, because such free motions lead to the excitation of the Fourier modes resonating near the plasma edge and the possibility that low- $n$  global interchange modes under the fixed boundary condition with  $\xi^s(a) = 0$  change into ballooning modes for  $\xi^s(a) \neq 0$ , where  $\xi^s = \vec{\xi} \cdot \nabla s$  is the normal component of the displacement vector  $\vec{\xi}$ .

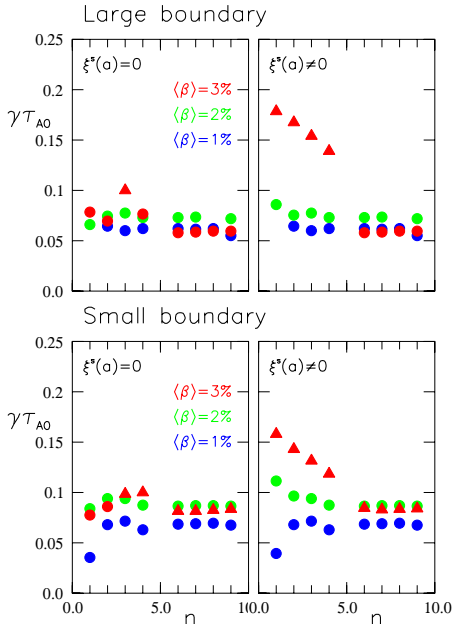


FIG. 5:  $\gamma\tau_{A0}$  vs  $n$  for equilibria with original vacuum boundary (Type  $S$  (lower row) and Type  $L$  (upper row)). The left (right) column corresponds to fixed (free) boundary stability analyses. The circles (triangles) denote interchange (ballooning) modes.

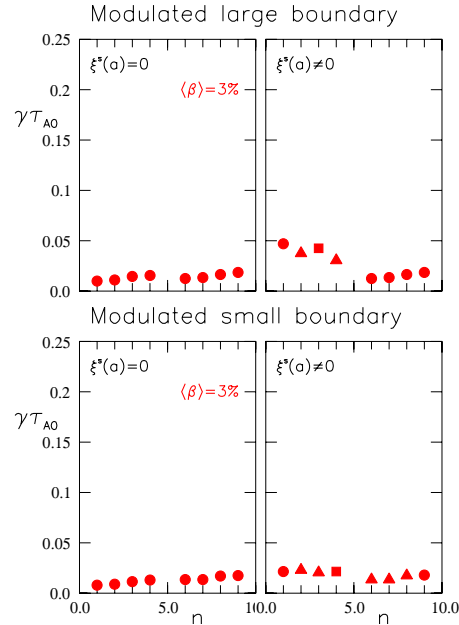


FIG. 6:  $\gamma\tau_{A0}$  vs  $n$  for equilibria with modulated boundary (Type  $S$ -mod (lower row) and Type  $L$ -mod (upper row)) and  $\langle\beta\rangle = 3\%$ . The notations are same as Fig. 5, and additional rectangles indicate ballooning modes with external components.

Figure 6 shows  $\gamma\tau_{A0}$  vs  $n$  for equilibria with modulated boundary Type  $S$ -mod or Type  $L$ -mod. Significant stabilizing effects by the boundary modulation simulating the free boundary motion of equilibrium plasma are quite clear. The stability properties between Type  $S$  and Type  $L$  boundary, and between Type  $S$ -mod and Type  $L$ -mod boundary do not change so much that it may be concluded that the size effects of the plasma boundary are weak. It should

be emphasized that a small change of the boundary shape leads to the significant improvement of the MHD stability through the geometrical change of the MHD equilibrium brought by the Shafranov shift.

One of characteristic points are that the experimentally observed modes with  $(m, n) = (2, 3)$  [11], whose resonant surface may be considered to be outside of the plasma, are weakly excited like external modes as is shown in Fig. 7. Since the magnitude of vacuum magnetic perturbations is determined by the  $\xi^s$  on the plasma-vacuum surface,  $(m, n) = (2, 3)$  mode is dominantly observed in these perturbations.

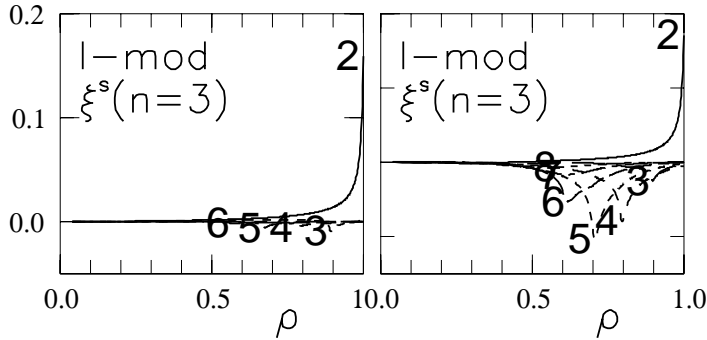


FIG. 7: Radial profiles of Fourier component of eigenfunctions with an external Fourier component:  $(m, n) = (2, 3)$  for  $\langle\beta\rangle = 2\%$  (left column) and  $\langle\beta\rangle = 3\%$  (right column) equilibria with boundary Type L-mod. Attached numbers indicate the poloidal mode numbers  $m$ .

The other characteristic point is that the core region stays in the second stability region of the ballooning modes. This point will be intensively examined in near future.

### 3.2 In MHD equilibria with free boundary

Free boundary currentless equilibria in various  $\beta$  values are created by keeping the contained toroidal flux constant. Each contained toroidal flux corresponds to the vacuum rotational transform  $t_v = 1.48$ ,  $t_v = 1.58$ , and  $t_v = 1.72$ . The surface corresponding to  $t_v = 1.48$  is a clear nested flux surface, however, surfaces corresponding to  $t_v = 1.58$ , and  $t_v = 1.72$  are averaged flux surfaces existing in the stochastic magnetic field region. Corresponding  $t$  in finite- $\beta$  equilibria with  $\langle\beta\rangle = 3\%$  are  $t = 1.49$ ,  $t = 1.60$ , and  $t = 1.77$ , respectively, where the same pressure profile as that in the previous cases is used. In order to distinguish effects of the equilibrium free motions on MHD stability from stability properties in the fixed boundary MHD equilibria, corresponding fixed plasma boundaries are created from the free boundary equilibrium with a quite low plasma pressure. Hereafter, only free boundary stability analyses are done for incompressible perturbations. Roughly speaking, the growth rate of the compressible perturbation is one-third of that of the incompressible perturbation. Figure 8 shows the comparison of stability analyses between fixed boundary MHD equilibria and free boundary MHD equilibria. As well as the MHD equilibria with boundary modulation, free boundary MHD equilibria are quite stable compared with the corresponding MHD equilibria with fixed boundary. By comparing Fig. 8 with the right column of Fig. 5 and Fig. 6, it is understood that significant stabilizing effects by a free motion of MHD equilibrium related to the Shafranov shift mainly correspond to the elimination of the bumpy components from the plasma boundary ( $\gamma\tau_{A0}$  for compressible perturbations is around one-third of that for incompressible perturbations).

One of characteristics of the stability analyses for free boundary MHD equilibria is that interchange modes with an external Fourier component of  $(m, n) = (1, 2)$  are excited, when a larger plasma boundary is chosen as shown in Fig. 9. These modes are recently observed in an inward-shifted configuration with a little bit different coil aspect ratio. In this perturbation given in Fig. 9,  $(m, n) = (1, 2)$  mode may be dominantly observed experimentally.

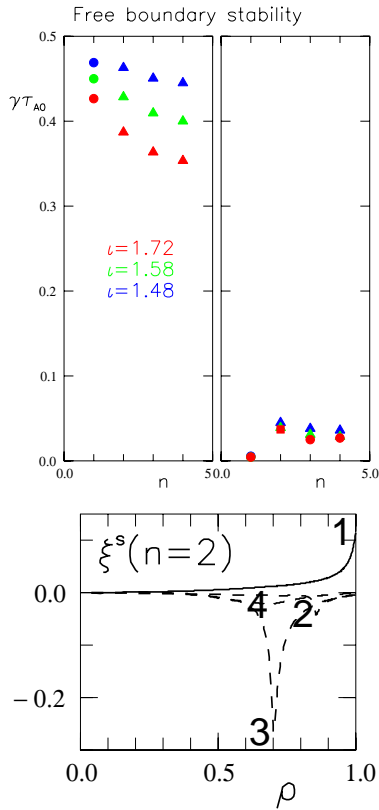


FIG. 8:  $\gamma\tau_{A0}$  vs  $n$  for MHD equilibria ( $\langle\beta\rangle = 3\%$ ) with fixed boundary (left column) and with free boundary (right column). Blue, green, and red colors correspond to the equilibrium with the rotational transform at the plasma boundary of  $\iota_v = 1.48$ ,  $\iota_v = 1.58$ , and  $\iota_v = 1.72$  in the vacuum states. Circles (triangles) denote interchange (ballooning or ballooning-like) modes. The red square indicates the interchange modes with external Fourier component shown in Fig. 9.

FIG. 9: Radial profiles of Fourier components of eigenfunctions with an external Fourier component:  $(m, n) = (1, 2)$  for the free boundary MHD equilibrium with  $\iota_v = 1.72$  and  $\langle\beta\rangle = 3\%$ , which corresponds to the growth rate denoted by red square in Fig. 8. Attached numbers denote the poloidal mode numbers  $m$ .

## 4 Discussions

It has been shown that the boundary modulation by a free motion of MHD equilibrium related to Shafranov shift has significant stabilizing properties for ideal pressure-driven modes, where essential modulation is reduction of the bumpy components of the plasma boundary. These stabilizing effects do not depend on the choice of the averaged flux surfaces with a long connection length and a definite rotational transform from the vacuum magnetic field. Depending on the chosen boundary, however, various external modes, which have same Fourier spectrum as those experimentally observed, are excited. In experiments, both the plasma boundary and the pressure profile will change in  $\beta$  ramp-up phases, according to the heating and the density control. Adequate choice of the plasma boundary and pressure profile might lead to better coincidences between theory and experiment.

The author(N.N) greatly acknowledges Dr.K.Y.Watanabe for his quite fruitful discussions.

## References

- [1] MOTOJIMA, O., et al., Nucl. Fusion **43** (2003) 1674.
- [2] NAKAJIMA, N., To appear in J. Plasma Fusion and Res. SER. **6** (2004).
- [3] ICHIGUCHI, K., NAKAJIMA, N., et al., Nucl. Fusion **33** (1993) 481.
- [4] ICHIGUCHI, K., NAKAJIMA, N., and GARDNER, H. J, Nucl. Fusion **36** (1996) 1157.
- [5] MORISAKI, T., et al., J. Nucl. Materials **313-316** (2003) 548.
- [6] HIRSHMAN, S. P., Phys. Fluids **26** (1983) 3553.
- [7] NÜHRENBERG, C, Phys. Plasmas **6** (1999) 137.
- [8] HARAFUJI, K, et al., J. Comput. Phys. **81** (1989) 169.
- [9] NAKAJIMA, N, Phys. Plasmas **3** (1996) 4556.
- [10] CHEN, J., NAKAJIMA, N, and OKAMOTO, M., Phys. Plasmas **6** (1999) 1562.
- [11] SAKAKBARA, S., et al., Plasma Phys. Control. Fusion **44** (2002) A217.

# Velocity-Space Structures of Distribution Function in Toroidal Ion Temperature Gradient Turbulence

T.-H.Watanabe and H.Sugama

*National Institute for Fusion Science / The Graduate  
University for Advanced Studies, Toki, Gifu, 509-5292, Japan*

(Dated: revised December 20, 2004)

## Abstract

Velocity-space structures of ion distribution function associated with the ion temperature gradient (ITG) turbulence and the collisionless damping of the zonal flow are investigated by means of a newly developed toroidal gyrokinetic-Vlasov simulation code with high velocity-space resolution. The present simulation on the zonal flow and the geodesic acoustic mode (GAM) successfully reproduces the neoclassical polarization of trapped ions as well as the parallel phase mixing due to passing particles. During the collisionless damping of GAM, finer-scale structures of the ion distribution function in the velocity space continue to develop due to the phase mixing while preserving an invariant defined by a sum of an entropy variable and the potential energy. Simulation results of the the toroidal ITG turbulent transport clearly show generation of the fine velocity-space structures of the distribution function and their collisional dissipation. Detailed calculation of the entropy balance confirms the statistically steady state of turbulence, where the anomalous transport balances with the dissipation given by the weak collisionality. The above results obtained by simulations with high velocity-space resolution are also understood in terms of generation, transfer, and dissipation processes of the entropy variable in the phase space.

PACS numbers: 52.25.Fi, 52.35.Ra, 52.65.Tt

## I. INTRODUCTION

Numerical simulations based on the gyrokinetic formalism for drift wave turbulence, such as the ion temperature gradient (ITG) mode [1], have been extensively performed with the aim of understating anomalous transport mechanism in a core region of magnetically confined plasmas. Transport suppression by self-generated zonal flows [2, 3] is one of the important results confirmed by the numerous simulations as well as theoretical investigations. In a high-temperature plasma, where mean-free-paths of ions and electrons are much longer than device sizes, the one-body velocity distribution function,  $f$ , involves a substantial difference from the thermal equilibrium with the Maxwellian,  $F_M$ . This is why kinetic approaches are indispensable for studying the core turbulent transport. Velocity-space structures of the distribution function and their relation to the turbulent transport, however, have rarely been discussed in the conventional kinetic simulations.

Regarding the velocity-space structures of  $f$  in plasma turbulence, it has been theoretically pointed out that, if a steady transport flux is observed in collisionless turbulence driven by constant density or temperature gradients, a quasisteady state should be realized [4–6], where high-order velocity-space moments of the perturbed distribution function  $\delta f$  continue to grow but the low-order ones are constant in average. Here, the deviation of  $f$  from the equilibrium is defined by  $\delta f \equiv f - F_M$ . Our gyrokinetic-Vlasov (Eulerian) simulation manifested existence of the quasisteady state of the collisionless slab ITG turbulence [7], where continuous generation of micro velocity-scale structures of  $\delta f$  through the phase mixing is responsible for the growth of the high-order moments. The quasisteady state is also characterized by a balance between monotonic increase of an entropy variable defined by a square-integral of  $\delta f$  and the turbulent transport. Recently, it has been shown numerically and analytically how the whole velocity-space spectrum of  $\delta f$  from macro to micro scales is determined by processes of the anomalous heat transport, the phase mixing, and the dissipation in the steady state of the weakly collisional slab ITG turbulence [8]. As the macro velocity-space structures of  $f$  directly related to the turbulent transport flux are hardly influenced in the weak collisionality limit, the transport coefficient asymptotically approaches the value for the collisionless case for sufficiently low collision frequency, while a logarithmic dependence on relatively large values of  $\nu$  has also been obtained [8]. It is emphasized that only a kinetic simulation with high velocity-space resolution and negligible

numerical dissipation enables one to quantitatively investigate how the turbulent transport depends on the weak collisionality.

We have now developed a new toroidal gyrokinetic-Vlasov simulation code with high velocity-space resolution [9], which can precisely deal with the phase-mixing processes of  $f$  in toroidal configurations. With this code, detailed velocity-space structures produced by collisionless dynamics of the zonal flow [10] and the geodesic acoustic mode (GAM) [11] are successfully simulated and the transport flux in the toroidal ITG turbulence consistent with the entropy balance can be obtained. In this paper, we present the numerical simulation results of the zonal flow dynamics and the ITG turbulent transport in a tokamak configuration, focusing on the velocity-space structures of the ion distribution function.

This paper is organized as follows. After introduction of the physical model in Section II, the balance equation for the entropy variable in a toroidal flux tube configuration is described in Section III. In Section IV, we report velocity-space structures of  $\delta f$  during the collisionless damping of GAM associated with the zonal flow, of which the level is considered to be critical to determination of the transport flux in the toroidal ITG turbulence. Nonlinear simulation results of the toroidal ITG turbulent transport are shown in Section V, where the entropy balance and the velocity-space structures of the distribution function are discussed. The results are summarized in Section VI.

## II. MODEL

We consider the gyrokinetic equation [12] for the ion distribution function in the low- $\beta$  (electrostatic) limit. By applying the flute reduction for a large-aspect-ratio tokamak with concentric circular magnetic surfaces and the major radius  $R_0$ , the governing equation is written as

$$\frac{\partial \delta f}{\partial t} + v_{\parallel} \mathbf{b} \cdot \nabla \delta f + \frac{c}{B_0} \{\Phi, \delta f\} + \mathbf{v}_d \cdot \nabla \delta f - \mu (\mathbf{b} \cdot \nabla \Omega_i) \frac{\partial \delta f}{\partial v_{\parallel}} = (\mathbf{v}_* - \mathbf{v}_d - v_{\parallel} \mathbf{b}) \cdot \frac{e \nabla \Phi}{T_i} F_M + C(\delta f) \quad (1)$$

where  $\mathbf{b}$ ,  $B_0$ ,  $c$ ,  $\Phi$ ,  $e$ , and  $T_i$  are the unit vector parallel to the magnetic field, magnetic field strength on the magnetic axis, the speed of light, the electrostatic potential averaged over the gyromotion, the elementary charge, and the ion temperature, respectively. The parallel velocity,  $v_{\parallel}$ , and the magnetic moment,  $\mu$ , are used as the velocity-space coordinates, where  $\mu$  is defined by  $\mu \equiv v_{\perp}^2 / 2\Omega_i$  with the ion cyclotron frequency  $\Omega_i = eB/m_i c$  ( $m_i$  is the

ion mass) and the perpendicular velocity  $v_{\perp}$ . The collision term is shown by  $C(\delta f)$ . The Maxwellian distribution is given by

$$F_M = n_0 \left( \frac{m_i}{2\pi T_i} \right)^{3/2} \exp \left[ -\frac{m_i (v_{\parallel}^2 + 2\Omega_i \mu)}{2T_i} \right] \quad (2)$$

with poloidal angle dependence through  $\Omega_i$  since  $\mu$  is chosen as one of the independent variables (the phase-space coordinates).

In the toroidal flux tube coordinates [13],  $x = r - r_0$ ,  $y = \frac{r_0}{q_0} [q(r)\theta - \zeta]$ , and  $z = \theta$  [where the safety factor  $q(r = r_0) = q_0$  at the minor radius  $r = r_0$ ], background gradients and magnetic shear parameters are assumed to be constant, such that  $L_n = -(d \ln n / dr)^{-1}$ ,  $L_T = -(d \ln T_i / dr)^{-1}$ , and  $q(r) = q_0 [1 + \hat{s}(r - r_0) / r_0]$ . The poloidal and toroidal angles are denoted by  $\theta$  and  $\zeta$ , respectively. The abbreviations are defined by

$$\begin{aligned} \mathbf{b} \cdot \nabla &= \frac{1}{q_0 R_0} \frac{\partial}{\partial z}, \quad \{\Phi, \delta f\} = \frac{\partial \Phi}{\partial x} \frac{\partial \delta f}{\partial y} - \frac{\partial \Phi}{\partial y} \frac{\partial \delta f}{\partial x}, \quad B = B_0 \left( 1 - \frac{r_0}{R_0} \cos z \right), \\ \mathbf{v}_d &= -\frac{v_{\parallel}^2 + \Omega_i \mu}{\Omega_i R_0} [\hat{x} \sin z + \hat{y} (\cos z + \hat{s} z \sin z)], \quad \mathbf{v}_* = -\hat{y} \frac{c T_i}{e L_n B_0} \left[ 1 + \eta_i \left( \frac{m_i v^2}{2 T_i} - \frac{3}{2} \right) \right], \end{aligned}$$

where  $\eta_i = L_n / L_T$  and  $v^2 = v_{\parallel}^2 + 2\Omega_i \mu$ . Unit vectors in the  $x$  and  $y$  directions are denoted by  $\hat{x}$  and  $\hat{y}$ , respectively. The radially-localized flux tube model enables us to impose the periodic boundary condition both in the  $x$  and  $y$  directions so that the Fourier spectral method can be applied to calculation of the convection (the Poisson brackets) term in Eq.(1). In the perpendicular wave number space  $(k_x, k_y)$ ,  $\Phi$  is related to the electrostatic potential,  $\phi$ , such that

$$\Phi_{k_x, k_y} = J_0(k_{\perp} v_{\perp} / \Omega_i) \phi_{k_x, k_y}. \quad (3)$$

Here,  $J_0$  is the zeroth order Bessel function and  $k_{\perp}^2 = (k_x + \hat{s} z k_y)^2 + k_y^2$ . The potential acting on particle positions,  $\phi_{k_x, k_y}$ , is determined by the quasi-neutrality condition,

$$\int J_0 f_{k_x, k_y} d^3 v - \frac{e \phi_{k_x, k_y}}{T_i} n_0 (1 - \Gamma_0) = n_{e, k_x, k_y}, \quad (4)$$

where the Fourier component of  $\delta f$  is denoted by  $f_{k_x, k_y}$ . Also,  $\Gamma_0 = e^{-b} I_0(b)$  with  $b = (k_{\perp} v_{ti} / \Omega_i)^2$ . The zeroth order modified Bessel function and the ion thermal speed are represented by  $I_0$  and  $v_{ti} = \sqrt{T_i / m_i}$ , respectively. The ratio of the electron density perturbation,  $n_{e, k_x, k_y}$ , to the averaged one,  $n_0$ , is assumed to be given in terms of the electron

temperature,  $T_e$ , by

$$\frac{n_{e,k_x,k_y}}{n_0} = \begin{cases} \tau \frac{e(\phi_{k_x,k_y} - \langle \phi_{k_x,k_y} \rangle)}{T_i} & \text{for } k_y = 0 \\ \tau \frac{e\phi_{k_x,k_y}}{T_i} & \text{for } k_y \neq 0 \end{cases}, \quad (5)$$

where  $\tau = T_i/T_e$  and  $\langle \dots \rangle$  means the flux surface average defined by

$$\langle A \rangle = \int_{-N_\theta\pi}^{+N_\theta\pi} \frac{A}{B_p} dz \Big/ \int_{-N_\theta\pi}^{+N_\theta\pi} \frac{1}{B_p} dz = \int_{-N_\theta\pi}^{+N_\theta\pi} \frac{A}{B} dz \Big/ \int_{-N_\theta\pi}^{+N_\theta\pi} \frac{1}{B} dz. \quad (6)$$

Here, the poloidal magnetic field is denoted by  $B_p$ . The last equality in Eq.(6) holds for the concentric circular magnetic surfaces with  $\mathbf{B} = B(r, \theta)[\hat{e}_\zeta + (r/qR_0)\hat{e}_\theta]$ , by neglecting  $O[(r/R_0)^2]$  terms, where  $\hat{e}_\theta$  and  $\hat{e}_\zeta$  denote the orthogonal unit vectors in the poloidal and toroidal directions, respectively. The parallel length of the flux tube is set to  $2N_\theta\pi$  where the modified periodic boundary condition is used in the  $z$  direction [13]. Hereafter, physical quantities are normalized as follows;  $x = x'/\rho_i$ ,  $t = t'v_{ti}/L_n$ ,  $v = v'/v_{ti}$ ,  $B = B'/B_0$ ,  $\phi = e\phi'L_n/T_i\rho_i$ , and  $f = f'L_nv_{ti}^3/\rho_in_0$ , where prime means dimensional quantities and  $\rho_i = v_{ti}/\Omega_{i0}$  with  $\Omega_{i0} = eB_0/m_ic$ .

### III. ENTROPY BALANCE

Multiplying the Fourier-transformed form of Eq.(1) by  $f_{k_x,k_y}/F_M$ , and taking the velocity-space integral, summation over  $k_x$  and  $k_y$ , and the magnetic surface average of it, one can derive the entropy balance equation (normalized),

$$\frac{d}{dt}(\delta S + W) = \eta_i Q_i + D_i, \quad (7)$$

by use of Eqs.(4) and (5). Here, the entropy variable,  $\delta S$ , the potential energy,  $W$ , the ion heat transport flux,  $Q_i$ , and the collisional dissipation,  $D_i$ , are, respectively, defined as

$$\begin{aligned} \delta S &= \sum_{k_x,k_y} \delta S_{k_x,k_y} = \frac{1}{2} \sum_{k_x,k_y} \left\langle \int \frac{|f_{k_x,k_y}|^2}{F_M} d^3v \right\rangle, \\ W &= \sum_{k_x,k_y} W_{k_x,k_y} = \frac{1}{2} \sum_{k_x,k_y} [\langle (1 - \Gamma_0 + \tau)|\phi_{k_x,k_y}|^2 \rangle - \tau |\langle \phi_{k_x,k_y} \rangle|^2 \delta_{k_y,0}], \\ Q_i &= \sum_{k_x,k_y} Q_{i,k_x,k_y} = \frac{1}{2} \sum_{k_x,k_y} \left\langle ik_y \phi_{-k_x,-k_y} \int v^2 J_0 f_{k_x,k_y} d^3v \right\rangle, \\ D_i &= \sum_{k_x,k_y} D_{i,k_x,k_y} = \sum_{k_x,k_y} \left\langle \int \left[ \left( J_0 \phi_{-k_x,-k_y} + \frac{f_{-k_x,-k_y}}{F_M} \right) C(f_{k_x,k_y}) \right] d^3v \right\rangle. \end{aligned}$$

The entropy balance in the flux tube coordinates is represented in the same form as that in the slab ITG turbulence [8]. In the derivation of Eq.(7), contribution of the second and fifth terms on the left-hand-side of Eq.(1) cancels out because of the  $z$ -dependence of  $F_M$ . A more general form of the entropy balance equation in a toroidal configuration is considered in Refs.[5] and [14].

Our slab ITG turbulence simulations with high velocity-space resolution have confirmed that the quasisteady state,  $d(\delta S)/dt \approx \eta_i Q_i$ , is realized in a collisionless turbulence with the statistically steady  $W$  and  $Q_i$ , where monotonic increase of  $\delta S$  is attributed to continuous generation of fine-scale structures of  $\delta f$  by the phase mixing through the parallel advection term [7]. Contrarily, the statistically steady state of turbulence appears in a weakly collisional case, where  $\eta_i Q_i \approx -D_i$  and  $d(\delta S)/dt \approx dW/dt \approx 0$ , and is understood in terms of the production, transfer, and dissipation processes of  $\delta S$  [8]. The steady and quasisteady states are, therefore, represented by two limiting cases of the entropy balance equation. It is purposed in the present paper to confirm the statistically steady state of the weakly collisional ITG turbulence in the toroidal flux tube configuration. The simulation results are shown in Section V.

The phase-mixing processes in a torus are more complicated than that in the slab geometry because of the toroidal magnetic drift and mirror motions as represented in Eq.(1). A power-law decay of a density perturbation due to the phase mixing caused by the toroidal drift [15], which can be precisely simulated by our toroidal flux tube code [9], is one of the examples. In the next section, we investigate the collisionless damping process of the zonal flow and GAM by means of the gyrokinetic-Vlasov simulation code, where the phase-mixing processes in the tokamak configuration as well as the mirror motion are taken into account. Time-evolution of a zonal flow component with  $k_y = 0$  (the toroidal mode number  $n = 0$ ) is considered as an initial value problem of a linearized version of Eq.(1). Solution of the initial value problem is equivalent to the response kernel of the zonal flow to a source term [10]. The entropy balance equation for an axisymmetric component with a radial wave number  $k_x$  is written as

$$\frac{d}{dt} (\delta S_{k_x,0} + W_{k_x,0}) = D_{i,k_x,0} , \quad (8)$$

which corresponds to a subset of Eq.(7) with  $k_y = 0$ . During the collisionless ( $D_{i,k_x,0} = 0$ ) damping of the zonal flow and GAM, thus,  $G \equiv \delta S_{k_x,0} + W_{k_x,0}$  is invariant. It means that decrease of the potential energy  $W_{k_x,0}$  due to the collisionless damping leads to increase

of the entropy variable  $\delta S_{k_x,0}$ . It is, thus, expected that, according to the enhancement of  $\delta S_{k_x,0}$ , fine-scale fluctuations of  $\delta f$  should develop in the phase space, while a coherent structure corresponding to the neoclassical polarization [10] can remain in association with the residual zonal flow level.

For precise reproduction of the entropy balance, high velocity-space resolution is necessary, since  $\delta S$  reflects fine-scale structures of  $\delta f$  which are artificially dissipated in numerical simulations with low resolution. (If the subgrid-scale fluctuations are not smoothed out, they will often cause the numerical instability.) The balance equation, Eqs.(7) or (8), thus, offers a good measure of judging whether the micro velocity-space structures consistent with the turbulent transport are correctly resolved or not.

#### IV. COLLISIONLESS DAMPING OF ZONAL FLOW AND GAM

The residual level of the zonal flow after the collisionless damping is considered to affect a saturation amplitude of the ITG turbulence [10]. Then, the initial value problem of the zonal flow and GAM, where a response function of a  $k_y = 0$  mode is dealt with [10], has been investigated as an important benchmark test of toroidal gyrokinetic simulation codes [16–19]. The conservation property given in Eq.(8) and velocity-space profiles of the distribution function are useful for manifesting the physical mechanism of the collisionless damping of the zonal flow and GAM as well as confirming accuracy of the numerical simulations, while they have not been examined in the previous studies.

The collisionless damping of the GAM oscillation will be seen in the time-evolution of the zonal flow amplitude,  $\langle \phi_{k_x,0} \rangle$ , when the initial distribution function is given by the Maxwellian in Eq.(2) with  $m = n = 0$ , where  $m$  and  $n$  mean the poloidal and toroidal mode numbers, respectively. The time-history of  $\langle \phi_{k_x,0} \rangle$  obtained by the toroidal flux tube simulation for the Cyclone DIII-D base case parameters [16] is shown in Fig.1 (a), where the radial wave number  $k_x = 0.1715\rho_i^{-1}$ . The used parameters are as follows;  $R_0/L_T = 6.92$ ,  $\epsilon \equiv r_0/R_0 = 0.18$ ,  $r_0/\rho_i = 80$ ,  $\hat{s} = 0.78$ ,  $q_0 = 1.4$ ,  $\eta_i = 3.114$ , and  $\tau = 1$ . For discretization of the velocity space,  $-5v_{ti} \leq v_{\parallel} \leq 5v_{ti}$  and  $0 \leq \mu \leq 12.5v_{ti}^2/\Omega_{i0}$ , we have employed  $1025 \times 65$  grid points, while 128 grid points are used for  $-\pi \leq z < \pi$ . Phase-space derivatives in the  $z$  and  $v_{\parallel}$  directions are approximated by the fifth- and fourth-order finite difference, respectively. The numerical time-integration is calculated by the fourth-order Runge-Kutta-

Gill method.

The residual level of  $\langle \phi_{k_x,0} \rangle$  shown in Fig.1 (a) agrees well with the theoretical estimate,  $\lim_{t \rightarrow \infty} \langle \phi_{k_x,0}(t) \rangle / \langle \phi_{k_x,0}(t=0) \rangle = 1/(1+1.6q^2/\epsilon^{1/2})$  [10]. The collisionless damping of the zonal flow and GAM is caused by the phase mixing processes which generate fine-scale structures of  $\delta f$  in the velocity space. According to Eq.(8), in the collisionless case, the entropy variable associated with the fine structures should increase so as to compensate the decrease of the potential energy. The simulation result shown in Fig.1 (b) confirms the entropy balance. During the collisionless damping of zonal flow and GAM with decrease of the potential energy,  $W_{k_x,0}$ , the entropy variable  $\delta S_{k_x,0}$  increases while accurately preserving  $G$ . The high phase-space resolution enables us to reproduce the conservation of  $G$  with a relative error less than 3%.

The analytical solution for the zonal-flow component of the perturbed gyrocenter distribution function is given by

$$f_{k_x,0}(t) = F_M \frac{e\langle \phi_{k_x,0}(0) \rangle}{T_i} \left[ \frac{k_x^2 \bar{\rho}^2}{2} + \frac{ik_x (\bar{\rho}_b - \rho_b) + k_x^2 \left( \rho_b \bar{\rho}_b - \frac{1}{2} \bar{\rho}_b^2 - \frac{1}{2} \rho_b^2 \right)}{1 + 1.6q^2/\epsilon^{1/2}} \right], \quad (9)$$

where  $\rho = v_{\perp}/\Omega_i$ ,  $\rho_b = (q/\epsilon)(v_{\parallel}/\Omega_i)$ ,

$$\bar{\rho}_b = \begin{cases} 0 & \text{for trapped particles} \\ \pi(q/\epsilon\Omega_{i0})(\mu\Omega_{i0}\epsilon)^{1/2}\kappa/K(\kappa^{-1}) & \text{for passing particles,} \end{cases}, \quad (10)$$

$$\bar{\rho}_b^2 = \begin{cases} 4(q/\epsilon\Omega_{i0})^2(\mu\Omega_{i0}\epsilon)[E(\kappa)/K(\kappa) - 1 + \kappa^2] & \text{for trapped particles} \\ 4(q/\epsilon\Omega_{i0})^2(\mu\Omega_{i0}\epsilon)\kappa^2 E(\kappa^{-1})/K(\kappa^{-1}) & \text{for passing particles,} \end{cases}, \quad (11)$$

and  $\kappa^2 = [v^2/2 - \mu\Omega_{i0}(1-\epsilon)]/(2\mu\Omega_{i0}\epsilon)$ . Here,  $K$  and  $E$  denote the complete elliptic integrals of the first and second kinds, respectively. The above analytical solution is derived by using the expression for the gyrocenter distribution function  $f_{\mathbf{k}}(t) = -J_0(e\phi_{\mathbf{k}}(t)/T_i)F_M + g_{\mathbf{k}}(t)$  with  $\phi_{\mathbf{k}}(t)$  and  $g_{\mathbf{k}}(t)$  given by the Rosenbluth-Hinton theory [10], which describes the long-time behavior of the zonal flow and drops out rapid oscillations such as the GAM.

Velocity-space profiles of  $\text{Re}[f_{k_x,0}]$  at different time steps are shown in Fig.2, where the boundary of trapped and passing ions is represented by blue lines. Contribution of the trapped ions to the neoclassical polarization [10] is clearly identified by a mean negative value of  $f_{k_x,0}$  for trapped particles. The profile of the distribution function resulting from the numerical simulation agrees with a bounce-averaged analytical solution given by Eq.(9)

(see also Fig.3), except for fine-scale oscillations caused by the phase mixing and the mirror motion. Generating fine-scale structures of  $f_{k_x,0}$  in the direction of the parallel velocity ( $v_{\parallel}$ ), the phase mixing due to the passing particles largely deforms the initial Maxwellian distribution as seen in Fig.2, and results in damping of GAM. The increase of  $\delta S_{k_x,0}$  balancing with decrease of  $W_{k_x,0}$  stems from the development of the fine-scale fluctuations of  $f_{k_x,0}$  in the velocity space. The continuous development of fine-scale structures of  $f_{k_x,0}$  after  $t = 20L_n/v_{ti}$  represents the transfer of the entropy variable from macro to micro velocity-scales, while its velocity-space integral, that is  $\delta S_{k_x,0}$ , oscillates around a constant level [see Fig.1 (b)].

## V. TOROIDAL ITG TURBULENCE

Nonlinear gyrokinetic-Vlasov simulations of the toroidal ITG turbulence are carried out by means of the flux tube model described in Section II. Used parameters are the same as those in Section IV but with finite collisionality. A model collision operator with the Lenard-Bernstein form averaged with respect to the gyrophase is employed, such as

$$C(f_{k_x,k_y}) = \nu_{ii} \left[ \frac{1}{v_{\perp}} \frac{\partial}{\partial v_{\perp}} \left( v_{\perp} \frac{\partial f_{k_x,k_y}}{\partial v_{\perp}} + \frac{v_{\perp}^2}{v_{ti}^2} f_{k_x,k_y} \right) + \frac{\partial}{\partial v_{\parallel}} \left( \frac{\partial f_{k_x,k_y}}{\partial v_{\parallel}} + \frac{v_{\parallel}}{v_{ti}^2} f_{k_x,k_y} \right) - \frac{k_{\perp}^2}{\Omega_i^2} f_{k_x,k_y} \right], \quad (12)$$

where  $\nu_{ii}$  denotes the ion-ion collision frequency.

Color contour plots of the electrostatic potential perturbations obtained by the toroidal ITG turbulence simulation are shown in Fig.4 for three different time moments, where  $\nu_{ii} = 10^{-3}v_{ti}/L_n$  (banana regime),  $N_{\theta} = 4$ ,  $k_{x,\min} = 0.1715$ ,  $k_{x,\max} = 5.145$ ,  $k_{y,\min} = 0.175$ , and  $k_{y,\max} = 1.75$  ( $31 \times 21$  Fourier components are involved in the  $k_x$ - $k_y$  space, excluding their complex conjugates as well as modes employed for de-aliasing). The minimum values of  $k_x$  and  $k_y$  correspond to  $\Delta q = 0.5$  and  $N_{\alpha} = 10$ , respectively, where  $\Delta q$  denotes a difference of the safety factor across the radial width. The toroidal periodicity of  $N_{\alpha}$  is also assumed [13]. In a latter phase of the linear growth of the ITG instability ( $t \approx 60L_n/v_{ti}$ ), the zonal flow components are spontaneously excited, and reduce the turbulence level. As seen in Fig.4, vortices with larger scales than that of the linearly most unstable mode dominate in the turbulence and are mainly responsible for the ion heat transport. A statistically steady turbulence with finite amplitudes of zonal flows is observed after  $t \approx 120L_n/v_{ti}$ .

The entropy balance in the ITG turbulence simulation is shown in Fig.5 (a), where time-histories of four terms in Eq.(7) are plotted. The relative error  $\Delta/D_i$  [defined by

$\Delta \equiv d(\delta S + W)/dt - \eta_i Q_i - D_i]$  in the saturated turbulence after  $t \approx 80L_n/v_{ti}$  is suppressed at 7-8% by use of high resolution, where 960 and  $129 \times 48$  grid points are employed in the  $z$ - and  $v_{\parallel}$ - $v_{\perp}$  space, respectively. Better balancing of Eq.(7) is found for finer grid spacings,  $\Delta z$ ,  $\Delta v_{\parallel}$ , and  $\Delta v_{\perp}$ , or for higher collision frequency,  $\nu_{ii}$ , since fine-scale fluctuations of  $\delta f$  generated in the turbulence are damped by collisions. In the steady turbulence, the collisional dissipation nearly balances with the transport flux,  $\eta_i Q_i \approx -D_i$ , in the same way as seen in the slab ITG simulation [8]. The ion heat transport coefficient,  $\chi_i \equiv Q_i/\eta_i$ , is shown in Fig.5 (b), where the time-averaged value of  $\chi_i \approx 1.4\rho_i^2 v_{ti}/L_n$  from  $t = 200$  to  $250L_n/v_{ti}$  in the saturated turbulence is comparable with results of other gyrokinetic simulations for the Cyclone base case ( $\chi_i \sim 2\rho_i^2 v_{ti}/L_n$ ) [16].

A quantitative estimate of the transport flux by means of collisionless or weakly collisional turbulence simulations, generally speaking, may suffer from a numerical error unless enough resolution for the velocity space is employed, as has been demonstrated in Ref.[9]. The entropy balance is a useful benchmark test for checking the soundness of simulation results as considered in the above. Introduction of the numerical diffusion may contribute to reduction of the aliasing error, while convergence of the transport coefficient against the artificial dissipation should be thoroughly evaluated in the same way as the systematic study on the collisionality dependence given in Ref.[8].

The balance relation,  $\eta_i Q_i \approx -D_i$ , suggests that fine-scale structures of  $\delta f$  generated by the phase mixing in the turbulence are dissipated by the finite collisionality. Velocity-space profiles of  $\text{Re}(f_{k_x, k_y}/\phi_{k_x, k_y})$  observed at  $t = 250L_n/v_{ti}$  are shown in Fig.6 for the longest wavelength mode ( $k_y = 0.175\rho_i^{-1}$ ), the linearly most unstable mode ( $k_y = 0.35\rho_i^{-1}$ ) and a stable mode ( $k_y = 0.7\rho_i^{-1}$ ), where  $\theta = z = 0$  and  $k_x = 0$ . The distribution function of the linear stable mode with  $k_y = 0.7\rho_i^{-1}$  mainly consists of small scale structures in the velocity space. As seen in cross-sectional plots of  $f_{k_x, k_y}$  at  $t = 50$  (linear growth phase) and  $250L_n/v_{ti}$  (nonlinear saturation phase) in Fig.7, the velocity-space profile of  $\text{Re}(f_{k_x, k_y})$  for the dominant long wavelength mode ( $k_y = 0.175\rho_i^{-1}$ ) is similar to that of the linear unstable eigenfunction. The same feature of  $f_{k_x, k_y}$  has also been observed in the slab ITG turbulence simulations [7]. This means that the entropy variable produced in the macro velocity-scale by the unstable modes is transferred to and is dissipated in the micro scales by the finite collision.

It is remarked that the present gyrokinetic-Vlasov simulation with high velocity-space

resolution enables one to quantitatively study the entropy balance in the five-dimensional phase space in association with the toroidal ITG turbulent transport. The simulation result of the toroidal ITG turbulence confirms the scenario on the steady state of the entropy balance originally derived from the slab ITG turbulence simulations [8], and also provides one with detailed information on the distribution function which could be useful for construction of a toroidal kinetic-fluid closure model [6]. For example, the profile of  $f_{k_x, k_y}$  for the most unstable mode ( $k_y = 0.35$ ) in the turbulence shown in Figs.6 and 7 also has a significant difference from the linear eigenfunction, which suggests that the phase-relation between the temperature and the parallel heat flux may not be fixed to a constant value governed by the linear eigenfunction, but can vary in time as is supposed in the nondissipative closure model [6].

## VI. SUMMARY

We have studied detailed velocity-space structures of ion distribution functions and related entropy balance in the collisionless damping of the zonal flow and GAM as well as in the toroidal ITG turbulence with the anomalous ion thermal transport, by means of the newly developed toroidal gyrokinetic-Vlasov simulation code for the flux tube geometry. The kinetic simulations with high velocity-space resolution enable us to quantitatively discuss the entropy balance which has rarely been evaluated in conventional studies. Our detailed numerical simulation on dynamics of the axisymmetric modes reveal the whole picture of the collisionless damping of the zonal flow and GAM in association with the phase space structures of the ion distribution function. Specifically, the neoclassical polarization of trapped ions as well as the parallel phase mixing due to passing particles is successfully reproduced. The velocity-space profile of the distribution function obtained by the simulations is also consistent with the bounce-averaged analytical solution in Eq.(9). During the collisionless damping of GAM, finer-scale structures of the distribution function in the velocity space continue to develop due to the phase mixing while preserving an invariant defined by a sum of the entropy variable and the potential energy. Thus, the collisionless dynamics of the zonal flow and GAM are comprehended in terms of a transfer process of the entropy variable from macro to micro velocity-scales.

It is considered that finite collisionality leads to a slow decay of the residual zonal flow

[20]. In addition, the entropy variable in the micro velocity-scale and the fine-scale structures of the distribution function are dissipated by collisions. Thus, a long time simulation also becomes possible at a smaller computational cost than that in the collisionless case. This is because collisionless kinetic simulations need a lot of computer resources in order to reproduce the fine structures of the distribution function, and are reliable only in a finite time period before the smallest scale-length of  $f$  in the phase space reaches the grid scale [7]. Recently, the collisionless zonal flow dynamics in helical systems is also studied based on the gyrokinetic theory and simulation [21], where the entropy balance and the velocity-space structures of  $f$  are quantitatively investigated. The detailed results will be reported elsewhere.

Simulation results of the anomalous transport in the toroidal ITG turbulence, in attention to the velocity-space structures of the distribution function and the entropy balance, are also presented. The statistically steady toroidal ITG turbulence is observed in terms of the saturated states of the entropy variable, the potential energy, the ion heat transport flux, and the collisional dissipation. Detailed calculation of the entropy balance for the toroidal flux tube geometry confirms the steady state of the turbulence where the transport balances with the collisional dissipation in the same way as found in the slab ITG system [8]. Fine velocity-space structures of the perturbed ion distribution function clearly appear in fluctuations with large wavenumbers, while the heat transport flux is mainly produced by vortices with long wavelengths. Accordingly, the entropy variable produced by the unstable modes with a macro velocity-scale is transferred in the wave number and velocity spaces, and is finally dissipated in the micro scale by the finite collision. Thus, the statistically steady toroidal ITG turbulence can be sustained, as we have seen in the slab case.

Introduction of the finite collisionality also makes the long-time simulation of the turbulent transport possible by smoothing out the fine-scale structures of the distribution function. According to our previous studies on the slab ITG turbulence, the collision frequency used in the present study ( $\nu_{ii} = 10^{-3}v_{ti}/L_n$ ) is in a regime where the transport flux has a logarithmic dependence on  $\nu_{ii}$ . Even if one employs numerically-enhanced diffusivity instead of the collision term with coarser phase-space resolution so as to carry out a *collisionless* turbulence simulation for the same parameters as used here, the transport coefficient may deviate from that in the true collisionless limit. Therefore, in order to quantitatively study the collisionality dependence of the velocity-space structures of the distribution function,

one needs to perform numerical simulations with higher phase-space resolution for a lower collision frequency, which remains for future works.

### Acknowledgments

This work is partially supported by grants-in-aid of Ministry of Education, Culture, Sports, Science and Technology (No. 14780387 and 16560727).

- 
- [1] Horton, W., *Rev. Mod. Phys.* **71**, 735 (1999).
  - [2] Terry, P.W., *Rev. Mod. Phys.* **72**, 109 (2000).
  - [3] Diamond, P.H., Itoh, S.-I., Itoh, K., Hahm, T.S., submitted to *Plasma Phys. Contl. Fusion* (2004).
  - [4] Krommes, J.A., Hu, G., *Phys. Plasmas* **1**, 3211 (1994).
  - [5] Sugama, H., Okamoto, M., Horton, W., Wakatani, M., *Phys. Plasmas* **3**, 2379 (1996).
  - [6] Sugama, H., Watanabe, T.-H., Horton, W., *Phys. Plasmas* **8**, 2617 (2001); Sugama, H., Watanabe, T.-H., Horton, W., *Phys. Plasmas* **10** 726 (2003).
  - [7] Watanabe, T.-H., Sugama, H., *Phys. Plasmas* **9**, 3659 (2002).
  - [8] Watanabe, T.-H., Sugama, H., *Phys. Plasmas* **11**, 1476 (2004).
  - [9] Watanabe, T.-H., Sugama, H., to appear in *J. Plasma Fus. Res. SERIES* **6** (2004).
  - [10] Rosenbluth, R.M., Hinton, F.L., *Phys. Rev. Lett.* **80**, 724 (1998).
  - [11] Winsor, N., Johnson, J.L., Dawson, J.J., *Phys. Plasmas* **11**, 2448 (1968).
  - [12] Frieman, E.A., Chen, L., *Phys. Fluids* **25**, 502 (1982).
  - [13] Beer, M.A., Cowley, S.C., Hammett, G.W., *Phys. Plasmas* **2**, 2687 (1995); Beer, M.A, Ph.D thesis, Princeton University, 1994.
  - [14] Sugama, H., Horton, W., *Phys. Plasmas* **4**, 405 (1997).
  - [15] H.Sugama, *Phys. Plasmas* **6**, 3527 (1999).
  - [16] Dimits, A.M., et al., *Phys. Plasmas* **7**, 969 (2000).
  - [17] Lin, Z., et al., *Phys. Plasmas* **7**, 1857 (2000).
  - [18] Candy, J., Waltz, R.E., *J. Comput. Phys.* **186**, 545 (2003).
  - [19] Idomura, Y., Tokuda, S., Kishimoto, Y., *Nucl. Fusion* **43**, 234 (2003).

- [20] Hinton, F.L., Rosenbluth, R.M., Plasma Phys. Control. Fusion **41**, A653 (1999).
- [21] Sugama, H., Watanabe, T.-H., Proceedings of the 12th International Congress on Plasma Physics (Nice, France, 2004), 084 & P2-100 (topic D).

## Figure Captions

FIG. 1: Time-evolutions of (a) the zonal flow potential, (b) the entropy variable,  $\delta S_{k_x,0}$ , and the potential energy,  $W_{k_x,0}$ , obtained by the toroidal flux tube simulation of the collisionless damping of the axisymmetric ( $n = 0$ ) mode, where  $G_0 = \delta S_{k_x,0} + W_{k_x,0}$  at  $t = 0$ .

FIG. 2: Velocity-space profiles of real part of the perturbed distribution function at  $\theta = 0$  for different time steps of simulation. The horizontal and vertical axes are defined by  $v_{\parallel}$  and  $\sqrt{2\mu\Omega_i}$ , respectively, where  $\mu$  is the magnetic moment. Positive and negative parts are colored by red and green, respectively. Blue lines show the boundary of trapped and passing particles.

FIG. 3: A velocity-space profile of real part of the perturbed distribution function at  $\theta = 0$  given by the bounce-averaged analytical solution in Eq.(9). Format of the plot is the same as those in Fig.2.

FIG. 4: Color contours of the electrostatic potential obtained by the toroidal ITG turbulence simulation at (a)  $t = 50$ , (b) 120, and (c)  $250L_n/v_{ti}$ , where only a part of the flux tube in the range of  $-\pi \leq z \leq \pi$  is plotted.

FIG. 5: Time-evolutions of (a) the entropy balance and (b) the ion thermal transport coefficients  $\chi_i$  obtained by the toroidal ITG turbulence simulation.

FIG. 6: Velocity-space profiles of real part of the perturbed distribution function observed in the toroidal ITG turbulence simulation at  $t = 250L_n/v_{ti}$  for (a)  $k_y = 0.175$ , (b) 0.35, and (c)  $0.7\rho_i^{-1}$  where  $\theta = z = 0$  and  $k_x = 0$ . The horizontal and vertical axes are defined by  $v_{\parallel}$  and  $\sqrt{2\mu\Omega_i}$ , respectively. The contour interval in (c) is twice the size of that in (a) and (b).

FIG. 7: The cross-sectional plots of real and imaginary parts of the perturbed distribution function at  $\mu = 0$  for (a) the longest wavelength ( $k_y = 0.175\rho_i^{-1}$ ) and (b) the most unstable ( $k_y = 0.35\rho_i^{-1}$ ) modes observed at  $t = 50$  (linear growth phase) and  $250L_n/v_{ti}$  (nonlinear saturation phase).

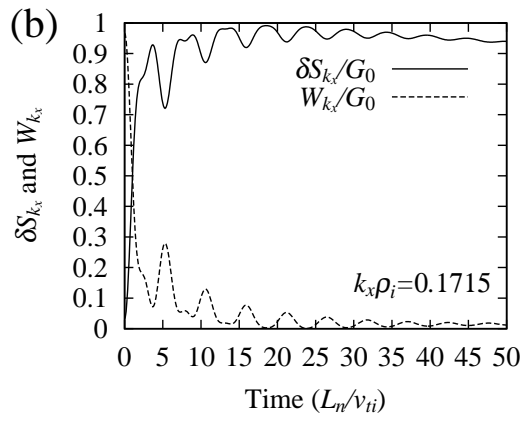
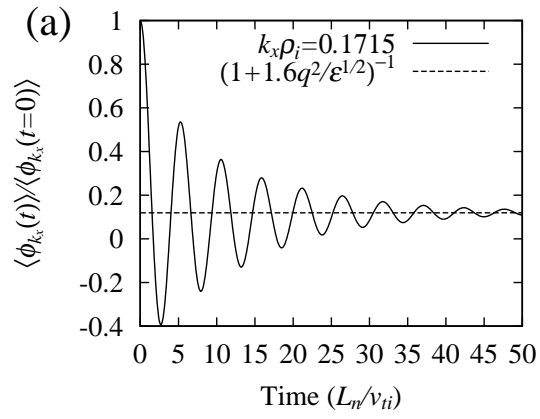


FIG. 1: Watanabe and Sugama

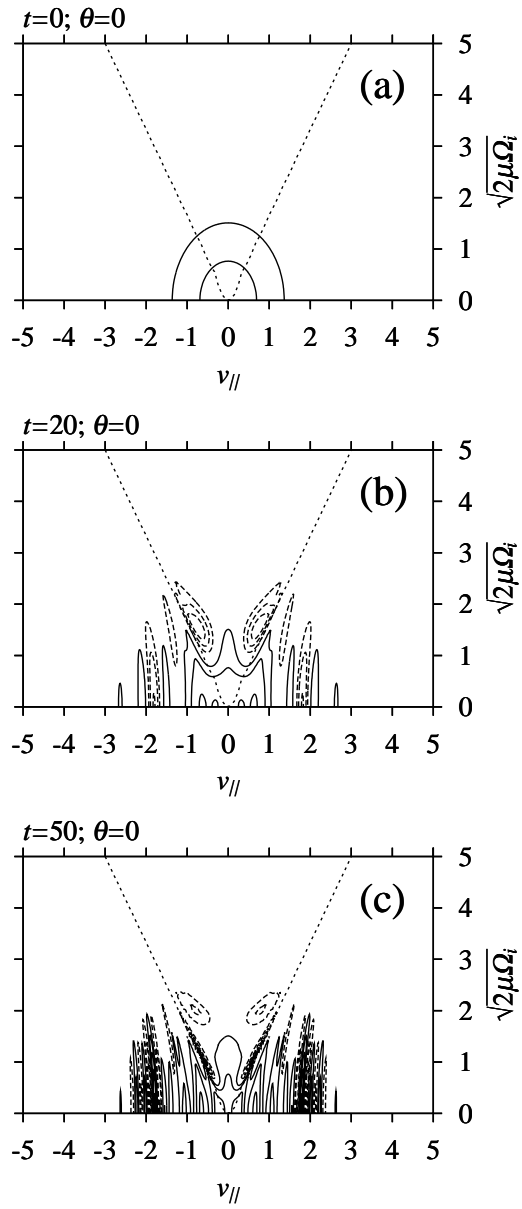


FIG. 2: Watanabe and Sugama

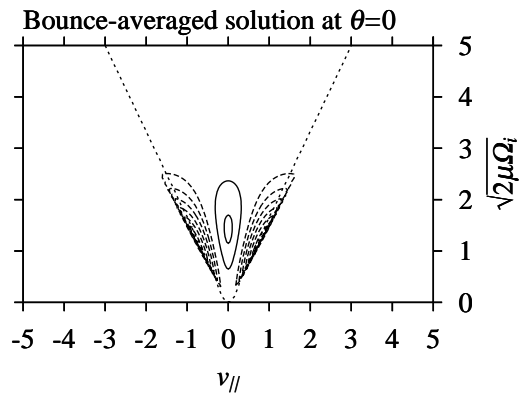


FIG. 3: Watanabe and Sugama

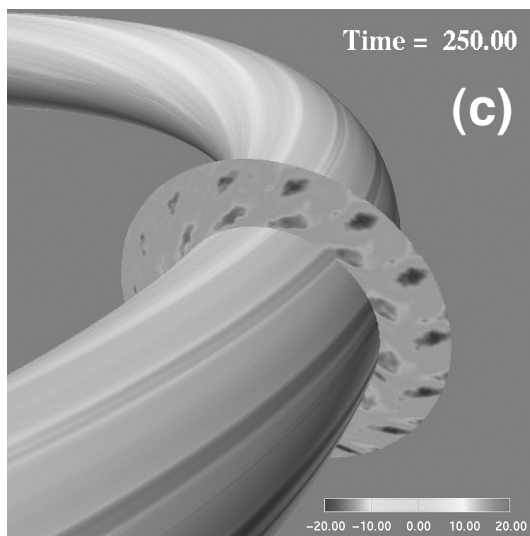
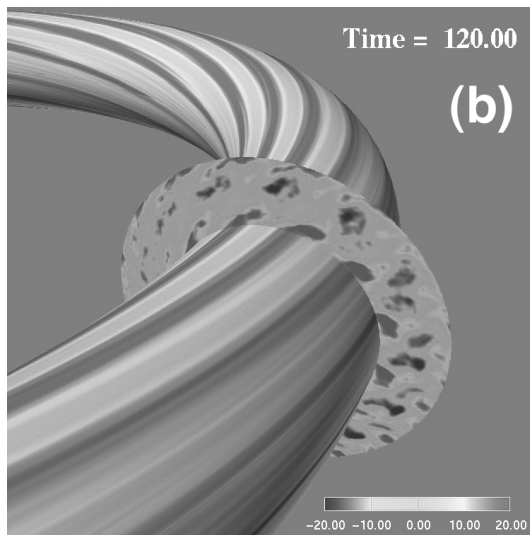
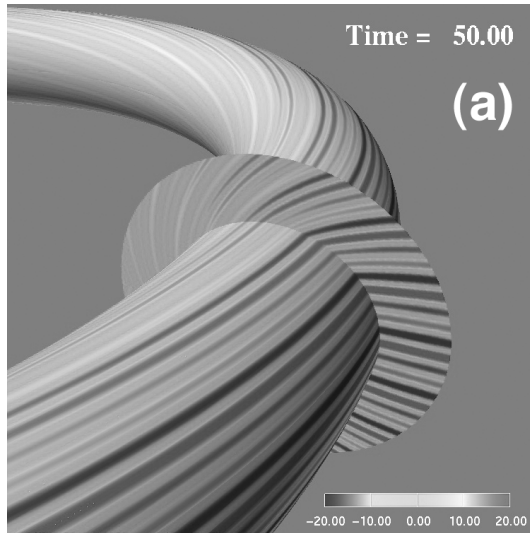


FIG. 4: Watanabe and Sugama

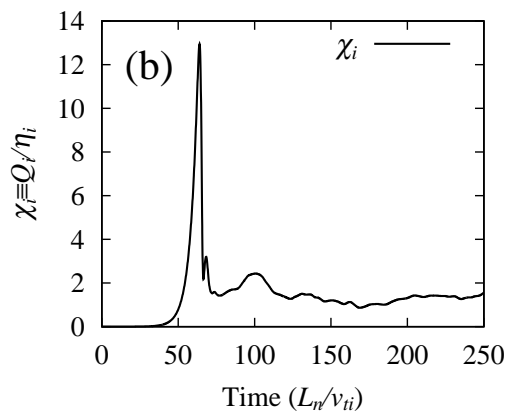
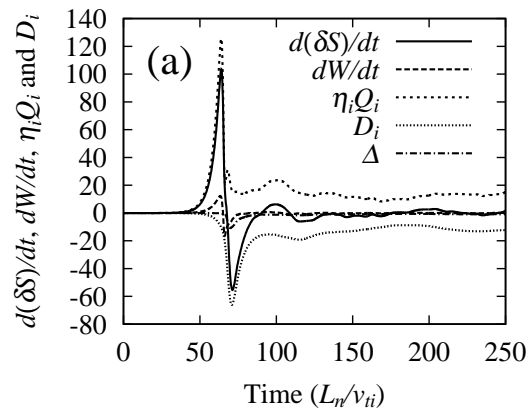


FIG. 5: Watanabe and Sugama

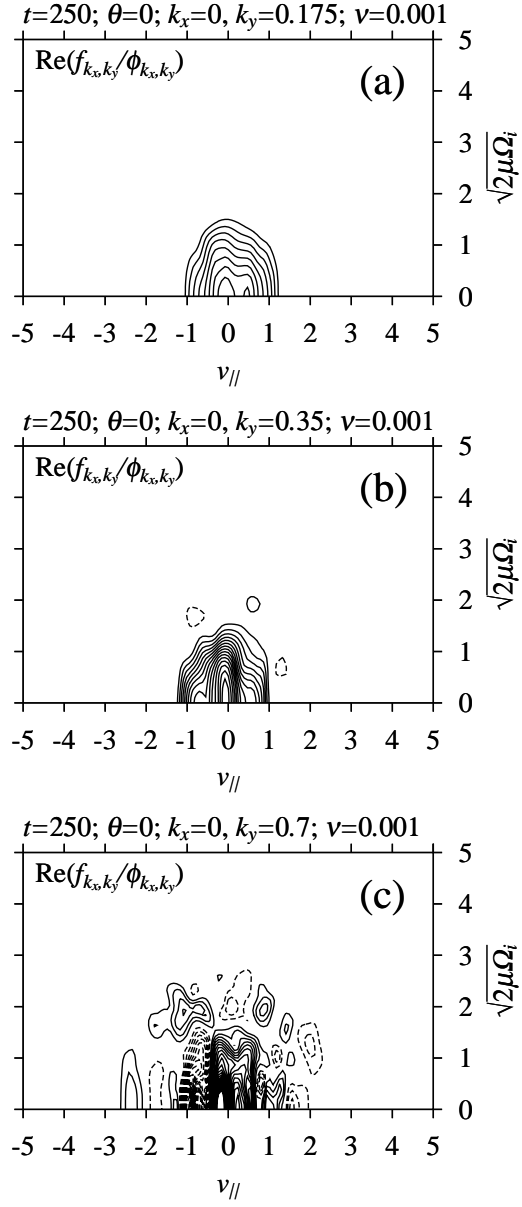


FIG. 6: Watanabe and Sugama

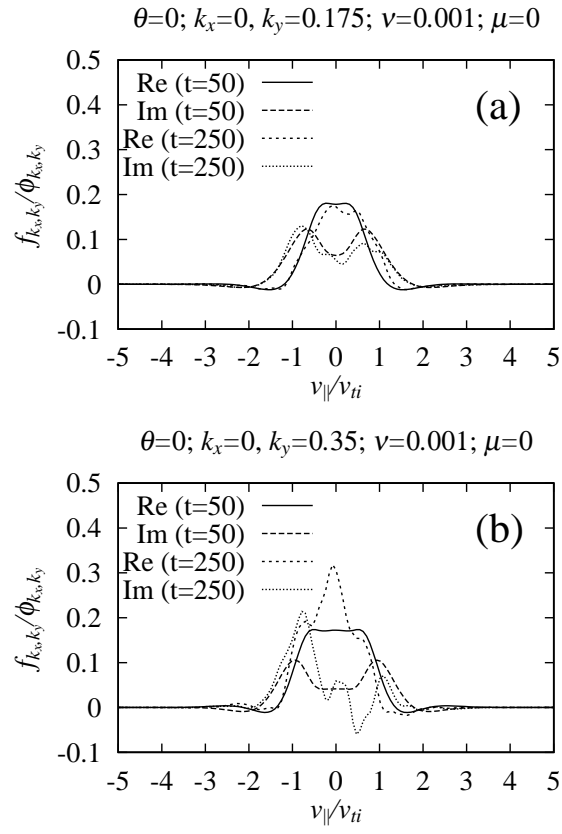


FIG. 7: Watanabe and Sugama

# Finite-Orbit-Width Effect and the Radial Electric Field in Neoclassical Transport Phenomena

S. Satake 1), M. Okamoto 1), N. Nakajima 1), H. Sugama 1), M. Yokoyama 1), and C. D. Beidler 2)

1) National Institute for Fusion Science, Toki, Japan

2) Max-Planck-Institut für Plasmaphysik, Greifswald, Germany

e-mail contact of main author : satake.shinsuke@nifs.ac.jp

**Abstract.** Modeling and detailed simulation of neoclassical transport phenomena both in 2D and 3D toroidal configurations are shown. The emphasis is put on the effect of finiteness of the drift-orbit width, which brings a non-local nature to neoclassical transport phenomena. Evolution of the self-consistent radial electric field in the framework of neoclassical transport is also investigated. The combination of Monte-Carlo calculation for ion transport and numerical solver of ripple-averaged kinetic equation for electrons makes it possible to calculate neoclassical fluxes and the time evolution of the radial electric field in the whole plasma region, including the finite-orbit-width(FOW) effects and global evolution of geodesic acoustic mode (GAM). The simulation results show that the heat conductivity around the magnetic axis is smaller than that obtained from standard neoclassical theory and that the evolution of GAM oscillation on each flux surface is coupled with other surfaces if the FOW effect is significant. A global simulation of radial electric field evolution in a non-axisymmetric plasma is also shown.

## 1. Introduction

Neoclassical(NC) transport theory has been successfully established under the assumption of the local transport model(small-orbit-width (SOW) limit)[1,2]. However, there are some cases in recent experiments where the assumption is not valid, for example, at the internal transport barrier(ITB) and in the core region of tokamak where potato orbits[3] appear. The potato width becomes several tens % of the plasma minor radius in a reversed-shear configuration, and to evaluate transport level in such cases the finite-orbit-width(FOW) effect of trapped particles should be considered. Neoclassical transport theory for 3-dimensional stellarator configurations has also been considered in the SOW-limit[4,5]. The drift orbits in stellarators are much complicated compared to those in tokamaks. Though the orbit widths of ripple-trapped particles are small, transit particles in stellarators have large orbit scales, and energetic particles trapped helically are easy to lose from the confinement region. In order to take account of those particles in NC transport calculation, conventional analytical method is hard to apply, and global properties of particle motion should be taken into account.

Another interest in recent study on NC transport is the formation of the radial electric field  $E_r$ . Since the lowest-order NC flux is intrinsic ambipolar in tokamaks, the higher-order terms appeared from the FOW effect must be retained to evaluate the time evolution of  $E_r$ . In stellarators, the radial flux is non-ambipolar even in the lowest order. Because NC fluxes in non-axisymmetric plasmas are sensitive to electric field, determination of the self-consistent ambipolar electric field is one of the main task of neoclassical theory.

However, the role of the FOW effects in the evolution of radial electric field has not been investigated in detail.

To carry out a general and detailed research on neoclassical transport phenomena including the finite-orbit-width effects and radial electric field, we develop a numerical transport simulation code FORTEC-3D using the  $\delta f$  Monte-Carlo method[6,7]. It solves the time evolution of neoclassical fluxes as well as the self-consistent radial electric field, in multidimensional MHD equilibrium configurations obtained from VMEC[8]. The original FORTEC has been developed to solve NC transport for ions in tokamaks, in which the electron particle flux  $\Gamma_e$  is negligible to determine ambipolar  $E_r$ . In non-axisymmetric cases  $\Gamma_e$  is comparable to  $\Gamma_i$  and is needed to calculate the evolution of ambipolar electric field. To reduce the time consumption for simulation, we adopt a hybrid model. While the ion transport is solved by the  $\delta f$  method, the electron flux is obtained from GSRAKE[9], a numerical solver of ripple-averaged kinetic equation. Thus FORTEC-3D enables us to investigate neoclassical transport and the evolution of radial electric field including the FOW effects of ions in general 3D configurations, from a microscopic point of view.

The remainder of the paper is organized as follows. In Sec. 2, formulation of  $\delta f$  Monte-Carlo method and our simulation modeling are explained. In Sec. 3, NC transport simulation in a tokamak configuration is shown. It is shown that the geodesic-acoustic-mode (GAM) oscillation in tokamak is affected by the FOW effects. The evolution of  $E_r$  on each flux surface is found to be coupled if the banana width is large. Effects of potato particles on transport are also shown. We have developed an extended transport theory including the FOW effects[10]. From the new neoclassical theory we show that the potato orbits around the axis plays an important role to the decreasing tendency of ion heat conductivity around the magnetic axis. In Sec. 3, a test calculation of NC transport in a LHD-like configuration in combination with GSRAKE is presented. The relaxation process of GAM oscillation toward ambipolar steady state is simulated precisely.

## 2. Simulation model

Consider a general toroidal plasma in the magnetic coordinates  $(\rho, \theta, \zeta)$ , where  $\rho = \sqrt{\psi/\psi_a}$  is a normalized radial coordinate and  $\psi_a$  is the toroidal flux label on the boundary. To solve the time development of a plasma distribution function in the phase space  $(\rho, \theta, \zeta, \mathcal{K} = v^2, \mu = mv_\perp^2/2B)$ , the linearized drift kinetic equation

$$\frac{D\delta f}{Dt} \equiv \left[ \frac{\partial}{\partial t} + \dot{\mathcal{K}} \frac{\partial}{\partial \mathcal{K}} + (\mathbf{v}_\parallel + \mathbf{v}_d) \cdot \nabla - C_{tp}(\cdot, f_M) \right] \delta f = -\mathbf{v}_d \cdot \left( \nabla f_M - \frac{e\mathbf{E}_\rho}{T} \right) f_M + \mathcal{P}f_M \quad (1)$$

is considered. Here,  $\mathbf{E}_\rho = -d\Phi/d\rho\nabla\rho$  is radial electric field,  $\mathbf{v}_d$  is the drift velocity of a guiding center, and  $f_M = f_M(\rho, \mathcal{K})$  is Maxwellian of a flux-surface function. The linearized test-particle collision operator  $C_{tp}$  is implemented numerically as a random kick in the velocity space. The field-particle collision operator  $\mathcal{P}f_M$  is defined so as to satisfy the conservation laws for collision operator

$$\int (C_{tp} + \mathcal{P}f_M) \mathcal{M}_{\{0,1,2\}} d\mathbf{v} = 0, \quad (2)$$

where  $\mathcal{M}_0 = 1$ ,  $\mathcal{M}_1 = \mathbf{v}$ , and  $\mathcal{M}_2 = \mathcal{K}$ , respectively[11]. The use of the operator which acts correctly as the linearized Fokker-Planck collision term is an advantage of our code to apply it to general toroidal geometry. Because of the break of the momentum-conservation law, it is known that the pitch-angle scattering operator, though it is a good approximation for neoclassical theory in helical systems, cannot be simply applied to the transport analysis in axisymmetric plasmas[12]. Note also that in the  $\delta f$  formulation, the FOW effect is included in the term  $\mathbf{v}_d \cdot \nabla \delta f$ , which is usually dropped in standard local transport models. We adopted the 2-weight scheme[6] to solve eq. (1) by Monte-Carlo method. Two weights  $w$  and  $p$  which satisfy the relation  $wg = \delta f$ ,  $pg = f_M$  are introduced, where  $g$  is the distribution function of simulation markers. Each marker follows the track in the phase space according to the lhs of eq. (1), that is,  $Dg/Dt = 0$  is satisfied. Then the problem is reduced to solve the evolution of weights for each markers

$$\dot{w} = \frac{p}{f_M} \left[ -\mathbf{v}_d \cdot \left( \nabla - \frac{e\mathbf{E}_\rho}{T} \right) + \mathcal{P} \right] f_M, \quad (3)$$

$$\dot{p} = \frac{p}{f_M} \mathbf{v}_d \cdot \left( \nabla - \frac{e\mathbf{E}_\rho}{T} \right) f_M. \quad (4)$$

We have also adopted a weight averaging technique to suppress the dispersion spreading of the weight fields[13].

The self-consistent evolution of the radial electric field is solved according to

$$\left( \langle |\nabla \rho|^2 \rangle + \left\langle \frac{c^2}{v_A^2} |\nabla \rho|^2 \right\rangle \right) \epsilon_0 \frac{\partial E_\rho(\rho, t)}{\partial t} = -e (Z_i \Gamma_i^{neo} - \Gamma_e^{neo}), \quad (5)$$

where the ion particle flux is obtained from  $\Gamma_i^{neo} = \langle \int d^3\mathbf{v} \dot{\rho} \delta f_i \rangle$ . In tokamak cases,  $\Gamma_e^{neo}$  is negligible since  $|\Gamma_e/\Gamma_i| \sim O(\sqrt{m_e/m_i})$ . In non-axisymmetric cases, however,  $\Gamma_e^{neo}$  is comparable to  $\Gamma_i^{neo}$  and the balance between these two fluxes determines the ambipolar  $E_r$ . Since ion and electron fluxes are strongly dependent on  $E_r$  in the collisionless  $1/\nu$  regime and the ambipolar condition  $\Gamma_i(E_r) = \Gamma_e(E_r)$  sometimes has a multiple solution, we need a proper evaluation for  $\Gamma_e$  as well as  $\Gamma_i$  in order to investigate important phenomena in NC transport in stellarators such as time evolution and bifurcation of electric field. However, solving both ion and electron transport by  $\delta f$  scheme is not practical way because the orbit time scales of two species are too separated, and because it is expected that the FOW effect on transport is significant only for ions. In FORTEC-3D only the ion part is solved by using the  $\delta f$  method. The table of  $\Gamma_e(E_\rho, \rho)$  for a given profile is prepared by GSRAKE, and  $\Gamma_e$  is referred from the table at each time step in solving eq. (5) in FORTEC-3D. GSRAKE is designed to give a general solution for ripple-averaged kinetic equation. The solution is valid throughout the entire long-mean-free-path (LMFP) regime. It is applicable to general, multi-helicity 3-dimensional configurations in which the magnetic field strength is given in a form

$$B = B_0 + \sum_{n=0}^{\infty} B_{0,n}(\rho) \cos n\zeta + \sum_{m=1}^{\infty} \sum_{n=-\infty}^{\infty} B_{m,n}(\rho) \cos(n\zeta - m\theta). \quad (6)$$

In our simulation system, the table of Fourier components of  $B$  are extracted from MHD equilibrium field solved by VMEC, and it is transferred to FORTEC-3D and GSRAKE. The

adaptability of GSRAKE to transport calculation in LHD plasmas has been benchmarked by comparing other numerical codes or analytical expressions previously[9].

Adopting the hybrid model, our simulation system is capable of solving neoclassical transport in general 2D and 3D configurations without missing the important role of the FOW effects of ions, within a practical calculation time. A typical simulation using 50 million markers in 3D configuration takes 20 hours to run a simulation to reach a steady state solution. It also enables us to investigate neoclassical transport dynamics in the whole plasma region from a microscopic point of view. The issues to be interested in with FORTEC-3D code are (1) the FOW effects on neoclassical transport (2) the propagation and damping of GAM oscillation in the entire plasma region (3) the effects of direct orbit-loss or some external sources and (4) precise simulation of the bifurcation phenomena and evolution of ambipolar  $E_r$  field in non-axisymmetric systems. In the following chapter our recent simulation results in tokamak and a LHD-like configuration are shown.

### 3. Transport simulation in 2D configurations

It has been revealed that the NC ion heat conductivity  $\chi_i$  calculated by Monte-Carlo method decreases in the near-axis region of tokamaks[6,14,15]. To explain this, we have developed a new transport formulation for axisymmetric plasma to include the large-scale orbital properties of potato particles into NC theory[10]. It is based on Lagrangian description of drift-kinetic equation[16], in which the kinetic equation is solved in the phase space of the constants of motion  $(\mathcal{E}, \mu, \langle\psi\rangle)$  in the collisionless limit. Here,  $\mathcal{E}$  is the total energy,  $\mu$  is the magnetic moment, and  $\langle\psi\rangle$  is averaged radial position of guiding-center motion. The reduced drift-kinetic equation for the averaged distribution function  $\bar{f}(\mathbf{z}) = \bar{f}(\mathcal{E}, \mu, \langle\psi\rangle)$  is as follows

$$\frac{\partial \bar{f}}{\partial t} = \frac{1}{J_c} \frac{\partial}{\partial \mathbf{z}} \cdot J_c \frac{\nu(\mathcal{E}, \langle\psi\rangle)}{2} \left[ \left\langle \frac{\partial \mathbf{z}}{\partial \mathbf{v}} \cdot \mathbf{v} \cdot \frac{\partial \mathbf{z}}{\partial \mathbf{v}} \right\rangle \frac{\partial \bar{f}}{\partial \mathbf{z}} - \left\langle \frac{m u_{\parallel}}{T} \frac{\partial \mathbf{z}}{\partial \mathbf{v}} \cdot \mathbf{w} f_M \right\rangle \right] \quad (7)$$

where  $\mathbf{V}(\mathbf{v}) = v^2 \mathbf{1} - \mathbf{v}\mathbf{v}$ ,  $\mathbf{w} = v^2 \mathbf{b} - v_{\parallel} \mathbf{v}$ ,  $\nu$  is collision frequency, and  $J_c$  is Jacobian. The rhs of eq.(7) describes the orbit-averaged collision operator, and  $\langle \dots \rangle$  is the orbit averaging operator. This equation can be interpreted as a description of the diffusion process of averaged radial position of particles by collisions. Since the orbit average is taken along real orbit, orbital properties of fat potato particles are included in the formulation. Equation (7) is solved by expanding  $\bar{f} = \bar{f}_0 + \bar{f}_1 + \dots$  and calculate the non-vanishing lowest order  $\partial \bar{f} / \partial t$  in the second order. The final solution is obtained in the form of transport coefficients in an usual manner such as  $D_i$  and  $\chi_i$ . The details of how to solve eq. (7) numerically is summarized in [10].

Typical potato orbit width is estimated as  $\Delta_p \sim (q^2 \rho_i^2 R_0)^{1/3}$ , where  $\rho_i$  is ion Larmor radius. Therefore,  $\Delta_p$  becomes larger in reversed-shear configuration where  $q \gg 1$  around the magnetic axis. To see the dependence of  $\chi_i$  on  $\Delta_p$  we show in Fig. 1 the example of calculation of  $\chi_i$  in two configurations, one is a normal-shear case  $q_{axis} = 1.5$ ,  $q_{edge} = 4$  and  $\Delta_p \simeq 0.08$ , and the other is a reversed-shear case  $q_{axis} = 8$ ,  $q_{min} = 1.5$  at  $r = 0.5$ ,  $q_{edge} = 4$ , and  $\Delta_p \simeq 0.18$  respectively. The results are compared with the fitting formula of neoclassical theory in the standard local analysis[17], and the result from FORTEC-3D for the reversed-shear case. As shown in other Monte-Carlo simulations,  $\chi_i$  obtained from

Lagrangian theory decreases in the near-axis region and the decreasing region width is proportional to  $\Delta_p$ . The FORTEC calculation shows qualitatively the same decreasing tendency of  $\chi_i$  though it is somewhat weaker compared with Lagrangian theory. In conclusion, the reduction of  $\chi_i$  around the magnetic axis can be explained by the existence of potato particles which is not considered in standard neoclassical theory.

Next example is GAM oscillation and damping. By a similar mechanism of Landau damping, GAM damps if  $q \simeq 1$ . Though the damping occurs even in the local transport model as in [18] by solving the kinetic equation only on the sole flux surface, the oscillation of  $E_r$  on neighboring surfaces are expected to couple through the particle motion passing these surfaces. The simulation results by FORTEC-3D are shown in Fig. 2 and 3 for a reversed-shear configuration  $q_{axis} = 3$ ,  $q_{min} = 1.2$  at  $r = 0.5$ , and  $q_{edge} = 8$ , varying banana width by changing  $B$  and  $T_i$ . A strong coupling effect can be seen in large-width case where the damping of  $E_r$  oscillation occurred on the resonant surface  $r \sim 0.5$  affects the time evolution of  $E_r$  on inner and outer surfaces. On the other hand, GAM oscillation on each flux surface seems to be decoupled in the small-width case. The beat patterns of the oscillation amplitude seen in these figures are also explained by the coupling effect of GAM oscillation because the GAM frequency varies in space proportional to thermal velocity on each surfaces. Thus the global evolution of GAM oscillation is found to have a non-local dependency if the orbit scale is large.

#### 4. Transport simulation in 3D configurations

As a benchmark of our hybrid model combining FORTEC-3D and GSRAKE, we show here a simulation results in a LHD-like configuration. The simulation parameters are  $R_{axis} = 3.7m$ ,  $\beta_{axis} = 0.08\%$ ,  $B_0 = 1.6T$ , and whole plasma region is well in the LMFP (plateau -  $1/\nu$ ) regime. The table of  $\Gamma_e(E_\rho, \rho)$  calculated from GSRAKE is shown in Fig. 4. By referring the table, FORTEC-3D solves time evolution of radial electric field and neoclassical transport for ions. In Fig. 5, the contour plot of radial electric field in the  $(\rho, t)$  plane is shown. The  $\iota$  profile is monotonically increasing and it has  $\iota = 1$  surface at  $\rho \simeq 0.8$ . GAM oscillation is strongly damped there and never appears at  $\rho > 0.8$ , while the oscillation sustains long time at the inner region. Therefore, the relaxation time scale of  $E_r$  and  $\Gamma_i$  to a steady, ambipolar state varies in radial direction depending on the rotational transform profile. The ambipolar electric field at the steady state is shown in Fig. 6. In GSRAKE we can calculate  $\Gamma_i$  as well as  $\Gamma_e$  and ambipolar electric field can be predicted by seeking the roots satisfies  $\Gamma_e = \Gamma_i$ . It is also shown in Fig. 6. In the present case only one negative root is found in the entire region. These two simulation results show a little different ambipolar  $E_r$ . The ion flux calculated in FORTEC-3D contains several effects which is neglected in calculating  $\Gamma_i$  in GSRAKE such as the FOW effects, neoclassical polarization drift in a time-dependent field, energy-scattering in collision term, and orbit loss at the boundary, etc. These differences are considered to be attributed to the difference in  $\Gamma_i$ (FORTEC-3D) and  $\Gamma_i$ (GSRAKE) as large as several tens % seen in the simulation result, and it leads to the difference in the ambipolar electric field profile.

## 5. Summary

We have developed a global neoclassical transport simulation code FORTEC-3D which is applicable both to axisymmetric and non-axisymmetric toroidal configurations including the finite-orbit-width effect and self-consistent time evolution of radial electric field. By using it, we have demonstrated several transport phenomena which contains non-local effects both in tokamak and stellarator plasmas. It is a promising tool to investigate non-local transport phenomena and global transport dynamics. We are planning to utilize the simulation system to reveal the non-local process in the evolution of ambipolar electric field in LHD plasmas including the bifurcation phenomenon.

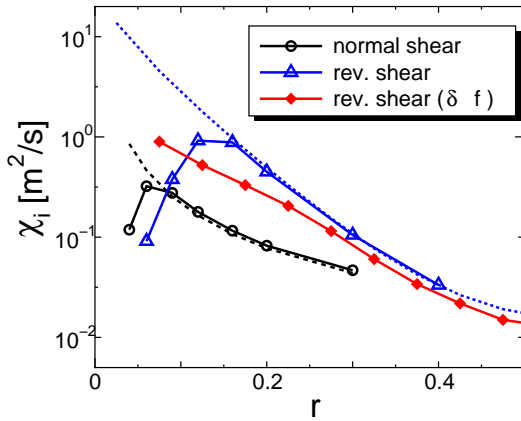


FIG. 1:  $\chi_i$  calculated in normal and reversed shear configurations from Lagrangian neoclassical theory. Dotted lines are fitting formula by Chang and Hinton. The line with diamonds is a result from FORTEC-3D.

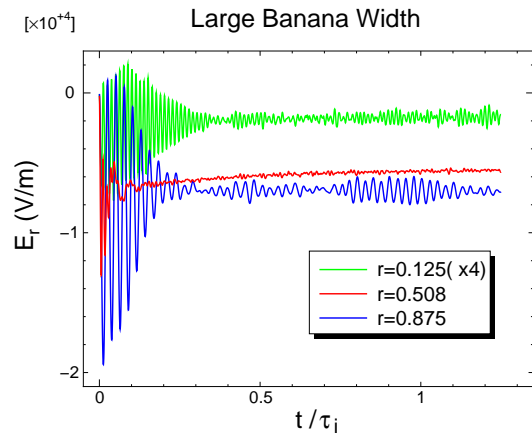


FIG. 2: Time evolution of  $E_r$  on three radial positions in a reversed-shear tokamak,  $q_{min} = 1.2$  at  $r = 0.5$ . The typical banana orbit width  $\Delta r \sim 10$  cm.

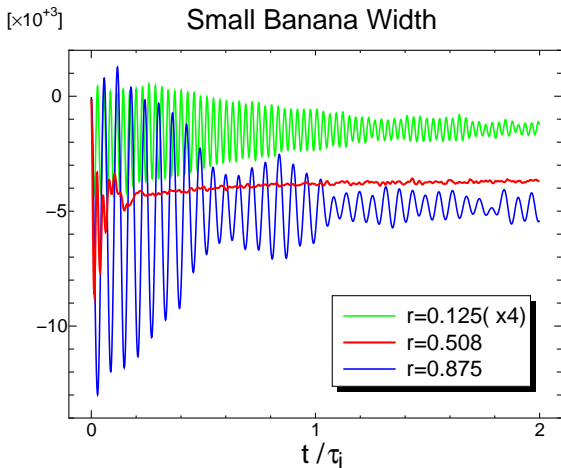


FIG. 3: Time evolution of  $E_r$  in the same configuration as in Fig. 1 but  $\Delta r$  is about 1/3 times narrower by changing the strength of B-field and ion temperature.

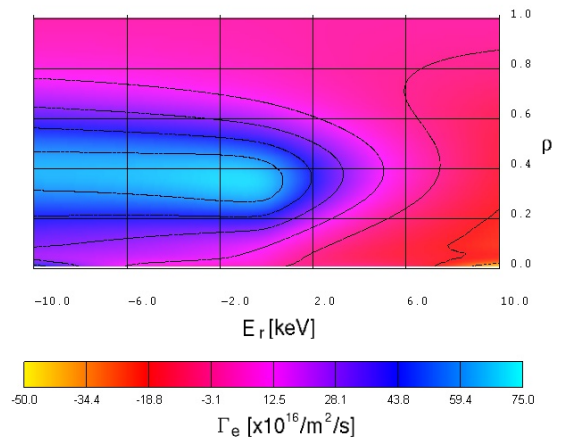


FIG. 4: Electron particle flux in a LHD-like configuration from GSRAKE.

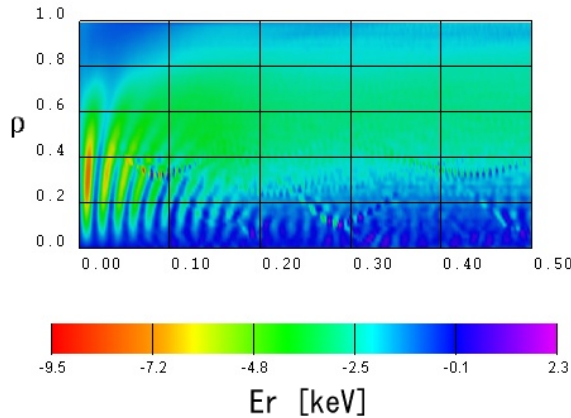


FIG. 5: Time evolution of  $E_r$  in a LHD-like configuration calculated by coupling FORTEC-3D and GSRAKE.

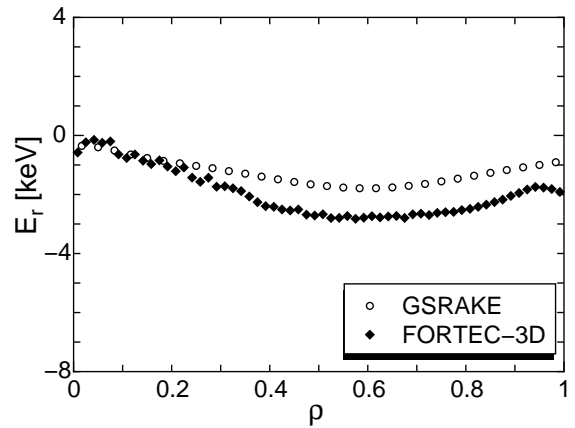


FIG. 6: Comparison of ambipolar electric field profile. Open circles are predicted from GSRAKE and diamonds are the result from FORTEC-3D when it reached a steady state.

## References

- [1] HINTON, F. L. and HAZELTINE, R. D., Rev. Mod. Phys. **48** (1976) 239.
- [2] HIRSHMAN, S. P. and SIGMAR, D. J., Nuclear Fusion **21** (1981) 1079.
- [3] SATAKE, S., et al., Journal. Plasma. Fusion Res. **77** (2001) 573.
- [4] KOVRIZHNYKH, L. M., Nulc. Fusion **24** (1984) 851.
- [5] SHAING, K. C. and CALLEN, J. D., Phys. Fluids **26** (1983) 3315.
- [6] WANG, W. X., et al., Plasma Phys. Control. Fusion **41** (1999) 1091.
- [7] OKAMOTO, M., et al., Journal of Plasma and Fusion Research **78** (2002) 1344.
- [8] HIRSHMAN, S. P. and Betancourt, O., J. Comput. Phys. **96** (1991) 99.
- [9] BEIDLER, C. D. and MAAßBERG, H., Plasma Phys. Control. Fusion **43** (2001) 1131.
- [10] SATAKE, S., et al., Phys. Plasmas **9** (2002) 3946.
- [11] LIN, Z., et al., Phys. Plasmas **2** (1995) 2975.
- [12] SUGAMA, H. and NISHIMURA, S., Phys. Plasmas **9** (2002) 4637.
- [13] BRUNNER, S., et al., Phys. Plasmas **6** (1999) 4504.
- [14] LIN, Z., et al., Phys. Plasmas **4** (1997) 1707.
- [15] BERGMANN, A., et al., Phys. Plasmas **8** (2001) 5192.
- [16] BERNSTEIN, I. B. and MOLVIG, K., Phys. Fluids **26** (1983) 1488.
- [17] CHANG, C. H. and HINTON, F. L., Phys. Fluids **25** (1982) 1493.
- [18] NOVAKOVSKII, S. V., et al., Phys. Plasmas **4** (1997) 4272.

## Finite-Orbit-Width Effect and the Radial Electric Field in Neoclassical Transport Phenomena

S. Satake 1), M. Okamoto 1), N. Nakajima 1), H. Sugama 1), M. Yokoyama 1), and C. D. Beidler 2)

1) National Institute for Fusion Science, Toki, Japan

2) Max-Planck-Institut für Plasmaphysik, Greifswald, Germany

e-mail contact of main author : satake.shinsuke@nifs.ac.jp

**Abstract.** Modeling and detailed simulation of neoclassical transport phenomena both in 2D and 3D toroidal configurations are shown. The emphasis is put on the effect of finiteness of the drift-orbit width, which brings a non-local nature to neoclassical transport phenomena. Evolution of the self-consistent radial electric field in the framework of neoclassical transport is also investigated. The combination of Monte-Carlo calculation for ion transport and numerical solver of ripple-averaged kinetic equation for electrons makes it possible to calculate neoclassical fluxes and the time evolution of the radial electric field in the whole plasma region, including the finite-orbit-width(FOW) effects and global evolution of geodesic acoustic mode (GAM). The simulation results show that the heat conductivity around the magnetic axis is smaller than that obtained from standard neoclassical theory and that the evolution of GAM oscillation on each flux surface is coupled with other surfaces if the FOW effect is significant. A global simulation of radial electric field evolution in a non-axisymmetric plasma is also shown.

### 1. Introduction

Neoclassical(NC) transport theory has been successfully established under the assumption of the local transport model(small-orbit-width (SOW) limit)[1,2]. However, there are some cases in recent experiments where the assumption is not valid, for example, at the internal transport barrier(ITB) and in the core region of tokamak where potato orbits[3] appear. The potato width becomes several tens % of the plasma minor radius in a reversed-shear configuration, and to evaluate transport level in such cases the finite-orbit-width(FOW) effect of trapped particles should be considered. Neoclassical transport theory for 3-dimensional stellarator configurations has also been considered in the SOW-limit[4,5]. The drift orbits in stellarators are much complicated compared to those in tokamaks. Though the orbit widths of ripple-trapped particles are small, transit particles in stellarators have large orbit scales, and energetic particles trapped helically are easy to lose from the confinement region. In order to take account of those particles in NC transport calculation, conventional analytical method is hard to apply, and global properties of particle motion should be taken into account.

Another interest in recent study on NC transport is the formation of the radial electric field  $E_r$ . Since the lowest-order NC flux is intrinsic ambipolar in tokamaks, the higher-order terms appeared from the FOW effect must be retained to evaluate the time evolution of  $E_r$ . In stellarators, the radial flux is non-ambipolar even in the lowest order. Because NC fluxes in non-axisymmetric plasmas are sensitive to electric field, determination of the self-consistent ambipolar electric field is one of the main task of neoclassical theory.

However, the role of the FOW effects in the evolution of radial electric field has not been investigated in detail.

To carry out a general and detailed research on neoclassical transport phenomena including the finite-orbit-width effects and radial electric field, we develop a numerical transport simulation code FORTEC-3D using the  $\delta f$  Monte-Carlo method[6,7]. It solves the time evolution of neoclassical fluxes as well as the self-consistent radial electric field, in multidimensional MHD equilibrium configurations obtained from VMEC[8]. The original FORTEC has been developed to solve NC transport for ions in tokamaks, in which the electron particle flux  $\Gamma_e$  is negligible to determine ambipolar  $E_r$ . In non-axisymmetric cases  $\Gamma_e$  is comparable to  $\Gamma_i$  and is needed to calculate the evolution of ambipolar electric field. To reduce the time consumption for simulation, we adopt a hybrid model. While the ion transport is solved by the  $\delta f$  method, the electron flux is obtained from GSRAKE[9], a numerical solver of ripple-averaged kinetic equation. Thus FORTEC-3D enables us to investigate neoclassical transport and the evolution of radial electric field including the FOW effects of ions in general 3D configurations, from a microscopic point of view.

The remainder of the paper is organized as follows. In Sec. 2, formulation of  $\delta f$  Monte-Carlo method and our simulation modeling are explained. In Sec. 3, NC transport simulation in a tokamak configuration is shown. It is shown that the geodesic-acoustic-mode (GAM) oscillation in tokamak is affected by the FOW effects. The evolution of  $E_r$  on each flux surface is found to be coupled if the banana width is large. Effects of potato particles on transport are also shown. We have developed an extended transport theory including the FOW effects[10]. From the new neoclassical theory we show that the potato orbits around the axis plays an important role to the decreasing tendency of ion heat conductivity around the magnetic axis. In Sec. 3, a test calculation of NC transport in a LHD-like configuration in combination with GSRAKE is presented. The relaxation process of GAM oscillation toward ambipolar steady state is simulated precisely.

## 2. Simulation model

Consider a general toroidal plasma in the magnetic coordinates  $(\rho, \theta, \zeta)$ , where  $\rho = \sqrt{\psi/\psi_a}$  is a normalized radial coordinate and  $\psi_a$  is the toroidal flux label on the boundary. To solve the time development of a plasma distribution function in the phase space  $(\rho, \theta, \zeta, \mathcal{K} = v^2, \mu = mv_\perp^2/2B)$ , the linearized drift kinetic equation

$$\frac{D\delta f}{Dt} \equiv \left[ \frac{\partial}{\partial t} + \dot{\mathcal{K}} \frac{\partial}{\partial \mathcal{K}} + (\mathbf{v}_\parallel + \mathbf{v}_d) \cdot \nabla - C_{tp}(\cdot, f_M) \right] \delta f = -\mathbf{v}_d \cdot \left( \nabla f_M - \frac{e\mathbf{E}_\rho}{T} \right) f_M + \mathcal{P}f_M \quad (1)$$

is considered. Here,  $\mathbf{E}_\rho = -d\Phi/d\rho\nabla\rho$  is radial electric field,  $\mathbf{v}_d$  is the drift velocity of a guiding center, and  $f_M = f_M(\rho, \mathcal{K})$  is Maxwellian of a flux-surface function. The linearized test-particle collision operator  $C_{tp}$  is implemented numerically as a random kick in the velocity space. The field-particle collision operator  $\mathcal{P}f_M$  is defined so as to satisfy the conservation laws for collision operator

$$\int (C_{tp} + \mathcal{P}f_M) \mathcal{M}_{\{0,1,2\}} d\mathbf{v} = 0, \quad (2)$$

where  $\mathcal{M}_0 = 1$ ,  $\mathcal{M}_1 = \mathbf{v}$ , and  $\mathcal{M}_2 = \mathcal{K}$ , respectively[11]. The use of the operator which acts correctly as the linearized Fokker-Planck collision term is an advantage of our code to apply it to general toroidal geometry. Because of the break of the momentum-conservation law, it is known that the pitch-angle scattering operator, though it is a good approximation for neoclassical theory in helical systems, cannot be simply applied to the transport analysis in axisymmetric plasmas[12]. Note also that in the  $\delta f$  formulation, the FOW effect is included in the term  $\mathbf{v}_d \cdot \nabla \delta f$ , which is usually dropped in standard local transport models. We adopted the 2-weight scheme[6] to solve eq. (1) by Monte-Carlo method. Two weights  $w$  and  $p$  which satisfy the relation  $wg = \delta f$ ,  $pg = f_M$  are introduced, where  $g$  is the distribution function of simulation markers. Each marker follows the track in the phase space according to the lhs of eq. (1), that is,  $Dg/Dt = 0$  is satisfied. Then the problem is reduced to solve the evolution of weights for each markers

$$\dot{w} = \frac{p}{f_M} \left[ -\mathbf{v}_d \cdot \left( \nabla - \frac{e\mathbf{E}_\rho}{T} \right) + \mathcal{P} \right] f_M, \quad (3)$$

$$\dot{p} = \frac{p}{f_M} \mathbf{v}_d \cdot \left( \nabla - \frac{e\mathbf{E}_\rho}{T} \right) f_M. \quad (4)$$

We have also adopted a weight averaging technique to suppress the dispersion spreading of the weight fields[13].

The self-consistent evolution of the radial electric field is solved according to

$$\left( \langle |\nabla \rho|^2 \rangle + \left\langle \frac{c^2}{v_A^2} |\nabla \rho|^2 \right\rangle \right) \epsilon_0 \frac{\partial E_\rho(\rho, t)}{\partial t} = -e (Z_i \Gamma_i^{neo} - \Gamma_e^{neo}), \quad (5)$$

where the ion particle flux is obtained from  $\Gamma_i^{neo} = \langle \int d^3\mathbf{v} \dot{\rho} \delta f_i \rangle$ . In tokamak cases,  $\Gamma_e^{neo}$  is negligible since  $|\Gamma_e/\Gamma_i| \sim O(\sqrt{m_e/m_i})$ . In non-axisymmetric cases, however,  $\Gamma_e^{neo}$  is comparable to  $\Gamma_i^{neo}$  and the balance between these two fluxes determines the ambipolar  $E_r$ . Since ion and electron fluxes are strongly dependent on  $E_r$  in the collisionless  $1/\nu$  regime and the ambipolar condition  $\Gamma_i(E_r) = \Gamma_e(E_r)$  sometimes has a multiple solution, we need a proper evaluation for  $\Gamma_e$  as well as  $\Gamma_i$  in order to investigate important phenomena in NC transport in stellarators such as time evolution and bifurcation of electric field. However, solving both ion and electron transport by  $\delta f$  scheme is not practical way because the orbit time scales of two species are too separated, and because it is expected that the FOW effect on transport is significant only for ions. In FORTEC-3D only the ion part is solved by using the  $\delta f$  method. The table of  $\Gamma_e(E_\rho, \rho)$  for a given profile is prepared by GSRAKE, and  $\Gamma_e$  is referred from the table at each time step in solving eq. (5) in FORTEC-3D. GSRAKE is designed to give a general solution for ripple-averaged kinetic equation. The solution is valid throughout the entire long-mean-free-path (LMFP) regime. It is applicable to general, multi-helicity 3-dimensional configurations in which the magnetic field strength is given in a form

$$B = B_0 + \sum_{n=0}^{\infty} B_{0,n}(\rho) \cos n\zeta + \sum_{m=1}^{\infty} \sum_{n=-\infty}^{\infty} B_{m,n}(\rho) \cos(n\zeta - m\theta). \quad (6)$$

In our simulation system, the table of Fourier components of  $B$  are extracted from MHD equilibrium field solved by VMEC, and it is transferred to FORTEC-3D and GSRAKE. The

adaptability of GSRAKE to transport calculation in LHD plasmas has been benchmarked by comparing other numerical codes or analytical expressions previously[9].

Adopting the hybrid model, our simulation system is capable of solving neoclassical transport in general 2D and 3D configurations without missing the important role of the FOW effects of ions, within a practical calculation time. A typical simulation using 50 million markers in 3D configuration takes 20 hours to run a simulation to reach a steady state solution. It also enables us to investigate neoclassical transport dynamics in the whole plasma region from a microscopic point of view. The issues to be interested in with FORTEC-3D code are (1) the FOW effects on neoclassical transport (2) the propagation and damping of GAM oscillation in the entire plasma region (3) the effects of direct orbit-loss or some external sources and (4) precise simulation of the bifurcation phenomena and evolution of ambipolar  $E_r$  field in non-axisymmetric systems. In the following chapter our recent simulation results in tokamak and a LHD-like configuration are shown.

### 3. Transport simulation in 2D configurations

It has been revealed that the NC ion heat conductivity  $\chi_i$  calculated by Monte-Carlo method decreases in the near-axis region of tokamaks[6,14,15]. To explain this, we have developed a new transport formulation for axisymmetric plasma to include the large-scale orbital properties of potato particles into NC theory[10]. It is based on Lagrangian description of drift-kinetic equation[16], in which the kinetic equation is solved in the phase space of the constants of motion  $(\mathcal{E}, \mu, \langle\psi\rangle)$  in the collisionless limit. Here,  $\mathcal{E}$  is the total energy,  $\mu$  is the magnetic moment, and  $\langle\psi\rangle$  is averaged radial position of guiding-center motion. The reduced drift-kinetic equation for the averaged distribution function  $\bar{f}(\mathbf{z}) = \bar{f}(\mathcal{E}, \mu, \langle\psi\rangle)$  is as follows

$$\frac{\partial \bar{f}}{\partial t} = \frac{1}{J_c} \frac{\partial}{\partial \mathbf{z}} \cdot J_c \frac{\nu(\mathcal{E}, \langle\psi\rangle)}{2} \left[ \left\langle \frac{\partial \mathbf{z}}{\partial \mathbf{v}} \cdot \mathbf{v} \cdot \frac{\partial \mathbf{z}}{\partial \mathbf{v}} \right\rangle \frac{\partial \bar{f}}{\partial \mathbf{z}} - \left\langle \frac{m u_{\parallel}}{T} \frac{\partial \mathbf{z}}{\partial \mathbf{v}} \cdot \mathbf{w} f_M \right\rangle \right] \quad (7)$$

where  $\mathbf{V}(\mathbf{v}) = v^2 \mathbf{1} - \mathbf{v}\mathbf{v}$ ,  $\mathbf{w} = v^2 \mathbf{b} - v_{\parallel} \mathbf{v}$ ,  $\nu$  is collision frequency, and  $J_c$  is Jacobian. The rhs of eq.(7) describes the orbit-averaged collision operator, and  $\langle \dots \rangle$  is the orbit averaging operator. This equation can be interpreted as a description of the diffusion process of averaged radial position of particles by collisions. Since the orbit average is taken along real orbit, orbital properties of fat potato particles are included in the formulation. Equation (7) is solved by expanding  $\bar{f} = \bar{f}_0 + \bar{f}_1 + \dots$  and calculate the non-vanishing lowest order  $\partial \bar{f} / \partial t$  in the second order. The final solution is obtained in the form of transport coefficients in an usual manner such as  $D_i$  and  $\chi_i$ . The details of how to solve eq. (7) numerically is summarized in [10].

Typical potato orbit width is estimated as  $\Delta_p \sim (q^2 \rho_i^2 R_0)^{1/3}$ , where  $\rho_i$  is ion Larmor radius. Therefore,  $\Delta_p$  becomes larger in reversed-shear configuration where  $q \gg 1$  around the magnetic axis. To see the dependence of  $\chi_i$  on  $\Delta_p$  we show in Fig. 1 the example of calculation of  $\chi_i$  in two configurations, one is a normal-shear case  $q_{axis} = 1.5$ ,  $q_{edge} = 4$  and  $\Delta_p \simeq 0.08$ , and the other is a reversed-shear case  $q_{axis} = 8$ ,  $q_{min} = 1.5$  at  $r = 0.5$ ,  $q_{edge} = 4$ , and  $\Delta_p \simeq 0.18$  respectively. The results are compared with the fitting formula of neoclassical theory in the standard local analysis[17], and the result from FORTEC-3D for the reversed-shear case. As shown in other Monte-Carlo simulations,  $\chi_i$  obtained from

Lagrangian theory decreases in the near-axis region and the decreasing region width is proportional to  $\Delta_p$ . The FORTEC calculation shows qualitatively the same decreasing tendency of  $\chi_i$  though it is somewhat weaker compared with Lagrangian theory. In conclusion, the reduction of  $\chi_i$  around the magnetic axis can be explained by the existence of potato particles which is not considered in standard neoclassical theory.

Next example is GAM oscillation and damping. By a similar mechanism of Landau damping, GAM damps if  $q \simeq 1$ . Though the damping occurs even in the local transport model as in [18] by solving the kinetic equation only on the sole flux surface, the oscillation of  $E_r$  on neighboring surfaces are expected to couple through the particle motion passing these surfaces. The simulation results by FORTEC-3D are shown in Fig. 2 and 3 for a reversed-shear configuration  $q_{axis} = 3$ ,  $q_{min} = 1.2$  at  $r = 0.5$ , and  $q_{edge} = 8$ , varying banana width by changing  $B$  and  $T_i$ . A strong coupling effect can be seen in large-width case where the damping of  $E_r$  oscillation occurred on the resonant surface  $r \sim 0.5$  affects the time evolution of  $E_r$  on inner and outer surfaces. On the other hand, GAM oscillation on each flux surface seems to be decoupled in the small-width case. The beat patterns of the oscillation amplitude seen in these figures are also explained by the coupling effect of GAM oscillation because the GAM frequency varies in space proportional to thermal velocity on each surfaces. Thus the global evolution of GAM oscillation is found to have a non-local dependency if the orbit scale is large.

#### 4. Transport simulation in 3D configurations

As a benchmark of our hybrid model combining FORTEC-3D and GSRAKE, we show here a simulation results in a LHD-like configuration. The simulation parameters are  $R_{axis} = 3.7m$ ,  $\beta_{axis} = 0.08\%$ ,  $B_0 = 1.6T$ , and whole plasma region is well in the LMFP (plateau -  $1/\nu$ ) regime. The table of  $\Gamma_e(E_\rho, \rho)$  calculated from GSRAKE is shown in Fig. 4. By referring the table, FORTEC-3D solves time evolution of radial electric field and neoclassical transport for ions. In Fig. 5, the contour plot of radial electric field in the  $(\rho, t)$  plane is shown. The  $\iota$  profile is monotonically increasing and it has  $\iota = 1$  surface at  $\rho \simeq 0.8$ . GAM oscillation is strongly damped there and never appears at  $\rho > 0.8$ , while the oscillation sustains long time at the inner region. Therefore, the relaxation time scale of  $E_r$  and  $\Gamma_i$  to a steady, ambipolar state varies in radial direction depending on the rotational transform profile. The ambipolar electric field at the steady state is shown in Fig. 6. In GSRAKE we can calculate  $\Gamma_i$  as well as  $\Gamma_e$  and ambipolar electric field can be predicted by seeking the roots satisfies  $\Gamma_e = \Gamma_i$ . It is also shown in Fig. 6. In the present case only one negative root is found in the entire region. These two simulation results show a little different ambipolar  $E_r$ . The ion flux calculated in FORTEC-3D contains several effects which is neglected in calculating  $\Gamma_i$  in GSRAKE such as the FOW effects, neoclassical polarization drift in a time-dependent field, energy-scattering in collision term, and orbit loss at the boundary, etc. These differences are considered to be attributed to the difference in  $\Gamma_i$ (FORTEC-3D) and  $\Gamma_i$ (GSRAKE) as large as several tens % seen in the simulation result, and it leads to the difference in the ambipolar electric field profile.

## 5. Summary

We have developed a global neoclassical transport simulation code FORTEC-3D which is applicable both to axisymmetric and non-axisymmetric toroidal configurations including the finite-orbit-width effect and self-consistent time evolution of radial electric field. By using it, we have demonstrated several transport phenomena which contains non-local effects both in tokamak and stellarator plasmas. It is a promising tool to investigate non-local transport phenomena and global transport dynamics. We are planning to utilize the simulation system to reveal the non-local process in the evolution of ambipolar electric field in LHD plasmas including the bifurcation phenomenon.

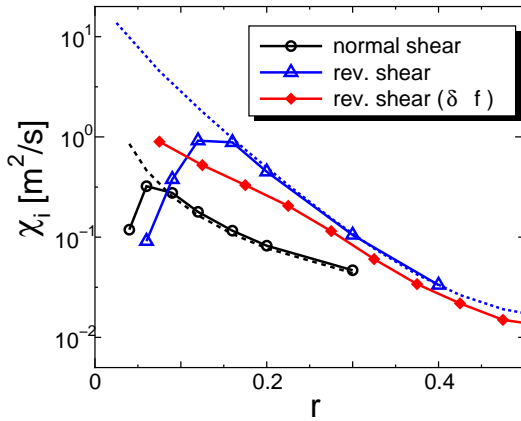


FIG. 1:  $\chi_i$  calculated in normal and reversed shear configurations from Lagrangian neoclassical theory. Dotted lines are fitting formula by Chang and Hinton. The line with diamonds is a result from FORTEC-3D.

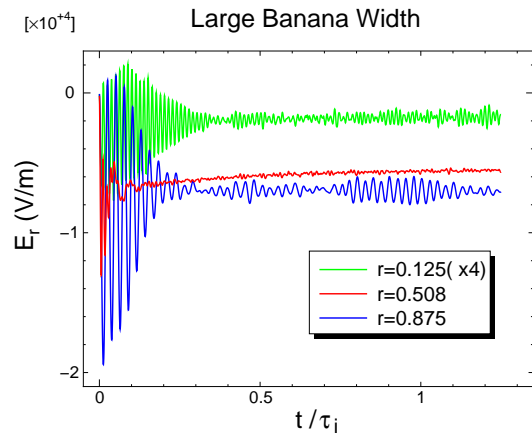


FIG. 2: Time evolution of  $E_r$  on three radial positions in a reversed-shear tokamak,  $q_{min} = 1.2$  at  $r = 0.5$ . The typical banana orbit width  $\Delta r \sim 10$  cm.

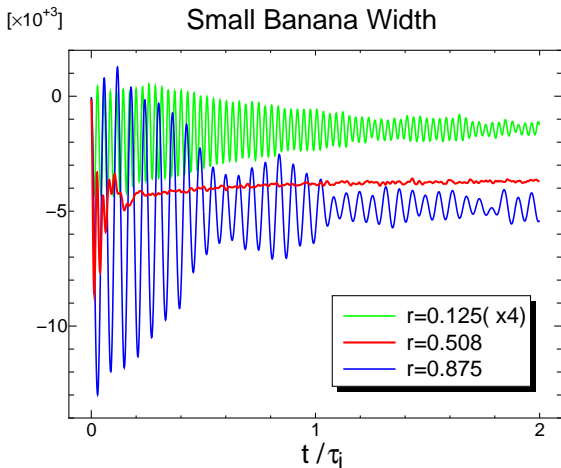


FIG. 3: Time evolution of  $E_r$  in the same configuration as in Fig. 1 but  $\Delta r$  is about 1/3 times narrower by changing the strength of B-field and ion temperature.

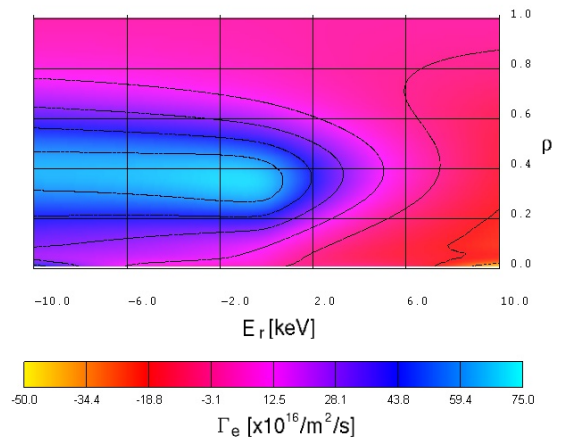


FIG. 4: Electron particle flux in a LHD-like configuration from GSRACE.

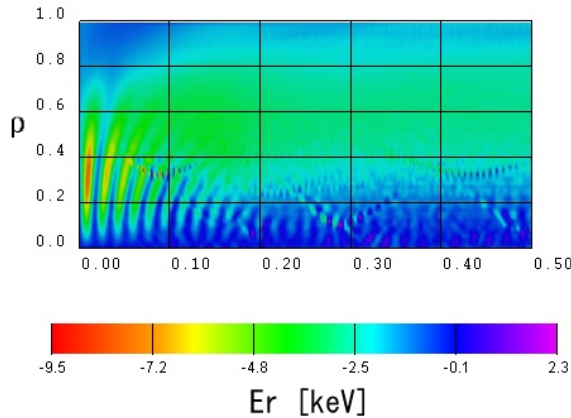


FIG. 5: Time evolution of  $E_r$  in a LHD-like configuration calculated by coupling FORTEC-3D and GSRAKE.

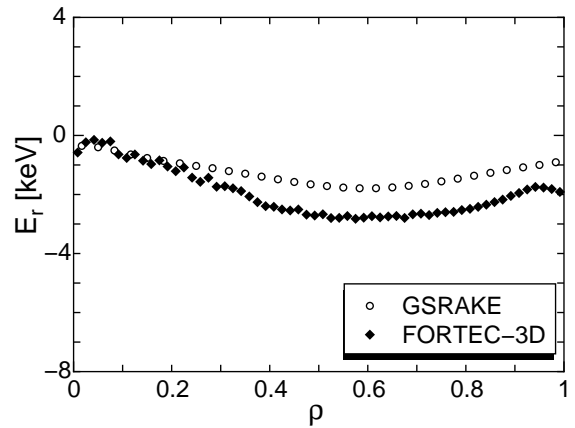


FIG. 6: Comparison of ambipolar electric field profile. Open circles are predicted from GSRAKE and diamonds are the result from FORTEC-3D when it reached a steady state.

## References

- [1] HINTON, F. L. and HAZELTINE, R. D., Rev. Mod. Phys. **48** (1976) 239.
- [2] HIRSHMAN, S. P. and SIGMAR, D. J., Nuclear Fusion **21** (1981) 1079.
- [3] SATAKE, S., et al., Journal. Plasma. Fusion Res. **77** (2001) 573.
- [4] KOVRIZHNYKH, L. M., Nulc. Fusion **24** (1984) 851.
- [5] SHAING, K. C. and CALLEN, J. D., Phys. Fluids **26** (1983) 3315.
- [6] WANG, W. X., et al., Plasma Phys. Control. Fusion **41** (1999) 1091.
- [7] OKAMOTO, M., et al., Journal of Plasma and Fusion Research **78** (2002) 1344.
- [8] HIRSHMAN, S. P. and Betancourt, O., J. Comput. Phys. **96** (1991) 99.
- [9] BEIDLER, C. D. and MAAßBERG, H., Plasma Phys. Control. Fusion **43** (2001) 1131.
- [10] SATAKE, S., et al., Phys. Plasmas **9** (2002) 3946.
- [11] LIN, Z., et al., Phys. Plasmas **2** (1995) 2975.
- [12] SUGAMA, H. and NISHIMURA, S., Phys. Plasmas **9** (2002) 4637.
- [13] BRUNNER, S., et al., Phys. Plasmas **6** (1999) 4504.
- [14] LIN, Z., et al., Phys. Plasmas **4** (1997) 1707.
- [15] BERGMANN, A., et al., Phys. Plasmas **8** (2001) 5192.
- [16] BERNSTEIN, I. B. and MOLVIG, K., Phys. Fluids **26** (1983) 1488.
- [17] CHANG, C. H. and HINTON, F. L., Phys. Fluids **25** (1982) 1493.
- [18] NOVAKOVSKII, S. V., et al., Phys. Plasmas **4** (1997) 4272.

## A Global Simulation of ICRF Heating in a 3D Magnetic Configuration

S. Murakami 1), A. Fukuyama 1), T. Akutsu 1), N. Nakajima 2), V. Chan 3), M. Choi 3), S.C. Chiu 4), L. Lao 3), V. Kasilov 5), T. Mutoh 1), R. Kumazawa 1), T. Seki 1), K. Saito 1), T. Watari 1), M. Isobe 1), T. Saida 6), M. Osakabe 1), M. Sasao 6) and LHD Experimental Group

1) Department of Nuclear Engineering, Kyoto University, Kyoto 606-8501, Japan

2) National Institute for Fusion Science, Oroshi, Toki, Gifu 509-5292, Japan

3) General Atomics, P.O. Box 85608, San Diego, California 92186-5608, USA

4) Sunrise R&M, Inc., 8585 Hopseed Lane, San Diego, California 92129, USA

5) Institute of Plasma Physics, National Science Center, KIPT, Kharkov, Ukraine

6) Graduate School of Engineering, Tohoku University, Sendai 980-8579, Japan

e-mail contact of main author: [murakami@nucleng.kyoto-u.ac.jp](mailto:murakami@nucleng.kyoto-u.ac.jp)

**Abstract.** A global simulation code for the ICRF heating analysis in a three-dimensional (3D) magnetic configuration is developed combining two global simulation codes; a drift kinetic equation solver, GNET, and a wave field solver, TASK/WM. Both codes take into account 3D geometry using the numerically obtained 3D MHD equilibrium. The developed simulation code is applied to the LHD configuration as an example. Characteristics of energetic ion distributions in the phase space are clarified in LHD. The simulation results are also compared with experimental results by evaluating the count number of the neutral particle analyzer using the obtained energetic ion distribution, and a relatively good agreement is obtained.

### 1. Introduction

ICRF heating experiments has been successfully done in helical systems[1-7] and have demonstrated the effectiveness of this heating method in three-dimensional (3D) magnetic configurations. In LHD, a significant performance of this method have also shown[8-11] and up to 500keV of energetic tail ions have been observed by fast neutral particle analysis (NPA)[12,13]. These measured results indicate a good property of energetic ion confinement in helical systems. However, the measured information by NPA is obtained as an integrated value along a line of sight and we need a reliable theoretical model for reproducing the energetic ion distribution to discuss the confinement of energetic ions accurately.

On the other hand, ICRF heating generates highly energetic trapped ions, which drift around the torus for a long time (typically on a collisional time scale) interacting with the RF wave field. Thus, the behavior of these energetic ions is strongly affected by the characteristics of the drift motions, that depend on the magnetic field configuration. In particular, in a 3D magnetic configuration, complicated drift motions of trapped particles would play an important role in the confinement of the energetic ions and the ICRF heating process.

Many efforts have been made to analyze the energetic particle distribution and the transport during ICRF heating, analytically and numerically (Fokker-Planck model and etc.), but most of the analyses using local approximation. A simple Orbit following Monte Carlo simulation has been used to take into account the non-local effect due to finite orbit size of energetic ions[1-3]. However, the energetic particle distribution changes in time and we can not obtain

a correct steady state by this type of Monte Carlo simulation[14]. To obtain a steady state we should consider the balanced state between particle source and sink correctly in a global simulation.

Additionally, since the wavelength of the ICRF heating is typically comparable to the plasma scale length and the 3D geometry effect on the RF wave field would be also important in a 3D magnetic configuration. Therefore a global simulation of ICRF heating is necessary for the accurate modeling of the plasma heating process in a 3D magnetic configuration.

In this paper we study the ICRF heating in a 3D magnetic configuration combining two global simulation codes; a drift kinetic equation solver GNET [15,16] and a wave field solver TASK/WM [17]. We apply the simulation code to the LHD configuration as an example. We make clear the characteristics of energetic ions distribution in the phase space, and also show the confinement property of LHD configurations by comparing the simulation and experimentally observed results.

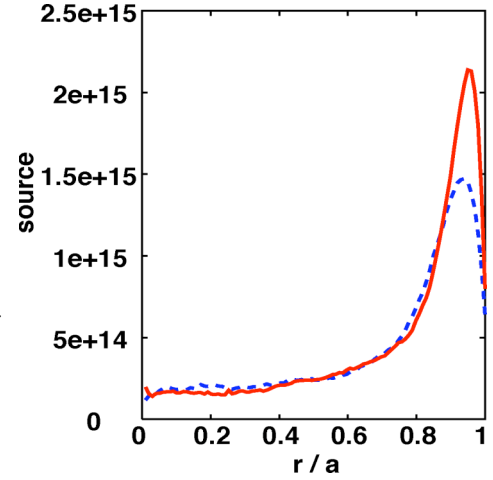


FIG. 1: Radial profiles of the minority ion sources;  $n_{e0}=2.0 \times 10^{19} \text{ m}^{-3}$  (solid line) and  $1.0 \times 10^{19} \text{ m}^{-3}$  (dotted line).

## 2. Simulation Model

In order to study the ICRF heating in a 3D magnetic field configuration we have developed a global simulation code combining two global codes; GNET and TASK/WM.

GNET solves a linearized drift kinetic equation for energetic ions including complicated behavior of trapped particles in 5-D phase space as where  $C(f)$  and  $Q_{ICRF}$  are the linear Coulomb Collision operator and the ICRF heating term.

$$\frac{\partial f}{\partial t} + (\mathbf{v}_{\parallel} + \mathbf{v}_D) \cdot \nabla f + \mathbf{a} \cdot \nabla_{\mathbf{v}} f - C(f) - Q_{ICRF}(f) - L_{particle} = S_{particle},$$

$S_{particle}$  is the particle source term by ionization of neutral particle and the radial profile of the source is evaluated using AURORA code. Figure 1 shows the typical profile of minority ion source for two densities. The particle sink (loss) term,  $L_{particle}$ , consists of two parts; one is the loss by the charge exchange loss assuming the same neutral particle profile as the source term calculation and the other is the loss by the orbit loss escaping outside of outermost flux surface.

In GNET code the minority ion distribution  $f$  is evaluated through a convolution of  $S_{particle}$  with a characteristic time dependent Green function evaluated using test particle Monte Carlo method. We follows the test particle orbits to evaluate the Green function in the Boozer coordinates.

The  $Q_{ICRF}$  term is modeled by the Monte Carlo method. When the test particle pass through the resonance layer where  $\omega - k_{\parallel}v_{\parallel} = n\omega_c$  the perpendicular velocity of this particle is changed by the following amount,

$$\begin{aligned}\Delta v_{\perp} &= \sqrt{\left(v_{\perp 0} + \frac{q}{2m} I |E_{+}| J_{n-1}(k_{\perp} \rho) \cos \phi_r\right)^2 + \frac{q^2}{4m^2} \left\{ I |E_{+}| J_{n-1}(k_{\perp} \rho) \right\}^2 \sin^2 \phi_r} - v_{\perp 0} \\ &\approx \frac{q}{2m} I |E_{+}| J_{n-1}(k_{\perp} \rho) \cos \phi_r + \frac{q^2}{8m^2 v_{\perp 0}} \left\{ I |E_{+}| J_{n-1}(k_{\perp} \rho) \right\}^2 \sin^2 \phi_r \\ I &= \sqrt{2\pi/n\dot{\omega}} \text{ or } 2\pi(n\dot{\omega}/2)^{-1/3} Ai(0)\end{aligned}$$

This expression includes the quadratic terms in wave amplitude and the averages of  $\Delta v_{\perp}$  and  $\Delta v_{\perp}^2$  over the random phase we obtain up to the leading order terms,

$$\langle \Delta v_{\perp} \rangle \approx \frac{q^2}{16m^2 v_{0\perp}} I^2 |E_{+}|^2, \quad \langle \Delta v_{\perp}^2 \rangle \approx \frac{q^2}{8m^2} I^2 |E_{+}|^2$$

and the following relation is fulfilled.

$$\langle \Delta v_{\perp} \rangle = \frac{1}{v_{0\perp}} \frac{\partial}{\partial v_{0\perp}} \left( v_{0\perp} \frac{\langle \Delta v_{\perp}^2 \rangle}{2} \right)$$

The spatial profile of RF wave electric field is necessary for the accurate calculation of the ICRF heating. The profile of RF wave field is an important factor on the ICRF heating and this profiles affect the particle orbit. We evaluate the RF wave field by the TASK/WM code. TASK/WM solves Maxwell's equation for RF wave electric field,  $\mathbf{E}_{RF}$ , with complex frequency,  $\omega$ , as a boundary value problem in the 3D magnetic configuration.

$$\nabla \times \nabla \times \mathbf{E}_{RF} = \frac{\omega^2}{c^2} \tilde{\epsilon} \cdot \mathbf{E}_{RF} + i\omega \mu_0 \mathbf{j}_{ext},$$

Here, the external current,  $\mathbf{j}_{ext}$ , denotes the antenna current in ICRF heating. The response of the plasma is described by a dielectric tensor including kinetic effects in a local normalized orthogonal coordinates.

In the simulation, first, we solve the RF wave field assuming the minority ion distribution and then we solve the minority ion distribution by GNET. Both codes assume a 3D magnetic configuration based on the MHD equilibrium by the VMEC code.

The developed code is benchmarked with ORBIT-RF [18] for 2-D geometry applying to the DIII-D configuration.

### 3. Simulation Results

We apply the global simulation code to a LHD configuration ( $R_{ax} = 3.6\text{m}$ ; the in-ward shifted configuration). This LHD configuration conforms the  $\sigma$ -optimized configuration and shows relatively good trapped particle orbit[19]. Most of ICRF heating experiments has been performed in this configuration.

The RF resonance position relative to magnetic flux surface has been tested mainly for two cases in the LHD experiments. One is the off-axis heating case in which the resonance surface almost crossing a saddle point of magnetic field at the longitudinally elongated cross section. In the off-axis case the resonance region only exists for  $r/a > 0.5$ . The other is the on-axis heating in which the resonance surface crossing a magnetic axis. The relation between the resonance surface and flux surfaces are shown in Fig. 2. The experimentally obtained results have shown the difference in the heating efficiencies and the decrease of energetic particle neutral count number detected by natural diamond detector (NDD-NPA) [20].

We, first, apply the TASK/WM code to evaluate the RF wave electric fields ( $E_+$  and  $E_-$ ) and, then, the obtained spatial profile of the RF field is used as a RF heating term in the GNET code. The similar heating and plasma parameters as the experimental ones are assumed in the calculation.

Figure 3 shows the steady state distribution of the minority ions during ICRF heating obtained by GNET. We plot the flux surface averaged tail ion distribution in the three dimensional space ( $r/a$ ,  $v_{||}$ ,  $v_{\text{perp}}$ ), where  $r/a$ ,  $v_{||}$  and  $v_{\text{perp}}$  are the normalized averaged minor radius, the parallel and perpendicular velocities normalized by the thermal velocity at the plasma center, respectively.

The RF wave accelerates minority ions perpendicularly in the velocity space and we can see perpendicularly elongated minority ion distributions. We find a peaked energetic tail ion distribution near  $r/a \sim 0.5$  in the off-axis heating case (Fig.3, left). Also, the energetic ions distribution has a triangular shape. This is because the large absorption of RF wave occurs when the banana tips of trapped particles are close to the resonance surface and those pitch angle of the particle depends on the minor radius (monotonically increase as a function of minor radius).

On the other hand we can see no strong peak in the distribution function in the on-axis heating case (Fig.3, right). The energetic particle distribution is broader than that of the off-axis case and the less energetic tail ion is obtained.

Figure 4 shows the minority ion pressure, which shows a population of energetic ions in the real space. We can see the clear difference between two heating cases. The high pressure regions are localized along the helical ripple where the magnetic field is weak and trapped particle are confined in this region. On the other hand the high pressure region is not localized and the a little stronger in the outer side (left side of the figure) of the torus.

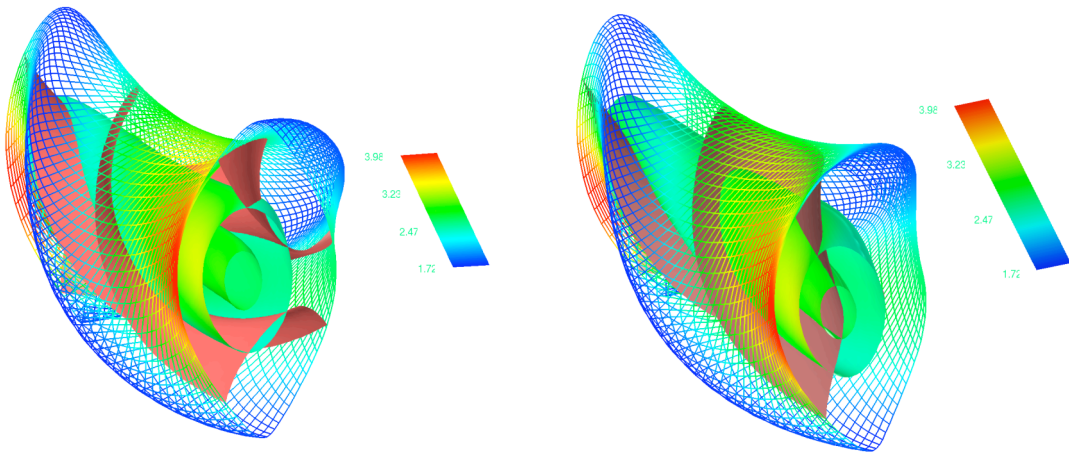


FIG. 2: 3D plots of the ICRF resonance surfaces in the off-axis point heating case (left) and on-axis heating case (right).

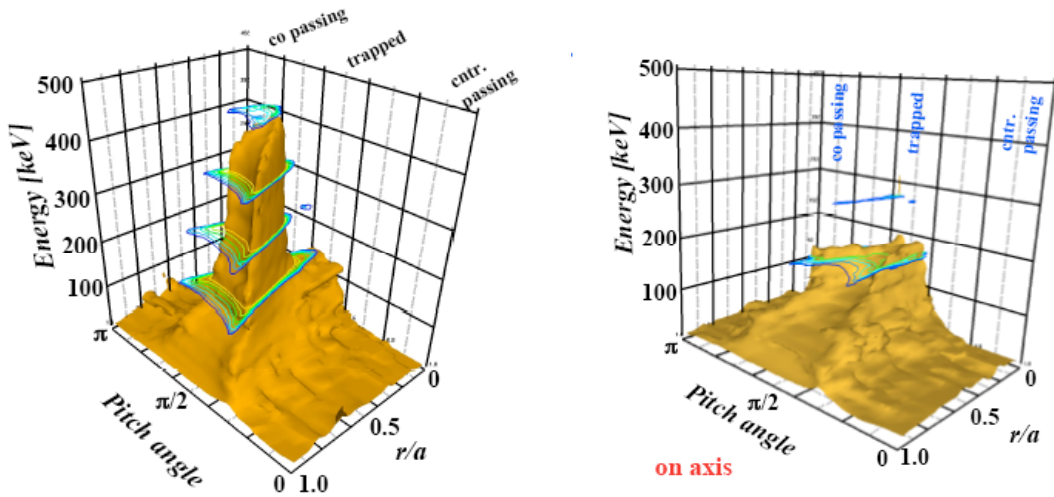


FIG. 3: Steady state distribution of energetic tail ions in the ( $r/a$ ,  $E$ , pitch angle) space in the off-axis point heating case (left) and on-axis heating case (right).

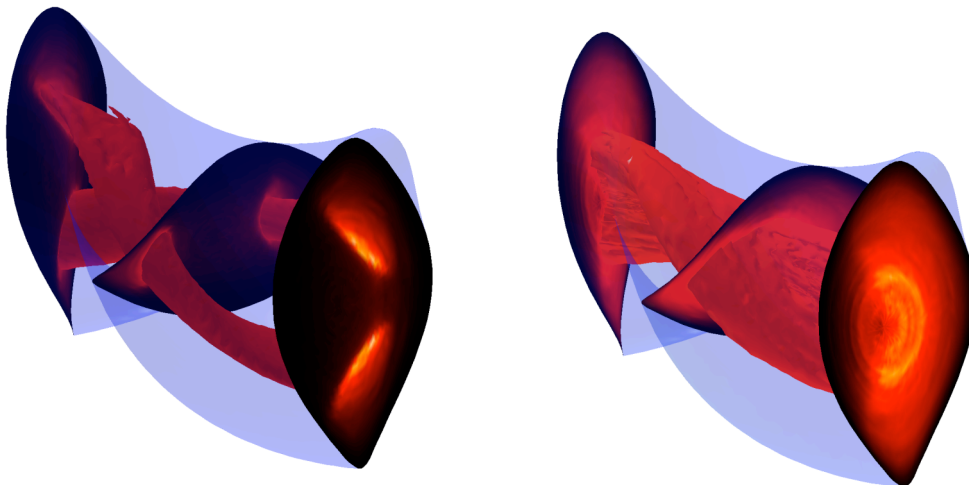


FIG. 4: 3D plots of the minority ion pressure in the off-axis point heating case (left) and on-axis heating case (right).

To understand this difference we plotted the resonance magnetic field strength with the modulation of magnetic field along the field line. Figure 5 shows the relative strength of the resonant magnetic field for two heating cases; the off-axis case (dotted line) and the on-axis heating case (dashed line).

The trapped particle whose banana tip is close to the resonance surface can absorb large energy from the RF wave. We can see, in the off-axis heating case, that the trapped particle absorbing large energy exists almost all region along the field line. This means that the those particle are resonate for a longer time and interact many times with the RF wave.

On the other hand the large absorbing trapped particle are a partly exist in the on-axis case. This means that the orbit of the large absorbing trapped particle is unstable and the transition between helically and toroidally trapped particles occurs. This transition takes place the stochastic behavior of the particle orbit and enhances the radial diffusion of energetic particles.

Therefore, we can conclude that the higher peak is observed in the distribution function in the off-axis case because the large absorbing trapped particles are more stable in the off-axis case than that of the on-axis heating case.

We can see the difference between two heating cases more clearly by the radial profile of the heating. Figure 6 shows the radial profiles of energetic ion pressure, heat deposition and minority ion density. The peaked pressure profile can be seen in the off axis case and the broader one is in the on-axis case. The heat deposition also shows the maximum near  $r/a=0.5$  in the off-axis case and flat one in the on axis case. The estimated heating efficiencies are about 70% for both cases and the difference of the radial profile does not influence the heating efficiency.

It is also found that the minority ions are pumped out near  $r/a=0.5$  in the off-axis case and near the axis in the on-axis case. These indicate that ICRF heating diffuse out the minority ions from the resonance layer.

To compare with the experimental results we have simulated the neutral count number detected by NDD-NPA using the simulation results. Relatively good agreement is obtained between the experimental and simulation results (Fig.7). Both the computed and the experimental counts have similar dependency on the energy spectrum.

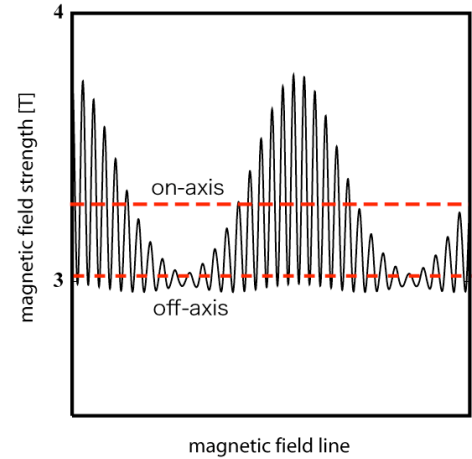


FIG. 5: Magnetic field strength along the field line at the flux surface of  $r/a=0.5$ .

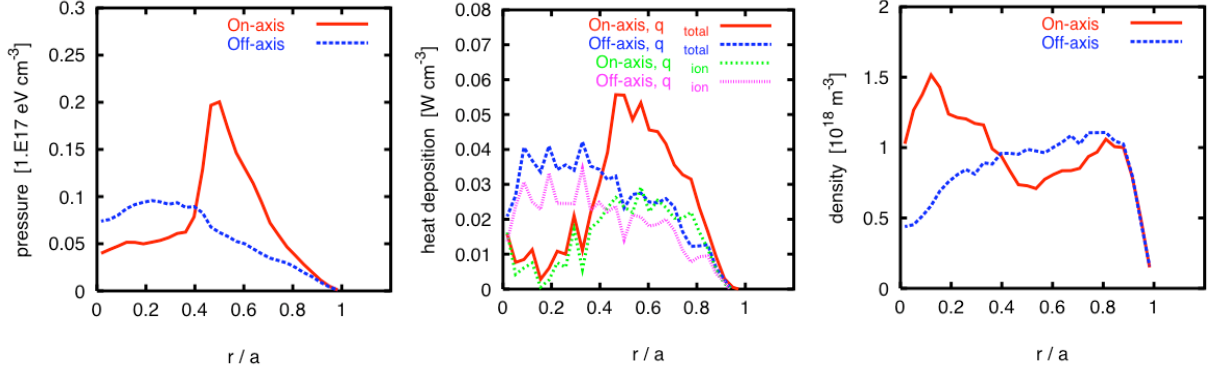


FIG. 6: Radial profiles of energetic ion pressure, heat deposition and minority ion density for the saddle point heating (red solid) and the on axis heating (blue dotted, closed).

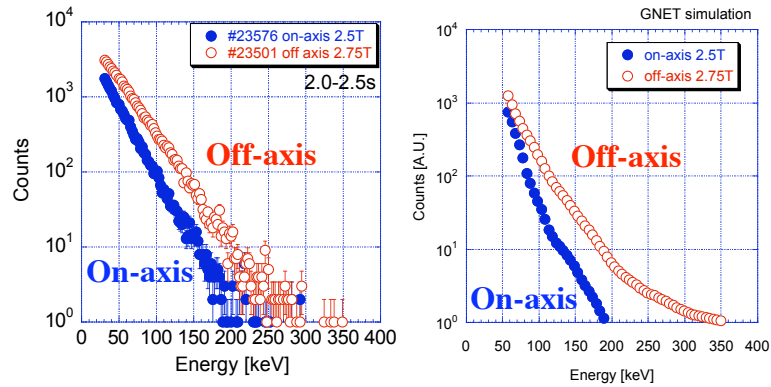


FIG. 7: Comparisons of the energy spectrum by the NDD-NPA results (left) and the simulation results (right) for the saddle point heating (red open) and the on axis heating (blue closed).

## 5. Conclusions

We have developed a global simulation code combining two code; GNET and TASK/WM. The GNET code solves a linearized drift kinetic equation for energetic ions including complicated behavior of trapped particles in 5-D phase space and the TASK/WM code solves Maxwell's equation for RF wave electric field with complex frequency as a boundary value problem in the 3D magnetic configuration.

The developed code has been applied to the analysis of energetic tail ion transport during ICRF heating in the LHD plasma. A steady state distribution of energetic tail ion has been obtained and the characteristics of distribution in the phase space are clarified. The resonance position dependency on the distribution have been shown and larger tail formation have been obtained in the off-axis heating case. This tendency agrees well with the experimental results. We have compared the GNET simulation results with the experimental results evaluating NDD count number and also obtained similar tendencies.

We have demonstrated that a global analysis is necessary for understanding the energetic particle transport in non-axisymmetric configurations.

**References**

- [1] MUTOH, T., et al., Nucl. Fusion **24** (1984) 1003.
- [2] NISHIMURA, K., et al., in Plasma Physics Controlled Nuclear Fusion Research 1994 (Proc. 15th Int. Conf. Seville, 1994), Vol. 1, IAEA, Vienna (1995) 679.
- [3] OKADA, H., et al., Nucl. Fusion **36** (1996) 465.
- [4] MASUDA, S., et al., Nucl. Fusion **37** (1997) 53.
- [5] NOTERDAEME, J.-M., et al., in Fusion Energy 1996 (Proc. 16th Int. Conf. Montreal, 1996) Vol. 3, IAEA, Vienna (1997) 335.
- [6] HARTMANN, D.A., et al., Contr. Fusion Plasma Phys., Proc. 24th EPS Conf., Berchtesgaden (Germany, 1997) p1633.
- [7] KWON, M., et al., Nucl. Fusion **32** (1992) 1225.
- [8] MUTOH, T., et al, Phys. Rev. Lett. **85** (2000) 4530.
- [9] KUMAZAEA, R., et al., Phys. Plasmas **8** (2001) 2139.
- [10] WATARI, T., et al. Nucl. Fusion **41** (2001) 325.
- [11] MUTOH, T., et al., Fusion Sci. Technol. **46** (2004) 175.
- [12] KRASHILNIKOV, A.V., et al., Nucl. Fusion **42** (2002) 759.
- [13] SAIDA, T., et al., Nuclear Fusion **44** (2004) 488.
- [14] MURAKAMI, S., et al, Nuclear Fusion **34** (1994) 913.
- [15] MURAKAMI, S., et al, Nuclear Fusion **40** (2000) 693.
- [16] MURAKAMI, S., et al., Fusion Sci. Technol. **46** (2004) 241.
- [17] FUKUYAMA, A., YOKOTA, E., AKUTSU, T., Proc. 18th IAEA Conf. on Fusion Energy (Sorrento, Italy, 2000) **THP2-26**.
- [18] CHOI, M., et.al., AIP Proceeding of the 15<sup>th</sup> Topical Conference in Radio Frequency Power in Plasmas 694 (2003) 86.
- [19] MURAKAMI, S., et al., Nucl. Fusion **42** (2002) L19.
- [20] ISOBE, M., et al., Rev. Sci. Instrum. **72** (2001) 611.

## Improvement of Negative Ion Source with Multi-Slot Grids for LHD-NBI

K. Tsumori 1), S. Asano 2), K. Nagaoka 1), M. Osakabe 1), K. Ikeda 1), Y. Takeiri 1), Y. Oka 1), O. Kaneko 1), Y. Suzuki 2), J. Watanabe 2), T. Okuyama 2), K. Ichihashi 2), M. Shibuya 1), T. Kawamoto 1), T. Kondo 1), M. Sato 1) and E. Asano 1).

1) National Institute for Fusion Science, 322-6 Oroshi Toki, Gifu, 509-5292 Japan.

2) Power and Industrial Systems R&D Center, Toshiba Corporation, 4-1 Ukishima-cho, Kawasaki-ku, Kawasaki 210-0862, Japan.

e-mail contact of main author: [tsumori@nifs.ac.jp](mailto:tsumori@nifs.ac.jp)

**Abstract.** In this article, we describe injection results on a negative ion source newly designed for one of the neutral beam injectors (NBI) in large helical device (LHD). The ion source consists of an accelerator with a combination of steering grid (SG) and multi-slot grounded grid (MSGG), whose transparency is about twice as large as that of conventional multi-hole grounded grid (MHGG). Due to the high transparency, the MSGG reduces the heat load carried by beam was much reduced comparing to the load onto MHGG. The maximum injection power increased drastically up to 4.4 MW at the energy of 180 keV in 2002 fiscal. In the ion source consisting of accelerator with MSGG, degradation of injection power was observed above the energy of more than 160 keV. The degradation was considered caused by saturation of yield of hydrogen negative ion ( $H^-$ ). In order to obtain further injection power, temperature of plasma grid rises up from 210 °C to 240 °C, and the arc balance was adjusted after changing total number of filaments from twenty-four to twenty-six. The injection power, consequently, reached 5.7 MW at the energy of 186 keV after improving the  $H^-$  yield. The maximum beam energy of 189 keV was obtained, and the power and pulse duration were 5.0 MW and 2 second at that time.

### 1. Introduction

Hydrogen negative ions have an advantage of higher neutral efficiency than protons in their energy range of more than 100keV [1], and negative-ion-based neutral beam injectors were built for the large scaled devices for nuclear fusion research [2,3]. In LHD, the experiments with neutral beams have been continued with two beam lines since 1998, and the third beam line has been added and injected beams since 2001. In case of LHD plasma, neutral injection is the most reliable heating method to improve the plasma parameters and to generate plasmas [4,5]. Enhancement of beam injection power was expected to improve the performance of LHD plasmas and to extend the boundary of experimental parameters. In order to improve plasma parameters, successive development of the ion sources has been carried out to improve beam injection power. The injection power and the energy were less than 4 MW and 170 keV for the pulse duration of 2 second after four-years improvements of the ion sources. The power, however, was limited by voltage breakdowns at beam accelerator of the ion source. In order to break through the power limit, newly designed beam accelerator has been developed and installed for the ion sources in one of beam lines for LHD since 2002. The new accelerator consisted of grounded grids with long slot-type

apertures instead of conventional circular apertures. The ion sources with MSGG succeeded to increase injection energy and power, while adjustment to the ion source was not sufficient. Some improvements were needed to obtain more injection power. The guideline to improve the injection power can be separated into following three issues. The first is to increase the maximum beam energy, which is strongly concerned with performance of beam accelerator. The next is to enhance  $H^-$  current, which relates to production rate of  $H^-$  ions and uniformity of  $H^-$  yield over whole beam extraction area. Although these issues link each other, we separate here to simplify the argument. The last is to improve the efficiency of neutral beam through beam injection port. In following sections, we report on the structures of ion source consisting of MSGG, on comparison of injection powers with use of accelerators with MHGG and MSGG, and on enhancement of  $H^-$  current by adjusting temperature of plasma grid and plasma uniformity.

## 2. Negative Ion Source with Multi-Slot Grounded Grid

Details of negative ion source with multi-slot grounded grid are described in elsewhere [6]. Figures 1(a) and 1(b) shows schematic cross-sectional views of negative ion source for LHD-NBI beam line 1 (BL1). The ion source is separated into two parts of the arc chamber and beam accelerator at an electrode called plasma grid, which divides the arc plasma and beam regions. The arc chamber is characterized by multi-cusp source with external magnetic filter. The chamber has hexagonal cross-sections in the both long and short sides

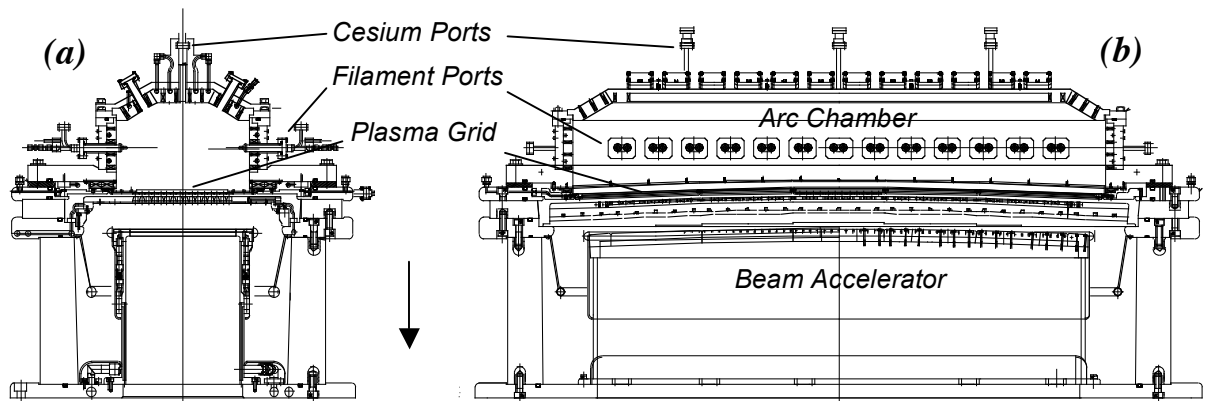


FIG. 1(a) and 1(b). Cross-sectional views on the short side (a) and long side (b) of a negative ion source for one of LHD-NBIs (Beam line 1). The arrow indicates beam direction.

to reduce magnetic lines of force connecting from filter magnet to cusp magnet and intersecting filaments. Those magnetic lines have a possibility to induce irregular arc discharge, which damages filaments and decreases the lifetime. Inner dimensions of the chamber are 1400 mm of the height, 350 mm of the width and 235 mm of the maximum depth. Cesium (Cs) vapor is seeded from three feeding lines equipped on the back plate to enhance the yield of hydrogen negative ions. Amount of Cs inside arc chamber is adjusted by remote-controlled pneumatic valves. Arc discharge is made by applying voltage of 40-80 V

between arc chamber and filaments installed from side plates via filament ports. Thirty filament-ports are installed on each side of the chamber and twenty-four filaments are usually feed from filament power supply.

Beam accelerator is divided into five segments in long side direction of the ion source. The single segment is composed by four electrode grids, which are plasma grid (PG), extraction grid (EG), steering grid (SG) and multi-slot grounded grid (MSGG). The segments are

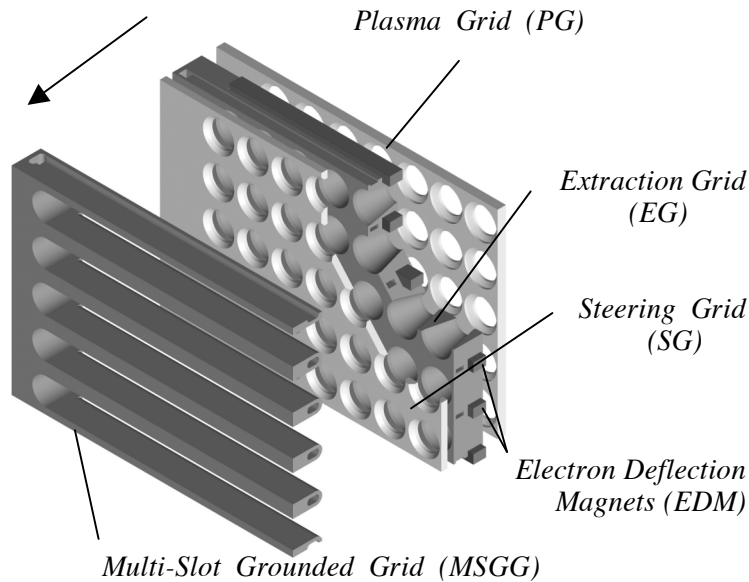


FIG. 2. Cut view of accelerator segment with multi-slot grounded grid. The segment consists of four grids of PG, EG, SG and MSGG. The arrow indicates direction of H<sup>+</sup> beam.

inclined for extrapolation of the centerlines of these five segments to intersect at the pivot point 13 m apart from the exit plane of grounded grid. A cut view of the accelerator is illustrated in FIG. 2. Plasma grid is made of molybdenum to increase the temperature; i.e. appropriate PG temperature increases the H<sup>+</sup> ion yield in Cs seeded negative ion source. As shown in FIG. 2, permanent magnet array is embedded in EG, and polarities of the magnetic field are alternated row by row. The array magnets called electron deflection magnets (EDM), and local magnetic fields induced by the magnets sweep electrons extracted from arc chamber accompanying with H<sup>+</sup> ions. The grid is made of oxygen free copper (OFC) with water-cooling channels to keep temperature of EDM lower than the Curie point. The material of SG is molybdenum to prevent hard sputtering due to high-energy back-streaming positive ions coming from the beam downstream region. Multi-slot grounded grid is made of OFC, water channels are installed in the grid to remove heat carried by beams. A power supply is connected to PG and EG to extract H<sup>+</sup> ions form arc chamber. The H<sup>+</sup> ions are extracted form apertures of PG and form multi-beamlets. The H<sup>+</sup> ions are accelerated by potential difference between SG and MSGG.

Each electrode segment performs to H<sup>+</sup> beamlets following three roles. The first role is beam focusing, which is defined by applied voltages to the grids and geometric structures of all the grids are defined. The second is beam converging. Each beamlets is converged at the pivot point by beam steering technique. Beamlets are steered by displacing the aperture axes of segment grids. The last is correction of beam trajectories deflected by EDM. The correction is also done by aperture displacement. In regard to BL1 of LHD-NBI, all the beamlet-axes are designed to intersect at the pivot point by beam focusing, converging and trajectory correction. Aperture axes in PG and EG are common and aperture of grounded grid (GG) were displaced in previous accelerator with MHGG. The maximum displacement

of MHGG apertures became more than 3 mm. Accelerator with MSGG cannot steer any beamlet in the direction of slot long side, and SG is added to control beamlet trajectories. The maximum displacement of the SG aperture is smaller than 2 mm, and this has an advantage from the point of view of beam aberration comparing to GG steering system.

### 3. Comparison of Injection Power and Energy in Accelerators with MHGG and MSGG

The largest difference between  $H^-$  and positive-ion accelerations is electron detachment by collisions of  $H^-$  ions with neutral hydrogen molecules. The collision occurs during the transport of  $H^-$  beam inside accelerator grids. Detached electrons, which are called stripped electrons, are independently accelerated from the collision points and are bent by magnetic field leaked from arc chamber. The stripped electrons scatter widely onto accelerator grids because of the randomness of the collision points in beam accelerating region and small Larmor radius of electrons. Acceleration voltage is higher than extraction voltage, and GG is exposed larger heat load carried by the stripped electrons. Neutralized hydrogen atoms and off-focus  $H^-$  ions carry heat load additionally. The neutralization process of  $H^-$  ions inside beam acceleration region is inevitable, because it is impossible to remove neutral gasses from the region. Energetic particles onto GG can cause gas emission and secondary ions emission via sputtering processes from the grid, and those emitted secondary particles can induce voltage breakdowns at the grid gap. One of the methods to reduce total heat load is to increase the beam transparency of GG. For this purpose, MSGG has been newly designed and replaced from previous MHGG. The beam transparency of MSGG is about twice as large as that of MHGG.

Figure 4 indicates Injection powers in both cases of accelerators with MHGG and MSGG. The data is plotted as a function of beam energy. The maximum injection power and energy are 3.6 MW and 165 keV for 2 second in pervious ion source with MHGG in LHD-NBI BL1. These values increased up to 4.4 MW and 180 keV by adopting MSGG to the accelerator. It took shorter time to reach the maximum power and energy in the accelerator equipping MSGG compared with MHGG. Main cause for shortening the attainable time was drastic decrease of breakdowns between accelerator grids, which is related to the reduction of heat load onto GG. Beam heat onto MHGG and MSGG was compared with the same beam condition by means of water-calorimetric measurement, and heat reduction rate was about 45 % in MSGG case. The reduction ratio is close to the ratio of beam interfarring area of GG [6]. Constitution of heat load due to

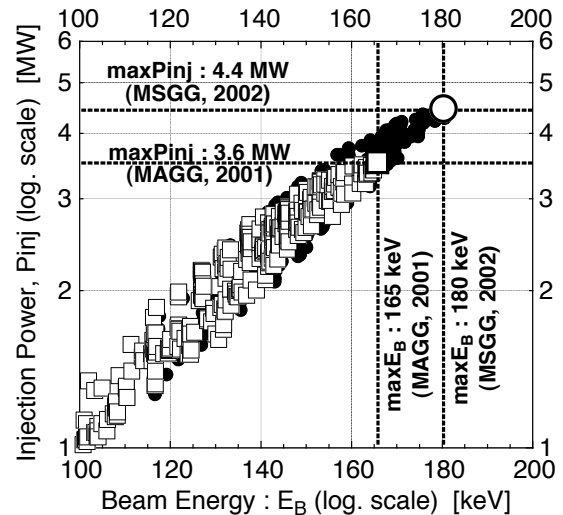


FIG. 4. Comparison of injection power with respect to beam energy. The power is summation of two ion sources. Solid circles and open squares indicate injection powers in the cases of accelerators with MSGG and MHGG, respectively.

The reduction ratio is close to the ratio of beam interfarring area of GG [6]. Constitution of heat load due to

stripped electron is considered not so large in total heat load to grounded grid, and the rest particles, neutralized  $H^0$  and  $H^-$  beam with strong aberration might deposit unexpected high heat load to GG.

## 4. Enhancement of $H^-$ Current

### 4.1 Saturation of $H^-$ Current

According to Child-Langmuir's law, injection power is approximately proportional to the  $5/2$  power of beam energy ( $E_B$ ) under the condition that beam perviance, grid gaps and the ratio of  $V_{ext} / V_{acc}$  ( $Rv$ ) are kept constant. Where the notations of  $V_{ext}$  and  $V_{acc}$  represent extraction and acceleration voltages, respectively, and beam energy is expressed as summation of these voltages. Injection power obtained by accelerator with MSGG is indicated with respect to beam energy in FIG. 5. Neutral beam line for LHD consists of two ion sources and injection power indicates summation of the powers obtained by those two ion sources here. Keeping beam energy constant,  $H^-$  current goes up linearly as increasing input arc power, and then reaches to the maximum value corresponding to the space charge limited current at that energy. The lines A and B are drawn to cross the limited powers. As indicated in the figure, injection power changes the raising rate from line A to B at about the energy of 160 keV. The line A is proportional to  $E_B^{5/2}$ , while line B changes linearly with respect to  $E_B$ . This suggests the  $H^-$  current saturates approximately in the energy above 160 keV. Following possibilities were expected in this situation. The first was mismatching of Cs condition for  $H^-$  production, and the next was caused by imbalanced distribution of arc plasma and the last was insufficiency of input power to generate the seeds of  $H^-$  ions; i.e. hydrogenous positive ions. The first and second were focused, because total  $H^-$  current did not change by increasing input arc power.

### 4.2 Enhancement of Cesium Effect

Assuming  $H^-$  ions are dominantly produced via surface process in Cs seeded ion sources, workfunction of PG surface should have strong influence to the production rate of  $H^-$  ions. In well-defined clean surface under ultra high vacuum condition, workfunction becomes minimum when Cs coverage is half monolayer [7]. In practical surface, such as PG surface

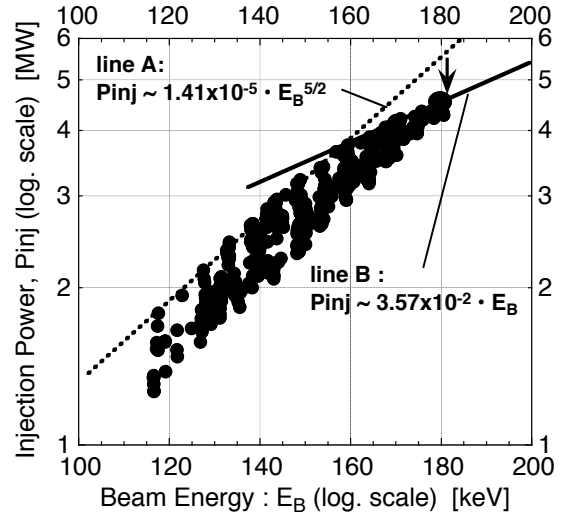


FIG. 5. Injection power with respect to beam energy. The power is summation of two ion sources consisting of accelerators with MSGG. The lines A and B are proportional to the  $5/2$  power of beam energy ( $E_B^{5/2}$ ) and to  $E_B$ , respectively.

of Cs seeded ion source, it is difficult to maintain the situation as static condition, because cesiated surface is exposed hydrogenous ions, electrons and other impurities. Nevertheless such violent situation of ion source,  $H^-$  production rate does not change so much once Cs is injected a certain amount inside the arc chamber. Although small amount of Cs vapor should be supplied to the chamber,  $H^-$  production rate becomes more sensitive to PG temperature. The PG temperature is risen by radiation form arc plasma and heat transfer of charged particles. Duty cycle of arc discharge is small, about 6 %, and thermal insulator is inserted between PG and PG retainer not to decrease the temperature quickly. Typical sensitivity of  $H^-$  production rate to PG temperature is shown in FIG. 6. The temperature is measured at a PG periphery without aperture holes. In this figure  $H^-$  current is normalized by the value at PG temperature of 210 °C. Averaged PG temperature was about 210 °C in beam injection of 2002 fiscal. Production rate of  $H^-$  ions still increases at PG temperature more than 210 °C as shown in FIG. 6. There are two ways to raise the temperature. One is to increase input arc power, which is a heat source. Another is to decrease heat transfer form PG via thermal insulator. Arc power was limited by arcing, irregular arc discharge, and it was impossible to increase the arc power. The latter, therefore, was chose to enhance  $H^-$  production rate. By changing the material of thermal insulator of PG from OFC to stainless steal and decreasing the contact area, PG temperature can keep much higher than previous condition.

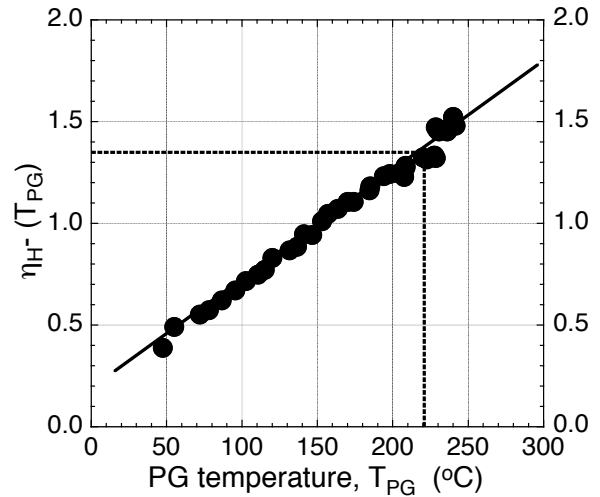


FIG. 6. Production rate of  $H^-$  ions as a function of temperature of plasma grid. The rate is normalized by the value of  $H^-$  current at 210 °C. The rate changes linearly to PG temperature in this temperature range.

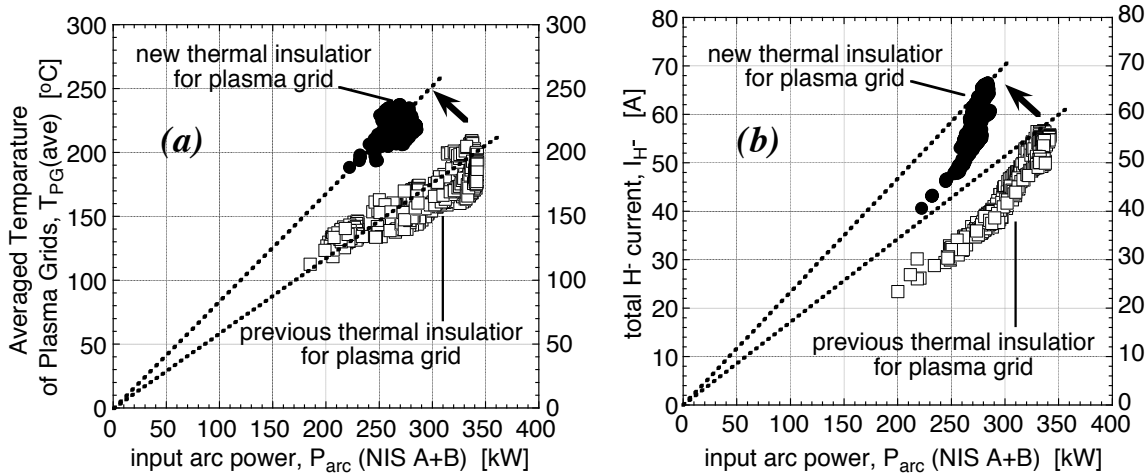


FIG. 7(a) and 7(b) (a) Averaged temperature of plasma grids over two sources is shown as a function of arc power input to two ion sources. (b) Arc efficiency of  $H^-$  current with respect to arc power. Solid circle and open square denote the data obtained by using new and old thermal insulators, respectively.

Figure 7a shows averaged temperature of ten plasma grids, which corresponds to whole plasma electrodes of two ion sources, as a function of input arc power. The ratio of PG temperature to input arc power increased from 0.6 to 0.8 °C / kW. The maximum averaged PG temperature of 240 °C was obtained at arc power of about 120 kW per ion source. Arc efficiency, which is defined as total  $H^-$  current to input arc power, enhanced after changing the thermal insulator. Larger current is obtained at lower arc power as shown in FIG. 7b. The efficiency changes from 0.172 to 0.235 [A/kW] at maximum. The higher efficiency of  $H^-$  production rate to input arc power contributes to decrease irregular discharge of arc chamber and to save the filament lifetime.

### 4.3 Improvement for Arc Distribution

The short and long inner sides of arc chamber for LHD negative ion source are 350 mm and 14000 mm, respectively. Imbalance of arc-plasma distribution is observed in such elongated ion sources. Uniform distribution of arc plasma is effective to obtain large  $H^-$  current and to avoid voltage breakdowns in accelerator due to spatial difference of beam perviance.

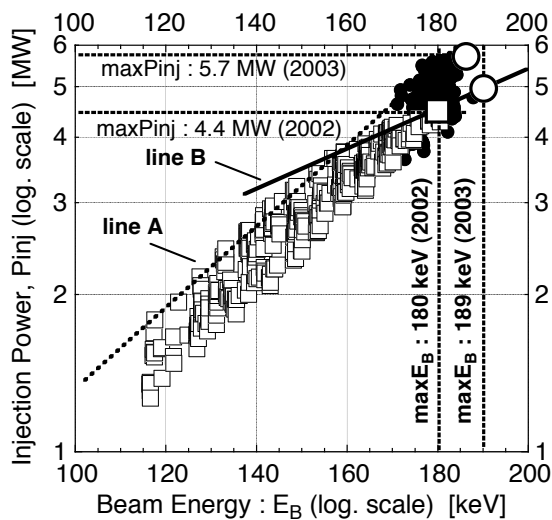


FIG. 8 Beam injection power before and after adjustments for PG temperature and for uniformity of arc plasma.

Twenty-six filaments are prepared for each arc chamber of LHD-NBI BL1; thirty filaments are installed on each long sidewall of the chamber. Usually twenty-four filaments are feed from twelve-filament power supply (PS). All the filaments were feed to obtain symmetric and uniform distribution of filament arrangement in long side of the arc chamber. Additionally, plasma distribution was adjusted by using external resistors connected between filament and arc power supplies. Injection power after adjustments for PG temperature and plasma uniformity is shown in FIG. 8. Injection result before the adjustments is indicated in the same figure for comparison. Degradation of injection power due to saturation of  $H^-$  current is shown as line A, and the feature is improved after the adjustments enhancing  $H^-$  current. As indicated in FIG. 8, power degradation is removed after the adjustments, and injection power reaches 5.7 MW at the beam energy of 186 keV. The beam duration was 1.6 second, and the duration is limited by experimental requirement. The injection power becomes proportional to  $E_B$  above the energy of 175 keV. In this energy range, drain current of acceleration PS, whose current includes about 75 % of  $H^-$  current, is limited by capacitance of the PS. High-energy limit has been examined using the accelerator with MSGG. So far, the maximum energy was limited 189 keV by the voltage limit of acceleration PS, the injection power and pulse duration were 5.0 MW and 2 seconds, respectively.

## 5. Summary

Beam accelerator with a combination of steering grid and multi-slot grounded grid was developed and applied to large scaled negative ion sources for LHD-NBI. Beam injection power increased from 3.6 MW to 4.4 MW by introducing the accelerator system in 2002 fiscal. The beam energy reached 180 keV, which is the design value of LHD-NBI. Although the beam energy attained the maximum value of power supply, injection power started to saturate above the energy of 160 keV. According to Child-Langmuir's law, injection power should be proportional to the  $5/2$  power of beam energy with some assumptions, while the power is linear to beam energy. This suggests the  $H^-$  yield is not sufficient to input arc power. In order to increase the beam power, two-steps adjustment has been applied for enhancement of the  $H^-$  current. The first one is to enhance cesium effect by rising averaged temperature of plasma grids from 210 °C to 240 °C. The saturation characteristic has been disappeared by this adjustment of PG temperature. Another is to adjust the uniformity of arc plasma by adding total number of filaments in arc chamber. The injection power, consequently, attained the maximum value of 5.7 MW at the energy of 186 keV and the pulse duration was 1.6 second. Both of the beam power and energy exceed the design value of LHD-NBI. The maximum beam energy of 189 keV, which was limited by capacity of acceleration power supply, was obtained at the power of 5.0 MW so far.

## References

- [1] BERKNER, K.H., et al., "Intense, Mixed-Energy Hydrogen Beams for CTR Injection", Nucl. Fusion, **15** (1975) 249-254.
- [2] USHIGUSA, K., and the JT-60 TEAM, Proceedings of 16th IAEA Fusion Energy Conference, Montreal, Canada, 1996, (unpublished), IAEA-CN-64/01-3.
- [3] MOTOJIMA, O., et al., "Initial physics achievements of large helical device experiments", Physics of Plasma **6** (1999) 1843-1850.
- [4] TAKEIRI, Y., et al., "Formation of electron internal transport barrier and achievement of high ion temperature in Large Helical Device", Phys. of Plasma, **10** No.5 (2003) 1788-1795.
- [5] KANEKO, O., et al., "Analysis of plasma initiation by neutral beams in the Large Helical Device", Nucl. Fusion, **42** No.4 (2002) 441-447.
- [6] TSUMORI, K., et al., "High power beam injection using an improved negative ion source for the large helical device", Rev. of Sci. Instrum, **75** No.5 (2004) 1847-1850.
- [7] KIEJNA, A., and WOJCIECHOWSKI, K. F., "Work function of metals: Relation between theory and experiment", Prog. Surf. Sci, **11**, (1981) 293-338.

## Improved Structure and Long-life Blanket Concepts for Heliotron Reactors

A. Sagara 1), S. Imagawa 1), O. Mitarai 2), T. Dolan 1), T. Tanaka 1), Y. Kubota 1), K. Yamazaki 1), K. Y. Watanabe 1), N. Mizuguchi 1), T. Muroga 1), N. Noda 1), O. Kaneko 1), H. Yamada 1), N. Ohyabu 1), T. Uda 1), A. Komori 1), S. Sudo 1), and O. Motojima 1)

1) National Institute for Fusion Science, Toki, Gifu 509-5292, Japan

2) Kyushu Tokai University, 9-1-1 Toroku, Kumamoto 862-8652, Japan

e-mail contact of main author: [sagara.akio@nifs.ac.jp](mailto:sagara.akio@nifs.ac.jp)

**Abstract.** New design approaches are proposed for the LHD-type heliotron D-T demo-reactor FFHR2 to solve the key engineering issues of blanket space limitation and replacement difficulty. A major radius over 14 m is selected to permit a blanket-shield thickness of about 1 m and to reduce the neutron wall loading and toroidal field, while achieving an acceptable cost of electricity COE. Two sets of optimization are successfully carried out. One is to reduce the magnetic hoop force on the helical coil support structures by adjustment of the helical winding coil pitch parameter and the poloidal coils design, which facilitates expansion of the maintenance ports. The other is a long-life blanket concept using carbon armor tiles that soften the neutron energy spectrum incident on the self-cooled Flibe-RAF blanket. In this adaptation of the Spectral-shifter and Tritium breeder Blanket (STB) concept a local tritium breeding ratio TBR over 1.2 is feasible by optimized arrangement of the neutron multiplier Be in the carbon tiles, and the radiation shielding of the super-conducting magnet coils is also significantly improved. Using the constant cross sections of helically winding shape, the “screw coaster” concept is proposed to replace in-vessel components such as the STB armor tiles. The key R&D issues to develop the STB concept, such as radiation effects on carbon and enhanced heat transfer of Flibe, are elucidated.

### 1. Introduction

Due to inherently current-less plasma, helical power reactors have attractive advantages, such as steady operation and no dangerous current disruption. Aiming at system integration for D-T fusion demo-reactors on the basis of physics and engineering results established in the LHD project [1], much progress has been made in design studies, including R&D works on engineering issues in the LHD-type heliotron power reactor FFHR [2]. In those studies the coil pitch parameter  $\gamma$  of continuous helical winding has been adjusted beneficially to reduce the magnetic hoop force while expanding the blanket space, and a self-cooled liquid blanket using molten salt Flibe ( $\text{BeF}_2\text{-LiF}$ ) has been proposed, due to its advantages of low MHD pressure loss, low reactivity with air, low pressure operation, and low tritium solubility.

In the direction of decreasing reactor size, however, many issues still remain, such as insufficient tritium breeding ratio (TBR) and nuclear shielding for superconducting (SC) magnets, and replacement of blanket due to high neutron wall loading and narrowed maintenance ports due to the support structure for high field coils. Thus, if we can accept some range of increased reactor size with decreased magnetic fields, then it may be possible to overcome all these issues at the same time by improving the support structure and introducing a long-life breeder blanket. Here the first results of these new design approaches are presented.

### 2. Optimized Design of a Long-life Breeder Blanket

In case of a liquid blanket, since the breeder liquid can be continuously circulated and refreshed during the reactor operation, the lifetime of blanket is essentially limited by the total displacement damage and He production in structural materials under irradiation by fusion neutrons. There are many candidates for structural materials such as reduced activation ferritic

steel (RAF), vanadium alloy, and SiC/SiC composite. In case of RAF, which has a very mature material database and is chemically compatible with Flibe, the design limit is about  $15\text{MWa/m}^2$  (about 120dpa). This means that the lifetime is 10 years under  $1.5\text{MW/m}^2$  as adopted so far in FFHR designs, and replacement is needed three times in the reactor life of 30 years. Therefore, if the effective wall loading could be reduced by a factor of 3, then no replacement would be required. This concept was proposed about 30 years ago as ISSEC (Internal Spectral Shifter and Energy Converter) by employing thick carbon shields as armor tiles on the blanket wall [3]. In this concept, therefore, the breeder blanket radioactive waste is largely reduced, while the carbon armors, low-level waste with no  $\gamma$ -ray, have to be replaced due to neutron damage. In that ISSEC study, however, the TBR was below 1.05 even with the Be neutron multiplier in C and 90% enriched liquid Li, and there was no practical means for actively cooling the carbon tiles below about  $2000^\circ\text{C}$  to avoid high carbon vapor pressure.

Figure 1 shows the new proposal of our STB (Spectral-shifter and Tritium breeder Blanket) of Flibe in the limited thickness of about 1m, where the position and thickness of the  $\text{Be}_2\text{C}$  layer between the 1<sup>st</sup> C and 2<sup>nd</sup> C layers and the Flibe zone are optimized as shown in Figs.2 and 3 with the MCNP-4C calculations for a simple torus model using JENDL3.2 nuclear data. Comparing with the original blanket [2] (not STB), results show that in this STB the flux of fast neutrons ( $> 0.1\text{MeV}$ ) at the first

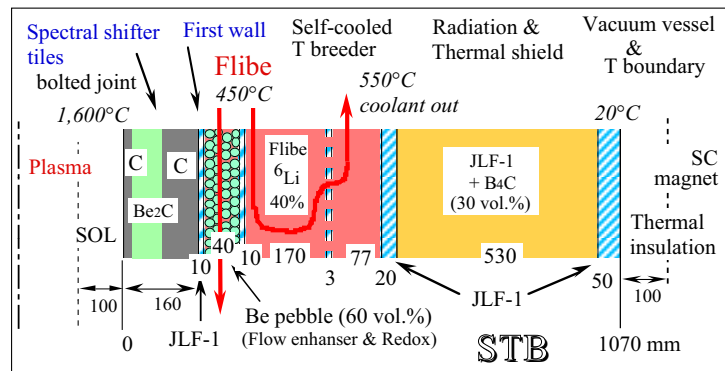


FIG.1 The radial build of the STB for FFHR2m1&2.

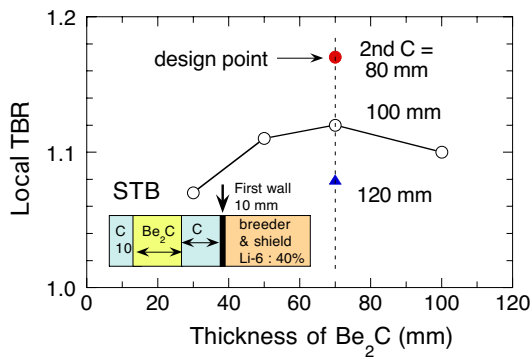


FIG.2 Local TBR as a function of the thickness of  $\text{Be}_2\text{C}$  zone.

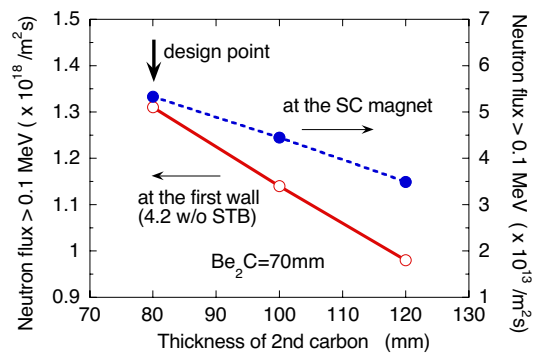


FIG.3 Fast neutron flux at the first wall and the SC magnet.

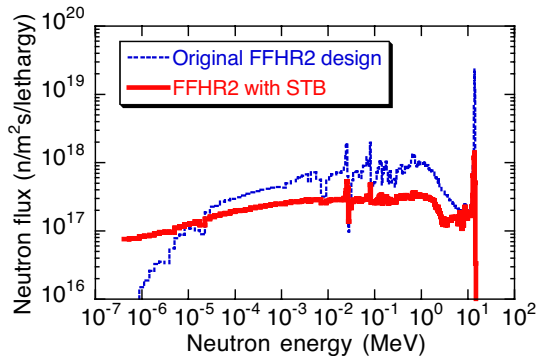


FIG.4 Neutron energy spectra at the first wall with and without STB

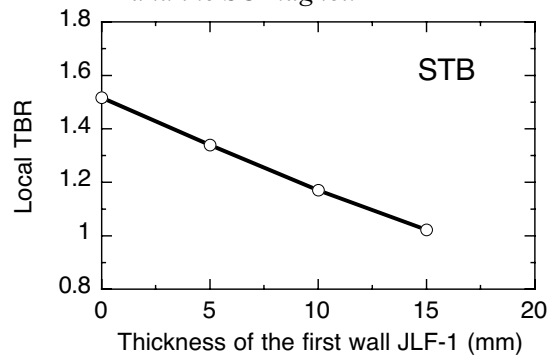


FIG.5 Local TBR as a function of thickness of the first wall.

wall of JLF-1 (RAF) is reduced to  $1.3 \times 10^{18}/\text{m}^2\text{s}$ , which is about 140dpa in 30 years and 1/3 of the original flux ( $4.2 \times 10^{18}/\text{m}^2\text{s}$ ) as shown in Fig.3 and 4. At the same time the local TBR of about 1.2 is obtained as shown in Fig.2, where the TBR strongly depends on the thickness of the first wall as shown in Fig.5 due to absorption of decelerated neutrons. And furthermore, as shown in Fig.3, the fast neutron fluence to SC magnets is one order reduced to  $5 \times 10^{22} \text{ n/m}^2$ , which is sufficient to keep  $T_c/T_{c0} > 0.9$  for  $\text{Nb}_3\text{Sn}$ , for instance. Coil winding and SC materials choice issues are under investigation.

According to a finite element (FE) thermal analysis, the carbon armor surface temperature is about  $1,600^\circ\text{C}$  under conditions of nuclear heating with surface heat flux of  $0.1 \text{ MW/m}^2$ , effective thermal conductivity of  $180 \text{ W/m/K}$  for C- $\text{Be}_2\text{C}$ -C bonded armors of 16cm thickness and heat transfer coefficient of  $6,000 \text{ W/m}^2/\text{K}$  for the bolted mechanical contact using a super-graphite sheet ( $100\mu\text{m}$ ) [4] between the armor and the first wall of JLF-1. At the first wall the heat removal of about  $1 \text{ MW/m}^2$  is required to self-cooling Flibe, where the packed-bed with Be pebbles (Fig.1) is promising to realize one order enhancement of heat transfer with a low flow rate [5] and to control REDOX chemical reactivity of molten salt [6]. Some key R&D issues are impurity shielding in edge plasma physics and armor tile lifetime. Carbon swelling and degradation of thermal and mechanical properties under high temperature neutron irradiation will determine the frequency of armor tile replacement, and a new replacement concept is proposed in Section 5. Fortunately the tritium inventory trapped in carbon and redeposited carbon is negligible at such high temperatures higher than  $800^\circ\text{C}$ [7], and the armor tiles are non  $\gamma$ -ray wastes.

### 3. Modified Design Parameters of FFHR2

According to the requirements of neutron wall loading below  $1.5 \text{ MW/m}^2$  and total blanket thickness of minimum 1.2m, the design parameters of FFHR2 are modified to those of FFHR2m, as shown in Table 1. The coil pitch parameter  $\gamma$  is 1.15 in FFHR2m1 to expand the blanket space and to reduce electromagnetic force, while  $\gamma$  is 1.25 in FFHR2m2 with inner shift of the plasma center as same as the standard condition in the present LHD [1]. FFHR2m2 is similar to the previous design LHR-S [8]. In both cases the major radius R is increased and the toroidal field  $B_0$  is decreased, compared with FFHR2.

The self-ignition analyses have been performed with zero-dimensional particle and power balance equations and ignition access algorithm using PID control

[9], where the alpha confinement time ratio  $\tau_\alpha^*/\tau_E=3$  and parabolic density and temperature

TTABLE 1 Design parameters of FFHR2m comparing with LHD and FFHR2.

Design parameters		LHD	FFHR2	FFHR2m1	FFHR2m2
Polarity	l	2	2	2	2
Field periods	m	10	10	10	10
Coil pitch parameter	$\gamma$	1.25	1.15	1.15	1.25
Coil major Radius	Rc m	3.9	10	14.0	17.3
Coil minor radius	ac m	0.98	2.3	3.22	4.33
Plasma major radius	Rp m	3.75	10	14.0	16.0
Plasma radius	ap m	0.61	1.2	1.73	2.80
Blanket space	$\Delta$ m	0.12	0.7	1.2	1.1
Magnetic field	B0 T	4	10	6.18	4.43
Max. field on coils	Bmax T	9.2	15	13.3	13.0
Coil current density	j MA/m2	53	25	26.6	32.8
Weight of support	ton	400	2880	3020	3210
Magnetic energy	GJ	1.64	147	154	142
Fusion power	Pf GW		1	1.9	3
Neutron wall load	MW/m2		1.5	1.5	1.3
External heating power	Pext MW		70	80	100
$\alpha$ heating efficiency	$\eta\alpha$		0.7	0.9	0.9
Density lim.improvement			1	1.5	1.5
H factor of ISS95			2.40	1.92	1.76
Effective ion charge	Zeff		1.40	1.34	1.35
Electron density	ne(0) $10^{19} \text{ m}^{-3}$		27.4	26.7	19.0
Temperature	Ti(0) keV		21	15.8	16.1
Plasma beta	$\langle\beta\rangle$ %		1.6	3.0	4.1

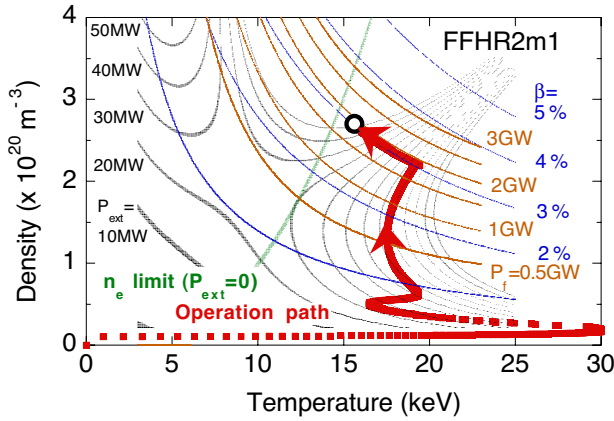


Fig.6 POPCON plot for FFHR2m1 showing the self-ignition operation path controlled under the density limit.

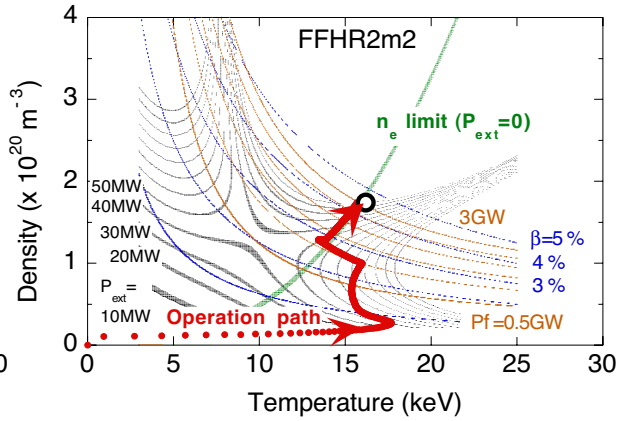


Fig.7 POPCON plot for FFHR2m2 showing the self-ignition operation path controlled under the density limit..

profiles are assumed. Figure 6 and 7 show the POPCON plots for FFHR2m1 and 2, respectively, where the fusion-power startup period is set at about 2 min and the self-ignition points are in the thermally stable region. In these analyses the density is controlled within 1.5 times the Sudo limit, as achieved in recent LHD results [10]. Therefore the enhancement factor  $H$  of the ISS95 confinement scaling is near the present LHD-achieved value of about 1.6. Evaluation studies using 3-dimensional equilibrium / 1-dimensional transport code [8] are also on going with neoclassical ripple transport as well as anomalous transport.

## 4. Improved Design of the Coil-Supporting Structure

### 4.1. Layout of Magnets

The layout of magnets is shown in Fig.8, where  $W$  and  $H$  are width and height of the helical coil in the cross-section. A high ratio of width to height is useful to reduce the maximum transverse field and to enlarge the blanket space, but it will bring problems for maintenance ports. The ratio of 2.0 was selected in this study as a moderate value. The pitch parameter  $\gamma$  of the helical coil is given by  $(ma_c)/(lR_c)$ , where  $R_c$ ,  $a_c$ ,  $l$ , and  $m$  are a coil major radius, a coil minor radius, a pole number, and a pitch number. It is set to 1.15 to reduce the electromagnetic force and to enlarge the distance between the helical coil and the plasma. The ratio of the highest magnetic field in the coil to the central toroidal field depends mainly on

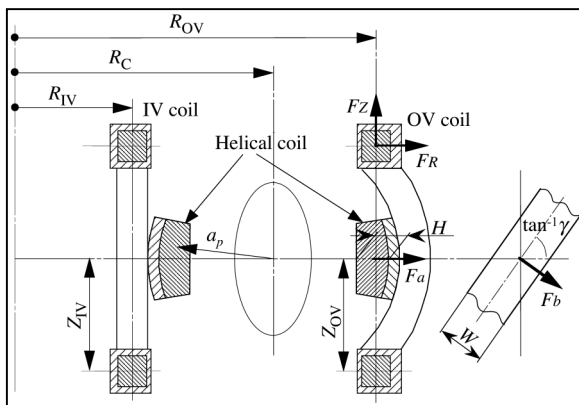


Fig.8 Layout of helical coils, poloidal coils, and magnetic force.

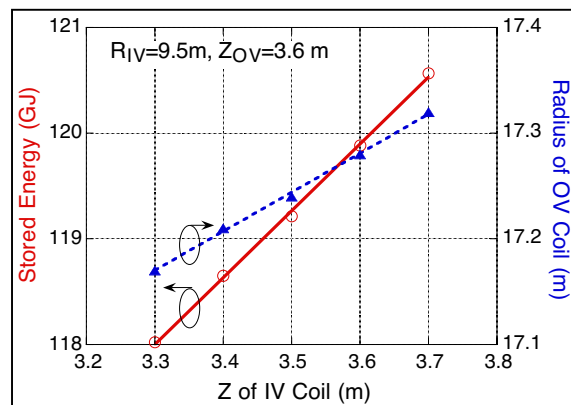


Fig.9 Stored energy of FFHR2m1 with two pairs of poloidal coils.

the ratio  $H/a_c$ . The height was determined to make the highest field 13 T that is a conservative value for A15 superconductors, such as  $Nb_3Sn$  or  $Nb_3Al$ . As the results, the current density of the helical coil becomes 25 to 30  $MA/m^2$  that is a suitable value for the large coil including a mechanical support inside. Though high density of the coil current is useful to enlarge the space for blankets and for maintenance, it is restricted with cryogenic stability, mechanical strength and the highest field.

One set of poloidal coils is necessary to adjust the major radius of the plasma, the quadrupole field, and the stray field. In the case of two sets of poloidal coils, the number of degrees of freedom is six, which additionally makes it possible to reduce the field near the center of the torus and the total stored magnetic energy. The position of the coils is not determined uniquely because of the rest of the degrees of freedom. An adequate position was determined by considering the layout of the mechanical support. Figure 9 shows an example of the dependence of the stored energy on the height of IV coil. It is about 120 GJ that is 80% of that in the case of one pair of the poloidal coils.

#### 4.2. Structural Analysis

Preliminary structural design for FFHR2m1 has been carried out. Electromagnetic forces on the coils are shown in Figures 10 and 11. Since sum of electromagnetic force on all coils is balanced, all coils were supported by each other. In considering the maintenance of blanket, large apertures are prepared at top, bottom and outer region. Since electromagnetic force on the helical coils is reduced by the 'force free' concept, the helical coils can withstand their electromagnetic forces by fixing them to inner and outer supporting structure around the mid-plane. A calculated stress by a FE model is shown in Fig. 12. Although the apparent maximum stress intensity exceeds 1,000 MPa here, it is due to insufficient accuracy in the present calculation. The maximum stress intensity is expected to be reduced less than 900 MPa by improving the accuracy. This value will be allowable for strengthened stainless steel.

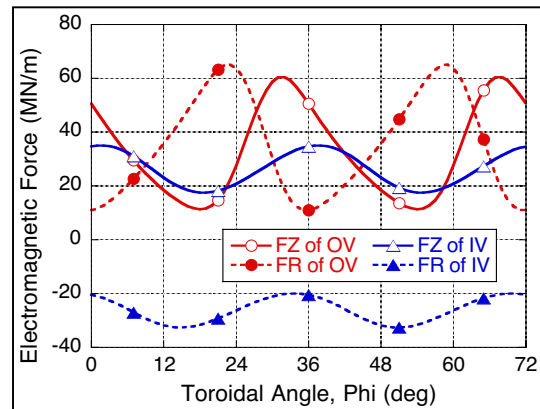


Fig.10 Electromagnetic forces on a helical coil of FFHR2m1.

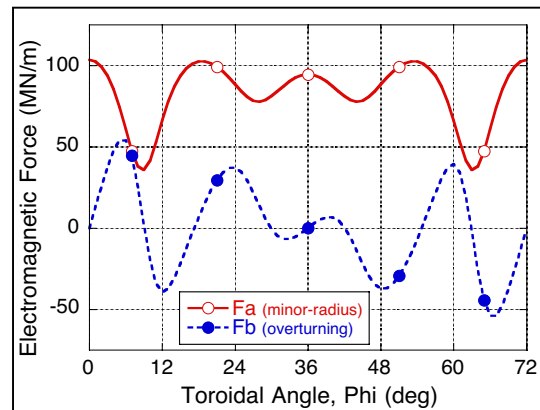


Fig.11 Electromagnetic forces on poloidal coils of FFHR2m1.

#### 5. Maintenance of In-Vessel Components

Figure 13 shows the typical poloidal cross sections in the 3D design of FFHR2m1 for a toroidal half pitch, where the field period  $m = 10$  and one pitch =  $36^\circ$ . Due to the simplified cylindrical supporting structure of helical and poloidal coils under the force reduced design, it is seen that large size maintenance ports can be opened at top, bottom, outer and inner sides of the torus, where the vacuum boundary is located just inside of the helical coils and supporting structure. Because the shielding zone of the blanket shown in Fig.1 is considered to be one of permanent structures, all blanket units can be supported on these shielding structures, which are helically wound and mainly supported at their bottom position.

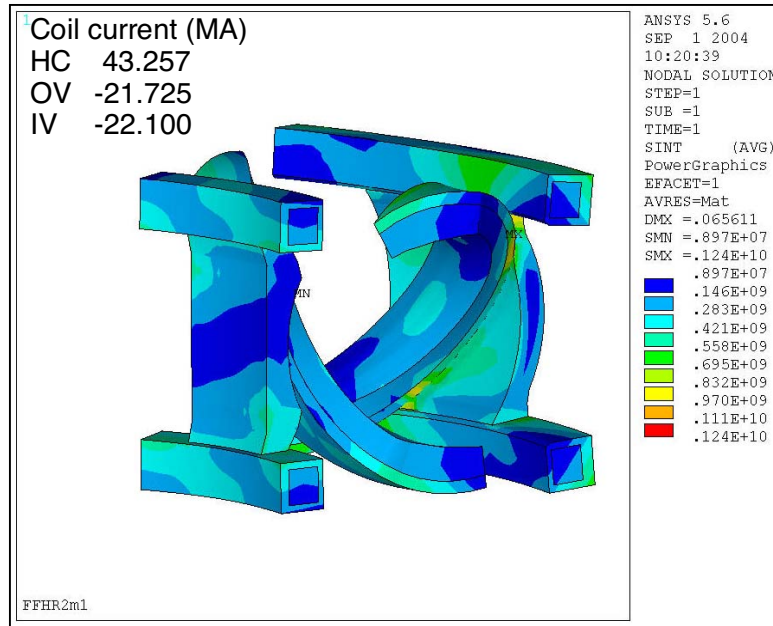


Fig.12 Finite element model of FFHR2m1.

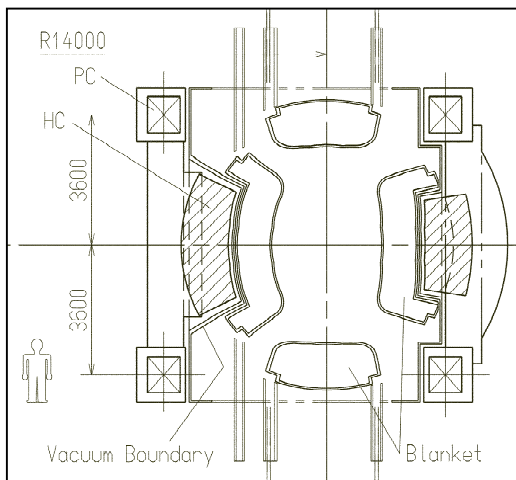


Fig.13a The poloidal cross section at the toroidal angle  $\theta=0^\circ$  of FFHR2m1.

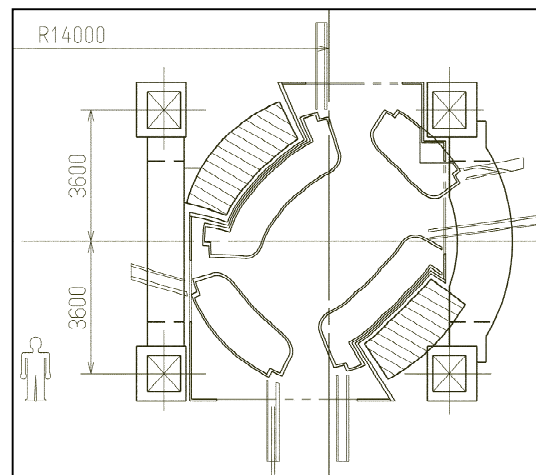


Fig.13b The poloidal cross section at  $\theta=36^\circ/4$  of FFHR2m1.

Within the present databases, due to dimensional changes and degradation of thermal and mechanical properties of carbon under neutron irradiations, armor tiles of STB should be replaced during the planned inspection period. For this purpose, as shown in Fig.14, the “screw coaster” concept [11,12] is adopted using the merit of continuously winding helical structure, where the normal cross section of blanket is constant. Therefore the screw coaster can move along the helical guides at the edge of blankets with adjusting toroidal effects by flexible actuators. Then the coaster replaces the bolted tiles under remote handling.

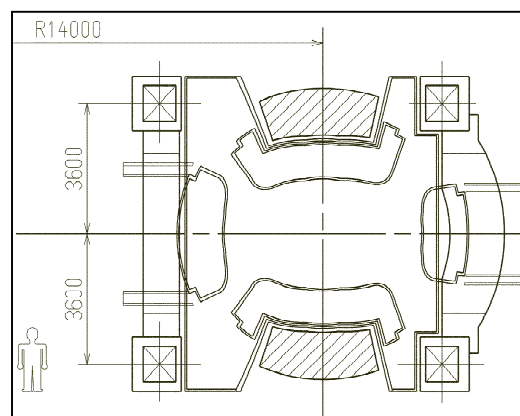


Fig.13c The poloidal cross section at  $\theta=36^\circ/2$  of FFHR2m1.

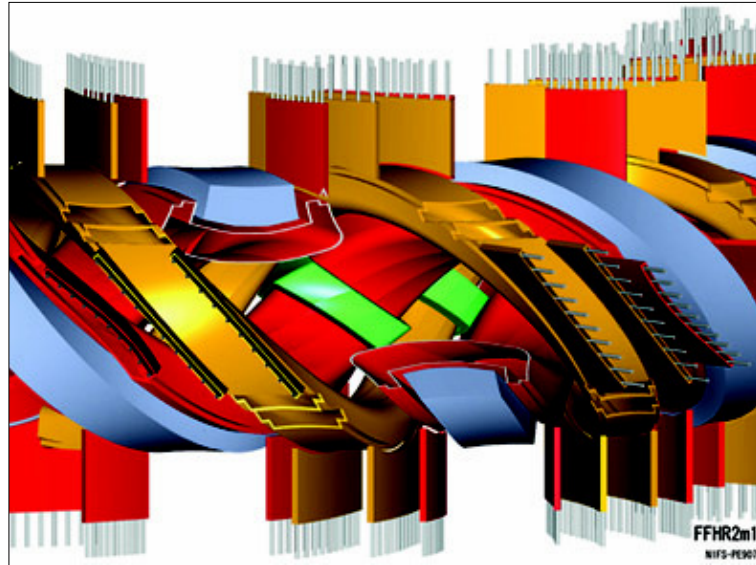


Fig.14 “Screw coasters” to replace STB armor tiles in FFHR2m1, where the helical coils and blankets with coolant pipes are only shown.

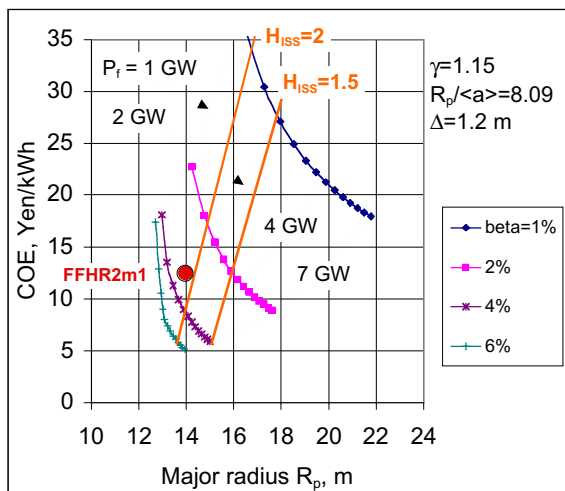


Fig.15 COE(Yen/kWh) of FFHR2m1, where the H factor of ISS95 is also indicated.

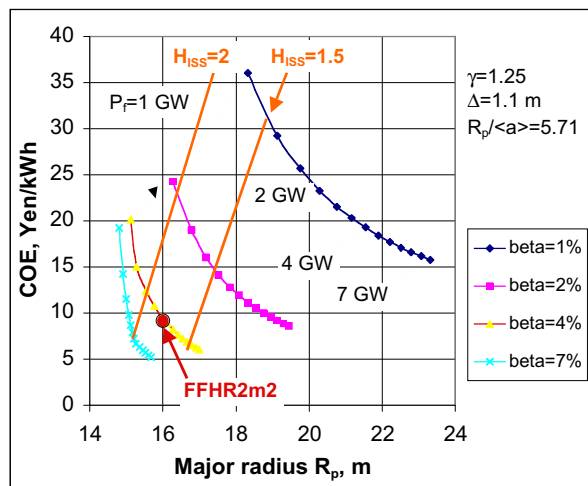


Fig.16 COE(Yen/kWh) of FFHR2m2, where the H factor of ISS95 is also indicated..

Detailed design of the divertor structure is under investigation, and it is seen in Fig.13 that there is an enough space for the double-null divertor pumping. As for replacement of divertor target tiles, the screw coaster can be basically used again during the planned inspection period.

### 6. Cost Estimation

The Physics-Engineering-Cost (PEC) code has been developed in NIFS. Recently by modifying it to include blanket-shield design data, a new cost structure, new unit costs, and

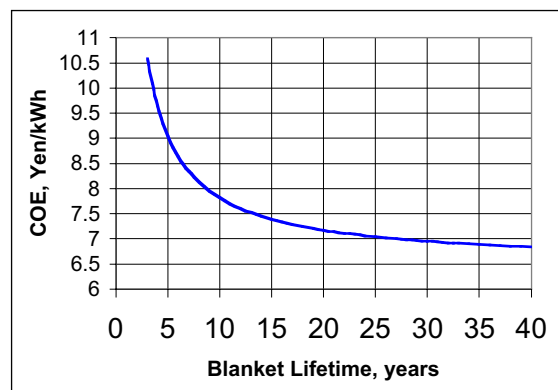


Fig.17 Variation of COE with blanket lifetime for FFHR2m2.

improved algorithms [13], the PEC code was calibrated by using it to model the ARIES-AT (advanced technology) tokamak and the ARIES-SPPS (stellarator power plant system), and it was found that the PEC Code COE estimates for each of these two cases differ from the published values by 5%, where those ARIES costs were escalated from 1992 \$ to 2003 \$ using an escalation factor of 1.223. Using this PEC code, COE's have been evaluated for FFHR2, FFHR2m1 and FFHR2m2, resulting in COE of 21.20, 12.95, and 9.53 Yen/kWh, respectively, as shown in Fig.15 and 16. The COE eventually decreases with increasing the reactor size, because the wall loading is fixed at about 1.5MW/m<sup>2</sup>, and the fusion output increases, while the weight of coil supporting structure does not significantly increase as shown in Table1.

The effect of long-life blanket on COE is also evaluated by the PEC code with a model, which assumes an availability factor that varies from the usual maximum 0.85 as

$$f_{\text{avail}} = 0.85 - f_{\text{avail}} * 1.4 G_w * t_m / Wt_b,$$

where  $G_w$  = average neutron wall load (MW/m<sup>2</sup>), 1.4 is the assumed peak to average ratio,  $t_m$  = blanket maintenance time (assumed to be 0.5 years), and  $Wt_b$  = blanket wall lifetime (MW-years/m<sup>2</sup>). The result is shown in Fig.17. As the blanket lifetime increases from 5 to 30 years, the COE drops about 20% from 9 to 7 Yen/kWh. The savings result from a higher availability and from a lower cost for replacement blankets.

## 7. Conclusions

Design studies on the LHD-type heliotron D-T power reactor FFHR have focused on concept improvement by new design approaches to solve the key engineering issues of blanket space limitation and replacement difficulty. The main conclusions are:

- (1) The combination of improved support structure and long-life breeder blanket STB is quite successful.
- (2) The "screw coaster" concept is advantageous in heliotron reactors to replace in-vessel components.
- (3) The COE can be largely reduced by those improved designs.
- (4) The key R&D issues to develop the STB concept are elucidated.

## References

- [1] A. Komori et al., Plasma Phys. Contr. Fusion 45 (2003) 671.
- [2] A. Sagara et al., 17th IAEA Fusion Energy Conf., Yokohama, FTP-3 (1998).
- [3] R.W. Conn, G.L. Kulchinski et al., Nucl. Technology 26 (1975) 125.
- [4] Y. Kubota et al., Fusion Eng. Des. 56-57 (2001) 205.
- [5] S. Chiba et al., in these proceedings.
- [6] S. Fukada et al., Proc. tritium 2004 (2004).
- [7] A. Sagara et al., J. Nucl. Mater., 220-222 (1995) 627.
- [8] K. Yamazaki et al., 18th IAEA Fusion Energy Conf., Sorrento, FTP2-12 (2000).
- [9] O. Mitarai et al., Fusion Eng. Des. 70 (2004) 247.
- [10] K. Nishimura et al., Annual Repo. of NIFS (2000) 13.
- [11] A.Sagara, US-J Workshop on Fusion Power Reactors(P246), JAERI-memo 07-100(1995).
- [12] A.Sagara et al, J. Nucl. Mater., 248 (1997) 147.
- [13] T. J. Dolan et al., to be published in Fusion Science and Technology.

## Development of Fabrication Technology for Low Activation Vanadium Alloys as Fusion Blanket Structural Materials

T. Nagasaka 1), T. Muroga 1), K. Fukumoto 2), H. Watanabe 3), M. L. Grossbeck 4), J. M. Chen 5)

- 1) National Institute for Fusion Science, Toki, Gifu 509-5292, Japan
  - 2) Institute for Materials Research, Tohoku University, Sendai 980-8577, Japan
  - 3) Research Institute for Applied Mechanics, Kyushu University, Kasuga 816-8580, Japan
  - 4) Oak Ridge National Laboratory, Oak Ridge, TN 37831-6376, USA
  - 5) Southwestern Institute of Physics, Chengdu 610041, China
- e-mail contact of main author: nagasaka@nifs.ac.jp

**Abstract.** High purity vanadium alloy products, such as plates, wires and tubes, were fabricated from reference high-purity V-4Cr-4Ti ingots designated as NIFS-HEAT, by using technologies applicable to industrial scale fabrication. Impurity behavior during breakdown, and its effect on mechanical properties were investigated. It was revealed that mechanical properties of the products were significantly improved by the control of Ti-C, N, O precipitation induced during the processes.

### 1. Introduction

Vanadium alloys are promising candidates for fusion blanket structural materials, because of their low activation property, high temperature strength, high resistance to neutron irradiation and good compatibility with liquid lithium[1, 2]. Large scale melting is essential to establish fabrication technology for components of the blanket system. In the 18th conference in this series, it has been reported that 30 kg and 166 kg scale ingots designated as NIFS-HEAT were melted in a collaboration program between the National Institute for Fusion Science, Japanese universities, and industries[3]. One of the critical issues for the melting was to reduce the levels of interstitial impurities, such as C, N and O, which were well known to deteriorate mechanical and irradiation properties of vanadium alloys. The oxygen level in the NIFS-HEAT ingots was successfully reduced to 130-180 wppm, which is half the level of previous large ingots produced by the U. S. Department of Energy program[4, 5]. The carbon and nitrogen levels were kept at about 60 and 100 wppm, respectively. In the present paper, fabrication processes for various products, such as plates, wires and tubes, were developed to maintain the higher purity and to obtain good mechanical properties, after investigation on the optimum process parameters and microstructures.

### 2. Fabrication process for plates, wires and tubes

The fabrication processes for plate, wire and tube products of NIFS-HEAT-2 were shown in Fig. 1. Since vanadium alloy is very reactive with the air above 700 K, the ingots were canned into stainless steel before hot working, such as hot forging, hot isostatic pressing (HIP) and shaping. Plates of 26 mm in thickness were obtained through hot working at 1173-1473 K, resulting in 52-55 % reduction in area, followed by removal of the can and the cold rolling to 68-74 % reduction in thickness. The surface of the plates was kept clean during the working.

The 26 mm-thick plate was cold rolled further into plates of 6.6, 4.0, 1.9, 1.0, 0.5 and 0.25 mm in thickness. The wires of 8 mm and 2 mm in diameter were swaged at room temperature

from the 26 mm-thick and the 6.6 mm-thick plates, respectively. For tubing, the 26 mm-thick plate was recrystallized at 1273 K for 2 hr in a vacuum. The annealed plate was machined into two kinds of pipes with 25 / 19, or 10 / 7 mm in outer diameter / inner diameter (OD / ID). Larger pipes were cold-rolled by 3-directional rolling into tubes with 10 mm in outer diameter and 0.5 mm in wall thickness ( $\phi 10-0.5t$ ), and the smaller into  $\phi 4.57-0.25t$  tube. During the 3-directional rolling, intermediate annealing at 1123 K for 1 hr was conducted after 1-3 pass each. The effects of final annealing temperature on the hardness and the microstructures were investigated at the temperature range from 673 – 1373 K. As a result, the reference final annealing condition was decided at 1273 K for 2 hr for the plates, the wires and the tube products[6]. Every annealing was performed in a vacuum, where the products were wrapped with Zr or Nb getter foils to avoid contamination with gaseous impurities, such as C, N and O. The products have been distributed for Round-Robin tests in universities and laboratories in Japan, US, China, Russia, Germany and Spain. The working degree after the hot working were summarized as Table 1. Table 2 shows the results of chemical analyses for the NIFS-HEAT products.

### 3. Evaluation procedure for the plates

The NIFS-HEAT plate products were evaluated by tensile tests, impact tests and microscopy. Tensile specimens were machined from the 26t, 4.0t and 0.25t plates after the final annealing at 1273 K X 2 hr. Gauge size of the specimen was 0.25 X 1.2 X 5 mm. Tensile tests were conducted with an initial strain rate of  $6.7 \times 10^{-4} \text{ s}^{-1}$  at 300 K. In the impact tests, 1/3 size Charpy V-notch specimens (1/3 CVN) and 1.5 mm-square size specimens (1.5 CVN) were used. The specimen size / notch depth were 3.3 X 3.3 X 25.4 mm / 0.66 mm and 1.5 X 1.5 X 20 mm / 0.3 mm, respectively. The impact tests were performed after the final annealing with a cross head speed of  $4.5 \text{ m s}^{-1}$  at 300 K and 77 K. Fig. 2 shows the definition of the position and the orientations of the specimens. For the 26t plate, homogeneity of the mechanical properties was investigated by the specimens from various positions in the thickness direction and with various orientations in

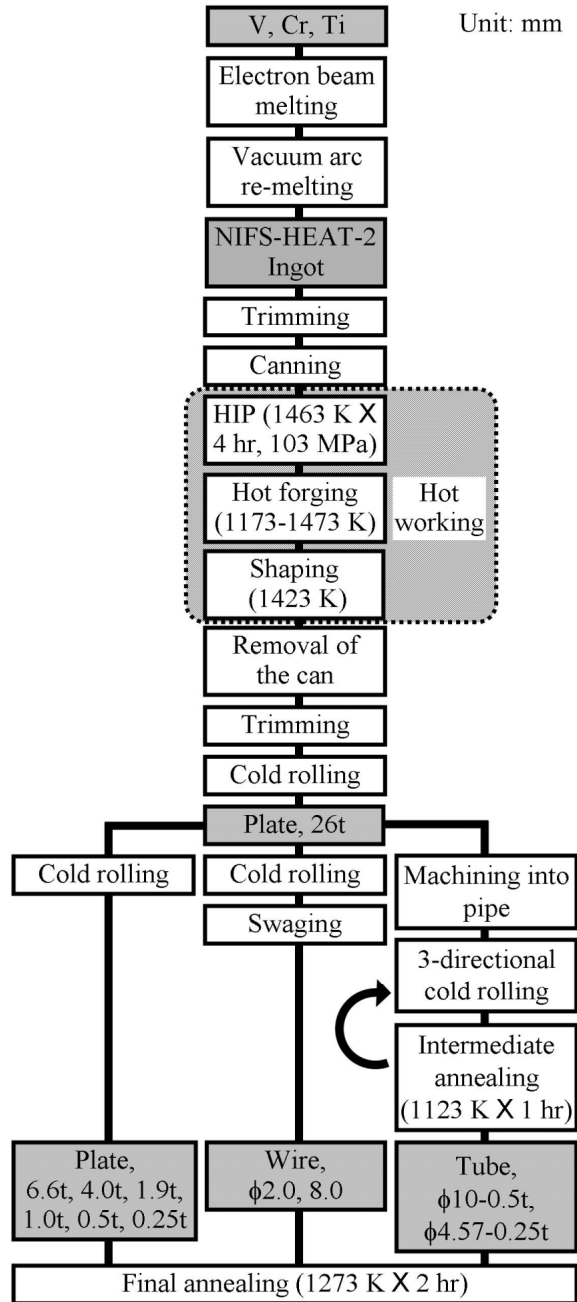


FIG. 1 Fabrication process for the plate, wire and tube products of NIFS-HEAT-2.

*Table 1 Working degree after hot working for the NIFS-HEAT products. The degree is defined as reduction in thickness for the plate products, whereas reduction in area for the wire and the tube products.*

Products	Size (ID) / mm	Working degree, R / %
Plate	26t	74
	6.6t	93
	4.0t	96
	1.9t	98
	1.0t	99
	0.5t	99.5
Wire	$\phi 8$	93
	$\phi 2$	99.4
Tube	$\phi 10-0.5t$	93
	$\phi 4.57-0.25t$	92

the plate. The microstructures during the fabrication process and the fracture surfaces after the mechanical tests were characterized by transmission electron microscopy (TEM), scanning electron microscopy (SEM), energy dispersive X-ray analysis (EDX) and optical microscopy (OM).

## 4. Results

### 4.1. Orientation and position dependence of mechanical properties

Stress-strain curves for tensile tests are shown in Fig. 3. The specimens at  $x = 0$  in all the orientations (dashed line curves) gave poor ductility as only 0.2 % in total elongation, whereas the near-surface specimens (solid line curves) at  $x = -12.4$  exhibited larger elongation than 10 %. Ductility was independent of specimen orientation, but dependent on the position in the thickness direction. Figure 4 shows

load-deflection curves in the impact tests on the 26t plate. The load levels were similar to each other, while the load drop rate after the maximum load was slightly smaller for the specimen at  $x = -12.4$  mm, than that at  $x = 0$  and 12.4 mm. The specimen at  $x = -12.4$  mm required larger load for crack propagation, and indicated larger absorbed energy, which is defined as the area enclosed by the load-deflection curve. Fig. 5 summarizes absorbed energy for the specimens at various positions in the thickness direction. In order to compare the absorbed energy among different size specimens, the energy is normalized with fracture volume parameter, which is given by  $(Bb)^{3/2}$ , where B is specimen width, 3.3 or 1.5 mm, and b is the ligament depth below the notch (width – notch depth), 2.64 or 1.2 mm, respectively[7]. The

*Table 2 Results of chemical analyses on impurities. (mass ppm, \*mass %)*

Product	Cr*	Ti*	H	C	N	O
Ingot /	4.00	4.02		50	96	122
As-melted	4.02	3.98		69	122	148
Plate 26t /						
As-rolled	4.33	3.95	146	80	108	124
Plate 26t /						
Annealed	4.07	3.88	52	50	89	178
Plate 4.0t /						
Annealed			29	51	123	139
Plate 0.25t /						
Annealed				62	84	158
Wire $\phi 2.0$ /						
Annealed			3.7	60	107	179
Tube						
$\phi 4.57-0.25t$ /			4.5	120	120	330
Annealed						
Tube						
$\phi 10-0.5t$ /			8	135	90	300
Annealed						

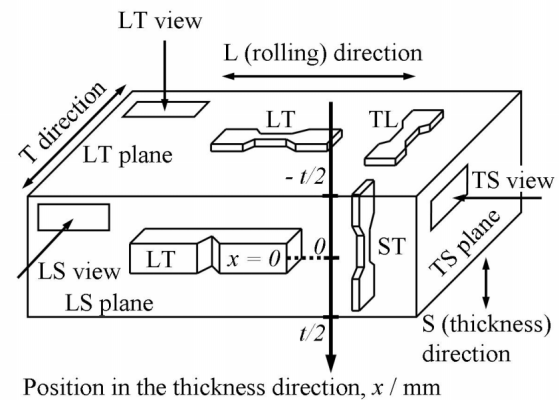


*FIG. 2 Definition of the specimen positions in the thickness direction and the orientation. For example, LT means that the specimen longitude is L direction and the crack for fracture propagates along to T direction. The axis for the position in the thickness direction,  $x$ , is taken along to the S direction. The origin for the position,  $x$ , is located at the center of the thickness,  $t$ . For example,  $x = 0$  means that the center of the specimen is at the origin.*

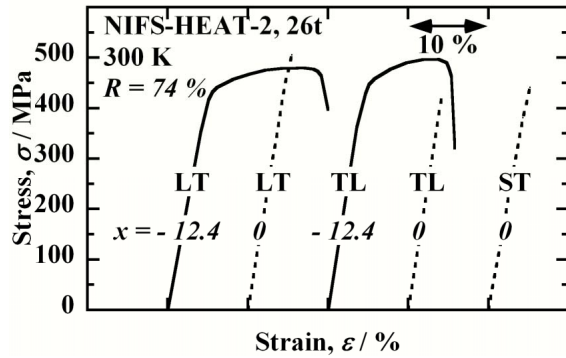


FIG. 3 Stress-strain curves obtained in the tensile tests on the 26t plate. Specimen position,  $x$ , and orientations are indicated.

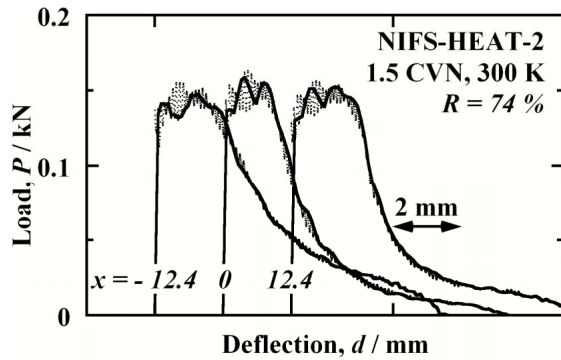


FIG. 4 Load-deflection curves for the impact tests at 300 K.

absorbed energy at 300 K around  $x = -12.4$  mm was higher than the other part, however the difference was not significant compared with the results of the tensile tests mentioned above. At 77 K, absorbed energy was reduced below half that at 300 K, but weakly dependent on the position in the thickness direction.

#### 4.2. Improvement of mechanical property by further working

Tensile and impact properties of the plate were significantly improved by an increase in the degree of working. As shown in Fig. 6, tensile elongation for the TL specimen at  $x = 0$  mm was quite lower than that at  $x = -12.4$  mm. The elongation, however, increased with increasing working degree,  $R$ , accompanied by decrease in tensile strength. On the other hand, standard size ( $\phi 6.25 \times 30$  mm for the parallel part) specimen has shown lower strength and larger elongation even with low  $R$  [8].

Fig. 7 shows load-deflection curves in the impact tests at 77 K. The plates with  $R = 74\%$  and  $93\%$  showed brittle fracture, and poor absorbed energy of less than  $0.054 \text{ J mm}^{-3}$ . By the increase in  $R$  up to  $96\%$ , the fracture mode was changed to ductile, and the absorbed energy was improved to  $0.17 \text{ J mm}^{-3}$ . Fig. 8 summarizes the absorbed energies obtained in the impact tests with 1/3 CVN and 1.5 CVN at 300 K and 77 K.

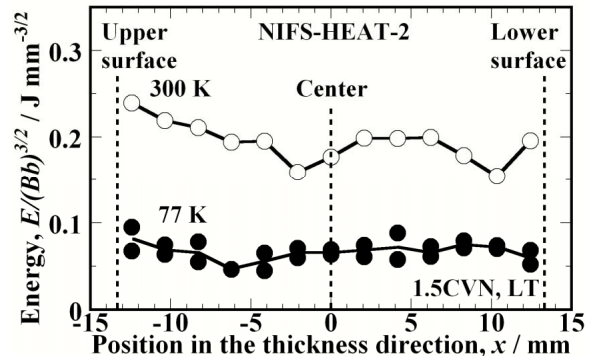


FIG. 5 Absorbed energy in the impact tests on the 26t at 300 K and 77 K.

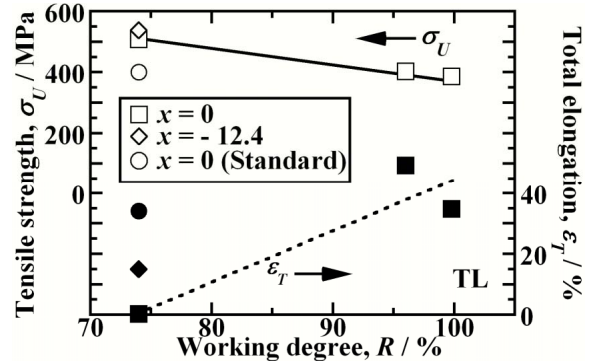


FIG. 6 Change in strength and ductility by working. The lines were drawn after the data on the specimen at  $x = 0$ . Data for standard size specimen is referred from [8].

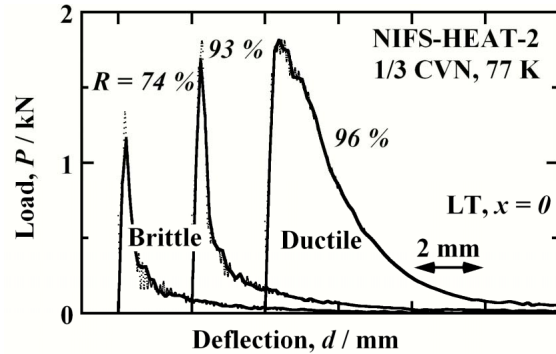


FIG. 7 Load-deflection curves in the impact tests on the plates with various working degree.

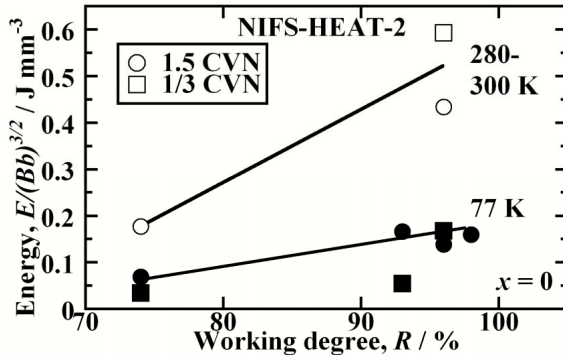


FIG. 8 Improvement of absorbed energy by working.

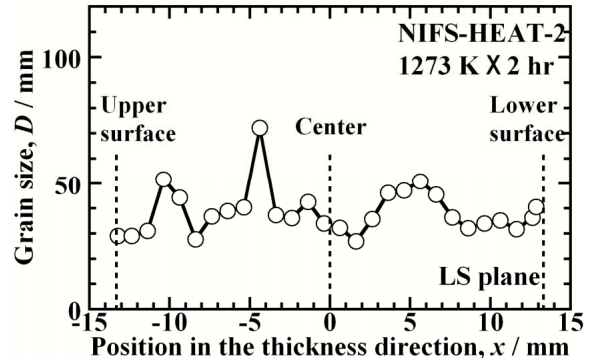


FIG. 9 Grain size distribution in the 26t plate determined by OM observations.

#### 4.3. Orientation and position dependence of microstructures

Figure 9 shows grain size distribution in the 26t plate. The average grain size was 39  $\mu\text{m}$ . No significant dependence of grain size on position was observed. From the SEM-EDX experiments, it was found that clusters of Ti-rich precipitates were produced during the hot working process. Fig. 10 shows the development of Ti-rich precipitates in the as-melted ingot by simulated annealing at the same temperature as hot working. In the as-melted ingot, no Ti segregation at the precipitates was detected. After annealing at 1273 K and 1423 K, clusters of Ti-rich precipitates were observed. The clusters of the precipitates were redistributed into precipitate bands aligned to the rolling direction with an increase in the degree of cold working,  $R$ . Fig. 11 shows the precipitate clusters and the bands in the 26t plate. Near the surface of the plates ( $x < -8.4$  mm), only the band structures were observed, while the precipitate clusters were observed as well as the bands around  $x = 0$  mm.

#### 4.4. Effect of working on microstructures and fracture mode

In the plates of the 6.6 mm and thinner, where  $R > 93$  %, no cluster were but narrow and

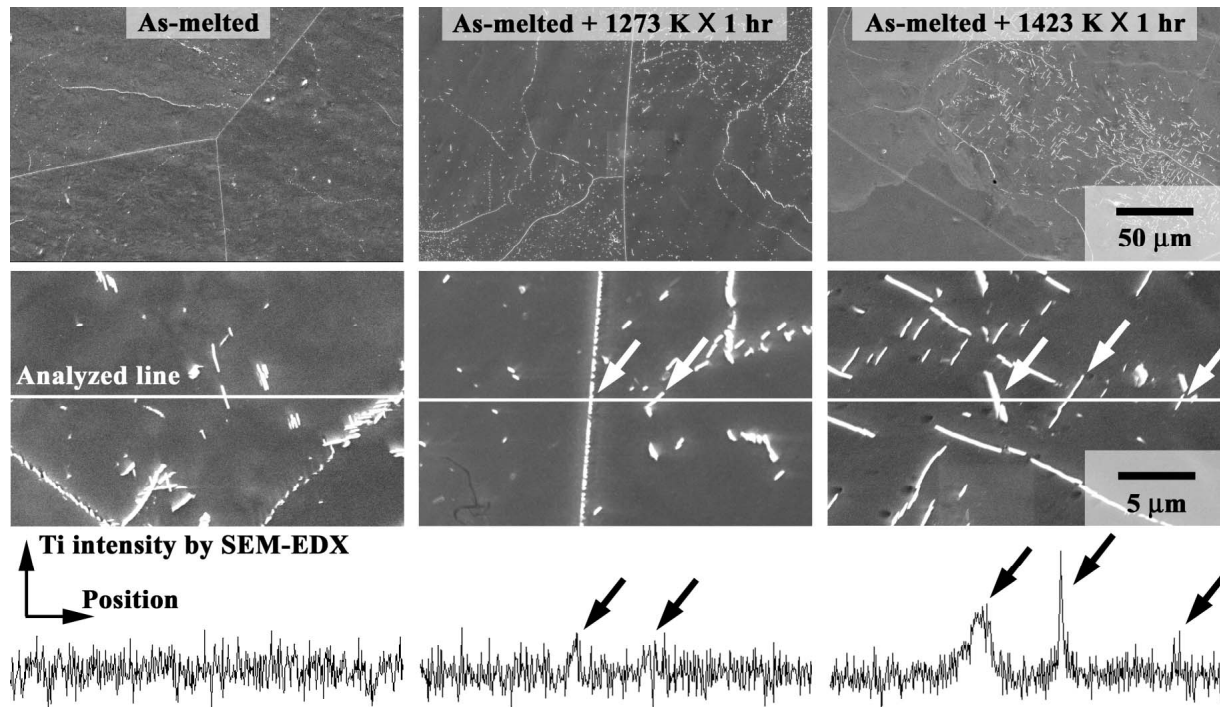


FIG. 10 SEM images and Ti intensity by EDX of precipitates in the as-melted ingot and after annealing at the same temperature as the hot working. White and black arrows indicate Ti-rich precipitates and Ti peaks at SEM-EDX spectra, respectively.

crowd bands were found. Fig. 12 shows typical band structures observed in the 4.0 mm-thick plate. Typical fracture surfaces after the impact tests were shown in Fig. 13. Secondary cracks were observed in all the specimens. In the plates with  $R = 74\%$  and  $93\%$  (26t and 6.6t), the secondary crack propagated to the random directions. On the contrary, the secondary crack in the plate with  $R = 96\%$  and  $98\%$  (4.0t and 1.9t) propagated along the precipitate bands.

## 5. Discussion

### 5.1. Impurity behavior in the fabrication process

In Table 2, impurity contaminations in the fabrication process can be estimated by the difference of the concentration in the products and that in the as-melted ingot. During the fabrication process, contaminations in the process except tubing were only 30, 33 and 56 mass ppm or less for carbon, nitrogen and oxygen, respectively. Hydrogen was removed by the vacuum annealing. The two kind of tube products were contaminated with 85 and 208 mass ppm of carbon and oxygen at the maximum, while nitrogen contamination was 24 mass ppm, which is similarly low to the other products. The additional contaminations of the carbon and oxygen are likely due to a number of intermediate annealing at 1123 K. Possible contamination sources are carbon, nitrogen, oxygen and their compound gases in the vacuum for annealing, and also the residual scale and lubricant on the surface of tube wall. Improvement of vacuum atmosphere and cleaning of the tube wall is required for getting further purity. It has been, however, reported that the  $\phi 4.57$ -0.25t tube did not show significant ductility loss and other mechanical property change[9]. Therefore the contamination level in the present fabrication process is acceptable and expected not to degrade the mechanical performance of NIFS-HEAT alloy. The NIFS-HEAT products maintain higher purity than previous work for the US DOE heat[4, 5]. Especially levels of oxygen in the plates and wires are half that in the US heat, so that superior weldability, irradiation resistance and so on are expected.

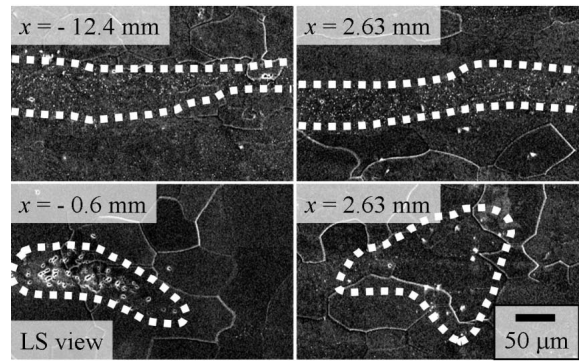


FIG. 11 SEM images of Ti-rich precipitates in the 26t plate. Dashed lines indicate the bands (top) and clusters (bottom) of the precipitates.

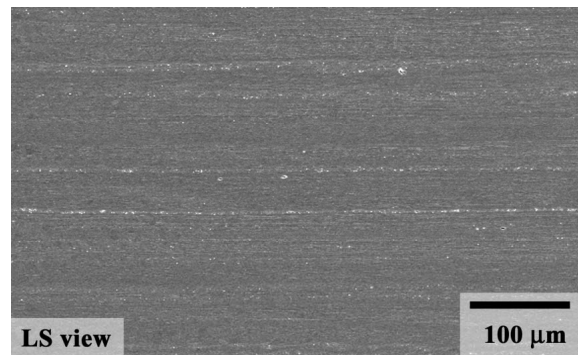


FIG. 12 Band structures of Ti-rich precipitates along to the rolling (L) direction.

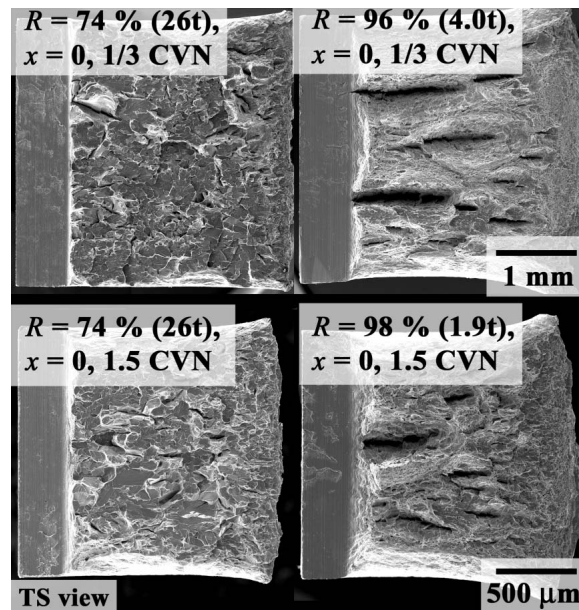


FIG. 13 Fracture surfaces after the impact tests. Notch is located at the left side.

The Ti-rich precipitates observed in Fig. 10 are considered as Ti-C, N, O type precipitates common in V-Cr-Ti alloy[10, 11]. In the as-melted ingot, solidification and cooling rate was thought too high to produce the Ti-C, N, O precipitates, however supersaturated carbon was extracted out as vanadium carbide type precipitates because of relatively low solubility of carbon in vanadium matrix[12]. Above 873 K, mobility of Ti becomes high enough to react with the supersaturated C, N and O. The Ti-C, N, O precipitates are well known to appear from 873 K and above[11]. The hot working at 1173-1473 K was considered to evolve the Ti-C, N, O precipitates. The precipitates made clusters shown in Fig. 10 without working. In the fabrication process, the precipitates in the clusters were redistributed into bands under the deformation stress for working.

## 5.2. Effect of oriented microstructure on mechanical properties

In the impact tests, secondary crack are possibly initiated at the precipitate, and propagate to the nearby precipitate. In the clusters, a crack is thought to propagate to random direction, whereas it goes along the bands, if formed. Since the random directional crack shown in Fig. 13 seems easy to connect with each other, the clusters of the precipitates are thought to induce the brittle fracture, while the oriented and parallel cracks could not affect to the next cracks, and also could terminate the propagation of the primary crack. From Fig. 11, the size of the clusters was about 100  $\mu\text{m}$ , which is comparable to 250  $\mu\text{m}$ , the thickness of the miniature tensile specimens used in the present study, therefore the tensile elongation was very sensitive to the position, and was small around the area containing the precipitates clusters (around  $x = 0$ ). In Fig. 6, the standard size specimens has not shown such ductility loss, because the size of the parallel part,  $\phi 6.25$  in diameter, was large enough relative to the cluster size. As shown in Fig. 11, precipitate band structures were observed near the surface of the 26t plate ( $x < -8.4$  mm), however they appeared much wavier compared with the thinner plate shown in Fig. 11. The wavy bands possibly cause the random directional cracks, and are considered to reduce absorbed energy at the thicker plates, as indicated in Fig. 4-8. From the results in Figs. 6 and 8, 74 % - 93 % seems to be a transition range for working degree from the brittleness to ductility. Working degree of 96 % is necessary for superior ductility both in the tensile and the impact tests.

In general, sufficient working to induce homogenization and recrystallization is necessary for improving ductility. Though the homogeneous grain structure was obtained as Fig. 9, mechanical properties significantly affected by the distribution of the Ti precipitates. In the case of vanadium alloys, it was revealed that sufficient working is critically required to obtain high ductility by the transition from precipitate clusters to bands.

## 5.3. Tubing and welding processes

It has been reported that the  $\phi 4.57$ -0.25t tube products had no precipitate clusters but precipitate bands aligned to the rolling direction[9]. The bands, however, were wavier than that in the 0.25t plates. It was indicated that surface cracks of the tubes were induced at the intersection point between the bands and the surface and propagated along the bands. Recovery of work hardening by periodic intermediate annealing at 1123 K for 1 hr was crucial to reduce deformation stress and to prevent surface cracking. The resulting tubes exhibited good tensile strength and ductility comparable to the plates[9, 13].

Weld joints of 6.6 mm and of 4.0 mm-thick plates were fabricated by gas-tungsten-arc welding and laser welding in a high-purity Ar gas. Both the plates showed excellent

weldability[14, 15]. All the precipitates in the weld metal were dissolved during welding. The re-precipitation of Ti-C, N, O with high number density around 873 K resulted in significant hardening of the weld metal and degraded its impact properties[16, 17]. Post-weld heat treatment (PWHT) at 1073 K was effective to reduce the number density of the precipitates and hence to recover the hardening and the impact properties[17]. For vanadium alloy, several mm-thick plates have been suggested as components for blanket structural materials[18]. Based on the superior mechanical properties and weldability of the sufficiently worked plate, such as 4.0t plates, production of the several mm-thick plates and their structures are feasible by applying the fabrication process developed in the present study.

## 6. Conclusions

The present study revealed critical technologies and optimum process parameters for vanadium alloy products having superior mechanical performance. The mechanical properties of the products were improved significantly not only by reducing the impurity levels of C, N and O, but also by controlling density, size and distribution of the Ti-C, N, O precipitates. Thus the large scale fabrication of vanadium alloy products for fusion blanket is feasible with appropriate management of the process.

## Acknowledgement

Authors are grateful to Prof. N. Noda in National Institute for Fusion Science and Dr. N. J. Heo in Center for Advanced Research of Energy Conversion Materials, Hokkaido University, the staff of International Research Center for Nuclear Materials Science, Institute for Materials Research, Tohoku University, for fruitful discussion and support in experiments.

## References

- [1] R. J. Kurtz, K. Abe, V. M. Chernov, D. T. Hoelzer, H. Matsui, T. Muroga and G. R. Odette, *J. Nucl. Mater.*, **329-333** (2004) 47.
- [2] Najmabadi et al., *Fusion Eng. Des.* **38** (1997) 3.
- [3] T. Muroga and T. Nagasaka, FTP1/09, Proc. 18th Intl. Conf. Fusion Energy (IAEA CN-77), Sorrento, Italy, Oct. 4-10, 2000.
- [4] H. M. Cheng, B. A. Loomis and D. L. Smith, *J. Nucl. Mater.*, **239** (1996) 139.
- [5] W. R. Johnson and J. P. Smith, *J. Nucl. Mater.*, **258-263** (1998) 1425.
- [6] N. J. Heo, T. Nagasaka, T. Muroga, *J. Nucl. Mater.*, **325** (2004) 53.
- [7] W. R. Corwin and A. M. Hougland, "The Use of Small-Scale Specimens for Testing Irradiated Material", Eds. W. R. Corwin and G. E. Lucas, ASTM-STP 888 (1986) 325.
- [8] A. Nishimura, T. Nagasaka and T. Muroga, *J. Nucl. Mater.*, **307-311** (2002) 571.
- [9] T. Nagasaka, T. Muroga and T. Iikubo, *Fusion Sci. Technol.*, **44** (2003) 465.
- [10] D. T. Hoelzer, *Fusion Mater. Semiannual Progress Rep.*, DOE/ER-0313/25 (1998) 59.
- [11] N. J. Heo, T. Nagasaka, T. Muroga and H. Matsui, *J. Nucl. Mater.*, **307-311** (2002) 620.
- [12] D. L. Harrod and R. E. Gold, *Int. Met. Rev.*, **25** (1980) 163.
- [13] K. Fukumoto, H. Matsui, M. Narui, T. Nagasaka and T. Muroga, *J. Nucl. Mater.*, **335** (2004) 103.
- [14] T. Nagasaka, M. L. Grossbeck, T. Muroga and J. F. King, *Fusion Technol.*, **39** (2001) 664.
- [15] N. J. Heo, T. Nagasaka, T. Muroga, A. Nishimura, K. Shinozaki and H. Watanabe, *Fusion Sci. Technol.*, **44** (2003) 470.
- [16] T. Nagasaka, T. Muroga, M. L. Grossbeck and T. Yamamoto, *J. Nucl. Mater.*, **307-311** (2002) 1595.
- [17] N.J. Heo, T. Nagasaka, T. Muroga, H. Watanabe, A. Nishimura, K. Shinozaki, *J. Nucl. Mater.* To be published.
- [18] L. A. El-Guebaly and the ARIES Team, *Fusion Eng. Des.* **38** (1997) 139.

# Interactions of Solid and Liquid Lithium with Steady State Hydrogen and Helium Plasmas

Y. Hirooka 1), M. Nishikawa 2), H. Ohgaki 2), and Y. Ohtsuka 2)

1) National Institute for Fusion Science, Oroshi, Toki, Gifu, Japan

2) Osaka University, Yamadaoka, Suita, Osaka, Japan

e-mail contact of main author: [hirooka@nifs.ac.jp](mailto:hirooka@nifs.ac.jp)

**Abstract.** A variety of innovative Plasma-Facing Component (PFC) concepts, employing moving solid or liquid surfaces, have recently been proposed in order to resolve technical issues, associated with the applications of currently used PFCs in future steady state fusion devices. As the first step to evaluate the concept using flowing-liquids for PFCs, steady state hydrogen and helium plasma interactions with solid and standing liquid lithium have been investigated in the present work, using the  $H_{\alpha}$  and He-I spectroscopy at the ion bombarding energies up to 150eV and at the lithium temperatures between room temperature and 480°C. Data indicate that hydrogen recycling over liquid lithium is clearly reduced, relative to that over solid lithium, whereas helium recycling does not show the same trend. From the kinetic analysis of these recycling time constant data, the activation energies for the overall recycling processes have been evaluated to be  $0.02 \pm 0.01$  eV, both for hydrogen and helium plasmas. Also, it has been found that the activation energy is nearly independent of ion bombarding energy.

## 1. Introduction

It is widely recognized in the magnetic fusion research community that since the discovery of TFTR's Supershot in late 80's, high performance core plasmas tend to favor low edge recycling conditions. Therefore, wall conditioning such as boronization has routinely been conducted in many confinement experiments. Unfortunately, however, due to the surface saturation with implanted particles, the efficacy of boronization to maintain low edge recycling conditions has finite lifetime, necessitating re-conditioning. This clearly points to a need for enabling wall concept development to provide reduced recycling even at steady state for future long-pulse and/or steady state fusion devices beyond the International Thermonuclear Experimental Reactor (ITER).

In an attempt to provide a possible resolution to this steady state recycling issue, the concept of Moving-Surface Plasma-Facing Component (MS-PFC) was proposed nearly a decade ago [1, 2]. Recently, laboratory-scale Proof-of-Principle (PoP) experiments have been conducted, employing a continuously Ti- or Li-gettered rotating drum exposed to hydrogen plasmas, and the results indicate that recycling can be reduced down to 95% for Ti and 75% for Li even at steady state, demonstrating "unsaturable walls" [3, 4, 5].

The success on these PoP experiments on moving-solid surfaces has now redirected our interest to moving-liquid surfaces, the concept often referred to as "liquid (metal) waterfall". In the this work, because of its high hydrogen absorptivity, low melting point, and low atomic number, lithium has been selected as a candidate material for this application. However, lithium is not yet set for flowing in the present experimental setup because we would rather obtain fundamental knowledge on standing liquid lithium interactions with steady state hydrogen and helium plasmas.

From this point of view, hydrogen and helium plasma recycling behavior over

solid and liquid lithium has been observed in a newly build facility: Vehicle-1 (for the Vertical and Horizontal positions Interchangeable test stand for Components and Liquids for fusion Experiments) [6]. Also, the relevant data taken from moving-solid lithium PFC experiments [3, 4, 5] will be referred to, as-needed, to make a comparison with those obtained from the moving-liquid cases.

## 2. Experimental

A schematic diagram of the Vehicle-1 facility is shown in Fig. 1-(a) and (b). Unlike other plasma-surface interactions research facilities such as PISCES-B [7], Vehicle-1 can take two positions, as can be seen, and is used in its vertical position in the present work. All the details of this facility have already been described elsewhere. However, for the sake of completeness, some of the most important features of Vehicle-1 will be briefly described below.

Vehicle-1 employs a 1kW ECR plasma source and can generate steady state hydrogen, helium, argon, nitrogen and oxygen plasmas with densities of the orders of  $10^{10-11}$   $1/\text{cm}^3$  and electron temperatures typically 4~5 eV. The ion temperature is believed to be near thermal unless associated with the Franc-Condon process. However, the ion bombarding energy can be controlled by applying a DC bias between the sample assembly and the plasma chamber at the floating and plasma potentials, respectively. The plasma column diameter is limited to about 3.5cm by a donut limiter made of tantalum, as shown later, providing a relatively flat density profile for the projected area over lithium in the form of circular disk with the diameter of 2.9cm and thickness of 2mm.

The diagnostics available for plasma-surface interactions include: a scanning Langmuir probe, partial and total pressure gauges, digital CCD camera, and an Optical Multi-channel Analyzer (OMA) connected with an optical fiber cable aiming at the pre-sheath region near the sample surface. Importantly, the temperature of lithium is measured with two thermocouples: one attached to the bottom of the crucible made of molybdenum; and the other attached to lithium directly on the plasma-facing surface. The crucible is 3cm in diameter and is mounted on a resistive heating assembly that can heat lithium up to around  $650^\circ\text{C}$ , sufficiently high to induce the decomposition of lithium hydride (LiH) in vacuum. Therefore, the sample temperature control was done using the combination of the plasma bombarding power flux and resistive heating.

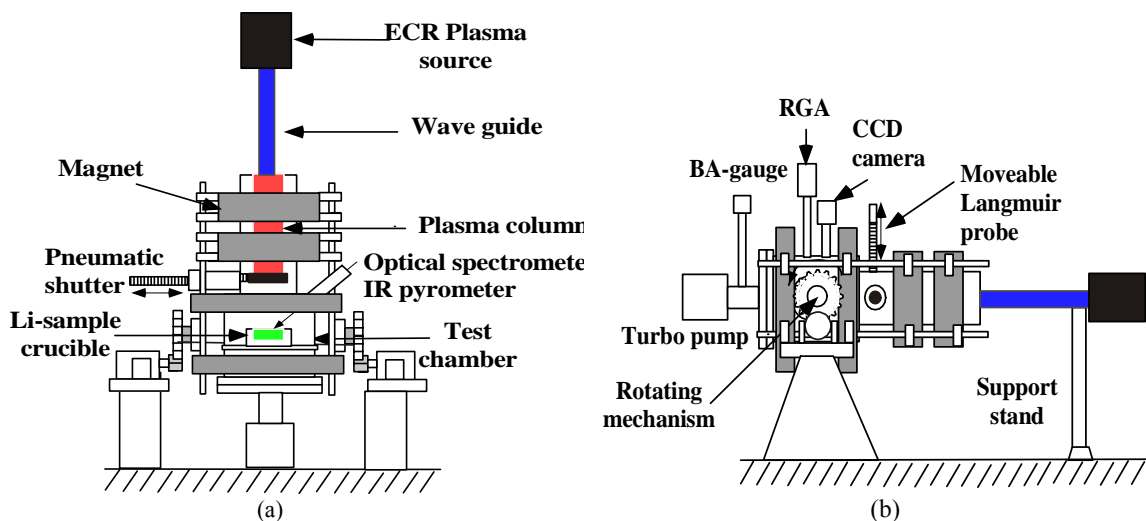


FIG. 1 A schematic diagram of the experimental facility: Vehicle-1[6] in its (a) vertical position; and (b) horizontal position.

### 3. Results and discussion

#### 3-1. Plasma characteristics in Vehicle-1

As presented in our recent paper [6], the plasma density increases from  $1 \times 10^{10}$  to  $1 \times 10^{11}$   $1/\text{cm}^3$  almost linearly with increasing ECR power from 100W to 1kW, whereas the electron temperature tends to remain 4~5 eV. In the present work, the ECR power was set at relatively low levels so that lithium temperature would not be overheated by the power flux associated with incident plasma ions.

Shown in FIG.2-(a) are the radial profiles of plasma density and electron temperature taken at the ECR power of 100W across the plasma column, the diameter of which is defined by a tantalum donut limiter. As seen, these profiles are rather flat.

Using the CCD video camera, the  $H_\alpha$  intensity profile was taken at the ECR region as that is viewed for hydrogen recycling measurements to be described next. Results are shown in FIG. 2-(b) with and without a DC-bias. Notice that the  $H_\alpha$  profile is raised with the DC-bias on, due to the enhanced reflection of electrons, while both exhibit the characteristic pre-sheath profiles.

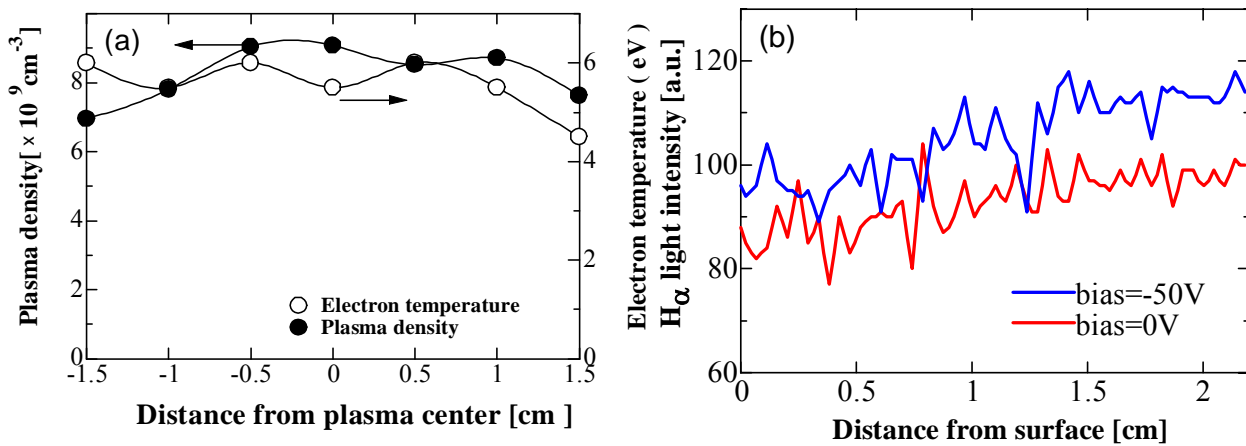


FIG.2 Plasma characteristics in Vehicle-1:(a) Radial profiles of plasma density and electron temperature; and (b) Axial profiles of  $H_\alpha$  intensity in the pre-sheath region.

#### 3-2. Hydrogen and helium plasma recycling measurements

Hydrogen and helium recycling measurements were conducted, setting the solid and liquid lithium temperature at  $50^\circ\text{C}$  and  $300^\circ\text{C}$ , respectively. Shown in FIG. 3-(a), (b) and (c) are the time evolution curves of  $H_\alpha$  and He-I light intensities that are taken as the measures of respective plasma recycling for the following reasons. In our recent experiments [3, 4, 5], the  $H_\alpha$  intensity has been found to be more closely related to the molecular hydrogen density in the pre-sheath region than to the atomic hydrogen density, the latter of which one would expect to be more relevant though. Similarly, we assume that the He-I intensity is governed by the neutral helium density recycled from the surface rather than by that in the host plasma.

These time evolution curves are fitted with the following empirical formula [8] to evaluate the recycling time constant,  $\tau_r$ :

$$I(t) = I^\infty \left\{ 1 - \exp\left(-\frac{t}{\tau_r}\right) \right\} \quad (1),$$

where  $I$  and  $I^\infty$  are the intensities of observed  $H_\alpha$  or He-I at  $t = t$  and at steady state (i.e.

$t = \infty$ ), respectively.

Notice that the steady state  $H_a$  measured for solid lithium (see FIG. 3-(a)) intensity generally increases with increasing ion bombarding energy, consistent with the data shown in FIG. 2-(b). It is also true that the recycling time constant tends to increase with increasing ion bombarding energy. This is because as the ion bombarding energy becomes larger, the implantation depth becomes larger, which then increases the particle retention capacity. Trends similar to these were observed in our

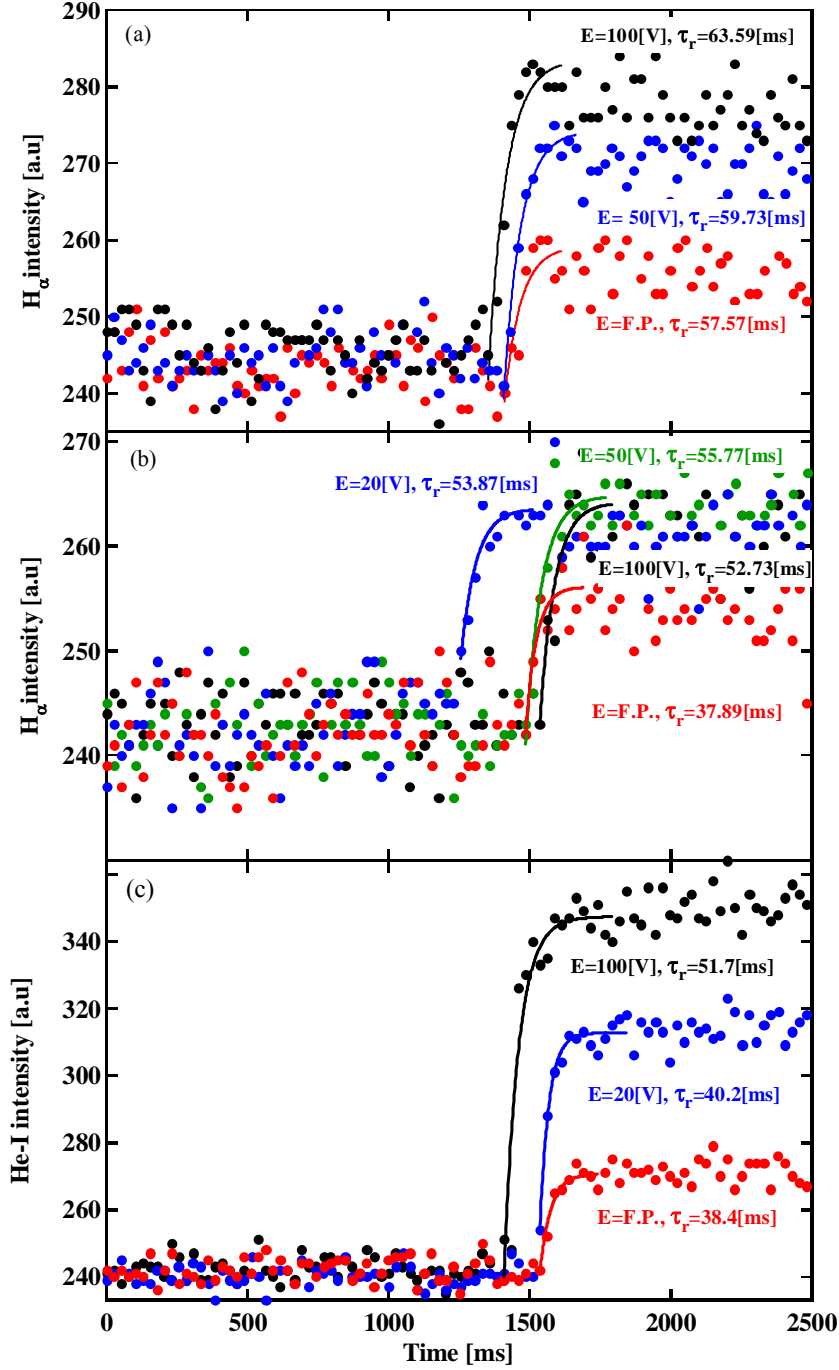


FIG. 2 Time evolution of (a) hydrogen recycling over solid lithium at 50°C, (b) hydrogen recycling over liquid lithium at 300°C, and (c) helium recycling over liquid lithium at 300°C, where  $E$  is the ion bombarding energy and F.P. is the floating potential ( $<10eV$ ).

recent MS-PFC experiments using a lithium-gettered rotating drum, the temperature of which is maintained essentially at room temperature [5].

It is extremely important to note here that hydrogen recycling over liquid lithium does not show these trends (see FIG. 3-(b)). In contrast, the steady state  $H_\alpha$  intensity tends to saturate only above 20V and the recycling time constant does not appear to increase even as the bias voltage increases. One might explain these findings as follows: Hydrogen migration in liquid lithium, obeying the Einstein-Stokes' law, is orders of magnitude faster than that in solid lithium, obeying the Fick's law. This in turn enhances the transport of hydrogen deeper into liquid lithium, which can then retard the saturation of the implantation range.

It is highly likely that under the present experimental conditions, implanted hydrogen exceeds the solid solution concentration within the range, forming lithium hydride (LiH). Interestingly, LiH is a solid up to its decomposition temperature of  $\sim 650^\circ\text{C}$ , leading to the two-phase condition of the Li-H system [9]. Therefore, perhaps forming clusters, segregated LiH tends to "sink" in the host liquid due to the microgravity effect. This again enhances the transport of hydrogen into the bulk of liquid lithium.

Therefore, it is considered that when hydrogen plasmas interact with liquid lithium, reemission of molecular hydrogen back to the surface will most likely be suppressed until the liquid is fully hydrogenated. This allows us to expect to see reduced hydrogen recycling over flowing liquid lithium even at steady state, as has been predicted elsewhere [10].

As shown in FIG. 3-(c), helium recycling over liquid lithium generally exhibits the similar trends to those observed over solid lithium. This is presumably because lithium has very little solubility of helium in it and they do not form any chemical compounds.

### 3-3. Kinetic analysis of hydrogen and helium plasma recycling behavior

In addition to the definition by eq. (1), the recycling time constant can also be given by the following relation [11]:

$$\tau_r = \frac{D}{k_r \nu \Phi} \quad (2),$$

where  $D$  is the diffusion coefficient of hydrogen in lithium,  $k_r$  is the surface recombination coefficient,  $\nu$  is the sticking (i.e. trapping) coefficient, and  $\Phi$  is the incoming particle flux. Generally, the reciprocal time constant is equivalent to the reaction rate constant, which may be expressed as follows:

$$\frac{1}{\tau_r} = \frac{k_o \nu_o \Phi}{D_o} \exp\left(-\frac{E_r - E_s - E_d}{kT}\right) \quad (3),$$

where  $k_o$ ,  $\nu_o$ , and  $D_o$ , and  $E_r$ ,  $E_s$ , and  $E_d$  are the frequency factors and the activation energies of the surface recombination, sticking and diffusion processes, respectively, and also  $k$  is the Boltzman constant, and  $T$  is the absolute temperature. Here, one must be aware that if the DC bias voltage is sufficiently large to induce ion implantation,  $\nu_o$ , and  $E_s$ , would be eliminated from eq. (3). Likewise, in the case of helium plasma bombardment,  $k_o$  and  $E_r$  should be ignored in eq. (3). Interestingly, although one might consider otherwise, in eq. (3) there is no factor related to the depth of implantation, i.e., the ion bombarding energy.

Shown in Fig. 3-(a) and (b) are the Arrhenius plots of these  $(1/\tau_r)$  data, taken

from hydrogen and helium recycling measurements, respectively. The activation energies evaluated from the straight lines have been found to be  $0.02 \pm 0.01$  eV, surprisingly for both hydrogen and helium plasmas, regardless whether lithium is a solid or liquid.

Immediately from eq. (3), one predicts not only that the activation energy for the overall recycling process could be a minute yet positive value, but also that it might possibly be a negative value, depending on the process dominating the overall recycling, as has actually been found in our recent work [6].

Shown in FIG. 5 are these activation energies plotted as a function of ion bombarding energy. One finds that there is almost no dependence on ion bombarding energy, as expected from eq. (3). However, because not all these individual activation energies are available from the literature, the further evaluation of the present data can not be done at this point, which no doubt warrants future work in this area.

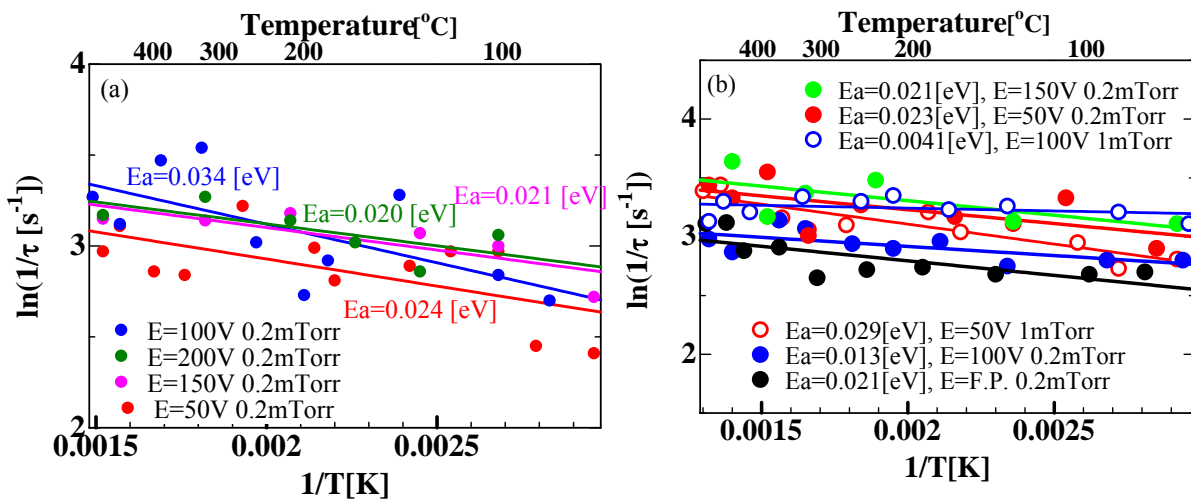


FIG. 4 Arrhenius plots of the reciprocal recycling time constants taken from: (a) hydrogen; and (b) helium recycling experiments, where  $E_a$  is the activation energy.

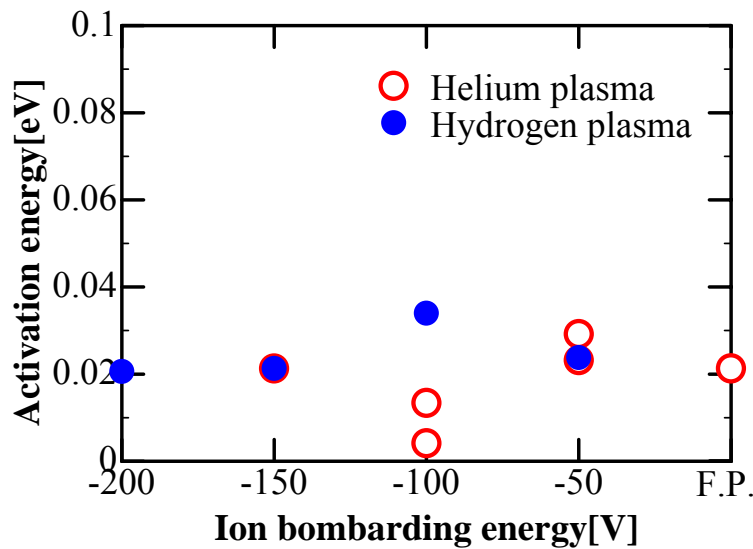


FIG. 5 Activation energies for hydrogen and helium plasma recycling over lithium as a function of ion bombarding energy.

#### 4. Summary and future plans

Steady state hydrogen and helium plasma recycling behavior over solid and liquid lithium has been measured with optical spectroscopy, using the newly built Vehicle-1 facility. Observations have indicated that hydrogen plasma recycling over liquid lithium tends to prevent the surface saturation, perhaps because of the rapid transport of implanted hydrogen into the bulk of liquid lithium. In contrast, this is not the case with helium because the solubility in lithium of which is known to be very little, hence leading to instant reemission.

From the kinetic analysis of the reciprocal recycling time constant data, the activation energies for the overall hydrogen and helium recycling have been evaluated and those obtained for hydrogen and helium are surprisingly close to each other and also they are nearly independent of ion bombarding energy.

In our separate experiments on the MS-PFC concept [5], employing a continuously lithium-gettered rotating drum, it has been demonstrated that steady state hydrogen recycling can be reduced down as low as 75%. From these data and together with the findings in the present work, one immediately expects that hydrogen recycling over flowing liquid lithium will also be reduced even at steady state. Nonetheless, more direct PoP experiments are awaited to be conducted on the liquid metal waterfall concept.

For this purpose, a two-reservoir “seesaw type” flowing liquid lithium setup is currently designed for the next step experiments. A schematic diagram of this setup is shown in FIG. 5. In this setup the liquid lithium flow is driven only by the gravity for the sake of simplicity. The depth of the liquid is determined by a small “dam” and the liquid flows from one reservoir into the other over a resistively heated bridge. Also, it is important to mention here that this seesaw setup takes advantage of the rotating mechanism of Vehicle-1 (see FIG.1), so that the plasma column and all the diagnostics will be inclined together when the flowing liquid interacts with the plasma, eliminating the possible errors in data due to the possible changes in relative distances between the spot of measurements and sensor heads, etc.

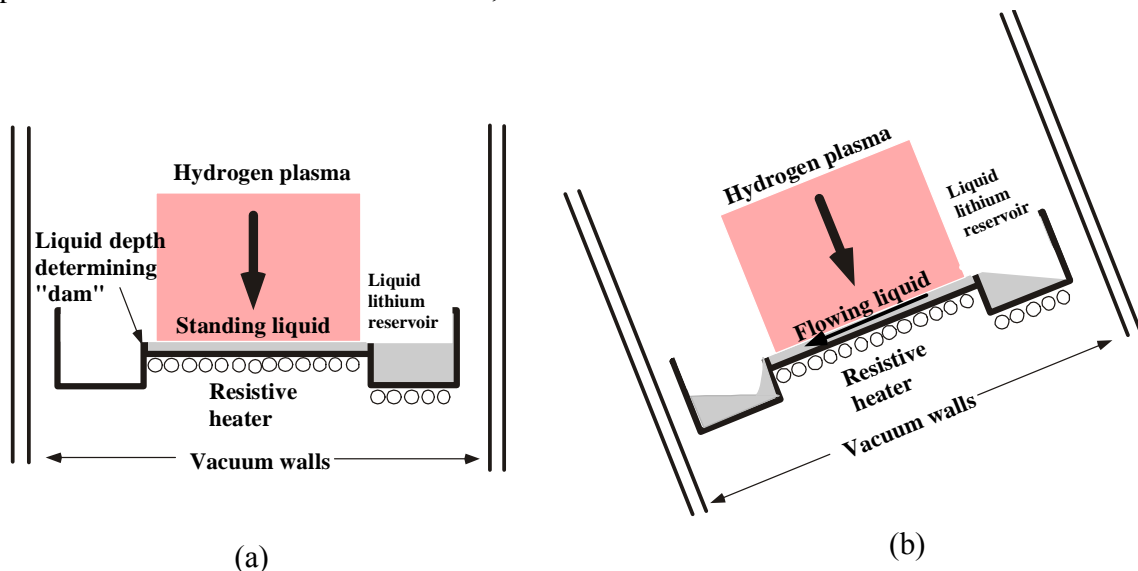


FIG. 4 A flowing liquid lithium experimental setup to be mounted in Vehicle-1 set in its: (a) vertical position; and (b) inclined position [towards the horizontal].

## References

- [1] Y. Hirooka et al., Proc. 17<sup>th</sup> SOFT, San Diego (1997)906.
- [2] Y. Hirooka and M. S. Tillack, Fusion Technol. **34**(1998)946.
- [3] Y. Hirooka et al., Fusion Eng. & Design, **65**(2003)413-421.
- [4] Y. Hirooka et al., Fusion Sci. & Technol. **45**(2004)60-64.
- [5] Y. Hirooka et al., “Particle Control in Steady State Magnetic Fusion Devices by Lithium-Gettered Moving-Surface Plasma-Facing Components”, paper presented at 15<sup>th</sup> ANS-TOFE, Madison (2004), to be published in Fusion Sci. & Technol.
- [6] Y. Hirooka et al. “A New Versatile Facility: Vehicle-1 for Innovative PFC Concepts Evaluation and its First Experiments on Hydrogen Recycling from Solid and Liquid Lithium”, paper presented at 16<sup>th</sup> PSI Conf., Portland (2004) and accepted for publication in J. Nucl. Mater.
- [7] Y. Hirooka et al., J. Vac. Sci. & Technol. **A8**(1990)1790.
- [8] Y. Hirooka et al., J. Vac. Sci. & Technol. **A6**(1988)2965.
- [9] T. B. Massalski et al. (Ed.), Binary Alloy Phase Diagrams, 2<sup>nd</sup> Ed., Vol.2, ASM Intl. (1990), pp. 2034.
- [10] M. J. Baldwin et al., Nucl. Mater. **306**(2002)15.
- [11] W. Moller and J. Roth in Physics of Plasma-Wall Interactions in Controlled Fusion D. E. Post and R. Behrisch (Ed.), Plenum Press, New York (1984).

## In-vessel Tritium Inventory in ITER Evaluated by Deuterium Retention of Carbon Dust

T. Hino 1), H. Yoshida 1), M. Akiba 2), S. Suzuki 2), Y. Hirohata 1) and Y. Yamauchi 1)

1) Laboratory of Plasma Physics and Engineering, Hokkaido University, Sapporo, 060-8628 Japan

2) Japan Atomic Energy Research Institute, Naka, 319-0193 Japan

e-mail contact of main author: tomhino@qe.eng.hokudai.ac.jp

**Abstracts.** In order to estimate in-vessel tritium inventory of carbon dust, deuterium gas absorption and deuterium ion irradiation experiments were conducted for a carbon dust prepared by using electron beam evaporation for graphite. The retained amount of deuterium after the deuterium gas absorption was very low,  $D/C=10^{-3}$  in the atomic ratio. The retained amount of deuterium after the deuterium ion irradiation was very similar with that for graphite. The deuterium concentration becomes close to zero if the wall temperature at divertor wall region is higher than 1000K. Co-deposited carbon dust was prepared by using a deuterium arc discharge apparatus with carbon electrodes at different gas pressure and substrate temperature. The co-deposited carbon dust had a largest deuterium concentration. In the ITER condition with gas pressure of 1 Pa and wall temperature of 573K, the deuterium concentration in the atomic ratio becomes approximately  $D/C=0.2$ . In DT discharge, the tritium concentration in the atomic ratio becomes  $T/C=0.1$ . This value is presumed to be a highest concentration of carbon dust in ITER. The present result shows that the accumulation speed of in-vessel tritium inventory is lower than that predicted so far.

### 1. Introduction

One of major issues in ITER is an evaluation of in-vessel tritium inventory since the tritium inventory has to be controlled less than operating limits set by safety considerations [1]. In the present design of ITER, it is presumed that a carbon dust produced by erosions of CFC divertor target has a highest tritium concentration, 0.4-2 in the atomic ratio of T/C. Though this value is based on hydrogen retention data of graphite, the data of carbon dust has not been obtained systematically so far. The precise evaluation of tritium inventory of the carbon dust is required to minimize a dwell time for tritium removal operation.

In order to evaluate the tritium concentration of carbon dust, a series of experiments on deuterium or hydrogen retention of carbon dust has been conducted at both Hokkaido University and JAERI [2, 3, 4]. The carbon dust produced by erosion of graphite is exposed to molecular fuel hydrogen, fuel hydrogen atom and ion. The fuel hydrogen also co-deposits on the wall with eroded carbon. To simulate these processes, we carried our (1) deuterium

molecular gas absorption experiment for carbon dust, (2) deuterium ion irradiation experiment for carbon dust, and (3) deuterium arc discharge experiment to prepare co-deposited carbon dust. The deuterium concentrations were measured after these experiments.

## 2. Experiments and Results

The carbon dust was prepared by using electron beam evaporation for isotropic graphite. This dust was used for the deuterium gas absorption experiments and the deuterium ion irradiation experiment. The surface morphology and crystal structure of the carbon dust prepared by electron beam evaporation were examined by using scanning microscope, SEM, and Raman spectroscopy, RS, respectively. The surface morphology and Raman spectrum are shown in **Fig. 1**. The carbon dust consisted with micron size particles and the crystal structure was amorphous carbon. In the preparation of co-deposited carbon dust, carbon electrodes were employed in deuterium arc discharge apparatus shown in **Fig. 2** to evaporate carbon atoms into the deuterium arc plasma. In the arc discharge, both the substrate temperature and discharge gas pressure were changed. The SEM photograph and the Raman spectra of the co-deposited carbon dusts are shown in **Fig. 3**. The crystal structure was amorphous for a case of low substrate temperature but the graphite like structure appeared for the case of high substrate temperature. The deuterium concentrations of the carbon dusts after the above experiments were measured by using a technique of thermal desorption spectroscopy, TDS.

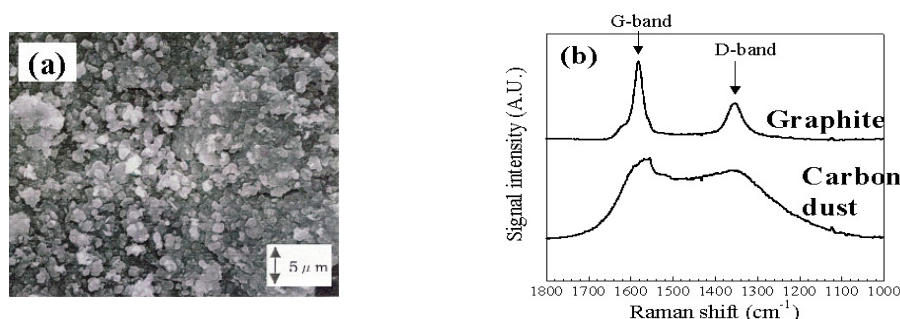


**Fig. 1** SEM photograph of carbon dust (a) and Raman spectra of carbon dust and isotropic graphite (b).

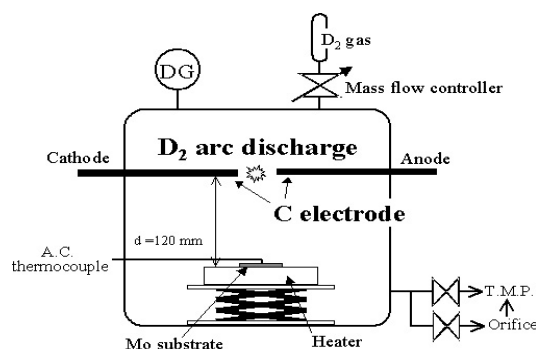


**Fig. 2** D<sub>2</sub> arc discharge apparatus with carbon electrodes.

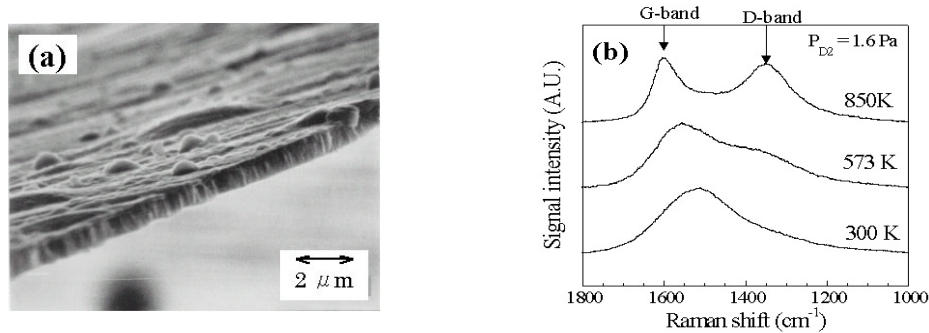


**Fig. 3** SEM photograph of co-deposited carbon dust (a) and Raman spectra of several co-deposited carbon dusts (b).

The carbon dust was exposed to  $D_2$  gas atmosphere in gas absorption apparatus at Hokkaido University. The equilibrium deuterium concentration after the deuterium gas absorption was measured. In this experiment, the gas pressure and the sample temperature were varied. For comparison, the concentrations of bulk graphite and the graphite powder with a size of  $1\mu\text{m}$  were similarly measured. The absorption amount of carbon dust was much larger than that of bulk graphite or graphite powders as shown in **Fig. 4**. The effective surface areas of these samples were measured using BET method. The absorption amount was roughly proportional with the effective surface area. The absorption of molecular fuel hydrogen takes place at the shadow of plasma facing wall. For the condition with a temperature of 573K and gas pressure of 1Pa, i.e. the ITER vacuum wall condition, the deuterium concentration became approximately  $10^{-3}$  in the atomic ratio of D/C. Thus, the absorption of fuel hydrogen molecular into the carbon dust can be ignored.

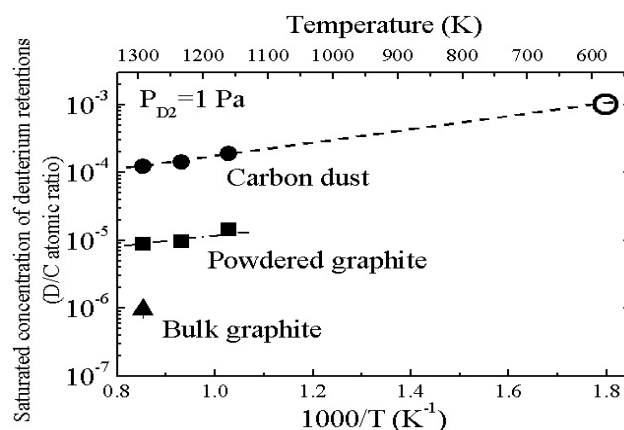


**Fig. 4** Equilibrium concentrations of carbon dust, powdered graphite and bulk graphite versus inverse of absorption temperature.

The carbon dust was irradiated by deuterium ions with energy of 1.7keV at RT in ECR ion irradiation apparatus at Hokkaido University. For comparison, isotropic graphite was similarly irradiated. **Fig.5** shows the deuterium concentrations of carbon dust and graphite

versus deuterium ion fluence. The fluence dependence of carbon dust shown in Fig.5 and the behavior of the thermal desorption were quite similar with those of graphite. In the deuterium ion irradiation, the structure in the implantation depth becomes amorphous in both the graphite and the carbon dust, and then the trapping behavior becomes the same. This is a possible reason for the concentration of carbon dust to be the same as that of graphite. For graphite, the temperature dependence of hydrogen concentration has been already obtained by several authors [5], and thus this result can be applied for the case of carbon dust. The divertor target region receives fuel hydrogen ion flux. The steady state wall temperature is approximately 1000K. The fuel hydrogen concentration of carbon dust becomes approximately zero, again negligible small.

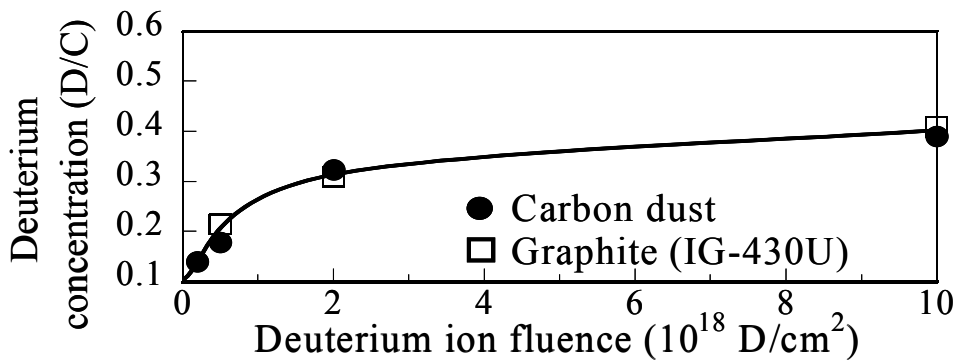


*Fig. 5 Amount of retained deuterium of carbon dust vs deuterium ion fluence.*

The co-deposited carbon dust is produced by the deposition of fuel hydrogen on the carbon dust in the formation process of carbon dust. The co-deposited carbon dust deposits on the wall in the vicinity of CFC target. The fuel hydrogen concentration may become large since the reactive species, i.e. fuel hydrogen atom or ion deposits on the carbon dust. The co-deposited carbon dust was prepared on the substrate in the deuterium arc discharge by changing the substrate temperature and the discharge pressure. **Fig. 6** shows the deuterium concentration of co-deposited carbon dust versus the substrate temperature for discharge pressures of 1.6Pa and 4Pa. **Fig. 7** shows the deuterium concentration versus the discharge pressure for the substrate temperature of 573K. In ITER, the highest concentration becomes 0.2 in the atomic ratio of D/C for the condition at wall temperature of 573K and discharge gas pressure of 1Pa. The co-deposited carbon dust had a highest deuterium concentration. For DT discharges, the tritium concentration becomes 0.1 in the atomic ratio of T/C. This value may be recognized as the highest tritium concentration of carbon dust in ITER. We now estimate the number of main discharge shot which accumulates the in-vessel tritium inventory of 500g. For the in-vessel inventory to reach 500g, the shot number becomes 400 if the erosion rate of CFC is 50g/shot and all the eroded carbon becomes co-deposited carbon dust.

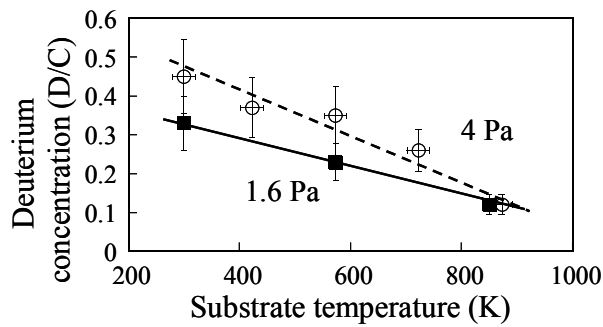


**Fig. 6** Deuterium concentration of co-deposited carbon dust versus substrate temperature.

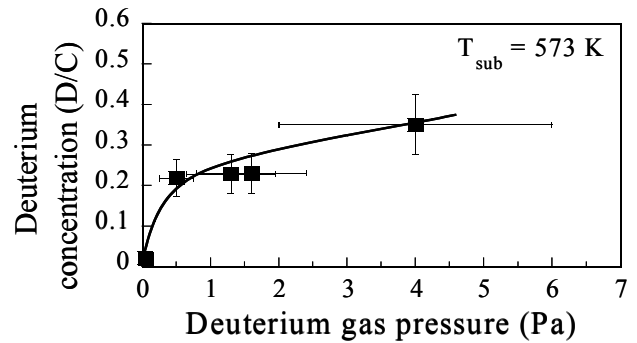


**Fig. 7** Deuterium concentration of co-deposited carbon dust versus deuterium gas pressure.

In the deuterium arc discharge, tungsten and carbon electrodes were employed for the anode and cathode, respectively, for the preparation of tungsten mixed carbon dust [6]. The deuterium concentration was observed to be higher than that of co-deposited carbon dust. The structure of the tungsten mixed carbon dust was more amorphous compared with that of co-deposited carbon dust. Thus, the deuterium might have been more trapped. However, the evaporation amount of tungsten is very small, and thus this contribution may be ignored for the in-vessel tritium inventory.

### 3. Summary and Conclusion

The deuterium concentration of carbon dust was measured after deuterium gas absorption and deuterium ion irradiation. The deuterium concentration after the deuterium gas absorption was very low,  $D/C=10^{-3}$  in the atomic ratio. The deuterium concentration of carbon dust after the deuterium ion irradiation was similar with that for graphite. The deuterium concentration becomes close to zero when the wall temperature is higher than 1000K. This contribution was also very small. The co-deposited carbon dust had a highest deuterium concentration. The deuterium concentration was  $D/C=0.2$  in the atomic ratio when the deuterium gas pressure of 1Pa and substrate temperature of 573K. For DT plasma, the tritium concentration becomes 0.1 in the atomic ratio of  $T/C$ . For the in-vessel tritium inventory of carbon dust to reach 500g, the number of plasma discharge shot becomes 400.

The carbon dust is produced mainly in the disruption phase. In the disruptions, the major erosion of CFC takes place by the emission of carbon particles with a size of  $\mu\text{m}$ . The tritium retention of the carbon particle may be much smaller than that of carbon atom or cluster. In addition, the tritium concentration significantly depends on the wall temperature.

The actual wall temperature becomes higher than 573K during the plasma discharge. The tritium concentration decreased by the elevated temperature. Hence, the tritium concentration of carbon dust may be smaller than  $T/C=0.1$ . Hence, the period required for dust cleaning is furthermore lengthened.

## References

- [1] G. Federici et al, Plasma-material interactions in Current Tokamaks and Their Implications for the Next Step Fusion Reactors, Nucl. Fusion **41**(2001)1967.
- [2] H. Yoshida et al, Deuterium Retention of Co-deposited Carbon Dust, Fusion Sci. Technol. **41**(2002)943.
- [3] T. Hino et al, Tritium Inventory of Carbon Dust in ITER, Fusion Eng. Design **61-62**(2003)605.
- [4] H. Yoshida et al, Hydrogen Retention of Carbon Dust Prepared by Arc Discharge and Electron Beam Irradiation, Fusion Eng. and Design **70**(2004)201.
- [5] J. W. Davis et al, Thermal desorption of graphite during deuterium ion bombardment, J. Nucl. Mater. **217**(1994)206.
- [6] H. Yoshida, Fuel Hydrogen Retention of Carbon Dust in Fusion Reactor, PhD Thesis, Hokkaido University, Sapporo (2004) (in Japanese).

## Research and Development of Steady-State EC/ICRF Heating in LHD and an Optimal Remote Steering Antenna

K. Ohkubo, S. Kubo, R. Kumazawa, W. Kasperek<sup>1)</sup>, T. Shimosuma, Y. Yoshimura, S. Inagaki, Y. Nakamura, K. Saito, T. Seki, T. Mutoh, T. Watari and LHD experimental group

National Institute for Fusion Science, Toki, Gifu, 509-5292, Japan

<sup>1)</sup> Institut für Plasmaforschung, Stuttgart, Germany

e-mail contact of main author: [Ohkubo@nifs.ac.jp](mailto:Ohkubo@nifs.ac.jp)

**Abstract.** In the LHD, steady-state plasma heating by EC wave with 72 kW and ICRF with 0.5 MW was achieved during 756 and 150 sec, respectively. An EC heated plasma with time-averaged radiation temperature of 240 eV and density of less than  $1 \times 10^{18} \text{ m}^{-3}$  was obtained. As for an ICRF heated plasma, plasmas with electron and ion temperatures of 2 keV and density of  $6 \times 10^{18} \text{ m}^{-3}$  were sustained until the discharge was terminated by increase in radiation loss. It is confirmed that an imaging property of the remote steering antenna has a branch structure and that recursiveness of input Gaussian beam is found even in a large-angle operation by means of the other branch. The directivity of radiation and power flow are analyzed in detail by using higher-order modes of Hermite-Gauss beam.

### 1. Introduction

In fusion-oriented experimental devices with superconducting coils such as Tore Supra, TRIAM-1M and LHD, studies on steady-state operation by lower hybrid current drive in tokamaks and ICRF heating in a helical device have been performed intensively. Up to now, two parameters such as discharge duration and input energy were attained to the order of hour and giga-joule in tokamaks. Since establishment of LHD, the steady-state heating by NBI, ICRF and EC waves has been carried out with development of high-power and long-pulse technology. The recent experimental results from steady-state heating on ICRF and EC waves are described. In addition, as to launching technology of millimeter wave by a remote steering antenna, investigations on an extension of the steering angle and optimization of input Gaussian beam were carried out theoretically and compared with experiment. By using the branches on image of both symmetric and asymmetric directions, an injection of Gaussian beam with the extent of 25 degrees enables us for application in ITER with good efficiency.

### 2. Steady-state EC/ICRF Heating

Steady-state ECH was carried out by an 84 GHz/200 kW diode CW gyrotron with a potential-depressed collector and a chemical vapor deposited diamond window. The high voltage power supplies for the gyrotron had been a little modified to use a body power supply. The body power supply controls the body voltage relative to the collector ground to keep the voltage between cathode and body constant. The gyrotron was installed on one of the gyrotron tanks and connected to the dummy load and transmission line that is extended from the end of evacuated 31.75 mm corrugated waveguide system used for the pre-existing system. Due to the increased reflection from transmission line or the dummy load, the gyrotron test had been limited below 150 kW /1000 sec.

The corrugated waveguide switches were introduced to select power from the pre-existing or the CW gyrotron, to couple the common corrugated waveguide, and to direct power to the dummy load or the LHD antenna. Since the pre-existing mirror antenna system had no cooling channel, the corrugated SUS waveguide of 88.9 mm in inner diameter is used as an

antenna by tapering up the corrugated waveguide from 31.75 mm inside LHD vacuum vessel. Another waveguide switch set just near the LHD port enables to select the mirror or corrugated waveguide antenna to launch an 84 GHz power to the LHD. The transmission line components of 31.75 mm in diameter including a diamond window at the LHD injection port were exchanged or reinforced to increase the heat handling capacities. The temperature rise of the waveguide components on the transmission line was measured by the thermocouples distributed along over the transmission line. In addition, the degree of vacuum on the MOU and the transmission line always was monitored and built in as an inter-lock circuit to avoid an arcing.

In FIG.1, waveforms of parameters are shown. With injecting ECH power of 72kW during 766 sec, an EC heated plasma with time-averaged density of  $2.4 \times 10^{17} \text{ m}^{-3}$  was sustained without radiation collapse during 756 sec. The density was always controlled by repetitive gas puff not to exceed a density limit for collapse due to limited ECH power. An ECE signal at plasma core increased and that at peripheral region decreased. The time-averaged ECE signal of which optical depth is not sufficiently thick is equivalent of the black body radiation with 240 eV. With time, waveguide temperature raised linearly as shown in FIG. 1.

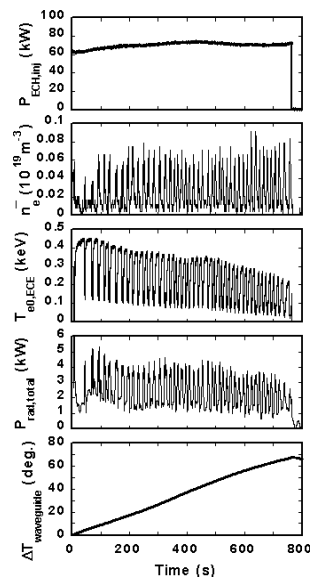


FIG. 1. Waveforms in steady-state ECH

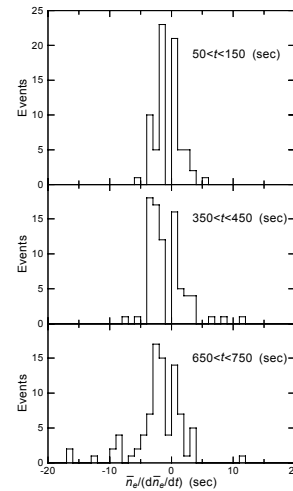


FIG. 2. The appearance counts distribution of the density response time to the gas puffing events for the time intervals of  $50 < t < 150$ ,  $350 < t < 450$  and  $650 < t < 750$  sec in Fig.1.

In the later stage of steady-state heating, decay rate of density just after the gas puffing pulse tends to decrease due to change in recycling from the vacuum wall. Figure 2 shows the appearance counts of the density response time  $\bar{n}_e / (d\bar{n}_e / dt)$  to the gas puffing events are plotted for the time intervals of  $50 < t < 150$ ,  $350 < t < 450$  and  $650 < t < 750$  sec during the discharge shown in FIG. 1. Here, the plus and minus sign of the response time corresponds to the density build-up and decay times after gas puffing, respectively. This figure clearly shows that the density decay time increases towards the end of discharge, while the build-up time stays almost constant. Most of parameters in the gyrotron were kept at the constant or saturated during the pulse. Collector and body voltages were well controlled and kept constant during the shot. Beam and body currents little increased with the time constant of 300 sec and then saturated to be constant toward the end of the pulse. This increase is ascribed to the cathode overheating due to the stray millimeter-wave power near the cathode.

Temperature differences between inlet and outlet of the gyrotron coolant are shown in FIG. 3. Although the coolant temperature near the end of such long-pulse operation increased slightly, it is demonstrated that this gyrotron can be operated well longer than 1000 sec with 200 kW. Pressure rise in the MOU and the waveguides due to the temperature rise had been the major cause of the termination of the pulse. The cooling of the transmission component was enforced during the experimental campaign, but the temperature of some components still kept increasing during 766 sec operation. The outgas from such high temperature component was far from saturation. The pressure inside the waveguide kept increasing due to the poor conductance in the small diameter of the waveguide. As a result, an interlock on degree of vacuum in the MOU and the evacuated waveguide due to the excess outgas was operated and the pulse was terminated. There exists competitive problem on creation of higher-order mode content by slits for increase in pumping speed at the pumping section and on leakage power from the increasing gap for withstanding voltage in the dc-break elements. Outgas in the heated transmission line due to joule loss becomes an important subject for CW power transmission with megawatts level.

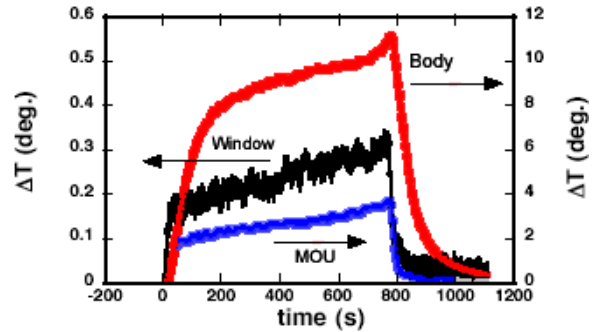


FIG. 3. Time evolutions of temperature differences between inlet and outlet of the coolant at the window, the gyrotron body and the MOU.

Since 1999, the steady-state operation by ICRF heating has been carried out and the pulse length was extended in every experimental campaign, but limited due to a defect on long-pulse operation in an RF generator. Recently, the RF emitter was tuned for the long-pulse operation by installing water-cooled ferrites between control and screen grids to suppress a parasitic oscillation. Time evolutions of plasma parameters of the long-pulse discharge are plotted in FIG. 4; this is the longest plasma discharge so far achieved in the ICRF heated plasma. The plasma with the electron density  $\bar{n}_e = 5\sim 6 \times 10^{18} \text{ m}^{-3}$  and the electron temperature and the ion temperature on the magnetic axis  $T_{e0} = T_{i0} = 2.0 \text{ keV}$  was sustained with the ICRF heating power of  $P_{\text{RF}} = 0.5 \text{ MW}$ . After 90 seconds, the electron density and the radiation power ( $P_{\text{rad}}$ ) increased with time and ended up with  $\bar{n}_e = 1 \times 10^{19} \text{ m}^{-3}$  and  $P_{\text{rad}} = 250 \text{ kW}$  before the plasma suddenly disappeared at 150 sec. The operation of the RF generator was automatically suspended by an increasing reflection power due to shrinking the plasma radius, when the plasma was collapsed. An electron density limit of the ICRF heated plasma was examined in the series of the experiments: the critical electron density  $\bar{n}_{\text{ecr}}$  is given in the relation of  $\bar{n}_{\text{ecr}} (10^{19} \text{ m}^{-3}) = 1.8 P_{\text{RF}} (\text{MW})$  [1].

A toroidal asymmetry in  $H\alpha$  intensity observed from the outside ports is shown in the circle-diagram of FIG. 5. Here, the values at  $t = 150 \text{ sec}$  are normalized by those at  $t = 90 \text{ sec}$ . It is easily found that the increase in  $H\alpha$  is prominent in 3-O and is about 2.5 times larger than that in 8-O. The ICRF heating antennas are installed at 3.5, that is between 3-O and 4-O. This increase in the  $H\alpha$  intensity is believed to be attributed to the temperature increase in the graphite plates located near 3-O in the toroidal direction. A toroidal asymmetry with respect to the temperature increase in the inboard side of the divertor plate is also shown in FIG. 5. It is found that the temperature increase in the 3-I (No.3 of inboard side divertor plate) is prominent. The 3-I divertor plate heated up to  $400^\circ\text{C}$  is thought to be a candidate of a hydrogen out-gassing source. This local temperature increase is compared with a calculated

result from particle orbit analysis. Two cyclotron resonance layers are separately located on the mod B surface in the employed magnetic configuration. The behavior of high-energy ions starting at the cyclotron resonance layer was examined using a full orbit calculation code under the RF electric field strength of 20kV/m [2]. About two thousands of high-energy ions with a low initial energy starting from the upper and the lower ion cyclotron resonance layers in various initial phase differences against the RF electric field. As the starting position, 100 points were selected from  $R = 4.15\text{m}$  to  $4.20\text{m}$  along the ion cyclotron layer, where the last magnetic closed surface is at  $R = 4.14\text{m}$ . Some of them hit the divertor plates within one circulation along the toroidal direction. The toroidal distribution on loss energy of high-energy ions is plotted in FIG. 5 to compare with the measured temperature increase. The orbit calculation suggests that the local temperature increase in divertor plates can be mitigated in two ICRF heating scenarios, in which the ion cyclotron resonance is located on the magnetic axis in the minority heating or is located near the low magnetic field region in the mode conversion heating; there exists no ion cyclotron resonance layer in front of the ICRF heating antennas.

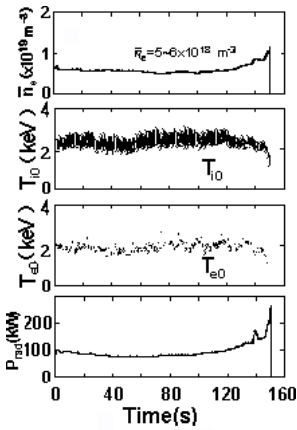


FIG. 4. Waveforms in steady-state ICRF heating.

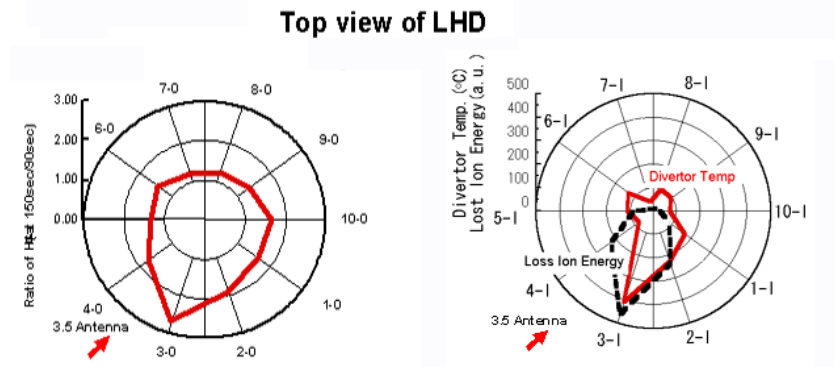


FIG. 5. Distributions along the toroidal direction of  $H\alpha$  signal and temperature at the divertor.

### 3. Branch Structure in a Remote Steering Antenna

To develop an ECH antenna without a steering mirror in the vacuum vessel, characteristics of a square corrugated waveguide antenna with the cross section of  $a \times a$  was examined theoretically and experimentally [3, 4]. In addition to the well-known optimum length  $L = 4a^2/\lambda$  for small-angle injection, existence of many branches with good imaging for large-angle injection was confirmed [4].

To find out the optimal waist size of injecting Gaussian beam, the imaging characteristics of the remote steering antenna with  $f = 158$  GHz and  $a = 60.08$  mm is calculated for various waist size  $w_0$  as a function of waveguide length  $L$ . In FIG. 6, the calculated results for first asymmetric direction with injection angle of 10 degrees and first symmetric one with 15 degrees, respectively are shown. The optimal waveguide length with respect to the imaging efficiency is almost the same for both branches as shown in FIG. 6 (a). Optimal  $w_0/a$  on the efficiency of the first asymmetric (symmetric) branch is around 0.30 (0.33). From the viewpoint of range in the waveguide length with the efficiency larger than 90%  $\Delta_{90}$ , optimal  $w_0/a$  is 0.30 for both branches. It is resulted from the minimum number of coupled waveguide modes and the large coupled content in a main mode.

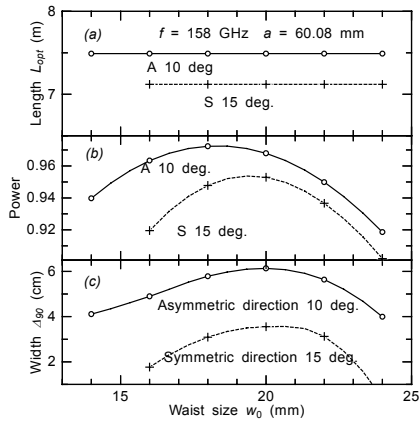


FIG. 6. (a) Optimal waveguide length and (b) imaging efficiency as a function of waist size. (c) The range of waveguide length where the efficiency is larger than 90%. Injection angle on asymmetric and symmetric directions is 10 and 15 degrees.

By changing the frequency instead of the waveguide length, the experimental confirmation of branch structure in recursiveness of input Gaussian beam was performed and compared with the numerical result [4]. All the scanning directions in the calculation and the experiment are perpendicular to the electric field. Calculated (left) and measured (right) results from the radiating power are shown in FIG. 7. Contour plots of (a) upper and (b) lower figures correspond to radiating for asymmetric and symmetric directions. All the data are also normalized with values at the normal injection to the waveguide mouth. Here,  $L = 6.5$  m,  $a = 60.08$  mm and  $w_0 = 22$  mm.

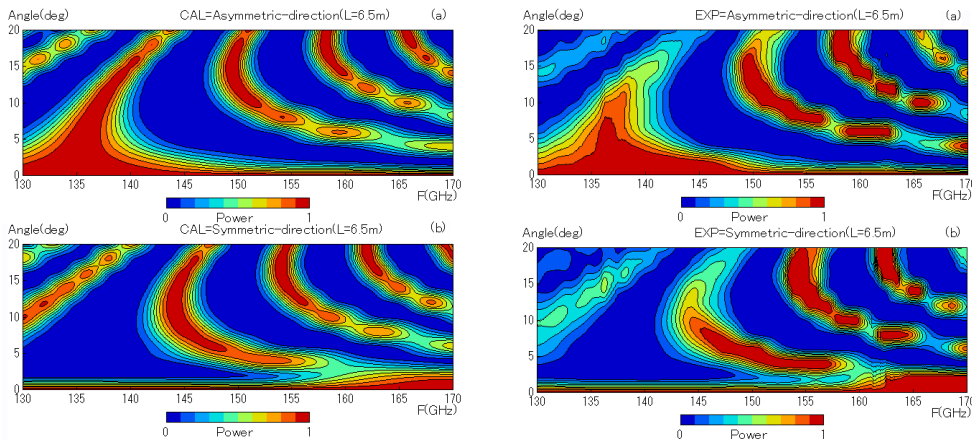


FIG. 7. Calculation (left) and experiment (right). The contour plots of power in (a) asymmetric and (b) symmetric directions with respect to the incident Gaussian beam

The wide contours corresponding to optimum frequency  $cL/(4a^2) = 135.0$  GHz at the small-angle injection in the asymmetric direction are seen. As for the second and third branches extending to the larger angle, the optimum frequency in the asymmetric direction is 150 and 158 GHz, respectively. Each branch with the symmetric direction fills partly a corresponding gap in the asymmetric direction. The measured dependence of efficiency (power) on the frequency and injection angle of Gaussian beam is in good agreement with the calculated results [5].

Using the orthonormality on Hermite's polynomial  $H_m$  or  $H_n$ , the EM fields propagating along the  $z'$ -axis can be written as the weighted sum of Hermite-Gauss beam  $HG_{mn}$  with mode numbers  $(m, n)$  and waist size of  $w'$ . Here,  $HG_{mn}$  mode is given by

$$E_{y'} = \frac{1}{w'} \sqrt{\frac{2Z_0}{\pi 2^{m+n} m! n!}} H_m \left( \frac{\sqrt{2}x'}{w'} \right) H_n \left( \frac{\sqrt{2}y'}{w'} \right) \exp \left[ -r'^2 \left( \frac{1}{w'^2} + \frac{jk_0}{2R'} \right) \right] \exp \left[ -jk_0 z' + j(m+n+1) \tan^{-1} \left( \frac{\lambda z'}{\pi w_0'^2} \right) \right]$$

and  $H_{x'} = -E_{y'} / Z_0$ .

The origins of beam coordinates  $(x', y', z')$  and waveguide coordinates  $(x, y, z)$  are at the center of the waveguide exit. The weighting coefficient of the  $HG_{mn}$  mode,  $B_{mn}$  is determined from the output electric field  $E_y$  at the waveguide exit using the integration on the waveguide exit:  $B_{mn} = -\iint E_y H_{x'}^* dS$

To overview the directivity of radiation, the viewing  $HG_{m0}$  beam with the same waist size as an injected fundamental  $HG_{00}$  is scanned around  $y$ -axis. The  $x'$ - $z'$  plane in beam coordinates is on the  $x$ - $z$  plane. To analyze a branch where radiation for the symmetric direction is main, waveguide parameters of  $L = 7.15$  m,  $a = 60.08$  mm and  $f = 158$  GHz [4] are used.

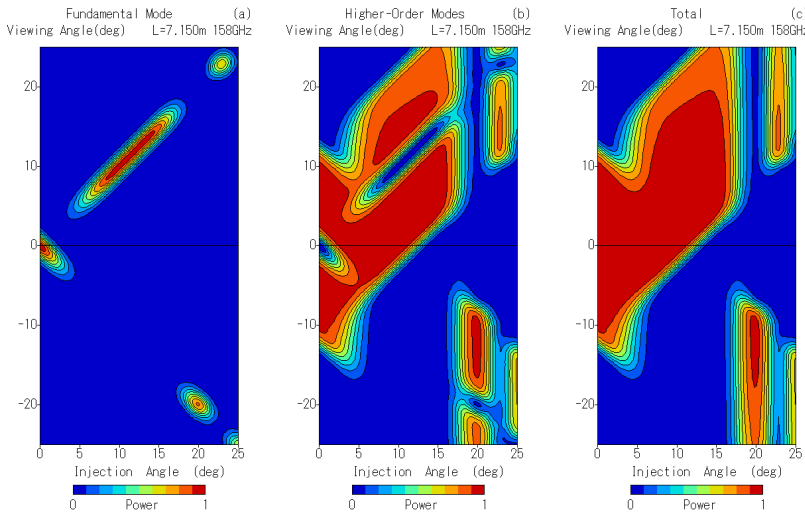


FIG. 8. Contour-plot of power content in the plane of injection and viewing angles. (a) Fundamental mode, (b) higher-order HG modes and (c) total of all the modes. Here,  $f = 158$  GHz and  $L = 7.150$  m. Calculation of the higher-order modes is carried out up to  $m = 60$ .

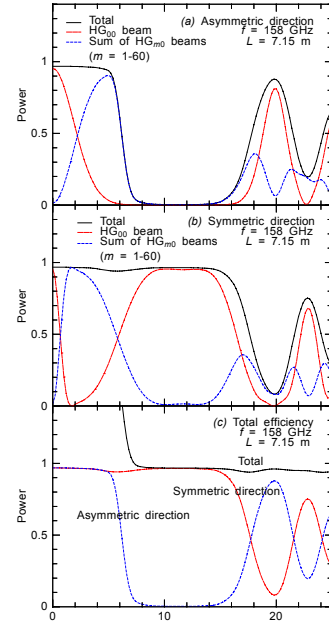


FIG. 9.  $|B_{00}|^2$ ,  $\Sigma|B_{m0}|^2$  (except  $m = 0$ ) and  $\Sigma|B_{m0}|^2$  where,  $L = 7.15$  m.

In FIG. 8, (a) the fundamental mode  $|B_{00}|^2$ , (b) higher-order modes  $\Sigma|B_{m0}|^2$  (except  $m = 0$ ) and (c) all the calculated modes  $\Sigma|B_{m0}|^2$  are contour-plotted in the plane of the injection angle and viewing one. As for higher-order modes, the value  $B_{m0}$  is calculated up to  $m = 60$ . The width of contour-plot on fundamental mode in FIG. 8 (a) corresponds to around  $3\theta$ , where a half angle of beam  $\theta$  is  $\lambda/\pi w_0$ . The higher-order HG modes have not central peak profile, which exists in a fundamental mode and its intensity extends to the wing in the profile. This property produces that a fundamental beam propagating along a direction appears as higher-order modes in the viewing beam looking along another direction. As a result, the width of the contour-plot on higher-order modes, which exists on both sides of fundamental mode, increases considerably. On the analysis, the radiating fundamental mode only in symmetric or asymmetric directions is double-counted as higher-order modes looking from the other direction. In the small angle injection, the  $HG_{00}$  beam radiates for the asymmetric direction.

With increasing an angle, radiating direction changes to the symmetric one. For the angle larger than 15 degrees, the direction changes again to asymmetric one.

The results from both the asymmetric and symmetric directions and also the total are shown in FIGs. 9 (a), (b) and (c), when a viewing angle is equal to injection one into the waveguide. In the range of 8-16 degrees power is launched for the symmetric direction. In the range larger than 16 degrees, power radiates alternatively for both directions. In the range smaller than 6 degrees, total power content in both directions becomes almost unity by appearance due to double counting as fundamental and higher-order modes in viewing beam as shown in FIG. 9 (c). It is noted that due to truncation of injecting beam, the total is slightly smaller than unity. The boundary angle where double counting disappears is denoted by  $\beta_d$ . When the Gaussian beam with the almost same  $w_0/a$  is injected into the smaller-size waveguide,  $\theta$  increases and  $\beta_d$  increases in proportional to  $\theta$ . At the intersection points in symmetric and asymmetric contents of FIG. 9 (c), the standing wave is formed near the side-wall of waveguide exit.

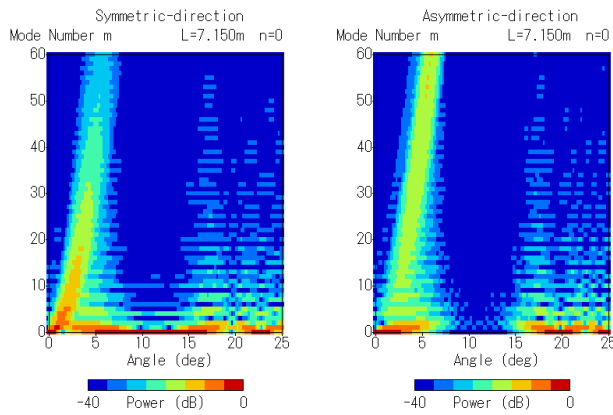


FIG. 10. The mode content of  $HG_{m0}$  for symmetric (left) and asymmetric (right) directions as a function of injection angle. Here, the scale of mode content is in decibel unit. Parameters in the figures are the same as those in FIG. 9.

The mode content of  $HG_{m0}$  for symmetric and asymmetric directions corresponding to FIG. 9 is shown in FIG. 10, as a function of injection angle. In a small angle lower than 6 degrees, a great number of higher-order modes with very small amount of content compose radiation. In the range of 8-16 degrees, the fundamental mode is main content. In the range larger than 16 degrees, higher-order modes increase to the medium level.

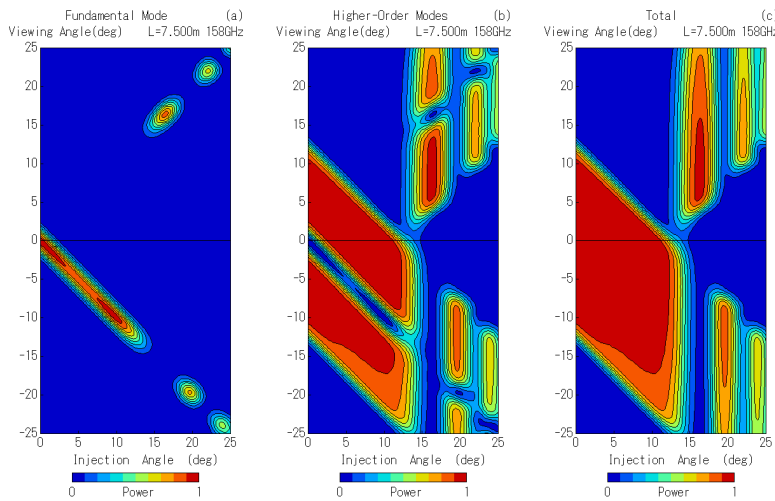


FIG. 11. Contour-plot of power content in the plane of injection and viewing angles. (a) Fundamental mode, (b) higher-order  $HG$  modes and (c) total of all the modes. Here,  $f = 158$  GHz and  $L = 7.50$  m. Calculation of the higher-modes is carried out up to  $m = 60$ .

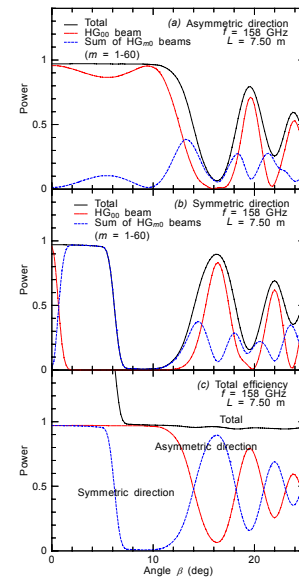


FIG. 12.  $|B_{00}|^2$ ,  $\sum |B_{m0}|^2$  (except  $m = 0$ ) and  $\sum |B_{m0}|^2$  where,  $L = 7.50$  m

When the waveguide length increases to  $L = 7.50$  m, the well-known first asymmetric branch appears. As to this branch, the directivity of radiation can be also examined by using the same technique. The contents of fundamental mode and the higher-order modes, and the total are shown as the contour plots on the plane of the injection angle and viewing one in FIGs. 11 (a), (b) and (c), and also plotted for various launching directions in FIGs. 12 (a), (b) and (c) when a viewing angle is equal to injection one for the waveguide. It is understood from the results of FIGs. 11 and 12 that the good imaging of  $HG_{00}$  mode is obtained up to injection angle of 12 degrees. By the analysis of mode content such as FIG. 10, it is found that the dip near 5 degrees on the  $HG_{00}$  mode is mainly due to a creation of  $HG_{10}$  modes. Beyond 15 degrees of injection angle, the main directivity of radiation changes alternatively between asymmetric and symmetric directions.

In FIG. 13, the calculated and the experimental results from the launching for the symmetric direction, where,  $f = 146$  GHz.  $w_0 = 22$  mm,  $a = 60.08$  mm and  $L = 6.5$  m. Several curves taking into account of some  $HG_{m0}$  modes are drawn. Because frequency of 146 GHz is slightly higher than the optimum value 144 GHz that is shown in calculation in FIG. 7, a deep dip in the content of  $HG_{00}$  mode appears near 13 degrees. By taking into account of the low-order modes as  $HG_{10}$  etc., the experimental results from the detection which are insensitive on the mode-selection can be explained well by the present calculation.

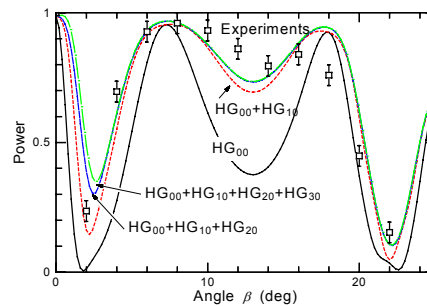


FIG. 13. The launching for the symmetric direction. Here,  $f = 146$  GHz.  $w_0 = 22$  mm,  $a = 60.08$  mm and  $L = 6.5$  m.

#### 4. Summary

We got the expected results in the first steady ECH in LHD despite of mild injection of 72 kW and also obtained medium parameters of density and temperature for steady ICRF heating of 0.5 MW. However, it turns out that wall conditioning and powerful injection are required for increasing density of ECH plasma and that careful treatment of high-energy particles is brought question in order to prolong ICRF heating pulse. The existence of branch structure in the remote steering antenna was found numerically and confirmed experimentally. By using the symmetric branch, we succeeded in the extension of operating angle in the remote steering antenna. The application to the ITER is expected with further development.

#### References

- [1] KUMAZAWA, R. et al., "Density increase during steady-state plasma discharge on the Large Helical Device", P5-108 in 31st European Society Conf. on Plasma Physics (London, 2004).
- [2] SAITO, K. et al., "Effects of RF field near ICRF antenna on edge plasma in LHD", to be published in *J. Nucl. Mater.*
- [3] OHKUBO, K., "Hybrid modes in a square corrugated waveguide", *Int. J. Infrared and Millimeter Waves* **22** (2001) 1709.
- [4] OHKUBO, K. et al., "Extension of steering angle in a square corrugated waveguide antenna", *Fusion Engineering and Design* **65** (2003) 657.
- [5] OHKUBO, K. and KASPAREK, W., "Extension of operating range in a remote steering waveguide antenna" Conf. digest. of 28th Int. Conf. on IRMMW (Otsu, 2003) p381.